

Sheffield Hallam University

The synthesis, characterisation and rheological properties of clay-polymer nanocomposites

JUDAH, Hassan

Available from the Sheffield Hallam University Research Archive (SHURA) at:

<http://shura.shu.ac.uk/27487/>

A Sheffield Hallam University thesis

This thesis is protected by copyright which belongs to the author.

The content must not be changed in any way or sold commercially in any format or medium without the formal permission of the author.

When referring to this work, full bibliographic details including the author, title, awarding institution and date of the thesis must be given.

Please visit <http://shura.shu.ac.uk/27487/> and <http://shura.shu.ac.uk/information.html> for further details about copyright and re-use permissions.

The Synthesis, Characterisation and Rheological Properties of Clay-Polymer Nanocomposites

Hassan Judah

A thesis submitted in partial fulfilment of the
requirements of Sheffield Hallam University for
the degree of Doctor of Philosophy

September 2019

Declaration

I hereby declare that:

1. I have not been enrolled for another award of the University, or other academic or professional organisation, whilst undertaking my research degree.
2. None of the material contained in the thesis has been used in any other submission for an academic award.
3. I am aware of and understand the University's policy on plagiarism and certify that this thesis is my own work. The use of all published or other sources of material consulted have been properly and fully acknowledged.
4. The work undertaken towards the thesis has been conducted in accordance with the SHU Principles of Integrity in Research and the SHU Research Ethics Policy.
5. The word count of the thesis is 61331.

Name	Hassan Ismaeel Hassan Judah
Award	PhD
Date of Submission	September 2019
Faculty	Business, Technology and Engineering
Director(s) of Studies	Prof. Chris Sammon Dr. Francis Clegg

بِسْمِ اللَّهِ الرَّحْمَنِ الرَّحِيمِ

Acknowledgements

I would like to thank Prof. Chris Sammon for the guidance, advice, expertise, supervision and invaluable words of wisdom throughout my PhD, thanks for giving me an opportunity to develop as a researcher and foremost as a person.

Thanks to Dr. Francis Clegg for the scientific input and continuous guidance, moral support and endless chats throughout stressful times. I feel very fortunate to have had such amazing supervisory team that was available for backup whenever needed.

Thanks to those who kindly have offered assistance in any stage throughout my PhD journey from MERI students, as well as MERI technical and administrative staff past and present. You are all exceptional people and I am grateful for the contribution you've all made to my experience at MERI.

Thanks to Sheffield for taking me in for the past eight years, thanks for all the warm and cold days, and thanks for being my home for all that time. You will most definitely be missed.

I'd like to thank my family; my father for his endless support, my mother for all her patience, and all of my six sisters for their wishes and support, as well as my two brothers for being by my side all that time.

Thanks to my small family, my lovely wife for being by my side and for the endless support. For the days and nights of stress I put you through, there are not enough words in the world to express my gratitude to you. To my kids Massa, Misk, and Azer, I promise to be more available from now on.

I dedicate this thesis to my father and my wife. I don't know what I'd have done without your love, support, and occasional nudge in the right direction. Thanks for believing in me and for the words of encouragement when I needed them most.

Abstract

This study aims to investigate the effect of different crosslinking agent and different crosslinking agent content on the material properties of the clay-polymer nanocomposite. A lot of materials were tried to be mixed to form a fully-reacted clay-polymer nanocomposite for the first time, which is a part of the novelty for this work. The overall properties governed by clay properties and clay/polymer relationship are prime aspects of this study. The Enhancement of significant properties of nanocomposites is a measure of clay platelets dispersion within the polymer matrix. Different approaches were adopted to understand the influence of clay properties on the nanocomposite; (i) by examining and comparing different clays as raw, dry, powder material using spectroscopy and thermogravimetric analysis (ii) mechanical examination of clay/water suspension of different clay types/grads, and different concentrations varying from 0.5 % - 10 % using rheological studies (iii) chemical and mechanical and morphological examination of Clay/Polymer nanocomposite with different clay types/grades, concentration, and polymers.

The synthesis of such material addresses issues including heterogeneity, processability, injectability, crosslinking and mechanical stability. The synthesis requires no purification steps no specialist equipment, and basic typical components of crosslinked nanocomposite/hydrogels (water, monomer, clay and initiator).

Morphological, pore size and scaffolding general arrangement which shows the effect of different crosslinking agents and crosslinking density were examined by Scanning Electron Microscope (SEM) to acquire information on wide/small pores are, diffusion kinetics in the system if required for further applications. The nature and elemental composition of the clay-polymer nanocomposites were determined by X-ray diffraction (XRD), X-ray fluorescence (XRF), and Fourier Transfer Infrared (FTIR) spectroscopy. The water content in the dry clay-polymer nanocomposite was determined and examined by Thermogravimetric analysis (TGA). Mechanical and rheological properties of the result were examined using a rheometer that operates on different modes (as a Dynamic Mechanical Analysis (DMA) technique) to evaluate the structure, performance, strength, and mechanical modules of these nanocomposites under different rotational and oscillatory loads. This offers the opportunity to relate the differences to the clays and polymers the hydrogels were synthesised from.

List of Abbreviations

~	Approximately
°Cmin ⁻¹	Degrees Celsius per minute
°	Degree
°C	Degree Celsius
3D	Three Dimension
A	Hypothetical functional groups
A	Shear area
Å	Angstrom (1 × 10 ⁻¹⁰ meters)
AIBN	Azobisisobutyronitrile
B	Hypothetical functional groups
BSE	Backscattered and secondary electrons
CEC	Cationic exchange capacity
cm ⁻¹	Wavenumber
C _{Na+}	Cloisite Na+
CST	Critical Solution Temperature
d	Interplanar spacing
DMAc	<i>N,N'</i> -Dimethylacrylamide
DTG	Derivative weight loss
EDS	Energy Dispersive X-ray spectroscopy

EDS	Energy-dispersive X-ray spectroscopy
F	Shear force
FTIR	Fourier Transform Infrared Spectroscopy
g	Gram
G	Elastic modulus
G'	Storage modulus
G''	Loss modulus
GMAc	<i>Glycidyl methacrylate</i>
h	Distance
h	Plank's constant ($6.625 \times 10^{-34} \text{ m}^2 \text{ kg s}^{-1}$ or J s)
HEMA	<i>Hydroxyethyl Methacrylate</i>
HPMA	<i>Hydroxypropyl methacrylate</i>
I	Initiator
I^*	Free radical initiator
IPN	Interpenetrating Polymer Network
IR	Infrared
kV	Kilovolt
LCST	Lower Critical Solution Temperature
L _{EL}	Laponite® EL
L _{FN}	Laponite® FN

LOG	Laponite® OG
LRD	Laponite® RD
LXL21	Laponite® XL21
m	Metre
M	Polymer chain
M*	Free radical polymer
mA	Milliamperes
mg	Milligram
min	Minute
mL	Millilitres
mΩ	Milliohm
n	Number of experiments
n ₁ , n ₂	Light refractive index
NIPAM	<i>N-Isopropylacrylamide</i>
nm	Nanometre
p	polymer
pDMAc	<i>Poly(N,N'-Dimethylacrylamide)</i>
pGMAc	<i>Poly(glycedyl methacrylate)</i>
pHEMA	<i>Poly(hydroxyethyl methacrylate)</i>
pHPMA	<i>Poly(hydroxypropyl methacrylate)</i>

pNIPAM	<i>Poly(N-isopropylacrylamide)</i>
R	Polymer chain
R'	Polymer chain
R*	Free radical polymer
SD	Standard deviation
SEM	Scanning electron microscopy
TEM	Transmission Electron Microscopy
TGA	Thermogravimetric Analysis
torr	101325 Pa
u	Velocity a fluid along a boundary
UCST	Upper Critical Solution Temperature
v	Velocity
wt%	Weight percentage
X	Hypothetical functional groups
XRD	X-Ray Diffraction
XRF	X-Ray Fluorescence
y	Height above the boundary
γ	Shear strain
$\dot{\gamma}$	Shear rate
η	Viscosity

θ_c	Critical angle
θ_i	Incident angle
μm	Micrometre
τ	Shear stress
T_{yield}	Yield stress
E	Energy of a photon
λ	Wavelength
ν	Frequency of the electromagnetic wave

Table of Contents

Chapter 1	Introduction	2
1.1	Polymers: An Overview	2
1.1.1	Polymeric Systems	3
1.1.1.1	Homopolymer / Copolymer.....	3
1.1.1.2	Polymer Blends.....	3
1.1.1.3	Amphiphilic Polymers.....	4
1.2	Hydrogels.....	4
1.2.1	Hydrogel Classification.....	6
1.2.1.1	Temperature Responsive Hydrogels.....	8
1.2.1.1.1	Positive Temperature Hydrogels	9
1.2.1.1.2	Negative Temperature Hydrogels.....	9
1.2.1.1.3	Thermo-Reversible Hydrogels	10
1.3	Polymerisation Reactions.....	10
1.3.1	Step Polymerisation.....	11
1.3.2	Chain Polymerisation	12
1.3.2.1	Initiation	12
1.3.2.2	Propagation.....	13
1.3.2.3	Termination.....	14
1.3.2.4	Other Reactions.....	14
1.4	Crosslinking in Hydrogels	15
1.4.1	Chemical Crosslinks	15
1.4.2	Physical Crosslinks	16
1.5	Clays.....	18
1.5.1	Clays Structure and Properties	18
1.5.2	Hectorite.....	19
1.5.3	Bentonite.....	25
1.6	Composite Materials.....	26
1.7	Nanocomposite Materials.....	27
1.7.1	Polymer-Matrix Nanocomposites	27

1.7.2	Clay-Polymer Nanocomposites	28
1.7.3	Clay-Polymer Based Hydrogels	30
1.7.4	Structural Properties of Clay-Polymer Based Hydrogels	31
1.8	Aims and Objectives.....	32
1.9	References	35
Chapter 2	Experimental	50
2.1	Analytical Techniques	50
2.1.1	X-Ray Diffraction (XRD)	50
2.1.1.1	XRD Experimental Parameters	52
2.1.2	X-Ray Fluorescence (XRF).....	52
2.1.2.1	XRF Experimental Parameters	53
2.1.3	Thermogravimetric Analysis (TGA)	54
2.1.3.1	TGA Experimental Parameters	55
2.1.4	Scanning Electron Microscopy (SEM).....	56
2.1.4.1	SEM Experimental Parameters	57
2.1.5	Infrared (IR) Spectroscopy	57
2.1.5.1	Fourier Transform Infrared (FTIR) Spectroscopy	59
2.1.5.2	FTIR Experimental Parameters	61
2.1.6	Rheology and Viscoelasticity.....	61
2.1.6.1	Viscosity	62
2.1.6.2	Shear Thinning.....	64
2.1.6.3	Shear Thickening	65
2.1.6.4	Yield Stress	66
2.1.6.5	Viscoelasticity.....	67
2.1.6.5.1	Elastic Behaviour	68
2.1.6.5.2	Viscous Behaviour	68
2.1.6.5.3	Viscoelastic Behaviour.....	69
2.1.6.6	Rheology Experimental Parameters	70
2.2	Materials and Sample Synthesis	71
2.2.1	Clays 71	
2.2.2	Polymers.....	74
2.2.2.1	Acrylamide	74

2.2.2.2 Methacrylates	74
2.3 Sample Synthesis and Preparation.....	77
2.3.1 Synthesis and Preparation of Clay Suspensions	77
2.3.2 Synthesis and Preparation on Clay-Polymer Nanocomposites	77
2.4 References	79
Chapter 3 Characterisation of Clay and Clay Suspensions	86
3.1 XRD Characterisation of Clays	87
3.2 XRF Characterisation of Clays.....	89
3.3 TGA Characterisation of Clays.....	93
3.4 FTIR Spectroscopy Analysis of Clays.....	96
3.5 Rheological Characterisation and Properties of Clay Dispersions	98
3.5.1 Clay Suspension Viscosity Behaviour	101
3.5.2 Clay suspensions Yield Stress.....	104
3.6 Summary.....	108
3.7 References	111
Chapter 4 Clay-PolyAcrylamide Nanocomposites/Hydrogels	
Characterisation.....	117
4.1 Clay-pNIPAM Characterisation and Rheological Properties	118
4.1.1 Clay-pNIPAM Nanocomposites	119
4.1.2 XRD Characterisation of Clay-pNIPAM Nanocomposites	122
4.1.3 TGA Characterisation of Clay-pNIPAM Nanocomposites	131
4.1.4 SEM Morphology Observation of Clay-pNIPAM Nanocomposites	138
4.1.5 FTIR Spectra Analysis of Clay-pNIPAM Nanocomposites	145
4.1.6 Rheological Analysis and Properties of Clay-pNIPAM Hydrogels.....	154
4.1.6.1 Temperature Effect on Clay-pNIPAM Hydrogels	156
4.1.6.1.1 Temperature Effect on Viscosity (Rotational Temperature Sweep)	156
4.1.6.1.2 Temperature Effect on the Loss (G') and Storage (G'') Moduli of the Clay-pNIPAM Hydrogel	159
4.1.6.2 Critical Yield Stress of Clay-pNIPAM Hydrogels	166
4.1.6.3 Storage (G') and Loss (G'') Moduli Behaviour	168

4.1.6.3.1	Amplitude Sweep (Function of Strain).....	168
4.1.6.3.2	Frequency Sweeps (Function of Frequency).....	171
4.2	Clay-pDMAc Characterisation and Rheological Properties.....	174
4.2.1	Clay-pDMAc Nanocomposites	174
4.2.2	XRD Characterisation of Clay-pDMAc Nanocomposites.....	177
4.2.3	TGA Characterisation of Clay-pDMAc Nanocomposites.....	181
4.2.4	SEM morphology observation of clay-pDMAc nanocomposite	187
4.2.5	FTIR Spectra Analysis of Clay-pDMAc Nanocomposites.....	196
4.2.6	Rheological Analysis and Properties of Clay-pDMAc Hydrogels.....	203
4.2.6.1	Critical Yield Test of Clay-pDMAc Hydrogels.....	203
4.2.6.2	Storage (G') and Loss (G'') Moduli Behaviour for Clay- pDMAc Hydrogels.....	206
4.2.6.2.1	Amplitude Sweep (Function of Strain).....	206
4.2.6.2.2	Frequency Sweep (Function of Frequency)	209
4.3	Summary.....	213
4.4	References	218
Chapter 5	Clay-PolyMethacrylate Nanocomposites/Hydrogels	
	Characterisation.....	228
5.1	Clay-pHEMA Characterisation and Rheological Properties	229
5.1.1	Clay-pHEMA Nanocomposites	230
5.1.2	XRD Characterisation of Clay-pHEMA Nanocomposites	232
5.1.3	TGA Characterisation of Clay-pHEMA Nanocomposites	239
5.1.4	SEM Morphology Observation of Clay-pHEMA Nanocomposite	243
5.1.5	FTIR Spectroscopic Analysis of Clay-pHEMA Nanocomposites...	247
5.1.6	Rheological Analysis and Properties of Clay-pHEMA Nanocomposites	252
5.1.6.1	Yield Stress for Clay-pHEMA Nanocomposites	252
5.1.6.2	Storage (G') and Loss (G'') Moduli Behaviour for Clay- pHEMA Nanocomposite	253
5.1.6.2.1	Amplitude Sweep (Function of Strain).....	253

5.1.6.2.2	Frequency Sweep (Function of Frequency)	254
5.2	Clay-pHPMA Characterisation and Rheological Properties	255
5.2.1	Clay-pHPMA Nanocomposites	255
5.2.2	XRD Characterisation of Clay-pHPMA Nanocomposites	258
5.2.3	TGA characterisation of Clay-pHPMA Nanocomposites.....	261
5.2.4	SEM Morphology Observation of Clay-pHPMA Nanocomposites	264
5.2.5	FTIR Spectra Analysis of Clay-pHPMA Nanocomposites	268
5.2.6	Rheological Analysis and Properties of Clay-pHPMA Nanocomposites	272
5.2.6.1	Yield Stress for Clay-pHPMA Nanocomposites	272
5.2.6.2	Storage (G') and Loss (G'') Moduli Behaviour for Clay- pHPMA Nanocomposites.....	273
5.2.6.2.1	Amplitude sweep (Function of Strain).....	273
5.2.6.2.2	Frequency Sweep (Function of Frequency)	274
5.3	Clay-pGMAc Characterisation and Rheological Properties	275
5.3.1	Clay-pGMAc Nanocomposite	276
5.3.2	XRD Characterisation of Clay-pGMAc Nanocomposites.....	278
5.3.3	TGA Characterisation of Clay-pGMAc Nanocomposite	281
5.3.4	SEM Morphology Observation of Clay-pGMAc Nanocomposites	284
5.3.5	FTIR Spectra Analysis of Clay-pGMAc Nanocomposites.....	288
5.3.6	Rheological Analysis and Properties of Clay-pGMAc Nanocomposites	292
5.3.6.1	Yield stress for clay-pGMAc nanocomposites.....	292
5.3.6.2	Storage (G') and Loss (G'') Moduli Behaviour for Clay- pGMAc Nanocomposites.....	295
5.3.6.2.1	Amplitude Sweep (Function of Strain).....	295
5.3.6.2.2	Frequency Sweep (Function of Frequency)	298
5.4	Summary.....	300
5.5	References	303

Chapter 6	Comparison Between Different Polymer-based nanocomposites/Hydrogels with L_{XL21} as a Crosslinking Agent	312
6.1	XRD Analysis of L _{XL21} -Polymer Nanocomposites.....	312
6.2	SEM Imaging Analysis of L _{XL21} -Polymer Nanocomposites.....	314
6.3	Rheological Analysis and Properties of L _{XL21} -Polymer Hydrogels	318
6.3.1	Yield Stress of L _{XL21} -Polymer Hydrogels	318
6.3.2	LVE Region of L _{XL21} -Polymer Hydrogels	319
6.4	Summary.....	321
Chapter 7	Conclusions and Further Work.....	323
7.1	Further Work	330
7.2	References	332

1

Introduction

Chapter 1 Introduction

1.1 Polymers: An Overview

Polymers occupy a major place in our materials map. With a wide range of potential applications and performance characteristics, they can be manufactured and used as rubbers, resins, composites, adhesives, laminates, and coatings. They offer novelty that can hardly be matched by other materials.

The word polymer (Greek poly- "many" and -mer "parts") was used for the first time by Berzelius in 1833. It was not fully understood until the 1920s when polymers were defined as we know them today, i.e. large molecules of very high molecular weights made up of molecular repeating units, known as monomers.

Polymers are synthesised by chemically joining many molecular units or "monomers" in a chemical process called polymerisation. Polymers found in nature are mostly water soluble which includes glycogen, proteins, deoxyribonucleic acid (DNA), silk, wool, cellulose and starches. Synthetic polymers have a wide range of uses depending on their behavioural properties. Many are produced commercially and include polyester, polyamides, poly(tetrahydrofuroethylene), and epoxy. A polymer can be prepared from a single or multiple monomers; and can be classified depending on shape (Figure 1.1), polymerisation process or the nature of the bonds in the final product. [1][2]

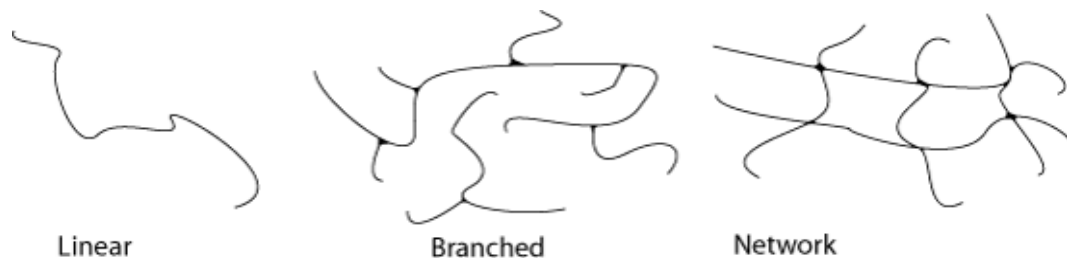


Figure 1.1 Representation of different polymer types. [3]

1.1.1 Polymeric Systems

1.1.1.1 Homopolymer / Copolymer

Polymers prepared from one monomer are called homopolymers. If two or more monomers are employed, the polymer is called a copolymer. The monomeric units in a copolymer (Figure 1.2) can take different arrangements: randomly (random copolymer), in blocks (block copolymer), or alternate (alternating copolymer).

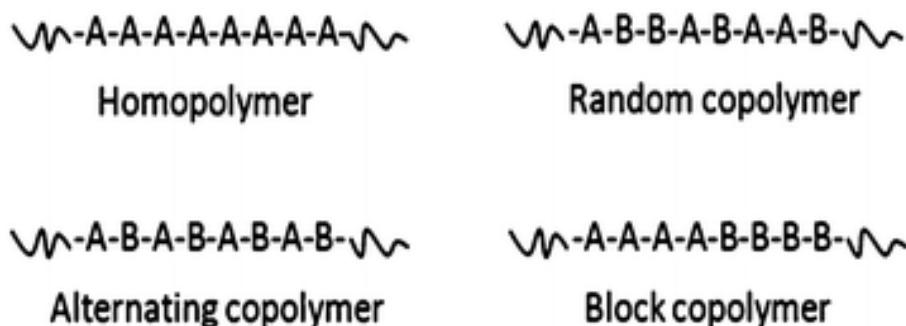


Figure 1.2 Representation of homopolymer and copolymers. [1][4]

Different types of block copolymers exist. If blocks A and B alternate in the backbone it is called an AB multi-block copolymer. If A and B form the backbone with a single block of each the polymer is known as an AB di-block copolymer. It is also possible to form a tri-block copolymer ABA (central B block with terminal A blocks) or ABC (one each of three blocks).

1.1.1.2 Polymer Blends

If two or more polymers or copolymers form a mixture without covalent bonds (i.e. a physical mixture), the product is called a polymer blend or polyblend. This concept is not new; the rubber industry has used it for many years. These polymer networks attracted a lot of attention recently due to the demand for a wider variety of engineering plastics and special grades of fibres and elastomers.

IPN (Interpenetrating Polymer Network) Figure 1.3 is defined by the IUPAC as a "polymer comprising two or more networks which are at least partially interlaced on a molecular scale but not covalently bonded to each other and cannot be

separated unless chemical bonds are broken". [5] IPN is one type of polyblend that uses the concept of crosslinking (Section 1.4).

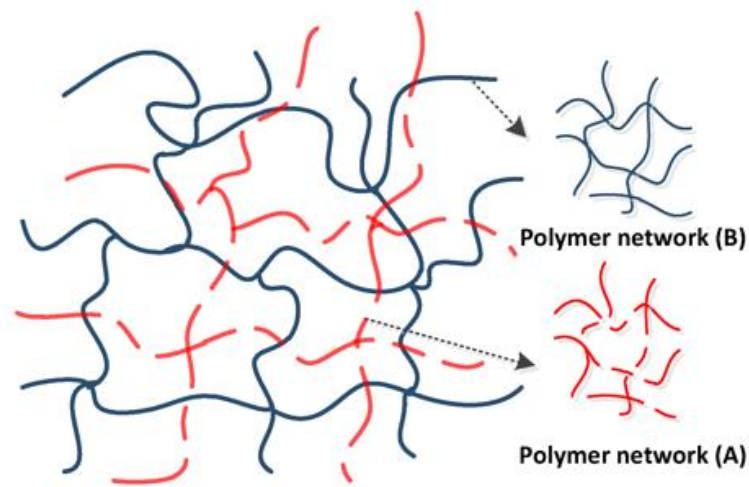


Figure 1.3 Schematic of interpenetrating polymer networks IPN. [6]

1.1.1.3 Amphiphilic Polymers

Amphiphile (from Greek amphis: both, philia: friendship) is a chemical compound which possesses hydrophobic (water-hating) and hydrophilic (water-loving) properties. Amphiphilic polymers contain hydrophobic and hydrophilic units, either as zones within a single monomer unit or by incorporating both hydrophilic and hydrophobic comonomers. The hydrophobic part is typically referred to as the tail and the hydrophilic part is referred to as a head group which may be charged or uncharged. Due to repulsion between hydrophobic and hydrophilic groups of the polymer phase separation may occur; such materials can often self-assemble into a range of morphologies and can be environmentally-responsive to changes in conditions such as temperature, pH, light frequency and type or concentration of electrolyte. Common amphiphilic substances are soaps, detergents and lipoproteins. [7][8]

1.2 Hydrogels

Polymer hydrogels are crosslinked, stable, three-dimensional, two- or multi-component polymeric network systems made of natural or synthetic materials,

which can form soft materials. They are capable of retaining substantial amounts of water that fills the space between macro-molecules in a swollen state up to thousands of times their dry volume; the water fills the interstitial space of the network giving the final product a high degree of flexibility. [9][10] Due to the unique properties of hydrogels: including reversible swelling/de-swelling behaviour, mechanical strength, permeability, environmental sensitivity, high ionic conductivity, [11] and extraordinary surface properties accredited to polar groups on their polymer backbone, they provide a promising platform for a range of applications as smart material. [12][13][14]

Around the 1890s, the term 'hydrogel' appeared in the scientific literature describing a colloidal gel of inorganic salts. In 1936, a paper was published by DuPont's scientists on synthesised methacrylic polymers in which poly 2-hydroxyethyl methacrylate (pHEMA) was described as a glassy, hard and brittle polymer. It was not considered of importance and was essentially forgotten until Wichterle and Lim reported a water-swollen, elastic and clear gel in 1960. [15] Today these gels are known as a hydrogel. Figure 1.4 shows important events in the history of the research. [16] Since then, crosslinked hydrogels have been used in many fields such as soft contact lenses, superabsorbent polymeric gels (disposable nappies), artificial burn dressings and refrigerants in medical and food industries. [17][15] Some polymers show sensitivity to external stimuli. Because of this; swellability, flexibility and adaptability it could be engineered to match natural living tissue. [18] The potential of these different polymeric hydrogels have been investigated and continued to be of interest for; cell encapsulation, photo-responsive gels [19], enzyme carriers, [20] separation devices, [21] and colloid crystals. Recently investigations have begun into the potential use of hydrogels for "tissue engineering" as cell-cultivation matrices for repairing and regenerating tissues and organs, as they can be biocompatible and biodegradable. [13]

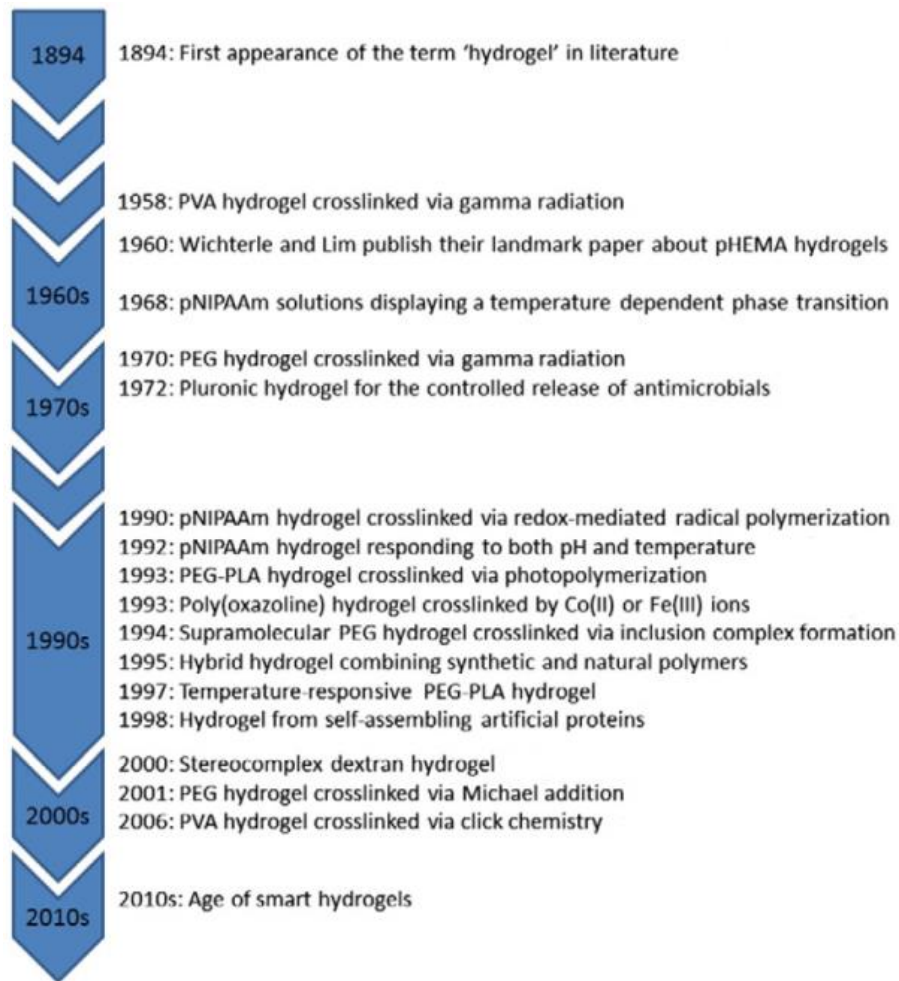


Figure 1.4 The most important events in the history of hydrogel research. [16]

1.2.1 Hydrogel Classification

Literature reports a number of classifications for hydrogels. Depending on the source, hydrogels may be natural like collagen, gelatine and polysaccharides such as starch; or synthetically prepared using chemical polymerisation methods. [22][23]

It is also possible to categorise hydrogels depending on their configuration or physical appearance (matrix, film, or microsphere). It is also possible to divide hydrogels into groups based on the charge on the bonded groups (nonionic, ionic, amphoteric electrolyte).

Hydrogels can also be classified depending on physical properties, method of preparation, polymeric composition, nature of swelling/de-swelling and type of

crosslinking. Figure 1.5 shows clearly that the classification for each type is complex and beyond the scope of this thesis. [11]

Based on polymeric composition, hydrogels may be classified as homopolymeric (derived from a single species of monomer), [24] copolymeric (comprised of two or more different monomers-one hydrophilic component at least), [25] semi-interpenetrating network (IPN) (where a linear polymer penetrates another crosslinked network without the aid of chemical bond) [11] or multipolymer IPN (made of two independent crosslinked synthetic and/or natural polymer components)

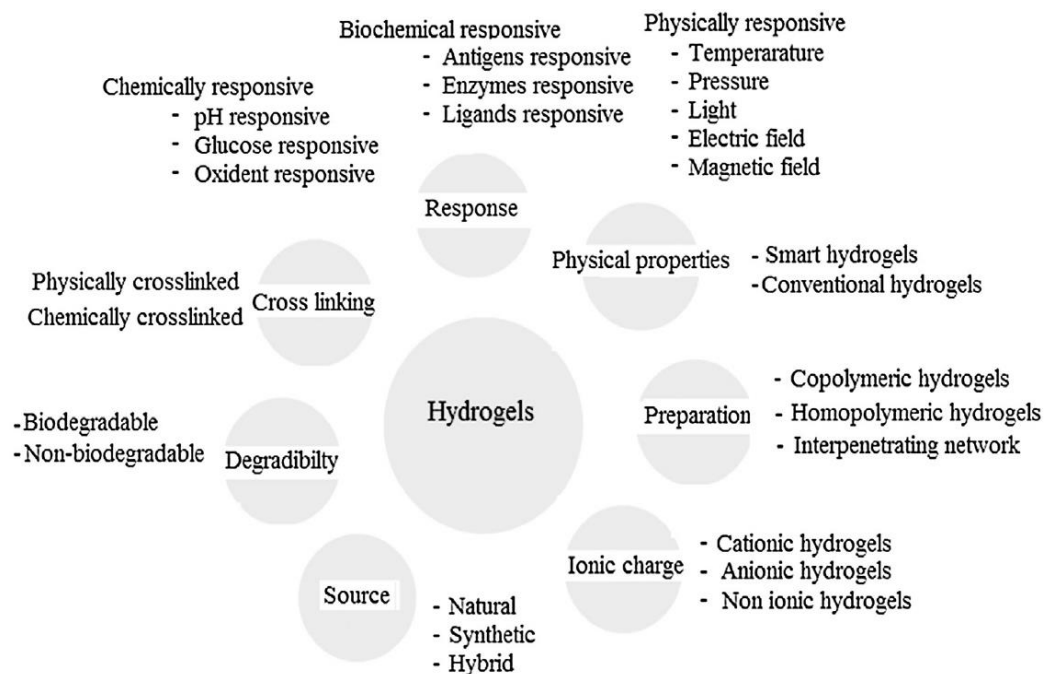


Figure 1.5 Classification of hydrogels based on different properties. [11]

Based on stimuli response; hydrogels can be classified as;

- Environmental: responding to physical stimuli, which can change their molecular interactions at critical onset points (including light levels, pressure, temperature, electric fields, magnetic fields and mechanical stress).[26]

- Chemical; which change their interactions between polymer chains and solvents at the molecular level (including pH, ionic factors and chemical agents).
- Biochemical; where hydrogels respond to enzyme, antigen, and other biochemical agents. This biologically responsive type of hydrogels has attracted a lot of attention as biomaterials for biomedical, biotechnology, pharmaceutical research and industry. [27]
- Dual stimulus hydrogels; where two stimuli responsive mechanisms work in one system. [28]

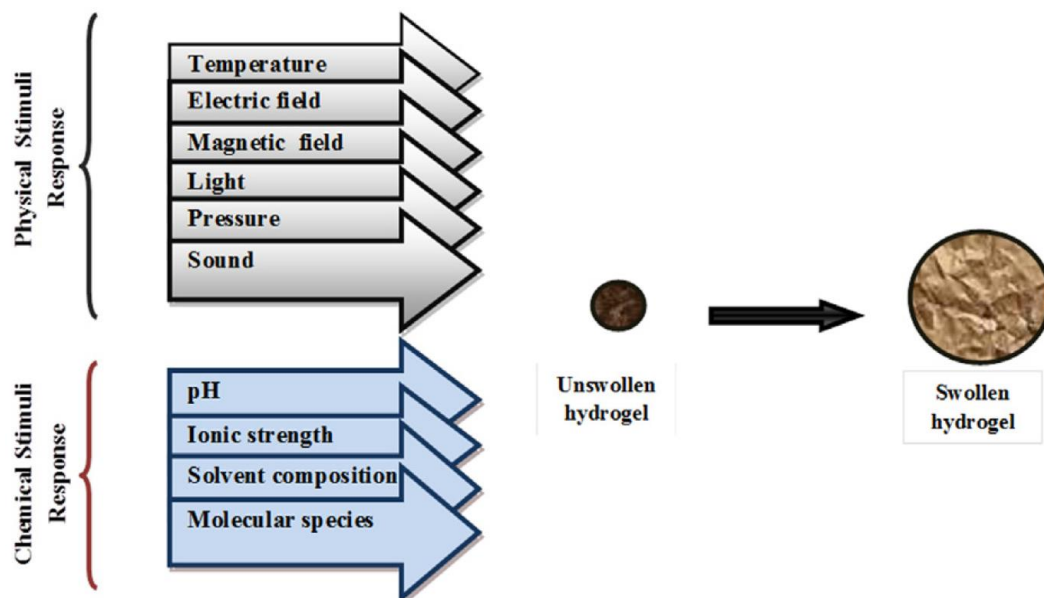


Figure 1.6 Stimuli response swelling hydrogel. [23]

1.2.1.1 Temperature Responsive Hydrogels

Temperature-sensitive hydrogels are a widely studied type of environmentally responsive systems known for their ability to swell and shrink as the surrounding fluid temperature changes. They can be classified as positive or negative temperature responsive systems (Sections 1.2.1.1.1. and 1.2.1.1.2). In general; water release reabsorption occurs as a result of the quest for thermodynamic stability. The temperature dependent balance of the physical entanglements, hydrogen bonding and hydrophobic interactions govern the thermo-sensitive

behaviour of the hydrogel giving it an advantage in a range of applications such as "*in-situ*" forming systems. For example, the ability of the material to be injected into tissue, organ or body cavity in a minimally invasive manner prior to gelation may reduce the necessity for surgery in many instances. [29] Temperature sensitive hydrogels are also utilised for the controlled delivery of pharmaceutical agents. The most studied temperature responsive hydrogels are chitosan-based copolymers i.e. methylcellulose, hydroxypropyl methylcellulose and N-isopropylacrylamide (pNIPAM) with poly N-2-hydroxypropyl methacrylate (pHPMA). [16][11]

1.2.1.1.1 Positive Temperature Hydrogels

An important temperature of note for temperature sensitive hydrogel is known as the upper critical solution temperature (UCST). [30] When the temperature is below the UCST the hydrogels release solvents (water, ethanol, methanol, acid etc) from the network (de-hydration). When the temperature is higher than the UCST, swelling occurs. Positive temperature hydrogels swell rapidly above the UCST as their structure dissociates due to the breaking of hydrogen bonds. Below the UCST positive temperature hydrogels shrink because of the formation of a complex structure of hydrogen bonding at the lower temperature. [31]

1.2.1.1.2 Negative Temperature Hydrogels

This kind of hydrogel is known by the lower critical solution temperature (LCST), meaning the hydrogel will shrink and expel fluid as the temperature increases above the LCST and will swell as temperature decreases below the LCST. [32]

The hydrophilic groups of the polymer interact with the fluid when the temperature is lower than the LCST forming hydrogen bonds which improve the dissolution and the swelling in crosslinked systems. With a dominant hydrophilic behaviour, water occupies the interstitial spaces of the gel in a swollen hydrated phase. The hydrogen bonds become weaker at temperatures above the LCST. This causes hydrophobic interactions within the hydrophobic parts to become stronger and dominate, while the ordering of water molecules becomes entropically

unfavourable in the presence of hydrophobic units. Shrinking occurs due to inter-polymer chain association and de-swelling processes force absorbed fluid to leave the network, making the polymer physically collapse. [33]

The LCST can be tailored in different ways by mixing the hydrogel with ionic copolymer or changing the solvent composition. In general, the greater the hydrophobic constituents present the lower the LCST for the polymer system. [34]

1.2.1.1.3 Thermo-Reversible Hydrogels

For thermo-reversible hydrogels the volume change mechanism and the bond type are different, here the hydrogels undergo a sol-gel phase transition instead of a swelling-shrinking process because the polymer chains are not covalently crosslinked. At the CST the hydrogen bonds (between the polymer and water molecules) become energetically unfavourable facilitating polymer-polymer and water-water interactions causing the release of water from the hydrogel and resulting in shrinkage of the polymeric network. In the swollen state, water forms hydrogen bonds with the polar groups of the polymer backbone in the hydrogels and organises itself around hydrophobic groups as a clathrate.

Thermo-reversible hydrogels are an important class of hydrogels since the solution responds to temperature by a sol-gel transition. The specific temperature at which the transition takes place depends on the hydrophilic and hydrophobic blocks, polymer concentration, and the chemical nature of the polymers. [11]

1.3 Polymerisation Reactions

The term polymerisation describes the chemical reaction monomers react through to form long-chain polymers. Polymerisation reactions can be classified as either addition or condensation processes. The basis of this classification was suggested by W. H. Carothers in 1929. It is based on whether the repeating unit of the polymer contains the same atoms as the monomer.

For addition polymerisation, the synthesised polymer has the same number of atoms as the monomer in its repeating unit, whereas for condensation polymerisation the polymers contain fewer because of the formation of by-products during the polymerisation process.

Polymerisation reactions are now more commonly characterised according to the reaction mechanism, in which polymerisation reactions are divided into step and chain processes.

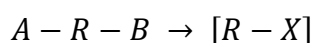
Step polymerisation: or step-growth polymerisation. Polymer chains are built up in a stepwise fashion by the random union of monomer molecules. Monomer concentration drops rapidly towards zero early in the reaction. Molar mass rises steadily during the reaction as groups of polymerised monomers continue to link together. Long reaction times are essential to obtain a high molar masses. [35]

Chain polymerisation: or chain-growth polymerisation. The molecular weight increases by the successive linking of single monomer molecules, monomer concentration decreases steadily with time. Long reaction times give higher yields. The reaction mixture contains only monomer, high molar mass polymer, and a low concentration of growing chains. [35]

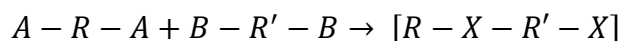
Polymers having identical repeating units but when formed by different reactions do not necessarily possess the same properties. Physical and mechanical properties may differ as different polymerisation processes may produce differences in molecular weight, stereochemistry, end groups, or chain branching. [1]

1.3.1 Step Polymerisation

Step polymerisations occur between functionally substituted monomers. There are two approaches to prepare linear step-reaction polymers. Consider hypothetical functional groups A and B that react to form group X. The first approach is having both reactive functional groups in one molecule:



and the other having two difunctional monomers:



Typically, these reactions take place between reactive components, such as dibasic acids with diamines to give polyamides, or dibasic acids with diols to form polyesters. This reaction has an important modification in the case of nylon 6,6 [poly(hexamethylenedipamide)], where the initial product of the reaction between hexamethylenediamine and adipic acid is a salt. This salt can be recrystallised readily in order to obtain the high-purity intermediate essential for conversion to high molar mass product. The condensation part of the reaction, in this case, is brought about by heating the intermediate salt. [1]

1.3.2 Chain Polymerisation

This polymerisation reaction often involves unsaturated monomers which means they have at least one C=C group. It begins with the chemical generation of reactive centres on selected monomer molecules. These reactive centres are typically free radicals, which react with other monomers without extinguishing the active centre. This way any active centre becomes responsible for the reaction of a number of monomers which add to the growing polymer, increasing its molar mass. [36]

Chain reactions do not continue indefinitely, the nature of the reactivity of the free radical is likely to react in ways that will destroy the reactivity.

Chain polymerisation consists of three phases, namely initiation, propagation, and termination. In detail:

1.3.2.1 Initiation

To carry out such polymerisations the monomer mixture must contain a trace of an initiator material. Initiators role is to start off the chemical process. Initiators readily fragment into free radicals through the application of heat (thermal), light (ultraviolet and visible), electricity (electrochemical), or any other process that

creates the essential free radicals (Figure 1.7). The two most commonly used free radical initiators are benzoyl peroxide and azobisisobutyronitrile (AIBN).

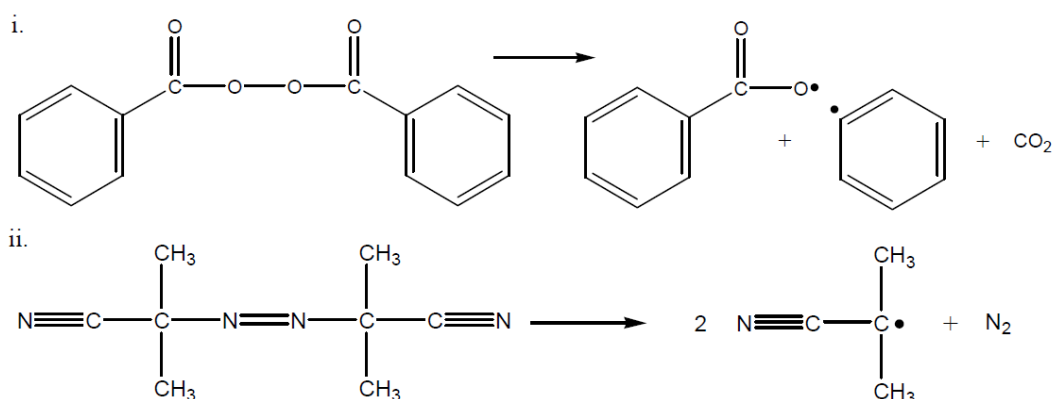


Figure 1.7 Initiator free radical creation.

This can be represented by the following reaction, where I represent the initiator molecule and I^* represents a free radical.



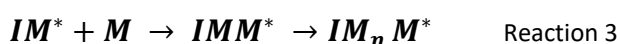
Once produced the active free radical formed can react rapidly with a molecule of monomer (M) to yield a new species that is a free radical of the monomer as shown in reaction 2.



The efficiency of the initiator is a measure of the extent to which the number of radicals formed reflects the number of polymer chains formed.

1.3.2.2 Propagation

Free radicals are transient compounds which have the ability to add to another monomer unit. Propagation is the series of reactions in which the free radical unit at the end of the growing polymer molecule reacts with the additional monomer to increase the length of the polymer chain, the resulting chain may contain thousands of monomer units (Reaction 3).

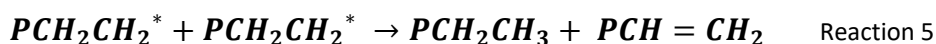


1.3.2.3 Termination

There are two methods of termination in radical polymerisations; the first is recombination which occurs when two radical species react together sharing their unpaired electrons to form a single and stable covalent bond and one reaction product (Reaction 4) where the polymer chain is represented as P.



The second method is disproportionate (Reaction 5) where two radicals can interact by a hydrogen atom transfer from one chain end to the free radical chain end of a growing chain, leading to the formation of two reaction products, one of which is saturated and the other having an unsaturated chain end. [37][36]



1.3.2.4 Other Reactions

The reactivity of the free radicals means other processes can also occur during polymerisation. This occurs when the reactivity of the free radical is transferred to another species which is capable of continuing the chain reaction. This is known as chain transfer. This reaction stops the polymer molecule from growing further without quenching the radical centre.

Generally, chain transfer reactions involve the abstraction of an atom from a neutral saturated molecule (solvent or agent added to control the final size and distribution of molar mass). It also involves more polymer molecules with a lower degree of polymerization. Some monomers and relevant polymers are also known to be effective as chain transfer agents, these may cause an increase in the number of polymer molecules; polymer transfer may lead to moderate to extensive chain branching. [1][35]

1.4 Crosslinking in Hydrogels

The crosslink is a major component in the creation of hydrogels and partially responsible for their unique properties.

Crosslinked polymers can be presented by a planar network as in graphite or space network, as in diamond. On crosslinking, basic structural changes in the polymers are introduced producing improvements in properties. Designing the process with the final application in consideration, different degrees and densities of crosslinking, high or low can be achieved, Figure 1.8. [2]

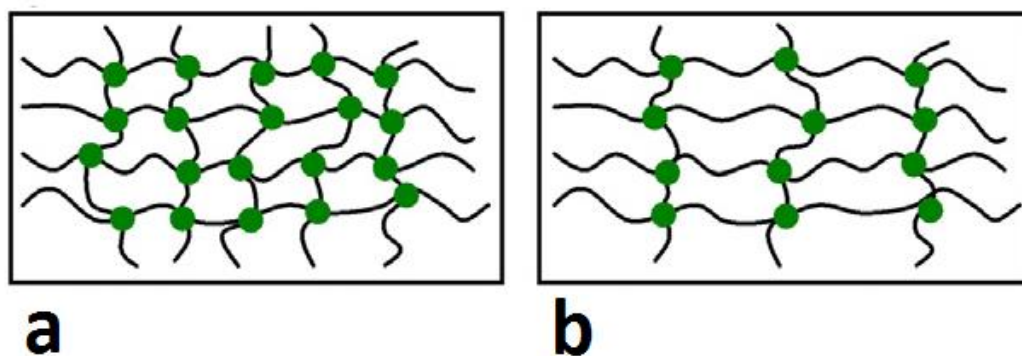


Figure 1.8 Schematic representation of network or cross-linked structures a) High crosslink density, and b) Low crosslink density. Modified from [38]

Depending on the nature of the crosslink, hydrogels can be divided into two categories; chemical and physical. Chemically crosslinked networks are composed of polymer networks with covalent bonding, while physically crosslinked networks have non-covalent interactions that may arise from polymer chain entanglements or physical interactions. The properties of the final hydrogel are highly dependent on the nature of the crosslink. [23][39] This study will investigate the influence of crosslink density and nature on the hydrogels; focusing mainly on physical crosslinks.

1.4.1 Chemical Crosslinks

In chemically crosslinked hydrogels, the crosslinking procedure is achieved through covalent bonds to form a polymer network via a crosslinking agent. As the most

severe mechanism for decreasing molecular freedom; chemically crosslinked hydrogels are permanent and the crosslinking process is irreversible. The initiation of chemical crosslinking may require the addition of a low molecular weight agent with the polymer into the reaction mixture.

Crosslinking can be effected through the application of heat, mechanical forces, exposure radiation and chemical agents, or a combination of these. [11][40][41] The crosslinking in the polymer networks may contain the same chemical and structural features as the main chains or they may be different depending on the way crosslinking was formed. Crosslinking induces a few changes; for example, the polymer will no longer dissolve if it was previously soluble and may swell in a solvent as solvent molecules penetrate the network. [1]

Chemically crosslinked hydrogels have some serious drawbacks, mainly the lack of mechanical toughness leaving the hydrogel weak and brittle. As the covalent bonding process is irreversible, bonds broken during the application of external stresses cannot reform rendering the 3D structure damaged. [42] Chemically crosslinked hydrogels have slow de-swelling rates that require a long time to reach equilibrium (e.g. up to a month), which puts it out of range for some applications such as drug delivery systems. [43][44]

The transparency of chemically crosslinked hydrogels can be lost when changing the polymerisation conditions and/or the composition, high concentrations of crosslinking agent lead to a permanent structural inhomogeneity therefore chemically crosslinked hydrogels become opaque even at temperatures below their LCST. [14][45]

1.4.2 Physical Crosslinks

Covalent crosslinking has disadvantages; once crosslinked the polymer cannot be dissolved, moulded or recycled. Many strategies have been explored to circumvent this; one approach investigated crosslinks that break apart on heating and reform on cooling, e.g. ionic crosslinks. Another approach introduced strong secondary

bonding attraction between polymer chains, which is termed "physical crosslinking". [1]

Physically crosslinked hydrogels can be synthesized through different methods like hydrogen bonding, amphiphilic graft and block polymers which can self-assemble in aqueous media to form hydrogels and polymeric micelles, crystallization, ionic interactions like alginate crosslinked via calcium ions, or by protein interactions. [44]

The physical junctions maintain the 3D structure of the swollen state. Non-covalent interactions and hydrophobic or hydrophilic interaction keep the polymer chains free and flexible allowing for solvent casting, ease of fabrication, reshaping, biodegradation and non-toxicity, which chemically crosslinked hydrogels lack. [41] Physically crosslinked hydrogels can be prepared by several methods, such as hydrophobic association, chain aggregation and crystallisation. [46] Physically crosslinked hydrogels can also disintegrate and dissolve; hence they are sometimes referred to as 'reversible' hydrogels. [11][13]

A noticeable improvement on the properties (mechanical, swelling/de-swelling rate and optical) of physically crosslinked hydrogels was reported in 2002 by Kazutoshi Haraguchi, [39] who replaced the conventional chemical crosslinks with exfoliated inorganic clay platelets. Prepared by *in situ* free radical polymerisation, this new hydrogel synthesis route showed an increase in viscosity and different behaviour on the stress-strain curves due to a primary network formation. The new material demonstrated a 1000 % improvement in elongation at break; fracture energy up to 3300 times that of its predecessors and a strength, modulus and swelling/shrinking capacity which could be modified and controlled by adjusting clay concentration. The clay platelets act as an effective multifunctional crosslinking agent through non-covalent interactions; free and flexible polymer chains are randomly distributed between clay platelets which are large distances apart. [14]

1.5 Clays

Clays are used in a range of applications. A key component in the formulation of ceramic products, drilling fluids, cement, paints and paper. Clays occur naturally as constituents of geological material, mainly as fine particles with a very large surface area and sheet-like structure. They have a high capacity for cation exchange, swelling properties, and high adsorption capacities. Clay minerals ability to disperse is key to obtain a uniform stable system under certain conditions, which leads to changes in properties required for specific applications; for example, the flow behaviour in drilling fluids. Clay minerals include kaolinite and smectite, of which the latter is the main clay type used in this study. [47]

1.5.1 Clays Structure and Properties

Clay minerals are natural silicates or aluminosilicates which dominantly make up soils, sediments and rocks. It is an inexpensive material but is not phase pure, which makes natural clay undesirable in some industrial applications. Synthetic clay is an inexpensive, nanoparticulate material with unique electrical, mechanical, and rheological properties, which are of interest to several industries. An added benefit of synthetic clay is that it can be produced at a high enough purity for critical manufacturing applications. [48]

Clays are crystalline structures that exist as layers. The structure is determined by the atomic arrangement within each clay layer. The simple blocks of a clay platelet consist of silica tetrahedral sheets and octahedral sheets. For silica tetrahedral, four oxygen atoms surround a central silicon atom. For octahedral sheets, six oxygen atoms (or hydroxyl anions) surround an aluminium or magnesium atom. Adjacent octahedral groups share these anions and a planar network sheet is formed (Figure 1.9). The tetrahedral and octahedral sheets are superimposed on one another and fused by the sharing of oxygen atoms; the fused sheets collectively constitute a clay layer. The layers form stacks with a large surface area and a high aspect ratio.

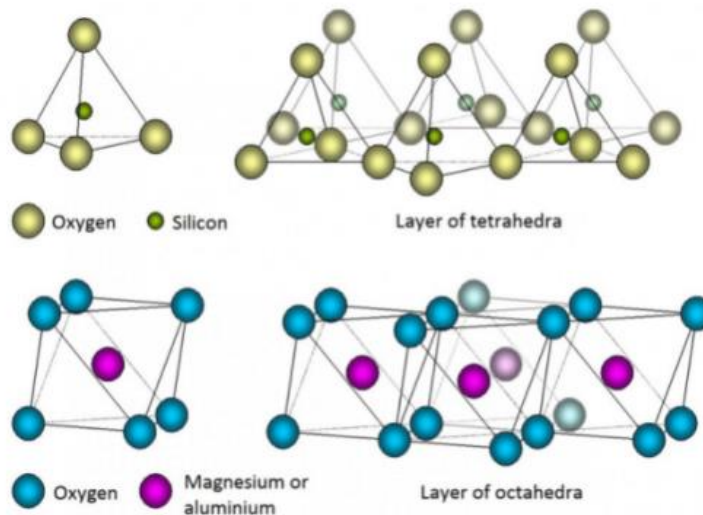


Figure 1.9 Clay structural units: tetrahedra and octahedra. [49]

Inter-layer ions within the sheets may be replaced with similar size and lower charge ions resulting in an excess of electrons (e.g. Si^{4+} is replaced by Al^{3+} in tetrahedral or Al^{3+} is replaced by Mg^{2+} in octahedral sheets). The net negative charge may be counteracted by the adsorption of K^+ , Ca^{2+} , Na^+ or Mg^{2+} providing a charged aqueous environment within the inter-layer space. The cationic charge is shared between the layers and results in the layers being attracted to one another.

1.5.2 Hectorite

Laponite[®] (Figure 1.10) is a synthetic hectorite, which is one of the trioctahedral subgroups of the smectite family of clays and produced by BYK[®] Additives & Instruments. It is a speciality additive synthetic clay mineral similar in structure and composition to the natural hectorite of the smectite group. It is a layered silicate manufactured from naturally occurring inorganic mineral sources.

The primary particle of Laponite[®] possesses an anisotropic nanometric shape. When dispersed in water it shows a rich variety of phase behaviours. It excels in applications as an active agent in many water based formulations. [50]

There are two key areas of functional use for Laponite[®]; either i) Rheology modifier, added to the formulation of many waterborne products such as surface coatings, household cleaners and personal care products. It will impart thixotropic shear

sensitive viscosity and improve stability and syntheses control. ii) Film former agent used to produce electrically conductive, antistatic and barrier coatings.

Table 1.1 shows the advantages of using Laponite[®] where it can be used depending on different grades for two groups of final application:

- Gel forming grades disperse under agitation in water to form clear colourless dispersions. The viscosity depends on the solids and electrolyte content of the water used. A highly thixotropic gel is formed at 2 wt.% in tap water, whereas the same concentration in deionised water will produce a low viscosity sol. Both forms of dispersion are suitable to use in or add to formulations at this point.
- Sol forming grades also disperse readily in water under agitation, but these grades contain dispersing agents which delay the formation of a thixotropic gel structure. At concentrations of up to 30 wt.% solids, low viscosity liquid sols can be produced. [51]

Table 1.1 Properties and Benefits of Laponite[®]

Property	Benefits
Synthetic layered silicate	<ul style="list-style-type: none"> • High purity • Colourless dispersion • Excellent consistency • Free from abrasives
Colloidal sized primary crystal	<ul style="list-style-type: none"> • Produces clear gels or sols in water to give ultra-clear products • Disperses rapidly in water without the need for high shear
Inorganic material	<ul style="list-style-type: none"> • Cannot support microbial growth • Not affected by high temperature • Non-yellowing • Non-toxic • Non-flammable • Free from crystalline silica

Laponite[®] dispersions are versatile components for waterborne formulated products due to the combination of key properties including; high viscosity at low shear rates which produce very effective anti-settling properties, and low viscosity at high shear rates.

With such properties and benefits, a small addition of Laponite[®] into polymer thickened systems can generate a very significant increase in low shear rate viscosity. It will also improve tolerance to “harsh conditions” in formulations containing high levels of electrolytes, surfactants, acids and alkalis. Precise rheological profiles can be engineered by combining Laponite[®] with polymeric thickeners. Pourable formulations with stable suspended particles can be easily formulated.

Laponite[®] has a layered structure (Figure 1.10). Each layer comprises three sheets, two outer tetrahedral silica sheets and a central octahedral magnesia sheet. The Si and Mg are balanced by twenty oxygen atoms and four hydroxyl groups to maintain charge neutrality. [52]

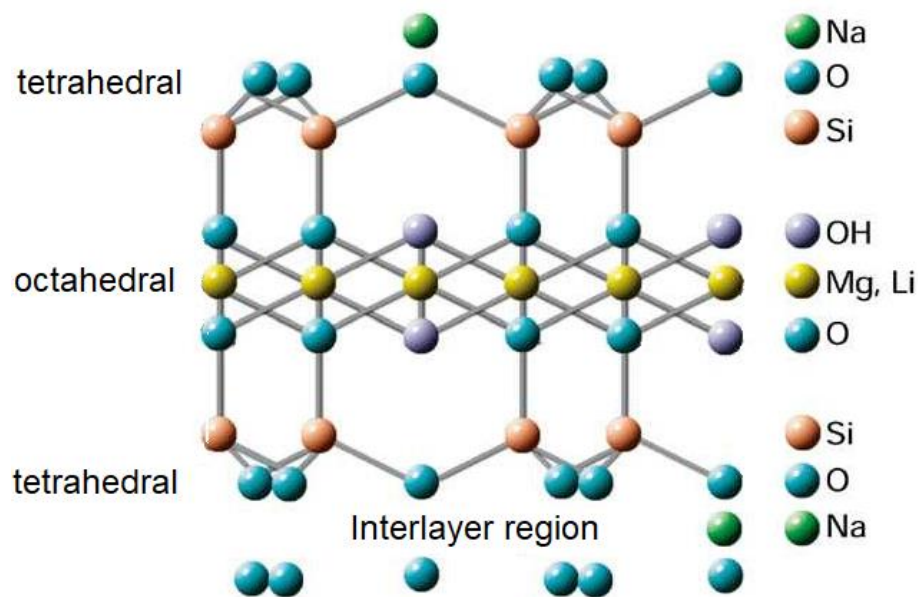


Figure 1.10 Hectorite Idealised Structural Formula. Modified from [51].

The idealised structure shown in Figure 1.10 would have a neutral charge with six divalent magnesium ions in the octahedral layer, giving a positive charge of twelve. In practice, however, some magnesium ions are substituted by lithium ions (monovalent) and some positions are empty to give a composition which typically has the empirical formula $Na_{0.7}^+ [(Si_8Mg_{5.5}Li_{0.3})O_{20}(OH)_4]^{0.7-}$.

A Laponite[®] particle (Figure 1.11) is defined as a repetition of layers many times in two directions, with a typical particle containing up to 2000 of these layers. Macromolecules of this size are known as colloids, examples include bentonite and hectorite, which are natural clay mineral thickeners and have a similar crystal structure but are more than one order of magnitude larger in diameter.

Laponite[®] dispersion in water has attracted attention from academia and industry due to the dependence of physical properties of the dispersion on time; particularly the increase in modulus and relaxation time. [51][53]

A Laponite[®] dilute dispersion in deionised water at low concentration may remain a low viscosity dispersion of non-interacting crystals for long periods of time, whereas the addition of Laponite[®] to tap water, typically beyond 2 wt.%, increases its viscosity and elastic modulus by several orders of magnitude over a shorter duration. [52] The phenomenon of gelation can be ascribed to interactions between the electrical double layers, these interactions are strong enough to limit translational diffusion and cause an equilibrium structure of almost immobile particles at high concentrations.

The gelation mechanism of Laponite[®] dispersions is likely to be similar to that which occurs with natural hectorite minerals which can also undergo osmotic swelling. [54] At 25°C in tap water and with rapid agitation, it takes 10 minutes for the clay to substantially disperse (high shear mixing, temperature or chemical dispersants are not required) Figure 1.11.

Gelation takes place within a period from a few hours to some days depending on the concentration of clay. Two different mechanisms for gelation in clay mineral dispersions are proposed, leading to different types of three-dimensional network structures of the clay dispersion.

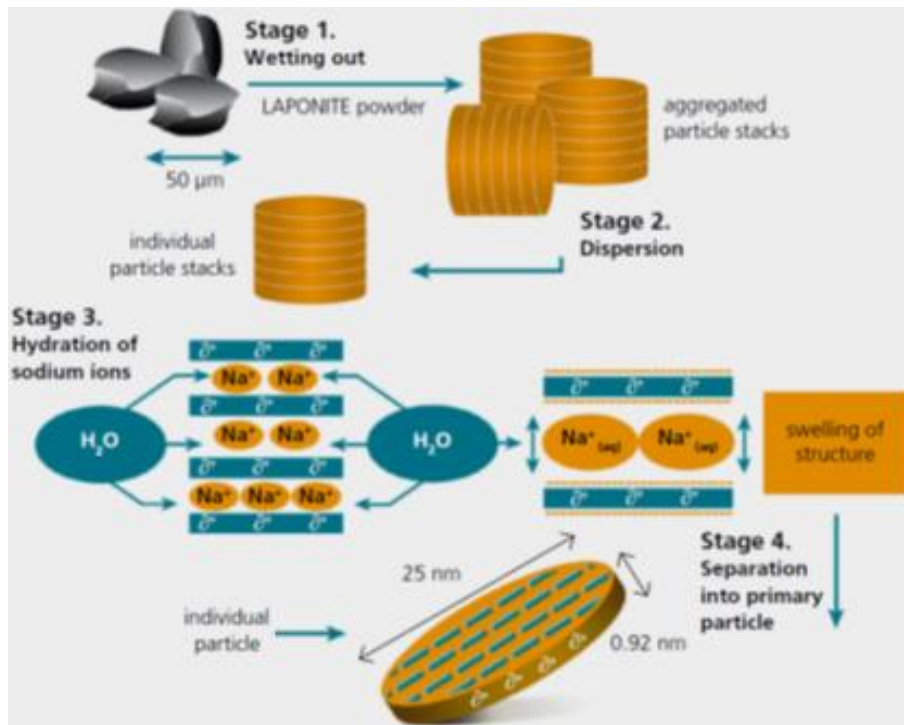


Figure 1.11 Addition of Laponite[®] to Water. [51]

The first case; formation of an equilibrium structure is induced by long-range electrostatic repulsion. Sodium ions are exchangeable; in aqueous dispersions, sodium ions are drawn towards the crystal surface by electrostatic attractions, where osmotic pressure from the bulk of water pulls them away, these ions diffuse into the water and plate-like particles with negatively charged faces are formed; This forms what is known as electrical double layers; an equilibrium structure where the sodium ions are held in a diffuse region on both sides of the dispersed Laponite[®] crystal Figure 1.12.

At higher ionic strength another mechanism is suggested where the double layers around the faces of the platelets are compressed and the electrostatic attraction between oppositely charged faces and edges (together with the attractive van der Waals forces between the particles) gives rise to edge-to-face as well as edge-to-edge associations, leading to a linked three-dimensional network flocculated in a so-called house of cards like structure (Figure 1.13). [51][52]

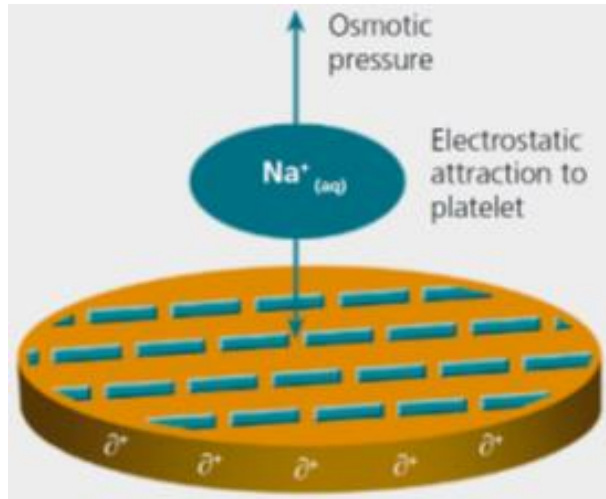


Figure 1.12 Dispersed Primary Particle. [51]

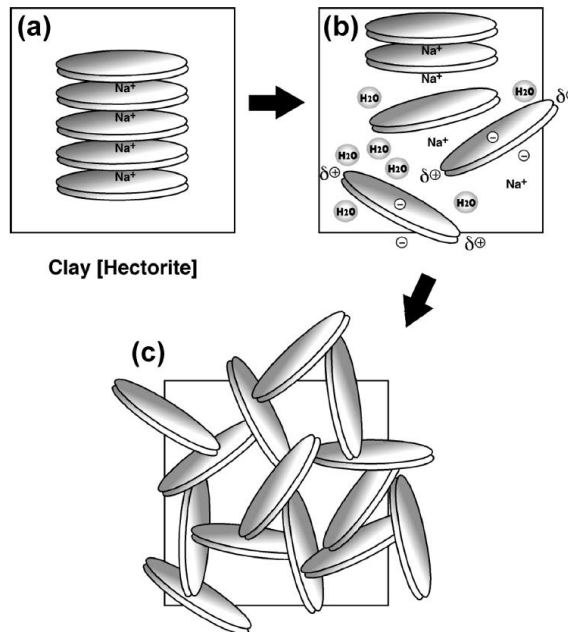


Figure 1.13 Gel formation of house-of-cards structure. [55]

The kinetics of gelation of aqueous dispersions has been rheologically probed by measurements of the storage modulus G' . [54] The dispersion of different grades of Laponite® in water exhibits a low viscosity and Newtonian type rheology, as their mutual positive charges repel particles from each other. The addition of polar compounds in solution to the dispersion will reduce the osmotic pressure holding the sodium ions away from the particle surface. This is of particular interest for the application of an emulsifying and thickening agent, as well as the gelation and flocculation of Laponite® dispersions caused by the addition of electrolytes or polar solvents. [52]

1.5.3 Bentonite

Bentonite also falls in the smectite group. In this study, A “BYK® Additives & Instruments” grade of montmorillonite called Cloisite® Na+ was provided. It has the same structural units as the three sheets as Laponite®. Montmorillonite structure classifies as dioctahedral, with two-thirds of the octahedral sites occupied by trivalent cations. Dioctahedral montmorillonite charge originates from the substitution of Mg^{2+} for Al^{3+} in the octahedral sheet (Figure 1.14). [47]

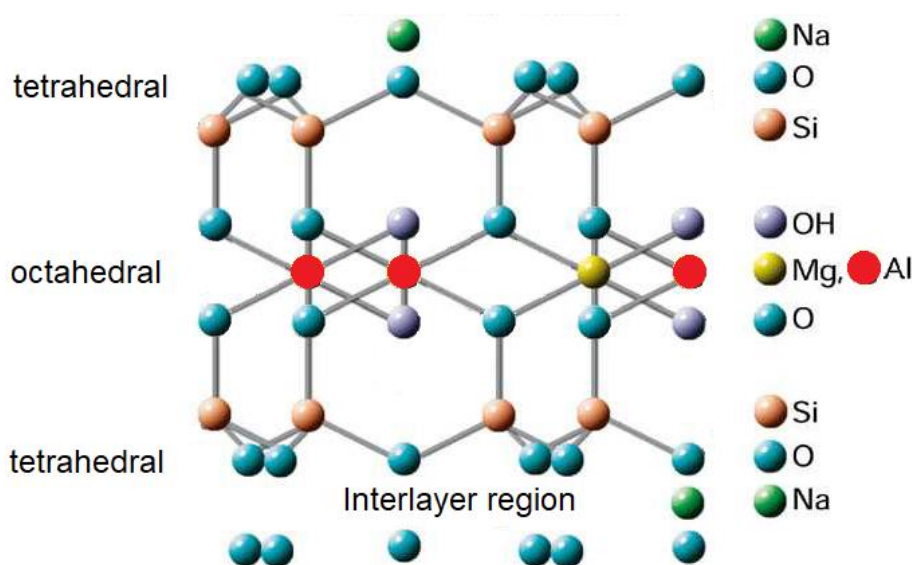


Figure 1.14 The layer structure of bentonite. Modified from [51][56].

Montmorillonite is known as *Na⁺-montmorillonite*, if Na^+ cations are exclusively in exchange with the surface or otherwise as bentonite. Montmorillonite idealised structural formula is $M_y^+ nH_2O(Al_{2y}Mg_y)Si_4O_{10}(OH)_2$ (cations intercalated between the structural units balance the negative charge, these cations may be alkaline earth ions (Ca^{2+} and Mg^{2+}) or alkali metals Na^+). The expanding lattice may provide the clay with a specific area of as high as 800 m²/g. The chemical formula for Na^+ montmorillonite is $Na_{0.33}[(Al_{1.67}Mg_{0.33})(O(OH))_2(SiO_2)_4]$. [47]

1.6 Composite Materials

Composites are composed of two or more individual components combined to obtain the ideal properties of each component, the result is a material with better properties than those of the individual components used on their own, to end up with unique behaviour and properties. A composite material was defined by Jartiz as “a multifunctional material system that provides characteristics not obtainable from any distinct material”. [57][58][59] Composites are traced back to 2500 years ago, where Egyptians used clay containing straw and to build their houses. [60][61][62] In 1980; Bonfield et al. showed the possibility of using composites in bone grafts. [63][64] Consequently, composites have been already in use for many different applications such as household appliances, aerospace, and medical devices. [65]

A polymer composite is a composite material in which one of its components is a polymer. Adding a second component will, hopefully, produce a new material that is relatively cheap with unique properties for applications such as house goods, construction materials and medical instruments.

Bone is a natural composite of an inorganic hard but brittle component called hydroxyapatite and an organic soft and flexible component called collagen, this gives the bones the unique properties that are needed to support the body and protect organs such as the brain and lungs. Recently; several studies investigated the possibility of using composites in medical applications. [63][66][67] Polymer/inorganic composites are attractive and promising in the field of biomedical and tissue culture, as enhancement is always a needed for mechanical properties and this can be obtained by incorporating nanoparticles into polymeric materials, [39][68][69][70-74] where tensile strength, [39][69][72][73][74] higher stiffness [75][76] and elongation at break [39][72][69][73][77] are improved by nanoparticles when compared to that of the pure polymer.

1.7 Nanocomposite Materials

Nanocomposites can be generally defined as multiphase solid material which incorporates one or more individual components (where one of the phases has one, two or three dimensions of < 100 nm) that are combined to obtain the optimal properties of each component and a unique property profile. [78]

The reasons nanocomposites differ from conventional composite materials are the high surface to volume ratio of the reinforcing phase and/or its exceptional aspect ratio. The nanocomposites reinforcing material can be made up of particles (e.g. minerals), sheets (e.g. exfoliated clay stacks) or fibres (e.g. carbon nanotubes or electrospun fibres). The area of the interface between the matrix and reinforcement is greater than for conventional composite materials. [79]

1.7.1 Polymer-Matrix Nanocomposites

Adding nanoparticulate (metals, carbon nanotubes or clays) to a polymer matrix enhances its performance. This strategy is particularly effective in yielding high-performance composites when good dispersion of the filler is achieved and the properties of the nanoscale filler are substantially different or better than those of the matrix, for example, reinforcing a polymer matrix by much stiffer nanoparticles of clays, or carbon nanotubes. [74][80]

Nanoscale dispersion in the composites can introduce new physical properties and novel behaviours, effectively changing the nature of the original matrix-like fire resistance and accelerated biodegradability. [78]

Well-arranged polymer nanocomposites materials display a rich morphology due to the variations in composition, structure, and properties on a nanometre scale allow the delivery of nanoscale therapeutic agents, small enough to be taken up by cells. The advantages of using such a delivery system are that different therapeutic agents can be encapsulated in the same nanogel without changing the agent's

attachment chemistry. Covalently bound systems also offer greater drug stability and can prevent a burst release. [81][82]

The result of the combination of clay minerals with polymers is a new family of composite materials that possess both the polymers' properties such as elasticity, stiffness and toughness and the inorganic materials' behaviour such as hardness and resistance ignition which improves the properties of final products. [83][84] At the end of 1980s Toyota began the advent of clay-polymer nanocomposites by developing clay/Nylon-6 nanocomposites. [85][86][87] The properties and applications of clay-polymer/ nanocomposite were further investigated. [39][71][72][73][74][88] Some nanocomposites showed appreciable improvements in certain properties, such as permeability, modulus and stiffness. [89]

1.7.2 Clay-Polymer Nanocomposites

Clay-polymer nanocomposites are of interest due to their wide range of novel physical properties. In 1989; researchers at Toyota patented clay-nylon composites with greatly improved tensile strength, tensile modulus, and heat resistant timing belt cover with only 5% of clay incorporation. [48] Research groups around the world are still spending significant effort to understand and develop these materials. [90]

Three main types of composites may be found when the clay is associated with a polymer. The type of composite depends on the method of preparation and the nature of clay used (Figure 1.15).

When the clay layers are not separated, the polymer will not be able to intercalate between the silicate sheets, as a result, a phase-separated micro-composite is obtained which has similar properties to the traditional micro-composite (Figure 1.15 a).

Dispersed clay with a single (or a few) polymer chains intercalated between the silicate layers, gives a well-ordered multilayer silicate known as an intercalated

structure (Figure 1.15 b). [91] The repetitive multilayer structure is preserved in intercalated structures making it easy to determine the interlayer spacing using X-ray diffraction (XRD). As silicate layers completely disperse, it allows multiple polymer chains to extend in-between, resulting in an exfoliated structure (Figure 1.15 c). [92] Exfoliated structures allow a large number of clay-polymer interactions, and the result may be a nanocomposite with excellent properties. When dispersed in water clays exhibit different rheological behaviours as the clay content increases with the presence of polymers the interaction between the polymer chains and clay platelets causes a change in the rheological behaviour of dispersions. In suspensions, these clay platelets can only adsorb a maximum amount of polymer. The polymer and clay build a network-like structure containing excess polymer and water. [93]

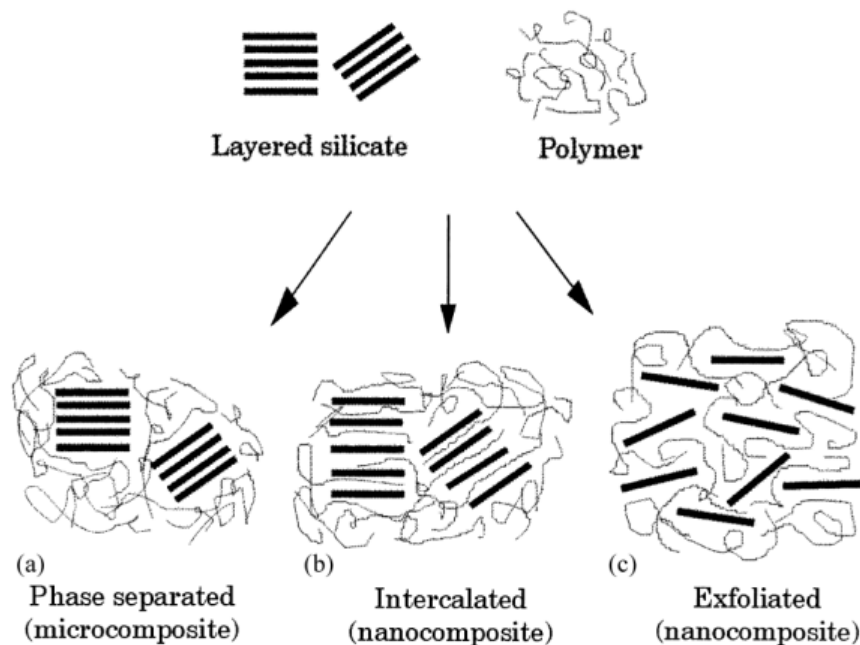


Figure 1.15 Composites arising from the interaction of layered silicates and polymers. [91]

Clay-polymer nanomaterials have been of interest to several industries in the last twenty years, which is due to clay being an inexpensive, environmentally benign, transparent suspension creator, nanoparticulate material. [48] Clay can be produced at high purity as a result of its availability. This allows the use of clay suspensions for critical applications that require improvements on mechanical, and

rheological properties for the clay suspensions and the clay nanocomposites depending at low and high loading. [94] Applications that require suspension or gels can be engineered to use, shear thinning and thickening applications can also make use of such property.

1.7.3 Clay-Polymer Based Hydrogels

Haraguchi et al developed a clay-pNIPAM nanocomposites composed of specific polymers and a water-swelling organic clay in 2002 where the inorganic clays are exfoliated and uniformly dispersed in an aqueous media, then neighbouring clay sheets are connected by polymer chains [74] which is a very similar technique to what is used in this work, they documented the swelling, optical and mechanical properties on the final product. [39][72][95] The purpose of producing composite materials is to improve the general properties of the composite and incorporating inorganic particles (clay) to pNIPAM could improve several properties. The interesting properties of pNIPAM thermal response, [96] ability to absorb large volumes of water, [13] biocompatibility [76][97][98] make it a promising material for different applications, such as artificial soft tissues [99][100][101] and drug delivery. [102]

In pNIPAM, the thermoresponsive behaviour can be modified to be used as an injectable scaffold, where cells could suspend in the hydrogel in a flowing state above LCST, then gel will encapsulate the cells within its structure when temperature decreased below the LCST. [97] Scarpa et al investigation of LCST for free pNIPAM dates to 1967, they presented a study describing precipitation and resolving of pNIPAM from the solution as an "inverse temperature coefficient of solubility". [103]

The major purpose of producing composite materials is improving their general properties and reducing the cost. In the same context, incorporating inorganic particles such as clays to other polymers in this study may improve a number of their properties.

Several parameters can influence the mechanical properties on the composites, such as crosslink density, monomer type and concentration, polymerization method and temperature, and swelling and de-swelling rate. [13][39][104][105][106][107] Due to its importance in controlling the mechanical properties of viscoelastic networks Crosslink density of hydrogel materials has received significant attention over the last decade. [108] The increase in the crosslink density was shown to increase the stiffness of hydrogel materials as was reported by Haraguchi et al and Djonlagic, [75][45] to meet different application requirements, mechanical properties of hydrogel materials can be tuned.[109] In the current study, the influence of composition on the mechanical properties (Rheological properties) of pNIPAM based hydrogels as well as pDMAc, pHEMA, pHPMA, and pGMAc based hydrogels has been studied.

As previously mentioned, hydrogels are 3D polymeric network structures containing water and have the ability to absorb a huge amount of water or other fluids in their structures. [110] High water contents are very important for hydrogel's biocompatibility. [36] To understand the water within hydrogel materials Fourier Transform Infrared spectroscopy (FTIR) has been used to investigating hydrogen bonding between water and polymer molecules. [104][111] [112]

1.7.4 Structural Properties of Clay-Polymer Based Hydrogels

Morphological and structural properties of polymer-based hydrogels were impacted by crosslink density. [75][113][114][115] It was found by Jang J, et al. that average pore size of hydrogels was decreased by increasing crosslink density. [116] The pore size modification of hydrogel materials is important as it improves fluid

transportation through the structure rapidly and effectively when used in tissue culture. [117] In addition, structural and morphological properties influence other properties, such as swelling degree [118][119] and the mechanical behaviour. [75][76][119] This study focused on influences of crosslink density, type and concentrations on the morphology and structure of clay-polymer based hydrogels, as well as the relationship between changing hydrogel structure and the effect on rheological properties within these materials.

1.8 Aims and Objectives

The initial focal point from which the research stems is a novel, developing and relatively well researched hydrogel system based on pNIPAM. From this, we have investigated different, yet comparative polymer and clay chemistries with the aim to better understand the formation and interactive processes of the components within the hydrogel nanocomposite system. Furthermore, the new formulations and chemistries have led to new nanocomposite morphologies other than hydrogels, e.g. films and coatings.

- 1) What are the new polymer chemistries, how do they compare/differ and why were they chosen? This is all based on free radical polymerisation and thermally initiated.
- 2) What are the new clay chemistries (i.e. the crosslinkers), how do they compare/differ and why were they chosen?
- 3) How did we characterise the interactions - rheology, XRD, SEM, etc?

The novelty of this study lies in the control of the clay-polymer nanocomposite by combination and variation of different clays and monomers. While earlier studies described alteration by changing the polymer to clay ratio, the polymer molecular weight, the amount of metal salt, and the amount of water. [93]

The aim of this research was to explore applying existing nanotechnology to address technical challenges in the development of new clay-polymer

nanocomposite materials. Using clay with different chemistry, sizes and surface areas gives the chance to understand how clay interacts and affects the structure and characteristics of clay-polymer based nanocomposites, some of these materials are already used for a number of high-value applications such as drug delivery, and biological tissue scaffolding and cosmetics.

This study also aims to investigate the effect of different crosslinking agent and different crosslinking agent content on the material properties of the clay-polymer nanocomposite. The overall properties governed by clay properties and clay-polymer relationship are prime aspects of this study. The Enhancement of significant properties of nanocomposites is a measure of clay platelets dispersion within the polymer matrix. Different approaches were adopted to understand the influence of clay properties on the nanocomposite; (i) by examining and comparing different clays as raw, dry, powder material using spectroscopy and thermogravimetry analysis (ii) mechanical examination of clay/water suspension of different clay types/grads, and different concentrations varying from 0.5 %-10 % using rheological studies (iii) chemical and mechanical and morphological examination of clay-polymer nanocomposite with different clay types/grades, concentration, and polymers. [120]

Morphological, pore size and scaffolding general arrangement which shows the effect of different crosslinking agents and crosslinking density were examined by Scanning Electron Microscope (SEM) to acquire information on how wide/small pores are, diffusion kinetics in the system if required for further applications. The nature and elemental composition of the clay-polymer nanocomposites were determined by X-ray diffraction (XRD), X-ray fluorescence (XRF), and Fourier Transfer Infrared (FTIR) spectroscopy. The water content in the dry clay-polymer nanocomposite was determined and examined by Thermogravimetric analysis (TGA).

Mechanical and rheological properties of the hydrogels were examined using a rheometer that operates on different modes (as a Dynamic Mechanical Analysis

(DMA) technique) to evaluate the structure, performance, strength and torsional mechanical modules of these nanocomposites under different rotational and oscillatory loads.

Here is presented an investigation study the of clay-polymer nanocomposite which addresses all the previous issues. Polymerised at a high temperature as a low or high viscosity, opaque liquid, or as solid material. Investigations were undertaken to examine the mechanical, chemical and morphological properties of the nanocomposite at different state controlled by surrounding environment temperature when possible. This study allows the development of new and exciting technologies which can be tailored to specific high end medical and industrial applications. [121]

1.9 References

- [1] P. M. P. Stevens, *Polymer Chemistry, An Introduction (2nd ed.)*. New York: Oxford University Press., 1990.
- [2] P. P. Ghosh, "POLYMER SCIENCE,FUNDAMENTALS OF POLYMER SCIENCE, Basic Concepts." Kolkata, 2006.
- [3] J. Gwynne, "Polymer basics," *University of Cambridge*. [Online]. Available: <https://www.doitpoms.ac.uk/tlplib/polymerbasics/printall.php>.
- [4] W.-F. Su, "Principles of Polymer Design and Synthesis, Chapter 1: Interoduction," in *Principles of Polymer Design and Synthesis*, vol. 82, 2013, pp. 137–183.
- [5] Z. Maolin, L. Jun, Y. Min, and H. Hongfei, "The swelling behavior of radiation prepared semi-interpenetrating polymer networks composed of polyNIPAAm and hydrophilic polymers," *Radiat. Phys. Chem.*, vol. 58, no. 4, pp. 397–400, Jun. 2000.
- [6] Y. S. Ye, J. Rick, and B. J. Hwang, "Water soluble polymers as proton exchange membranes for fuel cells," *Polymers*, vol. 4, no. 2. pp. 913–963, 2012.
- [7] X. Li, Y. Yang, J. Eastoe, and J. Dong, "Rich self-assembly behavior from a simple amphiphile," *ChemPhysChem*, vol. 11, no. 14, pp. 3074–3077, 2010.
- [8] L. Dougan, J. Crain, J. L. Finney, and A. K. Soper, "Molecular self-assembly in a model amphiphile system," *Phys. Chem. Chem. Phys.*, vol. 12, no. 35, pp. 10221–10229, 2010.
- [9] Y. Hirokawa, T. Tanaka, and E. S. Matsuo, "Erratum: Volume phase transition in a nonionic gel (Journal of Chemical Physics (1984) 81 (6379))," *The Journal of Chemical Physics*, vol. 96, no. 11. p. 8641, 1992.
- [10] S. Hirotsu, Y. Hirokawa, and T. Tanaka, "Volume-phase transitions of ionized

- N-isopropylacrylamide gels," *J. Chem. Phys.*, vol. 87, no. 2, pp. 1392–1395, 1987.
- [11] F. Ullah, M. B. H. Othman, F. Javed, Z. Ahmad, and H. M. Akil, "Classification, processing and application of hydrogels: A review," *Mater. Sci. Eng. C*, vol. 57, pp. 414–433, Dec. 2015.
- [12] L. Liang *et al.*, "Surfaces with reversible hydrophilic/hydrophobic characteristics on cross-linked poly(N-isopropylacrylamide) hydrogels," *Langmuir*, vol. 16, no. 21, pp. 8016–8023, Oct. 2000.
- [13] A. S. Hoffman, "Hydrogels for biomedical applications," *Adv. Drug Deliv. Rev.*, vol. 64, pp. 18–23, 2012.
- [14] K. Haraguchi, H. J. Li, K. Matsuda, T. Takehisa, and E. Elliott, "Mechanism of forming organic/inorganic network structures during in-situ free-radical polymerization in PNIPA-clay nanocomposite hydrogels," *Macromolecules*, vol. 38, no. 8, pp. 3482–3490, Apr. 2005.
- [15] O. WICHTERLE and D. LÍM, "Hydrophilic Gels for Biological Use," *Nature*, vol. 185, no. 4706, pp. 117–118, 1960.
- [16] S. J. Buwalda, K. W. M. Boere, P. J. Dijkstra, J. Feijen, T. Vermonden, and W. E. Hennink, "Hydrogels in a historical perspective: From simple networks to smart materials," *J. Control. Release*, vol. 190, pp. 254–273, Sep. 2014.
- [17] H. Li and K. Haraguchi, "Mechanical and swelling/de-swelling properties of nanocomposite gel with high clay content," vol. 55, Jan. 2006.
- [18] M. E. Byrne, K. Park, and N. A. Peppas, "Molecular imprinting within hydrogels," *Adv. Drug Deliv. Rev.*, vol. 54, no. 1, pp. 149–161, Jan. 2002.
- [19] R. Akashi, H. Tsutsui, and A. Komura, "Polymer Gel Light-Modulation Materials Imitating Pigment Cells," *Adv. Mater.*, vol. 14, no. 24, p. 1808, 2002.

- [20] P. S. Stayton *et al.*, "Control of protein–ligand recognition using a stimuli-responsive polymer," *Nature*, vol. 378, no. 6556, pp. 472–474, Nov. 1995.
- [21] S. Champ, W. Xue, and M. B. Huglin, "Concentrating aqueous dispersions of Staphylococcus Epidermidis bacteria by swelling of thermosensitive poly[(N-isopropylacrylamide)-co-(acrylic acid)] hydrogels," *Macromol. Chem. Phys.*, vol. 201, no. 17, pp. 2505–2509, Nov. 2000.
- [22] W. Zhao, X. Jin, Y. Cong, Y. Liu, and J. Fu, "Degradable natural polymer hydrogels for articular cartilage tissue engineering," *J. Chem. Technol. Biotechnol.*, vol. 88, no. 3, pp. 327–339, Mar. 2013.
- [23] E. M. Ahmed, "Hydrogel: Preparation, characterization, and applications: A review," *J. Adv. Res.*, vol. 6, no. 2, pp. 105–121, 2015.
- [24] T. Iizawa, H. Taketa, M. Maruta, T. Ishido, T. Gotoh, and S. Sakohara, "Synthesis of porous poly(N-isopropylacrylamide) gel beads by sedimentation polymerization and their morphology," *J. Appl. Polym. Sci.*, vol. 104, no. 2, pp. 842–850, Apr. 2007.
- [25] L. Yang, J. S. Chu, and J. A. Fix, "Colon-specific drug delivery: New approaches and in vitro/in vivo evaluation," *Int. J. Pharm.*, vol. 235, no. 1–2, pp. 1–15, Mar. 2002.
- [26] E. S. Gil and S. M. Hudson, "Stimuli-responsive polymers and their bioconjugates," *Prog. Polym. Sci.*, vol. 29, no. 12, pp. 1173–1222, Dec. 2004.
- [27] N. Kashyap, N. Kumar, and M. N. V. R. Kumar, "Hydrogels for pharmaceutical and biomedical applications," *Crit. Rev. Ther. Drug Carrier Syst.*, vol. 22, no. 2, pp. 107–149, 2005.
- [28] S. Il Kang and Y. H. Bae, "A sulfonamide based glucose-responsive hydrogel with covalently immobilized glucose oxidase and catalase," *J. Control. Release*, vol. 86, no. 1, pp. 115–121, Jan. 2003.

- [29] E. Ruel-Gariépy and J. C. Leroux, "In situ-forming hydrogels - Review of temperature-sensitive systems," *Eur. J. Pharm. Biopharm.*, vol. 58, no. 2, pp. 409–426, Sep. 2004.
- [30] C. Gong *et al.*, "Thermosensitive Polymeric Hydrogels As Drug Delivery Systems," *Curr. Med. Chem.*, vol. 20, no. 1, pp. 79–94, Dec. 2012.
- [31] B. Jeong, S. W. Kim, and Y. H. Bae, "Thermosensitive sol-gel reversible hydrogels," *Advanced Drug Delivery Reviews*, vol. 64, no. SUPPL. pp. 154–162, Dec-2012.
- [32] and A. L. M. Behl, J. Zotzmann, *Shape-Memory Polymers*. Springer-Verlag Berlin Heidelberg, 2010.
- [33] Y. Qiu and K. Park, "Environment-sensitive hydrogels for drug delivery," *Adv. Drug Deliv. Rev.*, vol. 64, no. SUPPL., pp. 49–60, Dec. 2012.
- [34] C. M. Yakacki, "Shape-memory and shape-changing polymers," *Polym. Rev.*, vol. 53, no. 1, pp. 1–5, Jan. 2013.
- [35] J. Nicholson, *The Chemistry of Polymers*. The Royal Society of Chemistry, 2006.
- [36] C. Maldonado-Codina and N. Efron, "Hydrogel Lenses Materials and Manufacture_ A Review," *Optom. Pract.*, vol. 4, pp. 101–115, 2003.
- [37] "FREE-RADICAL POLYMERIZATION." pp. 1–13.
- [38] K. U. Claussen, R. Giesa, and H. W. Schmidt, "Longitudinal polymer gradient materials based on crosslinked polymers," *Polymer (Guildf)*, vol. 55, no. 1, pp. 29–38, 2014.
- [39] K. Haraguchi, R. Farnworth, A. Ohbayashi, and T. Takehisa, "Compositional effects on mechanical properties of nanocomposite hydrogels composed of poly(N,N-dimethylacrylamide) and clay," *Macromolecules*, vol. 36, no. 15, pp.

5732–5741, Jul. 2003.

- [40] J. Charles E. Carraher, *Polymer Chemistry*. NEW YORK • BASEL: MARCEL DEKKER, INC, 2003.
- [41] M. J. Park, S. M. Hur, and H. K. Rhee, "Online estimation and control of polymer quality in a copolymerization reactor," *AIChE J.*, vol. 48, no. 5, pp. 1013–1021, May 2002.
- [42] S. Hirotsu and A. Onuki, "Volume Phase Transition of Gels under Uniaxial Tension," *Journal of the Physics Society Japan*, vol. 58, no. 5. pp. 1508–1511, 1989.
- [43] K. Haraguchi, H. J. Li, L. Song, and K. Murata, "Tunable optical and swelling/deswelling properties associated with control of the coil-to-globule transition of poly(N-isopropylacrylamide) in polymer - Clay nanocomposite gels," *Macromolecules*, vol. 40, no. 19, pp. 6973–6980, Sep. 2007.
- [44] M. F. Akhtar, M. Hanif, and N. M. Ranjha, "Methods of synthesis of hydrogels ... A review," *Saudi Pharm. J.*, vol. 24, no. 5, pp. 554–559, Sep. 2016.
- [45] K. Haraguchi, T. Takehisa, and S. Fan, "Effects of clay content on the properties of nanocomposite hydrogels composed of poly(N-isopropylacrylamide) and clay," *Macromolecules*, vol. 35, no. 27, pp. 10162–10171, Dec. 2002.
- [46] P. Gupta, K. Vermani, and S. Garg, "Hydrogels from controlled release to pH-responsive drug delivery," *Res. Focus*, vol. 7, no. 10, pp. 1–11, 2002.
- [47] P. F. Luckham and S. Rossi, "Colloidal and rheological properties of bentonite suspensions," *Adv. Colloid Interface Sci.*, vol. 82, no. 1, pp. 43–92, Oct. 1999.
- [48] T. N. Blanton, D. Majumdar, and S. M. Melpolder, "MICROSTRUCTURE OF CLAY-POLYMER COMPOSITES," vol. 42. JCPDS-International Centre for Diffraction Data, New York, pp. 562–568, 2000.

- [49] A. Jordán, "Lightening the clay (II)," *Soil System Sciences (SSS) Division*, 2014. [Online]. Available: <https://blogs.egu.eu/divisions/sss/2014/09/page/3/>.
- [50] S. Jatav and Y. M. Joshi, "Chemical stability of Laponite in aqueous media," *Appl. Clay Sci.*, vol. 97–98, pp. 72–77, 2014.
- [51] BYK Additives & Instruments, "LAPONITE LAPONITE-Performance Additives," Geretsried.
- [52] N. Willenbacher, "Unusual thixotropic properties of aqueous dispersions of Laponite RD," *J. Colloid Interface Sci.*, vol. 182, no. 2, pp. 501–510, Sep. 1996.
- [53] A. Shahin and Y. M. Joshi, "Physicochemical effects in aging aqueous laponite suspensions," *Langmuir*, vol. 28, no. 44, pp. 15674–15686, Nov. 2012.
- [54] R. G. Avery and J. D. F. Ramsay, "Colloidal properties of synthetic hectorite clay dispersions. II. Light and small angle neutron scattering," *J. Colloid Interface Sci.*, vol. 109, no. 2, pp. 448–454, 1986.
- [55] B. Ferse, S. Richter, K. F. Arndt, and A. Richter, "Investigation of gelling aqueous clay dispersions with dynamic light scattering," *Macromol. Symp.*, vol. 254, pp. 378–385, 2007.
- [56] U. Hofmann, K. Endell, and D. Wilm, "Kristallstruktur und Quellung von Montmorillonit," *Cryst. Mater.*, no. 86, pp. 340–348, 2015.
- [57] S. Divagar, M. Vigneshwar, and S. T. Selvamani, "Impacts of Nano Particles on Fatigue Strength of Aluminum Based Metal Matrix Composites for Aerospace," *Mater. Today Proc.*, vol. 3, no. 10, pp. 3734–3739, 2016.
- [58] S. P. Shukla, "Investigation in To Tribo Potential of Rice Husk (Rh) Char Reinforced Epoxy Composite Investigation in To Tribo Potential of Rice Husk (Rh) Char Reinforced Epoxy," vol. 008, 2011.
- [59] D. Verma, P. C. Gope, M. K. Maheshwari, and R. K. Sharma, "Bagasse fiber

- composites-A review," *J. Mater. Environ. Sci.*, vol. 3, no. 6, pp. 1079–1092, 2012.
- [60] W. D. (Rik) Brouwer, "Natural Fibre Composites in Structural Components: Alternative Applications," 2000.
- [61] Robert W. Hurter, "Sisal Fibre: Market Opportunities in the Pulp and Paper Industry," 2000.
- [62] P. Vimla, "Synthesis and Characterization of a Biocomposite Derived From Banana Plants (Musa," Durban University of Technology, 2015.
- [63] M. Wang, "Developing bioactive composite materials for tissue replacement," *Biomaterials*, vol. 24, no. 13, pp. 2133–2151, 2003.
- [64] W. Bonfield and J. Charnley, "Composites for bone replacement," vol. 10, no. 1, pp. 522–526, 1988.
- [65] Aleksendric Dragan and P. Carlone, *Soft Computing in the Design and Manufacturing of Composite Materials*, 1st Editio. Woodhead Publishing, 2015.
- [66] K. Haraguchi, "Development of soft nanocomposite materials and their applications in cell culture and tissue engineering," *J. Stem Cells Regen. Med.*, vol. 8, no. 1, 2012.
- [67] H. Davis and J. Leach, "Hybrid and Composite Biomaterials in Tissue Engineering," *Top. Multifunct. Biomater. devices*, no. 530, pp. 1–26, 2008.
- [68] M. Okamoto and B. John, "Synthetic biopolymer nanocomposites for tissue engineering scaffolds," *Prog. Polym. Sci.*, vol. 38, no. 10–11, pp. 1487–1503, 2013.
- [69] Y. I. Tien and K. H. Wei, "High-tensile-property layered silicates/polyurethane nanocomposites by using reactive silicates as pseudo chain extenders,"

Macromolecules, vol. 34, no. 26, pp. 9045–9052, 2001.

- [70] S. Wang, C. Long, X. Wang, Q. Li, and Z. Qi, "Synthesis and properties of silicone rubber/organomontmorillonite hybrid nanocomposites," *J. Appl. Polym. Sci.*, vol. 69, no. 8, pp. 1557–1561, 1998.
- [71] I. Tsvintzelis, S. I. Marras, I. Zuburtikudis, and C. Panayiotou, "Porous poly(l-lactic acid) nanocomposite scaffolds prepared by phase inversion using supercritical CO₂ as antisolvent," *Polymer (Guildf.)*, vol. 48, no. 21, pp. 6311–6318, 2007.
- [72] K. Haraguchi and H. J. Li, "Mechanical properties and structure of polymer-clay nanocomposite gels with high clay content," *Macromolecules*, vol. 39, no. 5, pp. 1898–1905, Mar. 2006.
- [73] S. Sinha Ray, K. Yamada, M. Okamoto, and K. Ueda, "New polylactide-layered silicate nanocomposites. 2. Concurrent improvements of material properties, biodegradability and melt rheology," *Polymer (Guildf.)*, vol. 44, no. 3, pp. 857–866, 2002.
- [74] K. Haraguchi and T. Takehisa, "Nanocomposite Hydrogels: A Unique Organic–Inorganic Network Structure with Extraordinary Mechanical, Optical, and Swelling/Deswelling Properties," *Adv. Mater. - ADVAN MATER*, vol. 14, Aug. 2002.
- [75] J. Djonlagic, A. Lancuski, M. S. Nikolic, J. Rogan, S. Ostojic, and Z. Petrovic, "Hydrogels reinforced with nanoclays with improved response rate," *J. Appl. Polym. Sci.*, vol. 134, no. 9, pp. 1–14, 2017.
- [76] R. H. Dosh, A. Essa, N. Jordan-Mahy, C. Sammon, and C. L. Le Maitre, "Use of hydrogel scaffolds to develop an in vitro 3D culture model of human intestinal epithelium," *Acta Biomater.*, vol. 62, pp. 128–143, 2017.
- [77] Y. Ou, F. Yang, and Z. Z. Yu, "A new conception on the toughness of nylon

- 6/silica nanocomposite prepared via in situ polymerization," *J. Polym. Sci. Part B Polym. Phys.*, vol. 36, no. 5, pp. 789–795, 1998.
- [78] R. Raj, A. Kaushik, and R. Kundu, "Theoretical aspects about bright future of polymer nano-composites in mechanical engineering," *Int. J. Enhanc. Res. Sci. Technol. Eng.*, vol. 2, no. 9, pp. 34–37, 2013.
- [79] P. M. Ajayan, L. S. Schadler, and P. V. Braun, "Nanocomposite Science and Technology," in *Nanocomposite Science and Technology*, Wiley-VCH, 2003, pp. 1–20.
- [80] X. Liu, K. Liu, S. Gou, L. Liang, C. Luo, and Q. Guo, "Water-soluble acrylamide sulfonate copolymer for inhibiting shale hydration," *Ind. Eng. Chem. Res.*, vol. 53, no. 8, pp. 2903–2910, Feb. 2014.
- [81] E. A. Stefanescu, W. H. Daly, and I. I. Negulescu, "Hybrid polymer/clay nanocomposites: Effect of clay size on the structure of multilayered films," *Macromol. Mater. Eng.*, vol. 293, no. 8, pp. 651–656, Aug. 2008.
- [82] S. J. Buwalda, T. Vermonden, and W. E. Hennink, "Hydrogels for Therapeutic Delivery: Current Developments and Future Directions," *Biomacromolecules*, vol. 18, no. 2, pp. 316–330, Feb. 2017.
- [83] A.S Edelstein and R. . Cammaratra, *Nanomaterials Synthesis, Properties and Applications*, Second Edi. CRC Press, 1996.
- [84] B. Brunier, N. Sheibat-Othman, M. Chniguir, Y. Chevalier, and E. Bourgeat-Lami, "Investigation of Four Different Laponite Clays as Stabilizers in Pickering Emulsion Polymerization," *Langmuir*, vol. 32, no. 24, pp. 6046–6057, 2016.
- [85] P. Jan, "PROCESS FOR PRODUCING COMPOSITE MATERIAL," 4,810,734, 1989.
- [86] Y. Kojima *et al.*, "Mechanical properties of nylon 6-clay hybrid," *J. Mater. Res.*, vol. 8, no. 5, pp. 1185–1189, 1993.

- [87] A. Usuki *et al.*, "Synthesis of nylon 6-clay hybrid," *J. Mater. Res.*, vol. 8, no. 5, pp. 1179–1184, 1993.
- [88] J. J. Luo and I. M. Daniel, "Characterization and modeling of mechanical behavior of polymer/clay nanocomposites," *Compos. Sci. Technol.*, vol. 63, no. 11, pp. 1607–1616, 2003.
- [89] K. Haraguchi, M. Ebato, and T. Takehisa, "Polymer-clay nanocomposites exhibiting abnormal necking phenomena accompanied by extremely large reversible elongations and excellent transparency," *Adv. Mater.*, vol. 18, no. 17, pp. 2250–2254, Sep. 2006.
- [90] A. USUKI, M. KAWASUMI, Y. KOJIMA, A. OKADA, and T. KURAUCHI, "Synthesis and properties of diamine-modified nylon 6-clay hybrid," *Kobunshi ronbunshu*, vol. 52, no. 7. Tsukiji daisan nagaoka, pp. 440–444.
- [91] M. Alexandre and P. Dubois, "Polymer-layered silicate nanocomposites: Preparation, properties and uses of a new class of materials," *Mater. Sci. Eng. R Reports*, vol. 28, no. 1, pp. 1–63, Jun. 2000.
- [92] D. Schmidt, D. Shah, and E. P. Giannelis, "New advances in polymer/layered silicate nanocomposites," *Curr. Opin. Solid State Mater. Sci.*, vol. 6, no. 3, pp. 205–212, 2002.
- [93] E. A. Stefanescu, C. Stefanescu, W. H. Daly, G. Schmidt, and I. I. Negulescu, "Hybrid polymer-clay nanocomposites: A mechanical study on gels and multilayered films," *Polymer (Guildf.)*, vol. 49, no. 17, pp. 3785–3794, Aug. 2008.
- [94] A. Blumstein, "Polymerization of adsorbed monolayers. II. Thermal degradation of the inserted polymer," *J. Polym. Sci. Part A Gen. Pap.*, vol. 3, no. 7, pp. 2665–2672, Jul. 1965.
- [95] K. Haraguchi, R. Farnworth, A. Ohbayashi, and T. Takehisa, "Compositional

effects on mechanical properties of nanocomposite hydrogels composed of poly(N,N-dimethylacrylamide) and clay," *Macromolecules*, vol. 36, no. 15, pp. 5732–5741, 2003.

- [96] H. Yim *et al.*, "Temperature-Dependent Conformational Change of PNIPAM Grafted Chains at High Surface Density in Water," *Macromolecules*, vol. 37, no. 5, pp. 1994–1997, 2004.
- [97] A. A. Thorpe *et al.*, "Thermally triggered hydrogel injection into bovine intervertebral disc tissue explants induces differentiation of mesenchymal stem cells and restores mechanical function," *Acta Biomater.*, vol. 54, pp. 212–226, 2017.
- [98] A. A. Thorpe, S. Creasey, C. Sammon, and C. L. Le Maitre, "Hydroxyapatite nanoparticle injectable hydrogel scaffold to support osteogenic differentiation of human mesenchymal stem cells," *Eur. Cells Mater.*, vol. 32, pp. 1–23, 2016.
- [99] R. Yoshida, "Self-Oscillating Gels," in *Soft Actuators: Materials, Modeling, Applications, and Future Perspectives*, K. Asaka and H. Okuzaki, Eds. Tokyo: Springer Japan, 2014, pp. 55–78.
- [100] L. Liang, J. Liu, and X. Gong, "Thermosensitive poly(N-isopropylacrylamide)-clay nanocomposites with enhanced temperature response," *Langmuir*, vol. 16, no. 25, pp. 9895–9899, 2000.
- [101] C. H. Zhang, Y. L. Luo, Y. S. Chen, Q. B. Wei, and L. H. Fan, "Preparation and theophylline delivery applications of novel PMAA/MWCNT-COOH nanohybrid hydrogels," *J. Biomater. Sci. Polym. Ed.*, vol. 20, no. 7–8, pp. 1119–1135, 2009.
- [102] Y. Dogu and O. Okay, "Swelling-deswelling kinetics of poly(N-isopropylacrylamide) hydrogels formed in PEG solutions," *J. Appl. Polym. Sci.*, vol. 99, no. 1, pp. 37–44, 2006.

- [103] J. S. Scarpa, D. D. Mueller, and I. M. Klotz, "Slow Hydrogen-Deuterium Exchange in a Non- α -helical Polyamide," *J. Am. Chem. Soc.*, vol. 89, no. 24, pp. 6024–6030, 1967.
- [104] Z. H. Ping, Q. T. Nguyen, S. M. Chen, J. Q. Zhou, and Y. D. Ding, "States of water in different hydrophilic polymers - DSC and FTIR studies," *Polymer (Guildf.)*, vol. 42, no. 20, pp. 8461–8467, 2001.
- [105] C. C. Lin and A. T. Metters, "Hydrogels in controlled release formulations: Network design and mathematical modeling," *Adv. Drug Deliv. Rev.*, vol. 58, no. 12–13, pp. 1379–1408, 2006.
- [106] T. Takigawa, T. Yamawaki, K. Takahashi, and T. Masuda, "Change in Young's modulus of poly(N-isopropylacrylamide) gels by volume phase transition," *Polym. Gels Networks*, vol. 5, no. 6, pp. 585–589, 1998.
- [107] F. A. Aouada, B.-S. Chiou, W. J. Orts, and L. H. C. Mattoso, "Physicochemical and Morphological Properties of Poly(acrylamide) and Methylcellulose Hydrogels: Effects of Monomer, Crosslinker and Polysaccharide Compositions," *Society*, pp. 2–9, 2006.
- [108] M. M. E. Koenigs, A. Pal, H. Mortazavi, G. M. Pawar, C. Storm, and R. P. Sijbesma, "Tuning cross-link density in a physical hydrogel by supramolecular self-sorting," *Macromolecules*, vol. 47, no. 8, pp. 2712–2717, 2014.
- [109] D. S. Achilias and P. I. Sifaka, "Polymerization kinetics of poly(2-hydroxyethyl methacrylate) hydrogels and nanocomposite materials," *Processes*, vol. 5, no. 2, Jun. 2017.
- [110] M. Hamidi, A. Azadi, and P. Rafiei, "Hydrogel nanoparticles in drug delivery," *Adv. Drug Deliv. Rev.*, vol. 60, no. 15, pp. 1638–1649, 2008.
- [111] S. B. Black, Y. Chang, C. Bae, and M. A. Hickner, "FTIR characterization of water-polymer interactions in superacid polymers," *J. Phys. Chem. B*, vol.

117, no. 50, pp. 16266–16274, 2013.

- [112] M. Gierszewska-Drużyńska, J. Ostrowska-Czubenko, and A. Kwiatkowska, “Effect of ionic crosslinking on density of hydrogel chitosan membranes,” *Prog. Chem. Appl. Chitin its Deriv.*, vol. 18, no. December, pp. 49–58, 2013.
- [113] S. M. Choi, D. Singh, Y. W. Cho, T. H. Oh, and S. S. Han, “Three-dimensional porous HPMA-co-DMAEM hydrogels for biomedical application,” *Colloid Polym. Sci.*, vol. 291, no. 5, pp. 1121–1133, May 2013.
- [114] K. Haraguchi, T. Takehisa, and S. Fan, “Effects of clay content on the properties of nanocomposite hydrogels composed of poly(N-isopropylacrylamide) and clay,” *Macromolecules*, vol. 35, no. 27, pp. 10162–10171, 2002.
- [115] L. W. Xia, R. Xie, X. J. Ju, W. Wang, Q. Chen, and L. Y. Chu, “Nano-structured smart hydrogels with rapid response and high elasticity,” *Nat. Commun.*, vol. 4, pp. 1–11, 2013.
- [116] J. Jang, Y. J. Seol, H. J. Kim, J. Kundu, S. W. Kim, and D. W. Cho, “Effects of alginate hydrogel cross-linking density on mechanical and biological behaviors for tissue engineering,” *J. Mech. Behav. Biomed. Mater.*, vol. 37, pp. 69–77, 2014.
- [117] E. Karpushkin, M. Dušková-Smrčková, M. Šlouf, and K. Dušek, “Rheology and porosity control of poly(2-hydroxyethyl methacrylate) hydrogels,” *Polymer (Guildf)*, vol. 54, no. 2, pp. 661–672, Jan. 2013.
- [118] N. Yacob and K. Hashim, “Morphological effect on swelling behaviour of hydrogel,” *AIP Conf. Proc.*, vol. 1584, no. February, pp. 153–159, 2014.
- [119] S. M. Lanasa, I. T. Hoffecker, and S. J. Bryant, “Presence of pores and hydrogel composition influence tensile properties of scaffolds fabricated from well-defined sphere templates,” *J. Biomed. Mater. Res. - Part B Appl.*

Biomater., vol. 96 B, no. 2, pp. 294–302, 2011.

- [120] J. Díez, L. Barral, R. Bellas, J. López, C. Ramírez, and A. Rodríguez, “Exfoliated/intercalated silicate/hot styrene butadiene rubber nanocomposites: Structure-properties relationship,” *J. Appl. Polym. Sci.*, vol. 125, no. SUPPL. 1, Jul. 2012.
- [121] V. Boyes, “The Synthesis and Development of Novel, Easily Processable Poly(N-Isopropylacrylamide)-Based Hydrogels,” Sheffield Hallam University, Material and Engineering Research Institute, Sheffield, 2012.

2

Experimental

Chapter 2 Experimental

2.1 Analytical Techniques

2.1.1 X-Ray Diffraction (XRD)

XRD is a technique used to identify atomic and molecular crystalline phases and crystal orientation within a sample. Crystals are regular arrays of atoms, and X-rays are high-energy electromagnetic radiation with a wavelength between that of ultraviolet (UV) radiation and gamma-rays in the electromagnetic spectrum. Short wavelength X-rays are suited for the examination of atomic structural arrangements.

The diffractometer generates X-rays by bombarding a metal target (Cu in the instrument used) with a beam of electrons emitted from a hot filament. The X-rays then are focused on a solid sample. The crystals in the sample cause the X-rays to diffract generating a continuous stream of parallel monochromatic X-rays. Measuring the angles and intensities of the diffracted beam provides information about the crystals structure such as the mean positions of the atoms in the crystal. [1][2]

Crystalline material atoms are arranged into atomic planes with interplanar-spacings (denoted by “d”). The angle of incidence of parallel rays is denoted θ . Figure 2.1 is a schematic of a wave scattered from two planes separated by a spacing, d. The difference in path length for the X-rays scattered from top and bottom planes is given by $2d \sin \theta$. Constructive wave interference occurs when waves leave the sample “in phase” with the difference in path length for the top ray and bottom ray equal to an integer number of wavelengths ($n\lambda = 2d \sin \theta$). This gives a reflected beam of maximum intensity. [2]

$$n\lambda = 2d \sin \theta \quad \text{Equation 1}$$

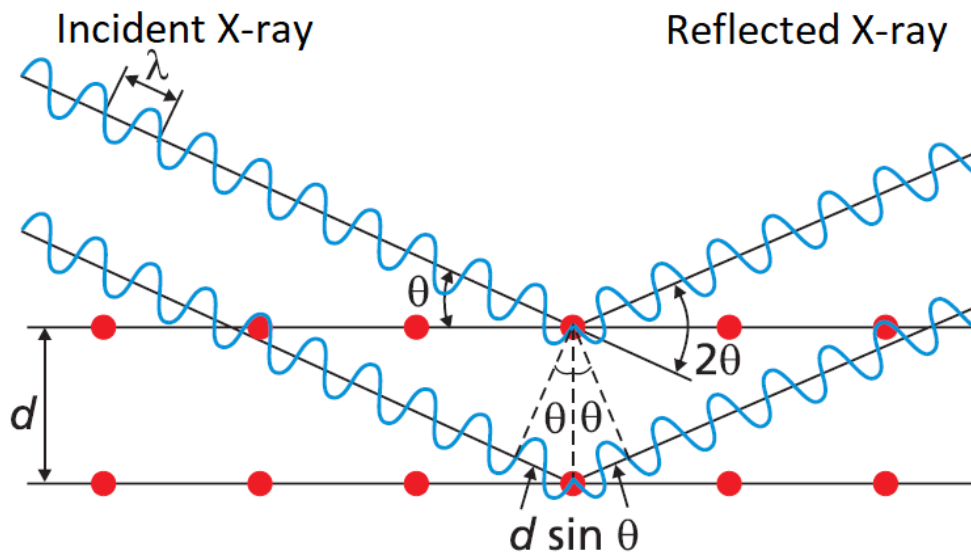


Figure 2.1 Schematic of a wave scattered from two planes separated by spacing d . Modified from [3]

Diffracted beams are received by a detector (Figure 2.2) and their intensity is recorded using a counter mounted on a rotating arm which moves at constant angular velocity. The resulting trace produced gives the diffracted beam intensity as a function of angle 2θ .

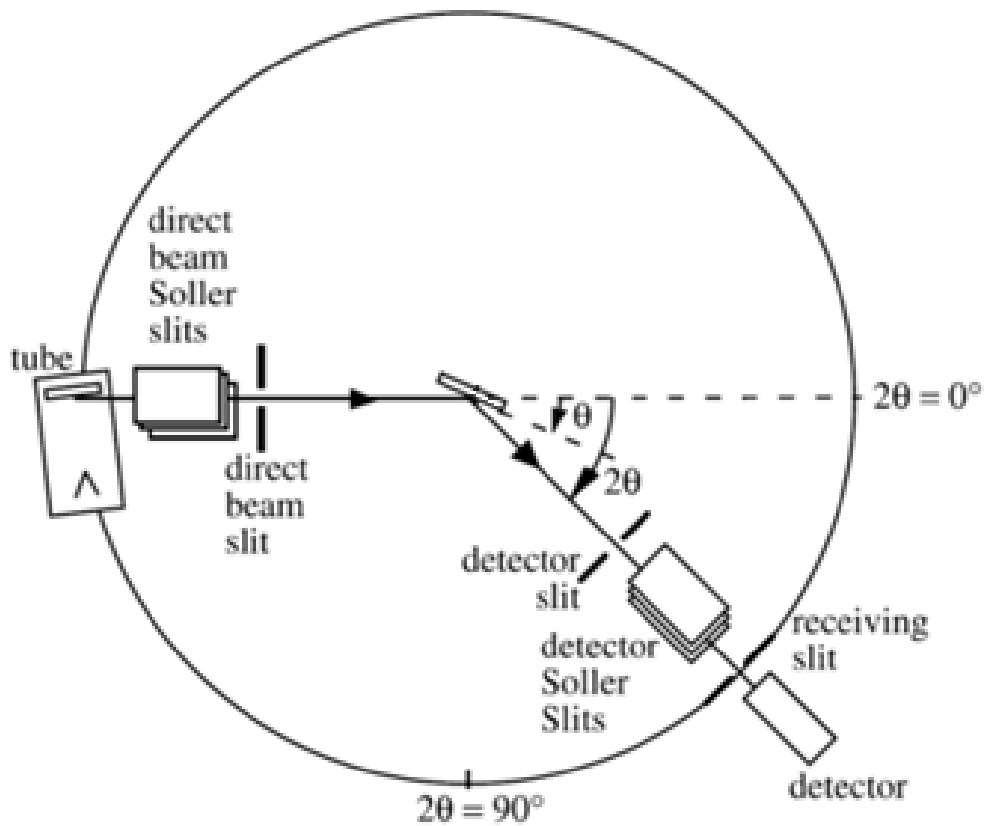


Figure 2.2 Schematic typical components and angles for a θ - 2θ X-ray diffractometer. The flat specimen is at the centre of the goniometer circle. Modified from [4]

2.1.1.1 XRD Experimental Parameters

Diffracted traces were collected using a Phillips-Xpert Diffractometer with Cu X-ray source ($\lambda=1.542 \text{ \AA}$, 40 kV, 40 mA) and a Philips mini prop detector. Standard masks for the X-ray beam ($\frac{1}{4}$ inch divergence slit, $\frac{1}{2}$ inch anti-scatter slit, and a 15 cm fixed mask). Dry powder clay samples and dried fine ground clay-polymer nanocomposite samples were tested.

Clay-polymer hydrogels were synthesised and then oven-dried at 60 °C for five days. Fine powder clay samples (or clay-polymer samples ground by a mortar and pestle) were filled in the sample holder with the top face of the sample holder held down using a solid steel cylinder (Figure 2.3). [5] The sample is then packed into the sample holder to create a flat upper surface and to achieve a random distribution of lattice orientations. [6]

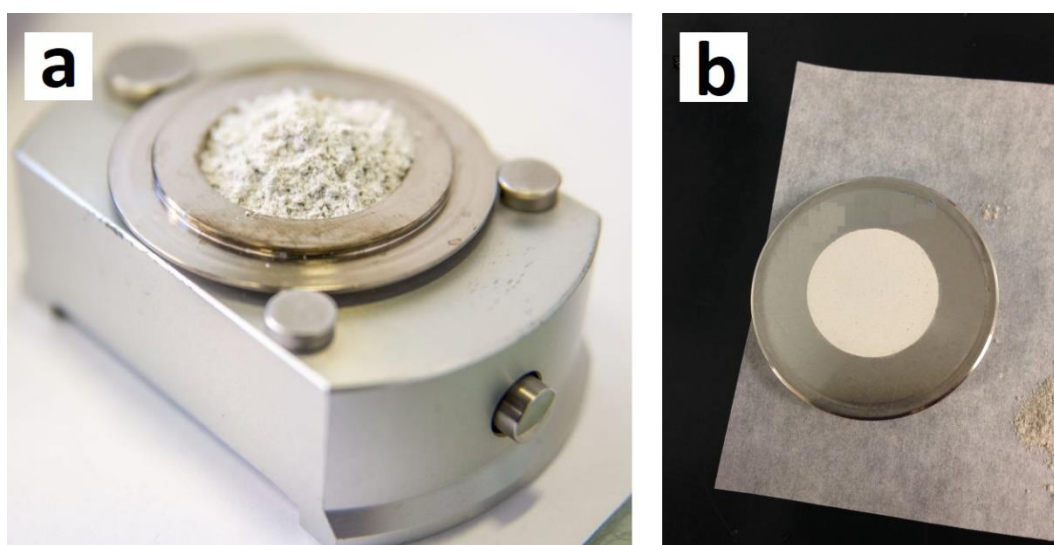


Figure 2.3 XRD a) Sample holder loading with top face down b) smooth surface with top face up.

2.1.2 X-Ray Fluorescence (XRF)

XRF spectrometry is a widely used elemental analysis technique based on the principle that when atoms are excited by an external energy source certain characteristic energies and wavelengths are emitted. X-rays with energy greater than the binding energy of an inner shell electron dislodge and eject an electron (Figure 2.4). An electron from a higher energy orbital shell drops down to the empty

space emitting the energy of a characteristic wavelength (a fluorescent X-ray) and the atom regains stability. The instrument detects the energy of X-rays and matches this to a database to determine what elements are present in the sample.

Counting the photons of the X-ray energy emitted from a sample identify and quantify the elements presented in it. Modern XRF instruments analyse solid and liquid samples for major and trace level components. The analysis time is short and sample preparation is minimal. XRF is not suitable for analysis of very light elements (H to Ne). [7]

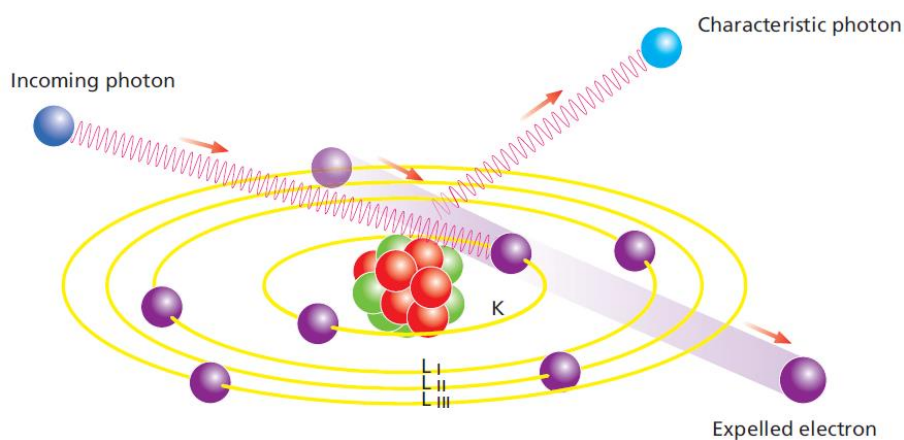


Figure 2.4 Production of characteristic radiation. [7]

2.1.2.1 XRF Experimental Parameters

XRF data was collected using a "PANalyticalMagiX Pro XRF spectrometer" instrument with "PANalytical IQ+" software to interpret the X-ray spectra and to give quantitative results. XRF data from clay powder samples were collected using a fused bead analysis method, where samples are fused into a glass bead at 1100 °C then poured into a mould and allowed to cool. ~1 g of sample is mixed with 10 g of fusion flux (5 g of $\text{Li}_2\text{B}_4\text{O}_7$ and 5 g of LiBO_2). This flux consists of elements which will not be detected by XRF as the elements present in the flux are too light to give strong enough XRF lines that can be easily detected; thus, only XRF lines from the sample of interest will be observed.

The analysis was performed by a laboratory technician (Dr Tony Bell) at the Materials and Engineering Research Institute at Sheffield Hallam University.

2.1.3 Thermogravimetric Analysis (TGA)

Thermogravimetry (TG) is the study of the relationship between a sample's mass and its temperature. [8] Thermogravimetric analysis (TGA) is a technique used to characterise a wide variety of materials in which an excellent precision of the substance mass is monitored. It can be used to study physical (e.g. evaporation) or chemical process (e.g. thermal degradation). Upon heating or cooling a material, the weight increases or decreases as these physical and chemical processes occur. TGA measures the amount and rate of change in the mass of a sample in a controlled atmosphere.

The measurements are used primarily to determine the thermal and/or oxidative stabilities of materials as well as their compositional properties. TGA can quantify significant weight loss of water or solvent, decarboxylation, pyrolysis, oxidation, or decomposition associated with sample degradation. Weight gain indicates a chemical process like oxidation which can be prevented by continuously purging the system with an inert gas that flows over the sample and exits through an exhaust. [9] These measurements provide valuable information that can be used to select materials for certain end-use applications, predict product performance and improve product quality.

The differences of polymers thermal stabilities are easily detected by TGA in terms of temperature range, extent, and kinetics of decomposition and so the technique provides a rapid means to distinguish between polymeric materials. These measurements are useful for the study of polymeric materials such as; thermoplastics, thermosets, composites, films, fibres, and coatings. [10]

The TGA arrangement consists of a sample crucible able to withstand the highest temperature used in the experiment, and not chemically interact with the sample. The crucible is loaded with a sample and supported on a high precision balance. The crucible (residing in a temperature-controlled furnace) is heated and the sample mass is monitored as it is heated by a linear temperature gradient (which can exceed 1000 °C if required). The sample weight is plotted relative to the

temperature in real-time using appropriate software. The resulting weight loss/gain curve is affected by several factors like the sample mass and size, the sample form (block or powder), the gas purge rate and type (oxidative or pyrolysis). Generally, a slower heating rate reveals a more detailed weight loss curve and ensures the recorded temperature is closer to that of the whole sample. [11]

Figure 2.5 shows the weight change as a function of temperature. A transformation to 1st derivative weight loss curve (DTG) is often useful to help distinguish subtle event differences when weight loss curves look similar. The peak of the 1st derivative indicates the point of the greatest rate of change on the weight loss curve. [11]

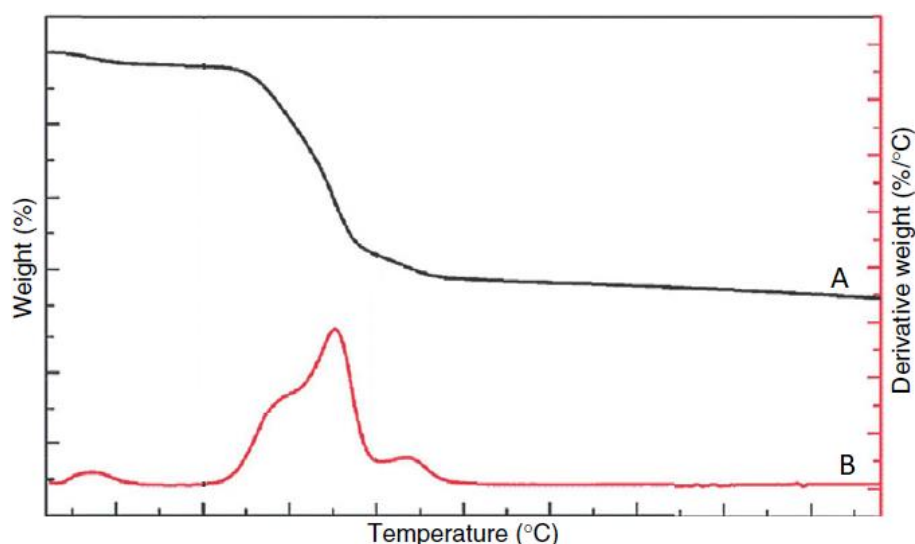


Figure 2.5 A) TG thermogram curves. B) DTG derivative thermogram curves. Modified from [12].

2.1.3.1 TGA Experimental Parameters

Thermogravimetric analysis was performed using a Mettler TG50 with 40 ml min⁻¹ N₂ purge. Placed into a clean, dry alumina crucible, clay and clay polymer nanocomposites samples were heated from 20 °C to 900 °C at a constant rate of 20 °C min⁻¹. Powder clay samples were weighed and loaded to the instrument. Clay-polymer nanocomposites were oven-dried and ground using a pestle and mortar prior to analysis.

2.1.4 Scanning Electron Microscopy (SEM)

Scanning electron microscopy (SEM) is an analytical technique used to obtain high-resolution images of samples surfaces. It requires an electron optical system to produce an electron beam, a stage to place the specimen on, an electron detector, and a display unit.

As the SEM instrument fires electrons at the sample, several different signals can be given as a result of electron-sample collisions (Figure 2.6). Among the various signals, three of the most important are backscattered electrons, secondary electrons, and X-rays. The X-rays are used for elemental analysis of the sample (Energy Dispersive X-ray spectroscopy EDS). SEM imaging utilises the other two types of electrons (Backscattered and Secondary Electrons BSE) to form an image by scanning the electron beam across the sample and recording the electrons ejected from the sample using detectors which pick up the signals to create a magnified image of the sample. [13]

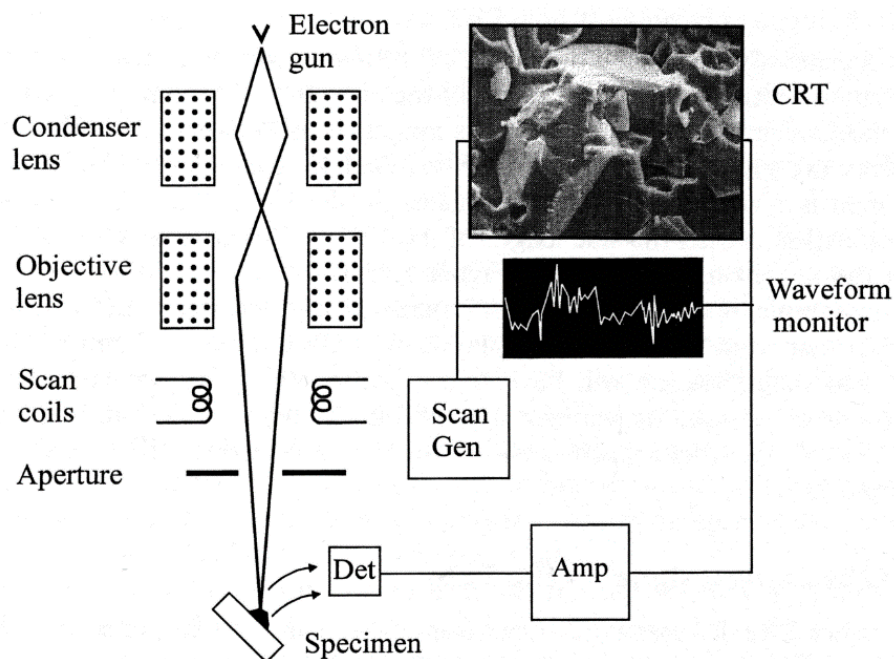


Figure 2.6 Schematic of a Scanning Electron Microscope. [14][15]

High-resolution SEM images are produced by the detection of secondary electrons emitted from the specimen by a secondary electron detector, the secondary electrons are attracted to the tip of the detector due to the high voltage applied to

it. The output signals from the secondary electron detector are amplified and then transferred to the display unit. [14][15]

With a magnification capability of approximately 10x to 500,000x a surface area of between approximately 5 μm to 1 cm can be imaged at any one time with a conventional SEM setup. Details of the structure and surface texture are revealed as a 3-dimensional image is constructed. Samples typically are around 10 cm in width and not more than 4 cm in height to fit into the chamber and must be self-supporting. The chamber is vacuumed to 10^{-5} - 10^{-6} torr, and as such samples must be stable under these conditions. [16] Electrically insulating samples must have an electrically conductive coating (usually carbon or gold) for study in conventional SEM systems.

2.1.4.1 SEM Experimental Parameters

The electron micrographs were taken at the Materials and Engineering Research Institute at Sheffield Hallam University using a FEI NOVA nanoSEM 200 Scanning Electron Microscope. A Backscattered and Secondary Electrons “Helix Detector” insert was used to obtain the images together with an accelerating voltage of 5 kV and a spot size of 4.0. In this thesis, all SEM data was collected in conventional SEM mode for the gold coating samples. Clay-polymer hydrogels were flash-frozen in liquid nitrogen and then were freeze-dried overnight in an attempt to maintain the 3D structure. The ImageJ images processing software was used for the measurement of the pore size, it is a software that helps to measure distances and areas on images after a known scale is presented.

2.1.5 Infrared (IR) Spectroscopy

Infrared spectroscopy is one of the most important analytical techniques available to scientists. The principal advantage of infrared spectroscopy is that any sample in any state may be studied. In basic terms, IR spectroscopy relies on the absorption of electromagnetic radiation at frequencies that correlate to the vibrational energy level of specific chemical bonds within a molecule. [17] The vibrational spectrum of

a molecule is characteristic of the molecular structure of the molecule. The infrared spectrum of the sample is obtained by passing infrared radiation through a sample, and by determining the absorbed fraction of the radiation at each particular energy level. Comparing the spectrum from an “unknown” substance to previously recorded reference spectra allows an infrared spectrum to be used as an identification fingerprint for organic and inorganic compounds. [18]

For IR spectroscopy, the wavelength (λ) is presented as “wavenumbers” in cm^{-1} . The wavenumber is equal to $1/\lambda \text{ cm}^{-1}$. Electromagnetic radiation is absorbed by molecules at only specific wavelengths. [19]

The vibrational energy corresponds to the absorption of energy by a molecule as the atoms vibrate about the mean centre of their chemical bonds. The Planck-Einstein equation (Equation 2) shows the relationship between the energy of a photon (E) in J/photon, Planck’s constant (h) ($6.625 \times 10^{-34} \text{ m}^2 \text{ kg s}^{-1}$ or Js), and the frequency of the electromagnetic wave (ν) in 1/s:

$$E = h\nu \quad \text{Equation 2}$$

Vibrational frequency is proportional to the square root of the ratio of the vibrational force which in turn is proportional to the masses of the corresponding atoms. So, the lower the atomic mass is (stronger bond), the higher the vibrational frequency. i.e. $\text{C}\equiv\text{N}$ and $\text{C}\equiv\text{C}$ bond stretches occur at higher frequencies than those of $\text{C}=\text{O}$, $\text{C}=\text{C}$, and $\text{C}=\text{N}$ which have higher frequencies than $\text{C}-\text{H}$, $\text{O}-\text{H}$, $\text{C}-\text{C}$, $\text{C}-\text{N}$, and $\text{N}-\text{H}$. In addition, $\text{C}-\text{H}$ stretching occurs at a higher frequency than $\text{C}-\text{C}$, and $\text{C}-\text{O}$ stretching occurs at a frequency lower than both.

The fundamental requirement for infrared activity is that specific vibrational energies for a given system are possible, so photons with specifically related energies will only be absorbed. Therefore, a change in molecular vibration occurs when the photon frequency matches the vibrational frequency of the molecule, leading to the absorption of infrared radiation. For absorption to occur, a net change in dipole moment during the vibration is also required. [17]

2.1.5.1 Fourier Transform Infrared (FTIR) Spectroscopy

(FTIR) spectroscopy is based on the interference of radiation between two beams to yield a signal produced as a function of the change of pathlength between the two beams. The distance and frequency are interconvertible by *Fourier-transformation*.

The source emerging radiation is passed through an interferometer to the sample then to a detector. Upon signal amplification, the data are converted from analogue to digital and transferred to the computer for Fourier-transformation Figure 2.7. [18]

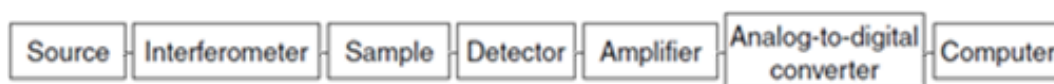


Figure 2.7 Basic components of an FTIR spectrometer. [18]

The most common interferometer used in FTIR spectrometry is a Michelson interferometer, which consists of two perpendicular plane mirrors, with one travelling in a perpendicular direction to the plane (Figure 2.8). A beamsplitter (*semi-reflective film*), bisects the planes of these two mirrors. When a radiation beam with wavelength λ (cm) is passed into a beamsplitter half of it reflects at a moving mirror while the other half transmits to a fixed mirror. The two beams combine at the beam splitter again and changes in the relative position of the mirrors generate an interference pattern.

Half of the beam reflected from the fixed mirror is transmitted through the beamsplitter while the other half is reflected back to the source. The beam which emerges from the interferometer at 90 degrees to the input beam is called the transmitted beam and this is the beam detected in FTIR spectrometry. Applying a Fourier Transform mathematical operation to the intensity of the path-length difference over the recombined beam contains information about the frequencies present in the beam as a graph. [20][18]

When high refractive index light (n_1) propagates through the material at a certain angle ($\theta_i > \theta_c$) it reflects internally with a lower refractive index (n_2). At the

reflection, a wave with components in all directions is formed (evanescent wave). For the beam to reflect, the crystal refractive index must be greater than that of the sample.

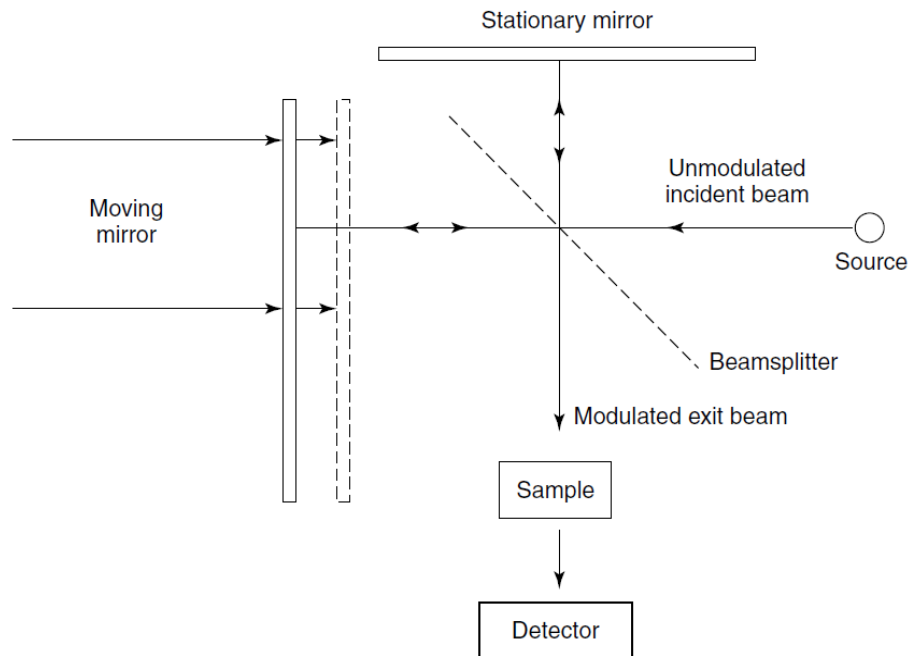


Figure 2.8 Schematic of a Michelson interferometer.

Sample setup can be different depending on the phase of the sample, full contact between the sample and the crystal is essential. A small amount of a liquid sample poured directly onto the crystal is enough whereas a plate presses the sample onto the diamond crystal surface for solid sample analysis (Figure 2.9). [20]

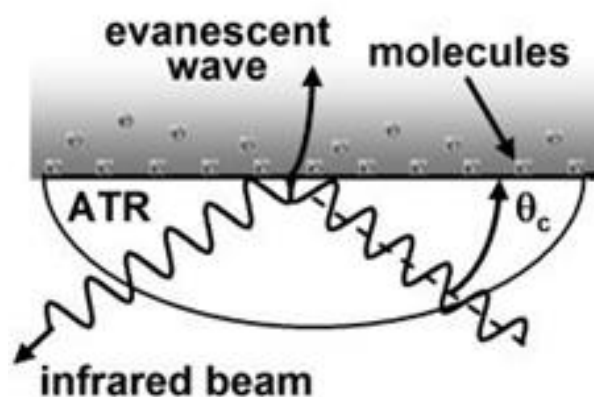


Figure 2.9 Schematic of ATR apparatus.

2.1.5.2 FTIR Experimental Parameters

Spectra were collected using "Graseby Specac Single Reflection Golden Gate ATR" sampling accessory, attached to "Thermo Nicolet Nexus Spectrometer". The spectra for clay powder samples and hydrogels were collected using 64 scans at a resolution of 4 cm^{-1} . The clay-polymer nanocomposites used were the same oven-dried ground powders described in Sections 2.1.3.1 and 2.1.4.1.

2.1.6 Rheology and Viscoelasticity

Rheometry is the technique used to determine the rheological properties of materials experimentally; this assists in defining rheology as the science which studies flow and deformation of matter for a better understanding of the interrelation between force, deformation, and time. The term was invented by Professor Bingham of Lafayette College. It is a branch of physics since the most important variables come from the field of mechanics: forces, deflections, and velocities. The term rheology (*rheos*: Greek for flowing or streaming) literally means flow science.

Rheological experiments reveal information about the deformation behaviour of solid-like materials produced by shear forces and the flow of liquid-like materials, particularly about the behaviour of complex viscoelastic materials (which represent most real materials). For example, gum eraser is a viscoelastic solid and wallpaper paste is a viscoelastic liquid.

Before 1980, rheological experiments were carried out as rotational tests which enabled the characterisation of flow behaviour at medium and high velocities. As measurement technology has developed, investigations were expanded on deformation and flow behaviour which also covers the low-shear range. The rheometrical study is motivated by the hope that flow behaviour can be correlated to measured geometrical function. Hence it is of potential importance for the industry in quality and process control. In future rheometry may also be relevant in

process modelling when the full potential of computational fluid dynamics is realised within a rheological context. [21][22][23]

2.1.6.1 Viscosity

Materials clearly showing a flow behaviour are referred to as fluids (liquids and gases). Molecules show relative motion between one another for all flowing fluids, in the shear flow, they shear past one another, whilst in the extensional flow, they flow away or towards one other, this process is always combined with internal frictional forces. The easiest flow to measure on a rheometer or viscometer is shear flow. A certain flow resistance occurs for all fluids in motion which may be determined in terms of the viscosity.

To understand viscosity, terms related to it need to be defined. The simplest explanation of shear flow is to imagine layers sliding over each other; the uppermost layer has maximum velocity while the bottom layer is stationary. Shear force takes the form of shear stress (τ) which is defined as a force (F) over a unit area (A) (Figure 2.10). The upper layer moves a distance x , while the bottom layer remains stationary. The term shear strain (γ) defines a displacement gradient created across the sample (x/h). For a solid, no flow is possible, so the strain is finite for applied stress. For a fluid, the shear strain will continue to increase for the period of applied stress. This creates a velocity gradient called shear rate or strain rate ($\dot{\gamma}$) which is the rate of change of strain with time ($d\gamma/dt$). It is easier to understand the relation of these terms to viscosity mathematically.

- Shear Stress:

$$\tau = F/A \text{ (Pa)} \quad \text{Equation 3}$$

where:

τ : Shear stress (Pa), F : Shear force (N) and A : Shear area (m^2).

- Shear Strain

$$\gamma = x/h \quad \text{Equation 4}$$

Where:

γ : Shear Strain, x : Distance (m), h : Height (m).

- Shear Rate or Strain Rate:

$$\dot{\gamma} = v/h \text{ s}^{-1} \quad \text{or} \quad \dot{\gamma} = d\gamma/dt \text{ s}^{-1} \quad \text{Equation 5}$$

where:

$\dot{\gamma}$: Shear rate (s^{-1}), v : Velocity (ms^{-1}) and h : Distance (m).

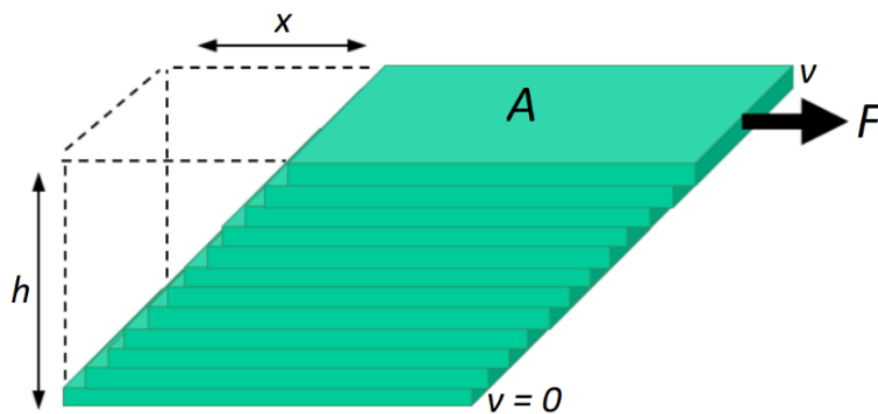


Figure 2.10 Plates-Model for shear illustrating the velocity distribution of a flowing fluid

When the shear stress is applied to a fluid, the momentum is transferred through the layers of fluid by collisions and interactions. The ratio of shear stress to shear rate is defined as the shear viscosity or dynamic viscosity (η) measured at constant pressure and temperature, and can be calculated as:

$$\eta = \tau/\dot{\gamma} \text{ (Pa.s)} \quad \text{Equation 6}$$

where:

η : Viscosity (Pa)

For Newtonian fluids, the shear stress is linearly related to the shear rate (Figure 2.11). Newtonian fluids include water, simple hydrocarbons, and dilute colloidal dispersions. For non-newtonian fluids, the viscosity varies with the applied shear rate or shear stress.

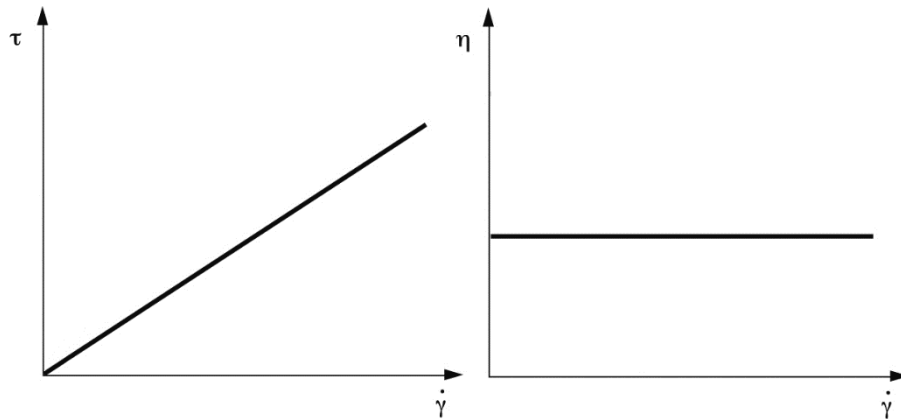


Figure 2.11 Left) Viscosity curve of a Newtonian fluid, Right) Flow curve of a Newtonian fluid.

2.1.6.2 Shear Thinning

For non-Newtonian fluids, if viscosity decreases as shear rate increases it is described as Shear Thinning (pseudoplastic) flow. Shear thinning fluids show a constant viscosity at low shear rates η_0 , and a large drop in viscosity is observed at critical shear stress or shear rate.

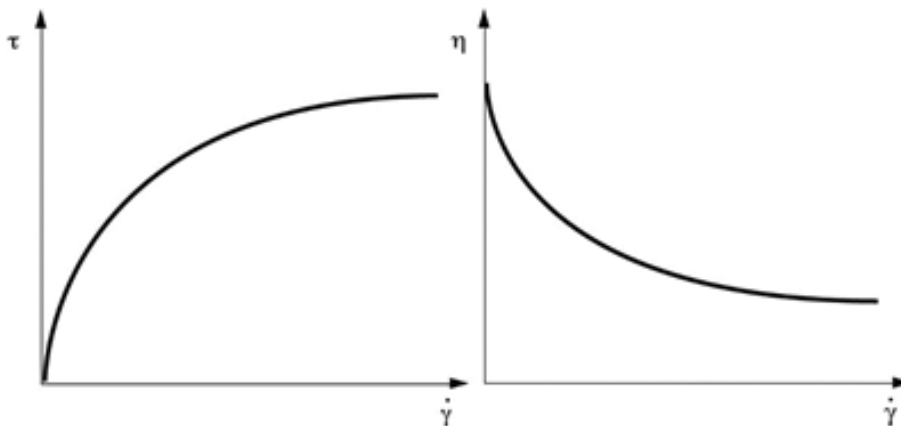


Figure 2.12 Left) Viscosity curve of shear thinning liquid, Right) Flow curve of shear thinning liquid.

A shear thinning region can be viewed on a double logarithmic scale (Figure 2.12). At very high shear rates another constant viscosity can be observed, called the infinite shear viscosity η_∞ . Polymer solutions (e.g. methylcellulose), unfilled polymer melts, most coatings, glues, and shampoos are all examples of shear-thinning materials. Shear thinning is the result of micro-structural rearrangements occurring in the plane of applied shear and is observed for dispersions as well as polymer solutions. In polymer solutions at rest, each macromolecule is in the state of the lowest level of energy consumption; therefore, it shows the shape of a three-

dimensional coil. Coils show a semi-spherical shape and are entangled with neighbouring macromolecules. As the shear process occurs, the molecules become oriented in the shear direction. When in motion, the molecules disentangle, and flow resistance reduces. An illustration of shear-induced orientation which can occur for various shear thinning material (polymer chain as an example) is shown in Figure 2.13.

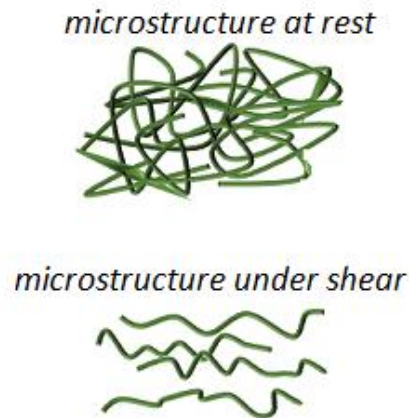


Figure 2.13 Macromolecules, showing coiled and entangled chains at rest and oriented and partially disentangled chains under shear load.

2.1.6.3 Shear Thickening

Shear-thickening and dilatant materials have an identical meaning; their viscosity increases as the shear rate or shear stress increases (Figure 2.14). Shear-hardening, or solidifying are also terms which are sometimes used to describe the same phenomenon.

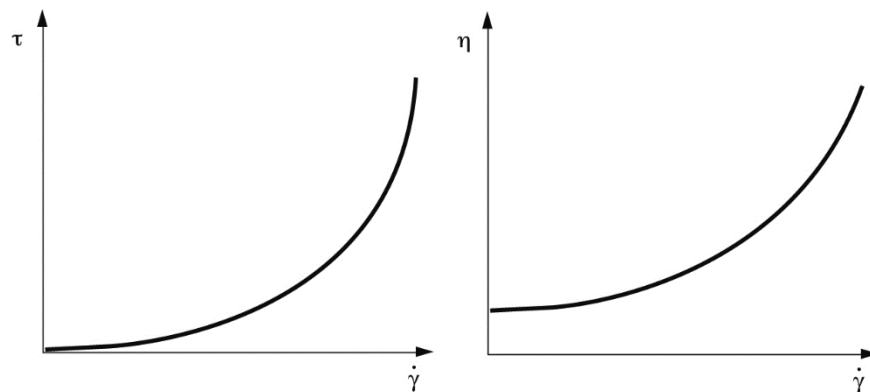


Figure 2.14 Left) Flow curve of a shear-thickening Liquid, Right) Viscosity curve of a shear thickening liquid.

Suspensions or dispersions which have a high concentration of solid particles usually show shear thickening. Shear thickening materials are less common in industrial applications however these materials are useful in specific applications such as high impact protective equipment and shock absorbers. However, shear thickening can lead to problems with flow processes, so it is often an unwanted effect. If tested or in use flow should be carefully observed. To investigate this, tests need to be repeated several times under identical conditions for reproducibility.

Generally, shear thickening occurs for suspensions that show shear thinning at lower shear rates and stresses. In suspensions with high particle concentrations at high shear rates, the particles come into contact with each other more regularly. Softer and gel-like particles may become compressed and flow resistance will increase. The particle shape plays a crucial role. Shear gradients occurring in each flowing liquid cause the particles to rotate and move in the shear direction.

Shearing highly concentrated, chemically unlinked, polymer solutions and melts may cause shear-thickening due to mechanical entanglements between the molecule chains. The higher the shear rate or shear stress the more the molecule chains open-up and stretch causing some exposure of the chain that can create transient intermolecular associations that can then prevent relative motion between neighbouring molecules.

2.1.6.4 Yield Stress

A sample will not begin to flow before the external forces F_{ext} acting on it are larger than the internal structural forces F_{int} ; The term “yield stress” is used to indicate that point. The yield point is also referred to as the yield stress or yield value. Below that point, the sample exhibits an elastic behaviour with a degree of deformation that recovers after removing the load.

Many shear thinning fluids have both liquid and solid-like properties. At rest, they form intermolecular networks because of polymer entanglements, or other interactions.

Figure 2.15 shows shear stress against shear rate for different fluid types. For fluids with a yield stress, the curves intercept the shear stress axis at a higher value greater than zero.

To measure the yield stress, applying a shear stress ramp can be useful (Figure 2.15 b), as a viscosity peak can be observed indicating the value of the yield point. Prior to that peak, the sample deformation is elastic. The peak represents the point at which the material starts to flow, and structure breaks down. If there is no peak this indicates that the material does not have yield stress under the conditions of the test. Understanding yield stress helps the industry to relate and improve properties such as stability of a suspension and sagging of film on vertical surfaces.

There are many examples of such material both in research fields and in the industry, gels, dispersions with a high concentration of solid particles, conductor pastes, sealants, ceramic masses, semi-solid materials. Examples can also be seen in daily life; toothpaste, margarine, lipsticks, creams, ketchup, mayonnaise, chocolate melts, and yoghurts.

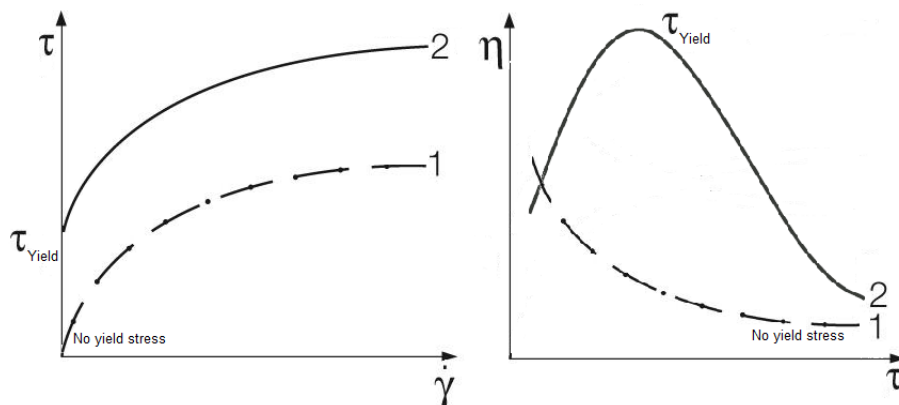


Figure 2.15 Left) Without and with τ_y , τ_y is interception on the τ - axis, Right) With and without yield stress corresponding to viscosity, τ_y is the point the peak.

2.1.6.5 Viscoelasticity

Viscoelasticity describes materials which show behaviour between that of an ideal liquid (viscous) and ideal solid (elastic). Oscillatory shear rheometry is the primary technique that is used to measure viscoelasticity.

2.1.6.5.1 Elastic Behaviour

Structured fluids have a minimum energy state associated with an 'at rest' microstructure. Applying an external force to a structured fluid creates an elastic force that tries to restore the microstructure to its initial state. The applied stress is proportional to the resultant strain if the elastic limit is not exceeded, and the structured fluid will start to return to its initial shape as soon as the stress is removed. If the applied stress exceeds the elastic limit the relationship will become non-linear and the structured fluid may be permanently distorted.

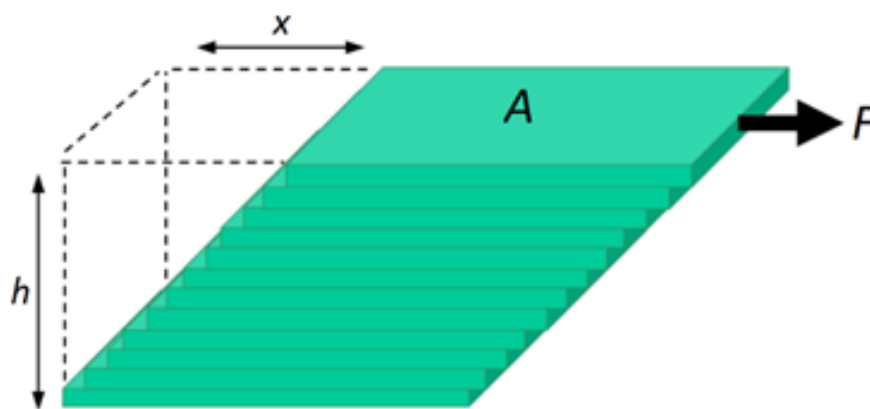


Figure 2.16 Solid deforming elastically under shear force

The elastic modulus (G) is the constant of proportionality for elastic shear deformation. Similar to how viscosity is a measure of the resistance to flow the elastic modulus is a measure of resistance to deformation (Figure 2.16).

$$\gamma = \tau / G \quad \text{Equation 7}$$

Where:

τ : Shear stress (Pa), γ : Shear Strain, G : Elastic Modulus

2.1.6.5.2 Viscous Behaviour

When a stress is applied to a fluid, the dashpot starts to deform immediately at a constant strain rate. For an ideal liquid, the strain is expressed as:

$$\gamma = \tau/\eta$$

Equation 8

Where:

γ : Shear Strain, τ : Shear stress (Pa), η : Viscosity (Pa)

2.1.6.5.3 Viscoelastic Behaviour

Viscoelastic materials show viscous and elastic behaviour simultaneously. Most of the materials exhibit rheological behaviour that puts them in this region. It is possible to illustrate a viscoelastic liquid using a combination of a spring and a dashpot connected in series. The spring portion of the model represents the elastic behaviour, and the dashpot part of the model represents the viscous behaviour (Hooks law and Newtons law, respectively) which is called the Maxwell model in honour of James C. Maxwell (1831 to 1879), who first presented the mathematical fundamentals. To represent a viscoelastic solid, the Kelvin-Voigt model (Figure 2.17) is used which utilizes the same combination of elements in parallel.

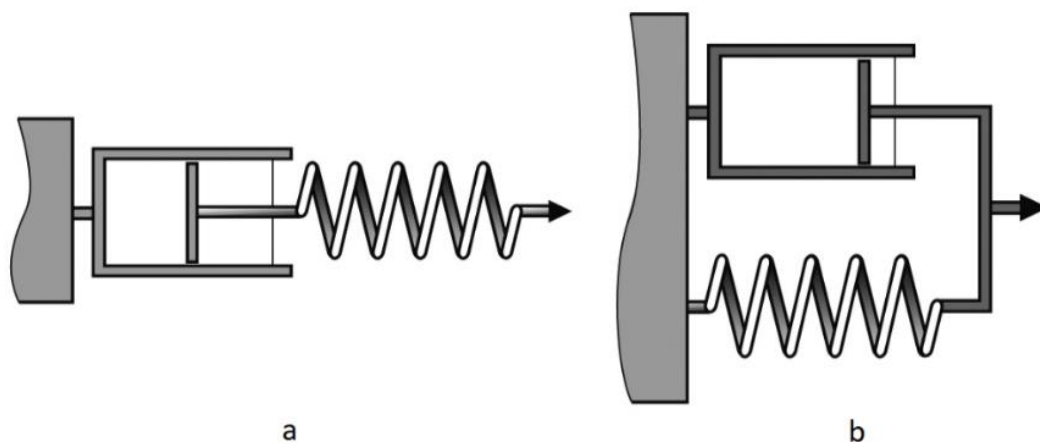


Figure 2.17 (a) Maxwell model (simple viscoelastic liquid); (b) Kelvin-Voigt model (viscoelastic solid).

If a stress is applied to a Maxwell model, the response is predominantly elastic at short times and governed by G , and has a viscous response at longer times and governed by η .

2.1.6.6 Rheology Experimental Parameters

Rheological experimental analysis was performed using an Anton Paar "Physica MCR Series" rheometer using a parallel-plate measuring system (PPMS) geometry (Figure 2.18) for testing clay suspensions and clay-polymer hydrogels.

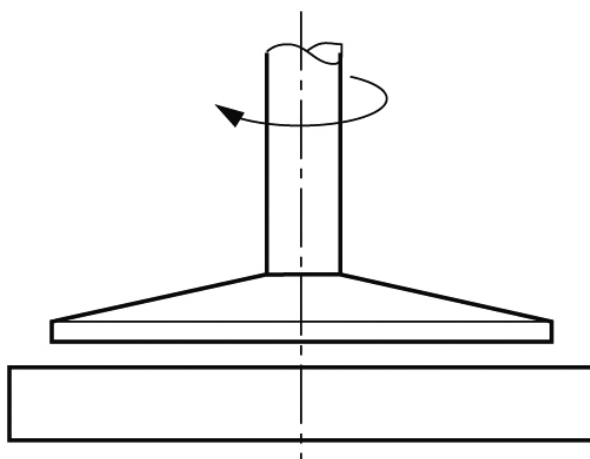


Figure 2.18 Parallel-plate measuring system (PPMS) geometry. Modified from [23].

Placed between the clean parallel plates, clay suspensions and clay-polymer hydrogels were subjected to a constant temperature to reach thermal equilibrium before the testing start. To better control the environment around the samples and to prevent dehydration a moisture control tool was used on top of the samples (Figure 2.19), however still some dehydration was noted, and a wet sponge was used on top of this for a better seal.

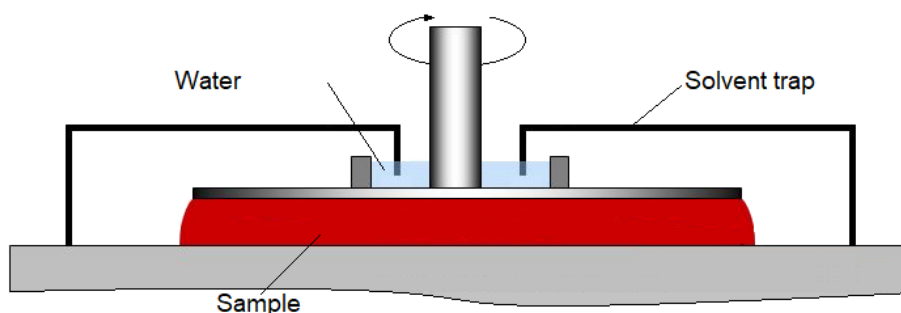


Figure 2.19 Moisture control device provided by the instrument manufacturer.

For the clay suspensions, a simple viscosity curve was determined by performing a shear rate run to find the values of clay suspensions viscosity at the different shear rate and the way clay suspension behave over a range of shear rate (shear thinning or shear thickening).

For clay-polymer hydrogels. At first, a time sweep was performed to determine how long it takes the samples to reach an equilibrium state. Strain sweep was then performed to determine the linear viscoelastic region (LVE) of the sample with respect to strain. A frequency sweep determines the linear equilibrium modulus plateau, the values from these three test were then used to design:

- Temperature sweep to show the viscosity behaviour over a cooling temperature sweep for thermo-responsive hydrogels.
- Strain sweep to show the different yield point on a flow curve and the behaviour of the storage modulus (G') and loss modulus (G'') values as a function of strain up to 100 % strain.
- Frequency sweep to show the behaviour of the storage modulus (G') and loss modulus (G'') values as a function of frequency up to 100 Hz.
- Oscillatory cooling temperature sweep at a constant strain and frequency to determine the behaviour of the loss modulus and storage modulus as a function of temperature for the thermo-responsive nanocomposites.

2.2 Materials and Sample Synthesis

2.2.1 Clays

In this work, the clay material used is synthetic smectite that resembles the natural clay mineral hectorite in both structure and composition. Five grades of Laponite[®] (Laponite EL, Laponite FN, Laponite OG, Laponite RD, Laponite XL21) supplied by BYK Additives & Instruments as a white powder, and a bentonite Cloisite[®] Na⁺ (CNa⁺) as a yellowish powder, were used as received without any further purification. [24][25][26][27][28]

Laponite[®] **EL** is a lithium magnesium sodium silicate which was developed to be more tolerant in higher **EL**ectrolyte conditions. It produces shear sensitive and thixotropic structure products when dispersed in water. It is particularly useful with

formulations that contain high levels of salts or surfactants, showing an increased efficiency and gel strength in such systems compared with other Laponite grades. Laponite[®] **OG** is a very similar grade which was developed to be compatible with an **OrGanic** modification. Laponite[®] **RD** falls in the same chemical category, it is a very early grade in the development of Laponite for **Rapid-Dispersing**, it swells producing a translucent and colourless colloidal dispersion, but it is water insoluble. [29][30][31]

Laponite[®] **FN** is a synthetic layered fluorosilicate which contains structural **F**luorine, the **N** refers to the project that it was developed for by the manufacturer. This grade is water insoluble but hydrates and swells producing translucent and colourless colloidal dispersions. Its particles are primarily larger with higher cation exchange capacity than other Laponite[®] grades. [32]

Laponite[®] **XL21** is a sodium magnesium fluorosilicate, a high purity grade, certified low heavy metal and low microbiological content developed to control the rheological properties of personal care and cosmetic products, this is still an experimental grade and as such limited data is available in the literature and little data is provided by the supplier. The **XL21** included in the name of this Laponite[®] has no relation to any particular properties of the material; it behaves like Laponite[®] **FN** and Laponite[®] **RD** in water. [33][34]

The Laponite[®] clay platelets vary in surface dimensions and are approximately 1 nm thick charged discs. Clay crystals carry a charge caused by the substitutions of certain atoms in their structure where the Si^{4+} may be replaced by trivalent cations (Al^{3+} or Fe^{3+}) in the tetrahedral sheet, or the Al^{3+} may be replaced by divalent cations (Mg^{2+} or Fe^{2+}) in the octahedral sheet. As the replacement happens a negative potential is created at the surface of the clay due to the charge deficiency. [35] The negative potential is balanced by the adsorption of cations on the surface. In aqueous suspension, ions may exchange with ions in the bulk solution (known as exchangeable cations). The total amount of cations adsorbed on the clay is called

the cation exchange capacity (CEC). It is an important characteristic of the material. [36]. The general chemical composition of the dry powder is $Na_{0.7}^+[(Si_8Mg_{5.5}Li_{0.3})O_{20}(OH)_4]^{0.7-}$. [26][27][28] Table 2.1 shows the particle size, CEC and the chemical composition (dry basis) for the different Laponite[®] grade as provided by the manufacturer. Most of the Laponite[®] grades produce an optically transparent suspension in water.

Table 2.1 Clay platelet size, CEC, and chemical composition by weight %. [29][30][31][32][33][34]

Laponite	Platelet Size (nm)	CEC (meq/100g)	Chemical Composition				
			SiO ₂	MgO	Li ₂ O	Na ₂ O	F
EL	44	75	59.5	27.5	0.8	2.8	0.0
FN	140	130	62.4	21.7	2.5	2.2	4.2
OG	83	60	59.5	27.5	0.8	2.8	0.0
RD	40	55	59.5	27.5	0.8	2.8	0.0
XL21	60	107	No data available				

The Cloisite[®] Na+ platelets are 100 nm wide across the surface and are 1 nm thick and produce an opaque suspension. The chemical composition of the dry Cloisite[®] Na+ is $Na_{0.33}[(Al_{1.67}Mg_{0.33})(O(OH))_2(SiO_2)_4]$. The Cloisite Na+ CEC is on average 90 meq/100g. Figure 2.20 shows the differences in chemical structure and composition between hectorite (presenting the Laponite[®]) and bentonite (presenting the Cloisite[®] Na+). [24][25][37][38]

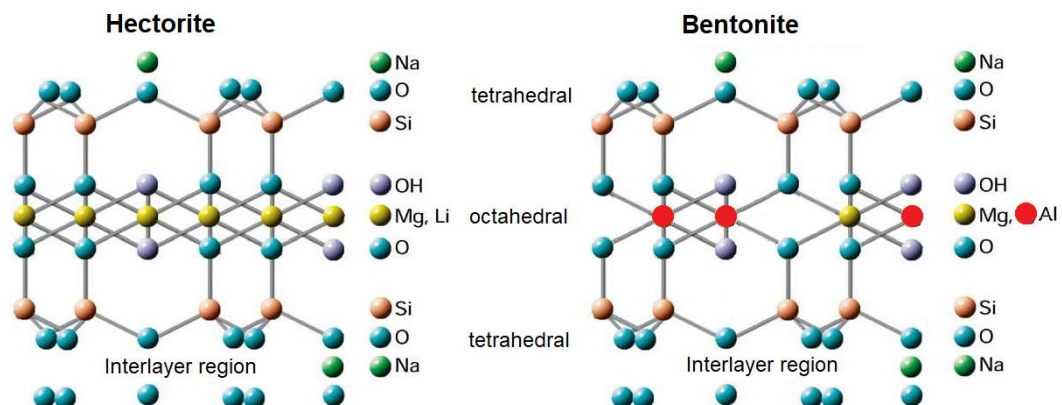


Figure 2.20 The layer structure of Hectorite and Bentonite. [33][39]

2.2.2 Polymers

2.2.2.1 Acrylamide

Poly(N-isopropylacrylamide) (pNIPAM) is a water-soluble polymer; which has a well-defined thermoresponsive stimulus sensitivity. [40] Around its lower critical solution temperature (LCST) the pNIPAM undergoes a fast and reversible transition in aqueous media. Above the LCST the pNIPAM chains are dehydrated. Below the LCST the pNIPAM chains are hydrated and flexible in the water. pNIPAM is being studied extensively in both fundamental and application based studies and there is a constant drive to engineer the functionality of its thermo-responsivity. [41] [42] [43]

Thermo-stable poly(N,N-dimethylacrylamide) (pDMAc) can also absorb large amounts of water similar to poly(N-isopropylacrylamide) (pNIPAM). pDMAc can be easily altered because it dissolves in water, the polymer solutions formed are stable against temperature changes. [44][45] pDMAc can be used in contact-lens fabrication and adhesives manufacturing and drug delivery. [46]

2.2.2.2 Methacrylates

The interest in the polymerisation of methacrylate is due to its relatively easy radical reactions with the hydroxyl groups that provide hydrophilicity.

Hydroxyethyl methacrylate (HEMA) is a hydrophilic monomer used to prepare hydrogels. Its polymer (pHEMA) is an excellent biocompatible material and has physicochemical properties like living tissues. It is widely used to manufacture contact lenses due to its homogeneous network structure and water distribution which results in optical clarity. [47][48]

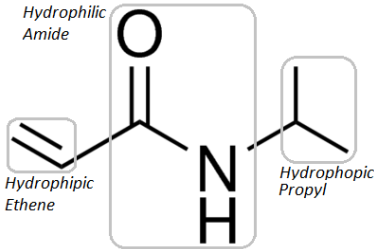
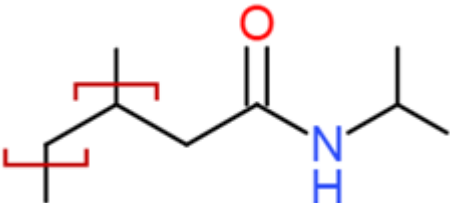
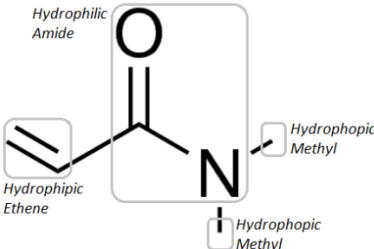
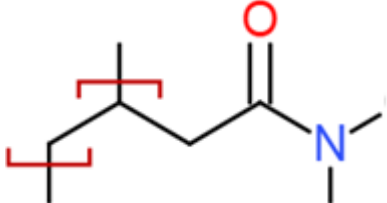
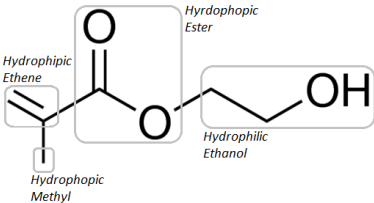
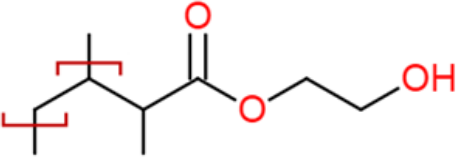
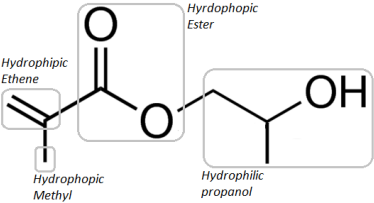
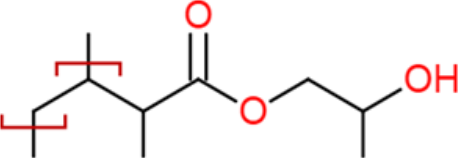
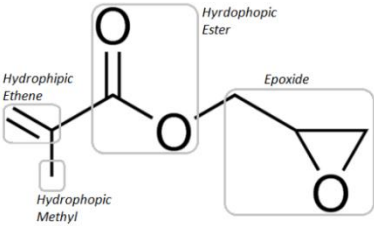
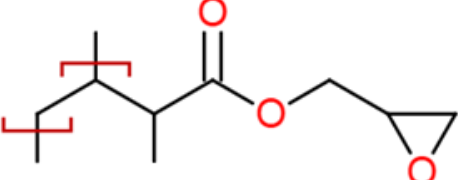
Most of the hydrophilic behaviour of pHEMA is due to the hydroxyl group (-OH) present. At this location, hydrogen bonding with water molecules occurs, causing them to be drawn into the polymer matrix. [49]

Hydroxypropyl methacrylate (HPMA) is a water-soluble monomer, it contains a functional group that can be easily polymerized and crosslinked. Poly(hydroxypropyl methacrylate) pHPMA has better shrinkage resistance and water resistance than pHEMA. It is biocompatible and can be easily copolymerized with another water-soluble block. [50][51]

2,3-Dihydroxypropyl methacrylate, otherwise known as glycerol methacrylate [GMAc], has highly hydrophilic functional monomers which contain two hydroxyl groups and epoxy group. It is of interest for the preparation of biocompatible amphiphilic networks, [49][52] and It can be used in soft contact lenses. [51] It is a low-cost reagent as it is widely used for the industrial production of epoxy-functional methacrylic resins used in coatings and adhesives. [53]

N-Isopropylacrylamide 99% (NIPAM) monomer, *N,N*-Dimethylacrylamide 99% (DMAc) monomer, Hydroxyethyl methacrylate 99% (HEMA) monomer, Hydroxypropyl methacrylate 99% (HPMA) monomer, and Glyceryl methacrylate 99% (GMAc) monomer were purchased from Sigma-Aldrich chemicals and were used without further treatment or purification. 2-2'-azobisisobutyronitrile (AIBN) was purchased from Sigma-Aldrich chemicals, it was recrystallised from methanol and dried in vacuum. All water was 18 mΩ, distilled and deionized.

Table 2.2 Monomers and polymers names, composition and structure

Monomer Name/Chemical Composition	Monomer Structure	Polymer Structure
N-Isopropyl Acrylamide (NIPAM) $C_6H_{11}NO$		
N,N-Dimethyl Acrylamide (DMAc) C_5H_8NO		
Hydroxyethyl Methacrylate (HEMA) $C_6H_8O_3$		
Hydroxypropyl Methacrylate (HPMA) $C_7H_{10}O_3$		
Glycidyl Methacrylate (GMAc) $C_7H_8O_3$		

2.3 Sample Synthesis and Preparation

2.3.1 Synthesis and Preparation of Clay Suspensions

All glassware, including sample vials, were thoroughly washed using base and acid baths, rinsed with acetone and dried in a drying cupboard overnight prior to use. An appropriate amount of Laponite[®] and Cloisite[®] Na⁺ clays were weighed before being dispersed in deionised water and exfoliated under rapid stir for 24 hours. [54] Clay suspensions of 0.5 % (or 0.5 g clay to 99.5 g water), 1 % (or 1 g clay to 99 g water), 2 % (or 2 g clay to 98 g water), 5 % (or 5 g clay to 95 g water), and 10% (or 10 g clay to 90 g water) in water were prepared for Laponite[®]EL, Laponite[®]FN, Laponite[®]OG, Laponite[®]RD, Laponite[®]XL21, Cloisite[®] Na⁺ (otherwise noted as L_{EL}, L_{FN}, L_{OG}, L_{RD}, L_{XL21}, and C_{Na+} respectively)

2.3.2 Synthesis and Preparation on Clay-Polymer Nanocomposites

All glassware, including sample vials, were thoroughly washed using base and acid baths, rinsed with acetone and dried in a drying cupboard overnight prior to use. An appropriate amount of clay was weighed before being dispersed in deionized water and exfoliated under rapid stir for 24 hours. Monomers and initiator (AIBN) were weighed and added to the mixture, before stirring for a further 2 hours. Pure polymer formulations were prepared identically, omitting the presence of clay.

To prepare a precursor solution which contains 10 wt.% solids of which 1 wt.% is clay (otherwise denoted 1Lanomite grade-p(monomer) or 1Cloisite-p(monomer), an aqueous solution consisting of water (9 g) exfoliated inorganic clay (0.1 g) (or 9.1 g of the original exfoliated suspension), AIBN (0.009 g) and monomer (0.9 g) was prepared (N.B. In all cases, the ratio of monomer to AIBN was kept at 99:1). And to prepare a precursor solution which contains 10 % solids of which 2% is clay (otherwise denoted 2Lanomite[®] grade-p(monomer) or 1Cloisite[®]-p(monomer), an aqueous solution consisting of water (9 g) exfoliated inorganic clay (0.2 g) (or 9.2 g of the original exfoliated suspension), AIBN (0.008 g) and monomer (0.8 g) was

prepared (N.B. In all cases, the ratio of monomer to AIBN was kept at 99:1). Then, polymerisation was allowed to proceed in an oven pre-set to 80 °C for 24 hours. [15][48]

As there are six different clay grades and five different monomers, a naming convention was required. To avoid confusion the grade and concentration of clay and the monomer used are included in the name, and the nomenclature format is as follows:

$$x (L \text{ or } C)_{\text{grade initials}} - p(\text{monomer acronym})$$

Where x is the overall percentage of clay by weight without the percentage symbol (%), L is for Laponite[®], C is for Cloisite[®], and p is for the polymer. For example, “1L_{EL}-pNIPAM” indicates a sample of clay-polymer nanocomposite prepared using 90 wt.% water, 9 wt.% NIPAM, 1 wt.% Laponite[®] EL discounting AIBN, therefore clay + monomer. All of the 1 % clay composites were made for the first investigation, depending on the results of these trials only specific 2% clay composites were made based on the processability and ability to test on the rheometer. A full trial of a monomer with all clay grades and a clay grade with all types of monomer was also considered that is why DMAc was polymerised with all clays and the L_{XL21} was incorporated with all monomers. Table 2.3 shows composites made with each crosslinker concentration.

Table 2.3 Composites made for different crosslinker concentration

	NIPAM	DMAc	HEMA	HPMA	GMAc
Laponite EL	1L _{EL} -pNIAPM	1L _{EL} -pDMAc	1L _{EL} -pHEMA	1L _{EL} -pHPMA	1L _{EL} -pGMAc
	2L _{EL} -pNIAPM	2L _{EL} -pDMAc			
Laponite FN	1L _{FN} -pNIAPM	1L _{FN} -pDMAc	1L _{FN} -pHEMA	1L _{FN} -pHPMA	1L _{FN} -pGMAc
		2L _{FN} -pDMAc			
Laponite OG	1L _{OG} -pNIAPM	1L _{OG} -pDMAc	1L _{OG} -pHEMA	1L _{OG} -pHPMA	1L _{OG} -pGMAc
		2L _{OG} -pDMAc			
Laponite RD	1L _{RD} -pNIAPM	1L _{RD} -pDMAc	1L _{RD} -pHEMA	1L _{RD} -pHPMA	1L _{RD} -pGMAc
		2L _{RD} -pDMAc			
Laponite XL21	1L _{XL21} -pNIAPM	1L _{XL21} -pDMAc	1L _{XL21} -pHEMA	1L _{XL21} -pHPMA	1L _{XL21} -pGMAc
		2L _{XL21} -pDMAc			
Cloisite Na⁺	1L _{Na⁺} -pNIAPM	1L _{Na⁺} -pDMAc	1L _{Na⁺} -pHEMA	1L _{Na⁺} -pHPMA	1L _{Na⁺} -pGMAc
		2L _{Na⁺} -pDMAc			

2.4 References

- [1] C. Suryanarayana and M. G. Norton, *X-Ray Diffraction - A Practical Approach*. 1998.
- [2] B. Fultz and J. Howe, *Transmission Electron Microscopy and Diffractometry of Materials*, (Third Edi. Heidelberg: Springer Berlin Heidelberg, 2007).
- [3] M. Ermrich and D. Opper, *XRD for the analyst : getting acquainted with the principles. .*
- [4] B. Fultz, J. M. Howe, B. Fultz, and J. M. Howe, "Diffraction and the X-Ray Powder Diffractometer," in *Transmission Electron Microscopy and Diffractometry of Materials*, Springer Berlin Heidelberg, 2002, pp. 1–61.
- [5] SHIMADZU, "SHIMADZU XRD-7000 X-RAY DIFFRACTOMETER Operating Instructions." pp. 1–17.
- [6] Barbara L Dutrow and C. M. Clark, "X-ray Powder Diffraction (XRD)," 2019. [Online]. Available: https://serc.carleton.edu/research_education/geochemsheets/techniques/XRD.html. [Accessed: 01-Jan-2019].
- [7] P. Brouwer, "Theory of XRF," *PANalytical BV*. PANalytical B.V., Almelo, p. 59, 2010.
- [8] D. M. Price, D. J. Hourston, and F. Dumont, "Thermogravimetry of Polymers," *Encycl. Anal. Chem.*, pp. 8094–8105, Sep. 2000.
- [9] PerkinElmer, "A Beginner's Guide to Thermogravimetric Analysis (TGA)." PerkinElmer, Inc, Waltham, pp. 1–19.
- [10] W. J. Sichina and M. Manager, "Characterization of Polymers Using TGA," *Therm. Anal. Appl. note*, pp. 1–5.
- [11] C. M. Earnest, "Compositional Analysis by Thermogravimetry," *Therm. Meas.*

ASTM Comm. E-37, no. 997, 1988.

- [12] H. M. Ng, N. M. Saidi, F. S. Omar, K. Ramesh, S. Ramesh, and S. Bashir, "Thermogravimetric Analysis of Polymers," *Encycl. Polym. Sci. Technol.*, pp. 1–29, Nov. 2018.
- [13] J. Ltd, "SEM Scanning Electron Microscope A To Z." Tokyo, pp. 1–32.
- [14] "Introduction to scanning electron microscopy."
- [15] V. Boyes, "The Synthesis and Development of Novel, Easily Processable Poly(N-Isopropylacrylamide)-Based Hydrogels," Sheffield Hallam University, Material and Engineering Research Institute, Sheffield, 2012.
- [16] N. D. HALLAM, "Electron Microscopy and Cytochemistry of Plant Cells," *Biochem. Soc. Trans.*, vol. 8, no. 1, pp. 159 LP – 159, Feb. 1980.
- [17] J. Coates, "Interpretation of Infrared Spectra, A Practical Approach," in *Encyclopedia of Analytical Chemistry*, John Wiley & Sons, Ltd, 2006.
- [18] B. H. Stuart, *Infrared Spectroscopy: Fundamentals and Applications*. John Wiley & Sons, Ltd, 2004.
- [19] W. Struve and I. Mills, "Fundamentals of Molecular Spectroscopy," *Vib. Spectrosc.*, vol. 1, no. 1, pp. 103–104, Dec. 1990.
- [20] V. L. Boyes *et al.*, "One-Pot Precipitation Polymerisation Strategy for Tuneable Injectable Laponite®-pNIPAM Hydrogels." .
- [21] M. I. Limited, "A Basic Introduction to Rheology Shear Flow." .
- [22] H. A. Barnes, J. F. (John F. Hutton, and K. Walters, *An introduction to rheology*. Elsevier, 1989.
- [23] T. G. Mezger, *The Rheology Handbook : 4th Edition*. Vincentz Network, 2014.
- [24] E. A. Stefanescu, W. H. Daly, and I. I. Negulescu, "Hybrid polymer/clay

- nanocomposites: Effect of clay size on the structure of multilayered films,” *Macromol. Mater. Eng.*, vol. 293, no. 8, pp. 651–656, Aug. 2008.
- [25] T. N. Blanton, D. Majumdar, and S. M. Melpolder, “MICROSTRUCTURE OF CLAY-POLYMER COMPOSITES,” vol. 42. JCPDS-International Centre for Diffraction Data, New York, pp. 562–568, 2000.
- [26] K. Haraguchi, T. Takada, and R. Haraguchi, “Nanocomposite Gels by Initiator-Free Photopolymerization: Role of Plasma-Treated Clay in the Synthesis and Network Formation,” *ACS Appl. Nano Mater.*, vol. 1, no. 1, pp. 418–425, Jan. 2018.
- [27] P. K. Paul, S. A. Hussain, D. Bhattacharjee, and M. Pal, “Preparation of polystyrene-clay nanocomposite by solution intercalation technique,” *Bull. Mater. Sci.*, vol. 36, no. 3, pp. 361–366, Jun. 2013.
- [28] N. Negrete-Herrera, J. L. Putaux, and E. Bourgeat-Lami, “Synthesis of polymer/Laponite nanocomposite latex particles via emulsion polymerization using silylated and cation-exchanged Laponite clay platelets,” *Prog. Solid State Chem.*, vol. 34, no. 2–4, pp. 121–137, Jul. 2006.
- [29] BYK Additives & Instruments, “Laponite EL Technical Data Sheet,” Wesel, Germany, 2013.
- [30] BYK Additives & Instruments, “Laponite OG Technical Data Sheet.” 2015.
- [31] BYK Additives & Instruments, “Laponite RD Technical Data Sheet,” 2015.
- [32] BYK Additives & Instruments, “Laponite FN Technical Data Sheet,” 2015.
- [33] BYK Additives & Instruments, “LAPONITE LAPONITE-Performance Additives,” Geretsried.
- [34] BYK Additives & Instruments, “Laponite XL21 Technical Data Sheet,” 2015.
- [35] “Layer Lattices and the Base-Exchange Clays ,” *Zeitschrift für Kristallographie*

- *Crystalline Materials* , vol. 91. p. 433, 1935.

- [36] T. Al Ani and S. Olli, "Clay and clay mineralogy." 2008.
- [37] S. Mallakpour and M. Dinari, "Biomodification of cloisite Na + with L-methionine amino acid and preparation of poly(vinyl alcohol)/organoclay nanocomposite films," *J. Appl. Polym. Sci.*, vol. 124, no. 5, pp. 4322–4330, Jun. 2012.
- [38] B. Rafiei and F. A. Ghomi, "Preparation and characterization of the Cloisite Na+ modified with cationic surfactants Caspian sea View project Organoclay synthesis View project," *J. Crystallogr. Mineral.*, vol. 21, pp. 25–32, 2013.
- [39] U. Hofmann, K. Endell, and D. Wilm, "Kristallstruktur und Quellung von Montmorillonit," *Cryst. Mater.*, no. 86, pp. 340–348, 2015.
- [40] S. A. Jadhav, V. Brunella, I. Miletto, G. Berlier, and D. Scalarone, "Synthesis of poly(N-isopropylacrylamide) by distillation precipitation polymerization and quantitative grafting on mesoporous silica," *J. Appl. Polym. Sci.*, vol. 133, no. 44, pp. 1–8, Nov. 2016.
- [41] K. Haraguchi, K. Murata, and T. Takehisa, "Stimuli-responsive nanocomposite gels and soft nanocomposites consisting of inorganic clays and copolymers with different chemical affinities," *Macromolecules*, vol. 45, no. 1, pp. 385–391, Jan. 2012.
- [42] K. Haraguchi, T. Takehisa, and S. Fan, "Effects of clay content on the properties of nanocomposite hydrogels composed of poly(N-isopropylacrylamide) and clay," *Macromolecules*, vol. 35, no. 27, pp. 10162–10171, Dec. 2002.
- [43] K. Haraguchi and H. J. Li, "Mechanical properties and structure of polymer-clay nanocomposite gels with high clay content," *Macromolecules*, vol. 39, no. 5, pp. 1898–1905, Mar. 2006.

- [44] K. Haraguchi, T. Takehisa, and M. Ebato, "Control of cell cultivation and cell sheet detachment on the surface of polymer/clay nanocomposite hydrogels," *Biomacromolecules*, vol. 7, no. 11, pp. 3267–3275, Nov. 2006.
- [45] K. Haraguchi, R. Farnworth, A. Ohbayashi, and T. Takehisa, "Compositional effects on mechanical properties of nanocomposite hydrogels composed of poly(N,N-dimethylacrylamide) and clay," *Macromolecules*, vol. 36, no. 15, pp. 5732–5741, Jul. 2003.
- [46] C. Fang, Y. Jing, Y. Zong, and Z. Lin, "Effect of N,N-dimethylacrylamide (DMA) on the comprehensive properties of acrylic latex pressure sensitive adhesives," *Int. J. Adhes. Adhes.*, vol. 71, pp. 105–111, Dec. 2016.
- [47] D. S. Achilias and P. I. Siafaka, "Polymerization kinetics of poly(2-hydroxyethyl methacrylate) hydrogels and nanocomposite materials," *Processes*, vol. 5, no. 2, Jun. 2017.
- [48] S. J. Buwalda, T. Vermonden, and W. E. Hennink, "Hydrogels for Therapeutic Delivery: Current Developments and Future Directions," *Biomacromolecules*, vol. 18, no. 2, pp. 316–330, Feb. 2017.
- [49] C. Maldonado-Codina and N. Efron, "Hydrogel Lenses Materials and Manufacture_ A Review," *Optom. Pract.*, vol. 4, pp. 101–115, 2003.
- [50] M. Zhai, F. Ma, J. Li, B. Wan, and N. Yu, "Preparation and properties of cryogel based on poly(hydroxypropyl methacrylate)," *J. Biomater. Sci. Polym. Ed.*, vol. 29, no. 12, pp. 1401–1425, Aug. 2018.
- [51] M. Save, J. V. M. Weaver, S. P. Armes, and P. McKenna, "Atom transfer radical polymerization of hydroxy-functional methacrylates at ambient temperature: Comparison of glycerol monomethacrylate with 2-hydroxypropyl methacrylate," *Macromolecules*, vol. 35, no. 4, pp. 1152–1159, Feb. 2002.

- [52] R. Haigh, S. Rimmer, and N. J. Fullwood, "Synthesis and properties of amphiphilic networks. 1: The effect of hydration and polymer composition on the adhesion of immunoglobulin-G to poly(laurylmethacrylate-stat-glycerolmonomethacrylate-stat-ethylene-glycol- dimethacrylate) networks," *Biomaterials*, vol. 21, no. 7, pp. 735–739, 2000.
- [53] M. Benaglia, A. Alberti, L. Giorgini, F. Magnoni, and S. Tozzi, "Poly(glycidyl methacrylate): A highly versatile polymeric building block for post-polymerization modifications," *Polym. Chem.*, vol. 4, no. 1, pp. 124–132, Jan. 2013.
- [54] N. Willenbacher, "Unusual thixotropic properties of aqueous dispersions of Laponite RD," *J. Colloid Interface Sci.*, vol. 182, no. 2, pp. 501–510, Sep. 1996.

3

Characterisation of Clay and Clay Dispersions

Chapter 3 Characterisation of Clay and Clay Suspensions

Clays are a key component in a wide range of applications like ceramic products, drilling fluids, moulding sands, paints, and paper. [1] Clays can provide a convenient particle dispersion for these applications which is necessary to obtain a uniform and stable system.

The purpose of this chapter is to highlight the characteristics of clay powders and clay suspensions in order to help understand the characteristics, structure, and behaviour of the clay-polymer nanocomposites. [2]

Clays are hydrous silicates or aluminosilicates which make up the dominant colloidal fraction of soils, sediments or rocks. [3] The clay minerals structure is composed of layers containing silica and alumina or magnesia sheets joined together, and these layers are stacked on top of each other.

Generally, two structural sheets are involved in the clay layer (as described previously in Figure 2.19). One consists of closely packed oxygens and hydroxyls in which aluminium or magnesium atoms are embedded in octahedral coordination (the octahedral sheet). The second is built of silica tetrahedrons (the tetrahedral sheet) in which each silicon atom is equidistant from four oxygen atoms or hydroxyls to balance the structure. The silica tetrahedral groups are arranged to form a hexagonal network, and a sheet of composition $\text{Si}_4\text{O}_6(\text{OH})_4$. [4]

Smectites are a class of clay minerals which have a range of characteristics e.g. (swelling capacity, polymer adsorption, and gel-like structures) as a result of its ionic charged surfaces that attract the attention of several fields. [5][2]

In order to understand the interaction between the different clay grades used in this study and the range of polymers, it is essential to understand the structure of clay and the interaction of clay particles in the aqueous medium. Clay powder and

clay suspensions were characterised using the experimental methodology described in Chapter 2. The names and some manufacturer-provided information regarding their character are given in Table 3.2.

3.1 XRD Characterisation of Clays

XRD is a technique used to evaluate the d-spacing between clay layers by using the position and intensity of the basal reflections from the distributed silicate layers. [6]

Representative XRD traces of the L_{EL} , L_{FN} , L_{OG} , L_{RD} , L_{XL21} , and C_{Na+} powder samples are shown in Figure 3.1. They are consistent with hectorite and montmorillonite type powder traces characterised by the broad d_{001} (Figure 3.4) between of 12.6 – 18.2 Å ($2\theta = 4.86^\circ - 7.02^\circ$). [7][8] The notation used here in this section will be used throughout this study for the purposes of saving space and clarity.

The d_{001} spacing of the clay defines the distance from a plane in one layer to the corresponding plane in another parallel layer of the crystal, so the d_{001} includes information about the geometry of stacking of the layers and any material present between the layers. [9][4] The d_{001} values are calculated by following Braggs Law, ($n\lambda = 2d \sin\theta$) at the observed reflections. Pure clay shows broad XRD reflections due to relatively low and broad range of crystallinity and small particle size. [10][11]

L_{EL} shows the largest d_{001} at 18.2 Å while L_{OG} shows the smallest d_{001} -spacing of 12.6 Å. The d-spacing values can vary as a function of relative humidity (RH); the higher the RH the larger the d-spacing value due to water incorporation in the clay interlayer. [4] The extent of water intercalation in different clays, at fixed RH and temperature, reflects the polarity and hygroscopic nature of the clay.

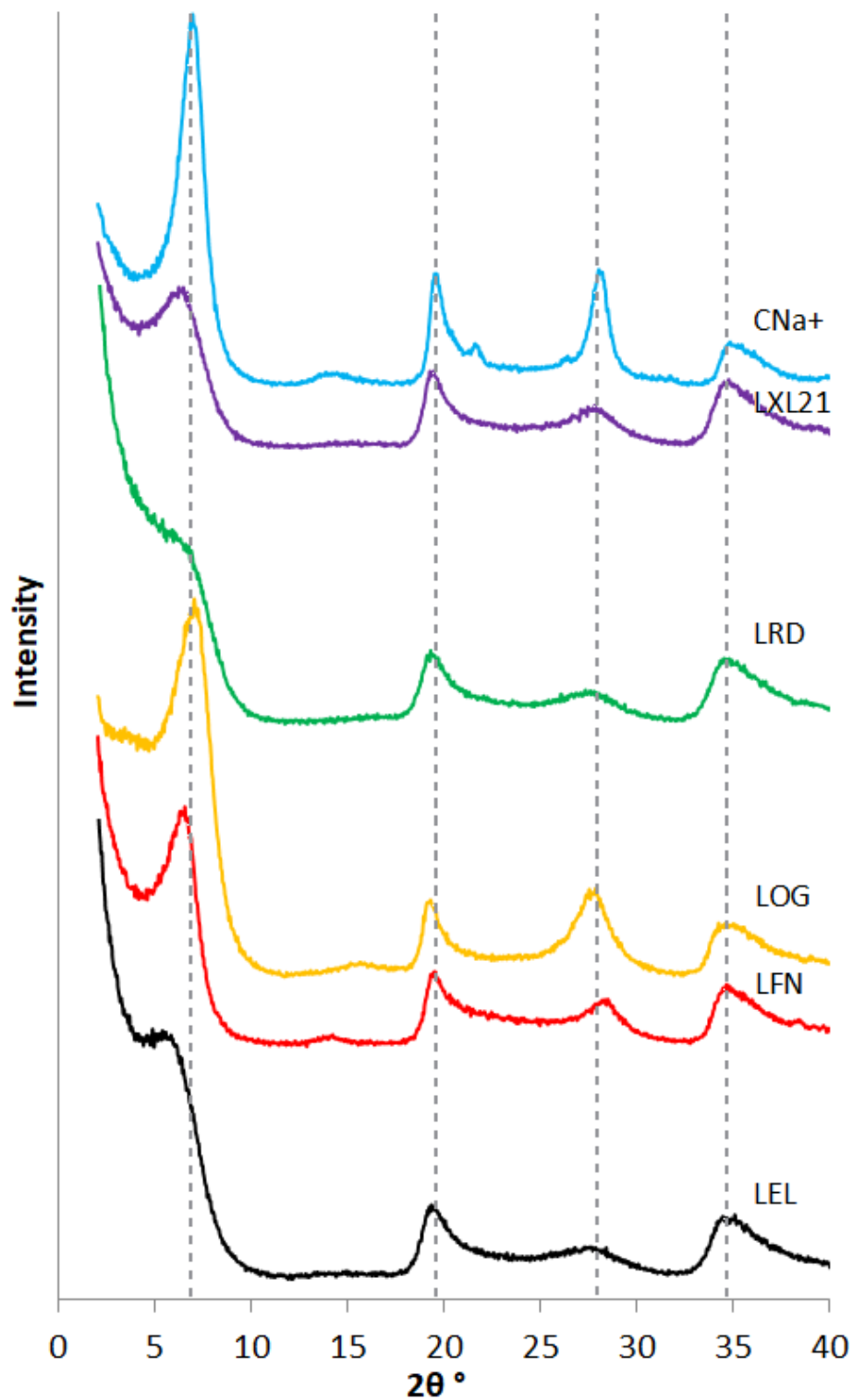


Figure 3.1 X-ray diffraction traces for as received powders; LEL, LFN, LOG, LRD, LXL21, and CNa+ showing reflections for 001, 100, 005, and 110 (dotted lines) basal spacing, respectively.

Reflections present at 2θ values ($19 - 20^\circ$), ($27 - 28^\circ$) and ($34 - 35^\circ$) are attributed to (100), (005) and (110) crystal planes, respectively (the dotted lines on Figure 3.1). Table 3.1 summarises the reflections positions and the corresponding d-spacing

values. [12][13][14] The intensity of the d_{001} -spacing relative to the d_{100} -spacing reflects the order within the clay layers. An increase in the ordering of the clay layers is easier to achieve when the layer diameters (i.e. platelet size) become larger, this could explain that the relative intensities of the d_{001} of L_{FN} , L_{OG} and C_{Na+} compared to their d_{100} 's are higher than those of L_{EL} , L_{RD} , and L_{XL21}

Table 3.1 d-spacing values calculated by Braggs Law and crystal planes.

Samples	d_{001}		d_{100}		d_{005}		d_{110}	
	2θ	d (Å)	2θ	d (Å)	2θ	d (Å)	2θ	d (Å)
L_{EL}	4.86	18.2	19.2	4.6	27.3	3.3	35.1	2.6
L_{FN}	6.54	13.5	19.5	4.5	28.2	3.2	34.6	2.6
L_{OG}	7.02	12.6	19.3	4.6	27.5	3.2	34.2	2.6
L_{RD}	5.86	15.1	19.3	4.6	27.3	3.3	34.7	2.6
L_{XL21}	6.22	14.2	19.4	4.6	27.8	3.2	34.7	2.6
C_{Na+}	6.94	12.7	19.6	4.5	28.0	3.2	34.8	2.6

3.2 XRF Characterisation of Clays

Table 3.2 shows the elemental chemical analysis of the Laponite[®] clays as provided by “BYK[®] Additives & Instrument”, they clearly contain major quantities of magnesium, silicon, sodium, and other elements in minor quantities. [15]

Table 3.2 Chemical analysis of Laponite[®] clays produced by “BYK[®] Additives & Instrument” as per Datasheet provided by “BYK[®] Additives & Instrument”.

		L_{EL}	L_{FN}	L_{OG}	L_{RD}	L_{XL21}
Chemical Composition Weight (%)	Na ₂ O	2.8	2.2	2.8	2.8	No data provided by manufacturer
	MgO	27.5	21.7	27.5	27.5	
	SiO ₂	59.5	62.4	59.5	59.5	
	Li ₂ O	0.8	2.5	0.8	0.8	
	F	0	4.2	0	0	
Loss on ignition Weight (%)		8.2	7.0	8.2	8.2	
Platelet size (nm)		44	140	83	40	60
CEC (meq/100 g)		75	129	60	55	107

XRF was performed to determine a better understanding and confirmation of the elements present in the clay. Elemental composition for the Laponite[®] and Cloisite[®] samples determined using XRF is shown in Figure 3.2 and Table 3.3. Silicon and magnesium are present in major quantities in the Laponite[®] clays as expected since silica is the main component in the two tetrahedral sheets that comprise the clay layers, and magnesium is the main component in the octahedral sheet. Aluminium

is present in major quantities in the C_{Na+} as it contains aluminium octahedral layers. [15] Unfortunately elements such as F and Li cannot be detected using XRF as described earlier in Chapter 2; the lack of such details makes it harder to relate the elemental composition to the CEC for different clays.

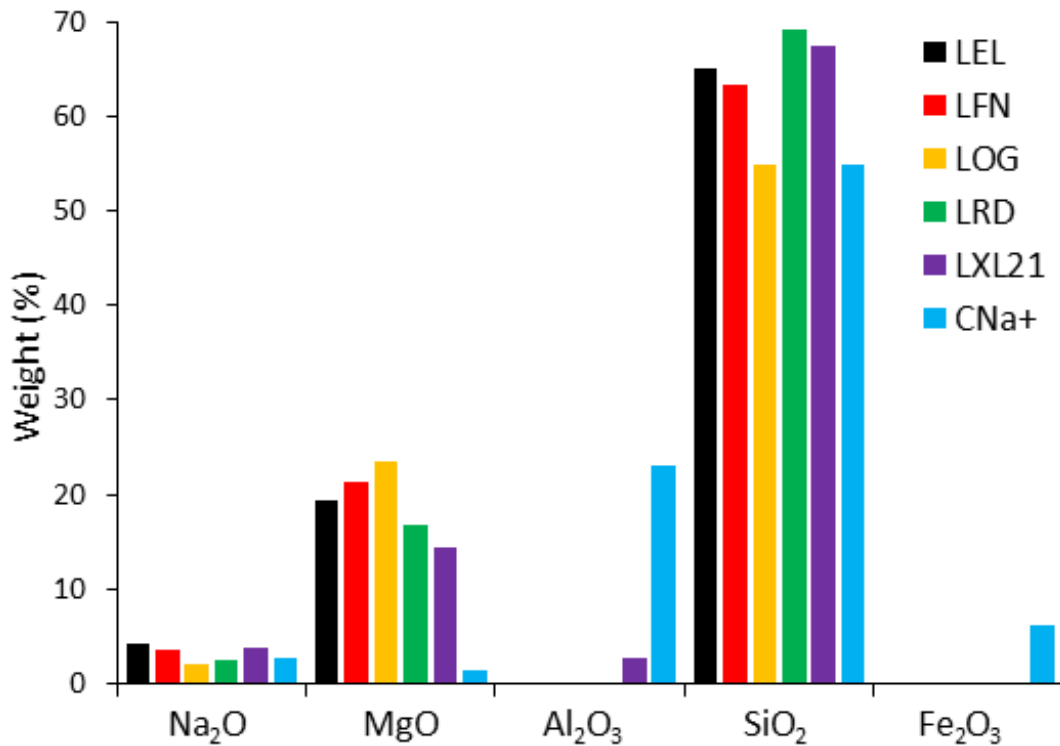


Figure 3.2 Comparison of the elemental composition of LEL, LFN, LOG, LRD, LXL21, and CNa+ as per XRF analysis.

LEL, LFN, and LXL21 have the highest concentration of Na₂O (Table 3.3). Sodium ions are held in the diffuse region on both sides of the dispersed clay platelets and may be responsible for the formation of electrical double layers. The ionic strength defines the structure of the clay suspension. [2]

The Li is substituted for Mg in the octahedral layer which results in a net negative charge. This negative charge is compensated by exchangeable cations (sodium cations) located in the interlayer region. The number of Na ions should reflect the CEC, however, NaSO₄ is a by-product of the clay synthesis and not all of it is washed away, the presence of the NaSO₄ can help in controlling the rheological properties of the clay dispersion. The sodium ions may also be associated with other anions such as chlorine.

Table 3.3 Chemical analysis of fractions of clay by XRF.

Chemical Composition	L _{EL}	L _{FN}	L _{OG}	L _{RD}	L _{XL21}	C _{Na+}
	Weight (%) of clay					
Na ₂ O	4.9	3.9	2.5	2.7	4.2	3.0
MgO	21.7	24.1	28.9	18.8	16.3	1.6
Al ₂ O ₃	-	-	-	-	3.1	25.9
SiO ₂	73.2	71.4	67.6	78.1	75.9	61.7
CaO	0.3	0.3	0.4	0.2	0.2	0.5
Fe ₂ O ₃	-	-	-	-	-	6.9

L_{EL}, L_{OG}, and L_{RD} have similar Na content as reported by the manufacturer. The XRF analysis agrees with the reported amounts for L_{OG} and L_{RD} but it shows that the L_{EL} has considerably more Na (Figure 3.3); this may reflect the higher CEC for L_{EL}, but it could also be accounted for by the sodium cations present in excess of the CEC.

The L_{XL21} has a high CEC and therefore one might expect it to contain more Na when compared to the L_{OG} and L_{RD}, which is the case. While L_{FN} is the exception in that, it has the highest CEC but not the highest Na content; this may reflect it being an F-based clay with F in the octahedral layer that contributes to the negative charge within the layer (and hence the high CEC) and the high level of Li-ions could be the compensating exchangeable cations (rather than the sodium ions). Figure 3.3 shows the relationship between the Na₂O amount and the CEC values.

L_{FN} contains comparable amounts of the Li and Na as per data provided from BYK[®], however, the formula suggests that the Na is significantly higher in content than Li. L_{XL21} is different when compared to the other Laponite[®] clays as it contains Al in its chemical composition as per the XRF analysis results. Presumably, this resides in the mostly magnesium octahedral sheets and enables the clay to achieve a relatively higher CEC. The L_{XL21} is still predominantly hectorite-like clay with some montmorillonite-like characteristics.

L_{XL21} elemental analysis shows the presence of Al₂O₃, which makes it the only Laponite[®] that contains Al₂O₃ and may explain its CEC value when compared to its particle size and other Laponites[®]. The L_{XL21} is an experimental grade with very limited info available on research or provided by “BYK[®] Additives & Instrument”.

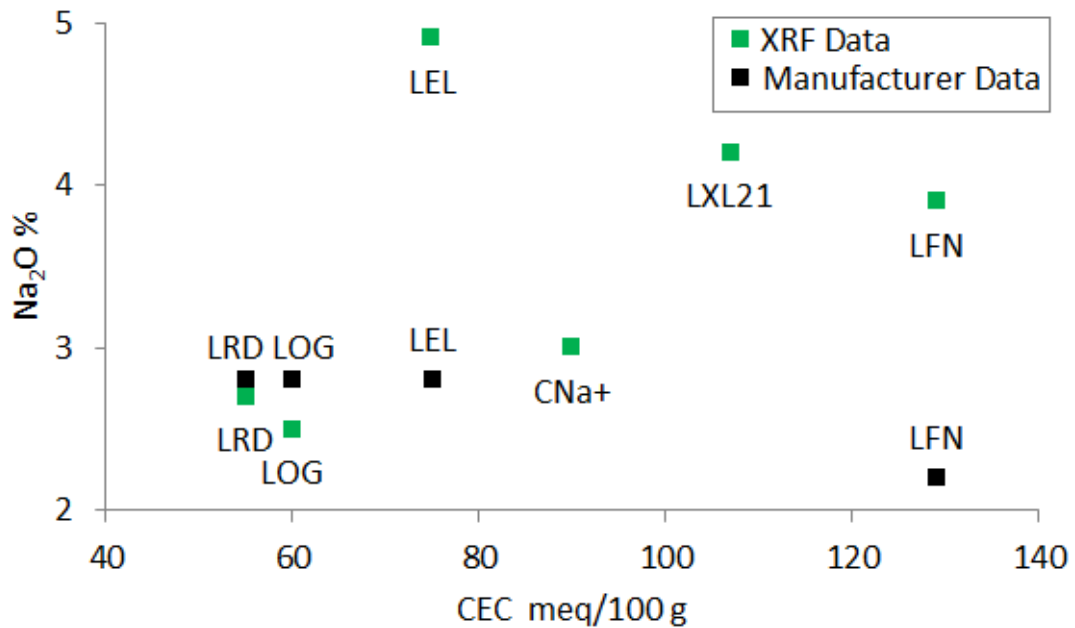


Figure 3.3 Na₂O (as per XRF and manufacturer) as a function of the CEC showing the relationship between the L_{OG} and L_{RD} low CEC and their low Na₂O content.

Figure 3.3 shows a comparison between the amounts of Na₂O in different clay grades as per the XRF analysis and the BYK[®] data provided. The data provided by BYK[®] for the L_{EL}, L_{OG} and L_{RD} have the same amount of Na₂O. In both (the XRF analysis and the BYK[®] data) LFN includes less amount of Na₂O than other Laponite[®] grades.

Certain clays can swell in an aqueous environment and form a gel-like structure. A proportion of the cations in the clay balances the negative layer charge resulting from isomorphous substitution (e.g. Li for Mg) spread across the external surfaces, the cations are present in the interlayer space between the clay platelets and also at layer edges (~ 20 %). The negatively charged sheets are held together by the electrostatic forces between alternate layers of bridging cations (for the clays in this section Na⁺ and some Li). Swelling is the disjoining of the clay layers until they reach their equilibrium separation. The degree of expansion of the layers (Figure 3.4) depends on the cations located in the interlayer region. For example, if the interlayer cations are monovalent and strongly hydrated (Na⁺, Li⁺), then the interplatelet repulsion is strong, and the degree of platelet separation is larger. The interlayer spacing may increase abruptly with water content. [2]

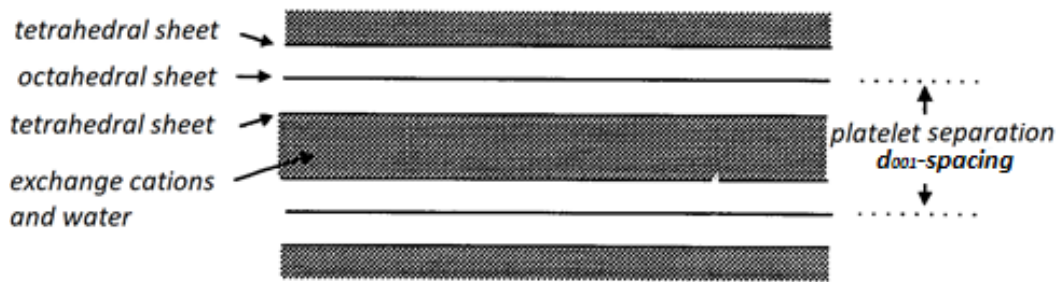


Figure 3.4 Schematic of expanding clay basal spacing as water enters the interlayer region. Modified from [2].

3.3 TGA Characterisation of Clays

The thermal stability of the clay samples was studied by thermogravimetric analysis, weight loss was monitored as a function of temperature between 20 °C and 900 °C (20 °C min⁻¹) under a 40 ml min⁻¹ N₂ purge. [12] Different decomposition steps were observed including dehydration and dehydroxylation. Samples were tested as received from the manufacturer without further purification or pre-drying.

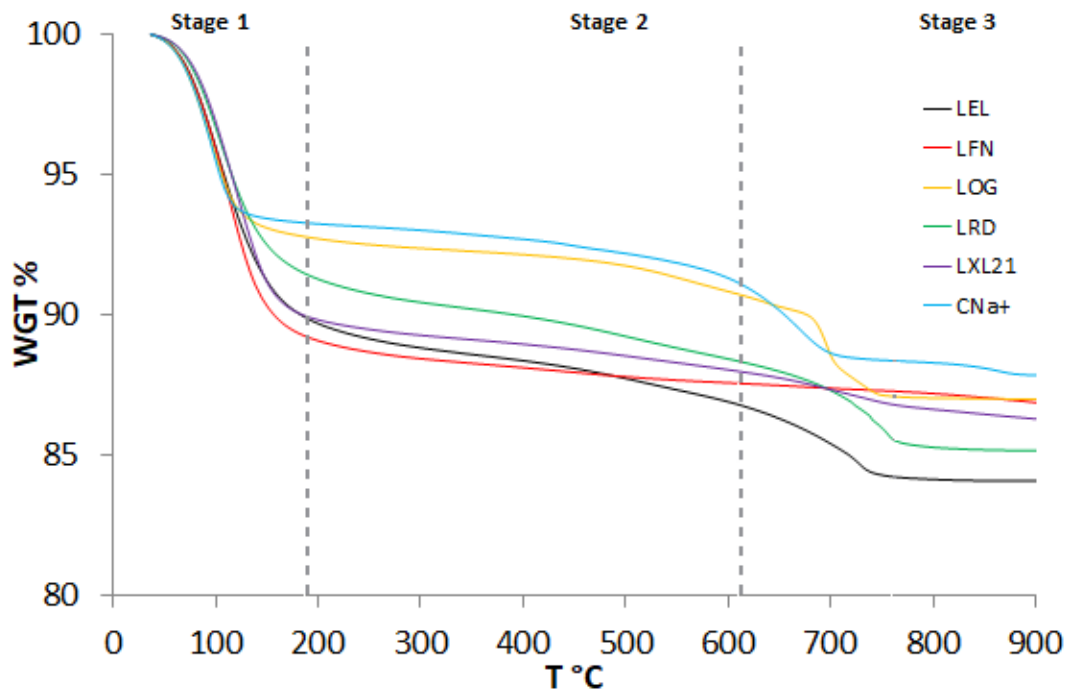


Figure 3.5 TGA curves of LEL, LFN, LOG, LRD, LXL21, and CNa+ showing the main weight loss stages in the temperature range 20 – 900 °C. samples were tested as received from the manufacturer with no further purification.

Table 3.4 TGA thermograms analysis showing the three main weight loss stages Laponite® and Cloisite®.

	Stage 1: 25 - 200 °C	Stage 2: 200 - 600 °C	Stage 3: 600 - 900 °C	Total
	Weight loss %			
L_{EL}	10.30	2.78	2.82	15.90
L_{FN}	10.91	1.49	0.71	13.12
L_{OG}	7.28	1.86	3.85	12.99
L_{RD}	8.72	2.82	3.28	14.82
L_{XL21}	10.16	1.77	1.76	13.69
C_{Na+}	6.75	1.89	3.49	12.13

Typical thermogravimetric (TG) curves for all clay samples are illustrated in Figure 3.5. Three different decomposition stages can be observed for most of the clays except the L_{FN} and the L_{XL21}. The first decomposition stage occurred between 25 - 200 °C and can be attributed to free water evaporation from the edges of the clay platelets, the interlayer and between platelets stacks. The biggest weight losses in this stage were observed in the L_{EL}, L_{FN}, and L_{XL21} (10.3, 10.9 and 10.2 %, respectively), whereas the lowest were L_{OG} and C_{Na+} with 7.3 and 6.8 % respectively (Table 3.4). These amounts reflect the hydrophilic nature. [2][16] The second decomposition stage was observed between 200 - 600 °C. During this stage a gradual, non-significant weight loss was observed mainly due to the dehydroxylation of interlayers, it could also include the loss of very strongly held water molecules at the lower temperature. The last decomposition stage can be ascribed to dehydroxylation of the layers (600 - 900 °C), the main loss event happens at around 700 °C in which all clays showed major mass loss except for L_{FN} and L_{XL21}, these clays are fluorine-containing clays, which explains their different behaviour when compared to all other clays. [11][17][18][19]

The relationship between the CEC and the weight loss can be seen in Figure 3.6, there was no clear relationship between the total weight loss and the CEC values of the different clay. However, it can be noticed that the clays with higher CEC values show lower total weight loss. The relationship not being clear can be caused by a lot of different reasons, the first reason is that the behaviour of the weight loss of these clays depends on other factors not only the CEC, surface area of clay platelets also plays a role in it as can also be seen in Figure 3.7, the platelet size show a better relationship for the decrease of weight loss with the increase of the size of

the platelets except for the L_{EL} and L_{FN} providing more evidence that the weight loss is a complicated property that depends on many factors at one time. The elemental analysis of different clays has a role also as seen in Figure 3.5 where fluorine-containing clays (L_{FN} and L_{XL21}) show only two stages of weight loss.

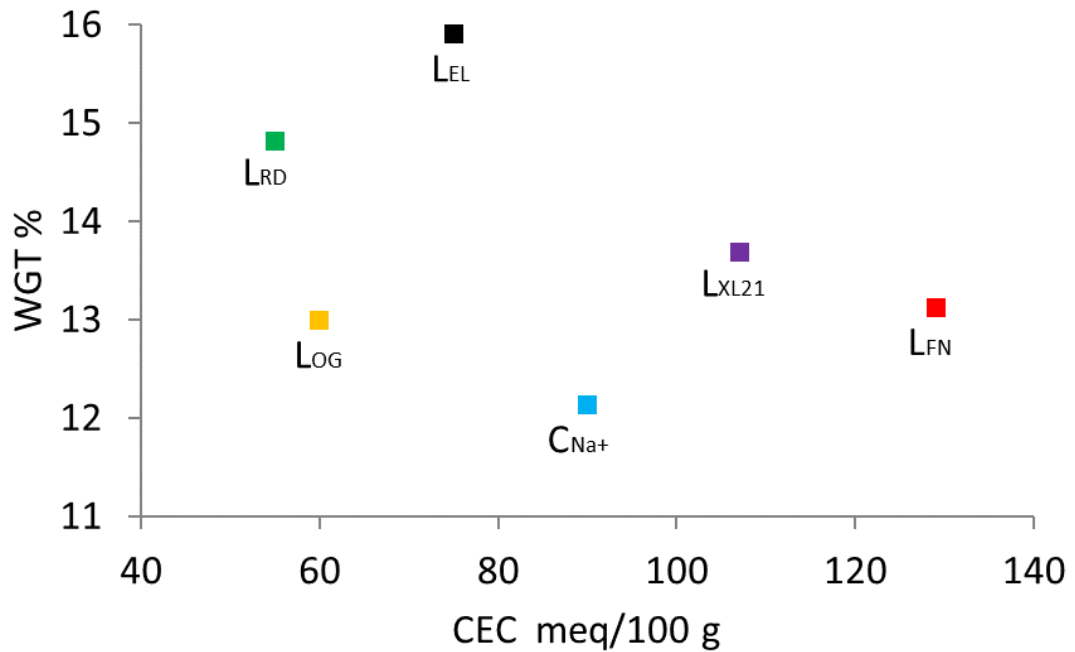


Figure 3.6 WGT% total weight loss as a function of the CEC for the TGA test for different clays showing no clear relationship between the CEC values and the weight loss. However, it can be noted from the plot that clays with higher CEC have less weight loss on the right side of the plot (C_{Na+}, L_{XL21} and L_{FN}).

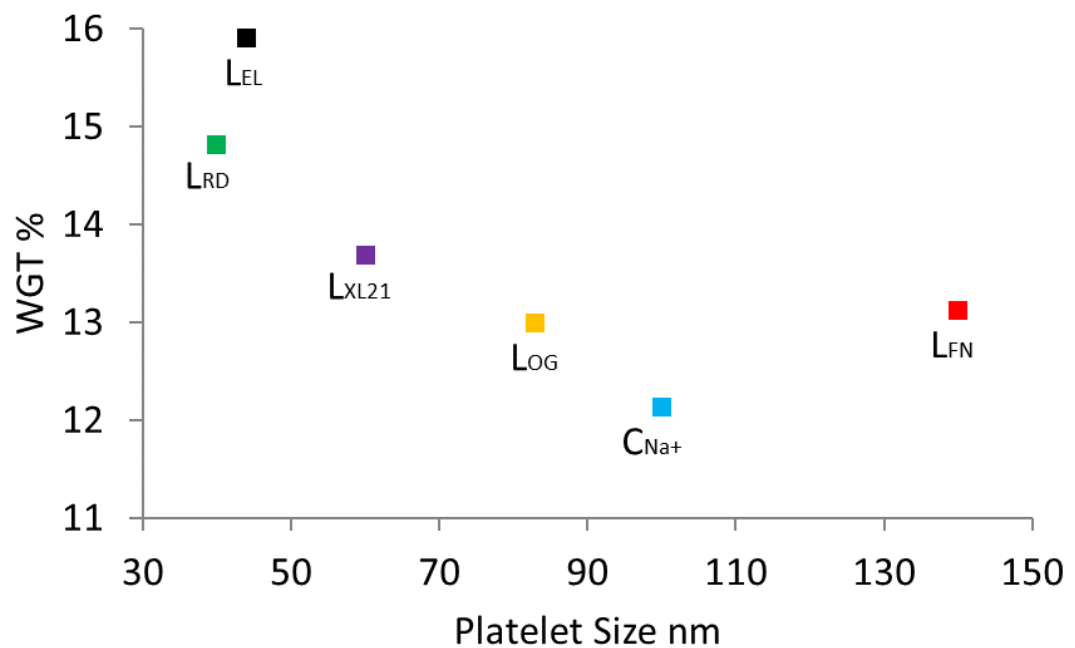


Figure 3.7 WGT% total weight loss as a function of the platelet size for the TGA test for different clays showing the relationship between the platelet size and the weight loss.

3.4 FTIR Spectroscopy Analysis of Clays

It is important to understand the infrared spectra of clays as a reference in its initial unintercalated and undispersed state in order to determine interactions with polymers once they are dispersed in them. Layered silicates are a complicated subject for IR analysis. The Si-O stretching vibration gives rise to strong absorption bands in the range 1100 - 1000 cm^{-1} . Some of these bands correspond to Si-O-Si bonds at the surface of the clay layers and have their transition moment in the plane of the layer and are referred to as “in-plane” (Figure 3.8). Others correspond to the Si-O bands pointing towards aluminium or magnesium ions at the centre of the layer; with their transition moment perpendicular to the layer and are referred to as “out-of-plane” (Figure 3.8). The type of clay, elemental composition platelet size, and structure can affect the FTIR spectrum. It was reported that four overlapping bands (three in-plane at 1120, 1048, 1025 cm^{-1} and one out-of-plane at 1080 cm^{-1}) are strongly influenced by layer separator due to intercalation of various molecules. [6][20][21][22]

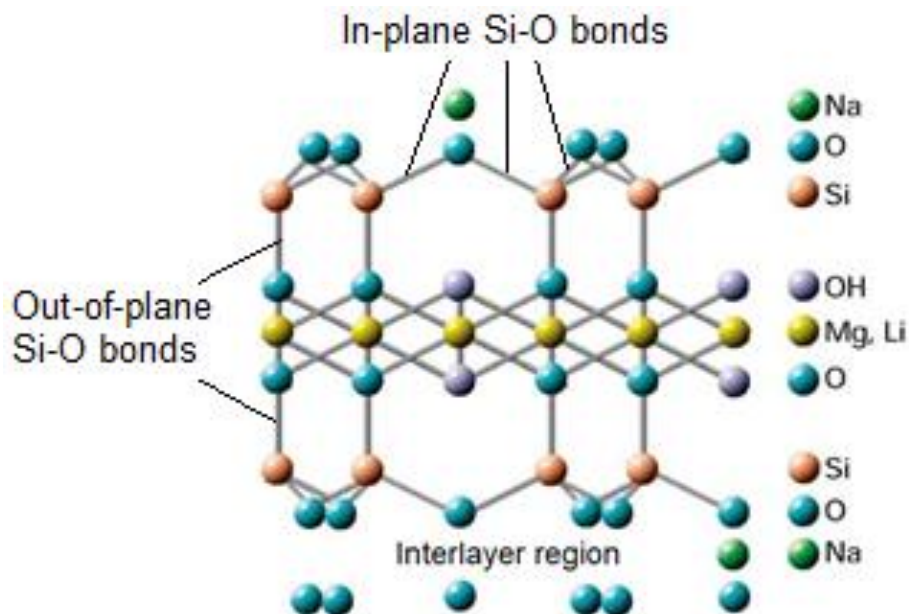


Figure 3.8 Schematic of a smectite clay layer. In-plane (Si-O) bonds absorb infrared at a different frequency than the out-of-plane (Si-O) bonds. [23] Modified from [24].

Figure 3.9 shows the infrared spectra of the Laponite[®] and Cloisite[®] powders in the region 3800 cm^{-1} to 700 cm^{-1} . All spectra of Laponite[®] grades show very similar FTIR

characteristics and exhibit broad bands around 3200 - 3700 cm^{-1} , this range of frequencies is assigned to the stretching of the surface hydroxyl groups (3625 cm^{-1} for Si-OH and Al-OH) and sorbed water (3440 cm^{-1} for -OH). The bands at around 1637 cm^{-1} are due to interlayer water O-H bending vibration. [12] The broad bands around 850 - 1100 cm^{-1} observed in all spectra of Laponite[®] grades are due to the four overlapping (three in-plane and one out-of-plane) Si-O vibration. [9][25]

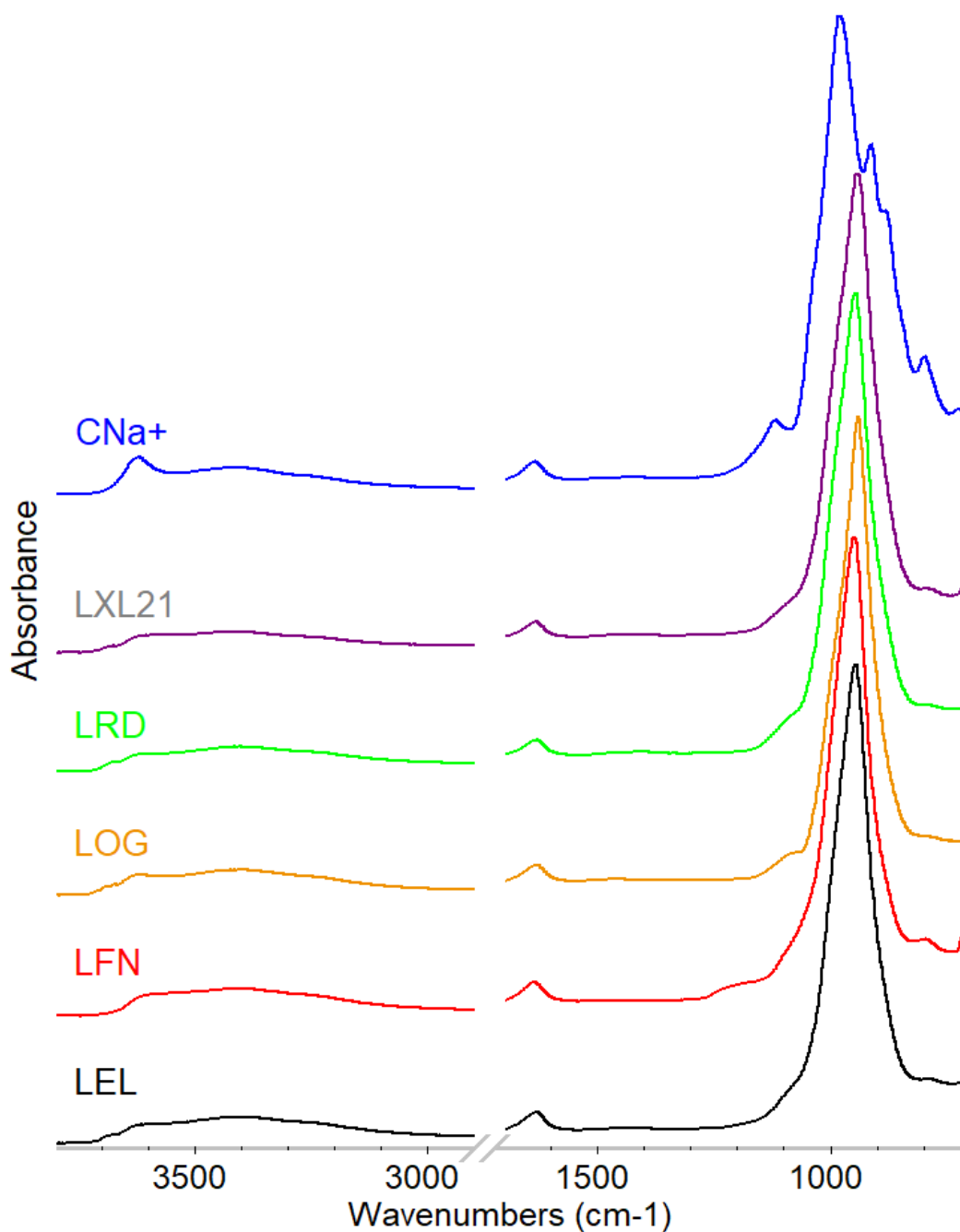


Figure 3.9 FTIR spectra of different grades of LEL, LFN, LOG, LRD, LXL21, and CNa+ showing a strong peak at around 1000 cm^{-1} attributed to Si-O.

The spectrum of Cloisite[®] Na⁺ is characterised by similar stretching and bending bands of both -OH and Si-O but also contains stretching bands due to Al-O. The Si-O stretching band is observed at 990 cm⁻¹ as well as Al-OH bending at 915 cm⁻¹. [11][9] The fact that the Si-O region for C_{Na+} appears more complex than the Laponite[®] grades is due to more impurities and the presence of the Al in its structure.

3.5 Rheological Characterisation and Properties of Clay Dispersions

The dispersion quality and stability of clay in water are crucial for reproducible synthesis of the final properties of nanocomposite properties. [26] The lamellar clay crystal structure swells in water into detached plate-like nanosheets. The exfoliated nanosheets have a thickness of 1 nm and diameters that vary over a large range from tens up to hundreds of nanometres according to the clay type (25 - 150 nm for synthetic hectorite and 300 - 1000 nm for natural montmorillonite). [27] Figure 3.10 depicts the gradual exfoliating progress of clay to a homogeneous suspension in water. [28] Since clay platelets have high aspect ratios and negative surface charges, they can form stable aqueous dispersions with house-of-cards like structures when the clay concentration (C_{clay}) is sufficiently high. The extent of clay dispersion affects the viscosity of the dispersion. [29][30]

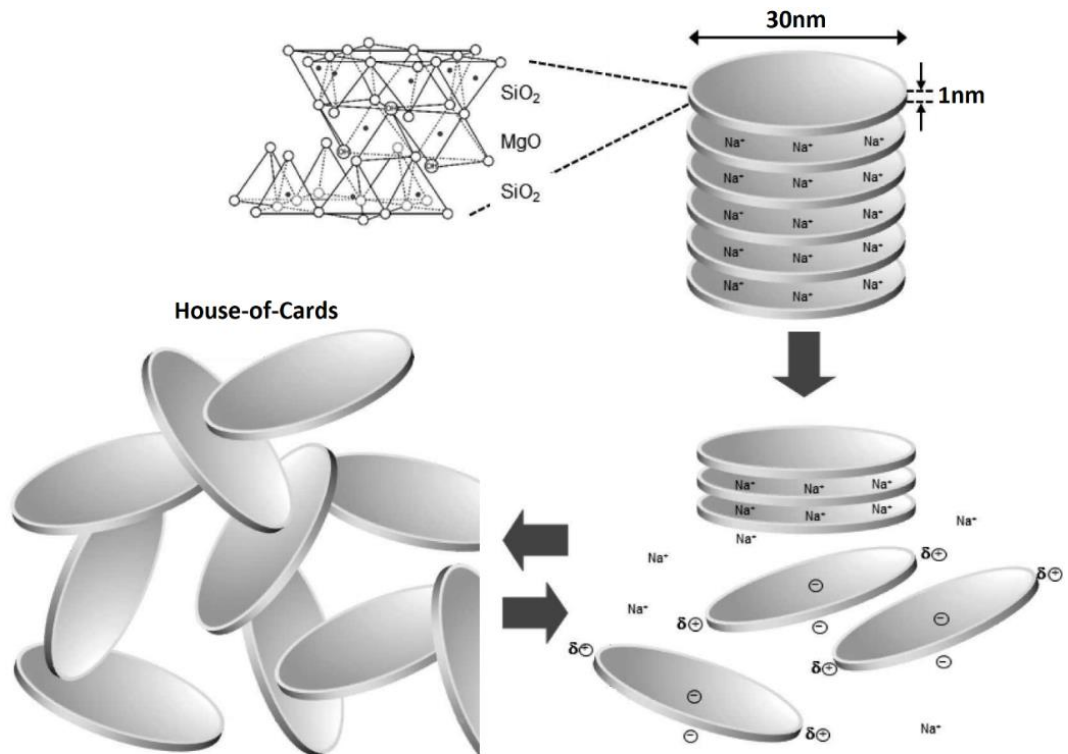


Figure 3.10 Schematic of the clay crystal structure and the exfoliation states of clay nanosheets in water to form the house-of-cards structure and the reverse of the process as the suspension dries. Modified from [29][30].

A series of aqueous clay dispersions of L_{EL} , L_{FN} , L_{OG} , L_{RD} , L_{XL21} , and C_{Na^+} were prepared by adding the appropriate amount of clay to deionised water at different concentrations (clay = 0.5, 1.0, 2.0, 5.0, and 10.0 weight% (wt.%)). For 0.5 wt.%; 0.5 g Laponite[®] was added to 99.5 g deionised water to form 0.5 g/100 g. [16] The dispersions were sealed from the atmosphere and stirred continuously with a high-speed magnetic stirrer for 24 hours at room temperature. [31][32] Due to their high purity and small crystallite size; L_{EL} , L_{RD} , and L_{XL21} form clear transparent dispersions at low concentration (clay \leq 2 wt.%) while L_{OG} , L_{FN} and C_{Na^+} form opaque dispersions at the same concentration (Figure 3.11). At 2.0 wt.%, clays with particle size \geq 80 nm suspensions are opaque. [33] To achieve fully dispersed state clay can require many hours or days depending on many factors (platelet size, agitation, concentration, etc.). [34][35]

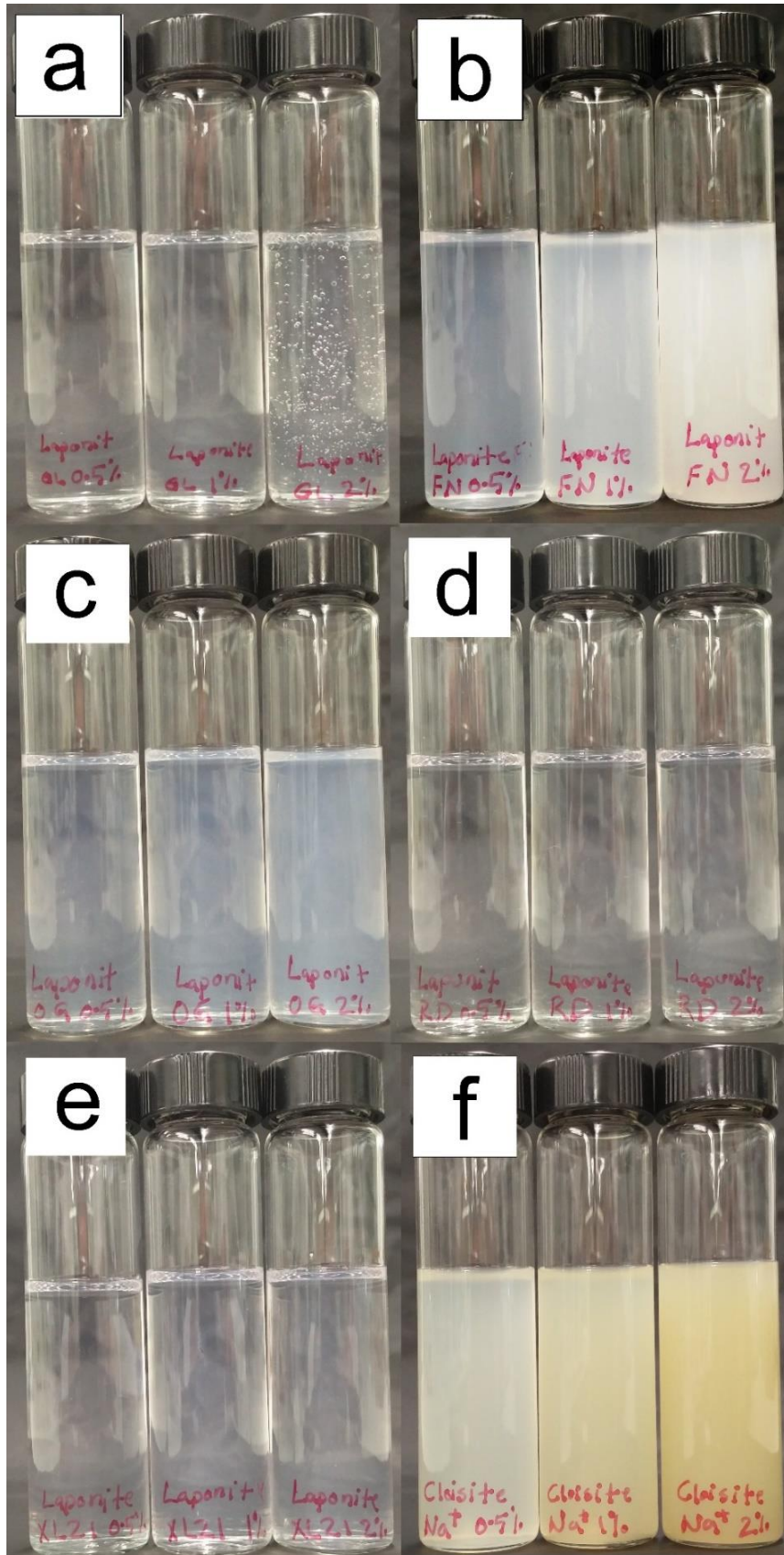


Figure 3.11 Clay dispersions at (from left) 0.5, 1.0, and 2.0 wt.% for a) LEL, b) LFN, c) LOG, d) LRD, e) LXL21, and f) CNa⁺.

The properties of the aqueous clay dispersions at different clay content have been studied using rheological measurement protocols. [26][29] The rheological behaviour of clay suspension can be used to identify any relationships between different clay grades and their concentrations under certain types of loads. Using parallel plate geometry, $\sim 1.95 \times 10^{-3} \text{ mm}^3$ of each aqueous clay dispersion was dispensed on the lower stationary plate of the plate-plate geometry and the mobile upper plate was lowered to a gap height of 1 mm (Figure 3.12). Different testing sequences were then applied and a fresh sample was used for every test. [36]

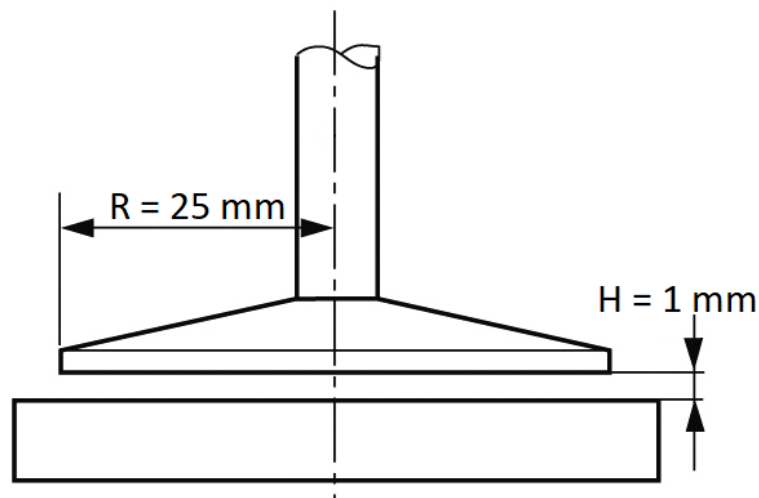


Figure 3.12 A schematic showing the dimensions on the geometry of the parallel plate used, the sample size is $H\pi R^2 \sim 1.95 \times 10^{-3} \text{ mm}^3$.

3.5.1 Clay Suspension Viscosity Behaviour

A shear-thinning behaviour is generally observed in the viscosity curves for the clay suspensions (Figure 3.13). The viscosity and shear thinning behaviours are enhanced as the clay concentration increases. Low clay concentration suspensions 0.5 wt.% generally show low viscosity and Newtonian-type properties. The low concentration suspensions (clay ≤ 2 wt.%) behaviour is rather complex as the increase in viscosity value after $\dot{\gamma} = 100 \text{ s}^{-1}$ is due to turbulence in the flow, not a shear thickening behaviour. The viscosity values at low shear rates ($< 10 \text{ s}^{-1}$) were lower than the sensitivity limits of the instrument so are not shown.

A clear shear thinning behaviour is observed over the whole range of shear rate for the 5.0 wt.% and 10.0 wt.% clay suspensions with a clear decrease in viscosity as a

function of shear rate (Figure 3.14). [13] Generally, the highest viscosity values are associated with the smallest platelet size clays at clay concentrations of 5 and 10 wt.%, however, at ≤ 2 wt.% the opposite trend is observed where smaller platelet clays show lower viscosities, this may be as a results of clays behaving different at certain concentration where clays facilitate the dispersion flow to a certain concentration and it makes it harder for it to flow beyond that point.

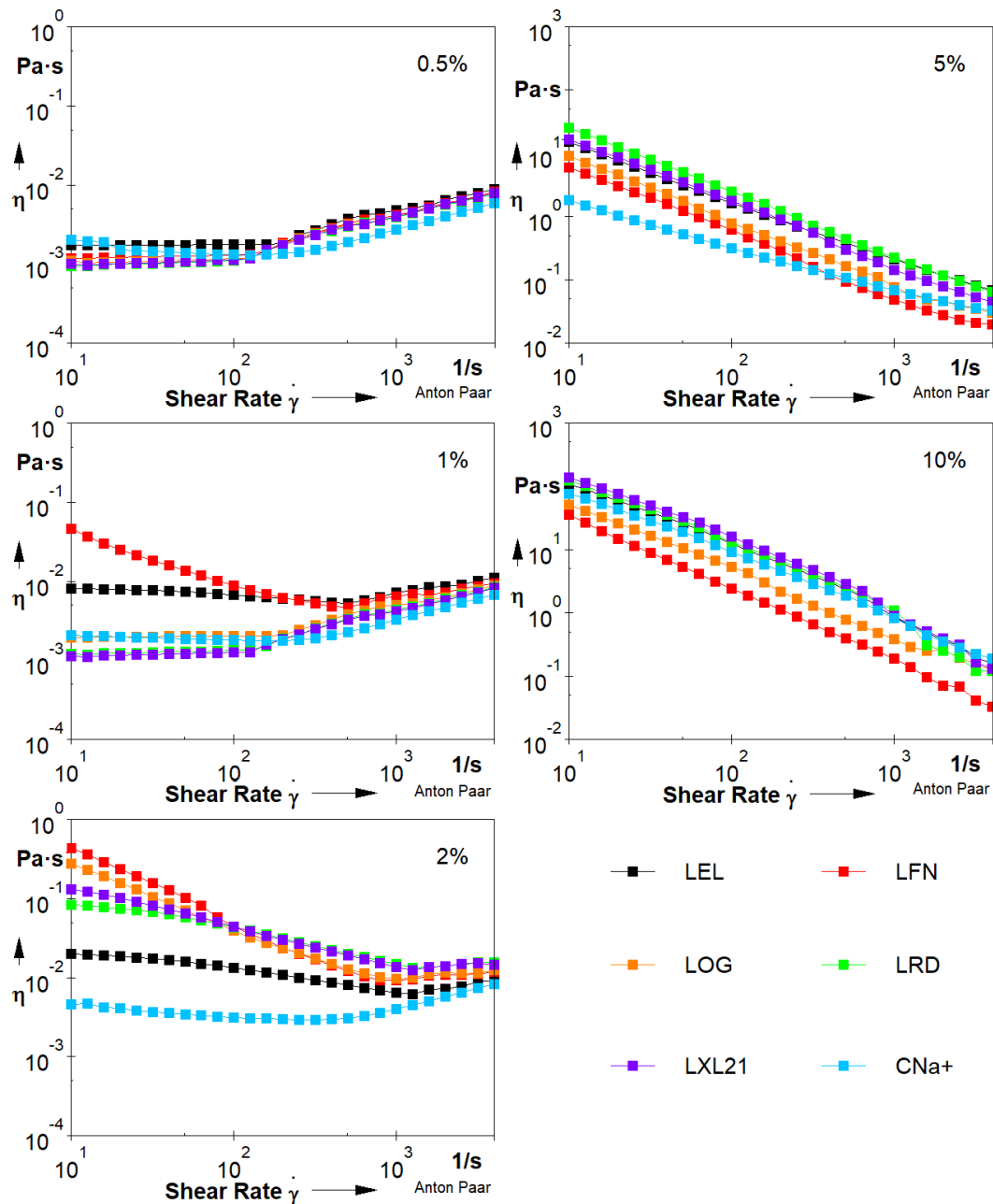


Figure 3.13 Viscosity curves (log-log scale) for clay suspensions at different clay wt.% dispersions showing shear thinning.

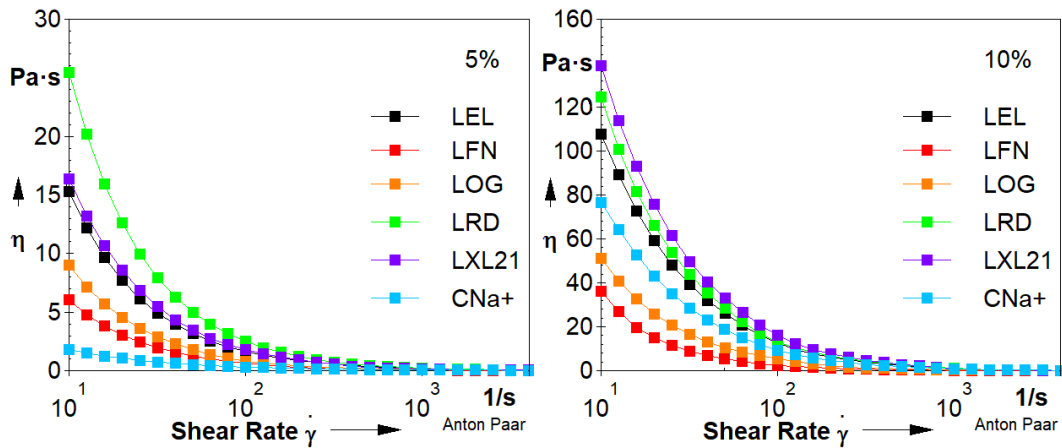


Figure 3.14 Viscosity curves (semi-log scale) for 5.0 and 10.0 wt.% clay dispersions showing a clear shear thinning behaviour.

The viscosity values for the higher clay concentration (Table 3.5 and Figure 3.15) demonstrate the relationship between particle size and viscosity, the smaller the particle size the higher the viscosity values. L_{EL}, L_{RD}, and L_{XL21} have larger viscosity values when compared to L_{OG}, L_{FN}, and C_{Na+}.

Table 3.5 Viscosity values at specific shear rates or clay dispersion at different clay content.

	Particle size (nm)	η (Pa.s) for 1%		η (Pa.s) for 2%		η (Pa.s) for 5%		η (Pa.s) for 10%	
		10 s^{-1}	10^3 s^{-1}	10 s^{-1}	10^3 s^{-1}	10 s^{-1}	10^3 s^{-1}	10 s^{-1}	10^3 s^{-1}
L _{EL}	44	0.008	0.007	0.020	0.006	15.30	0.21	114	0.15
L _{FN}	140	0.046	0.006	0.437	0.009	06.04	0.05	036	0.19
L _{OG}	83	0.002	0.005	0.276	0.010	09.01	0.08	051	0.38
L _{RD}	40	0.001	0.004	0.083	0.015	25.50	0.22	125	1.10
L _{XL21}	60	0.001	0.004	0.131	0.014	16.40	0.14	139	0.90
C _{Na+}	100	0.002	0.003	0.005	0.004	01.82	0.07	076	0.82

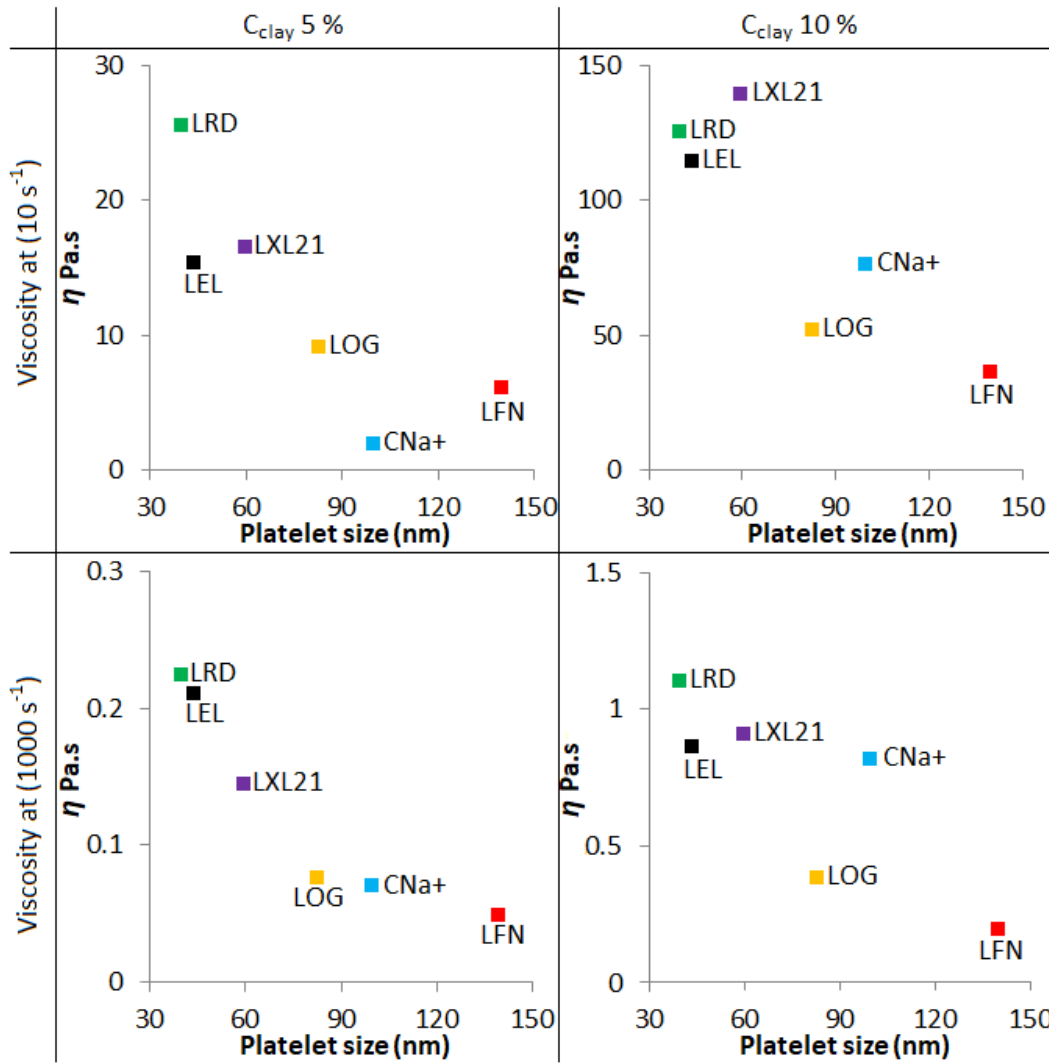


Figure 3.15 Viscosity value at for 5 and 10 wt.% clay dispersions at different shear rates as a function of platelet size.

3.5.2 Clay suspensions Yield Stress

The high viscosity values at a low shear rate effectively produce anti-settling properties which are a key for many applications in different fields like in drilling fluids production. [37] The stability of a clay suspension comes from the mutual repulsion between the intersecting electrical double layers interacting on approach. [38] The double-layer is made of the negatively charged surface and a positively charged edge. As they are oppositely charged the concentration of the counter-ions near the particle surface is high. With the distance increased from the surface the concentration of the counter-ions decreases as they tend to diffuse away to the bulk solution where the concentration is lower. [39][40][41] If the clay

concentration is high enough, gel structures build up slowly with time, as the particles orient themselves towards positions of minimum free energy (Figure 3.10). [2] This property is the reason why structured fluids do not often flow until they reach a certain stress level known as “yield stress or τ_{yield} ”. When below the yield point the material behaviour is elastic, when stress builds to reach above the yield point the material structure breaks and the material starts to flow. [42] Classically, flow curves are used to measure the yield, as the shear stress increases in steps or via a ramp the shear stress value is taken as the yield point. At which the measuring device is still detecting no sign of motion, this is the last measuring point at which the rotational speed is still displayed as $\omega = 0.0$ rpm or shear stress $\dot{\gamma} = 0.0$ 1/s on a flow curve. The yield point value occurs as an intersection on the τ -axis when plotted on a linear scale. If presented on a logarithmic scale, the yield point is the τ value at the lowest measured shear rate (Figure 3.16 a). [43] The shear ramp can also be used where yield stress is at the viscosity maximum, which is readily measurable for most structured fluids (Figure 3.16 b).[42]

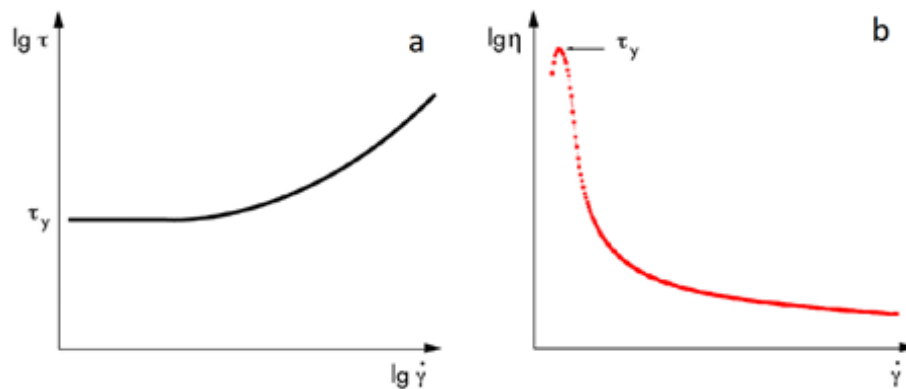


Figure 3.16 Yield stress values as observed on a) Flow curve (log-log scale) b) Viscosity curve (semi-log). Modified from [43].

Flow curves for different clay grades at different clay concentration shows that the yield stress increases as a function of clay concentration (Figure 3.17). At low clay concentration dispersion, the τ_{yield} is significantly lower than the τ_{yield} for suspensions with high clay concentration. In the high clay concentration suspensions; the edge-to-face bonds are operative (i.e. a house-of-cards structure), and the gel structures build up as the particles orient themselves towards positions

of minimum free energy, thus the structure break occurs at higher yield stress for the clay concentration. [31]

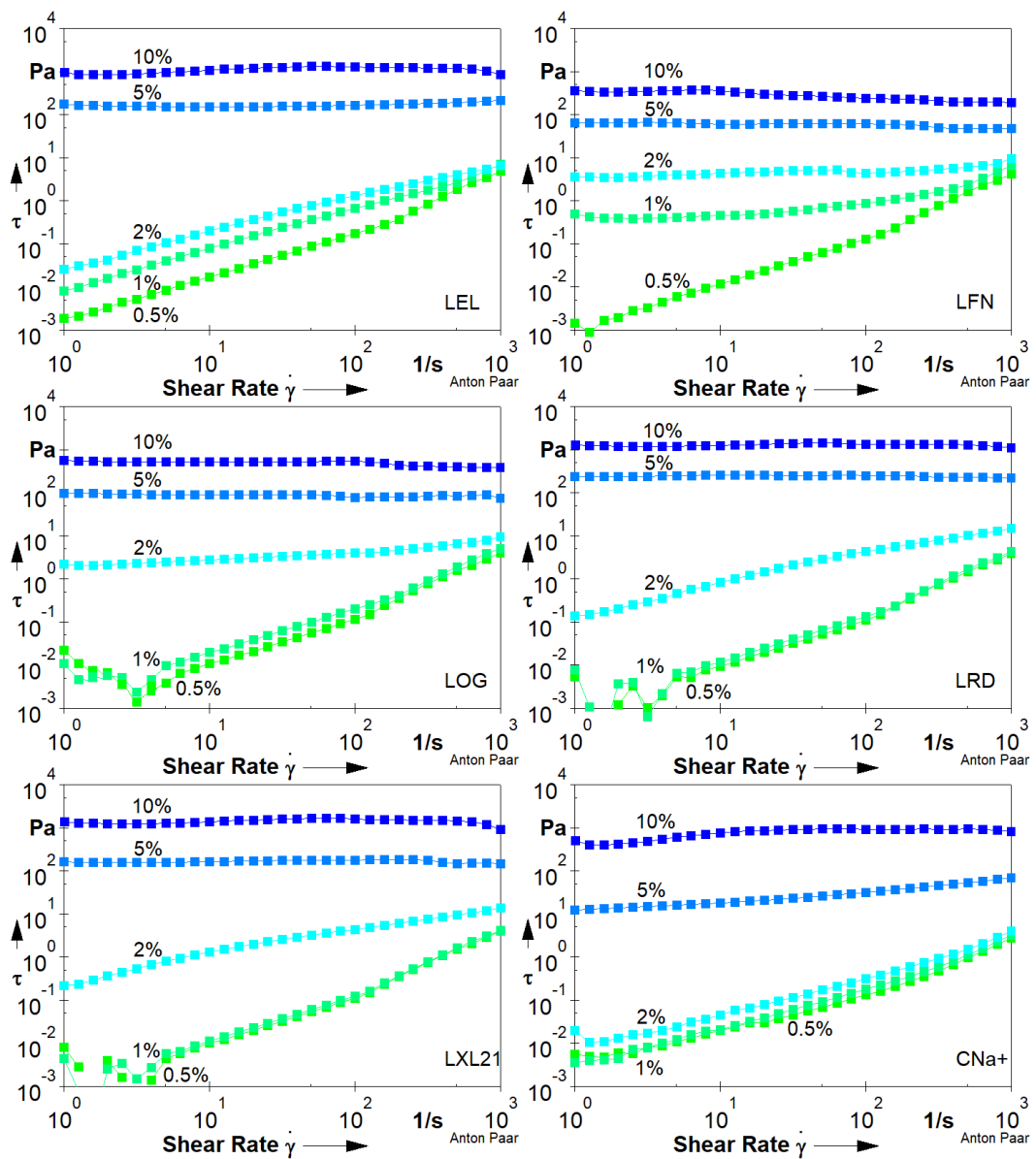


Figure 3.17 Flow curves for LEL, LFN, LOG, LRD, LXL21, and CNa+ dispersions at different clay concentration (0.5, 1.0, 2.0, 5.0, 10.0 wt.%) show the yield stress increases with increasing the clay concentration.

Clay dispersion yield stress depends mainly on the clay platelet size and the CEC of the type of clay used. Figure 3.18 shows a comparison between different clays of different platelet sizes and yield stress.

Generally, more clay in the dispersion increases the yield stress which is observed clearly from the graphs for the 2 wt%, 5 wt%, and 10 wt% as there is more platelet-

platelet interaction which requires more force to overcome the interaction. The 0.5 wt.% and 1 wt.% clay samples show similar weak values representing little platelet-claylet interaction.

The plots show different behavior for low and high clay concentrations. Yield stress value increases with larger platelets for clay dispersion with clay concentrations ≤ 2 wt.% for all clays except C_{Na+}, however, for clay dispersions with $C_{\text{clay}} \geq 5$ wt.% the relationship between platelet size and yield stress is opposite as the yield value decreases with larger platelet size.

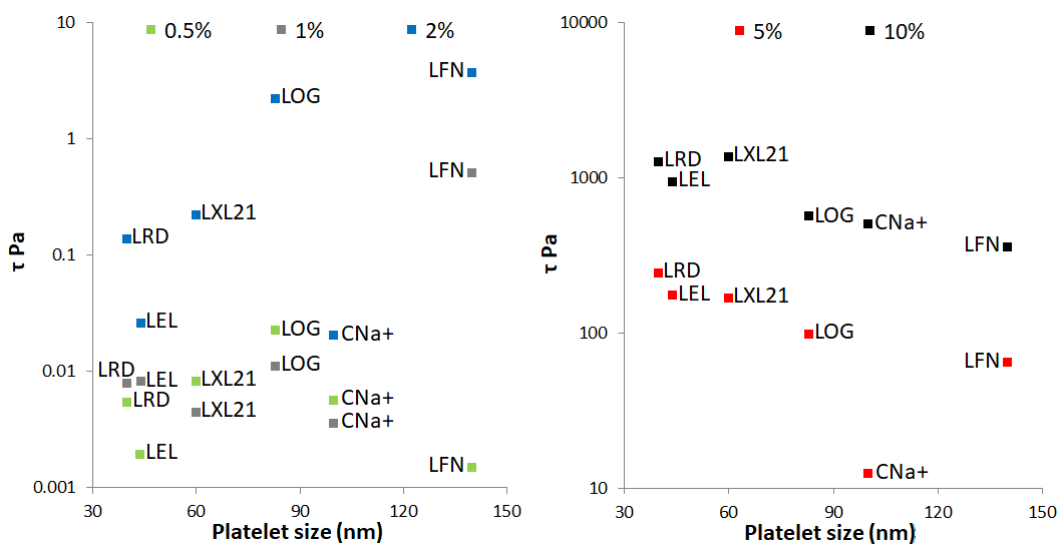


Figure 3.18 Yield stress vs platelet size for (left) low clay concentration dispersions (≤ 2 wt.%) and (right) high clay concentration (≥ 5 wt.%).

On the other hand, the relationship between the yield stress and the clay CEC is not different as shown by Figure 3.19. The comparison shows that as the clay CEC increases the yield stress is not following a certain decreasing trend. Table 3.6 shows the value of yield stress for all types of clays for dispersion of different clay concentrations.

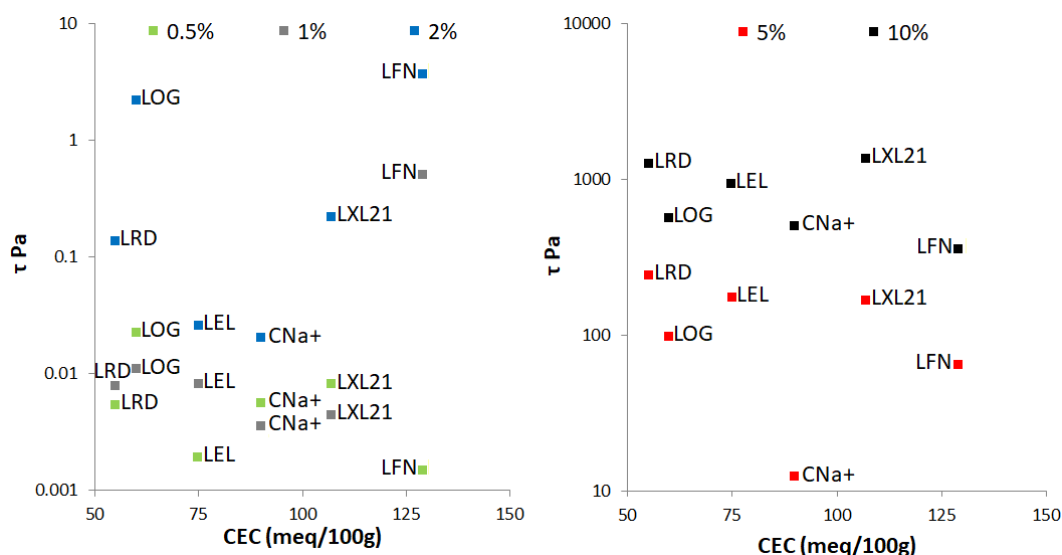


Figure 3.19 Yield stress vs CEC for (left) low clay concentrations dispersions (clay concentrations ≤ 2 wt.%) and (right) high clay concentrations dispersions (clay concentrations ≥ 5 wt.%).

Table 3.6 Yield stress value (Pa) for different clays dispersions at different clay concentrations.

Platelet size (nm)	CEC (meq/100 g)	clay concentration					
		0.5 wt.%	1 wt.%	2 wt.%	5 wt.%	10 wt.%	
Yield stress Pa							
L _{EL}	044	075	0.002	0.008	0.026	175	933
L _{FN}	140	129	0.002	0.502	3.620	064	353
L _{OG}	083	060	0.022	0.011	2.180	098	567
L _{RD}	040	055	0.005	0.008	0.137	241	1250
L _{XL21}	060	107	0.008	0.004	0.219	166	1350
C _{Na+}	100	090	0.006	0.004	0.020	12.4	503

3.6 Summary

This chapter described the characterisation of the physical and chemical properties of clays that will be used as crosslinking agents later in this work in the synthesis of a series of clay-polymer nanocomposite materials. The clays used were synthetic grades of hectorite and natural bentonite with good dispersion properties for gel creation.

The clays were all shown to be broadly similar in nature from the XRD and FTIR spectroscopic analysis, as anticipated. All clays have d_{001} and d_{100} in the ranges 2θ ($5 - 7^\circ$) and ($19.2 - 19.6^\circ$) respectively. The d_{001} (the interlayer spacing) have a bigger range as a result of the different structures and modifications made on each type. the smaller the platelet size clays had a weak reflection at d_{001} for the L_{EL}, L_{RD} and a smaller d_{001} spacing (4.86, 5.86 Å respectively) whereas clays with large platelet size

like L_{FN} , L_{OG} and C_{Na^+} had a sharp and clear reflection for the d_{001} and a spacing of 6.54, 7.02, and 6.94 Å, respectively. However, the XRF data show some elemental differences between the clays as shown in Table 3.3, although some question marks on the validity of the XRF data should be raised due to some elements that are 'XRF' silent in certain samples, As there may be issues with not being able to detect Li and F, but with their small quantities a little effect on the quantitative ability of XRF method is anticipated. Even if there was an effect the ratios of elements are still expected to correlate. As this cannot be seen perhaps the validity of the manufacturer's numbers can be questioned as the manufacturer's numbers could be reporting the concentration of the elements added to make the clay and do not account for elements that are washed away during the process. It could also be accounted for by batch variability. We cannot be sure with certainty and further experiments would be required. We can only look at the general trends for the purposes of this research.

These differences can be used to explain the different behaviours of the clay dispersions have and the clay's ability to form crosslinking points as the charge on the surface is related to the number of ions available as indicated by Figure 3.3 and Table 3.3.

The TGA data shows that the platelet size plays an important role in the thermal properties. Clays with smaller platelet size like L_{EL} and L_{RD} show the total weight loss of 15.90 % for L_{EL} and 14.82 % L_{RD} , whereas clays with large platelet size like L_{FN} and C_{Na^+} had less weight loss of 13.12 % and 12.13 % respectively. L_{OG} and C_{Na^+} had a higher onset temperature than all other clays, this behaviour still needs more investigation, but it may be related to the range of the platelets size or the ratio between the clay platelet size and the CEC. A higher CEC and more exchangeable cations could result in a more polar environment and thus they may be able to attract more water. However, if the CEC is high then the clay layers are going to be more tightly held together which will prevent more water molecules entering the interlayer. Smaller platelets would mean more surface edges relative to the bulk of the clay, these broken edges are likely to be more polar and will attract more water.

Different exchangeable cations with different polarisability could attract more water. If Li or Na or Ca are present these will affect the amounts of water present.

The FTIR spectroscopy analysis shows that the clays are chemically very similar, as expected, with a high-intensity Si-O band at the range of 990 – 1000 cm^{-1} , the C_{Na^+} has different fingerprint in that region due to its different chemical structure, as mentioned earlier, with Al included in it and more impurities in that grade. As clays are used as a crosslinking agent in the clay-polymer nanocomposites, the position of the Si-O bands could be informative when understanding clay-polymer interactions.

The Rheological properties for different clays dispersions at different clay concentrations show the effect of clay content on the rheological and mechanical properties. For low clay concentration dispersions (< 5 wt.%) the larger the particles, the higher the viscosity and yield stress, while for higher clay concentration dispersions (> 5 wt.%) the larger the clay particle size, the lower the viscosity and yield stress (Figure 3.13 and Figure 3.14). Dispersions with high clay content show a clear shear thinning behaviour as clay platelets facilitate the clay suspension flow, as the force affecting the hydrogel increases the clay platelets get in line with the flow direction, this leads to an improvement, as the platelets help to direct the flow making it easier to flow in the right direction and to avoid turbulence. The clay platelet size also plays a role in the rheological behaviour of the clay dispersions; larger clay-platelets dispersions (L_{FN} , L_{OG} , and C_{Na^+}) show a lower viscosity range when compared to other smaller clay-platelets dispersions (L_{EL} , L_{RD} , and L_{XL21}) as shown in Figure 3.14. The effect of clay platelet size can also be observed on the yield stress values as shown in Figure 3.15; the larger clay-platelets dispersions have lower yield stresses.

3.7 References

- [1] T. Al Ani and S. Olli, "Clay and clay mineralogy." 2008.
- [2] P. F. Luckham and S. Rossi, "Colloidal and rheological properties of bentonite suspensions," *Adv. Colloid Interface Sci.*, vol. 82, no. 1, pp. 43–92, Oct. 1999.
- [3] R. J. Hunter, "The Flow Behavior of Coagulated Colloidal Dispersions," *Adv. Colloid Interface Sci.*, vol. 17, pp. 197–211, 1982.
- [4] T. N. Blanton, D. Majumdar, and S. M. Melpolder, "MICROSTRUCTURE OF CLAY-POLYMER COMPOSITES," vol. 42. JCPDS-International Centre for Diffraction Data, New York, pp. 562–568, 2000.
- [5] R. E. Grim, *Clay mineralogy, 2nd ed.* New York : McGraw-Hill, 1968.
- [6] J. Díez, L. Barral, R. Bellas, J. López, C. Ramírez, and A. Rodríguez, "Exfoliated/intercalated silicate/hot styrene butadiene rubber nanocomposites: Structure-properties relationship," *J. Appl. Polym. Sci.*, vol. 125, no. SUPPL. 1, Jul. 2012.
- [7] D. M. C. MacEwan and M. J. Wilson, "Interlayer and Intercalation Complexes of Clay Minerals," *Crystal Structures of Clay Minerals and their X-Ray Identification*, vol. 5. Mineralogical Society of Great Britain and Ireland, p. 0, 01-Jan-1980.
- [8] G. E. Christidis *et al.*, "The nature of laponite: Pure hectorite or a mixture of different trioctahedral phases?," *Minerals*, vol. 8, no. 8, Aug. 2018.
- [9] S. Mallakpour and M. Dinari, "Biomodification of cloisite Na + with L-methionine amino acid and preparation of poly(vinyl alcohol)/organoclay nanocomposite films," *J. Appl. Polym. Sci.*, vol. 124, no. 5, pp. 4322–4330, Jun. 2012.
- [10] H. J. M. Hanley, C. D. Muzny, and B. D. Butler, "Surfactant adsorption on a

clay mineral: Application of radiation scattering," *Langmuir*, vol. 13, no. 20, pp. 5276–5282, Oct. 1997.

- [11] B. Rafiei and F. A. Ghomi, "Preparation and characterization of the Cloisite Na⁺ modified with cationic surfactants Caspian sea View project Organoclay synthesis View project," *J. Crystallogr. Mineral.*, vol. 21, pp. 25–32, 2013.
- [12] P. K. Paul, S. A. Hussain, D. Bhattacharjee, and M. Pal, "Preparation of polystyrene-clay nanocomposite by solution intercalation technique," *Bull. Mater. Sci.*, vol. 36, no. 3, pp. 361–366, Jun. 2013.
- [13] E. A. Stefanescu, C. Stefanescu, W. H. Daly, G. Schmidt, and I. I. Negulescu, "Hybrid polymer-clay nanocomposites: A mechanical study on gels and multilayered films," *Polymer (Guildf.)*, vol. 49, no. 17, pp. 3785–3794, Aug. 2008.
- [14] E. A. Stefanescu, W. H. Daly, and I. I. Negulescu, "Hybrid polymer/clay nanocomposites: Effect of clay size on the structure of multilayered films," *Macromol. Mater. Eng.*, vol. 293, no. 8, pp. 651–656, Aug. 2008.
- [15] P. S. Nayak and B. K. Singh, "Instrumental characterization of clay by XRF, XRD and FTIR," *Bull. Mater. Sci.*, vol. 30, no. 3, pp. 235–238, Jun. 2007.
- [16] Z. Q. Xiong, X. D. Li, F. Fu, and Y. N. Li, "Performance evaluation of laponite as a mud-making material for drilling fluids," *Pet. Sci.*, 2019.
- [17] S. H. Nair, K. C. Pawar, J. P. Jog, and M. V. Badiger, "Swelling and mechanical behavior of modified poly(vinyl alcohol)/laponite nanocomposite membranes," *J. Appl. Polym. Sci.*, vol. 103, no. 5, pp. 2896–2903, Mar. 2007.
- [18] J. M. Yeh, S. J. Liou, and Y. W. Chang, "Polyacrylamide-clay nanocomposite materials prepared by photopolymerization with acrylamide as an intercalating agent," *J. Appl. Polym. Sci.*, vol. 91, no. 6, pp. 3489–3496, Mar. 2004.

- [19] W. Xie, Z. Gao, W. P. Pan, D. Hunter, A. Singh, and R. Vaia, "Thermal degradation chemistry of alkyl quaternary ammonium Montmorillonite," *Chem. Mater.*, vol. 13, no. 9, pp. 2979–2990, 2001.
- [20] K. C. Cole, "Use of infrared spectroscopy to characterize clay intercalation and exfoliation in polymer nanocomposites," *Macromolecules*, vol. 41, no. 3, pp. 834–843, Feb. 2008.
- [21] L. Yan, C. B. Roth, and P. F. Low, "Changes in the Si-O vibrations of smectite layers accompanying the sorption of interlayer water," *Langmuir*, vol. 12, no. 18, pp. 4421–4429, Sep. 1996.
- [22] K. C. Cole, F. Perrin-Sarazin, and G. Dorval-Douville, "Infrared spectroscopic characterization of polymer and clay platelet orientation in blown films based on polypropylene-clay nanocomposite," *Macromol. Symp.*, vol. 230, pp. 1–10, 2005.
- [23] R. J. Gilkes, "Chemistry of Clays and Clay Minerals. Mineralogical Society/Longman Scientific and Technical, England," *Clay Miner.*, vol. 22, no. 4, pp. 485–486, 1987.
- [24] BYK Additives & Instruments, "LAPONITE LAPONITE-Performance Additives," Geretsried.
- [25] F. F. Fang, J. H. Kim, H. J. Choi, and C. A. Kim, "Synthesis and electrorheological response of nano-sized laponite stabilized poly(methyl methacrylate) spheres," *Colloid Polym. Sci.*, vol. 287, no. 6, pp. 745–749, 2009.
- [26] B. Strachota *et al.*, "Poly(N-isopropylacrylamide)-clay based hydrogels controlled by the initiating conditions: Evolution of structure and gel formation," *Soft Matter*, vol. 11, no. 48, pp. 9291–9306, 2015.
- [27] P. H. Nadeau, "The physical dimensions of fundamental clay particles," *Clay*

Miner., vol. 20, no. 4, pp. 499–514, Dec. 1985.

- [28] M. Dijkstra, J. P. Hansen, and P. A. Madden, “Gelation of a clay colloid suspension,” *Phys. Rev. Lett.*, vol. 75, no. 11, pp. 2236–2239, 1995.
- [29] Y. Kimura and K. Haraguchi, “Clay-Alcohol-Water Dispersions: Anomalous Viscosity Changes Due to Network Formation of Clay Nanosheets Induced by Alcohol Clustering,” *Langmuir*, vol. 33, no. 19, pp. 4758–4768, May 2017.
- [30] K. Haraguchi, H. J. Li, K. Matsuda, T. Takehisa, and E. Elliott, “Mechanism of forming organic/inorganic network structures during in-situ free-radical polymerization in PNIPA-clay nanocomposite hydrogels,” *Macromolecules*, vol. 38, no. 8, pp. 3482–3490, Apr. 2005.
- [31] B. S. Neumann and K. G. Sansom, “The rheological properties of dispersions of Laponite, a synthetic hectorite-like clay, in electrolyte solutions,” *Clay Miner.*, vol. 9, no. 2, pp. 231–243, Dec. 1971.
- [32] D. W. Thompson and J. T. Butterworth, “The nature of laponite and its aqueous dispersions,” *J. Colloid Interface Sci.*, vol. 151, no. 1, pp. 236–243, 1992.
- [33] J. D. F. Ramsay, “Colloidal properties of synthetic hectorite clay dispersions. I. Rheology,” *J. Colloid Interface Sci.*, vol. 109, no. 2, pp. 441–447, 1986.
- [34] T. Wang, D. Liu, C. Lian, S. Zheng, X. Liu, and Z. Tong, “Large deformation behavior and effective network chain density of swollen poly(N-isopropylacrylamide)-Laponite nanocomposite hydrogels,” *Soft Matter*, vol. 8, no. 3, pp. 774–783, 2012.
- [35] C. Martin *et al.*, “Osmotic compression and expansion of highly ordered clay dispersions,” *Langmuir*, vol. 22, no. 9, pp. 4065–4075, Apr. 2006.
- [36] J. M. Zuidema, C. J. Rivet, R. J. Gilbert, and F. A. Morrison, “A protocol for rheological characterization of hydrogels for tissue engineering strategies,” *J.*

Biomed. Mater. Res. - Part B Appl. Biomater., vol. 102, no. 5, pp. 1063–1073, 2014.

- [37] N. Willenbacher, “Unusual thixotropic properties of aqueous dispersions of Laponite RD,” *J. Colloid Interface Sci.*, vol. 182, no. 2, pp. 501–510, Sep. 1996.
- [38] P. M. P. Stevens, *Polymer Chemistry, An Introduction (2nd ed.)*. New York: Oxford University Press., 1990.
- [39] H. Li and K. Haraguchi, “Mechanical and swelling/de-swelling properties of nanocomposite gel with high clay content,” vol. 55, Jan. 2006.
- [40] M. E. Byrne, K. Park, and N. A. Peppas, “Molecular imprinting within hydrogels,” *Adv. Drug Deliv. Rev.*, vol. 54, no. 1, pp. 149–161, Jan. 2002.
- [41] R. Akashi, H. Tsutsui, and A. Komura, “Polymer Gel Light-Modulation Materials Imitating Pigment Cells,” *Adv. Mater.*, vol. 14, no. 24, p. 1808, 2002.
- [42] A. Franck, “Understanding Rheology of Structured Fluids.”
- [43] T. G. Mezger, *The Rheology Handbook : 4th Edition*. Vincentz Network, 2014.

4

Clay-Acrylamide Nanocomposites/Hydrogels Characterisation

Chapter 4 Clay-PolyAcrylamide

Nanocomposites/Hydrogels Characterisation

Polyacrylamides are a class of polymers commonly used in a variety of industries, over the last fifty years. There has been an increasing interest in acrylamide devoted research. Acrylamide ($\text{CH}_2=\text{CH}-\text{CO}-\text{NH}_2$) is a highly reactive organic substance, that easily dissolves in water and polar solvents such as methanol or ethanol. Acrylamide's high reactivity is due to the double bond and amide group within its structure. Acrylamide is polymerised under the influence of temperature and ultraviolet (UV) radiation with the presence of a suitable initiator. [1]

Polyacrylamide hydrogels are important in a variety of applications, such as superabsorbent materials, support for cell culture, and artificial muscles. However, the hydrogel structure and mechanical properties need to be engineered to meet the required specification of any particular application. [2]

Clay-polymer nanocomposites formed by adding polymer to a modified clay dispersion, are known for their enhanced mechanical properties. [3] Clay-polymer nanocomposite materials are of interest due to a wide range of novel physical properties. In these composites, the layered clay material is often exfoliated in the polymer matrix, and hence the improvement in physical properties as more polymeric chains can get to crosslink. [4]

The addition of nanosized clay with large surface area to acrylamide type polymers dramatically improve its mechanical and barrier properties which is a useful property for several medical applications particularly applications that require stronger support to certain areas when needed as the case with clay-pNIPAM-based hydrogels that show an increase in the tensile modulus to around 500 kPa compared to a tensile modulus of around 240 kPa for conventional chemically crosslinked composites, [5] and fracture energy up to 3300 times that of

conventional gels. A good example is to make stronger materials to provide greater support to degraded discs in the spine. [6][7]

In this chapter, two different acrylamide based polymers (pNIPAM and pDMAc) and six different types of clay were used to synthesis a range of clay-polymer products at 1% clay loading. pNIPAM composites were also studied at 2% clay loading with each clay, to determine the influence of clay loading on various properties. These include processability, compatibility for rheology testing without damaging the kit, reasonable testing time and the ability to grind the material without contamination. [8] In this chapter, we investigated pNIPAM and pDMAc homopolymer gels as well as clay-pNIPAM and clay-pDMAc nanocomposites at different clay-to-polymer ratios.

4.1 Clay-pNIPAM Characterisation and Rheological Properties

Clay-polymer nanocomposite hydrogels with high water content and soft nature have an important role in biomedical research fields. These include stimuli-responsive polymer hydrogels (polymers that sharply respond to small changes in physical or chemical conditions with large property changes also referred to as “environmentally-sensitive” or “smart” polymers). [9] As a type of functional soft material with the ability to change in volume in response to external environmental changes, poly(N-isopropylacrylamide) (pNIPAM) and its corresponding hydrogels have been intensively studied.

It is an attractive polymer that exhibits a clear phase transition within a specific temperature range, this is known as a lower critical solution temperature (LCST) and this property can be used to form smart gels for various applications [10][11] such as tissue engineering, enzyme immobilization, and drug-delivery systems which are usually in an aqueous environment. [12] pNIPAM exhibits a fast coil-to-globule transition around its LCST 32 °C in aqueous media (Figure 4.1) and can be

produced in the form of covalent-free crosslinked hydrogels using clay platelets as crosslinkers. [13]

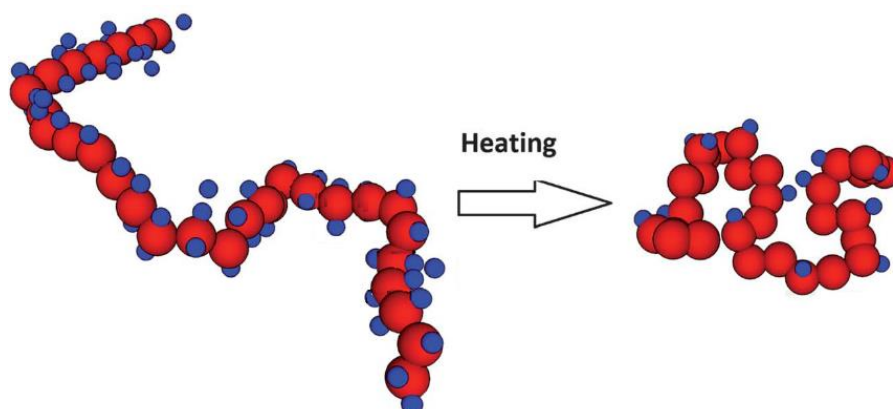


Figure 4.1 Schematic of the conformational change of poly (NIPAM) from a coil to a collapsed globule at LCST. Red balls correspond to NIPAM units and blue balls to water molecules. [14]

Below the LCST, pNIPAM chains adopt expanded random-coil conformations, which are hydrated and flexible in the water. Above the LCST, pNIPAM chains collapse to a globular tightly-packed confirmation and are dehydrated. The stimuli-responsive properties of pNIPAM enhance its potential to be used for the above-mentioned applications. In pNIPAM hydrogels, it was reported that many properties such as volume (i.e. swelling ratio) [15], optical transparency, and mechanical properties [16] change significantly because of the hydrophilic/hydrophobic transition at the LCST alongside it being crosslinked. [17]

4.1.1 Clay-pNIPAM Nanocomposites

The empirical observations of the synthesis of pNIPAM based clay-polymer composites were based on (a) ascertaining the physical state of the synthesis products immediately after synthesis, whilst still at moderately high T ($\sim 70\text{ }^{\circ}\text{C}$) and (b) determining the changes upon cooling to room T, i.e. below the reported LCST ($\sim 32\text{ }^{\circ}\text{C}$). The influence that changing the nature of the clay crosslinker on these observations was reported.

In order to create a 'benchmark' material, pNIPAM was synthesised using the same synthetic route but without any crosslinking agent. The pNIPAM homopolymer is a soft white gel at a temperature above LCST and solidifies as temperature decreases

to room temperature. The gel is easily poured out of a glass vial and is injectable using a syringe if its temperature is above the LCST.

Adding L_{EL} to the polymer to create the 1L_{EL}-pNIPAM nanocomposite changed some of its properties, for example, the composite is a free-flowing soft gel above the LCST, and however, after solidification below the LCST, the composite still has the ability to self-heal from damage.



















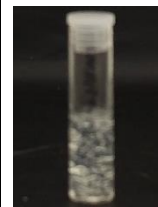

The addition of different Laponite[®] grades prior to synthesis resulted in a different set of properties to the final synthesis products. In general, the products 1L_{XL21}-pNIPAM, 1L_{EL}-pNIPAM and 1L_{RD}-pNIPAM had a lower apparent viscosity at higher temperatures than at lower temperatures and reduced in opacity as the T was reduced. Increasing the crosslink density increased the apparent viscosity but did not change the overall phenomena observed.

On the other hand, 1L_{FN}-pNIPAM and 1L_{OG}-pNIPAM formed hard rubbery materials upon polymerisation and only the viscosity seemed to change upon cooling.

1C_{Na+}-pNIPAM nanocomposite was different from the final product having what can be described as a soft scrambled egg-like consistency with evidence of phase at the bottom of the vial above and below the LCST.

Table 4.1 summarises with pictures the observations of clay-pNIPAM composites as it was synthesised after polymerisation at a temperature above pNIPAM LCST and after solidification at a temperature below the LCST.

Table 4.1 General properties of (1 % clay)-pNIPAM and (2 % clay)-pNIPAM at different temperatures above and below the LCST

	pNIPAM	1L _{EL} -pNIPAM	2L _{EL} -pNIPAM	1L _{FN} -pNIPAM	1L _{OG} -pNIPAM	1L _{RD} -pNIPAM	2L _{RD} -pNIPAM	1L _{XL21} -pNIPAM	2L _{XL21} -pNIPAM	1C _{Na+} -pNIPAM
Temperature; 60 °C	White, soft gel	White, soft flowing gel	White, soft gel, flows when shaken	White, hard elastic single block gel	White hard single block gel	White very soft flowing gel	White soft gel flows when shaken	White soft flowing gel	White soft gel, easier to flow than 2L _{EL} -pNIPAM and 2LRD-pNIPAM	Yellowish soft gel “scrambled egg-like”. Almost 15% clear water on the bottom
										
Temperature; Room temp.	Cloudy yellowish, hard gel	Cloudy, hard gel	Clear hard gel	Clear hard gel	Yellowish hard gel	Clear hard gel	Clear hard gel	Clear hard gel	Clear hard gel	Yellowish hard gel
										

4.1.2 XRD Characterisation of Clay-pNIPAM Nanocomposites

Whenever a polymer is associated with dispersed nanoclay, the clay interlayer spacing changes depending on different factors; such as the extent of diffusion of polymer chains within the interlayer, clay-to-polymer ratio, preparation method, the clay platelet size, and CEC. [18][19]

The interlayer spacing of different clay-pNIPAM nanocomposites was investigated by XRD after drying to remove water. The results are listed in Table 4.2. The as-prepared (2 % clay)-polymer nanocomposite contains 90 wt.% water and 2 wt.% of clay, but when dried to remove water, the clay content in the (2 % clay)-polymer nanocomposite is 20 wt.% based on the assumption that all water was lost during the drying process. [20] However, the TGA results analysis (Section 4.1.3) show that according to the drying protocol used in this study (Section 2.1.1.1) the clay content for the (2 % clay)-polymer nanocomposite is less than 20 wt.% as all nanocomposites show some weight loss of free water ($\approx 5 - 10$ wt% relative to the clay and polymer content) up to 150 °C.

The correlations between XRD and nanocomposite morphology are demonstrated in Figure 4.2. The XRD trace of clay displays an intense d_{001} peak, and for a conventional composite of non-intercalated or non-exfoliated clay in the polymer matrix, the resulting XRD trace is similar to that of the original clay particles.[21]

Ghaemi et al. [22] showed with XRD that clay in a polymer matrix can lead to two types of morphologies. In the intercalated morphology, the results are a displacement of the d_{001} reflection towards lower angles as the interlayer basal spacing of the clay sheets has increased by intercalation of the polymer. In an intercalated nanocomposite XRD trace, the d_{100} and d_{110} reflections of clay exist. In the exfoliated morphology the XRD result is the absence of a d_{001} diffraction reflection, which indicates that the sheets of the clay are delaminated and well spread among the polymer chains. [23][24] Despite the XRD results as explanations

and interpretations, XRD results cannot tell for sure if clay particles are exfoliated or not and Transmission Electronic Microscopy (TEM) is still required to provide evidence about what state the clay dispersions are, however the terms used in this work are mention for introducing the differences between the different samples based on literature available.

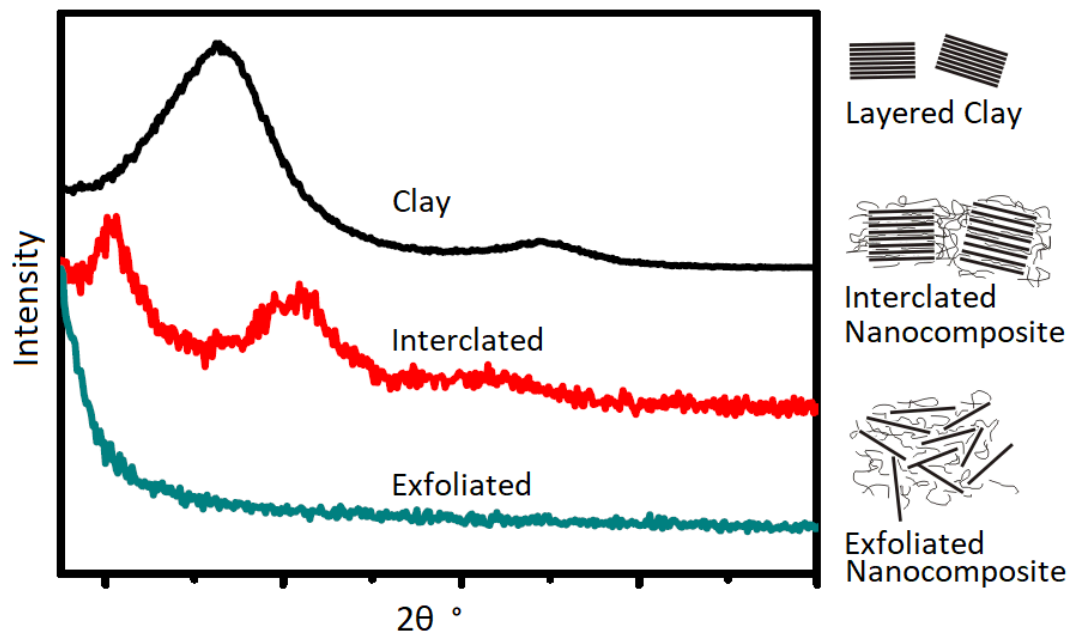


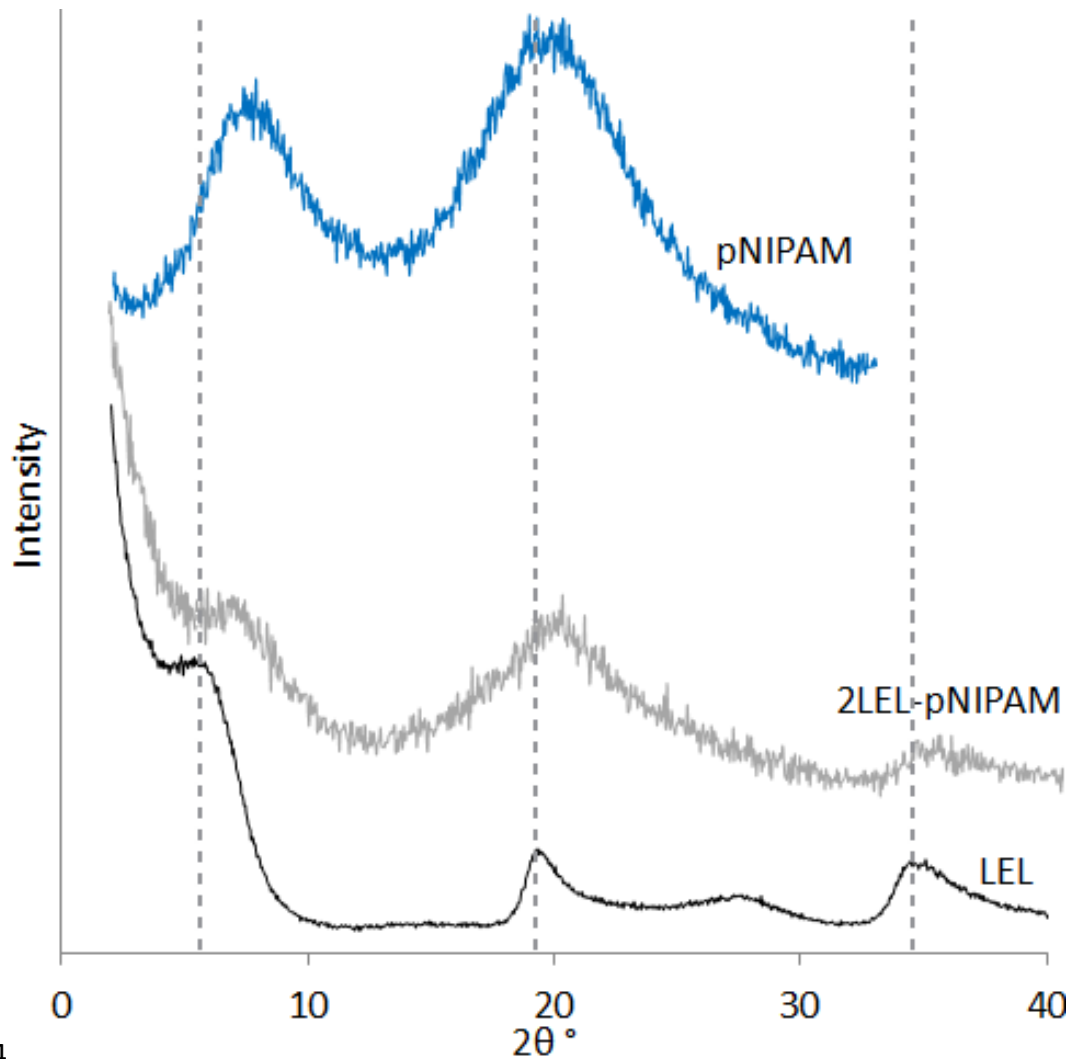
Figure 4.2 The correlations between XRD and nanocomposite morphology.

XRD traces of L_{EL} , pNIPAM and dried $2L_{EL}$ -pNIPAM are presented in Figure 4.3. The $1L_{EL}$ -pNIPAM composite sample was too hard to be ground using the same method used with all other samples (pestle and mortar), so a mechanical mill was used to grind it, but the results were not as hoped for, the form of the material was as small lumps and grey colour, and the mill was slightly dented. Data is not shown because it was suspected the different form would provide a different orientation of the sample in the XRD sample holder and affect the reflection shape and position. The XRD trace of $2L_{EL}$ -pNIPAM composite looks similar to that of pNIPAM. [25] The presence of pNIPAM chains between the clay platelets can be deduced by comparing the reflection positions in the XRD trace of the pure L_{EL} with those in the XRD trace of the nanocomposite. The increasing baseline in the XRD trace of the $2L_{EL}$ -pNIPAM at $2\theta < 5^\circ$ is likely to indicate exfoliation or a very disordered clay (due to a scattering effect), however, because the reflection at around $2\theta = 7.2^\circ$ in the trace of $2L_{EL}$ -pNIPAM could either be due to the clay or the pNIPAM there is

uncertainty in this description. For all the pNIPAM composites discussed herein the presence of the pNIPAM reflection at around $2\theta = 4$ to 12° makes the characterisation of the clay dispersion very difficult. Given the trends in the other polymer composites discussed below, it is believed the reflection at around $2\theta = 7.2^\circ$ ($d = 12.3 \text{ \AA}$) and $2\theta = 20.2^\circ$ ($d = 4.4 \text{ \AA}$) in the $2L_{EL}$ -pNIPAM nanocomposite trace are due to those at 7.4° and 20.2° in the pNIPAM, and the shift to a lower angle for the d_{100} is a result of mixing the pNIPAM with the clay (L_{EL}) and a change in crystallinity.

The reflection at $2\theta = 35.6^\circ$ ($d = 2.52 \text{ \AA}$) in the $2L_{EL}$ -pNIPAM nanocomposite trace did not show a significant shift to a higher or lower value compared to that of the clay (L_{EL}) as anticipated; this reflection corresponds to the d_{110} ($2\theta = 35.6^\circ$ ($d = 2.5 \text{ \AA}$)) of the clay and indicates the presence of the clay in the $2L_{EL}$ -pNIPAM nanocomposite. The reflection at $2\theta = 19.4^\circ$ in the clay should also be present in the nanocomposite to indicate the presence of the clay, but this overlaps with that of the pNIPAM reflections. [6][8]

XRD traces for $1L_{OG}$ -pNIPAM (Figure 4.5), $1L_{RD}$ -pNIPAM and $2L_{RD}$ -pNIPAM (Figure 4.6), and $1C_{Na^+}$ -pNIPAM (Figure 4.8) nanocomposites follow similar trends as described earlier for the $2L_{EL}$ -pNIPAM nanocomposites. However, some differences can be observed and are covered individually.



14

Figure 4.3 XRD traces for powder LEL, dried 2LEL-pNIPAM nanocomposite, and pNIPAM homopolymer showing the effect of clay platelets as they crosslink the pNIPAM chains. All samples are ground powders and offset for clearance.

L_{FN} has the biggest platelet size when compared to the other Laponite[®] grades. The XRD trace for L_{FN} is shown in Figure 4.4. A strong reflection at $2\theta = 6.6^\circ$ ($d = 13.39 \text{ \AA}$) (Table 4.2) in the L_{FN} corresponds to the spacing between clay layers (d_{001}). The dried $1L_{FN}$ -pNIPAM nanocomposite sample shows a reflection at around $2\theta = 6.6^\circ$; again, because this could overlap with the $2\theta = 7.4^\circ$ of the pNIPAM it is difficult to characterise the clay dispersion. If the intensity ratio of the pNIPAM reflections at $2\theta = 7.4^\circ$ and 20.2° is compared to that of the $1L_{FN}$ -pNIPAM nanocomposite then the increase at $2\theta = 7.4^\circ$ in the latter, and the fact the reflection is in the same position as the clay could indicate no intercalation has occurred (i.e. a microcomposite is formed). The reflection at $2\theta = 35.2^\circ$ in the $1L_{FN}$ -pNIPAM does

provide evidence that L_{FN} is present even though those for the L_{FN} at $2\theta = 19.4^\circ$ and 28.6° are difficult to discern.

$1L_{XL21}$ -pNIPAM and $2L_{XL21}$ -pNIPAM (Figure 4.7) nanocomposites have similar XRD traces to the $1L_{FN}$ -pNIPAM nanocomposites. However, some differences can be observed and are mentioned individually.

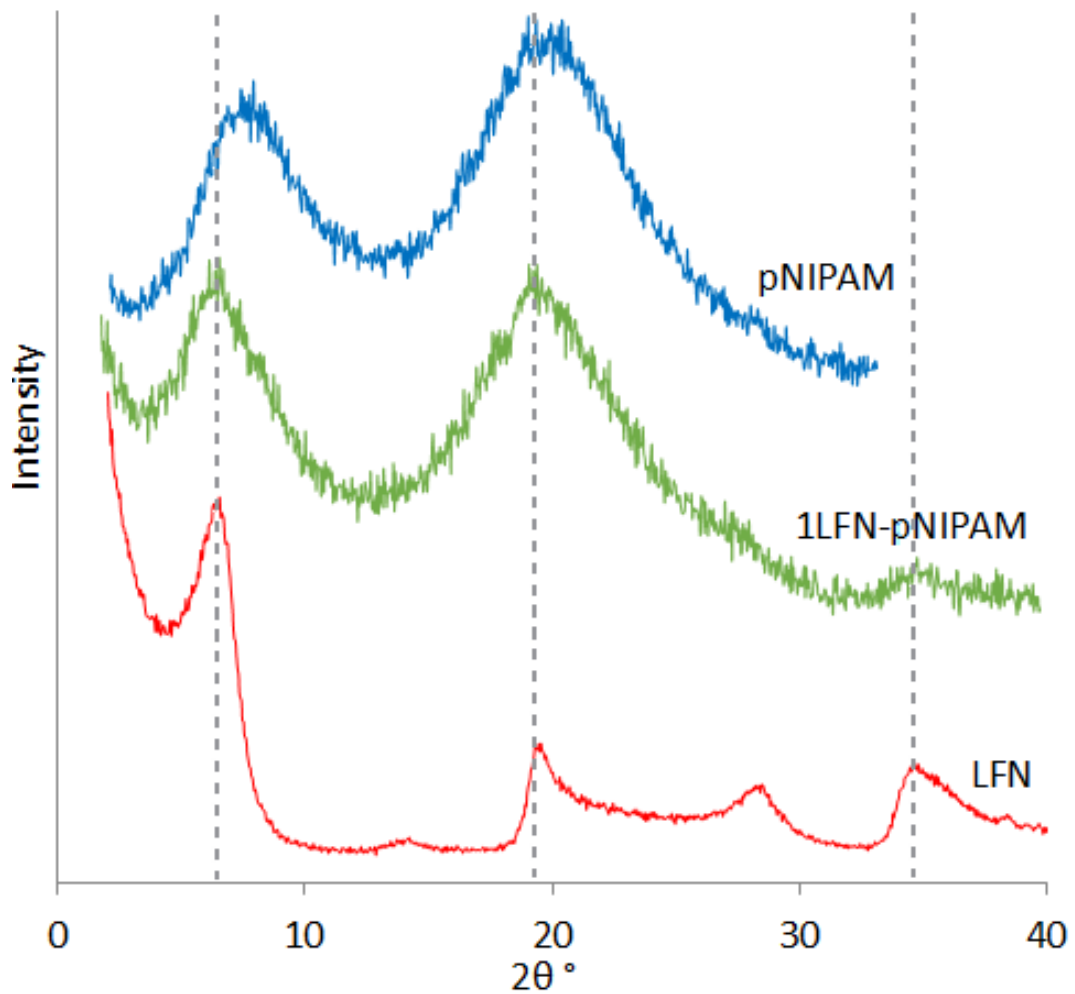


Figure 4.4 XRD traces for powder LFN, dried $1L_{FN}$ -pNIPAM nanocomposite, and pNIPAM homopolymer showing the effect of clay platelets as they crosslink the pNIPAM chains. All samples are ground powders and offset for clearance.

XRD traces of powder L_{OG} , pNIPAM homopolymer and dried $1L_{OG}$ -pNIPAM are presented in Figure 4.5. The observations in these traces are very similar to those for the L_{EL} samples, the increasing baseline at $2\theta < 5^\circ$ may suggest an exfoliated or very disordered clay dispersion. Again, it is difficult to ascertain the clay dispersion due to the overlapping pNIPAM reflection at $2\theta = 7.4^\circ$.

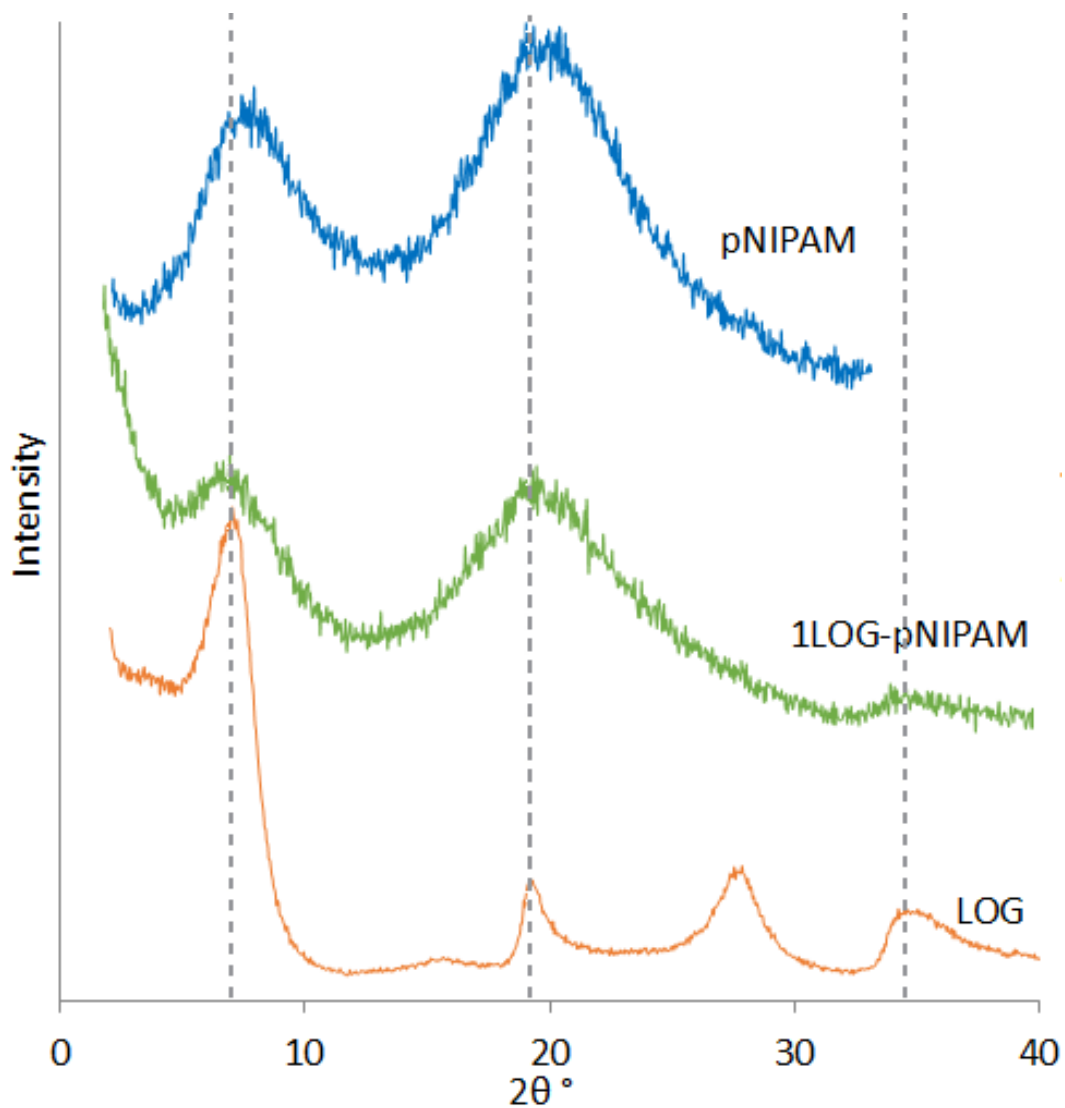


Figure 4.5 XRD traces for powder LOG, dried 1LOG-pNIPAM nanocomposite, and pNIPAM homopolymer showing the effect of clay platelets as they crosslink the pNIPAM chains. All samples are ground powders and offset for clearance.

The L_{RD} -pNIPAM nanocomposites at two different clay-to-polymer ratios have similar trends (Figure 4.6) as for the $2L_{EL}$ -pNIPAM. The increasing baseline in the XRD traces of the L_{EL} -pNIPAM nanocomposites at $2\theta < 5^\circ$ is likely to indicate exfoliation or a very disordered clay, however, because the reflection at $2\theta = 7.4^\circ$ of pNIPAM overlaps that of the d_{001} of LRD, it is not possible to state that intercalated or non-intercalated clay is present.

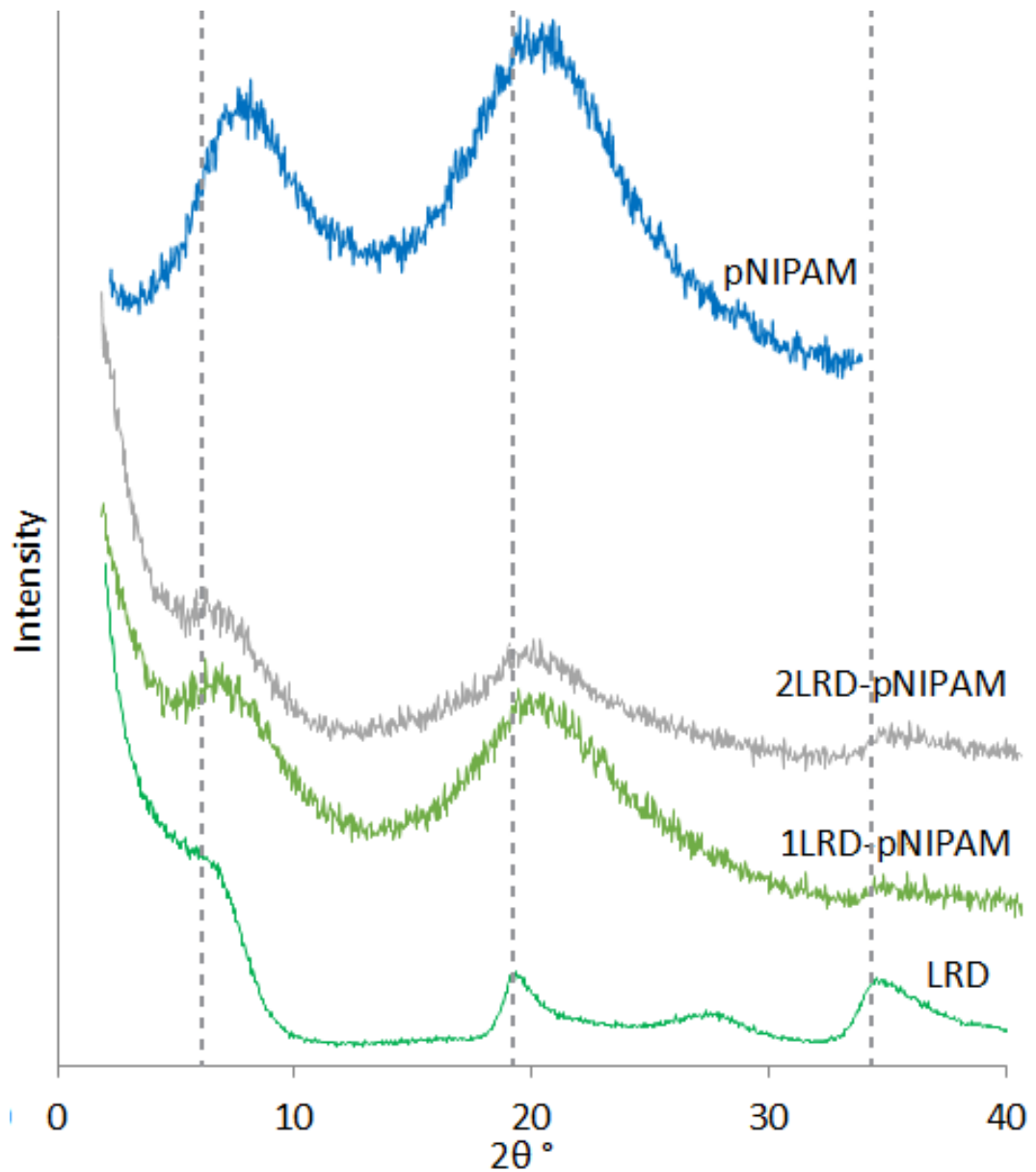


Figure 4.6 XRD traces for powder LRD, dried 1LRD-pNIPAM and 2LRD-pNIPAM nanocomposite, and pNIPAM homopolymer showing the effect of clay platelets as they crosslink the pNIPAM chains. All samples are ground powders and offset for clearance.

Figure 4.7 shows the XRD traces of the powder L_{XL21} and its corresponding pNIPAM nanocomposites at two different clay-to-polymer ratios. Again, the increasing baseline towards lower angles indicates an exfoliated structure, the potentially overlapping reflection from the pNIPAM does not rule out that intercalation has occurred. [26]

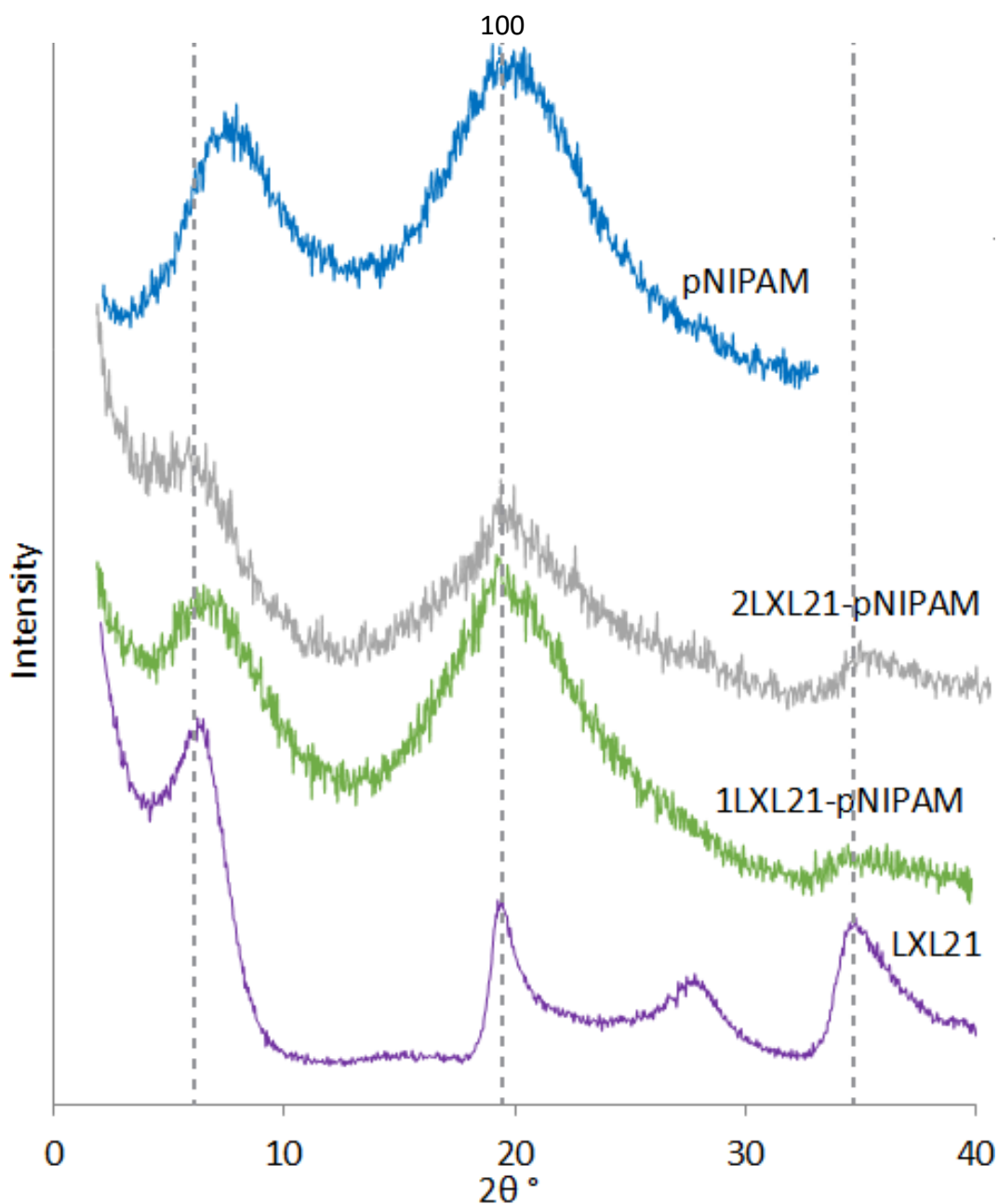


Figure 4.7 XRD traces for powder LXL21, dried 1LXL21-pNIPAM and 2LXL21-pNIPAM nanocomposite, and pNIPAM homopolymer showing the effect of clay platelets as they crosslink the pNIPAM chains. All samples are ground powders and offset for clearance.

In Figure 4.8, the $1C_{Na^+}$ -pNIPAM shows similar behaviour to the $2L_{EL}$ -pNIPAM where the XRD trace is dominated by the pNIPAM within the composite; there is an increasing baseline towards lower angles and thus the traces could indicate that exfoliated or very disordered clay dispersion is obtained. Moreover, it is interesting to note that in the C_{Na^+} trace the d_{001} -spacing is much higher than the d_{100} and d_{110} -reflections; if a non-intercalated microcomposite was formed then the d_{001} -reflection of the clay would significantly enhance the intensity of the reflection at

$2\theta = 7.2^\circ$ in the trace of the composite, which is it does not. This is supported by the presence of the sharper reflection at $2\theta = 19.8^\circ$ in the 1CNa^+ -pNIPAM strongly indicating the detection of clay in the composite. Thus, overall this supports exfoliated or very disordered clay dispersion. These observations could be applied, to some extent, to the composites containing Laponite[®] clays, but due to their relatively lower intensity d_{001} reflections, no enhancements are observed.

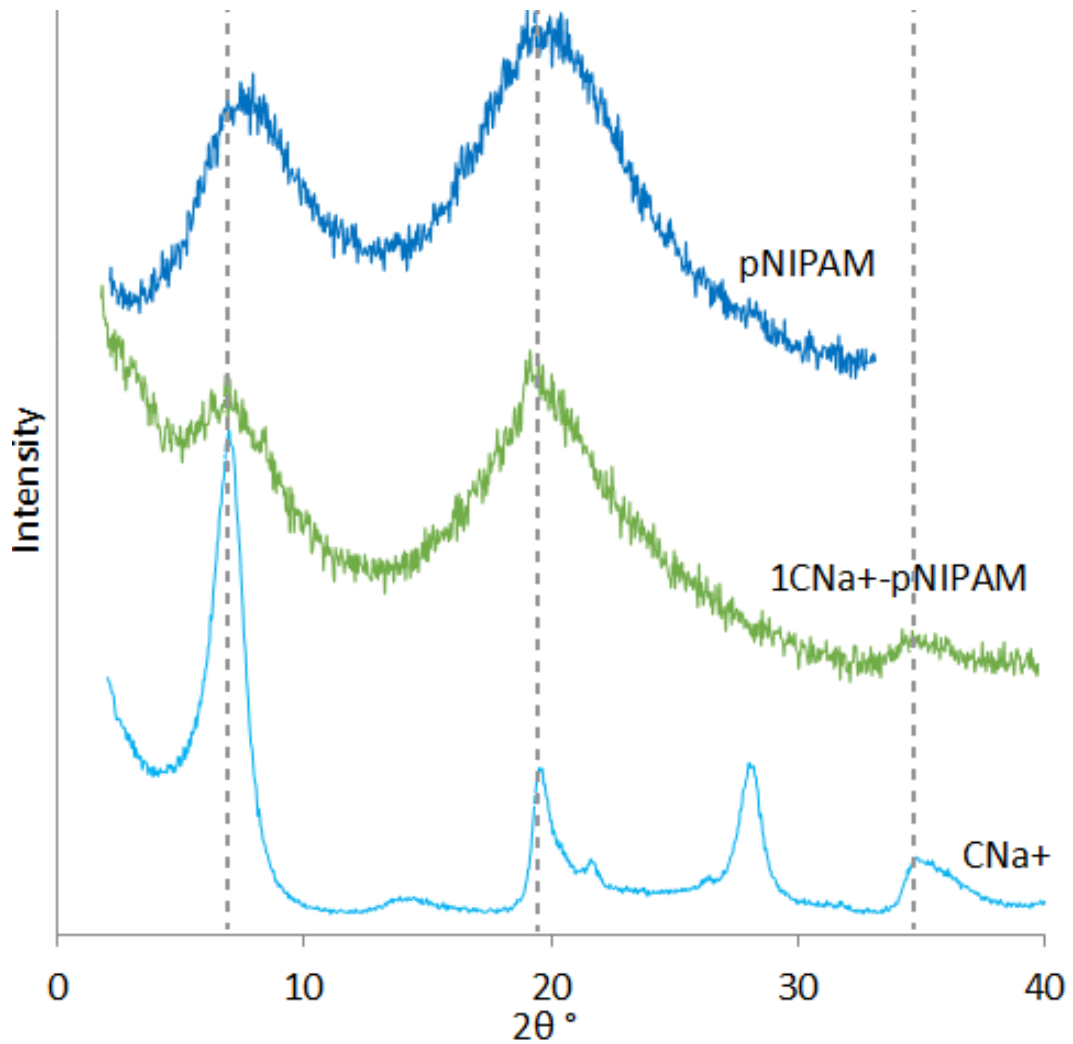


Figure 4.8 XRD traces for powder CNa^+ , dried 1CNa^+ -pNIPAM nanocomposite, and pNIPAM homopolymer showing the effect of clay platelets as they crosslink the pNIPAM chains. All samples are ground powders and offset for clearance.

Table 4.2 2 θ and d-spacing for clay-pNIPAM nanocomposites.

Sample	d_{001}		d_{100}		d_{110}	
	2 θ	d (Å)	2 θ	d (Å)	2 θ	d (Å)
pNIPAM	7.4	12.0	20.2	4.4	-	-
L_{EL}	5.8	15.3	19.4	4.6	35.6	2.5
2L_{EL}-pNIAPM	7.2	12.3	20.2	4.4	35.6	2.5
L_{FN}	6.6	13.3	19.4	4.6	34.9	2.6
1L_{FN}-pNIAPM	6.7	13.3	19.4	4.6	35.2	2.5
L_{OG}	7.1	12.4	19.1	4.6	34.7	2.6
1L_{OG}-pNIAPM	7.4	11.9	20.0	4.4	34.7	2.6
L_{RD}	6.5	13.6	19.4	4.6	34.6	2.6
1L_{RD}-pNIAPM	7.4	12.0	20.3	4.4	34.7	2.6
2L_{RD}-pNIAPM	7.3	12.2	20.1	4.4	34.7	2.6
L_{XL21}	6.4	13.8	19.3	4.6	34.7	2.6
1L_{XL21}-pNIAPM	7.1	12.4	19.9	4.5	34.7	2.6
2L_{XL21}-pNIAPM	5.9	14.9	19.8	4.5	34.7	2.6
C_{Na+}	7.0	12.6	19.5	4.6	34.7	2.6
1C_{Na+}-pNIAPM	7.2	12.2	19.8	4.5	34.8	2.6

The XRD results for the clay-pNIPAM suggest that the addition of all clays to NIPAM apart from L_{FN} results in a change in structure for such that when dried the polymer chains reside between the clay platelets. [27][28]

4.1.3 TGA Characterisation of Clay-pNIPAM Nanocomposites

Thermal stability plays an important role in determining both technological applications and processing conditions of polymeric nanocomposites. Thermal decomposition behaviour of polymeric materials, as well as polymer-based nanocomposites, is usually studied by TGA techniques. [19]

Thermal stability of pNIPAM and the influence of different clay types and clay-to-polymer ratios on the weight loss was studied by TGA in a temperature range of 25 – 900 °C with the heating rate set at 20 °C/min under a nitrogen purge. [29] The sample preparation process for TGA testing required drying the clay-polymer hydrogels by placing the samples in an oven at 80 °C for 3 days in a Petri dish. The nomenclature of the composition of the nanocomposite is based on its wet state, i.e. the (1 % clay)-polymer contains 1 wt.% clay, 9 wt.% polymer and 90 wt.% water. For TGA the samples were dried and so the (1 % clay)-pNIPAM composition is 10

wt.% clay to 90 wt.% polymer of the total sample weight (20 wt.% clay to 80 wt.% polymer of the total sample weight for the (2 % clay)-pNIPAM). The drying process used in this work involved no humidity control, however, at 80 °C humidity, this is not going to be a major factor as most weakly bonded water in the samples will be removed. The actual weight loss values at low temperatures (< 150°C) due to differences in water content may, therefore, can be different from one sample to another and thus may introduce an element of error for the wt.% value. However, the general behaviour of the materials as a function of temperature was still valid. After drying most of the samples were ground using a pestle and mortar; the 1L_{EL}-pNIAPM samples were too flexible to be ground so a sharp knife was used to cut the sample into small pieces to fit into the TGA crucibles, this may be the reason for the 1L_{EL}-pNIAPM composite showing more weight loss during “Stage 1” (Figure 4.9) however, sufficient drying time was allowed to remove weakly bound water. The likelihood is that the sample is more hygroscopic and holds on to water more, the held water will act as a plasticiser and thus the reason why the sample was more flexible.

TGA weight loss curves of the dried pNIPAM homopolymer and (1 % clay)-pNIPAM nanocomposites as a function of temperature are shown in Figure 4.9. Three main weight loss stages were observed in the TGA curves which correspond to evaporation of water and the structural decomposition of the polymers. The first weight loss stage takes place between 25 – 175 °C, and this is due to the evaporation of any remaining water after three days drying at 80 °C; the second stage at 175 – 450 °C predominantly involves polymer degradation. The third stage at 450 - 650 °C is more complex and includes the majority of the dehydroxylation and further degradation of polymer residues to yield carbon and hydrocarbons. [19] After approximately 650 °C the inorganic residues (i.e., Al, and Si) remain and the thermograms become flat. Also since the analysis was performed under nitrogen some organic carbonaceous char may remain. [28]

The thermal analysis results of pNIPAM and its clay nanocomposites are summarized in Table 4.3. The characteristic parameters selected are the main three

weight loss stages temperature range and the degradation temperature (onset temperature at which the highest rate of weight loss started “Stage 2”). [20]

Figure 4.9 and Table 4.3 show that the onset temperature of the clay-pNIPAM nanocomposites is lower than that of the pNIPAM homopolymer. [30] (1 % clay)-pNIPAM nanocomposites have good thermal stability up to 175 °C when compared to the pNIPAM homopolymer where weight loss is correlated to water evaporation. The highest weight loss in “Stage 1” of 8.62 % occurs for 1L_{EL}-pNIPAM. The onset temperature appeared in the range of 325 – 370 °C for both homopolymer and clay-polymer nanocomposite. The maximum weight loss in “Stage 2” was observed for 1L_{XL21}-pNIPAM of 76.64 %. During “Stage 3” 1C_{Na+}-pNIPAM had the maximum weight loss of 14.61 %. [31]

The weight loss measurements in Table 4.3 show that most nanocomposites lost more weight during “Stage 1” than the pNIPAM homopolymer except 1L_{XL21}-pNIPAM. The weight loss in this region represents the hygroscopic nature of the samples and thus the introduction of clay mostly results in a more hygroscopic sample, whereas with L_{XL} clay it becomes less hygroscopic. For “Stage 2” the % weight loss decreased when compared to the pNIPAM homopolymer because less polymer is present. The decrease in onset temperature suggests that the presence of clay may facilitate the degradation of the clay-polymer nanocomposites, in other words, (1 % clay)-pNIPAM nanocomposite has a weaker onset thermal stability than the pNIPAM homopolymer but the total weight loss in the nanocomposites is significantly less which can be related to the presence of clay platelets and less polymeric components. [29]

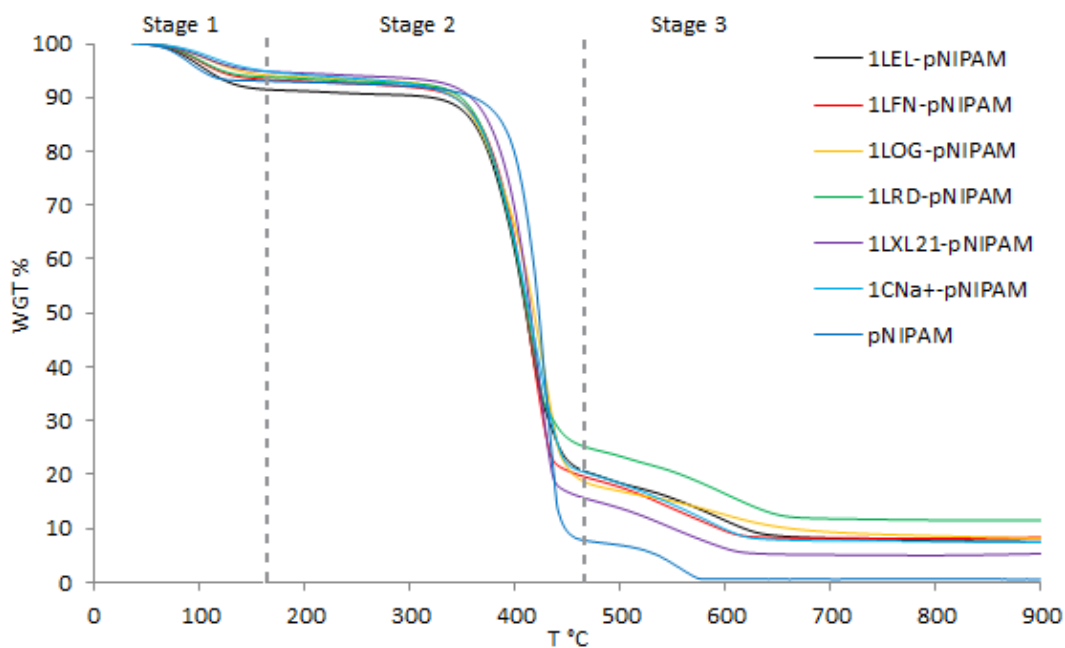


Figure 4.9 TGA thermograms of pNIPAM homopolymer and (1 % clay)-pNIPAM nanocomposites. Indicating the three stages of weight loss. Stage 1 (25 – 175 °C), Stage 2 (175 – 475 °C), and stage 3 (475 – 700 °C).

Figure 4.10 shows the TGA weight loss curves for pNIPAM compared to 2L_{EL}-pNIPAM, 2L_{RD}-pNIPAM and 2L_{XL21}-pNIPAM. The behaviour was the same as for the (1 % clay)-pNIPAM with three stages of weight loss and a polymer degradation onset temperature lower than of the pNIPAM homopolymer but with less total weight loss as the (2 % clay)-pNIPAM has more clay.

The results show the clay-to-polymer ratio incorporated in the nanocomposites did influence the onset temperature of the polymer degradation during stage 2 for the nanocomposites (Table 4.3) as more clay lowered the onset temperature.

At the end of “Stage 2” where most of the weight loss happens, 2L_{XL21}-pNIPAM still loses more weight than the 2L_{EL}-pNIPAM and 2L_{RD}-pNIPAM showing this clay does not reduce as much of the initial amount of polymer degradation (i.e. between 175-450 °C) and thus suggesting the slowing down of the degradation process.

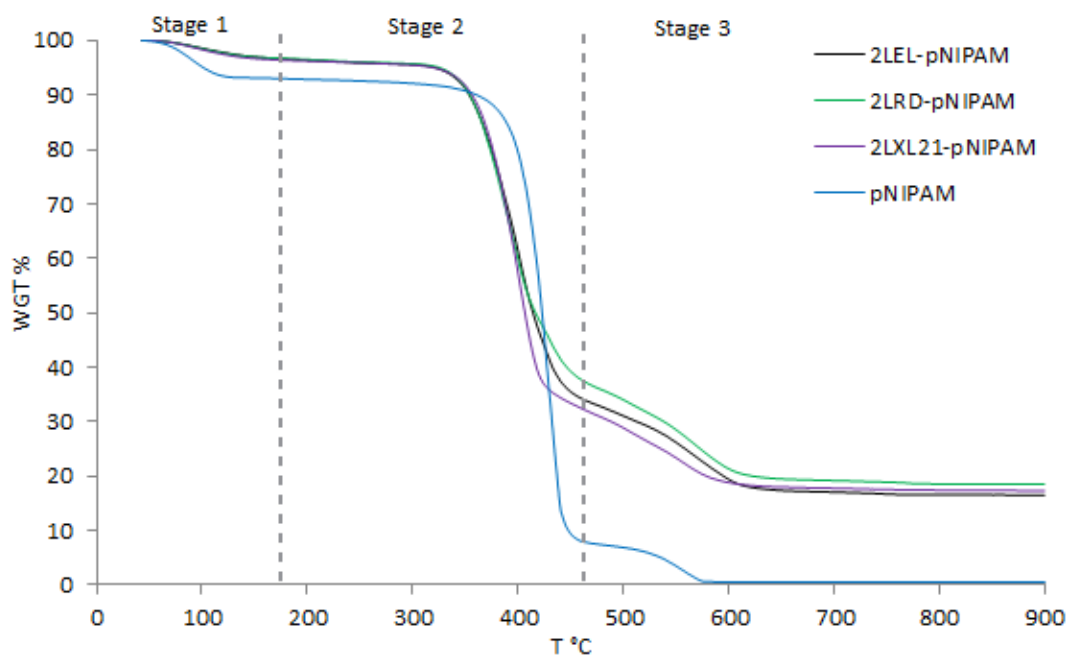


Figure 4.10 TGA thermograms of pNIPAM homopolymer, 2LEL-pNIPAM, 2LRD-pNIPAM and 2LXL21-pNIPAM nanocomposites. Indicating the three stages of weight loss. Stage 1 (25 – 175 °C), Stage 2 (175 – 475 °C), and stage 3 (475 – 600 °C).

Figure 4.11 shows a comparison between the same clay-pNIPAM nanocomposites at two different clay-to-polymer ratios. The L_{RD} different clay-to-polymer ratio shows a difference in the thermal stability of the L_{RD} -pNIPAM composites as the onset temperature dropped down from 344 °C for the $1L_{RD}$ -pNIPAM to 329 °C for the $2L_{RD}$ -pNIPAM (Figure 4.11 (b)). The weight loss rate (stage 2) was also different as the $1L_{RD}$ -pNIPAM had a higher weight loss rate than the $2L_{RD}$ -pNIPAM.

Figure 4.11 (c) shows the $1L_{XL21}$ -pNIPAM and $2L_{XL21}$ -pNIPAM weight loss curves. A drop in the onset temperature for the $2L_{XL21}$ -pNIPAM to 333 °C (the lowest onset temperature in all the clay-pNIPAM nanocomposite group) from 348 °C for the $1L_{XL21}$ -pNIPAM.

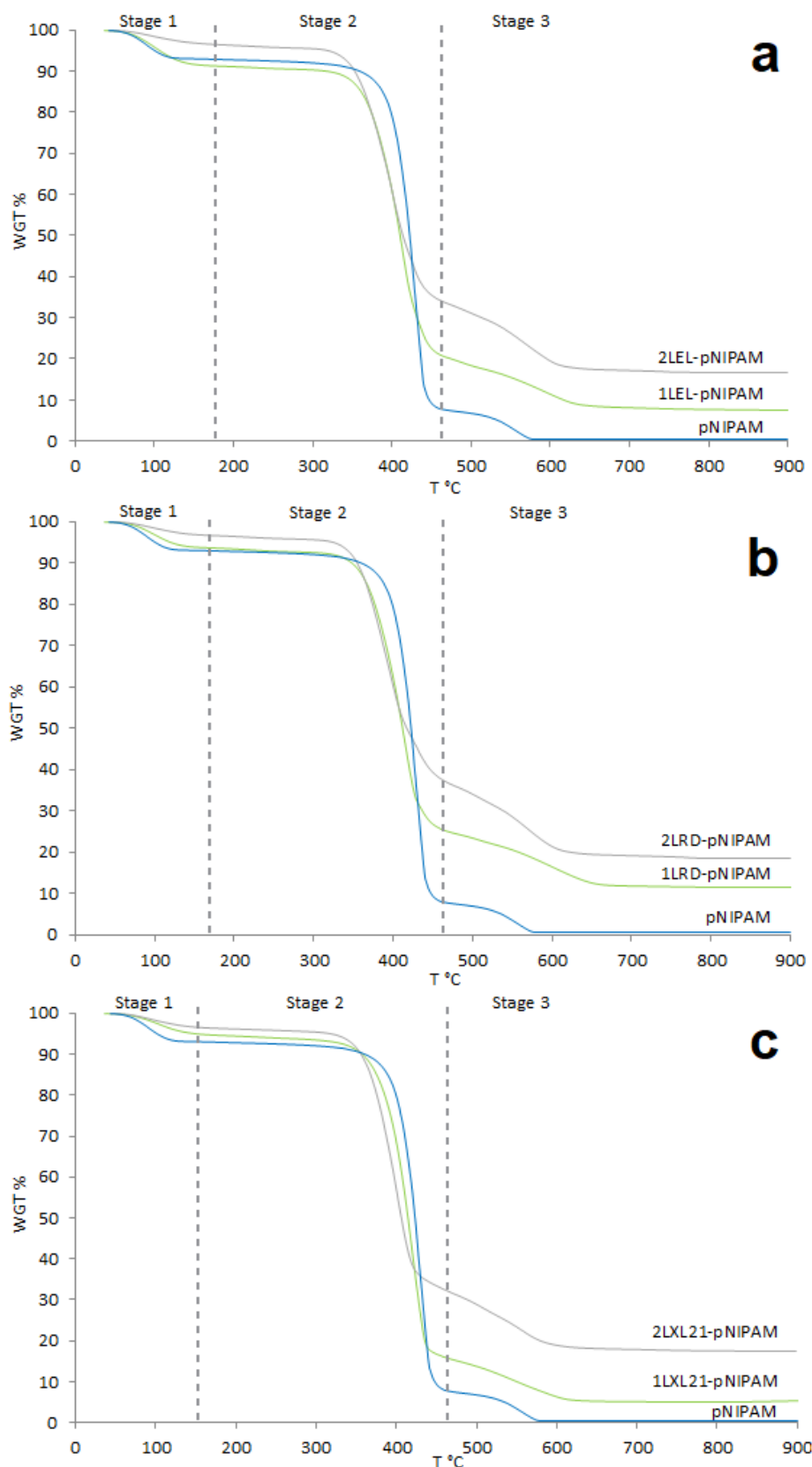


Figure 4.11 TGA thermograms of pNIPAM homopolymer compared to a) 1LEL-pNIPAM and 2LEL-pNIPAM, b) 1LRD-pNIPAM and 2LRD-pNIPAM, c) 1LXL21-pNIPAM and 2LXL21-pNIPAM nanocomposites. Indicating the three stages of weight loss. Stage 1 (25 – 175 °C), Stage 2 (175 – 475 °C), and stage 3 (475 – 650 °C).

Table 4.3 TGA of pNIPAM homopolymer (1 % clay)-pNIPAM and (2 % clay)-pNIPAM nanocomposites, showing weight loss at each stage and onset temperature (n=3).

Sample	Stage1: 25–175 °C	Stage2: 175–450 °C	Stage3: 450–650 °C	Total weight loss %	Onset Temp. °C
	weight loss %				
pNIPAM	6.99	83.41	9.04	99.44	370
1L _{EL} -pNIPAM	8.62	69.32	14.54	92.48	347
2L _{EL} -pNIPAM	3.37	59.47	20.63	83.47	341
1L _{FN} -pNIPAM	6.79	71.80	13.09	91.68	344
1L _{OG} -pNIPAM	6.03	72.12	13.56	91.71	343
1L _{RD} -pNIPAM	6.30	67.96	14.22	88.48	344
2L _{RD} -pNIPAM	3.27	57.52	20.68	81.47	329
1L _{XL21} -pNIPAM	5.28	76.64	12.74	94.66	348
2L _{XL21} -pNIPAM	3.60	59.38	19.70	82.68	333
1C _{Na+} -pNIPAM	5.26	72.67	14.61	92.54	340

The onset temperature was calculated using the extrapolated onset temperature that denotes the temperature at which the weight loss begins. The extrapolated onset temperature is a reproducible temperature calculation and was calculated for three samples of each composite (Figure 4.12). [32] To validate the data in this study, three test were done for each sample to provide quantitative values for repeatability and detection limit, for both the weight loss and onset temperatures. [33] The data did not vary over a huge range of values and strange or unusual trends or values were observed.

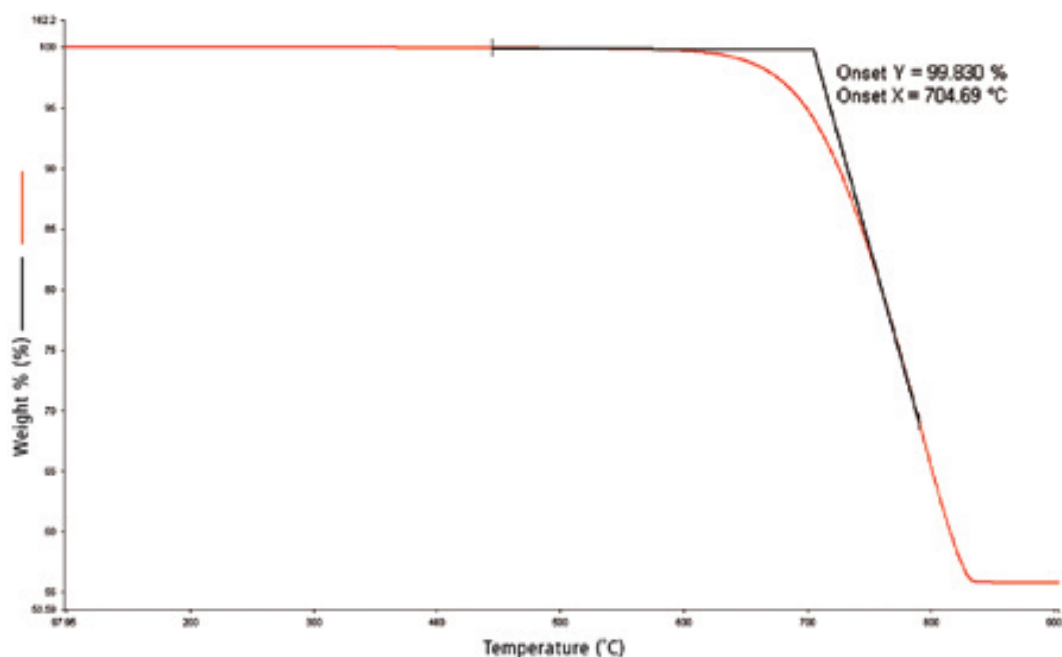


Figure 4.12 Extrapolated onset temperature

4.1.4 SEM Morphology Observation of Clay-pNIPAM Nanocomposites

Composites morphology is an important feature and describes the internal structure and void distribution within the matrix. It helps to provide an understanding of the physical and mechanical properties of the composite structure. The morphology of the clay-polymer nanocomposites can be observed to change by SEM with different clay types and clay-to-polymer ratios.

The morphology observed in Figure 4.13 shows the SEM image of homopolymer pNIPAM at 50 μm magnification bar. The pNIPAM sample preparation was similar to all other clay-pNIPAM nanocomposites. The general observation within the homopolymer pNIPAM was a solid material with low number of voids on the surface. Porosity was not observed, and the sample was a one piece, dense, solid block while all clay-pNIPAM samples were in a foamy structure.

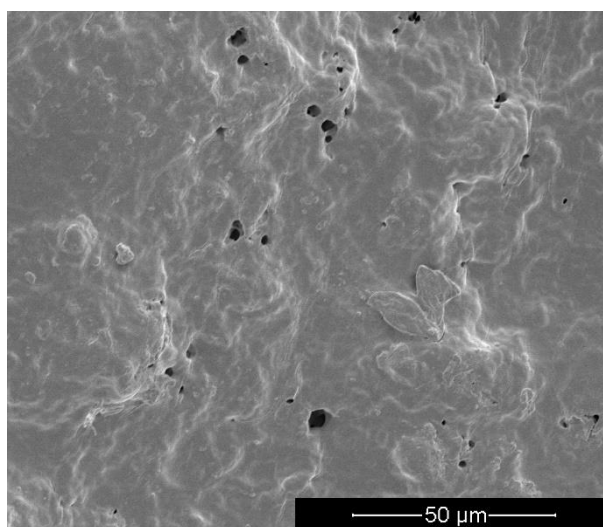


Figure 4.13 SEM images of homopolymer pNIPAM on scale bar 50 μm showing microstructure

The morphology discrepancies due to different clays observed in Figure 4.14 show the SEM images of (1 % clay)-pNIPAM nanocomposites at 100 μm magnification bar. The general observation within the (1 % clay)-pNIPAM nanocomposites is an interconnected porous microstructure, with different pore distributions. Porosity is clear for most of the (1 % clay)-pNIPAM except for 1C_{Na+}-pNIPAM nanocomposites (Figure 4.14 f) which does not show an interconnected clear porosity, it shows a

smooth mountain and valley-like textured surface. [19][34] The structures below show the impact that different clays have on the structure, however, these structures are mostly a result of the sample preparation method mentioned in the experimental section. These structures may not be a true representative of the real structure of the hydrogel's wet status since the samples have been flash-frozen with liquid nitrogen and the water removed by freeze-drying, however, they still provide comparable data. This approach is common in the literature as collecting SEM images of wet samples is not possible. [35][36]

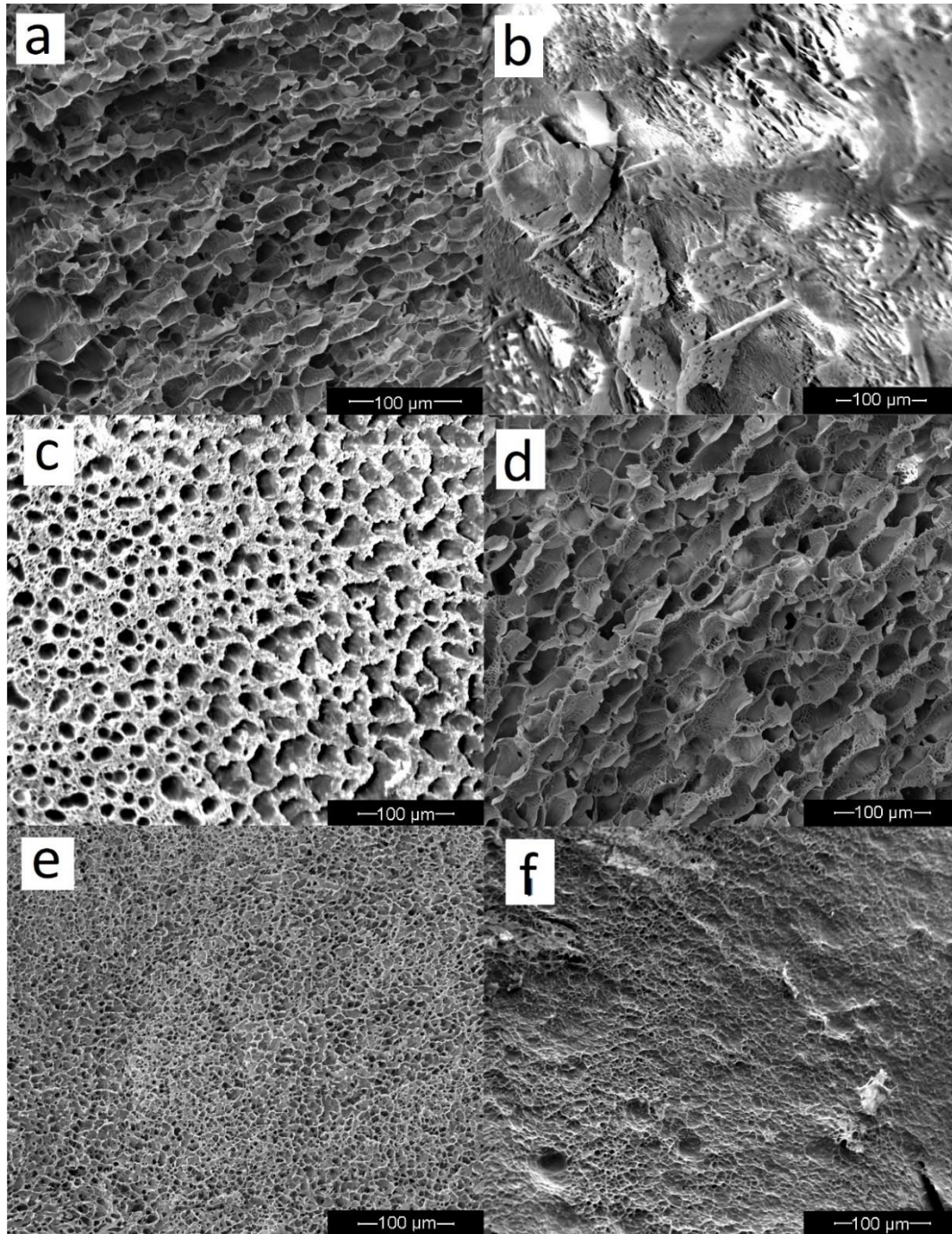


Figure 4.14 SEM images of (1 % clay)-pNIPAM nanocomposite on scale bar 100 μm showing microstructure and pore size differences as a result of the effect of the clay type used. a) 1LEL-pNIPAM b) 1LFN-pNIPAM c) 1LOG-pNIPAM d) 1LRD-pNIPAM e) 1XL21-pNIPAM f) 1CNa⁺-pNIPAM.

The 1L_{EL}-pNIPAM composite SEM images (Figure 4.14 b and Figure 4.15 a) show a rough surface and a uniformly distributed porous microstructure, it has thin and solid well-defined walls. The pore size has an average of 16.2 μm , which is considered large when compared to other (1 % clay)-pNIPAM nanocomposites. The

1L_{RD}-pNIPAM nanocomposite (Figure 4.15 d) has a similar morphology yet with a slightly wider average pore size of ~ 22.3 μm .

The SEM images of 1L_{FN}-pNIPAM (Figure 4.14 b and Figure 4.15 b) show a flake-like structure with layered texture and smooth surface when compared to 1L_{EL}-pNIPAM. Pore size varied as it was not easy to distinguish between pores and gaps between layers. The 1L_{FN}-pNIPAM composite also has a higher density structure with fewer gaps within the composite when compared to the 1L_{EL}-pNIPAM composite images. [27]

1L_{OG}-pNIPAM composite SEM images (Figure 4.14 c and Figure 4.15 c) show a porous structure, but with a different morphology. Thicker walls are present, within these are a lot of smaller pores, this nanocomposite was the only composite with an “internal bone” like structure. The pore size average is 17.0 μm , and the internal bone-like structure which formed the walls averaged a thickness around 9.1 μm .

The 1L_{XL21}-pNIPAM nanocomposite (Figure 4.14 e and Figure 4.15 e), has a significantly smaller pore size (average of 6.4 μm) with a reticular structure. Pores are uniformly distributed and there is a higher porosity than 1L_{EL}-pNIPAM, 1L_{OG}-pNIPAM and 1L_{RD}-pNIPAM which can be related to the high CEC and the crosslinking ability of L_{XL21}.

The SEM images of 1C_{Na+}-pNIPAM composite (Figure 4.14 f and Figure 4.15 f) show a solid “mountain-valley” morphology. [19] No pores through the thickness of the composite were noted, Figure 4.16 show more detailed images at a higher magnification of 30 μm .

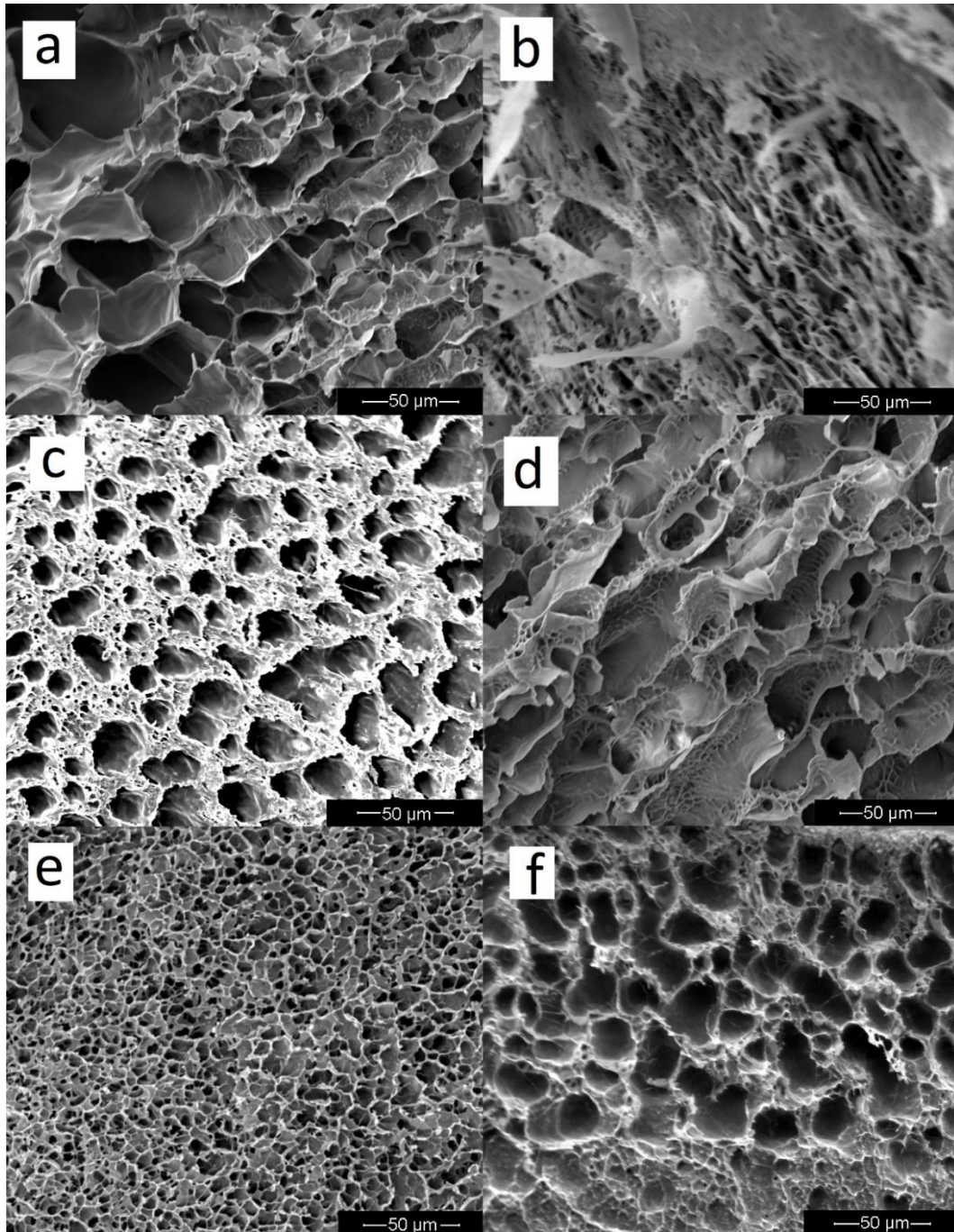


Figure 4.15 SEM images of (1 % clay)-pNIPAM nanocomposite on scale bar 50 μm showing more detailed microstructure and pore size differences as a result of the effect of the clay type used. a) 1LEL-pNIPAM b) 1LFN-pNIPAM c) 1LOG-pNIPAM d) 1LRD-pNIPAM e) 1LXL21-pNIPAM f) 1CNa+-pNIPAM.

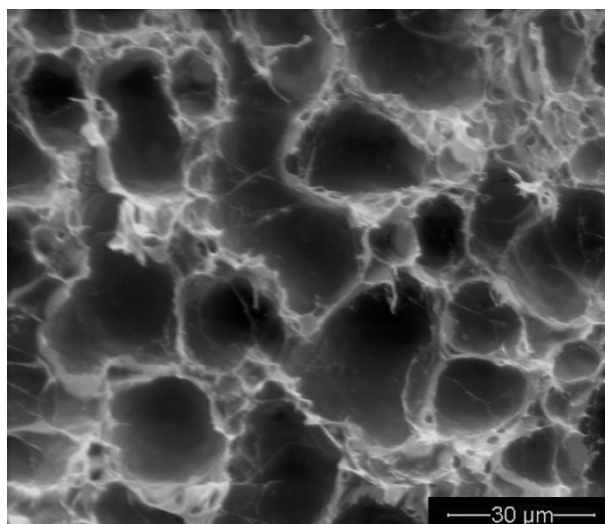


Figure 4.16 SEM images of 1CNa+-pNIPAM nanocomposite on scale bar 30 μm showing more detailed microstructure and no pores through the nanocomposite.

The porous microstructures of L_{EL}-pNIPAM nanocomposites with different clay-to-polymer ratios are shown in Figure 4.17. It is observed that more clay results in smaller pore size. When the clay content was increased to 2 wt.%, the pore sizes decreased to 4.9 μm, in comparison with an average of 16.2 μm for 1 wt.% clay. [37]. With (2 % clay)-polymer nanocomposites there are opportunities for more crosslinking points, and this may explain the reduction in pore size. With high clay contents, more crosslinks are made leading to the formation of micro-network structures resulting in a stronger and tougher material. [38][39][40][41]

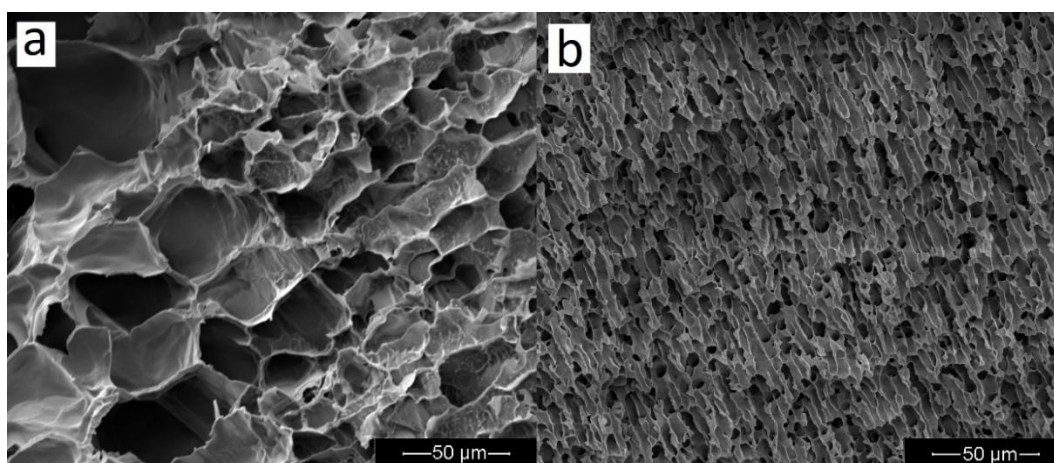


Figure 4.17 SEM images of LEL-pNIPAM nanocomposite on scale bar 50 μm. a) 1LEL-pNIPAM b) 2LEL-pNIPAM showing the effect of increasing clay content on the pore size and the microstructure.

Unfortunately, a comparison between the 1L_{RD}-pNIPAM and the 2L_{RD}-pNIPAM composites was not possible as it was impossible to create clear SEM images of the

2L_{RD}-pNIPAM. The samples were instantly damaged by the electron beam despite numerous attempts to capture images using a range of samples and electron beam intensities used to create the image.

Figure 4.18 shows the SEM images of L_{XL21}-PNIPAM composites at two different clay-to-polymer ratios. The 2L_{XL21}-pNIPAM had a structure with an average pore size of around 6.3 μm . It can also be seen that the 2L_{XL21}-pNIPAM had a more uniform structure and pore size with a lower standard deviation (Table 4.4), it was smoother with more crosslinks in the structure. The morphology of the surface changed to a well-structured wall formation when clay content was increased from the morphology of a sponge-like structure with the 1L_{XL21}-pNIPAM. The higher clay content accelerates the crosslinking action, which resulted in more polymer chains to be linked and shorter polymer chains in a uniform structure. [42]

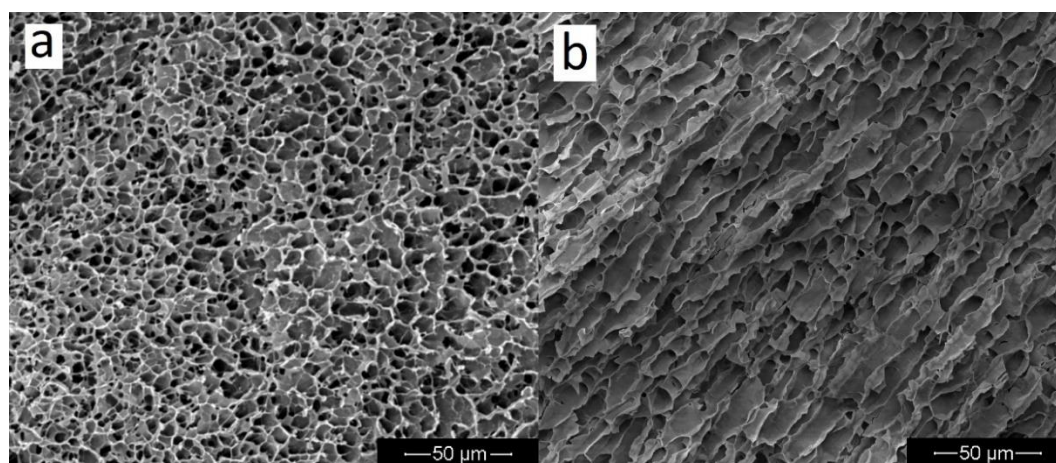


Figure 4.18 SEM images of LXL21-pNIPAM nanocomposite on scale bar 50 μm . a) 1LXL21-pNIPAM b) 2LXL21-pNIPAM showing the effect of increasing clay content on the pore size and the microstructure.

Table 4.4 Clay-pNIPAM pore size as an average of (n=25) different random measures across each SEM image and standard deviation

Sample	Pore size (μm)	SD
1L _{EL} -pNIPAM	16.2	5.5
2L _{EL} -pNIPAM	02.9	0.9
1L _{FN} -pNIPAM	05.0	2.5
1L _{OG} -pNIPAM	17.0	4.2
1L _{RD} -pNIPAM	22.3	4.5
1L _{XL21} -pNIPAM	06.4	1.4
2L _{XL21} -pNIPAM	06.3	1.2
1C _{Na+} -pNIPAM	06.7	1.2

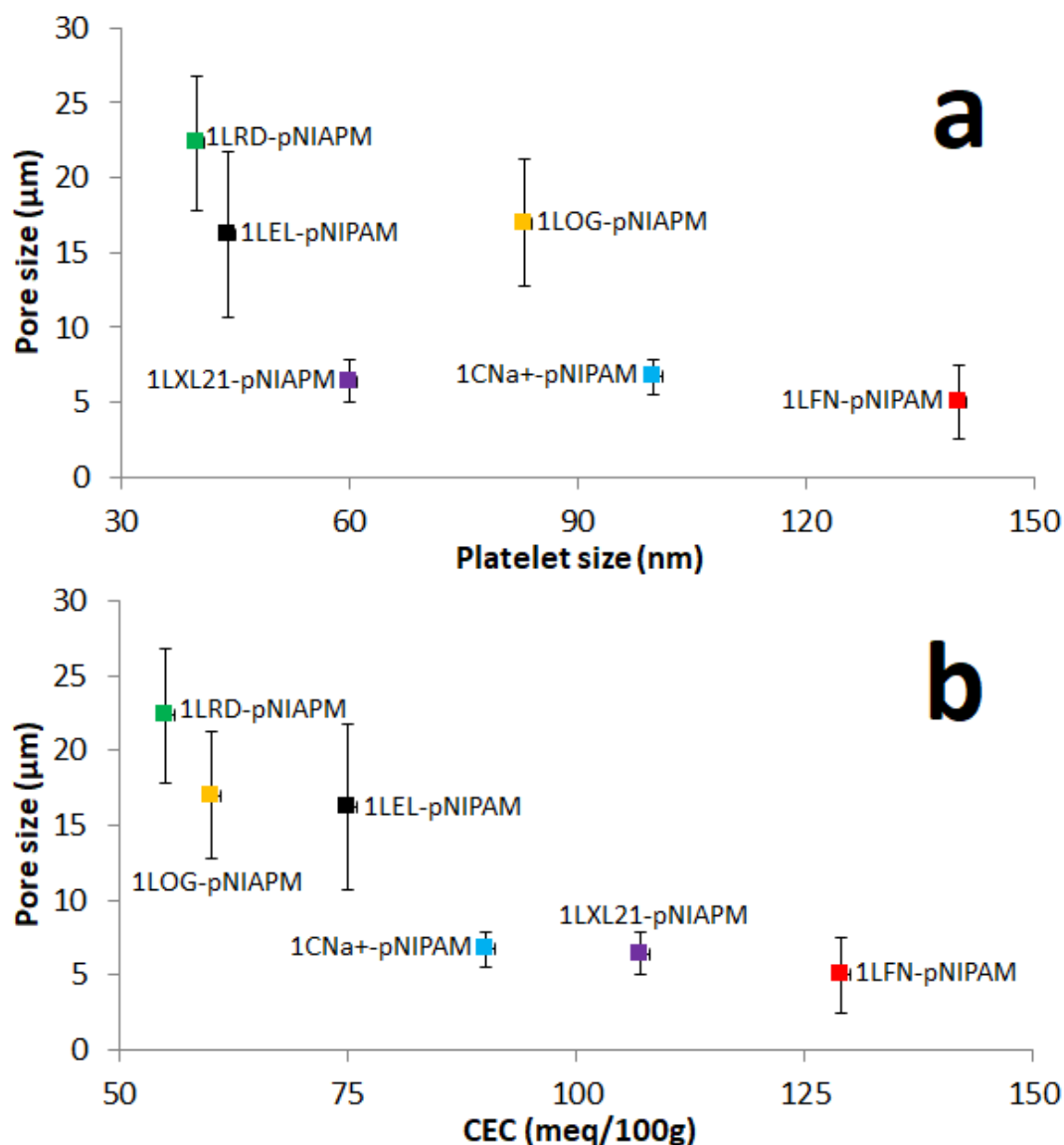
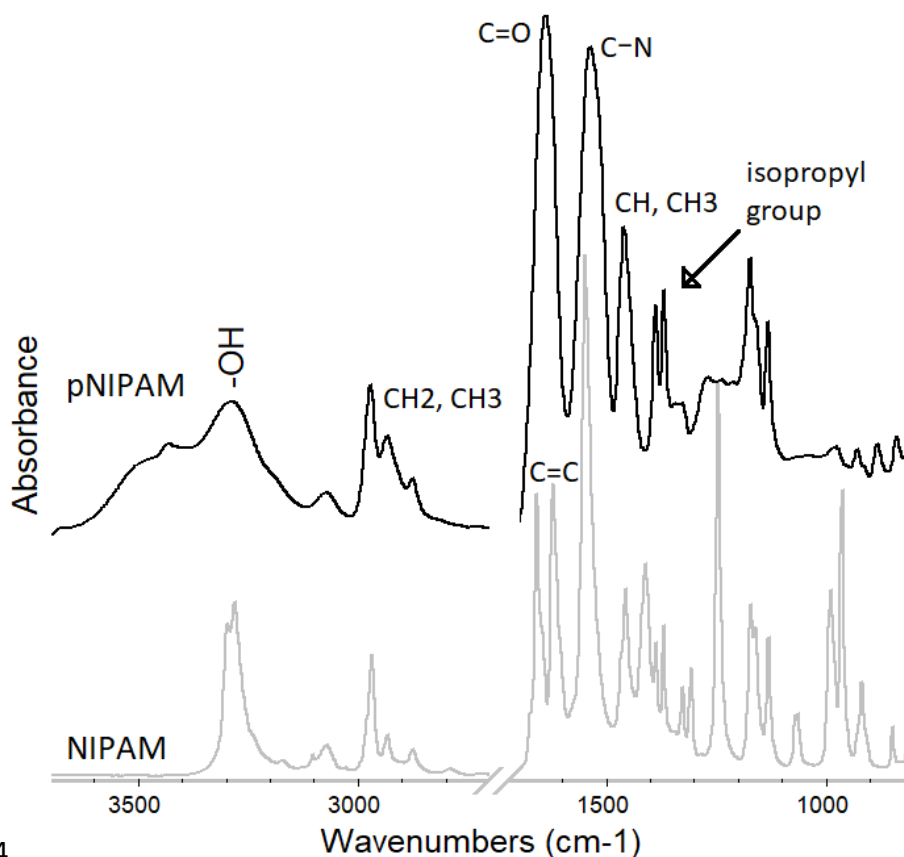


Figure 4.19 (1 % clay)-pNIPAM pore size as measured from the SEM images as a function of a) Clay platelet size, b) Clay CEC.

4.1.5 FTIR Spectra Analysis of Clay-pNIPAM Nanocomposites

FTIR spectroscopy is a useful method to study the interactions between the polymer chains and clay particles. [16] To help with the interpretation of clay-pNIPAM nanocomposites spectra, the FTIR spectra of NIPAM monomer and dried homopolymer pNIPAM were recorded at room temperature and are shown in Figure 4.20. The spectra are dominated by the C-H stretching region between 3000 - 2800 cm^{-1} and the CH bending/deformation region 1450 -1300 cm^{-1} . [43] The C-H

stretching has three bands at around 2980 cm^{-1} , 2935 cm^{-1} , and 2875 cm^{-1} . The C-H deformation region has bands at approximately 1460 cm^{-1} , 1393 cm^{-1} and 1372 cm^{-1} . An important band due to C=C stretching at 1620 cm^{-1} is no longer present upon polymerisation as double bonds are lost during polymerisation. However, broadband appears upon polymerisation around 1638 cm^{-1} , which is due to the stretching of the amide carbonyl group. The pNIPAM spectrum shows the main characteristic bands of the polymerised NIPAM at 1536 cm^{-1} (C-N stretching), 1643 cm^{-1} ($\text{C}=\text{O}$ stretching). [17][44]



14

Figure 4.20 FTIR spectra of monomer NIPAM and pNIPAM homopolymer showing the main characteristic bands of pNIPAM. Offset for clearance.

Figure 4.21 shows the main details of the FTIR spectra of LEL, pNIPAM, $1L_{EL}$ -pNIPAM and $2L_{EL}$ -pNIPAM nanocomposites to monitor any changes in the polymer bands and the effect of crosslinker density (clay-to-polymer ratio) on the nanocomposite.

The spectrum of L_{EL} in powder form in Figure 4.21 shows a typical Si-O band for layered silicate at 946 cm^{-1} . A general shift toward higher frequencies for Si-O modes in nanocomposite is observed when compared to neat clay. [18]

$1L_{EL}$ -pNIPAM and $2L_{EL}$ -pNIPAM spectra (Figure 4.21) show absorption bands at 3430 cm^{-1} and 3432 cm^{-1} , respectively, which are mainly the -OH vibration bands, these bands did not show any significant shift for both composites when compared to the pNIPAM homopolymer -OH band at (3432 cm^{-1}) these bands are related to sorbed water (Table 4.5). The bands at around 2970 cm^{-1} , 2920 cm^{-1} and 1459 cm^{-1} correspond to the C-H vibration. The C=O band was clear at 1633 cm^{-1} and 1637 cm^{-1} in the spectra of $1L_{EL}$ -pNIPAM for the $2L_{EL}$ -pNIPAM composites respectively, with no significant shift when compared to the 1635 cm^{-1} in the spectrum of pNIPAM. However, this band has a higher intensity in the spectrum of $1L_{EL}$ -pNIPAM composite as a result of the higher pNIPAM content it contains, compared to the $2L_{EL}$ -pNIPAM composite.

The C-N bending band at 1536 cm^{-1} in the spectrum of pNIPAM did not show any shift in the spectra of both $1L_{EL}$ -pNIPAM and $2L_{EL}$ -pNIPAM nanocomposites. [16] The observation of the absorption bands of the crosslinked pNIPAM nanocomposites and their similarity to those of the pNIPAM homopolymer is and the Si-O presence reasonable indication that the clay platelets were mixed with the pNIPAM chains. [42]

The Si-O bands at 996 cm^{-1} and 990 cm^{-1} in the spectra of $1L_{EL}$ -pNIPAM and $2L_{EL}$ -pNIPAM composites, respectively, shifted slightly to a higher frequency from the 946 cm^{-1} in the spectrum of L_{EL} . As the clay is dispersed another Si-O band can also be observed at 1074 cm^{-1} and 1072 cm^{-1} in the spectra of $1L_{EL}$ -pNIPAM and the $2L_{EL}$ -pNIPAM respectively, corresponding to the Si-O "out-of-plane" band. The observation of the Si-O "out-of-plane" band in the spectra of nanocomposites is an indication of well dispersed clay, [18] this supports the results observed in the XRD traces of the $2L_{EL}$ -pNIPAM composites were an increasing baseline for angle $< 5^\circ$ was considered as a dispersion indication. The intensities of the bands in the Si-O

stretching increase with increasing clay content as observed in the spectrum of 2L_{EL}-pNIPAM (clay-to-polymer ratio 2:8). And vice versa, the C=O and N-H bands have higher intensities in the spectrum of 1L_{EL}-pNIPAM with more polymer content. [18]

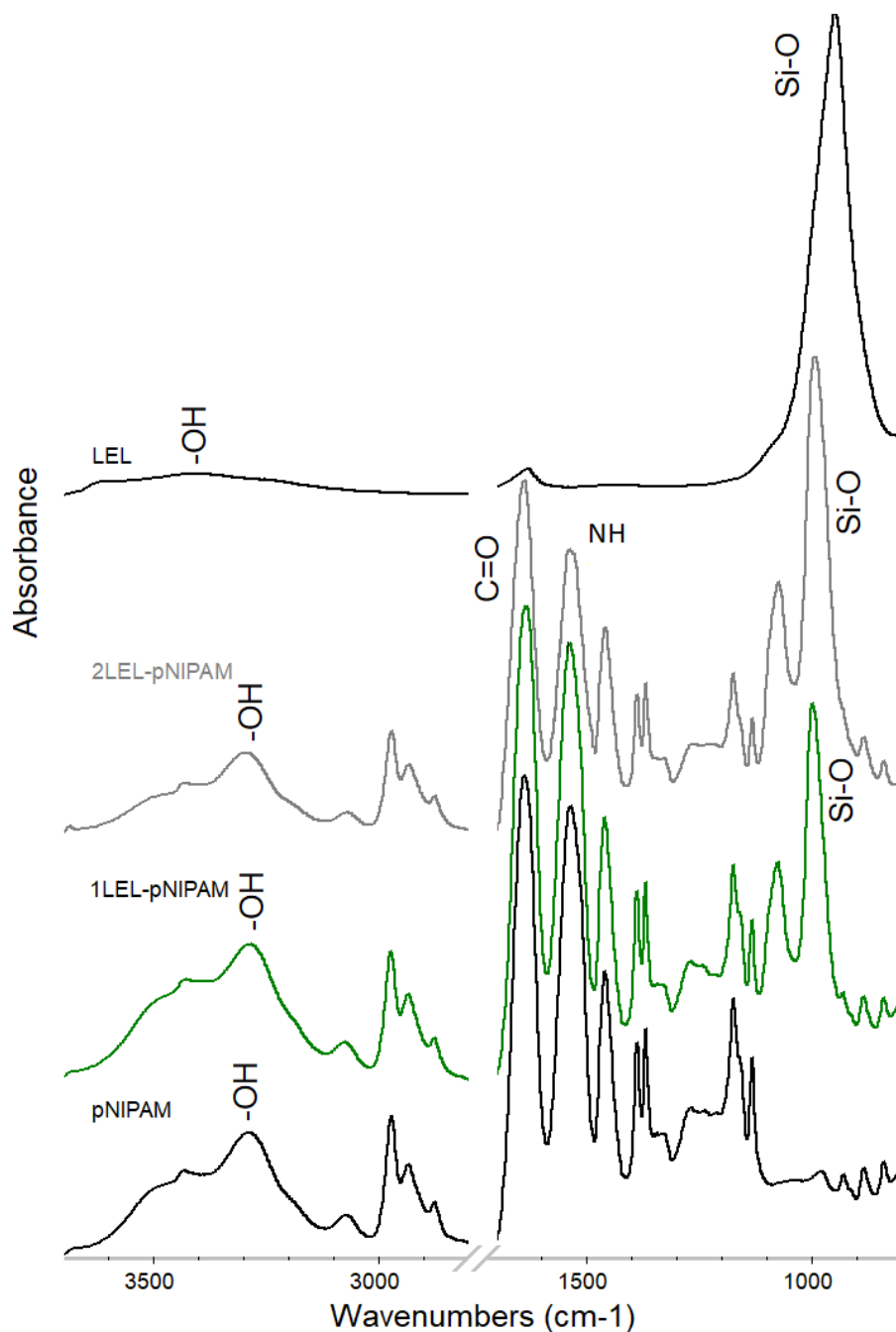


Figure 4.21 FTIR spectra of LEL, pNIPAM homopolymer, 1LEL-pNIPAM and 2LEL-pNIPAM composites showing regions of interest and offset for clearance.

Most of the clay-pNIPAM nanocomposites show similar FTIR spectra. However, some differences still can be observed as different clays have different properties and will be discussed below.

The spectra of the 1L_{FN}-pNIPAM and its related components are presented in Figure 4.22. The Si-O at 950 cm⁻¹ in L_{FN} spectra shows a shift to higher frequencies 995 cm⁻¹ in the spectrum of 1L_{FN}-pNIPAM composite. The Si-O “out-of-plane” in the spectrum of 1L_{FN}-pNIPAM shows a greater shift (to 1105cm⁻¹) when compared to the Si-O “out-of-plane” of L_{EL}-pNIPAM composite, this may be a result of a wider separation between clay platelets or as a result of the nature of the clay platelets, i.e. the chemistry, the larger platelet size or the higher CEC of the L_{FN} when compared to the L_{EL} and other clays. [16][45]. With the XRD data, it was less clear if the L_{EL}-pNIPAM composite contained well dispersed clay due to a not very strong increasing baseline towards lower angles, however, this FTIR data supports good clay dispersion, at least intercalated, if partly exfoliated.

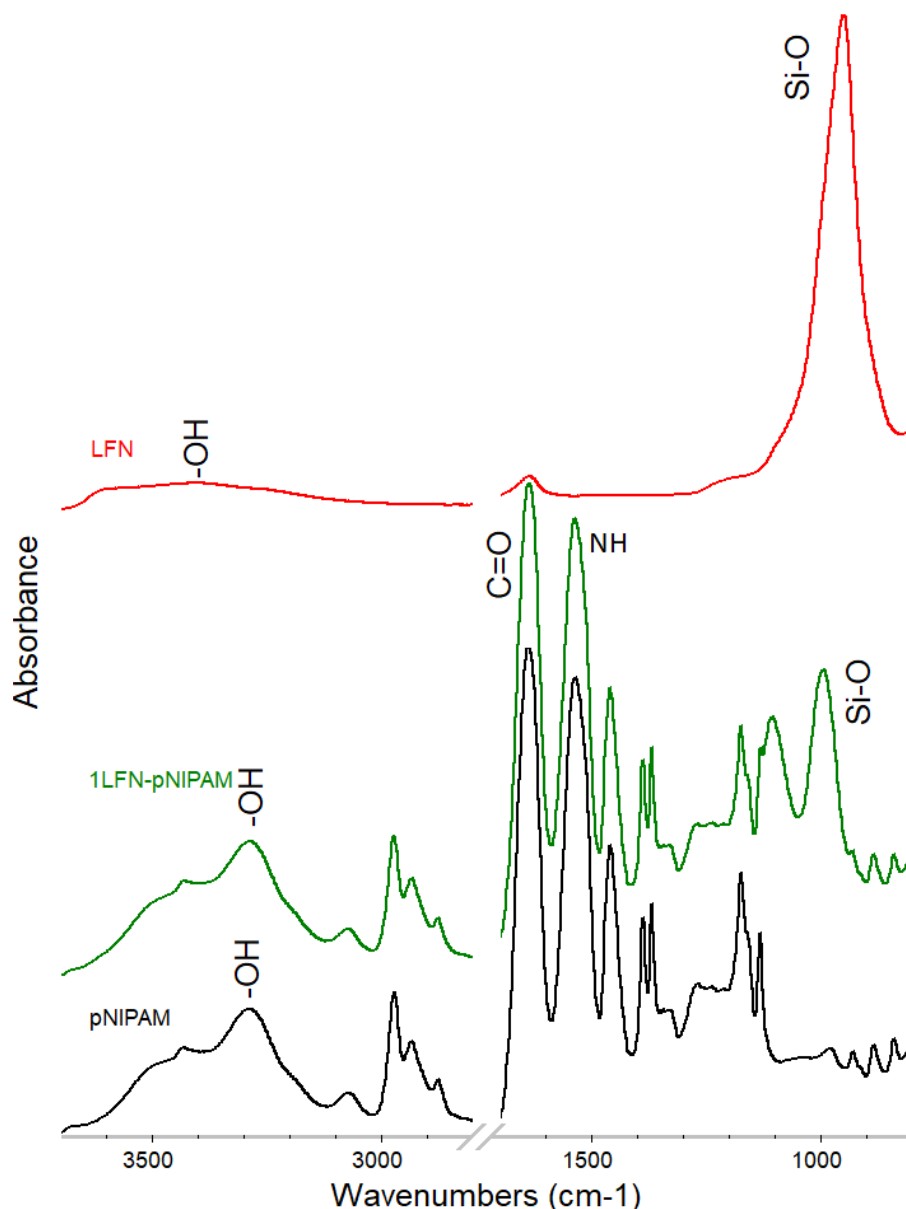


Figure 4.22 FTIR spectra of LFN, pNIPAM homopolymer, 1LFN-pNIPAM composites showing regions of interest and offset for clearance.

Figure 4.23 (a) shows spectra of L_{OG} , pNIPAM homopolymer and 1 L_{OG} -pNIPAM. The 1 L_{OG} -pNIPAM composite shows a very similar FTIR spectrum to that of the 1 L_{EL} -pNIPAM composite (Table 4.5). Both L_{RD} -pNIPAM nanocomposites with two different clay-to-polymer ratios also have spectra Figure 4.23 (b) similar to that of the 1 L_{EL} -pNIPAM, however, the Si-O “out-of-plane” bands have a lower wavenumber for the 1 L_{RD} -pNIPAM and 2 L_{RD} -pNIPAM (1068 cm^{-1} and 1067 cm^{-1} , respectively) when compared to similar bands from the 1 L_{EL} -pNIPAM, which may be related to the L_{RD} smaller platelet size and lower CEC than L_{EL} . Table 4.5 provides details about bands position for all clay-pNIPAM nanocomposites.

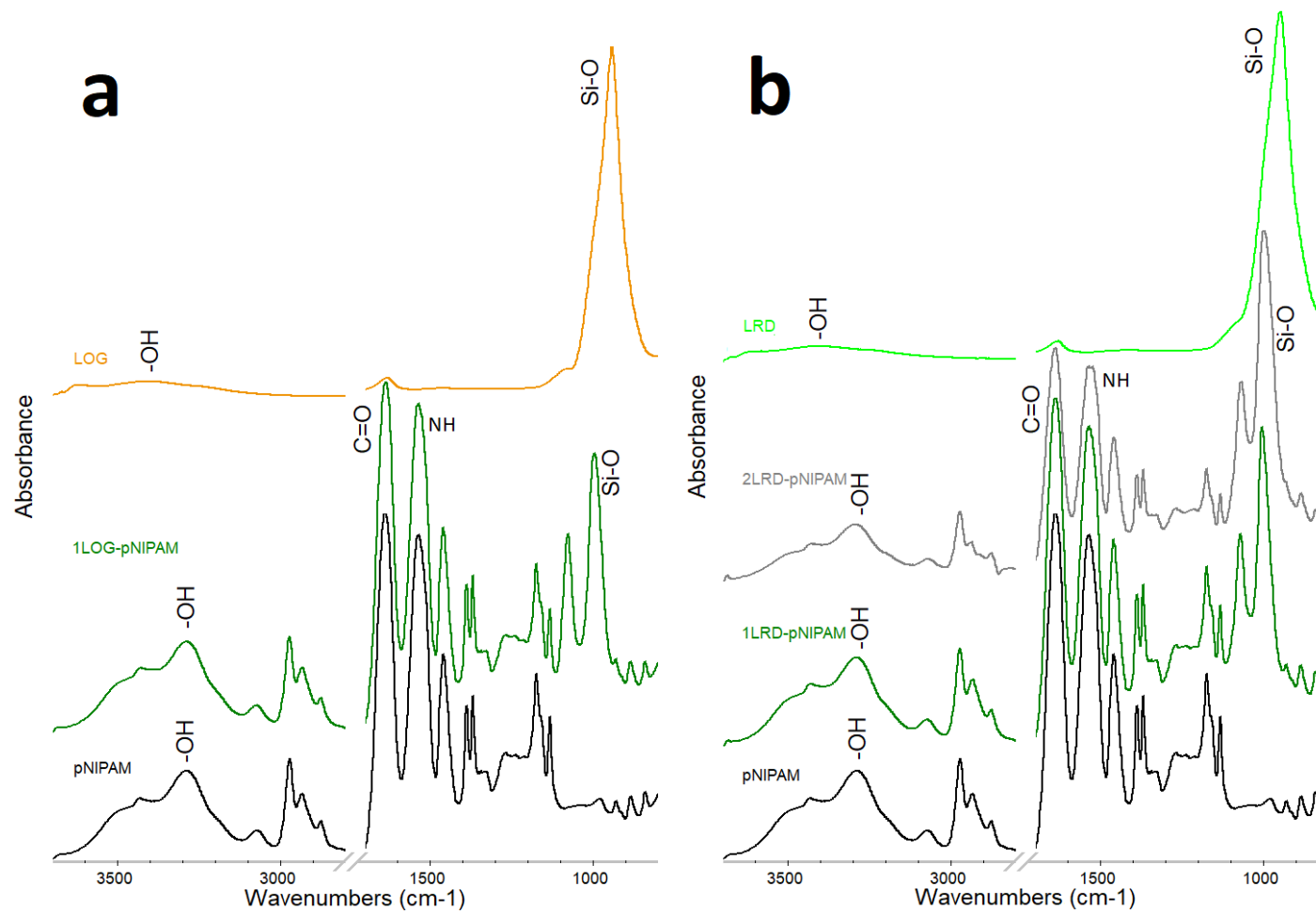


Figure 4.23 FTIR spectra of a) LOG, pNIPAM homopolymer, 1LOG-pNIPAM composites, b) LRD, pNIPAM homopolymer, 1LRD-pNIPAM and 2LRD-pNIPAM nanocomposites showing regions of interest and offset for clearance.

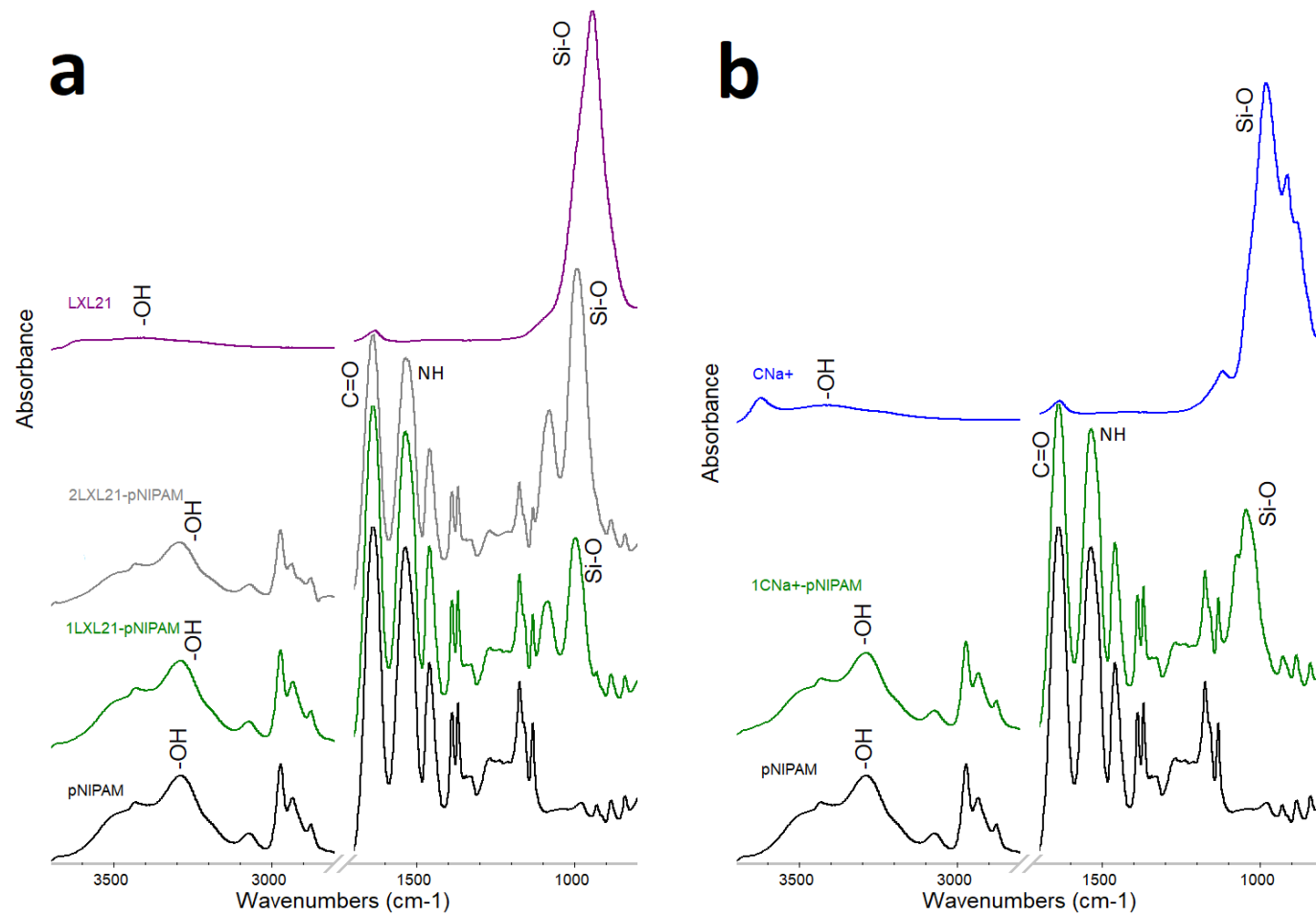


Figure 4.24 FTIR spectra of a) LXL21, pNIPAM homopolymer, 1LXL21-pNIPAM and 2LXL21-pNIPAM composites, b) CNa+, pNIPAM homopolymer, 1CNa+-pNIPAM nanocomposites showing regions of interest and offset for clearance.

Figure 4.24 (a) shows the FTIR spectra of the L_{XL21} , pNIPAM homopolymer and the corresponding nanocomposites at two different clay-to-polymer ratios. The Si-O band (in-plane mode) in the spectrum of the L_{XL21} can be observed at 942 cm^{-1} . [27] Respective, out-of-plane and in-plane Si-O bands are observed in the L_{XL21} -pNIPAM nanocomposites at 1084 cm^{-1} , 996 cm^{-1} in the spectrum of the $1L_{XL21}$ -pNIPAM composite and 1079 cm^{-1} , 990 cm^{-1} in the spectrum of the $2L_{XL21}$ -pNIPAM composite. As earlier mentioned, the observation of clear out-of-plane Si-O bands is an indication for a well dispersed L_{XL21} in both L_{XL21} -pNIPAM nanocomposites.[45]

Figure 4.24 (b) shows the change of bands for pNIPAM when crosslinked with C_{Na+} . The Si-O in-plane band of C_{Na+} is positioned at 980 cm^{-1} and when in the presence of pNIPAM, this shifts to 1043 cm^{-1} . The out-of-plane Si-O band also appears at 1070 cm^{-1} ; these two observations indicate that the C_{Na+} is well dispersed in the $1C_{Na+}$ -polymer. [45]

Table 4.5 FTIR bands positions for pNIPAM, (1 % clay)-pNIPAM, 2LEL-pNIPAM, 2LRD-pNIPAM and 2LXL21-pNIPAM composites

	-OH	Si-O	
		-out-of-plane	-in-plane
pNIPAM	3432	-	-
L_E	3408	-	946
$1L_{EL}$-pNIPAM	3430	1074	996
$2L_{EL}$-pNIPAM	3432	1072	990
L_{FN}	3408	-	949
$1L_{FN}$-pNIPAM	3431	1105	993
L_{OG}	3407	-	940
$1L_{OG}$-pNIPAM	3431	1075	995
L_{RD}	3405	-	945
$1L_{RD}$-pNIPAM	3431	1068	1001
$2L_{RD}$-pNIPAM	3431	1067	996
L_{XL21}	3417	-	942
$1L_{XL21}$-pNIPAM	3433	1084	996
$2L_{XL21}$-pNIPAM	3436	1079	990
C_{Na+}	3418	-	980
$1C_{Na+}$-pNIPAM	3432	1070	1043

4.1.6 Rheological Analysis and Properties of Clay-pNIPAM Hydrogels

Since rheology is sensitive, quick, requires small sample sizes and reveals differences (e.g. degree of crosslinking, structural homogeneity/heterogeneity) it is considered one of the most appropriate methods to characterise the mechanical properties of polymeric hydrogels. The rheological properties of hydrogels composed of different materials have been discussed in detail in several fields of research. [46][47] Materials with a uniform phase (solution, or pure substance) are referred to as simple fluids. If a material contains more than one phase (gas particles in foam, solid particles in liquid) it is considered to be a structured fluid as its rheological behaviour is dominated by the interactions of its components. [48]

There are several rheological techniques to characterise polymeric materials like small-amplitude oscillatory shear, frequency sweeps within the linear-viscoelastic range (LVE which can give information about the degree of crosslinking) and temperature sweeps useful polymers that have an upper and lower critical solution in which temperatures can form one or two phases can be formed. [49]

To be able to perform tests for viscoelastic materials with results that are not influenced by deformation occurring during an experiment, a check for the linear-viscoelastic region needs to be done. This can be done by performing a strain sweep (from 0.1 to 100% strain). Under the specified thermal conditions, a new sample was placed on the rheometer plates. Samples were given the time to rest as determined by a preceding time sweep test performed before the strain sweep, the frequency at which the strain sweep was chosen arbitrarily for the first test. Another time sweep was repeated with 15 % strain to check for equilibrium under the same condition.

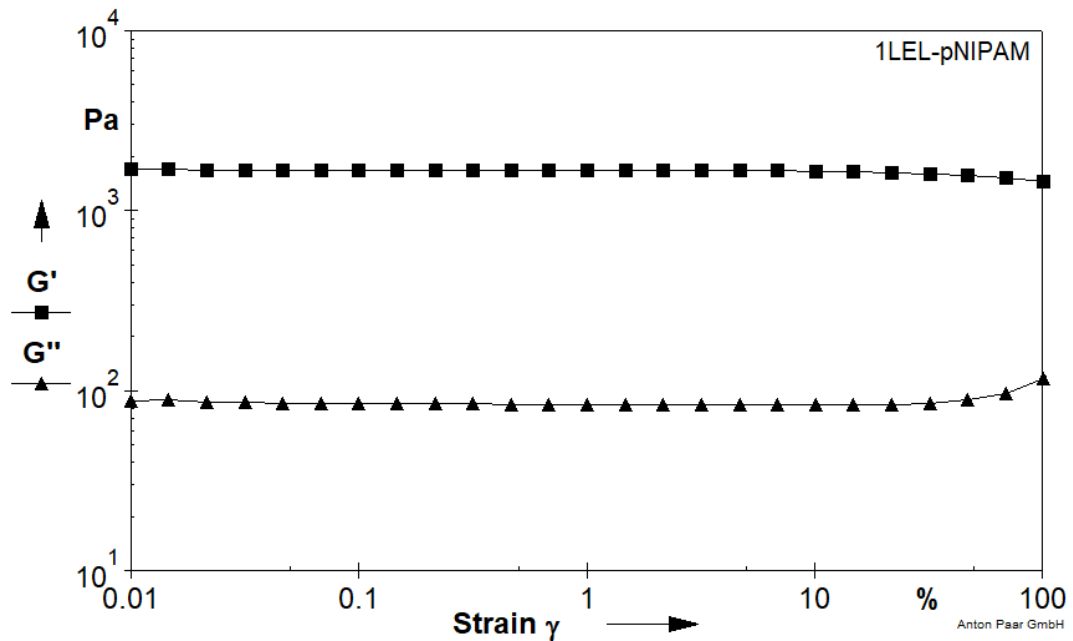


Figure 4.25 Strain sweep. The LVE limit was determined with respect to strain. G' was determined from 0.1 % to 100 % strain for 1LEL-pNIPAM.

The results of the strain sweep for the 1LEL-pNIPAM are shown as an example in Figure 4.25, the measurement was performed for fully formed hydrogel at 20 °C. The curve shows a linear behaviour (constant values as strain increases) of G' and G'' up to 10 % strain, therefore, a strain of 1 % was selected for subsequent sweeps. [49]

Homopolymer pNIPAM was not as easy to analyse, since as the test was started the sample slipped away from between the rheometer plates, however, it was clear that the pNIPAM homopolymer showed a lower viscosity in the test tubes compared to the pNIPAM clay samples. Other homopolymers were too hard (i.e. non-compressible) to be tested as was the case with homopolymers pHEMA and pHPMA since with these samples the upper plate was not able to reach the testing position to start the test. This made it hard to find the required parameters (time, strain, frequency) to run further tests on the homopolymers, as a result no homopolymers were tested further and only clay-polymer hydrogels were taken for further tests. The main point to look for in the rheological analysis section was to figure out the effect of different clay types/grades on the properties of hydrogels.

4.1.6.1 Temperature Effect on Clay-pNIPAM Hydrogels

4.1.6.1.1 Temperature Effect on Viscosity (Rotational Temperature Sweep)

A clay-polymer hydrogel is a flexible three-dimensional network structure. For the stimuli-responsive polymers, a change in the value of the mechanical properties can be observed with a simple viscosity check over a range of temperature to find out if the crosslinker presence will affect the LCST for NIPAM. An initial thermal equilibrium was essential for the clay-pNIPAM hydrogels, so the experimental setup started with an interval of five minutes with no forces applied at 40 °C to reach thermal equilibrium. Figure 4.26, when cooled the viscosity (η) values of (1 % clay)-pNIPAM hydrogel, increased to significantly higher values at ~ 32 °C. This behaviour is also clear in 1LEL-pNIPAM, 1LRD-pNIPAM, 1LXL21-pNIPAM, and 1CNa+-pNIPAM hydrogels; as these composites are soft, flowing materials when at temperatures higher than the LCST. The 1LOG-pNIPAM composite is a soft non-flowing material at temperatures \geq LCST and they became stiffer as the temperature decreases.

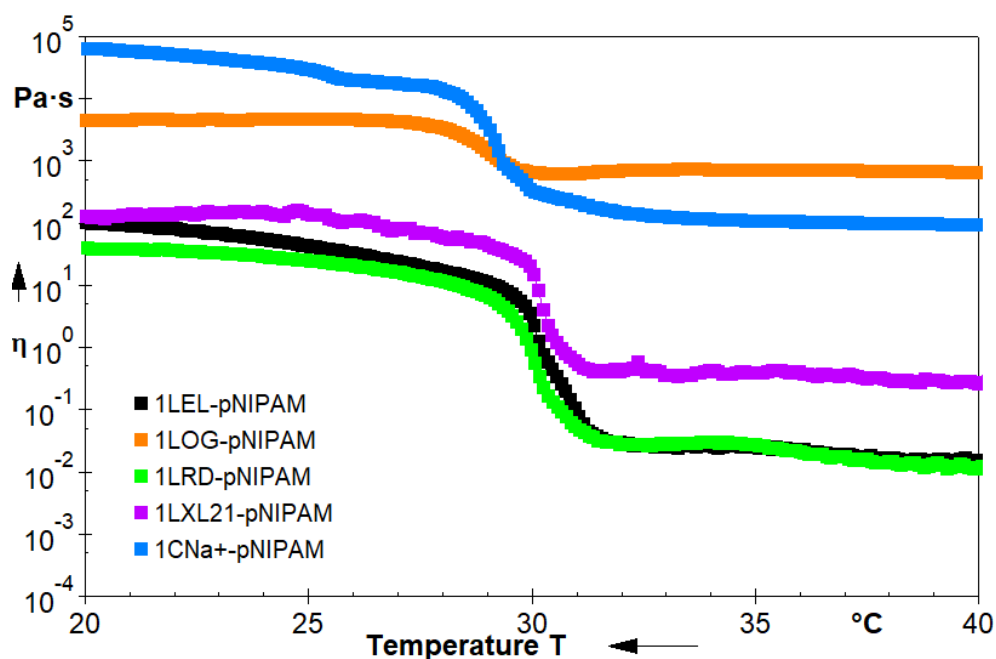


Figure 4.26 Viscosity (Pa.s) as a function of temperature (decreasing from 40 °C to 20 °C) for (1 % clay)-pNIPAM composites at a shear rate of 10 s⁻¹ and cooling rate of 1 °C.min⁻¹.

Figure 4.27 shows that there was no clear trend of the clay platelet size and CEC on the viscosity of the (1 % clay)-pNIPAM hydrogels.

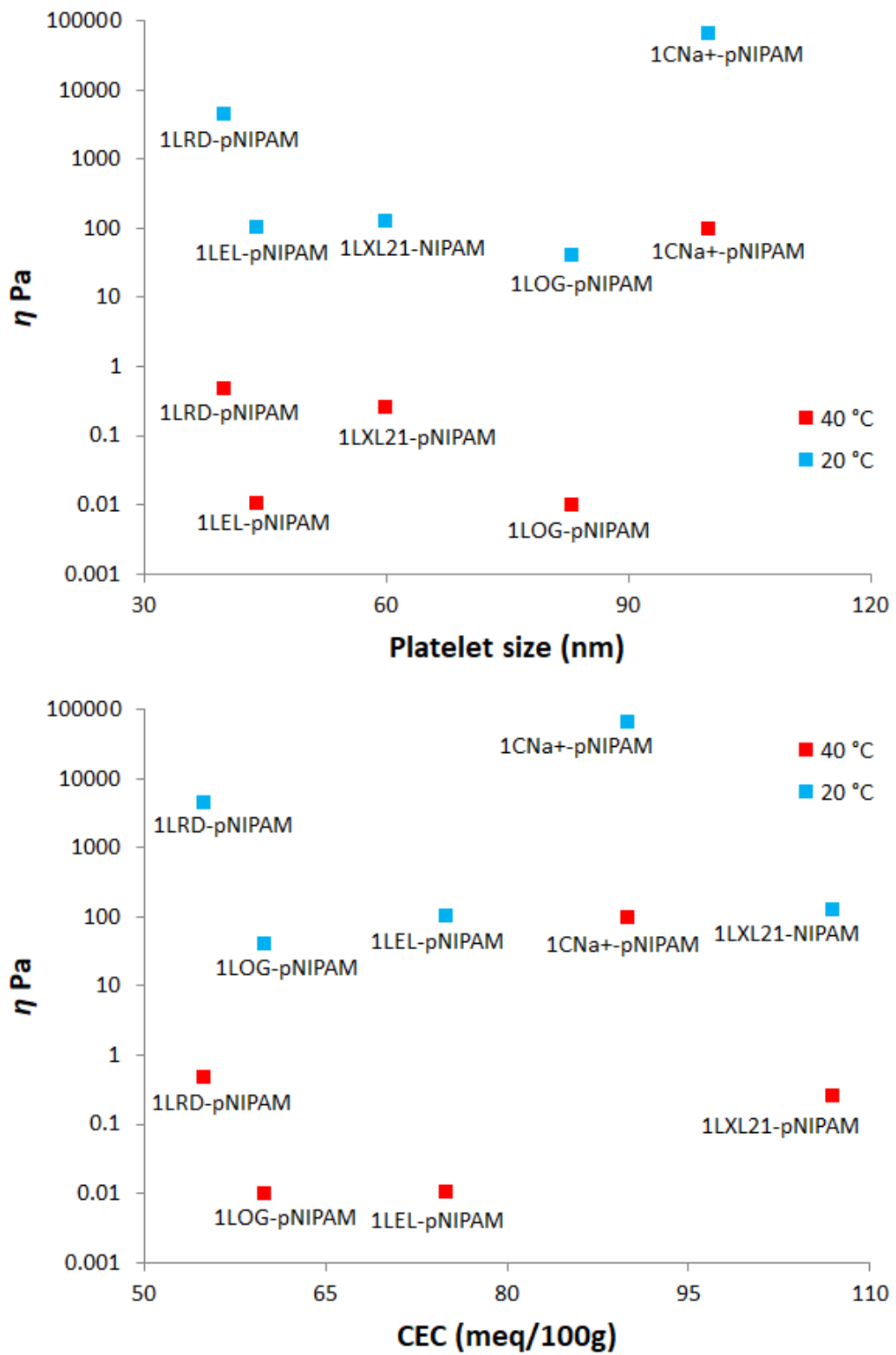


Figure 4.27 The effect of clay platelet size and CEC on the viscosity of (1 % clay)-pNIPAM hydrogels at temperatures above and below the pNIPAM LCST.

These measurements on 1L_{FN}-pNIPAM hydrogel samples were not possible because the sample was ejected from the plates and torn to pieces. Figure 4.28 shows the samples after being pushed out from between the plates. L_{FN} has the largest platelet size between the different clays used in this study, the 1L_{FN}-pNIPAM was more rubbery than other composites after solidification, which may be a result of the large clay platelet size. Other rheological tests were performed under oscillatory mode and more details about the 1L_{FN}-pNIPAM hydrogel are mentioned later in this chapter.

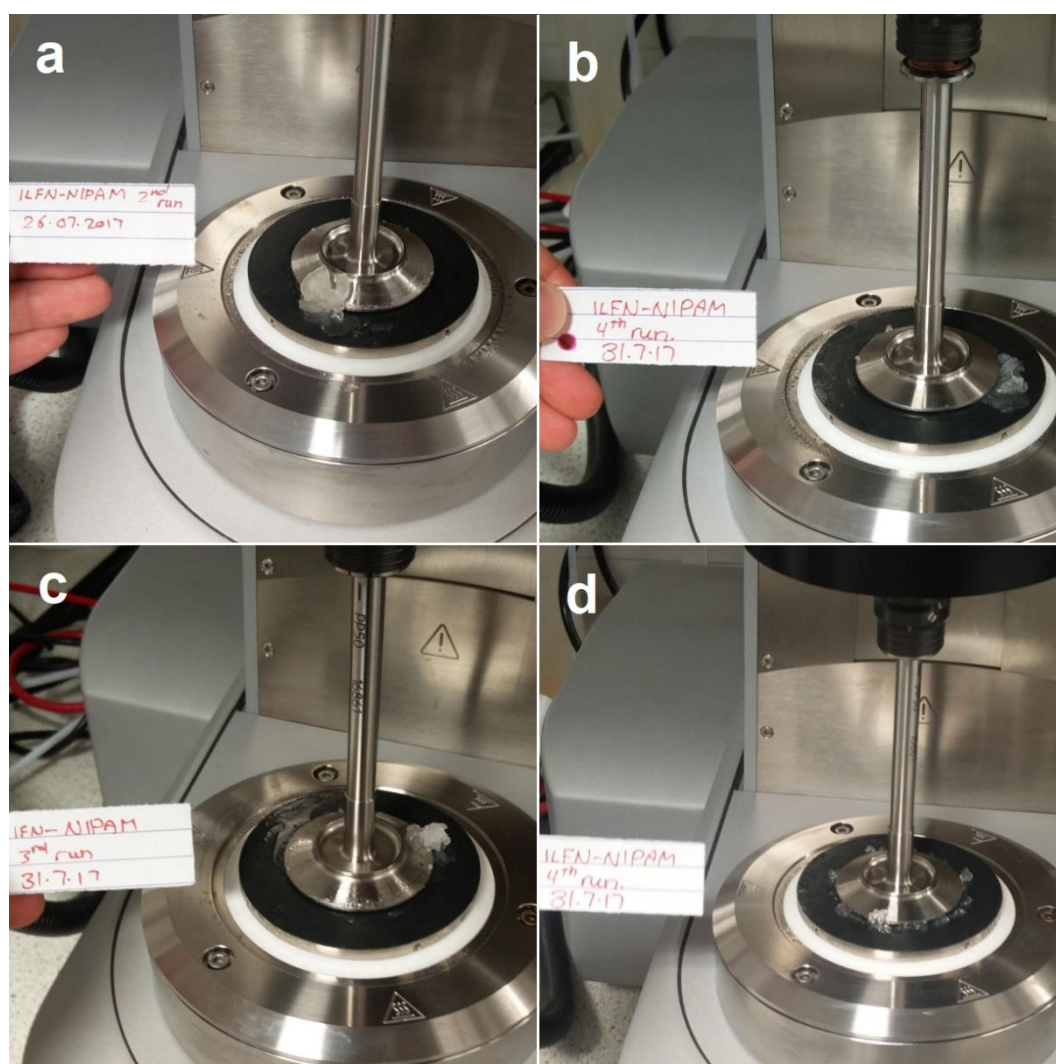


Figure 4.28 1L_{FN}-pNIPAM samples, samples pushed out from between the rheometer's parallel plates and inconsistent tests.

4.1.6.1.2 Temperature Effect on the Loss (G'') and Storage (G') Moduli of the Clay-pNIPAM Hydrogel

The rheological change of the clay-pNIPAM hydrogel systems over decreasing temperature was also investigated by monitoring the evolution of the storage modulus G' and loss modulus G'' . Both moduli increased and all systems progressed through three stages (Figure 4.29), a slow change in values between 40 -32 °C followed by a significant change between 32 – 30 °C, and finally a slow non-significant change between 30 – 20 °C. Based on visual observations it was expected that the clay-pNIPAM hydrogels would change from liquid to gel, however, in all the three stages $G'' < G'$, stating they are soft gels that change to a harder gel after passing through the LCST. After the LCST stage, the moduli gradually increase with the temperature decrease resulting in bigger differences between G' and G'' values. At this stage, the gels become stiffer as polymer chains change from globule to coil and crosslinking density gradually increases. [50]

The 1_{LFN}-pNIPAM, 1_{LOG}-pNIPAM and 1_{CNa+}-pNIPAM hydrogels (Figure 4.29) show a different behaviour as they pass through the LCST, this observation still needs further investigation. These three clays have bigger platelet sizes than others and this behaviour may be a result of the way big platelets interact with the pNIPAM chains as they change to coil form.

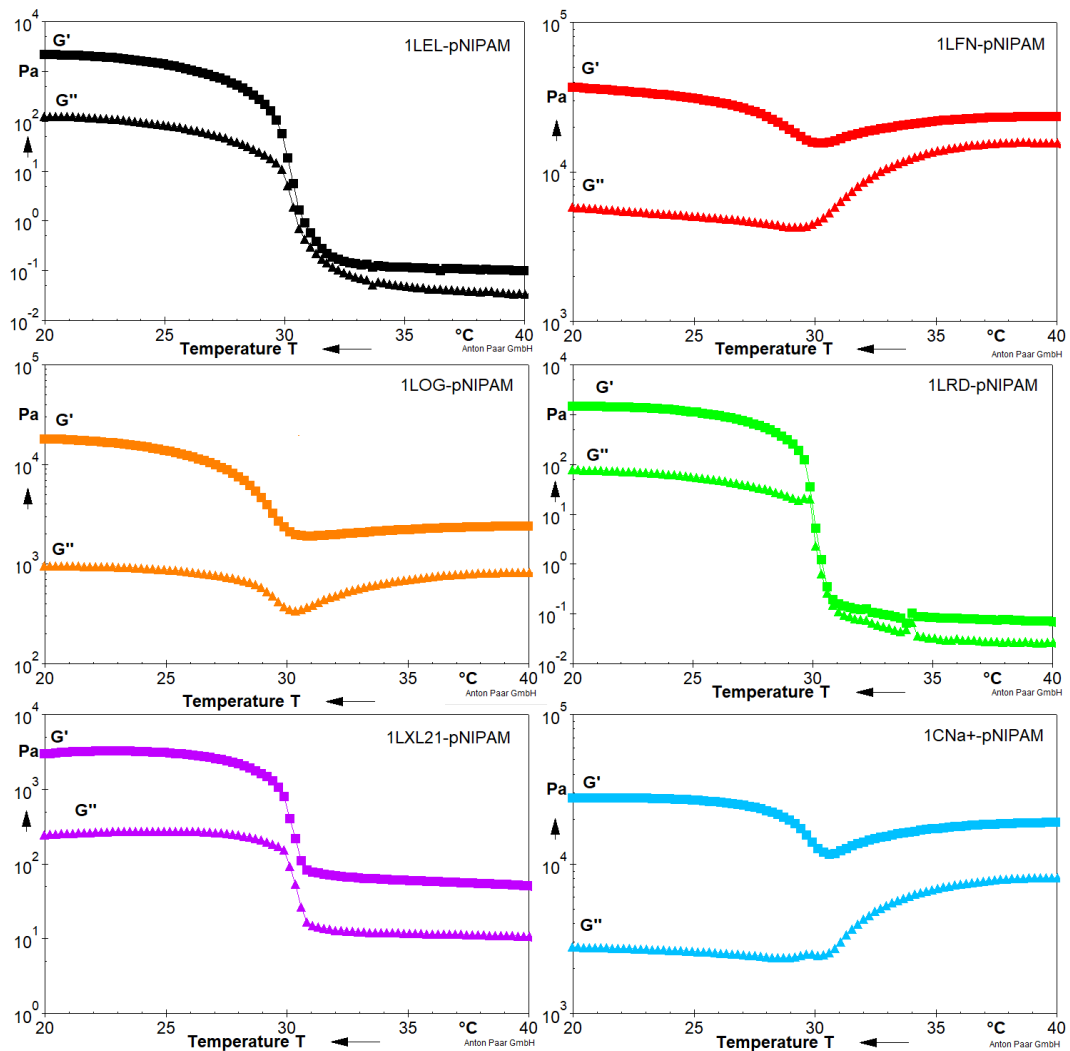


Figure 4.29 Evolution of storage modulus G' and loss modulus G'' during solidification of the (1 % clay)-pNIPAM hydrogel.

Figure 4.30 shows the relationship between the storage modulus and either the clay platelet size (top) or the clay CEC (bottom) at temperatures above ($40\text{ }^{\circ}\text{C}$) and below ($20\text{ }^{\circ}\text{C}$) the LCST for the (1 % clay)-pNIPAM hydrogels. Both parameters have a significant effect on the viscoelastic properties on the hydrogels, clays with larger platelets develop hydrogels with higher G' modules. The case is not the same with the effect of the CEC on the clay-pNIPAM hydrogels as the trend is not as clear, the clay platelet size influence on the viscoelastic properties is clearer as a linear relationship for the (1 % clay)-pNIPAM hydrogels at $20\text{ }^{\circ}\text{C}$ and as a clear increase in the values at $40\text{ }^{\circ}\text{C}$.

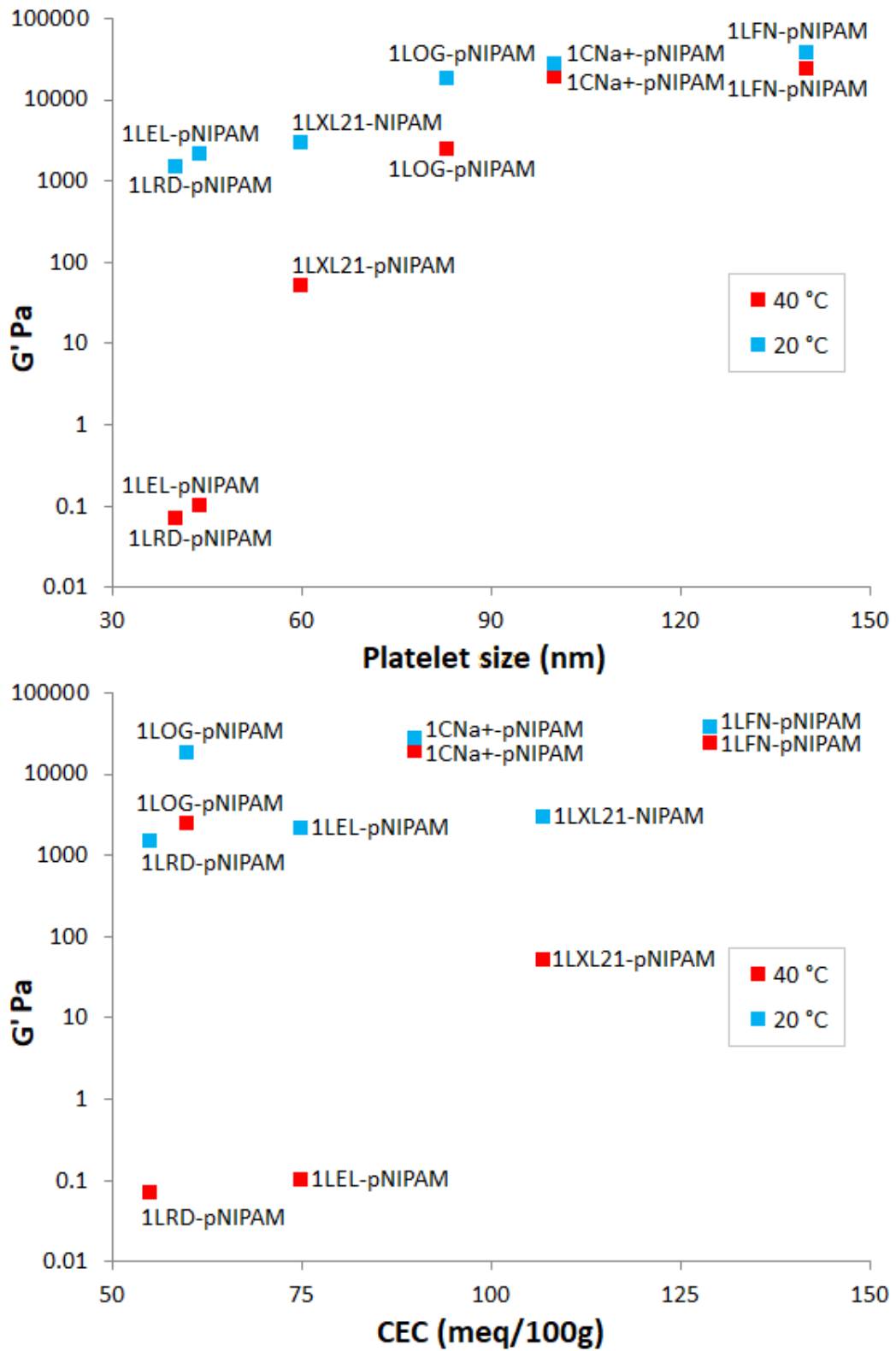


Figure 4.30 The relationship between G' and (top) clay platelet size and (bottom) clay CEC.

The (2 % clay)-pNIPAM hydrogels show similar behaviour with a significant difference in values before passing through the LCST for both moduli (Figure 4.31).

After passing through the LCST the G' and G'' values (Table 4.6) were similar to other values for L_{EL} -pNIPAM, L_{RD} -pNIPAM and L_{XL21} -pNIPAM hydrogels.

These results show that before passing through the LCST, the clay-to-polymer ratio has a great effect on the clay-polymer hydrogel rheological and mechanical properties depending on the amount of clay in the mixture, at this point the pNIPAM chains are still in globule conformation and it is not having a significant effect on the surroundings. After passing through the LCST the pNIPAM change to a coils conformation and has a greater effect on the mechanical properties of the hydrogel. This can be of a great benefit for certain application where composites need to be of a specific strength at below and above certain temperatures.

The plots in Figure 4.31 show the plots for three types of clays as a crosslinking agent (L_{EL} , L_{RD} and L_{XL21}). The $1L_{EL}$ -pNIPAM, $1L_{RD}$ -pNIPAM and $1L_{XL21}$ -pNIPAM hydrogel have a lower range of storage modulus in both plots in Figure 4.30 and different behaviour in Figure 4.29. L_{EL} , L_{RD} and L_{XL21} have a smaller range platelet size than other clays and as the relationship between the CEC and the storage modulus was not as clear, the platelet size was the only factor left affecting the rheological properties at a temperature above the pNIPAM LCST.

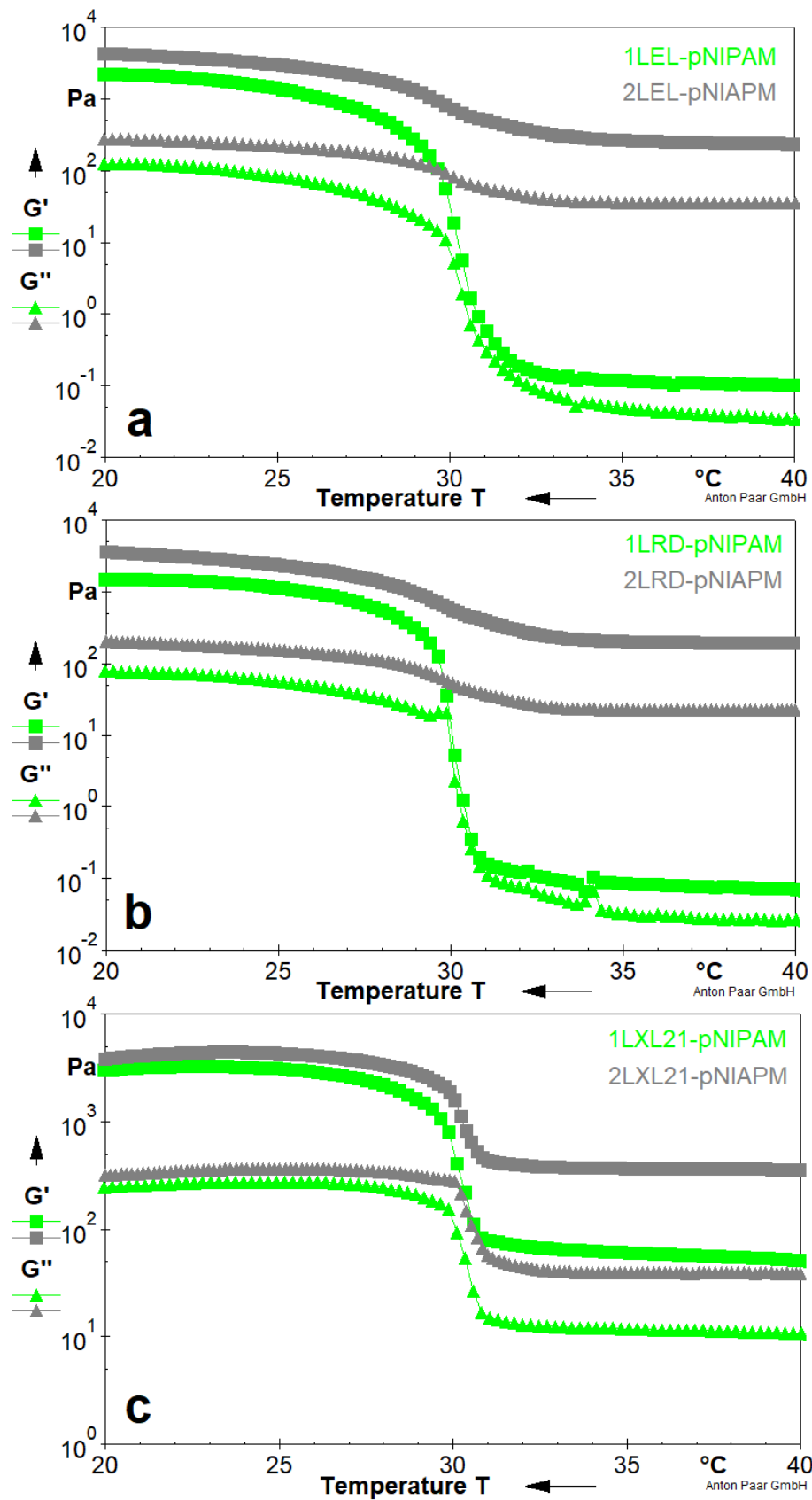


Figure 4.31 Evolution of storage modulus G' and loss modulus G'' through passing the LCST of the 1(LEL, LRD, LXL21)-pNIPAM and 2(LEL, LRD, LXL21)-pNIPAM hydrogels.

Figure 4.32 shows a comparison between the effect of different clay-to-polymer ratios on the storage moduli at different above (40 °C) and below (20 °C) the LCST. The figure also shows the relationship between the G' and the clay properties clay particle size (top) and clay CEC (bottom).

At temperature above the LCST, the effect of the clay-to-polymer ratio is clear; (Table 4.6) the G' values are significantly different between the (1 %clay)-pNIPAM and the (2 % clay)-pNIPAM hydrogels, whereas when the temperature is below the LCST the effect of the clay-to-polymer ratio is not as significant. This behaviour depends on which part of the hydrogel has a bigger effect on the rheological properties at different temperatures. When the temperature is above the LCST, the polymer chains are in a globule configuration and there are fewer interactions with one another or with the clay platelets and the clay dispersion properties have a greater effect on the overall hydrogel properties. As the temperature drops and the pNIPAM chains start to change to a coil configuration, it has more of an effect on the properties of the clay-pNIPAM hydrogels.

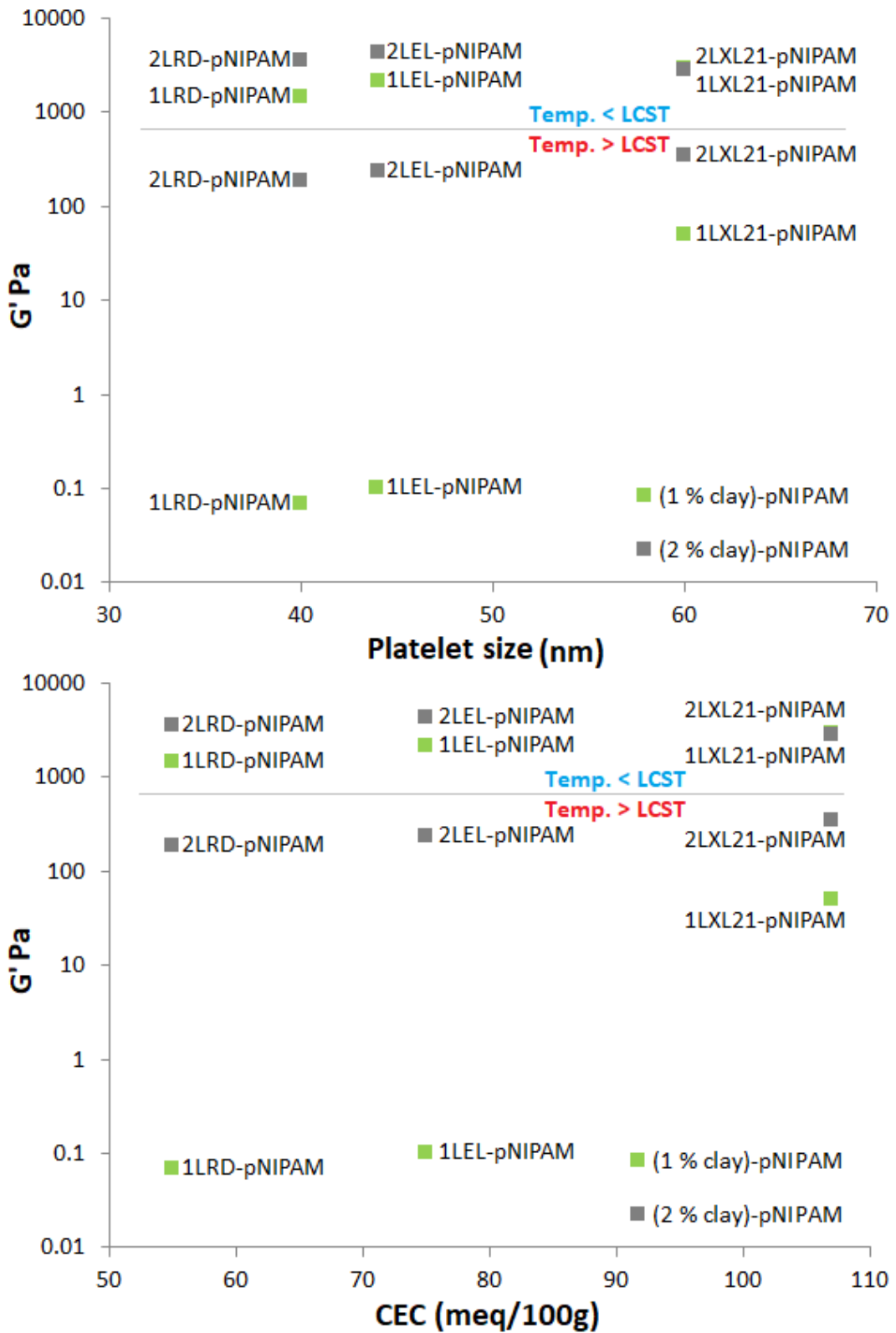


Figure 4.32 The effect of different clay-to-polymer ratios on the G' at temperatures above and below the pNIPAM LCST. The relationship between the G' and the clay properties (top) clay particle size and (bottom) clay CEC.

Table 4.6 storage (G') and loss (G'') moduli (Pa) at temperatures above (40 °C) and below (20 °C) the LCST.

Samples	At 40 °C				At 20 °C			
	G' Mean	G' SD	G'' Mean	G'' SD	G' Mean	G' SD	G'' Mean	G'' SD
1L_{EL}-pNIPAM	0.10	0.02	0.03	0.03	2181	11	126	0.86
2L_{EL}-pNIPAM	236	13	35	0.23	4296	922	277	60
1L_{FN}-pNIPAM	23354	7372	15550	5070	36877	10664	5811	1654
1L_{OG}-pNIPAM	2419	153	829	40	18106	1279	951	71
1L_{RD}-pNIPAM	0.07	0.01	0.03	0.01	1468	74	78	4.00
2L_{RD}-pNIPAM	188	10	22	0.76	3570	115	203	7.17
1L_{XL21}-pNIPAM	51	2.60	11	1.10	2960	26.	243	3.41
2L_{XL21}-pNIPAM	355	24	39	3.24	2822	621	314	5.43
1C_{Na+}-pNIPAM	18987	405017	8105	2377	27590	6707	2776	867

4.1.6.2 Critical Yield Stress of Clay-pNIPAM Hydrogels

Materials with a yield point (yield stress or yield value) begin to flow as the external forces acting on it become larger than the internal structural forces. Below the yield point, the material behaves like a solid. The classic method to determine the yield point is with a controlled shear stress experiment (it is the stress value at the onset of flow). When increasing the shear stress with time the shear stress value is taken when the measuring device is still detecting no sign of motion. This is the last measuring point at which the rotational speed $n = 0$ (or as $\dot{\gamma} = 0$). When presented on a logarithmic scale, the yield point is the τ -value at the lowest measured shear rate.[51]

Figure 4.33 shows the flow curves of L_{EL}-pNIPAM, L_{RD}-pNIPAM, and L_{XL21}-pNIPAM hydrogels at two different clay-to-polymer ratios and two different temperatures (40 °C and 20 °C). At 40 °C (above LCST) the (2 % clay)-pNIPAM shows the largest yield stress values, while after passing through the LCST at 20 °C (below LCST) the values for clays and clay concentrations are close to each other (Table 4.7). These results support the previous temperature oscillatory experiment showing that when the temperature is above the LCST the clay plays a big role in the properties of the clay-pNIPAM nanocomposite, but as the temperature decreases below the LCST and the polymer chains take a globule formation, it is the polymer within the hydrogel that has a bigger effect on the properties of the composite.

The 1L_{XL21}-pNIPAM hydrogel shows larger yield stress at 40 °C than the 1L_{EL}-pNIPAM and the 1L_{RD}-pNIPAM hydrogels which can be attributed to the larger platelet size and higher CEC. When at a different clay-to-polymer ratio, the 2L_{XL21}-pNIPAM hydrogel also has a higher yield stress value.

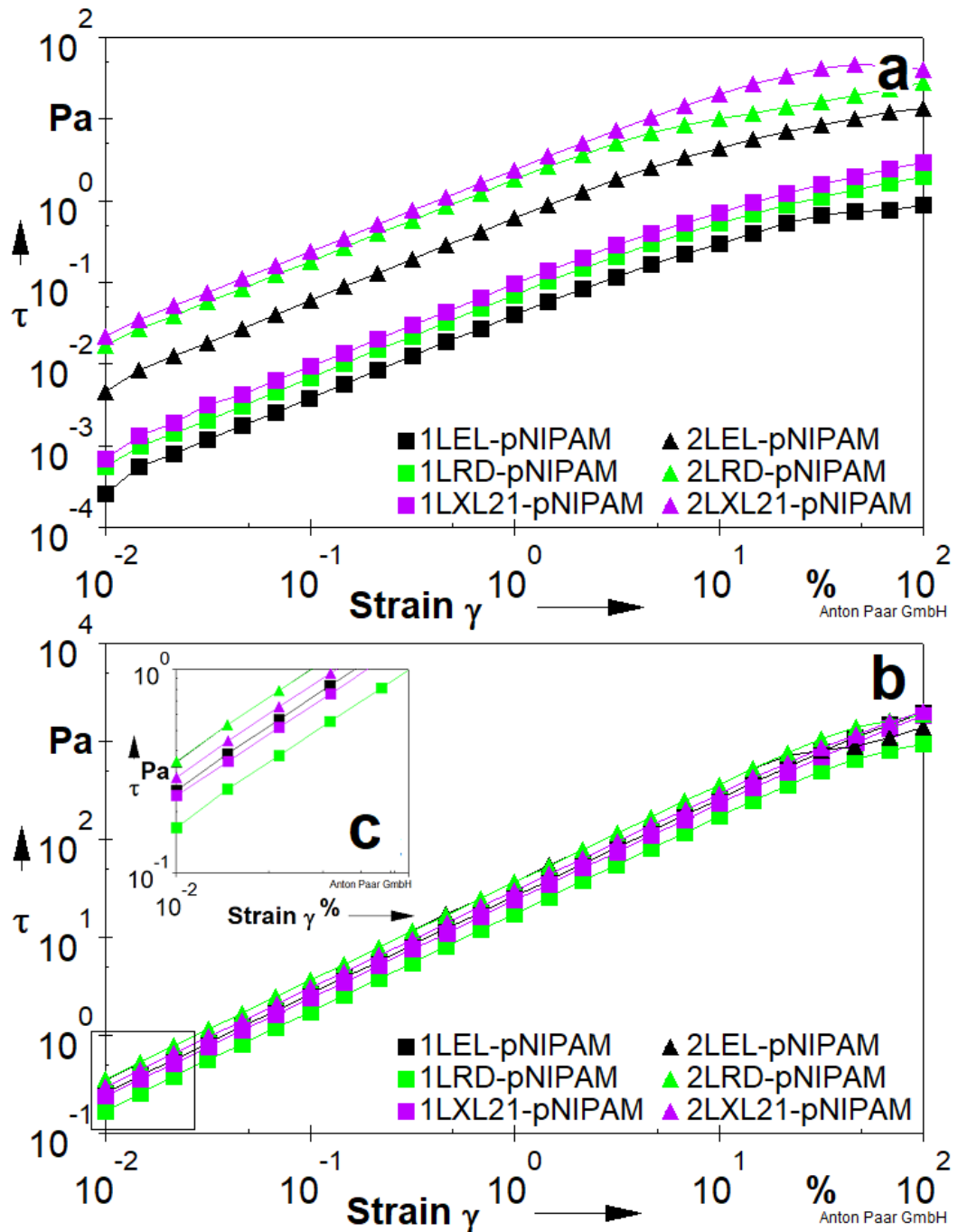


Figure 4.33 Yield stress values at temperatures a) Above LCST (40 °C) showing with the difference in value between the (1 % clay)-pNIPAM and the (2 % clay)-pNIPAM hydrogel. b) Below LCST (20 °C) showing how close the yield stress values after passing through the LCST.

Table 4.7 Average critical yield stress values and standard deviation (n=3) for LEL-pNIPAM, LRD-pNIPAM, and LXL21-pNIPAM hydrogels at two different clay-to-polymer ratios at temperatures above (40 °C) and below (20 °C) pNIPAM LCST.

Samples	At 40 °C		At 20 °C	
	τ Mean	τ SD	τ Mean	τ SD
1L_{EL}-pNIPAM	0.00030	0.00021	0.25699	0.05406
2L_{EL}-pNIPAM	0.00339	0.00135	0.32759	0.02189
1L_{RD}-pNIPAM	0.00054	0.00010	0.15835	0.01417
2L_{RD}-pNIPAM	0.01677	0.00101	0.34967	0.00797
1L_{XL21}-pNIPAM	0.00060	0.00055	0.21607	0.02101
2L_{XL21}-pNIPAM	0.02039	0.00115	0.30988	0.03348

4.1.6.3 Storage (G') and Loss (G'') Moduli Behaviour

4.1.6.3.1 Amplitude Sweep (Function of Strain)

The viscoelastic properties of the material are independent of strain up to a critical strain level, beyond this level the material behaviour is non-linear, and G' decreases. An amplitude (strain) sweep enables the observation of the viscoelastic behaviour by measuring the storage and loss moduli (G' , G''). It will establish the limit of the material's linearity at which the structure stops being intact (i.e. gel-like $G' > G''$) and the material network structure becomes disrupted (i.e. more liquid-like and $G' < G''$). [48][52]

Figure 4.34 shows a strain sweep for 1L_{EL}-pNIPAM, 2L_{EL}-pNIPAM, 1L_{RD}-pNIPAM, 2L_{RD}-pNIPAM, 1L_{XL21}pNIPAM, and 2L_{XL21}-pNIPAM hydrogels at temperatures above (40 °C) and below (20 °C) the pNIPAM LCST. The strain range 0.01 – 100 % shows the LVE for all nanocomposites but only shows the crossover points for 1L_{EL}-pNIPAM, 1L_{RD}-pNIPAM and 2L_{EL}-pNIPAM at 20 °C and 2L_{XL21}-pNIPAM at 40 °C. (Table 4.8) shows the mean values and standard deviation for G' and G'' from three runs.

Figure 4.34 (a, c, and e) show that G' and G'' meet at almost 100 % strain. However, the value (as by the plots) are very close, this shows that the nanocomposites are strain (amplitude) dependent, which helps to design and engineer the composites for certain final applications.

Figure 4.34 (b, d, f) shows more extended LVE (Linear ViscoElastic region) at 20 °C (Table 4.8) when compared to the same hydrogels at 40 °C where the polymer within the hydrogels dominates their mechanical properties; as the hydrogels reach the LVE limit they lose their elasticity quickly and their structures are destroyed. The G'' values at 20 °C show an increase at smaller strain values than for those at 40 °C.

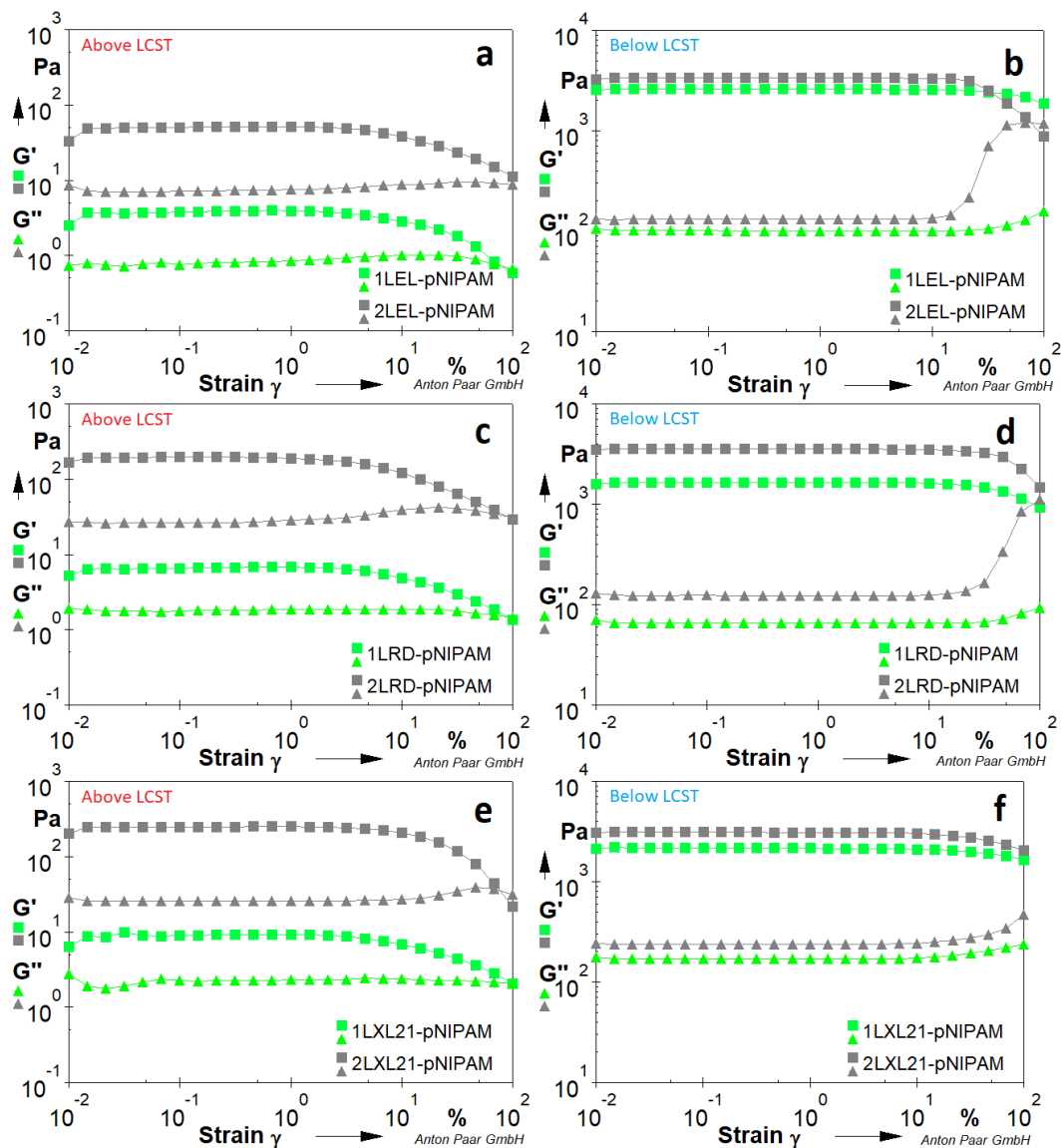


Figure 4.34 Evolution of storage modulus G' and loss modulus G'' as a function of strain from 0.01 - 100 % showing the LVE range and transition point. (gel-like to liquid-like) at temperatures above and below pNIPAM LCST for a) 1LEL-pNIPAM and 2LEL-pNIPAM at 40 °C, b) 1LEL-pNIPAM and 2LEL-pNIPAM at 20 °C, c) 1LRD-pNIPAM and 2LRD-pNIPAM at 40 °C, d) 1LRD-pNIPAM and 2LRD-pNIPAM at 20 °C, e) 1LXL21-pNIPAM and 2LXL21-pNIPAM at 40 °C, f) 1LXL21-pNIPAM and 2LXL21-pNIPAM at 20 °C.

The LVE range (Table 4.8) and the critical strain γ_c (if found) varies with changing temperature as expected. At 20 °C, the hydrogel is stiffer; the storage modulus has a greater effect on the hydrogel properties.

The LVE values show a clear relationship between the clay type and the clay-to-polymer ratio of the mechanical property of the hydrogels, the (2 % clay)-pNIPAM have larger LVE ranges than the (1 % clay)-pNIPAM hydrogels. In this case and as shown by the plots in Figure 4.35 (a, c), at a temperature above the LCST (40 °C) where the clay within the hydrogel has a bigger effect on the mechanical properties. At temperatures below the LCST (20 °C) the hydrogels with less clay give larger LVE ranges as the polymer part of the hydrogel has a bigger effect on the hydrogel properties with more polymer-to-polymer interaction.

The mechanical properties change as the clay changes because of the effect of the clay platelet size and their CEC, the relationship between these two parameters and any property is complex as it depends on both parameters at the same time and depends on the ratio between them. The larger the clay particle size the larger the LVE range and at the same time the higher the clay CEC the larger the LVE range. For example, L_{XL21}-pNIPAM hydrogels constantly show the largest LVE ranges (Figure 4.35, Table 4.8) and those have significantly larger platelet size and higher CEC when compared to L_{EL} and L_{RD}.

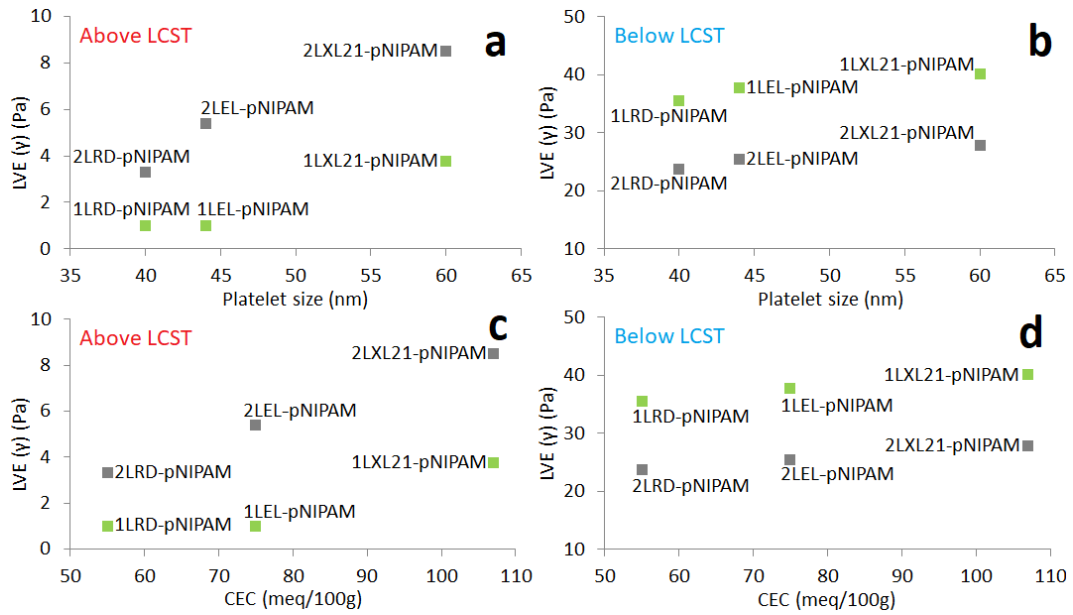


Figure 4.35 LVE range limit (γ %) to clay platelet size and CEC for 1LEL-pNIPAM, 2LEL-pNIPAM, 1LRD-pNIPAM, 2LRD-pNIPAM, 1LXL21-pNIPAM, and 2LXL21-pNIPAM at 40 °C (a, c) and 20 °C (b, d).

Table 4.8 Average crossover points (γ , G' value) and LVE range limits from (n=3) for 1LEL-pNIPAM, 2LEL-pNIPAM, 1LRD-pNIPAM, 2LRD-pNIPAM, 1LXL21-pNIPAM, and 2LXL21-pNIPAM hydrogels at 40 °C and 20 °C.

Samples	At 40 °C					At 20 °C				
	Crossover point				LVE (γ %)	Crossover point				LVE (γ %)
	γ %	γ SD	G' Pa	G' SD		γ %	γ SD	G' Pa	G' SD	
1 _{EL} -pNIPAM	79.56	-	0.72	-	1.01	-	-	-	-	37.80
2 _{EL} -pNIPAM	-	-	-	-	5.38	76.50	0.66	1197.2	62.93	25.50
1 _{RD} -pNIPAM	91.48	-	1.48	-	1.01	-	-	-	-	35.50
2 _{RD} -pNIPAM	-	-	-	-	3.30	-	-	-	-	23.80
1 _{XL21} -pNIPAM	-	-	-	-	3.75	-	-	-	-	40.10
2 _{XL21} -pNIPAM	76.62	19.80	35.07	9.896	8.52	-	-	-	-	27.90

4.1.6.3.2 Frequency Sweeps (Function of Frequency)

The frequency response of the clay-pNIPAM hydrogels to oscillatory shear stress was conducted to find an appropriate value of frequency to employ in further rheological experiments (time, strain, temperature sweeps) that defines the equilibrium strength and gelation parameters of such nanocomposites. But mainly the test was conducted to understand the behaviour of the nanocomposite under different frequencies. The applied stress amplitude was chosen in the linear viscoelastic region. For each test run a new clay-polymer nanocomposite solution was placed on the preheated rheometer plate (40 °C) and the appropriate amount of time elapsed for the samples to reach thermal equilibrium. A guard moisture trap was used to prevent evaporation.

The Frequency sweeps from 0.01 - 100 Hz were conducted at the LVE strain amplitude of 1 %. The variations of the viscoelastic moduli G' and G'' with the frequency are measured for the clay-pNIPAM hydrogels with different clay types and at different clay-to-polymer ratios. [49][53]

Figure 4.36 shows the storage modulus (G') and loss modulus (G'') values for 1L_{EL}-pNIPAM, 2L_{EL}-pNIPAM, 1L_{RD}-pNIPAM, 2L_{RD}-pNIPAM, 1L_{XL21}-pNIPAM, and 2L_{XL21}-pNIPAM hydrogels at two different temperatures, above (40 °C) and below (20 °C), the pNIPAM LCST. For 1L_{EL}-pNIPAM and 1L_{RD}-pNIPAM at 40° C (Figure 4.36 (a, c, e)) not all frequencies were measured since sample slippage was experienced above 10 Hz.

At 40 °C, the (2 % clay)-pNIPAM hydrogels show the LVE limits and the crossover point for the G' and G'' (Figure 4.36 (a, c, e)). Table 4.9 shows the value of the frequency (Hz) and the viscoelastic modulus (Pa), the LVE limits vary with different grades of clay, and as it was with the strain sweep results, the 2L_{XL21}-pNIPAM shows a larger LVE range.

At 20 °C, the clay-polymer nanocomposites look independent from frequency as G' value was almost constant throughout the frequency range, the LVE limits calculated by the analysis tool represent the change of the modulus (G') value over a certain number of measure point which explains the low-frequency values in the LVE column in Table 4.9. For the 1L_{EL}-pNIPAM and the 1L_{RD}-pNIPAM, there was no detectable change in the curve over the frequency range of the test.

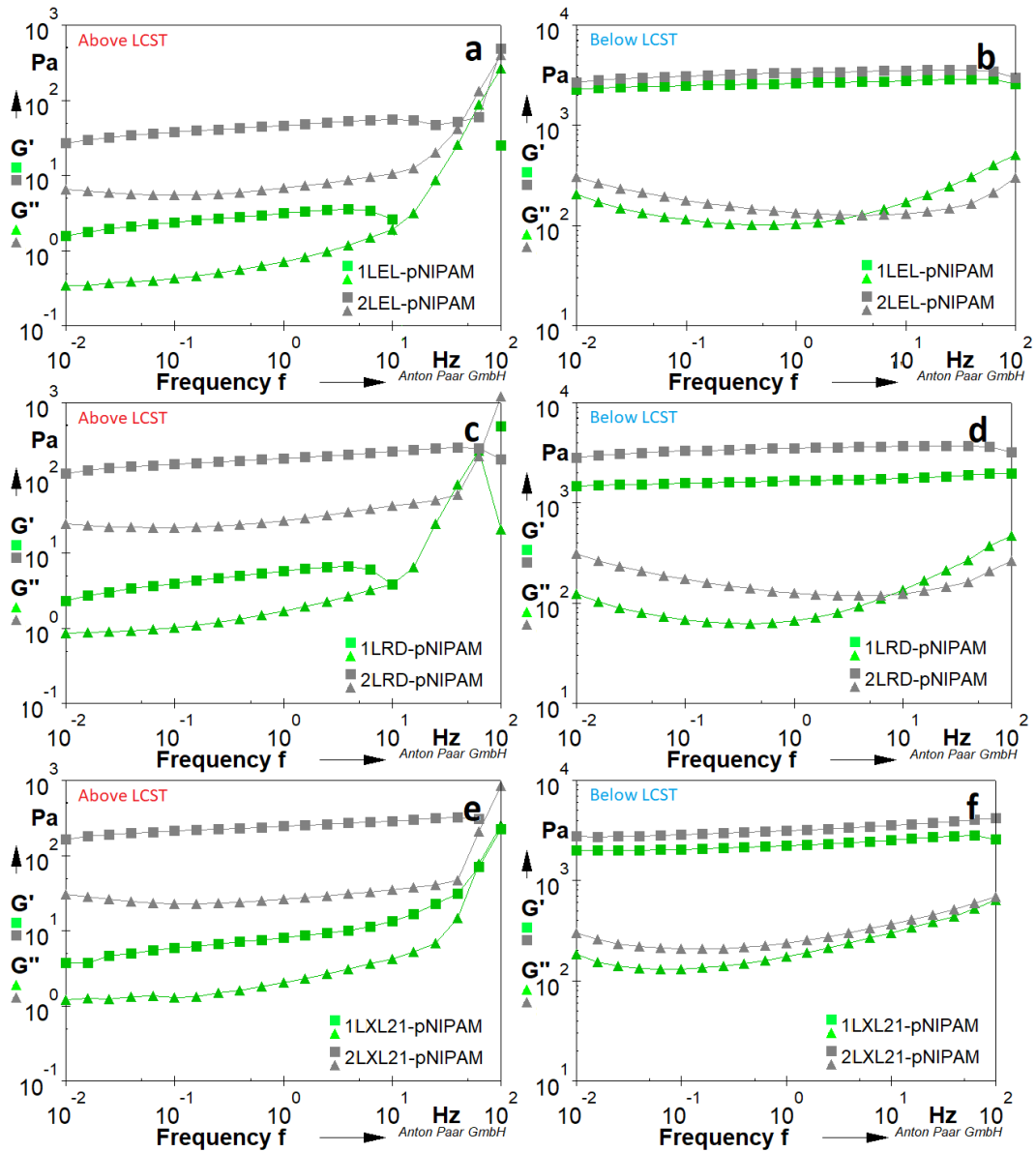


Figure 4.36 Evolution of storage modulus G' and loss modulus G'' as a function of frequency from 0.01 - 100 Hz showing the LVE range and transition point (gel-like to liquid-like) at temperatures above and below pNIPAM LCST for a) 1LEL-pNIPAM and 2LEL-pNIPAM at 40 °C, b) 1LEL-pNIPAM and 2LEL-pNIPAM at 20 °C, c) 1LRD-pNIPAM and 2LRD-pNIPAM at 40 °C, d) 1LRD-pNIPAM and 2LRD-pNIPAM at 20 °C, e) 1LXL21-pNIPAM and 2LXL21-pNIPAM at 40 °C, f) 1LXL21-pNIPAM and 2LXL21-pNIPAM at 20 °C.

Table 4.9 Average crossover points (f , G' value) and LVE range limits from (n=3) for 1LEL-pNIPAM, 2LEL-pNIPAM, 1LRD-pNIPAM, 2LRD-pNIPAM, 1LXL21-pNIPAM, and 2LXL21-pNIPAM hydrogels at 40 °C and 20 °C.

Samples	At 40 °C				At 20 °C	
	Crossover point				LVE (f) Hz	LVE (f) Hz
	f Hz	f SD	G' Pa	G' SD		
1LEL-pNIPAM	2.470	4.695	0.904	1.115	0.047	-
2LEL-pNIPAM	43.643	10.785	52.604	1.087	0.053	0.148
1LRD-pNIPAM	0.613	5.735	1.301	2.206	0.021	-
2LRD-pNIPAM	66.348	23.373	238.500	141.134	0.057	0.155
1LXL21-pNIPAM	-	-	-	-	0.055	4.440
2LXL21-pNIPAM	63.256	13.736	210.620	13.301	0.063	2.790

4.2 Clay-pDMAc Characterisation and Rheological Properties

Dimethylacrylamide (DMAc) is one of the most water-soluble, hydrophilic and biocompatible polymers. DMAc-based polymers have attracted increasing interest because of their suitability for several applications [54] and hydrogel-forming property [55] in biomedical fields such as drug-delivery hydrogels and medical diagnostics. Upon polymerisation, pDMAc is soluble in water as well as in various organic solvents allowing a better understanding of the polymer properties. pDMAc is stable against temperature changes and does not exhibit a stimuli-response to temperatures in the range of 0 - 80 °C. [11][56]

4.2.1 Clay-pDMAc Nanocomposites

The (1 % clay)-pDMAc hydrogels are easy to handle and process (Table 4.10), they can be described as highly viscous, free-flowing, elastic, and tacky gels; some were easier to flow than others and some were less tacky than others. The 1_{LEL}-pDMAc hydrogel was a homogeneous and opaque gel. The 1_{LOG}-pDMAc, 1_{LRD}-pDMAc and 1_{LXL21}-pDMAc hydrogels have similar observational properties to the 1_{LEL}-pDMAc. However, the 1_{FN}-pDMAc is a white coloured, less viscous hydrogel than the 1_{LEL}-pDMAc, and the 1_{C_{Na+}}-pDMAc is an off-white hydrogel.

The (2 % clay)-pDMAc were more elastic gels and do not flow without externally applied shear. Samples were dried at room temperature as film in PTFE (Polytetrafluoroethylene) boats to study their behaviour (Table 4.11). The drying process was performed over five days at room temperature, resulting in composites with a clay content of ~10 % and ~20 % by weight.

Table 4.10 General observational properties of (1 % clay)-pDMAc hydrogels upon pouring and poking with a small lab spatula.


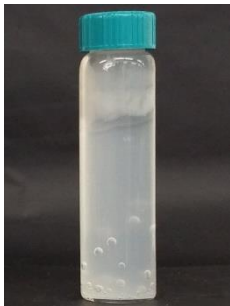





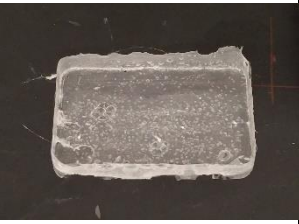

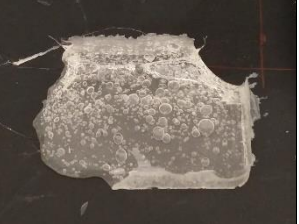








1L_{EL}- pDMAc	1L_{FN}- pDMAc	1L_{OG}- pDMAc	1L_{RD}- pDMAc	1L_{XL21}- pDMAc	1C_{Na+}- pDMAc
Opaque, tacky, highly elastic, highly viscous, and free-flowing gel	White, tacky, highly viscous, and free-flowing gel. Not as homogeneous as the 1L _{EL} -pDMAc and has some trapped air in it.	Opaque, tacky, highly elastic, highly viscous, and free-flowing gel.	Opaque, tacky, highly elastic, highly viscous, and free-flowing gel.	Opaque, tacky, highly elastic, highly viscous, and free-flowing gel.	Off-white, tacky, highly elastic, highly viscous, and free-flowing gel.
					

Table 4.11 pictures of clay-pDMAc nanocomposites after drying in PTFE boats for five days and a summary of observed properties.

1L_{EL}-pDMAc	1L_{FN}-pDMAc	1L_{OG}-pDMAc	1L_{RD}-pDMAc	1L_{XL21}-pDMAc	1C_{Na+}-pDMAc
Need to apply force (spatula) to take out of glass vial, does not take the shape of the container (PTFE boat) by gravity, and spread around with a spatula. Trapped air can be seen in the sample. Still elastic after drying.	A free-flowing gel takes the shape of the container (PTFE boat) by gravity. Trapped air can be seen in the sample. Still elastic after drying.	Need to apply force (spatula) to take out of glass vial, does not take the shape of the container (PTFE boat) by gravity, and spread around with a spatula. Trapped air can be seen in the sample. Still elastic after drying.	Need to apply force (spatula) to take out of glass vial, does not take the shape of the container (PTFE boat) by gravity, and spread around with a spatula. Trapped air can be seen in the sample. Still elastic after drying.	A free-flowing gel takes the shape of the container (PTFE boat) by gravity. Trapped air can be seen in the samples. Still elastic after drying.	A free-flowing gel takes the shape of the container (PTFE boat) by gravity. Trapped air can be seen in the samples. Still elastic after drying.
					
2L_{EL}-pDMAc	2L_{FN}-pDMAc	2L_{OG}-pDMAc	2L_{RD}-pDMAc	2L_{XL21}-pDMAc	2C_{Na+}-pDMAc
Need to apply force (spatula) to take out of glass vial, does not take the shape of the container (PTFE boat) by gravity or by spreading with a spatula. The sample contracts to a lump. Trapped air can be seen in the sample. Still elastic after drying, less elastic than the 1L _{EL} -pDMAc.	A free-flowing gel takes the shape of the container (PTFE boat) by gravity. Trapped air can be seen in the sample. Still elastic after drying, less elastic than the 1L _{FN} -pDMAc.	Need to apply force (spatula) to take out of glass vial, does not take the shape of the container by gravity or by spreading with a spatula, the sample contracts to a lump. Trapped air can be seen in the sample. Still elastic after drying, less elastic than the 1L _{OG} -pDMAc.	Need to apply force (with a spatula) to take out of glass vial, does not take the shape of the container (PTFE boat) by gravity or by spreading with a spatula, the sample contracts to a lump. Trapped air can be seen in the sample. Still elastic after drying, less elastic than the 1L _{RD} -pDMAc.	A free-flowing gel (honey-like consistency) takes the shape of the container (PTFE boat) by gravity. Trapped air can be seen in the sample. Still elastic after drying, less elastic than the 1L _{XL21} -pDMAc.	A free-flowing gel takes the shape of the container (PTFE boat) by gravity. Trapped air can be seen in the sample. Still elastic after drying, less elastic than the 1C _{Na+} -pDMAc.
					

4.2.2 XRD Characterisation of Clay-pDMAc Nanocomposites

The pDMAc homopolymer samples synthesised herein were too elastic to grind or section due to trapped air for appropriate XRD analysis. Figure 4.37 shows the XRD trace of pDMAc obtained from the literature [48] where powder samples were mounted on a sample holder and scanned with a step size of $2\theta = 0.02^\circ$ between $2\theta = 5^\circ$ and 50° . The absence of reflections in the XRD trace of pDMAc shows that it is predominantly non-crystalline. [57]

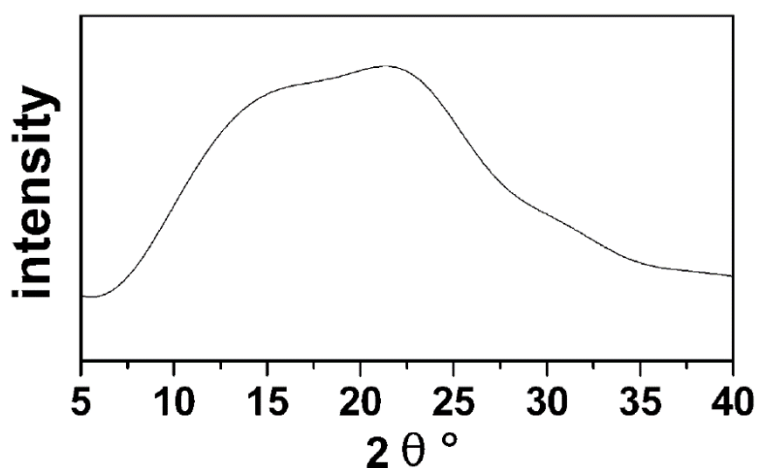


Figure 4.37 XRD trace of pDMAc from [58].

The same issue was presented when trying to characterise the 1L_{EL}-pDMAc, 2L_{EL}-pDMAc and 1L_{XL21}-pDMAc composite samples and no XRD traces were produced from them since they were too elastic to grind and the pieces that could be cut to size contained a lot of air bubbles trapped in the composite, that is why Figure 4.38 (a) is not presented. However, its slot was left empty to allow consistency in labelling and ease of comparison between clay diffraction traces from different polymers.

Figure 4.38 (b) shows the XRD traces of 1L_{FN}-pDMAc and 2L_{FN}-pDMAc nanocomposites. Towards low angles ($\leq 5^\circ$) the XRD traces of L_{FN}-pDMAc composites show an increasing baseline, which indicates that the clay platelets are very well dispersed, if not exfoliated. [25] The reflection at around $2\theta = 10.9^\circ$ ($d = 8.1 \text{ \AA}$) in the traces of the composites corresponds to the polymer as no reflection

in this area can be attributed to clay. The reflection at $2\theta = 21.0^\circ$ also is attributed to the polymer. The XRD trace obtained from the literature (Figure 4.34) of the pDMAc is different to those in the composites, which may be an influence of the clay on its morphology, however, broad reflections are observed in both. A comparison between the $1L_{FN}$ -pDMAc and $2L_{FN}$ -pDMAc composites show that the intensities for the reflections around $2\theta = 10.7^\circ$ are less for the $2L_{FN}$ -pDMAc composite as it contains less pDMAc. [34]

At $2\theta = 21.9^\circ$ ($d = 4.1 \text{ \AA}$) the XRD trace of the $1L_{FN}$ -pDMAc composite show a reflection mostly corresponds to the pDMAc within the composite, this is the clearest reflection in the composite XRD traces of both L_{FN} -pDMAc nanocomposites. It also of higher intensity in the XRD trace of the $1L_{FN}$ -pDMAc composite as a result of more pDMAc being contained in the $1L_{FN}$ -pDMAc. It is not possible to observe the L_{FN} diffraction reflection at $2\theta = 19.4^\circ$ ($d = 4.6 \text{ \AA}$) because of the high intensity of the polymer reflection in this area. However, the reflection in the XRD trace L_{FN} at $2\theta = 34.9^\circ$ ($d = 2.6 \text{ \AA}$) was observed in the XRD traces of $1L_{FN}$ -pDMAc and $2L_{FN}$ -pDMAc [6][8] providing evidence of clay in them (the reflection at $2\theta = 34.8^\circ$ ($d = 2.6 \text{ \AA}$) corresponds to the d_{110} in L_{FN}). Evidence for the presence of clay in the composite is important because an absence of a reflection in the region where clay reflections are anticipated (as is the case here) can be due to very poor mixing of the clay and no clay being present in the sampling area of the XRD experiment. Moreover, the absence of a reflection in the clay area (i.e. lower than $2\theta = 6^\circ$) in these composites further provide strong evidence that the clay is very well dispersed, if not exfoliated. Note that for the pNIPAM samples, a clear distinction was not possible due to the overlapping polymer reflection.

Other clay-pDMAc nanocomposites have similar traces, some differences were also observed as a function of the clay type used. Figure 4.38 (c) shows the XRD traces for the L_{OG} , $1L_{OG}$ -pNIPAM, and $2L_{OG}$ -pNIPAM. The XRD traces of these nanocomposites do not show a lot of clay corresponding details as they are mainly dominated by the pDMAc reflections. The XRD trace of $2L_{OG}$ -pDMAc does show a reflection at $2\theta = 8.9^\circ$ ($d = 10.0 \text{ \AA}$), which may be a result of collapsed clay (i.e.

dehydrated clay), but its position is believed to be at a too-high angle; it could also possibly be due to a change in the morphology of the polymer. Despite this uncertainty, the absence of any strong clay reflections and the increasing baseline towards lower angles strongly suggest the clay is very well dispersed.

Figure 4.38 (d) compares the XRD traces for L_{RD} to dried $1L_{RD}$ -pDMAc and $2L_{RD}$ -pDMAc. The XRD trace of $1L_{RD}$ -pDMAc shows a reflections at $2\theta = 7.2^\circ$ ($d = 12.3 \text{ \AA}$) which could be mainly due to the polymer, however this reflection could also be related to the clay reflection overlapped by the polymer at that region and $2\theta = 20.4^\circ$ ($d = 4.4 \text{ \AA}$) corresponding to the polymer within the composite. Both reflections can be observed in the $2L_{RD}$ -pDMAc trace with lower intensities and a slight shift to a lower angle $2\theta = 8.6^\circ$ ($d = 10.3 \text{ \AA}$) and $2\theta = 21.7^\circ$ ($d = 4.1 \text{ \AA}$). [8] The presence of the decreasing baseline suggests that clay in both nanocomposites was exfoliated. However the overlapping of the region at around $2\theta = 7^\circ$ also suggest that the clay did not really exfoliate and that the nanocomposite is a microstructure. [22][23][24]

The XRD trace of the $2L_{XL21}$ -pDMAc is presented in Figure 4.36 (e) along with the L_{XL21} trace. The decreasing baseline at $2\theta \geq 5^\circ$ suggests that clay in both nanocomposites was exfoliated. [24][23] The reflections at $2\theta = 8.6^\circ$ ($d = 10.3 \text{ \AA}$) and $2\theta = 20.8^\circ$ ($d = 4.3 \text{ \AA}$) correspond to the polymer within the composite and the reflection at $2\theta = 34.5^\circ$ ($d = 2.6 \text{ \AA}$) correspond to the clay. [26][59]

The XRD traces of C_{Na^+} and $1C_{Na^+}$ -pDMAc (Figure 4.38 (f)) show similar behaviour to the XRD trace of $1L_{FN}$ -pDMAc nanocomposite. As towards $2\theta \leq 5^\circ$ the XRD trace shows an increasing baseline, which indicates that the clay platelets are very well dispersed, if not exfoliated. [60] However, a sharp reflection was observed at $2\theta = 19.8^\circ$ ($d = 4.5 \text{ \AA}$) which correspond to the crystalline structure within a clay platelet. Table 4.12 summaries the reflection positions for all clay-pDMAc composites.

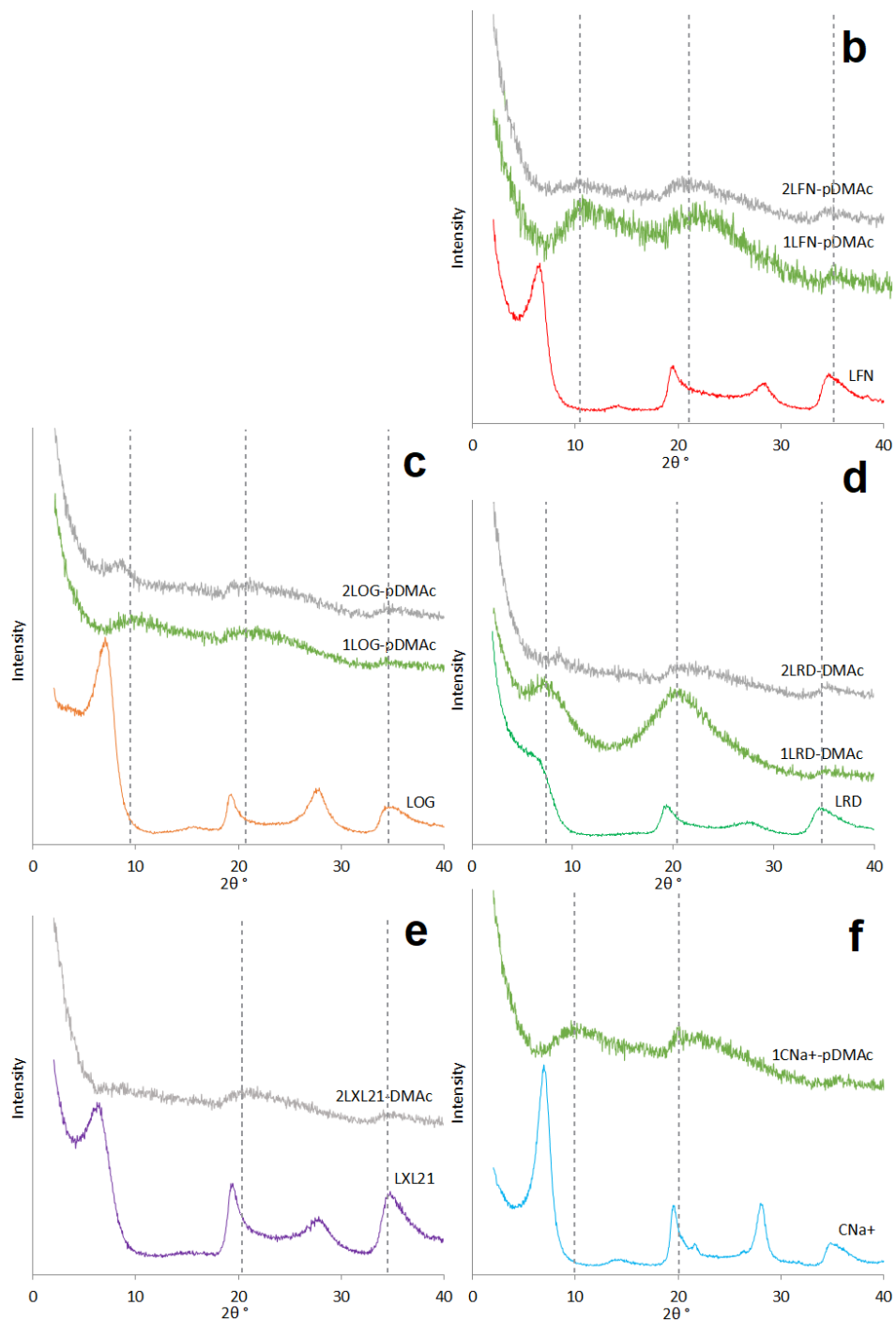


Figure 4.38 XRD traces for clay and dried clay-pDMAc nanocomposites showing the effect of different clay types on the clay-pDMAc composites. a) LEL-pDMAc XRD could not be obtained, its spot left empty to allow consistency in labelling and ease of comparison between clay diffraction traces from different polymers b) LFN, 1LFN-pDMAc and 2LFN-pDMAc c) LOG, 1LOG-pDMAc and 2LOG-pDMAc d) LRD, 1LRD-pDMAc, and 2LRD-pDMAc. 1LRD-pDMAc reflection at $2\theta = 7.2^\circ$ ($d = 12.3 \text{ \AA}$) from the polymer, however, this could also be due to the clay reflection overlapped by the polymer at that region and $2\theta = 20.4^\circ$ ($d = 4.4 \text{ \AA}$). Both reflections can be observed in the 2LRD-pDMAc trace with a slight shift to a lower angle $2\theta = 8.6^\circ$ ($d = 10.3 \text{ \AA}$) and $2\theta = 21.7^\circ$ ($d = 4.1 \text{ \AA}$). [6] The decreasing baseline suggests clay was exfoliated in both composites. However, the overlapping of the region $2\theta = 7^\circ$ also suggest that the clay did not really exfoliate but it is a microstructure. e) LXL21 and 2LXL21-pDMAc f) CNa+ and 1CNa+-pDMAc. All samples are ground powders and offset for clearance.

Table 4.12 Interplanar distances and 2θ of powder clay types and its corresponding clay-pDMAc nanocomposites samples obtained from XRD data.

Sample	d_{001}		d_{100}		d_{110}	
	2θ °	d (Å)	2θ °	d (Å)	2θ °	d (Å)
L_{FN}	6.6	13.3	19.4	4.6	34.9	2.6
1L_{FN}-pDMAc	10.9	8.1	21.9	4.1	34.8	2.6
2L_{FN}-pDMAc	10.4	8.5	21.2	4.3	34.8	2.6
L_{OG}	7.1	12.4	19.1	4.6	34.6	2.6
1L_{OG}-pDMAc	10.5	8.4	21.8	4.1	34.5	2.6
2L_{OG}-pDMAc	8.9	10.0	21.2	4.2	34.5	2.6
L_{RD}	6.5	13.6	19.4	4.6	34.6	2.6
1L_{RD}-pDMAc	7.2	12.3	20.4	4.4	34.5	2.6
2L_{RD}-pDMAc	8.6	10.3	21.7	4.1	34.6	2.6
L_{XL21}	6.4	13.8	19.3	4.6	34.7	2.6
2L_{XL21}-pDMAc	8.6	10.3	20.8	4.3	34.5	2.6
C_{Na+}	7.0	12.6	19.5	4.6	34.7	2.6
1C_{Na+}-pDMAc	9.5	9.3	21.5	4.1	34.9	2.6
			19.8	4.5		

In summary, there is a lack of any clay d_{001} reflection in the traces of clay-pDMAc composites and the increasing baseline towards angles less than 5° indicate the clay is very well dispersed in the composite matrix. [27][28][58]

4.2.3 TGA Characterisation of Clay-pDMAc Nanocomposites

Samples were analysed using the methods outlined in Section 2.1.3. TGA curves showing the weight loss of the dried pDMAc homopolymer and (1 % clay)-pDMAc nanocomposites as a function of temperature are shown in Figure 4.39. Three main weight loss stages were observed which correspond to evaporation of free water and the structural decomposition of the polymers.

“Stage 1” of weight loss takes place between $25 - 175^\circ\text{C}$, which is due to evaporation of the free water. The (1 % clay)-pDMAc nanocomposites have more weight loss up to 170°C when compared to the pDMAc homopolymer where weight loss is mainly due to water evaporation, max weight loss in “Stage 1” was correlated to 1L_{FN}-pDMAc composite (6.51 %).

“Stage 2” of weight loss takes place between $175 - 475^\circ\text{C}$, this stage involves mainly polymer degradation and some dehydroxylation. “Stage 2” also includes the

polymer degradation onset temperature of the nanocomposites, Figure 4.39 shows clearly that the onset of the polymer degradation temperature decreases for the clay-pDMAc nanocomposites when compared to the pDMAc homopolymer. [30][20] The maximum weight loss in “Stage 2” within the polymer clay nanocomposites was observed for 1L_{XL21}-pDMAc composite with 71.72 %. At “Stage 2” the clay-pDMAc composites weight loss decreased more when compared to the weight loss of the pDMAc homopolymer due to the addition of clay to the nanocomposite. [29]

The pDMAc curve shows an error between “Stage 2” and “Stage 3”, this due to a small glitch in the sample data collection, however, it does not significantly contribute to the overall profile of the curve.

“Stage 3” of weight loss takes place between 475 - 800 °C, which includes further degradation of polymer residues to yield carbon and hydrocarbons. [19] At “Stage 3” 1L_{EL}-pDMAc had the maximum mass loss of 19.48 %. [31]

After approximately 800 °C mainly the inorganic residues remain with the potential for some carbonaceous char and the curves become flat. [28]

The thermal analysis results of pDMAc and its corresponding clay nanocomposites are summarized in Table 4.13. The characteristic parameters selected were the main three weight loss stages and the degradation temperature (onset temperature). The data show that some composites lose more weight than others depending on the properties of the clay used as a crosslinking agent.

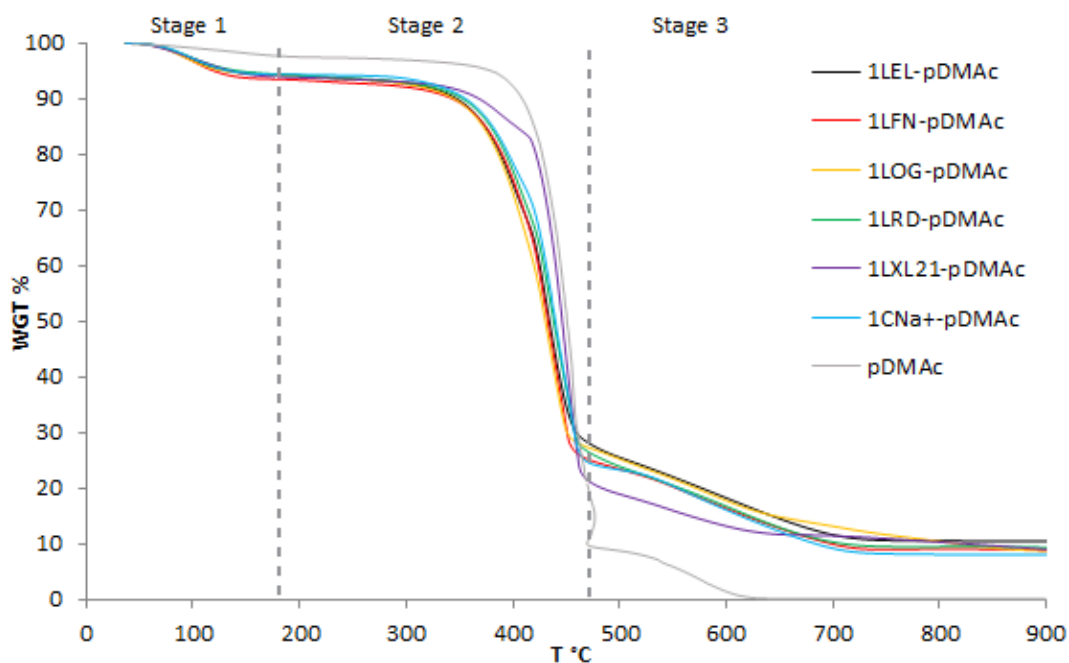


Figure 4.39 TGA thermograms of pDMAc and (1 % clay)-pDMAc nanocomposites. Indicating the main three stages of weight loss. Stage 1 (25 – 175 °C), Stage 2 (175 – 475 °C), and Stage 3 (475 – 800 °C).

Figure 4.40 shows the TGA weight loss curves of pDMAc compared to 2_{LEL}-pDMAc, 2_{LFN}-pDMAc, 2_{LOG}-pDMAc, 2_{LRD}-pDMAc, 2_{XL21}-pDMAc and 2_{CNa+}-pDMAc. The (2 % clay)-pDMAc behaviour is similar to the (1 % clay)-pDMAc; three stages of weight loss and onset temperatures lower than that of the pDMAc homopolymer but with less total weight loss as the (2 % clay)-pDMAc have more clay. By looking at the end of “Stage 2” where most of the weight loss happens, 2_{LEL}-pDMAc loses more weight than other nanocomposites. [61] The decrease of polymer onset degradation temperatures during “Stage 2” suggests that the presence of clay facilitate the degradation of the clay-pDMAc nanocomposites.

The 2_{LEL}-pDMAc had the highest degradation onset temperature (412 °C) during “Stage 2”, and also happened to lose more weight (67.84 %) during stage 2 than all other (2 % clay)-pDMAc nanocomposites (51 % - 67 %). This shows that L_{EL} had the least effect on the polymer degradation mechanism as it did not activate the early degradation of the polymer and produced the least amount of carbonaceous char up to 450 °C. The other 2% composites had very similar onset degradation temperatures in this region suggesting a similar effect on polymer degradation activation. The 2_{LRD}-pDMAc had a significantly lower weight loss than all other

composites and shows the enhanced ability of this clay to produce carbonaceous char.

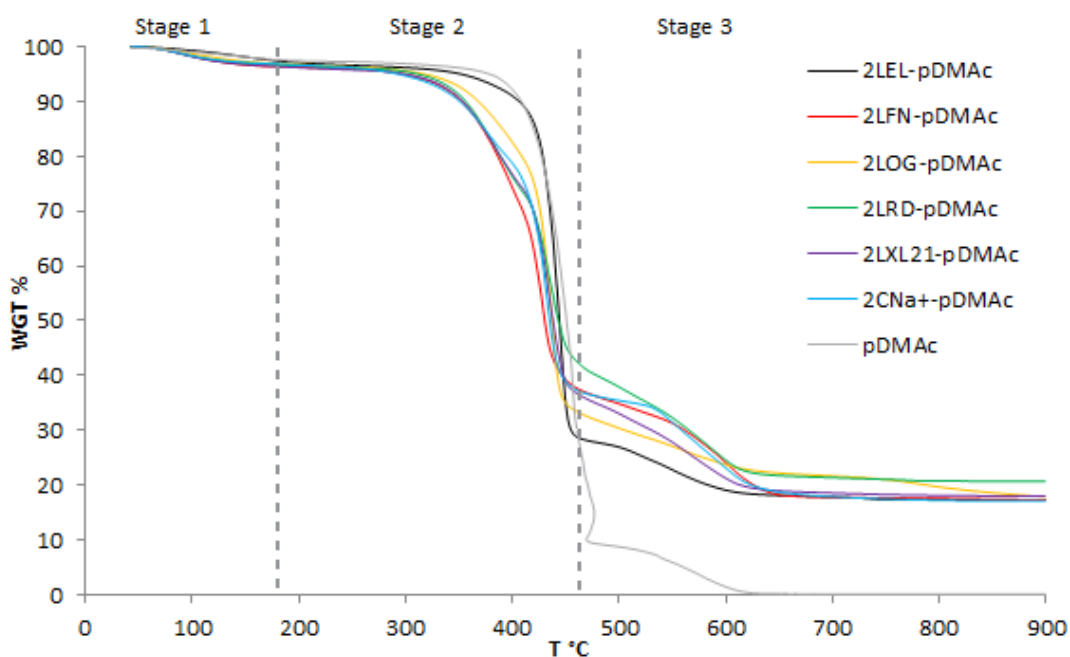


Figure 4.40 TGA thermograms of pDMAc and (2 % clay)-pDMAc nanocomposites. Indicating the three main stages of weight loss. Stage 1 (25 – 175 °C), Stage 2 (175 – 475 °C), and Stage 3 (475 – 800 °C).

Figure 4.41 shows comparisons between the same clay-pDMAc nanocomposites at two different clay-to-polymer ratios. With the higher amounts of clay in the 2LEL-pDMAc, 2LOG-pDMAc and nanocomposites higher onset temperatures in “Stage 2” region are observed when compared to their corresponding (1 % clay)-pDMAc composites (Figure 4.41 a and c). On the other hand, the 2LFN-pDMAc, 2LRD-pDMAc, 2LXL21-pDMAc and 2CNa+-pDMAc nanocomposites have lower onset temperatures when compared to their (1 % clay)-pDMAc nanocomposites (Figure 4.41 b, c, e and f). The reason for this behaviour is currently uncertain but does correlate to the clay platelet size as the second set of (2 % clay)-pDMAc nanocomposites have a higher range of clay platelet size. The remaining weight % of the composite at 900 °C is the clay within the composite and the carbonaceous char.

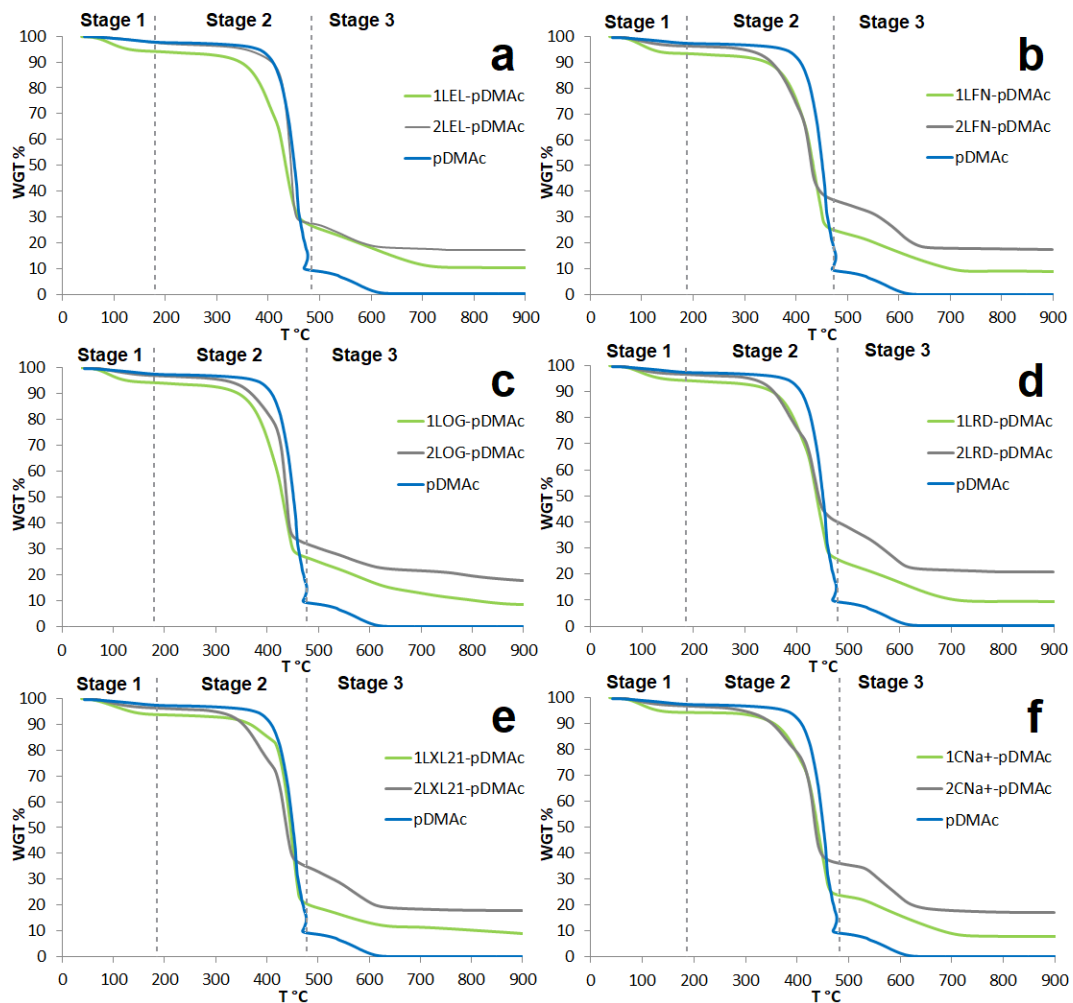


Figure 4.41 TGA thermograms of pDMAc compared to a) 1LEL-pDMAc and 2LEL-pDMAc, b) 1LFN-pDMAc and 2LFN-pDMAc, c) 1LOG-pDMAc and 2LOG-pDMAc, d) 1LRD-pDMAc and 2LRD-pDMAc, e) 1LXL21-pDMAc and 2LXL21-pDMAc, f) 1CNa⁺-pDMAc and 2CNa⁺-pDMAc composites. Indicating the main three stages of weight loss. Stage 1 (25 – 175 °C), Stage 2 (175 – 475 °C), and stage 3 (475 – 800 °C).

The differences in the thermal behaviour of clay-pDMAc nanocomposites, when compared to the pDMAc homopolymer, was due to the presence of the clay within the composites. The thermal stability presented by the onset temperature of the pDMAc degradation was compromised with the presence of clay. [19] The effect of the clay was also observed throughout “Stage 2” as the weight loss was less for the clay-pDMAc composites.

Table 4.13 TGA of pDMAc homopolymer and its (1 % clay)-pDMAc and (2 % clay)-pDMAc composites, showing weight loss % at each stage, total weight loss % and onset temperature.

Samples	Stage1: 25–200 °C	Stage2: 175–450 °C	Stage3: 450–800 °C	Total weight loss %	Onset Temp. °C
	Weight loss %				
1L _{EL} -pDMAc	5.70	64.40	19.48	89.57	350
2L _{EL} -pDMAc	2.46	67.84	12.38	82.69	412
1L _{FN} -pDMAc	6.51	67.65	17.01	91.17	362
2L _{FN} -pDMAc	6.58	53.50	22.65	82.73	351
1L _{OG} -pDMAc	5.75	65.32	20.19	91.27	363
2L _{OG} -pDMAc	3.02	61.77	17.34	82.13	351
1L _{RD} -pDMAc	5.59	66.88	18.17	90.64	358
2L _{RD} -pDMAc	3.22	51.76	24.33	79.32	335
1L _{XL21} -pDMAc	6.07	71.72	13.26	91.05	354
2L _{XL21} -pDMAc	3.55	58.54	19.94	82.03	338
1C _{Na+} -pDMAc	5.66	69.06	17.27	91.99	352
2C _{Na+} -pDMAc	3.11	58.02	21.76	82.90	331
pDMAc	2.31	87.74	9.83	99.88	393

The TGA analysis for the pNIPAM, pDMAc, clay-pNIPAM and clay-pDMAc nanocomposites appears to have similar stages of weight loss starting at approximately 20 °C and ending at 800 °C, which corresponds to the evaporation of physically adsorbed water from solvents and moisture [61][29] followed by the structural decomposition of the polymers. [62] However, the pDMAc homopolymer and clay-pDMAc have higher thermal stability than that of pNIPAM and clay-pNIPAM as an influence on the pDMAc increased thermal stability.[18]

The nanocomposites TGA curves show less weight loss during “Stage 2” for both pNIPAM and pDMAc upon the addition of clay. The best thermal stability can be attributed to the L_{RD} corresponding nanocomposites, preventing out-diffusion of the volatile decomposition products and the creation of more carbonaceous char. L_{RD} has the smallest particle size which would theoretically lead to a faster diffusion mechanism than those with larger platelet sized clays; other factors must therefore also be considered such as how the clay platelets are spatially arranged and their surface chemistry. [63]

4.2.4 SEM morphology observation of clay-pDMAc nanocomposite

The SEM images of nanocomposites at 100 μm in Figure 4.42 shows a general overview of the similarities and differences between the six different (1 % clay)-pDMAc composites. The images show porous micro-scaled structures. The porosity is clear for all (1 % clay)-pDMAc, even for the 1C_{Na+}-pDMAc nanocomposite, which did not show a clear interconnected porous structure when used a C_{Na+} was used as a crosslinker for 1C_{Na+}-pNIPAM nanocomposite earlier in this chapter. [19][34]

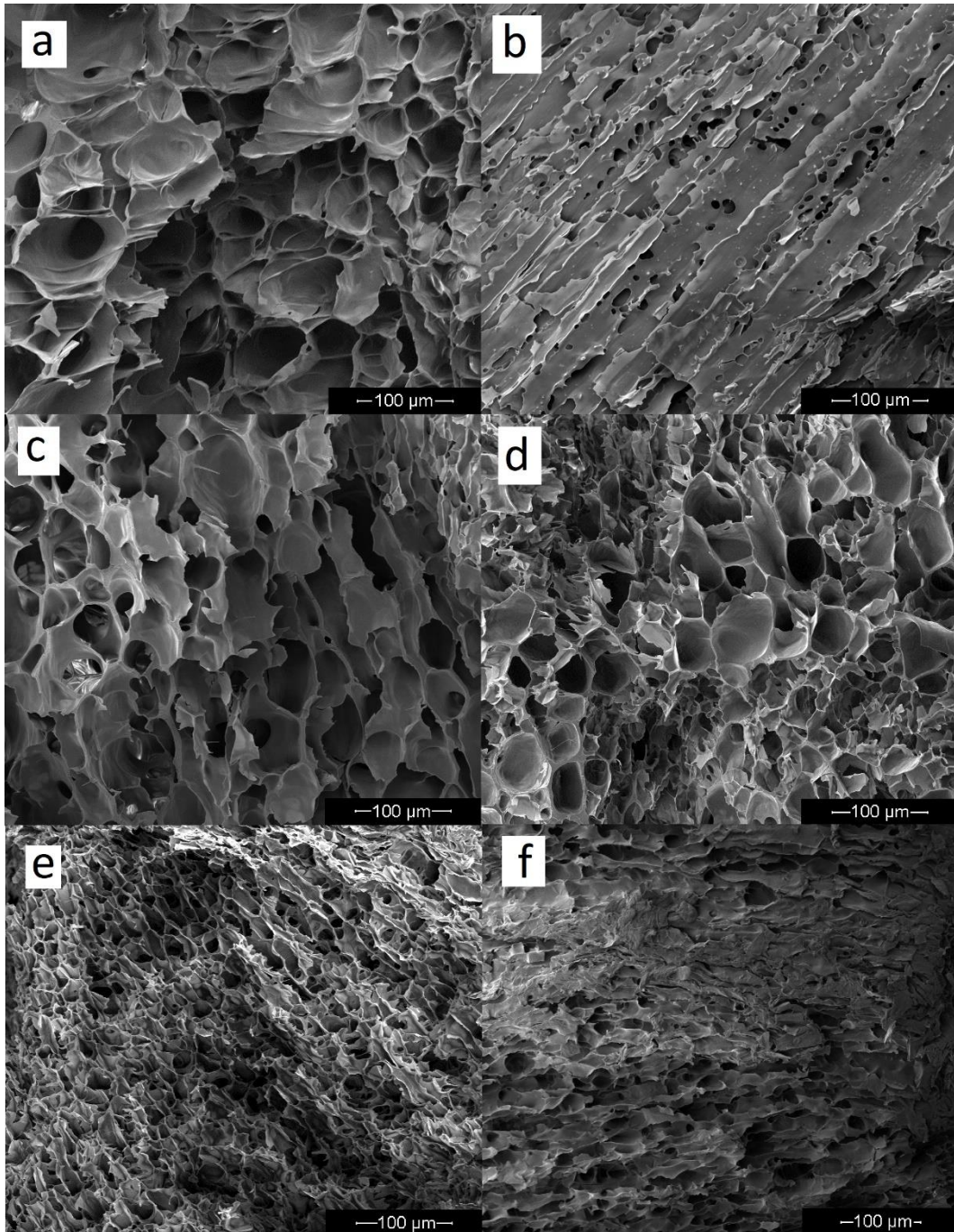


Figure 4.42 SEM images of 1clay-pDMAc nanocomposite on scale bar 100 μm showing microstructure and pore size differences as a result of the effect of clay grade used. a) 1LEL-pDMAc, b) 1LFN-pDMAc, c) 1LOG-pDMAc, d) 1LRD-pDMAc, e) 1LXL21-pDMAc, f) 1CNa+-pDMAc.

The 1LEL-pDMAc composite SEM images (Figure 4.42 a, Figure 4.43 a) show a wide porous, high-density microstructure, with thin well-defined walls. The pore size was on average 38.7 μm which is considered large when compared to other (1 % clay)-pDMAc nanocomposites. 1LOG-pDMAc (Figure 4.42 c, Figure 4.43 c) and 1LRD-pDMAc (Figure 4.42 d, Figure 4.43 d) have similar structures, however, the pore sizes were

different (average of 40.7 μm and 40.9 μm , respectively) as the L_{OG} and L_{RD} have different properties when compared to the L_{EL} . The average pore size and standard deviations are shown in Table 4.14.

The $1L_{FN}$ -pDMAc composite (Figure 4.42 b, Figure 4.43 b) show flake-like interconnected layered structure and smoother morphology than the $1L_{EL}$ -pDMAc. Pore size was on average 7.2 μm and is the smallest in the (1 % clay)-pDMAc group.

The $1L_{XL21}$ -pDMAc nanocomposite (Figure 4.42 e, Figure 4.43 e) show a different morphology and a significantly smaller pore size (average 14.1 μm) when compared to the $1L_{EL}$ -pDMAc, $1L_{OG}$ -pDMAc and $1L_{RD}$ -pDMAc, it also has higher porosity, which can be related to its high CEC and its effect on the crosslinking ability of L_{XL21} . (Figure 4.42 f, Figure 4.43 f) show that the porous morphology of $1C_{Na^+}$ -pDMAc composite is similar to the $1L_{XL21}$ -pDMAc with an average pore size of 16.6 μm .

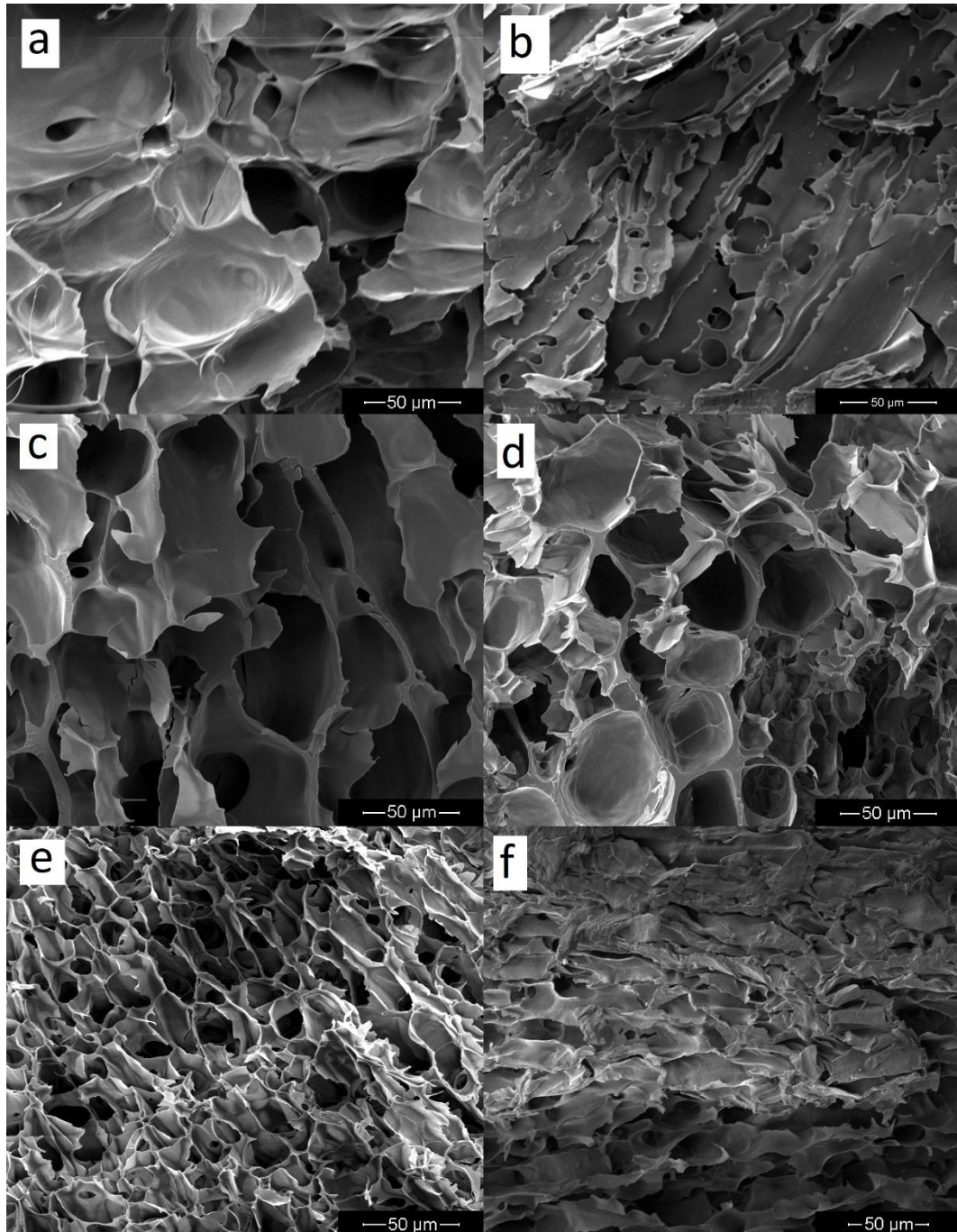


Figure 4.43 SEM images of (1 % clay)-pDMAc nanocomposite on scale bar 50 μm showing more detailed microstructure and pore size differences as a result of the effect of clay type used. a) 1LEL-pDMAc, b) 1LFN-pDMAc, c) 1LOG-pDMAc, d) 1LRD-pDMAc, e) 1LXL21-pDMAc, f) 1CNa+-pDMAc.

From the SEM images of the (2 % clay)-pDMAc composites, (Figure 4.44) it is clear that with the increase of the clay content the composites morphologies became more compact with a less porous structure. The morphological differences are mostly because of more crosslinking agent interacting with less pDMAc chains in the composites at different clay-to-polymer ratios. [31][34]

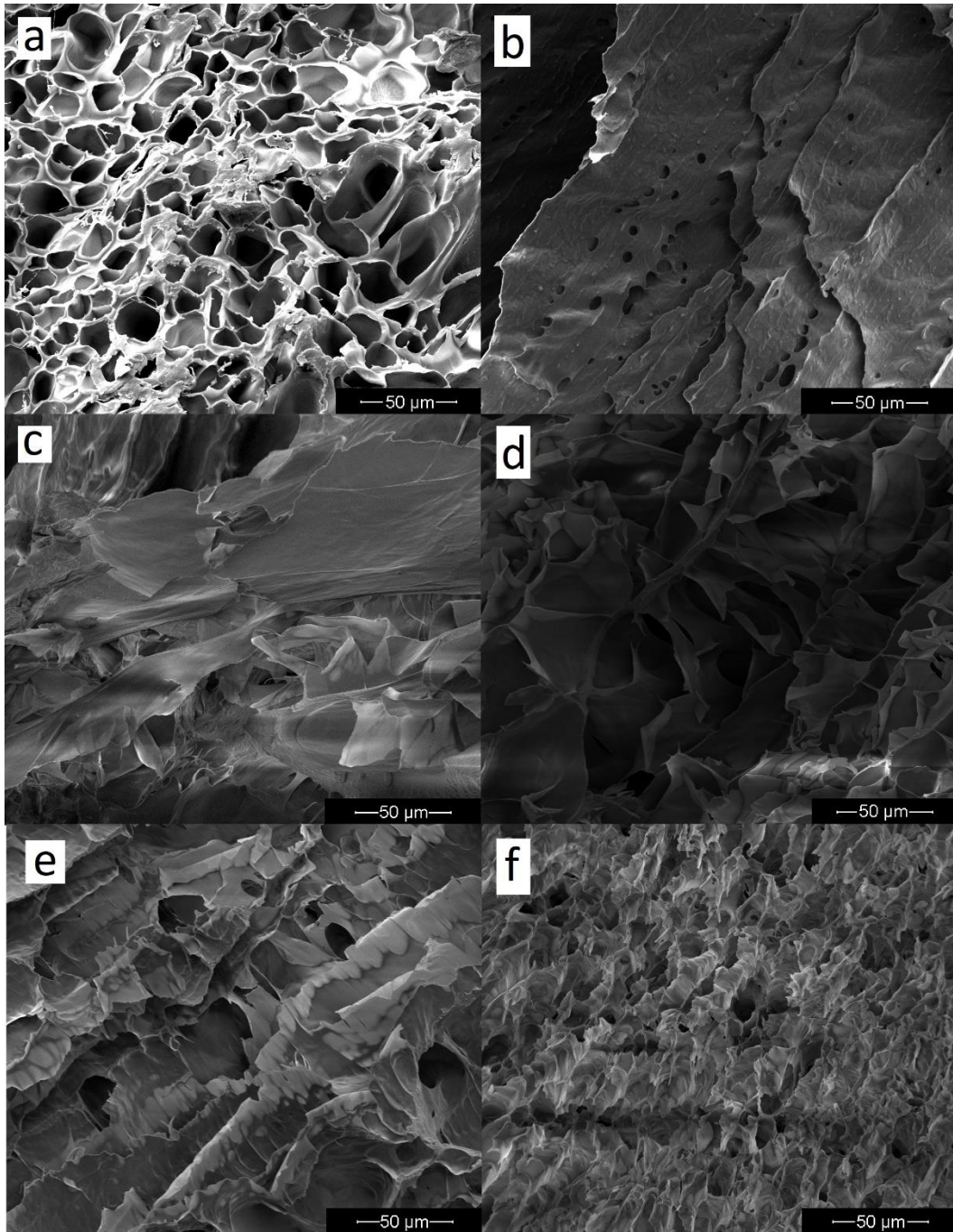


Figure 4.44 SEM images of (2 % clay)-pDMAc nanocomposite on scale bar 50 μm showing more detailed microstructure and pore size differences as a result of the effect of clay type. a) 2LEL-pDMAc, b) 2LFN-pDMAc, c) 2LOG-pDMAc, d) 2LRD-pDMAc, e) 2LXL21-pDMAc, f) 2CNa⁺-pDMAc.

Figure 4.45 shows a comparison between the SEM images of 1L_{EL}-pDMAc and 2L_{EL}-pDMAc nanocomposites. The 2L_{EL}-pDMAc nanocomposite has higher pore density, the sizes of the pores averaged around 18.4 μm with smaller variation in pore size when compared to the 1L_{EL}-pDMAc which show clearly the effect of the clay-to

polymer ratio on the pore sizes and the morphology of the L_{EL}-pDMAc composites. [64]

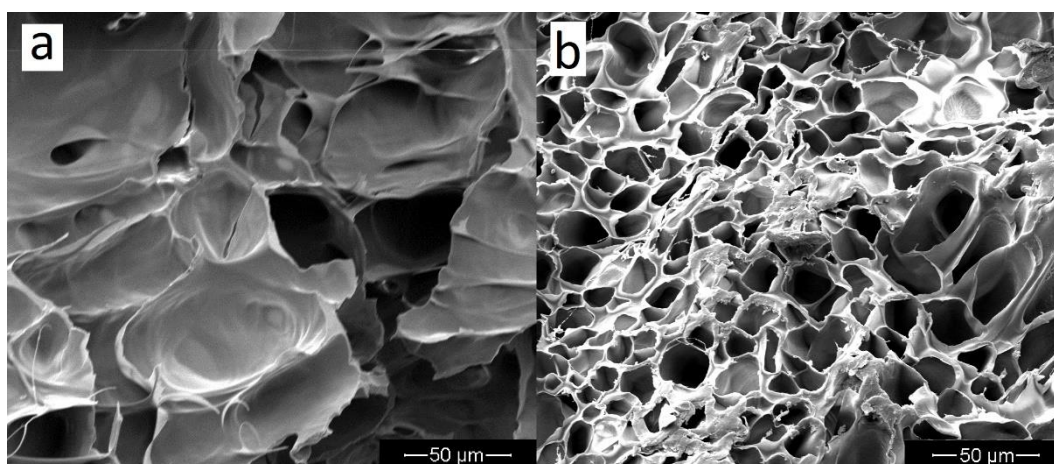


Figure 4.45 SEM images of LEL-pDMAc nanocomposite on scale bar 50 μm . a) 1LEL-pDMAc, b) 2LEL-pDMAc showing the effect of the clay-to-polymer ratio on the pore size and the microstructure.

The 2L_{FN}-pDMAc had a relatively smoother lower pore density when compared to the 1L_{FN}-pDMAc (Figure 4.46) with more defined layers and less flack-like pieces. The structure, in general, is more compact than the 1L_{FN}-pDMAc. Pore size averaged around 6.0 μm which is smaller than pores in the 1L_{FN}-pDMAc (7.2 μm). The 2L_{FN}-pDMAc shows a more uniform distribution of layers within the composite. [64]

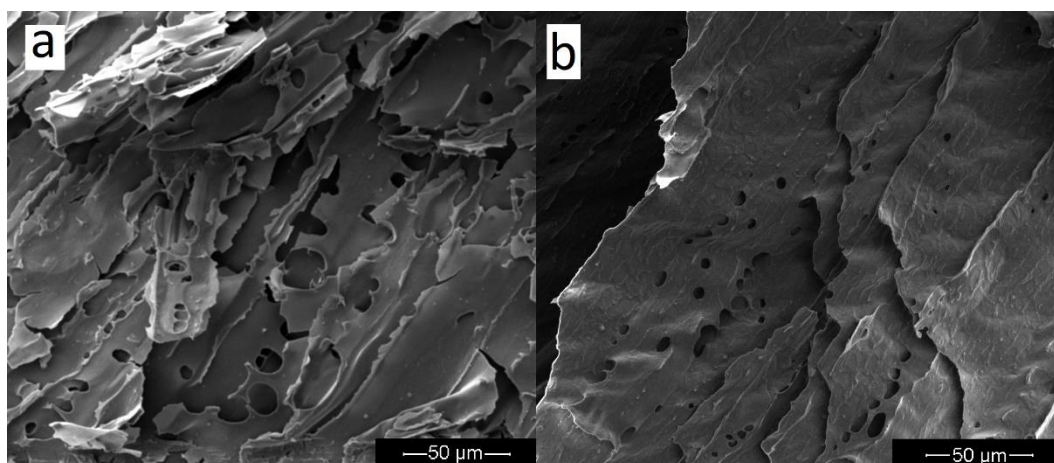


Figure 4.46 SEM images of LFN-pDMAc nanocomposite on scale bar 50 μm . a) 1LFN-pDMAc, b) 2LFN-pDMAc showing the effect of the clay-to-polymer ratio on the pore size and the microstructure.

The 1L_{OG}-pDMAc composite (Figure 4.47 a) showed a uniform and porous structure with an average pore size of 40.7 μm . However, as the clay-to-polymer ratio was different in the 2L_{OG}-pDMAc (Figure 4.47 b) a solid rough surface with uneven

distribution of spaces between walls/layers was created. As a result, there were no clear well-constructed pores to measure and compare. [64]

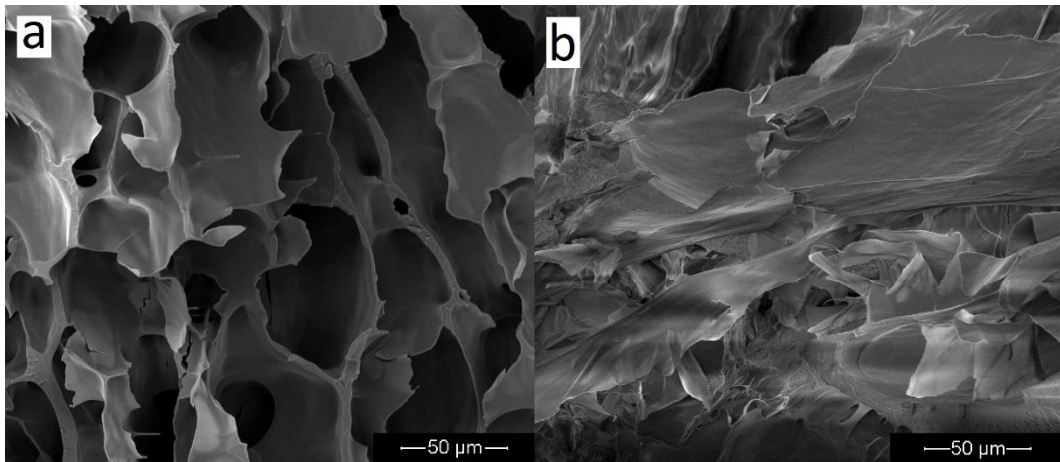


Figure 4.47 SEM images of LOG-pDMAc nanocomposite on scale bar 50 μm. a) 1LOG-pDMAc, b) 2LOG-pDMAc showing the effect of the clay-to-polymer ratio on the pore size and the microstructure.

The SEM images of 1_{LRD}-pDMAc and 2_{LRD}-pDMAc samples are shown in Figure 4.48 (a and b respectively). The structure of 2_{LRD}-pDMAc is porous with pore size averaged around 24.7 μm and has more flack-like texture when compared to the 1_{LRD}-pDMAc.

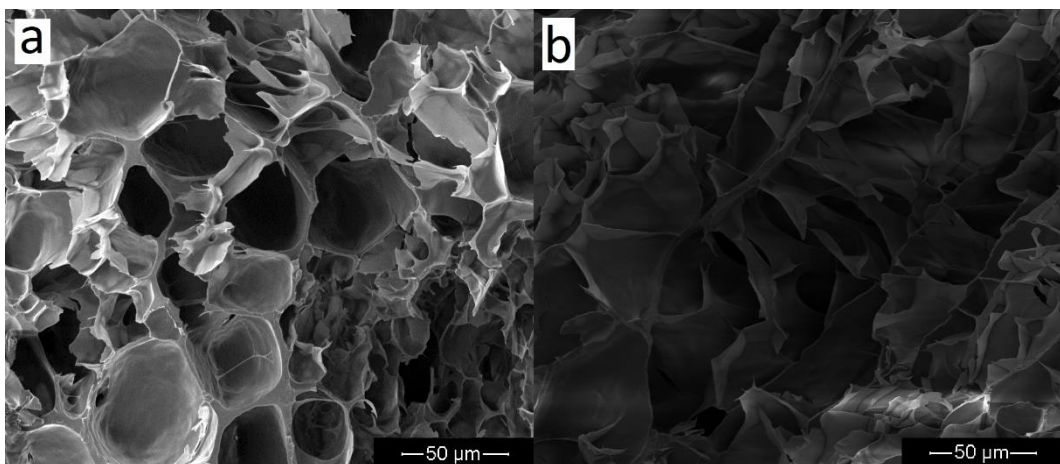


Figure 4.48 SEM images of LRD-pDMAc nanocomposite on scale bar 50 μm. a) 1_{LRD}-pDMAc, b) 2_{LRD}-pDMAc showing the effect of the clay-to-polymer ratio on the pore size and the microstructure.

The SEM images of the L_{XL21}-pDMAc samples at different clay-to-polymer ratio are shown in Figure 4.49. The differences can be observed as the 2_{L_{XL21}}-pDMAc had a relatively smoother less porous structure than the 1_{L_{XL21}}-pDMAc with a more defined layer like structure. Pore size averaged around 22.6 μm.

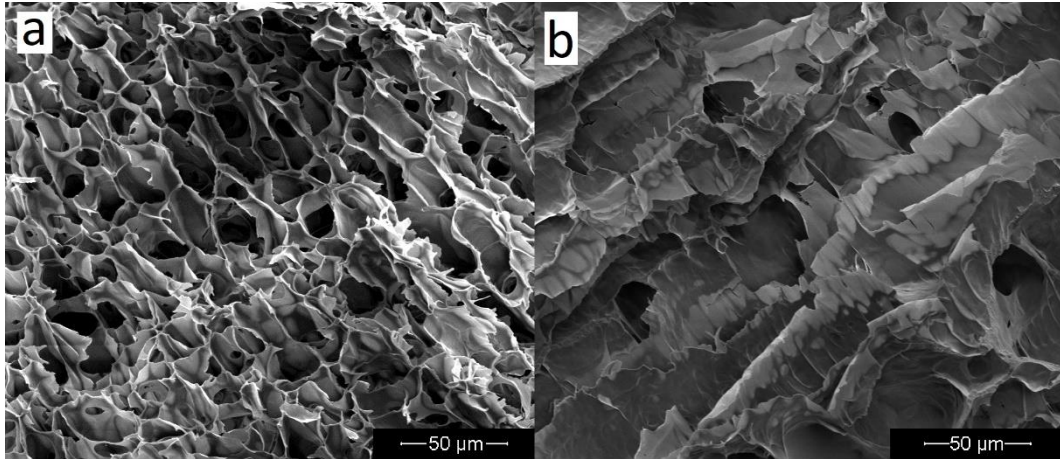


Figure 4.49 SEM images of LXL21-pDMAc nanocomposite on scale bar 50 μm . a) 1LXL21-pDMAc, b) 2L XL21-pDMAc showing the effect of the clay-to-polymer ratio on the pore size and the microstructure.

The morphology and characterization of C_{Na^+} -pDMAc samples at different clay-to-polymer ratio are shown in Figure 4.50. The $2C_{\text{Na}^+}$ -pDMAc structure is still uniform, with lower pore density (Figure 4.50 b) than $1C_{\text{Na}^+}$ -pDMAc. The pore size for the $2C_{\text{Na}^+}$ -pDMAc averaged around 10.6 μm while the average was 16.6 μm for the $1C_{\text{Na}^+}$ -pDMAc. The incorporation of more clay made the composite more uniform and more porous as the sodium hydration in C_{Na^+} causes massive aggregated morphology. [65][66] This means that the $2C_{\text{Na}^+}$ -pDMAc may be able to provide better mechanical properties compared to $1C_{\text{Na}^+}$ -pDMAc.

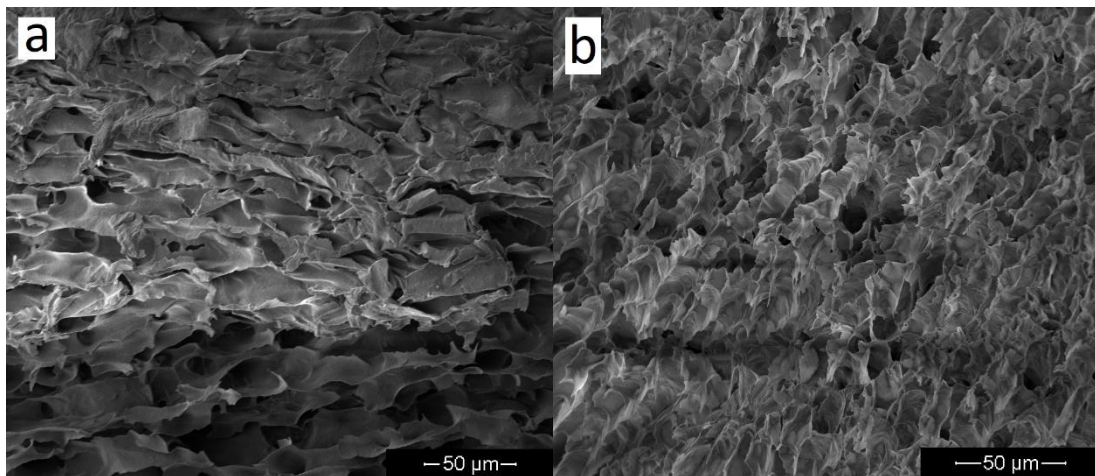


Figure 4.50 SEM images of C_{Na^+} -pDMAc nanocomposite on scale bar 50 μm . a) $1C_{\text{Na}^+}$ -pDMAc, b) $2C_{\text{Na}^+}$ -pDMAc showing the effect of the clay-to-polymer ratio on the pore size and the microstructure.

With higher clay content the clay-polymer nanocomposites are more compact due to more crosslinking agent available. However, looking at the morphology of the

resulting composites it appears that the interaction between the crosslinking agent (clay) and the chain (polymer) depends also on the properties of the clay. The clay effect on the clay-polymer interaction is a complex one depending on both clay particle size and the ECE at the same time.

Table 4.14 Average pore size and standard deviation of (n=25) for clay-pDMAc nanocomposites.

	Pore size (μm)	SD
1L_{EL}-pDMAc	38.7	6.3
2L_{EL}-pDMAc	18.4	3.0
1L_{FN}-pDMAc	7.2	2.6
2L_{FN}-pDMAc	6.0	1.4
1L_{OG}-pDMAc	40.7	6.2
2L_{OG}-pDMAc	28.3	12.0
1L_{RD}-pDMAc	40.9	8.2
2L_{RD}-pDMAc	28.7	7.7
1L_{XL21}-pDMAc	14.1	4.0
2L_{XL21}-pDMAc	22.6	5.2
1C_{Na+}-pDMAc	16.6	5.0
2C_{Na+}-pDMAc	10.6	1.8

Figure 4.51 shows that the smaller platelet size clays have bigger pore size composites showing the dependency on platelet size except for the L_{XL21} (Figure 4.51 a). Depending on the CEC; (Figure 4.51 b) shows that the higher the ECE the smaller the particle size for all clays including the L_{XL21}. The CEC has a bigger effect but still the effect is complex between both properties.

Figure 4.51 also shows that the (1 % clay)-pDMAc composite can be divided into two groups following the same trend as (1 % clay)-pDMAc (Figure 4.19) which suggest that the pore size depends to a certain limit on the clay platelet size.

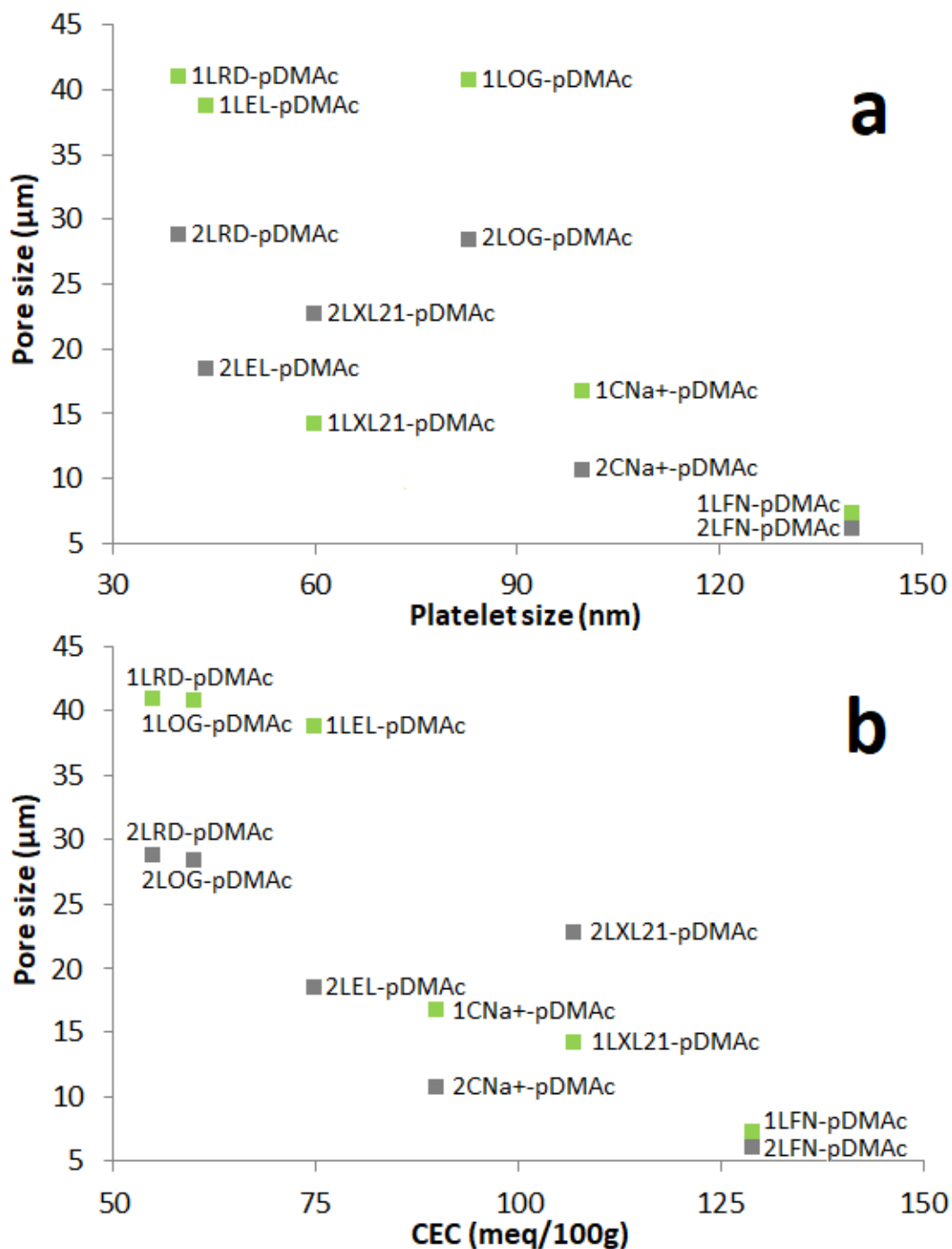


Figure 4.51 a) Platelet size (nm) against pore size (μm) and b) CEC (meq/100g) against pore size (μm) for clay-pDMAc at two clay-to-polymer ratios.

4.2.5 FTIR Spectra Analysis of Clay-pDMAc Nanocomposites

The FTIR spectra of DMAc monomer and dried pDMAc homopolymer at room temperature are shown in Figure 4.52. The DMAc spectrum shows the C=C band at 1615 cm^{-1} which is no longer observed upon polymerisation in pDMAc. A band was found upon DMAc polymerisation around 1620 cm^{-1} (carbonyl group stretching).

pDMAc spectrum shows the main characteristic bands of the pDMAc at 1459, 1435, and 1400 cm^{-1} (C-H bending), 1500 cm^{-1} (C-N stretching), 1620 cm^{-1} (C=O stretching), and 2925, 2855 cm^{-1} (C-H stretching). [17][44][67]

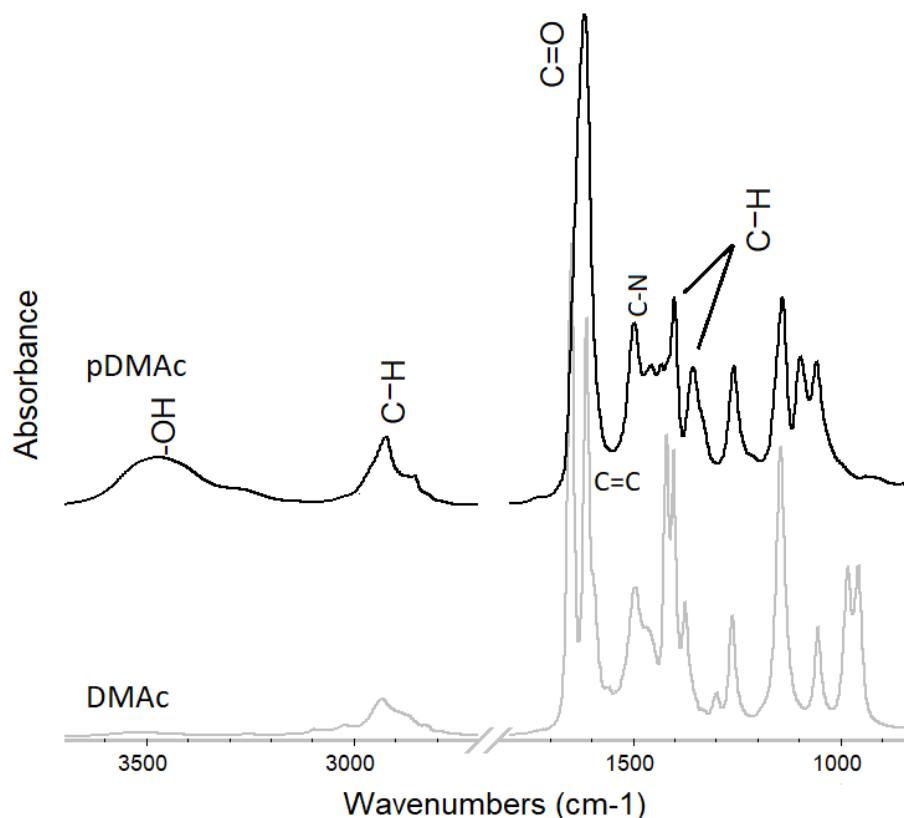


Figure 4.52 FTIR spectra of DMAc monomer and pDMAc homopolymer showing the main characteristic bands. Offset for clearance.

FTIR spectra of the clay, homopolymer pDMAc, and their corresponding dried (1 % clay)-pDMAc and (2 % clay)-pDMAc nanocomposites are presented in Figure 4.53, Figure 4.54 and Figure 4.55. Table 4.15 also provides details about the exact positions of the main bands in each spectrum. The FTIR spectra of the clay-pDMAc nanocomposites exhibit characteristics of both clay and pDMAc.

The FTIR spectra of L_{EL} (Figure 4.53 (a)) show the typical band for the layered silicate (Si-O) bands featured between 1100 cm^{-1} and 1000 cm^{-1} . As the clay platelets are dispersed in the 1L_{EL}-pDMAc nanocomposites the Si-O overlapping spectral features bands can be visualized, which correspond to in-plane and out-of-plane Si-O. The band at 990 cm^{-1} features the in-plane Si-O and the band at $\sim 1058 \text{ cm}^{-1}$ feature the out-of-plane Si-O which gets resolved when the clay is dispersed. A general shift

toward higher frequencies for Si-O bonds in the nanocomposite is observed when comparing the neat clay spectrum to the clay-pDMAc nanocomposite spectrum. [18] The band intensity in the Si-O stretching region increase with increasing clay content as observed from the spectrum of the 2L_{EL}-pDMAc (clay-to-polymer ratio 2:8) and 1L_{EL}-pDMAc (clay-to-polymer ratio 1:9). Vice versa the C=O and N-H bands increase in relative intensity in 1L_{EL}-pNIPAM with increasing polymer content.[18][45]

The 1L_{EL}-pDMAc nanocomposites showed absorption band around 1500 cm⁻¹ corresponding to the C-N in the acrylamide group, the C-N band did not show any significant changes in the L_{EL}-pDMAc composites. The bands at 2930, 2870, 2830 cm⁻¹ for and 1460, 1435, 1400 cm⁻¹ correspond to the C-H within the polymer, which also did not show any significant changes. The characteristic C=O stretching vibration bands exist in DMAc are observed to shift to a slightly higher wavenumber for the 2L_{EL}-pDMAc bands at 1618 cm⁻¹ and a slightly lower wavenumber for 1L_{EL}-pDMAc at 1613 cm⁻¹ for the form 1615 cm⁻¹ for the pDMAc homopolymer. [55][56]

Most of the clay-pDMAc nanocomposites follow the same trend and behave in a very similar manner when different clay types are used as a crosslinker with the pDMAc chains, however, some differences still exist as the clay types have different properties. FTIR spectra of L_{FN}, pDMAc, 1L_{FN}-pDMAc and 2L_{FN}-pDMAc nanocomposites (Figure 4.53 (b)) show absorption bands of the Si-O at 994, 1093 cm⁻¹ and 990, 1089 cm⁻¹ for the 1L_{FN}-pDMAc and the 2L_{FN}-pDMAc respectively. With a general shift to higher frequencies indicating that clay is dispersed in the clay-polymer matrix. [45]

FTIR spectra of L_{OG}, pDMAc, 1L_{OG}-pDMAc and 2L_{OG}-pDMAc nanocomposites are shown in Figure 4.54 (c), the Si-O related bands are positioned at 1072, 992 cm⁻¹ and 1062, 988 cm⁻¹ for 1L_{OG}-pDMAc and 2L_{OG}-pDMAc respectively, these bands positions have shifted to a higher wavenumber from the L_{OG} Si-O 940 cm⁻¹. The FTIR spectra for L_{RD}, pDMAc, 1L_{RD}-pDMAc and 2L_{RD}-pDMAc nanocomposites (Figure 4.54 (d)) show the same behaviour as beforementioned L_{EL}-pDMAc nanocomposites.

Table 4.15 provides details about the Si-O band positions for all L_{RD}-pDMAc composite.

Figure 4.55 shows the FTIR spectra for L_{XL21}, pDMAc, 1L_{XL21}-pDMAc and 2L_{XL21}-pDMAc nanocomposites (Figure 4.55 (e)). A different behaviour was observed on the L_{XL21}-pDMAc nanocomposites at both clay-to-polymer ratios, three different related Si-O bands are present at 1088, 1058, 991 cm⁻¹ and 1076, 1055, 989 cm⁻¹ for 1L_{XL21}-pDMAc and 2L_{XL21}-pDMAc, respectively. This behaviour was not observed with other L_{XL21}-polymer nanocomposites which highlight a different sort of interaction between the L_{XL21} and pDMAc. The L_{XL21}-pDMAc hydrogels are easier to handle and less sticky when compared to other composites with clays that have a platelet size in the same range (e.g. L_{EL}-pDMAc and L_{RD}-pDMAc hydrogels).

The FTIR spectra of C_{Na+}, pDMAc, 1C_{Na+}-pDMAc and 2C_{Na+}-pDMAc nanocomposites are presented in Figure 4.55 (f). The Si-O bands in the spectra of C_{Na+}-pDMAc nanocomposite show different behaviour related to the C_{Na+} and different Si-O band positions at 1076, 1045 cm⁻¹ and 1080, 1031 cm⁻¹ for 1C_{Na+}-pDMAc and 2C_{Na+}-pDMAc, respectively.

Table 4.15 FTIR peaks for clays, pDMAc, (1 % clay)-pDMAc, and (2 % clay)-pDMAc.

Sample	-OH	Si-O		
pDMAc	3477	-	-	-
L _{EL}	3408	-	-	946
1L _{EL} - pDMAc	3456	-	1058	990
2L _{EL} - pDMAc	3489	-	1073	986
L _{FN}	3408	-	-	949
1L _{FN} - pDMAc	3454	-	1056	994
2L _{FN} -pDMAc	3462	-	1058	990
L _{OG}	3407	-	-	940
1L _{OG} -pDMAc	3455	-	1072	992
2L _{OG} -pDMAc	3470	-	1062	988
L _{RD}	3405	-	-	945
1L _{RD} - pDMAc	3453	-	1059	998
2L _{RD} - pDMAc	3464	-	1058	993
L _{XL21}	3417	-	-	942
1L _{XL21} - pDMAc	3439	1088	1058	991
2L _{XL21} - pDMAc	3465	1076	1055	989
C _{Na+}	3418	-	-	912
1C _{Na+} - pDMAc	3457	-	1076	1045
2C _{Na+} -pDMAc	3470	-	1080	1031

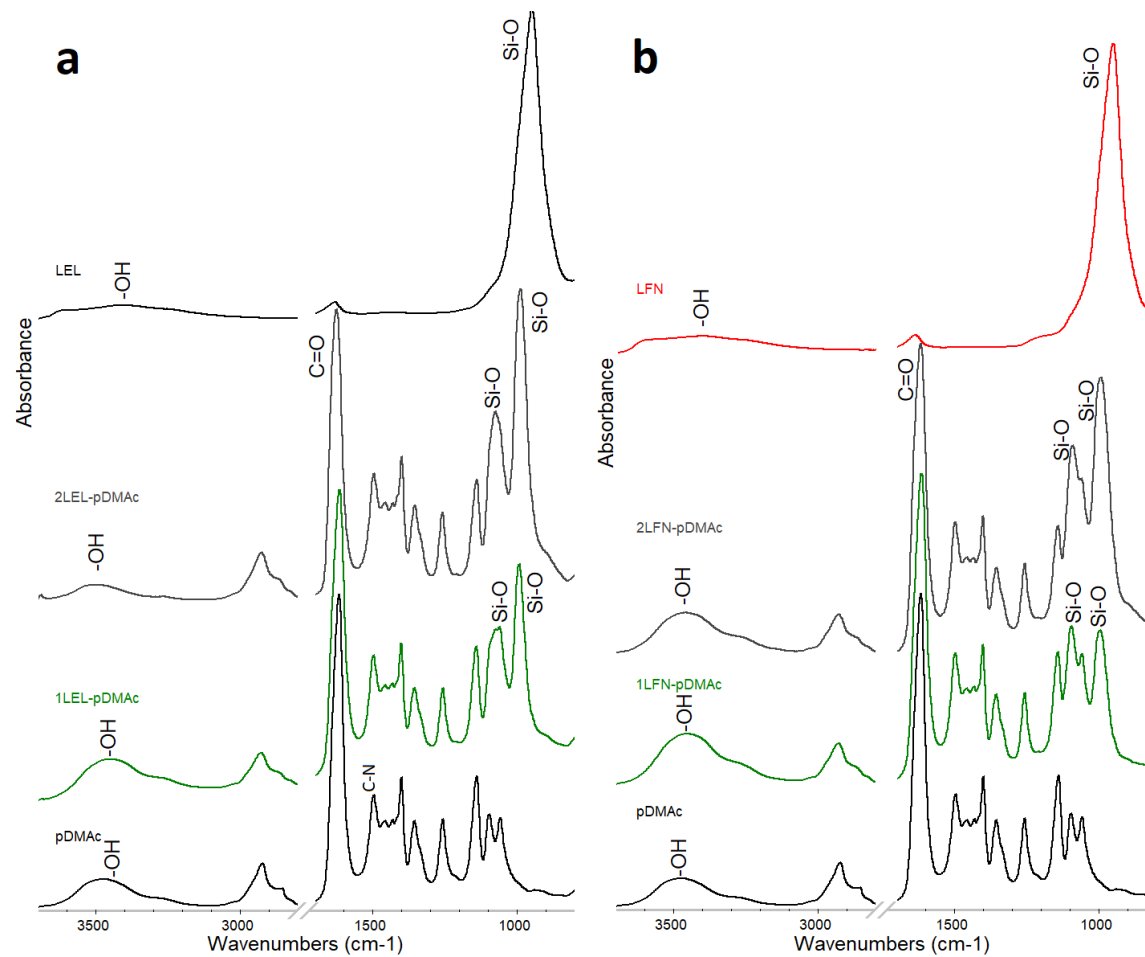


Figure 4.53 FTIR spectra of a) LEL, pDMAc, 1LEL-pDMAc and 2LEL-pDMAc composites. b) LFN, pDMAc, 1LFN-pDMAc and 2LFN-pDMAc composites, indicating major bands positions and offset for clearance.

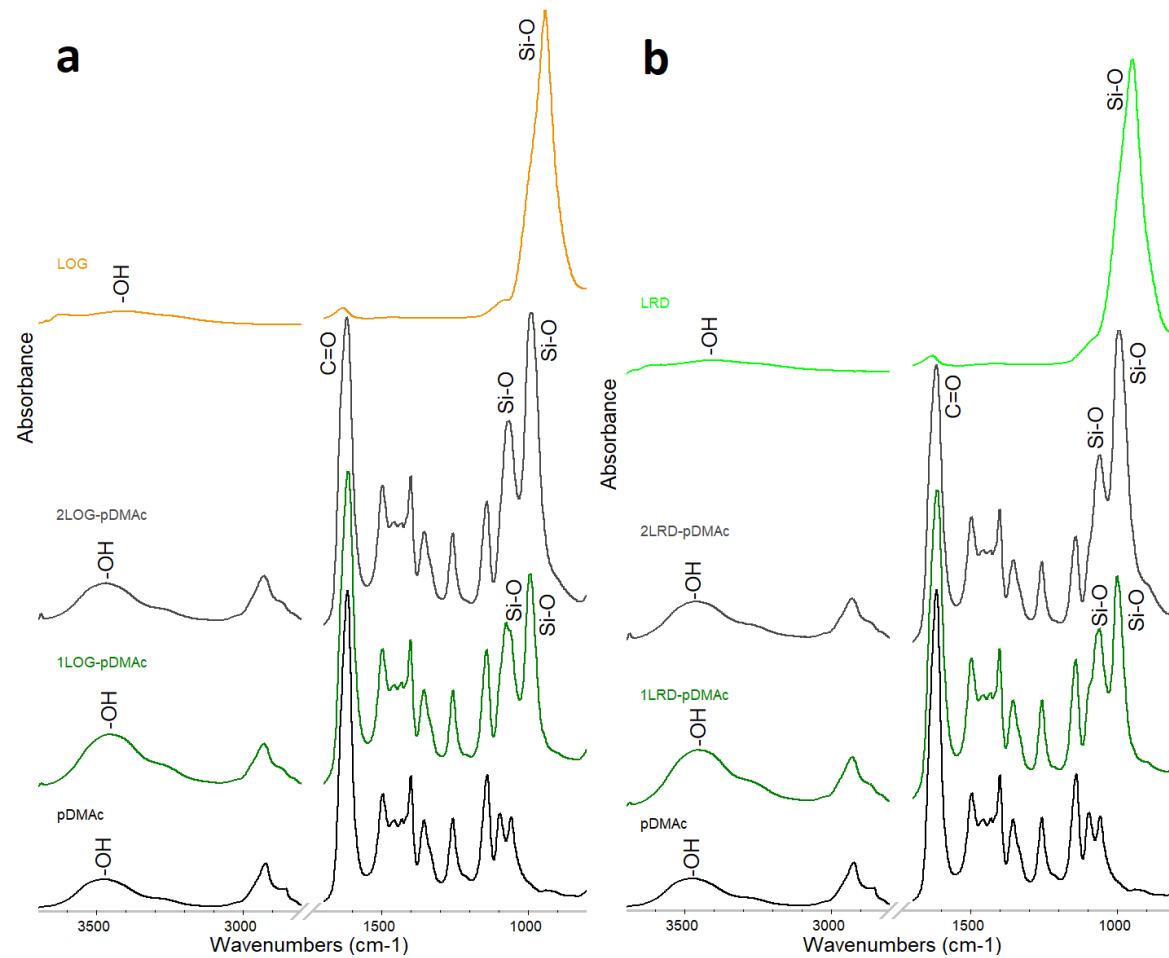


Figure 4.54 FTIR spectra of a) LOG, pDMAc, 1LOG-pDMAc and 2LOG-pDMAc composites. b) LRD, pDMAc, 1LRD-pDMAc and 2LRD-pDMAc composites, indicating major bands positions and offset for clearance.

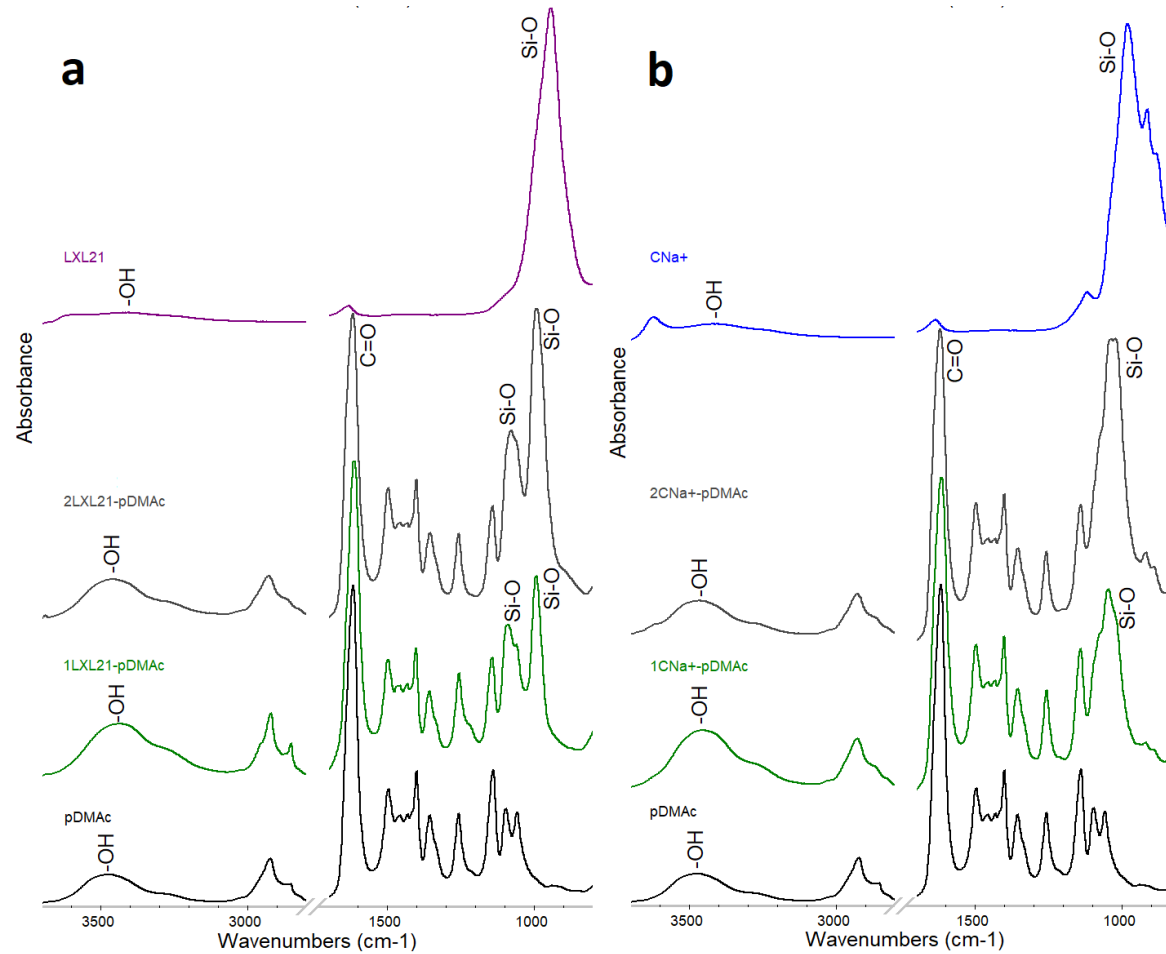


Figure 4.55 FTIR spectra of a) LXL21, pDMAc, 1LXL21-pDMAc and 2LXL21-pDMAc composites. b) CNa+, pDMAc, 1CNa+-pNIPAM, and 2CNa+-pDMAc composites, indicating major bands positions and offset for clearance.

4.2.6 Rheological Analysis and Properties of Clay-pDMAc Hydrogels

Generally, DMAc hydrogels exhibited better mechanical properties when compared to the NIPAM hydrogels. [68] DMAc and its corresponding clay-pDMAc hydrogels are not temperatures sensitive materials and no temperature-related rheology experiments were performed on them. [17]

4.2.6.1 Critical Yield Test of Clay-pDMAc Hydrogels

Figure 4.56 shows the flow curves for (1 % clay)-pDMAc and (2 % clay)-pDMAc hydrogels. The (1 % clay)-pDMAc hydrogels (Figure 4.56 a) have yield stress in the range 0.0037 – 0.0143 Pa (Table 4.16). The (2 % clay)-pDMAc hydrogels (Figure 4.56 b) have higher yield stress values as expected, the more clay in the hydrogel the larger the yield stress values.

(1 % clay)-pDMAc hydrogels yield values change as different clays are used in the hydrogels. The composites can be divided into two groups, the first one includes the 1L_{EL}-pDMAc, 1L_{RD}-pDMAc and the 1L_{OG}-pDMAc, and the other group includes the 1L_{FN}-pDMAc, 1L_{XL21}-pDMAc and the 1C_{Na+}-pDMAc. The yield values show that 1L_{RD}-pDMAc has the largest value (0.0143 Pa) followed by 1L_{EL}-pDMAc (0.0118 Pa), 1L_{OG}-pDMAc (0.0103 Pa) and the other group have closer yield stress values to one another (Table 4.16).

The same trend can be observed for the (2 % clay)-pDMAc hydrogels according to the clay used. The 2L_{RD}-pDMAc has the largest value followed by 2L_{EL}-pDMAc, 2L_{OG}-pDMAc hydrogels and then the 2L_{FN}-pDMAc, 2L_{XL21}-pDMAc and the 1C_{Na+}-pDMAc hydrogels.

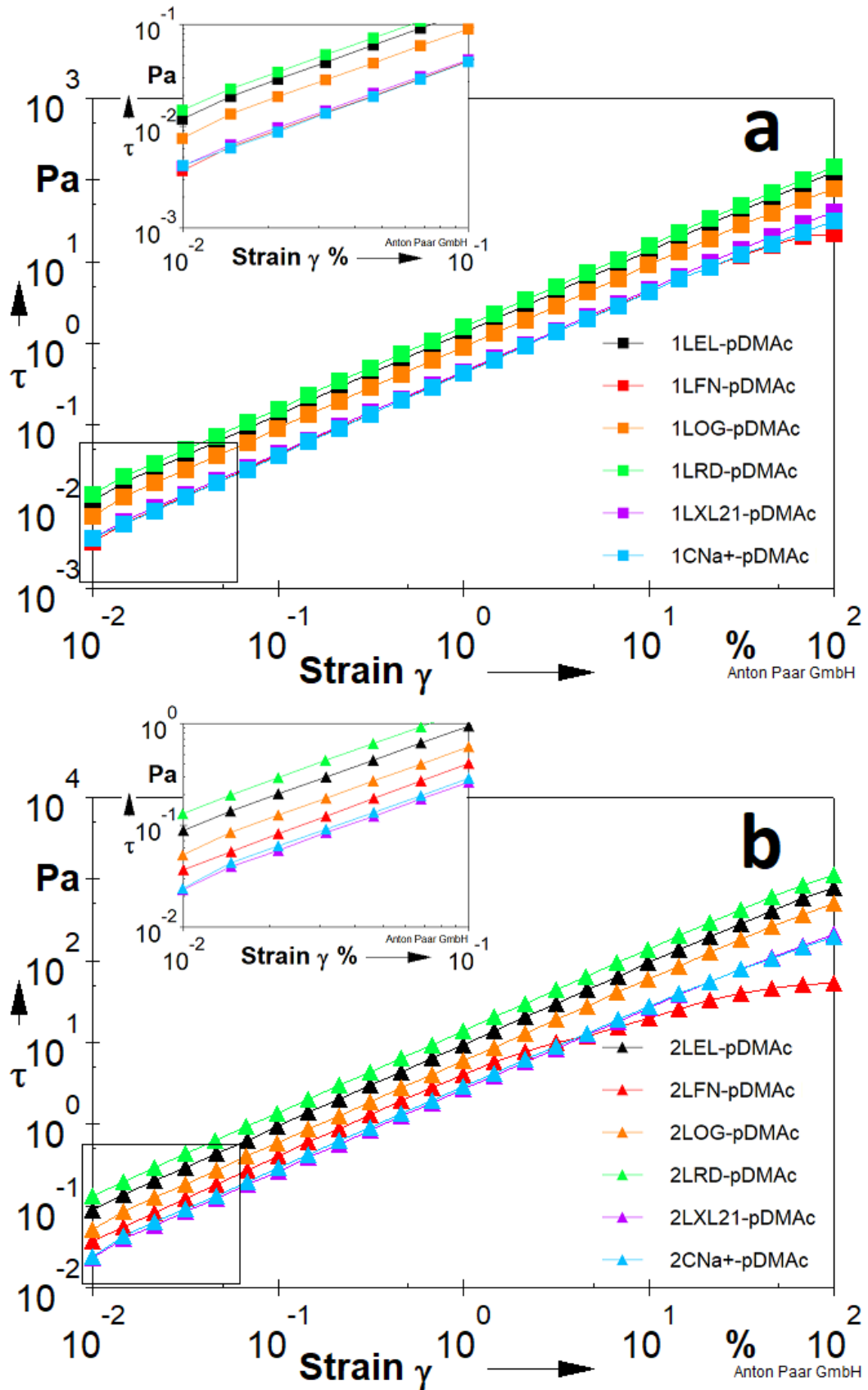


Figure 4.56 Yield stress values on flow curves for clay-pDMAc a) (1 % clay)-pDMAc. b) (2 % clay)-pDMAc.

Figure 4.57 shows the yield stress as a function of the clay platelet size (Figure 4.57 a) and the clay CEC (Figure 4.57 b). Both characteristics influence the yield stress of the clay-pDMAc hydrogels, however, the effect of the CEC values is clearer on the yield stress, the smaller the CEC the higher the yield stress when looking at the (1 % clay)-pDMAc and the (2 % clay)-pDMAc hydrogels. However, the trend can be observed in both plots suggesting that both properties affect the yield stress.

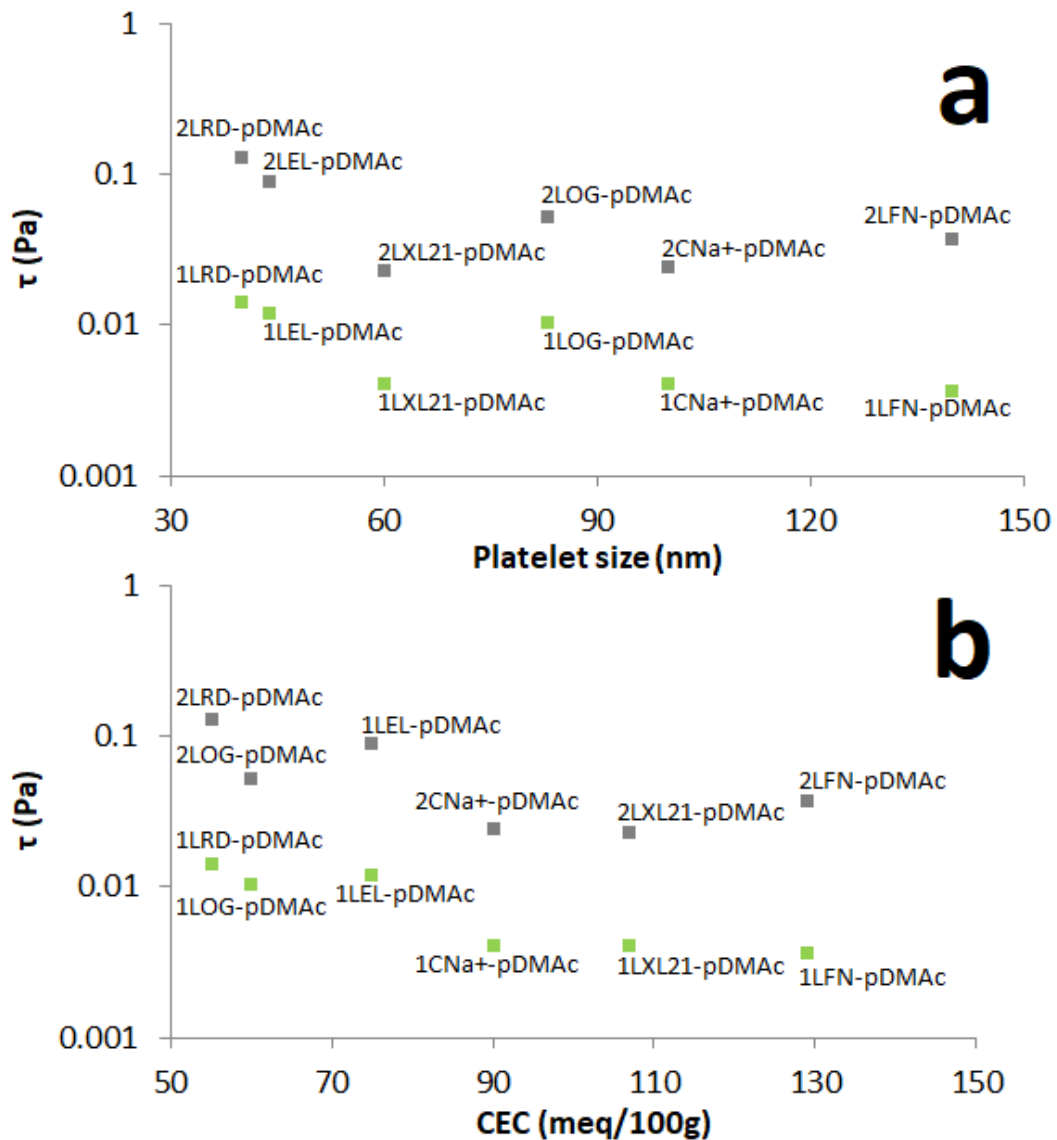


Figure 4.57 The relationship between yield stress and clay properties for clay-pDMAc hydrogel a) Yield stress to clay particle size. b) Yield stress to clay CEC.

Table 4.16 Average yield stress and standard deviation of (n=3) for (1 % clay)-pDMAc and (2 % clay)-pDMAc hydrogels.

Sample	τ (Pa)	τ SD	Properties of crosslinker (clay)	
			Particle size (nm)	CEC (meq/100g)
1L_{EL}-pDMAc	0.0118	0.0011	044	075
2L_{EL}-pDMAc	0.0890	0.0012	044	075
1L_{FN}-pDMAc	0.0037	0.0005	140	129
2L_{FN}-pDMAc	0.0368	0.0160	140	129
1L_{OG}-pDMAc	0.0103	0.0048	083	060
2L_{OG}-pDMAc	0.0514	0.0069	083	060
1L_{RD}-pDMAc	0.0143	0.0024	040	055
2L_{RD}-pDMAc	0.1304	0.0156	040	055
1L_{XL21}-pDMAc	0.0041	0.0003	060	107
2L_{XL21}-pDMAc	0.0232	0.0005	060	107
1C_{Na+}-pDMAc	0.0041	0.0047	500	090
2C_{Na+}-pDMAc	0.0241	0.0047	500	090

4.2.6.2 Storage (G') and Loss (G'') Moduli Behaviour for Clay-pDMAc Hydrogels

4.2.6.2.1 Amplitude Sweep (Function of Strain)

In pDMAc-based hydrogels containing enough water, the pDMAc chains behave as flexible polymer chains. Therefore, pDMAc hydrogels are expected to be soft materials with rubber-like elasticity and reversible deformation. An extended LVE region (Figure 4.58) was observed for clay-pDMAc hydrogel as some showed a $\gamma_c \geq 15\%$. Table 4.17 shows that a few of the clay-pDMAc hydrogels have a crossover point from a gel-like to a liquid-like material even at a high strain of 100%. [8]

The 1L_{XL21}-pDMAc and the 1C_{Na+}-pDMAc hydrogels show a different behaviour from all other composites, as they are a liquid-like material, over the whole strain range with close moduli values which was not observed before with these two clays or with any other clay or hydrogel.

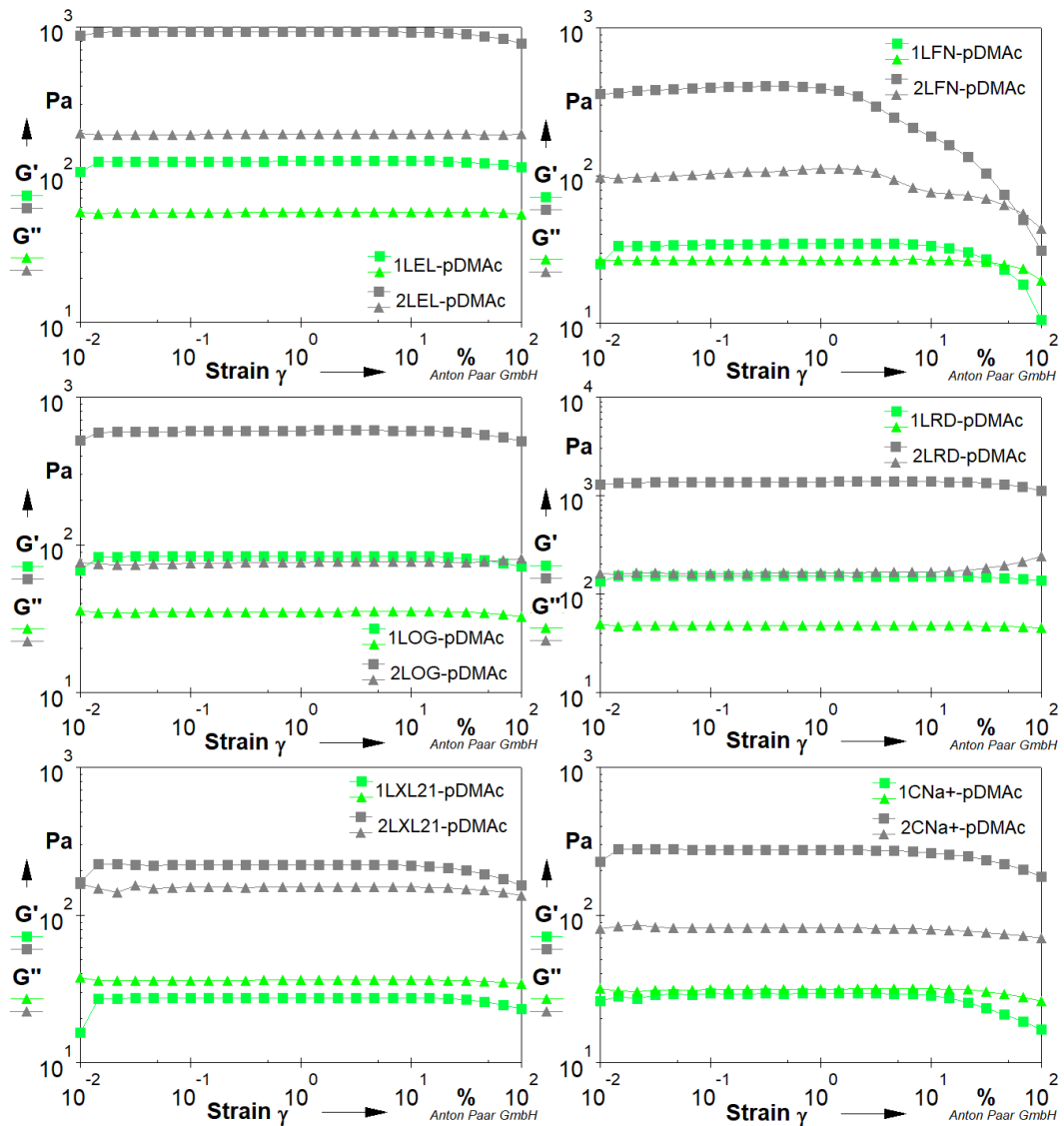


Figure 4.58 Evolution of storage G' and loss G'' moduli as a function of strain from 0.01 - 100 % strain showing the LVE range and transition point (gel-like to liquid-like) for; 1LEL-pDMAc and 2LEL-pDMAc, 1LFN-pDMAc and 2LFN-pDMAc, 1LOG-pDMAc and 2LOG-pDMAc, 1LRD-pDMAc and 2LRD-pDMAc, 1LXL21-pDMAc and 2LXL21-pDMAc, 1CNa+-pDMAc and 2CNa+-pDMAc.

Figure 4.59 shows the LVE limits of clay-pDMAc hydrogels as a function of the clay properties, (1 % clay)-pDMAc and (2 % clay)-pDMAc hydrogels show a clear relationship where the LVE limit decrease as the clay platelet size increases except for the 1_{LOG}-pDMAc hydrogel, whilst the effect of the CEC is not as clear as the effect of the particle size.

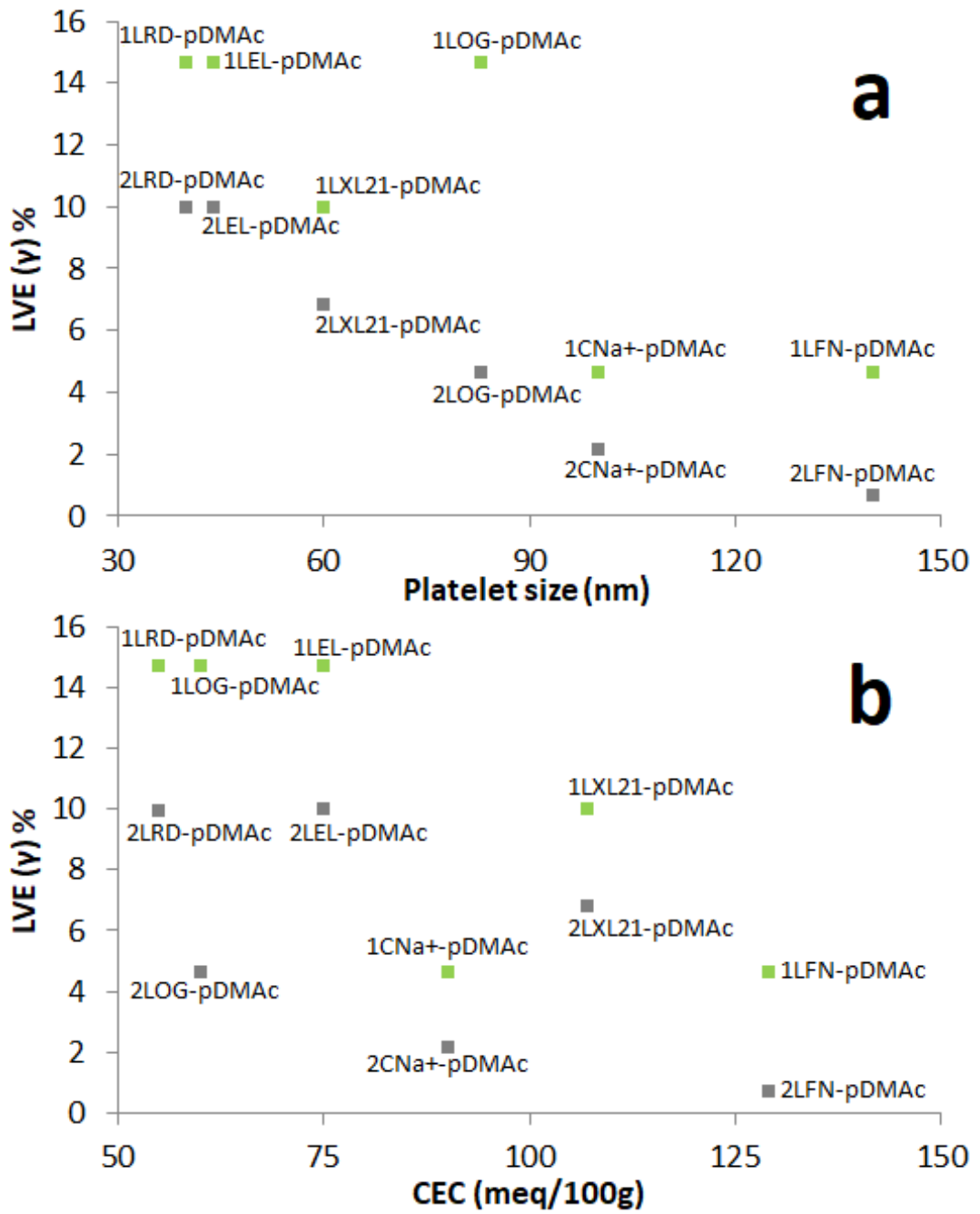


Figure 4.59 The relationship between strain at the LVE and clay properties for clay-pDMAc hydrogels a) Strain to clay platelet size. b) Strain to clay CEC.

Table 4.17 Average strain value at the LVE limit and standard deviation of (n=3) for (1 % clay)-pDMAc and (2 % clay)-pDMAc hydrogels.

Sample	Crossover Point				LVE (γ %)
	γ Mean (%)	γ SD	G' Mean (Pa)	G' SD	
1L _{EL} -pDMAc	-	-	-	-	14.6781
2L _{EL} -pDMAc	-	-	-	-	9.9923
1L _{FN} -pDMAc	36.5830	1.5335	25.5550	0.5409	4.6422
2L _{FN} -pDMAc	58.6700	4.0420	58.2510	31.3461	0.6910
1L _{OG} -pDMAc	-	-	-	-	14.6779
2L _{OG} -pDMAc	-	-	-	-	4.6318
1L _{RD} -pDMAc	-	-	-	-	14.6788
2L _{RD} -pDMAc	-	-	-	-	9.9670
1L _{XL21} -pDMAc	-	-	-	-	10.0008
2L _{XL21} -pDMAc	-	-	-	-	6.8137
1C _{Na+} -pDMAc	-	-	-	-	4.6420
2C _{Na+} -pDMAc	-	-	-	-	2.1549

4.2.6.2.2 Frequency Sweep (Function of Frequency)

The frequency sweeps for the clay-pDMAc hydrogels in the frequency range 0.01 to 100 Hz were conducted within the LVE at a strain of 1 %. The variations of the viscoelastic moduli G' and G'' with the frequency are measured for the clay-pDMAc with different clay types and at different clay-to-polymer ratios. [49]

Figure 4.60 show the storage (G') and loss (G'') modulus for (1 % clay)-pDMAc and (2 % clay)-pDMAc. The (1 % clay)-pDMAc hydrogels show crossover points at higher frequencies as expected for the hydrogels that show a frequency-independent behaviour at a strain of 1%. The (2 % clay)-pDMAc show higher moduli value when compared to the (1 % clay)-pDMAc as expected.

The 1L_{XL21}-pDMAc and 2L_{XL21}-pDMAc hydrogels show a liquid-like behavior as it did with the strain sweeps and the 1C_{Na+}-pDMAc show very close values for the viscoelastic moduli. This behaviour still needs more experimenting with different strain values.

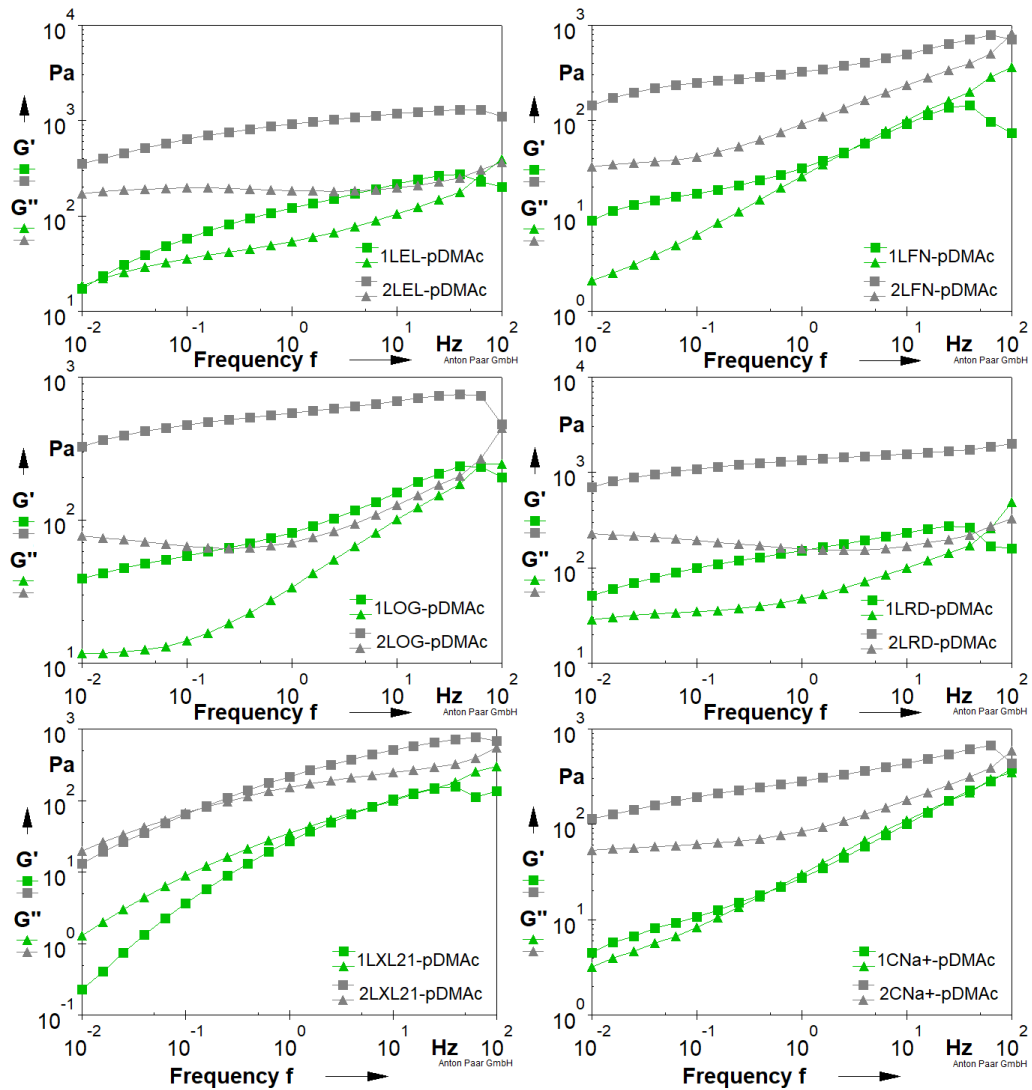


Figure 4.60 Evolution of storage G' and loss G'' moduli as a function of Frequency from 0.001 - 100 Hz transition point (gel-like to liquid-like) for; 1LEL-pDMAc and 2LEL-pDMAc, 1LFN-pDMAc and 2LFN-pDMAc, 1LOG-pDMAc and 2LOG-pDMAc, 1LRD-pDMAc and 2LRD-pDMAc, 1LXL21-pDMAc and 2LXL21-pDMAc, 1CNa+-pDMAc and 2CNa+-pDMAc.

Table 4.18 Average crossover points (f , G' value) from ($n=3$) for LEL-pDMAc, LFN-pDMAc, LOG-pDMAc LRD-pDMAc, LXL21-pDMAc, and CNa+-pNIPAM hydrogels at twodifferent clay-to-polymer ratios.

Samples	Crossover point			
	f Hz	f SD	G' Pa	G' SD
1L _{EL} -pDMAc	0.01	0.00	20.37	20.37
2L _{EL} -pDMAc	-	-	-	-
1L _{FN} -pDMAc	2.72	0.50	47.88	47.88
2L _{FN} -pDMAc	89.05	6.46	729.68	729.68
1L _{OG} -pDMAc	58.59	10.39	234.98	234.98
2L _{OG} -pDMAc	78.19	7.07	325.15	325.15
1L _{RD} -pDMAc	50.00	4.12	210.44	210.44
2L _{RD} -pDMAc	-	-	-	-
1L _{XL21} -pDMAc	36.12	11.09	149.49	149.49
2L _{XL21} -pDMAc	0.13	2.64	74.89	74.89
1C _{Na+} -pDMAc	0.52	0.02	20.46	20.46
2C _{Na+} -pDMAc	84.60	10.83	510.78	18.82

Figure 4.61 shows the crossover point (when happening) in the frequency sweeps of the clay-pDMAc hydrogels with relation to the clay platelet size and CEC. The plots do not show any correlation between the frequency and the clay properties when looking at the (1 % clay)-pDMAc or the (2 % clay)-pDMAc samples. Comparing the two clay-to-polymer ratios, where data was available, did not show a clear trend also as it can be seen the (2 % clay)-pDMAc does not have a higher crossover value and vice-versa. These results show that clay-pDMAc hydrogels properties are influenced by the properties of the pDMAc within the hydrogels in a greater manner than they are influenced by the properties of clay used.

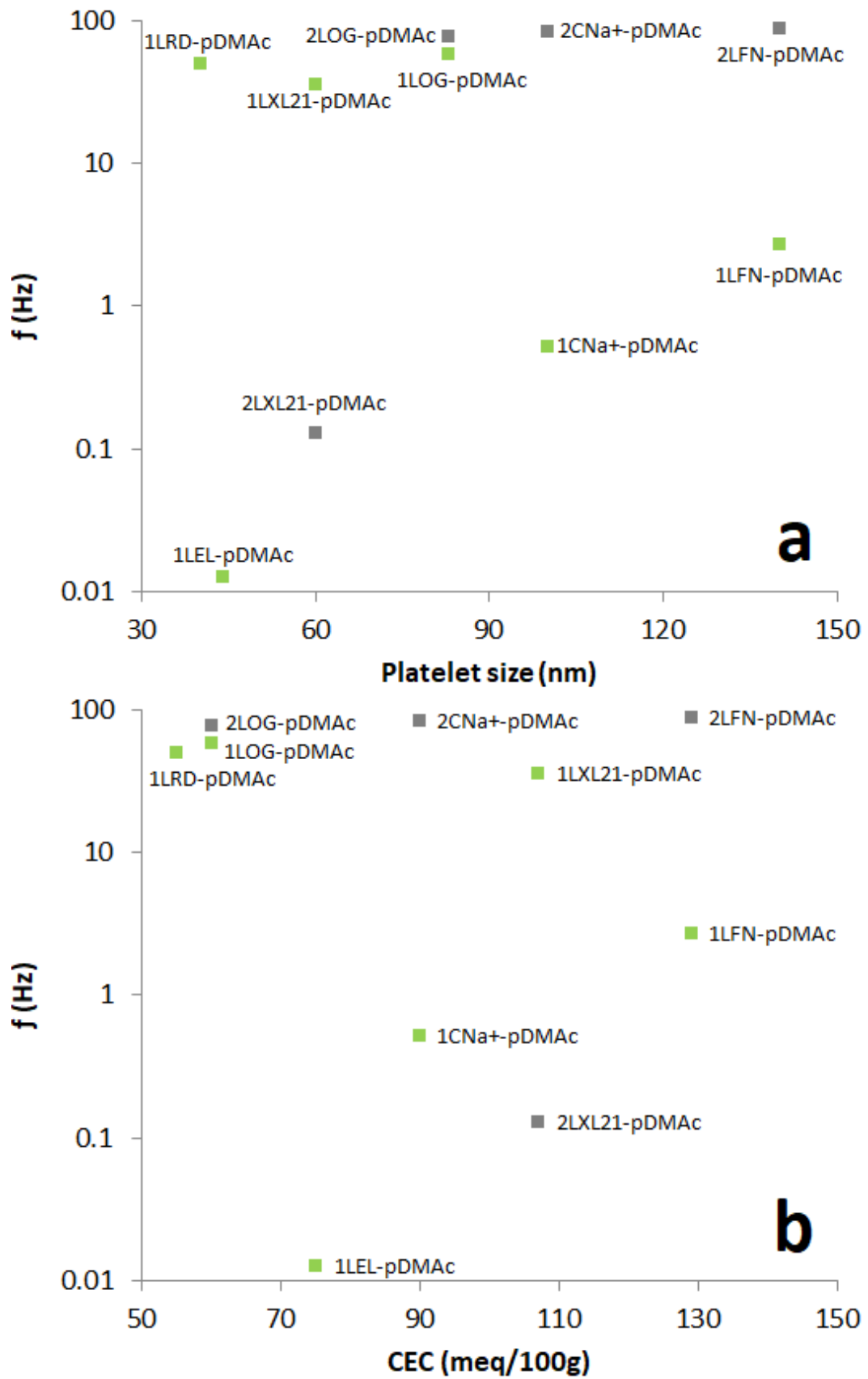


Figure 4.61 The relationship between the frequency at the crossover point and clay properties for clay-pDMAc hydrogels a) Frequency to clay platelet size. b) Frequency to clay CEC.

4.3 Summary

The main objective of this chapter was to determine the effect of different clay types on the rheological properties of acrylamide-based nanocomposites. Several rheological experimental methods were assessed for each formulation in order to control the overall conditions of the different tests such that the data is directly comparable. Several replicates of each test were done to assess repeatability.

For the pNIPAM-based nanocomposites the data is presented in Section 4.1. The characterisation techniques used (XRD and FTIR) show evidence about the dispersion of the clay platelets in the composite structure and the interaction between the clay platelets and the polymeric chains. The XRD shows an increasing baseline for $2\theta < 5^\circ$ which supports very well dispersed clay (if not exfoliated) in the nanocomposite's matrix. Most of the nanocomposites did not show any clay crystallinity reflection as their XRD traces were dominated by the pNIPAM within the composite. Table 4.2 shows that the (1 % clay)-pNIPAM d_{001} actually corresponds to the pNIPAM, however, some (2 % clay)-pNIPAM did show a shift to lower 2θ as a result of adding the clay to the polymer, however it was not easy to distinguish the changes in the clay reflections due to the overlapping between the clay and pNIPAM at 2θ around 7° but the clay is believed to be well dispersed (this is supported by the FTIR data). Information about the presence of the clay can be obtained from looking at the position and shape of the d_{110} peak, which can show that clay was present in all the samples and was detectable by the XRD technique.

The different clays effect on the composites can be observed in the SEM images. Adding any clay to the pNIPAM drastically changes the ability to make porous structures. Most composites show a clear interconnected porous network (Figure 4.14) except for the $1C_{Na^+}$ -pNIPAM and this reflects it being a different clay type; the platelet size, chemical composition and purity will also have an effect. The LOG -pNIPAM has a different morphology from all other composites as shown in Figure 4.15 with thicker walls and "internal bone" like structure. Table 4.4 shows the average pore size and standard deviation for all clay-pNIPAM nanocomposites and

Figure 4.19 helps to understand the effect of the clay type and its properties on the pore size on the nanocomposite. The clays CEC shows a clear effect on the pore size (clays with higher CEC values results in smaller pore size nanocomposites), this is possibility related to the ability of clay platelets to create crosslinking points through the cation exchange sites on the clay.

The main spectroscopic changes observed for FTIR spectra shown for all pNIPAM-based composites are changes in intensity and band position associated with the water and Si-O of the clay when comparing the neat clay and the pNIPAM homopolymer to the clay-pNIPAM composites (Table 4.5). The shifts in the Si-O stretching bands show that the clay platelets have moved apart from one another as a result of the polymeric chains being inserted between the layers. This observation supports the XRD observations indicating that the clay particles are very well dispersed. All these observations can be associated directly to the crosslinking action of the clay platelets.

Figure 4.30 shows the effect of clay platelet size on the storage modulus for (1 % clay)-pNIPAM at two different temperatures, the analysis shows that below the LCST of pNIPAM the G' values are closer to each other as a result of a bigger influence from the pNIPAM chains, which have taken the globule formation at such temperature and are having a greater effect on the physical and mechanical properties of the hydrogels. However the effect of clay platelet size can still be observed as larger clay-platelet hydrogels show higher G' values with L_{FN} -pNIPAM and C_{Na+} -pNIPAM showing values up to 20 times higher than $1L_{EL}$ -pNIPAM and L_{RD} -pNIPAM even at 20 °C. Note that the y-axis is a logarithmic scale and so these differences are significant. Figure 4.32 shows the effect of clay-to-polymer ratio on the elasticity of the clay-pNIPAM hydrogels, with more clay content and less polymer $2L_{EL}$ -pNIPAM, $2L_{RD}$ -pNIPAM, and $2L_{XL21}$ -PNIPAM show higher G' values than their corresponding (1 % clay)-pNIPAM at 40 °C, the $2L_{EL}$ -pNIPAM, $2L_{RD}$ -pNIPAM showed a greater differences by order of magnitude. The case is the same at 20 °C except for the L_{XL21} -pNIPAM hydrogels which shows no difference and may be a result of the L_{XL21} larger platelet size. Clay-pNIPAM nanocomposites with higher G'

values based on clay type or clay-to-polymer ratio are expected to show higher yield stress values, Table 4.7 shows the effect of clay-to-polymer ratio on the yield stress of the pNIPAM based hydrogels as clearly observed when comparing the τ_{yield} for the (2 % clay)-pNIPAM and (1 % clay)-pNIPAM hydrogels. With more clay presented in the hydrogel, more crosslinking points are created and as a result higher yield points.

Figure 4.35 and Table 4.8 show the effect of the clay-to-polymer ratios and clay properties on the LVE limits of the clay-pNIPAM hydrogels. The LXL₂₁-pNIPAM hydrogels show a larger LVE as a result of the L_{XL21} larger platelet size and higher CEC when compared to the L_{EL} and L_{RD}. The amplitude sweeps also show the different behaviour of these hydrogels based on temperature and the effect of changing the polymer chains conformation from coil-to-globule. The polymer part of the hydrogel dominates the properties of the material at temperatures higher than the LCST, whilst the effect of clay content is observed while at temperatures lower than the LCST – here the differences in the yield stress values are much smaller as a result of the polymer chains conformation changing from coil-to-globule Figure 4.1. This change leads to polymer chains getting more entangled with each other increasing the yield stress value of the hydrogel.

The pDMAc-based composites in Section 4.2 have similar XRD and FTIR results to one another and they show clearer evidence of dispersion to the pNIPAM-based nanocomposites (Figure 4.38 and Table 4.12) and most of the nanocomposites provided evidence for being very well dispersed unlike the pNIPAM-based nanocomposite where it was uncertain because of the reflections overlap. The pDMAc-based composites FTIR spectra showed shifts to higher wavenumber for the Si-O stretching band in a trend that was similar to the pNIPAM-based nanocomposites supporting the XRD evidence of very well dispersed clay. The SEM images (Figure 4.43 and Figure 4.44) and analysis results (Table 4.14) show the morphological differences as a result of different clay types and clay-to-polymer ratios on the pDMAc-based composites. An interconnected network structure can be seen for all composites and a clear layered effect can be observed for the (2 %

clay)-pDMAc especially for the L_{FN} and L_{XL21} corresponding nanocomposites. As earlier mentioned, the pore size correlates with the crosslinking ability of different clays. Figure 4.51 (b) shows the effect of the CEC on the pore size and how pore size is smaller with higher CEC. They can also be divided into two groups based on the CEC value and clay-to-polymer ratio; the low CEC value clays (L_{EL} , L_{RD} , L_{OG}) have much bigger differences (and are consistently higher) in pore sizes than high CEC value clays (L_{FN} , L_{XL21} , C_{Na+}) when decreasing the clay loading. These conclusions however, this still require more investigation as there could be other factors affecting the morphology, the pore size and pore size distribution of the clay-polymer nanocomposites.

The rheological analysis of the pDMAc-based composites presents a more complete understanding of the effect of different clay-to-polymer ratios as these were the only group in which all composites were synthesised using two different clay-to-polymer ratios. Figure 4.57 and Table 4.16 show that higher clay content in the hydrogel results in a higher τ_{yield} value, this is a result of more clay in the clay-polymer hydrogel dispersion and more crosslinking points between the clay platelets and polymer chains restricting the movement of it. The effect of the clay platelet size and CEC does not show a clear, consistent trend related to all of the clays, however, for the (1 % clay)-pDMAc hydrogels a lower τ_{yield} is observed when separating the clays to two different groups based on CEC (first group with L_{EL} , L_{RD} , L_{OG} and the second group with L_{FN} , L_{XL21} , C_{Na+}). These results show how complicated the relationships are between the clay and the polymer and that both clay properties (platelet size and CEC) have an effect at the same time. The influence of clay-to-polymer ratio and the clay platelet size on LVE limits can also be observed (Figure 4.59 and Table 4.17). The (1 % clay)-pDMAc hydrogels have higher LVE limit as the pDMAc flexible chains are less restricted by a fewer number of crosslinkers than that in the (2 % clay)-pDMAc hydrogels. A decrease in the LVE limit with larger platelet size (when separating the clays in to two different groups (first group with L_{EL} , L_{RD} , L_{OG} and the second group with L_{FN} , L_{XL21} , C_{Na+}) is also noted for the clay-pDMAc nanocomposites at both clay-to-polymer ratios .

Table 4.7 and Table 4.16 show the yield stress values for all clay-pNIPAM and clay-pDMAc hydrogels. Comparing the values for the hydrogels which contain the same clay type puts in perspective the differences between pNIPAM and pDMAc when used. The pNIPAM-based hydrogels require a much higher yield stress when the temperature is below LCST than the pDMAc-based hydrogels, this means that the pNIPAM-based hydrogels requires more force to move and that they have a stronger structure that can be of advantage or avoided when required for certain applications.

The clay-pNIPAM hydrogels show clear LVE ranges for the amplitude sweeps as shown in Figure 4.34, the pNIPAM containing hydrogels also showed a clear relationship between the clay platelet size and CEC and the LVE limits, the LVE limit increases with larger platelet size and higher CEC values weather the hydrogel temperature in higher or lower than the LCST as shown in Figure 4.35. The clay-pDMAc hydrogels also show an LVE range for the amplitude sweeps but the relationship between the clay platelet size and CEC was not as clear as no trends were observed with the clay platelet size or the CEC values when compared to the clay-pNIPAM hydrogels.

4.4 References

- [1] M. Semla, Z. Goc, M. Martiniaková, R. Omelka, and G. Formicki, "Acrylamide: A common food toxin related to physiological functions and health," *Physiol. Res.*, vol. 66, no. 2, pp. 205–217, 2017.
- [2] S. Lazzari, D. Pfister, V. Diederich, A. Kern, and G. Storti, "Modeling of acrylamide/N, N'-methylenebisacrylamide solution copolymerization," *Ind. Eng. Chem. Res.*, vol. 53, no. 22, pp. 9035–9048, Jun. 2014.
- [3] R. Fartaria, N. Javid, R. A. Pethrick, J. J. Liggat, J. Sefcik, and M. B. Sweatman, "Structure of laponite-styrene precursor dispersions for production of advanced polymer-clay nanocomposites," *Soft Matter*, vol. 7, no. 19, pp. 9157–9166, Oct. 2011.
- [4] T. N. Blanton, D. Majumdar, and S. M. Melpolder, "MICROSTRUCTURE OF CLAY-POLYMER COMPOSITES," vol. 42. JCPDS-International Centre for Diffraction Data, New York, pp. 562–568, 2000.
- [5] W. Dong, C. Huang, Y. Wang, Y. Sun, P. Ma, and M. Chen, "Superior mechanical properties of double-network hydrogels reinforced by carbon nanotubes without organic modification," *Int. J. Mol. Sci.*, vol. 14, no. 11, pp. 22380–22394, Nov. 2013.
- [6] E. A. Stefanescu, W. H. Daly, and I. I. Negulescu, "Hybrid polymer/clay nanocomposites: Effect of clay size on the structure of multilayered films," *Macromol. Mater. Eng.*, vol. 293, no. 8, pp. 651–656, Aug. 2008.
- [7] K. Haraguchi, H. J. Li, L. Song, and K. Murata, "Tunable optical and swelling/deswelling properties associated with control of the coil-to-globule transition of poly(N-isopropylacrylamide) in polymer - Clay nanocomposite gels," *Macromolecules*, vol. 40, no. 19, pp. 6973–6980, Sep. 2007.
- [8] K. Haraguchi, R. Farnworth, A. Ohbayashi, and T. Takehisa, "Compositional effects on mechanical properties of nanocomposite hydrogels composed of

- poly(N,N-dimethylacrylamide) and clay," *Macromolecules*, vol. 36, no. 15, pp. 5732–5741, Jul. 2003.
- [9] A. Hoffman, "Applications of thermally reversible polymers and hydrogels in therapeutics and diagnostics," *J. Control. Release*, vol. 6, pp. 297–305, 1987.
- [10] K. Haraguchi, K. Murata, and T. Takehisa, "Stimuli-responsive nanocomposite gels and soft nanocomposites consisting of inorganic clays and copolymers with different chemical affinities," *Macromolecules*, vol. 45, no. 1, pp. 385–391, Jan. 2012.
- [11] A. Pica and G. Graziano, "On urea's ability to stabilize the globule state of poly(: N -isopropylacrylamide)," *Phys. Chem. Chem. Phys.*, vol. 18, no. 21, pp. 14426–14433, 2016.
- [12] A. S. Hoffman, "Stimuli-responsive polymers: Biomedical applications and challenges for clinical translation," *Adv. Drug Deliv. Rev.*, vol. 65, no. 1, pp. 10–16, Jan. 2013.
- [13] K. Haraguchi, T. Takehisa, and M. Ebato, "Control of cell cultivation and cell sheet detachment on the surface of polymer/clay nanocomposite hydrogels," *Biomacromolecules*, vol. 7, no. 11, pp. 3267–3275, Nov. 2006.
- [14] S. Hocine and M. H. Li, "Thermoresponsive self-assembled polymer colloids in water," *Soft Matter*, vol. 9, no. 25, pp. 5839–5861, 10-Jul-2013.
- [15] M. Karg, S. Wellert, I. Pastoriza-Santos, A. Lapp, L. M. Liz-Marzán, and T. Hellweg, "Thermoresponsive core-shell microgels with silica nanoparticle cores: Size, structure, and volume phase transition of the polymer shell," *Phys. Chem. Chem. Phys.*, vol. 10, no. 44, pp. 6708–6716, 2008.
- [16] M. Shibayama, M. Morimoto, and S. Nomura, "Phase Separation Induced Mechanical Transition of Poly(N-isopropylacrylamide)/Water Isochore Gels," *Macromolecules*, vol. 27, no. 18, pp. 5060–5066, Aug. 1994.

- [17] K. Haraguchi, T. Takehisa, and S. Fan, "Effects of clay content on the properties of nanocomposite hydrogels composed of poly(N-isopropylacrylamide) and clay," *Macromolecules*, vol. 35, no. 27, pp. 10162–10171, Dec. 2002.
- [18] J. Díez, L. Barral, R. Bellas, J. López, C. Ramírez, and A. Rodríguez, "Exfoliated/intercalated silicate/hot styrene butadiene rubber nanocomposites: Structure-properties relationship," *J. Appl. Polym. Sci.*, vol. 125, no. SUPPL. 1, Jul. 2012.
- [19] S. Mallakpour and M. Dinari, "Biomodification of cloisite Na + with L-methionine amino acid and preparation of poly(vinyl alcohol)/organoclay nanocomposite films," *J. Appl. Polym. Sci.*, vol. 124, no. 5, pp. 4322–4330, Jun. 2012.
- [20] K. Haraguchi and H. J. Li, "Mechanical properties and structure of polymer-clay nanocomposite gels with high clay content," *Macromolecules*, vol. 39, no. 5, pp. 1898–1905, Mar. 2006.
- [21] C. Statement, "Multi-Scale Effects on Deformation Mechanisms of Polymer Nanocomposites : Experimental Characterisation and Numerical Study," *Scan. Electron Microsc.*, vol. 1994, no. April, 1994.
- [22] N. Ghaemi, S. S. Madaeni, A. Alizadeh, H. Rajabi, and P. Daraei, "Preparation, characterization and performance of polyethersulfone/organically modified montmorillonite nanocomposite membranes in removal of pesticides," *J. Memb. Sci.*, vol. 382, no. 1–2, pp. 135–147, 2011.
- [23] A. M. Asiri, "Nanocomposites and Importance of Nanofiller in Nanocomposites," *Dev. Prospect. Appl. Nanosci. Nanotechnol.*, no. January, pp. 157–179, 2016.
- [24] K. Zdiri, A. Elamri, and M. Hamdaoui, "Advances in Thermal and Mechanical Behaviors of PP/Clay Nanocomposites," *Polym. - Plast. Technol. Eng.*, vol. 56,

no. 8, pp. 824–840, 2017.

- [25] R. A. Pethrick, "Polymer–Clay Nanocomposites, Edited by TJ Pinnavaia and GW Beall John Wiley & Sons Ltd, Chichester, UK, 2000 0-471-6300-9 pp xi + 345, price £125.00," *Polym. Int.*, vol. 51, no. 5, p. 464, 2002.
- [26] M. Alexandre and P. Dubois, "Polymer-layered silicate nanocomposites: Preparation, properties and uses of a new class of materials," *Mater. Sci. Eng. R Reports*, vol. 28, no. 1, pp. 1–63, Jun. 2000.
- [27] X. Liu, K. Liu, S. Gou, L. Liang, C. Luo, and Q. Guo, "Water-soluble acrylamide sulfonate copolymer for inhibiting shale hydration," *Ind. Eng. Chem. Res.*, vol. 53, no. 8, pp. 2903–2910, Feb. 2014.
- [28] J. M. Yeh, S. J. Liou, and Y. W. Chang, "Polyacrylamide-clay nanocomposite materials prepared by photopolymerization with acrylamide as an intercalating agent," *J. Appl. Polym. Sci.*, vol. 91, no. 6, pp. 3489–3496, Mar. 2004.
- [29] U. Nakan *et al.*, "The effect of nanoparticle silver on the thermal stability of N-isopropylacrylamide (NIPAAm)," *World Appl. Sci. J.*, vol. 29, no. 3, pp. 359–364, 2014.
- [30] D. Wang, J. Zhu, Q. Yao, and C. A. Wilkie, "A comparison of various methods for the preparation of polystyrene and poly(methyl methacrylate) clay nanocomposites," *Chem. Mater.*, vol. 14, no. 9, pp. 3837–3843, Sep. 2002.
- [31] C. Basavaraja, R. Pierson, J. H. Kim, and S. H. Do, "Microscopic studies of polyaniline-poly-N-isopropylacrylamide/alumina composites containing dodecylbenzene sulfonic acid," *Bull. Korean Chem. Soc.*, vol. 29, no. 9, pp. 1699–1704, Sep. 2008.
- [32] PerkinElmer, "A Beginner's Guide to Thermogravimetric Analysis (TGA)." PerkinElmer, Inc, Waltham, pp. 1–19.

- [33] R. L. Blaine and J. E. Rose, "Validation of thermogravimetric analysis performance using mass loss reference materials," *TA Instruments*, no. 4, pp. 1–10, 2004.
- [34] P. K. Paul, S. A. Hussain, D. Bhattacharjee, and M. Pal, "Preparation of polystyrene-clay nanocomposite by solution intercalation technique," *Bull. Mater. Sci.*, vol. 36, no. 3, pp. 361–366, Jun. 2013.
- [35] V. Boyes, "The Synthesis and Development of Novel, Easily Processable Poly(N-Isopropylacrylamide)-Based Hydrogels," Sheffield Hallam University, Material and Engineering Research Institute, Sheffield, 2012.
- [36] A. A. Thorpe, S. Creasey, C. Sammon, and C. L. Le Maitre, "Hydroxyapatite nanoparticle injectable hydrogel scaffold to support osteogenic differentiation of human mesenchymal stem cells," *Eur. Cells Mater.*, vol. 32, pp. 1–23, 2016.
- [37] T. Dai, X. Qing, H. Zhou, C. Shen, J. Wang, and Y. Lu, "Mechanically strong conducting hydrogels with special double-network structure," *Synth. Met.*, vol. 160, no. 7–8, pp. 791–796, Apr. 2010.
- [38] Q. Wang, R. Hou, Y. Cheng, and J. Fu, "Super-tough double-network hydrogels reinforced by covalently compositing with silica-nanoparticles," *Soft Matter*, vol. 8, no. 22, pp. 6048–6056, Jun. 2012.
- [39] H. Tsukeshiba *et al.*, "Effect of polymer entanglement on the toughening of double network hydrogels," *J. Phys. Chem. B*, vol. 109, no. 34, pp. 16304–16309, Sep. 2005.
- [40] M. Huang, H. Furukawa, Y. Tanaka, T. Nakajima, Y. Osada, and J. P. Gong, "Importance of entanglement between first and second components in high-strength double network gels," *Macromolecules*, vol. 40, no. 18, pp. 6658–6664, Sep. 2007.

- [41] T. Nakajima, H. Furukawa, Y. Tanaka, T. Kurokawa, Y. Osada, and J. P. Gong, "True chemical structure of double network hydrogels," *Macromolecules*, vol. 42, no. 6, pp. 2184–2189, Mar. 2009.
- [42] L. Liang *et al.*, "Surfaces with reversible hydrophilic/hydrophobic characteristics on cross-linked poly(N-isopropylacrylamide) hydrogels," *Langmuir*, vol. 16, no. 21, pp. 8016–8023, Oct. 2000.
- [43] D. A. Beattie, J. Addai-Mensah, A. Beaussart, G. V. Franks, and K. Y. Yeap, "In situ particle film ATR FTIR spectroscopy of poly (N-isopropyl acrylamide) (PNIPAM) adsorption onto talc," *Phys. Chem. Chem. Phys.*, vol. 16, no. 45, pp. 25143–25151, Oct. 2014.
- [44] S. A. Jadhav, V. Brunella, I. Miletto, G. Berlier, and D. Scalarone, "Synthesis of poly(N-isopropylacrylamide) by distillation precipitation polymerization and quantitative grafting on mesoporous silica," *J. Appl. Polym. Sci.*, vol. 133, no. 44, pp. 1–8, Nov. 2016.
- [45] W. L. Ijdo, S. Kemnetz, and D. Benderly, "An infrared method to assess organoclay delamination and orientation in organoclay polymer nanocomposites," *Polym. Eng. Sci.*, vol. 46, no. 8, pp. 1031–1039, Aug. 2006.
- [46] C. Yan and D. J. Pochan, "Rheological properties of peptide-based hydrogels for biomedical and other applications," *Chem. Soc. Rev.*, vol. 39, no. 9, pp. 3528–3540, Sep. 2010.
- [47] D. R. Picout and S. B. Ross-Murphy, "Rheology of biopolymer solutions and gels," *ScientificWorldJournal.*, vol. 3, pp. 105–121, 2003.
- [48] A. Franck, "Understanding Rheology of Structured Fluids."
- [49] J. M. Zuidema, C. J. Rivet, R. J. Gilbert, and F. A. Morrison, "A protocol for rheological characterization of hydrogels for tissue engineering strategies," *J. Biomed. Mater. Res. - Part B Appl. Biomater.*, vol. 102, no. 5, pp. 1063–1073,

2014.

- [50] B. Strachota *et al.*, "Poly(N-isopropylacrylamide)-clay based hydrogels controlled by the initiating conditions: Evolution of structure and gel formation," *Soft Matter*, vol. 11, no. 48, pp. 9291–9306, 2015.
- [51] T. G. Mezger, *The Rheology Handbook : 4th Edition*. Vincentz Network, 2014.
- [52] M. I. Limited, "Measuring the rheology of polymer solutions." Malvern Instruments Limited, Worcestershire, pp. 1–17, 2017.
- [53] A. Mourchid, A. Delville, J. Lambard, E. Lécolier, and P. Levitz, "Phase Diagram of Colloidal Dispersions of Anisotropic Charged Particles: Equilibrium Properties, Structure, and Rheology of Laponite Suspensions," *Langmuir*, vol. 11, no. 6, pp. 1942–1950, Jun. 1995.
- [54] B. Başer, G. B. Demirel, and T. Caykara, "DNA adsorption on poly(N,N-dimethylacrylamide)-grafted chitosan hydrogels," *J. Appl. Polym. Sci.*, vol. 120, no. 3, pp. 1420–1425, May 2011.
- [55] T. Aoki *et al.*, "Temperature-Responsive Interpenetrating Polymer Networks Constructed with Poly(acrylic acid) and Poly(N,N-dimethylacrylamide)," *Macromolecules*, vol. 27, no. 4, pp. 947–952, Jul. 1994.
- [56] C. Fang, Y. Jing, Y. Zong, and Z. Lin, "Effect of N,N-dimethylacrylamide (DMA) on the comprehensive properties of acrylic latex pressure sensitive adhesives," *Int. J. Adhes. Adhes.*, vol. 71, pp. 105–111, Dec. 2016.
- [57] H. Yang, Q. Ma, L. Hu, J. Hao, and Y. Tan, "Synthesis and multi-stimuli-responsive behavior of copolymer of N,N'-dimethylacrylamide and complex pseudorotaxane," *Polym. Bull.*, vol. 69, no. 2, pp. 199–217, Jul. 2012.
- [58] H. Kang *et al.*, "Polymerization Kinetics of Poly(2-Hydroxyethyl Methacrylate) Hydrogels and Nanocomposite Materials," *Macromolecules*, vol. 5, no. 1, pp. 449–456, Jan. 2013.

- [59] J. M. Yeh *et al.*, "Enhancement of corrosion protection effect of poly(o-ethoxyaniline) via the formation of poly(o-ethoxyaniline)-clay nanocomposite materials," *Polymer (Guildf)*., vol. 43, no. 9, pp. 2729–2736, Mar. 2002.
- [60] R. A Vaia, *Polymer-clay nanocomposites*. John Wiley and Sons Ltd, 2000.
- [61] S. H. Nair, K. C. Pawar, J. P. Jog, and M. V. Badiger, "Swelling and mechanical behavior of modified poly(vinyl alcohol)/laponite nanocomposite membranes," *J. Appl. Polym. Sci.*, vol. 103, no. 5, pp. 2896–2903, Mar. 2007.
- [62] C. Tie Lan, P. D. Kaviratna, and T. J. Pinnavaia, "On the Nature of Polyimide-Clay Hybrid Composites," *Chem. mater*, vol. 6, no. 3, pp. 573–575, 1994.
- [63] G. Chen, S. Liu, S. Chen, and Z. Qi, "FTIR Spectra, Thermal Properties, and Dispersibility of a Polystyrene/Montmorillonite Nanocomposite," *Macromol. Chem. Phys*, vol. 202, pp. 1189–1193, 2001.
- [64] D. Kai, M. P. Prabhakaran, B. Stahl, M. Eblenkamp, E. Wintermantel, and S. Ramakrishna, "Mechanical properties and in vitro behavior of nanofiberhydrogel composites for tissue engineering applications," *Nanotechnology*, vol. 23, no. 9, Mar. 2012.
- [65] G. Jin, M. P. Prabhakaran, D. Kai, S. K. Annamalai, K. D. Arunachalam, and S. Ramakrishna, "Tissue engineered plant extracts as nanofibrous wound dressing," *Biomaterials*, vol. 34, no. 3, pp. 724–734, Jan. 2013.
- [66] B. Rafiei and F. A. Ghomi, "Preparation and characterization of the Cloisite Na⁺ modified with cationic surfactants Caspian sea View project Organoclay synthesis View project," *J. Crystallogr. Mineral.*, vol. 21, pp. 25–32, 2013.
- [67] Y. Liu *et al.*, "Thio-Michael addition of α,β -unsaturated amides catalyzed by Nmm-based ionic liquids," *RSC Adv.*, vol. 7, no. 68, pp. 43104–43113, 2017.
- [68] K. Haraguchi and T. Takehisa, "Nanocomposite Hydrogels: A Unique Organic–Inorganic Network Structure with Extraordinary Mechanical, Optical, and

Swelling/Deswelling Properties," *Adv. Mater.* - *ADVAN MATER*, vol. 14, Aug. 2002.

5

Clay-PolyMethacrylate Nanocomposite/Hydrogels Characterisation

Chapter 5 Clay-PolyMethacrylate

Nanocomposites/Hydrogels Characterisation

In this chapter, methacrylate-based nanocomposites with a nano-silicate (Laponite[®] and Cloisite[®]) as crosslinking agents were investigated. [1][2] The addition of large surface area nanosized clay fillers to a polymer has the potential to improve its water uptake ability and its mechanical and rheological properties. [3]

The crosslinker content is the main factor in the synthesis of clay-polymer nanocomposites in this study. Increasing/decreasing the clay-to-polymer ratio controls the crosslinking density, i.e. the number of crosslinking sites between polymer chains and clay platelets. This affects major properties in the clay-polymer composite of which an important one is water content as it is easy for water to penetrate with a loose crosslinked network. Increasing the clay-to-polymer ratio increases the number of crosslinking sites, this produces a composite with more hydrophobic nature. This can also be used to control the swelling properties of the nanocomposite; as increasing the density of crosslinked sites promotes a hydrophobic nature in the clay-polymer nanocomposite [4] by decreasing and restricting the mobility of water molecules in the nanocomposite network [5] which hinders the water uptake and slows the nanocomposite swelling rate. [6] By controlling the concentration of the crosslinking agent, the morphology and the crosslinking density can be regulated, and the optimum water content for specific applications (from delicate contact lenses to industrial drilling fluids) can be achieved.[7] Controlling the crosslinking density can also be used to control the stiffness and robustness of the structure. By controlling how the polymeric chains are crosslinked they can be designed to adapt and withstand external stress and to retain their mechanical performance over time with certain water content for longer (e.g. robust composites are required for biodegradable scaffolds for tissue regeneration). [6]

In this chapter, pHEMA, pHPMA, and pGMAc homopolymer as well as (clay-pHEMA), (clay-pHPMA) and (clay-pGMAc) nanocomposites at different clay-to-polymer ratios were investigated, this was performed through a series of tests which will help to understand the behaviour of clay-polymer nanocomposites as a function of the clay-to-polymer ratio. The tests described earlier (Chapter 2) will identify; how well the clay is integrated into the polymer matrix, the water content and its relationship to the crosslinking agent, any changes in the polymer backbone, and the effect of all these on the mechanical properties of the final clay-polymer nanocomposite. The aim was to be able to tune these properties based on this characterisation. [8]

HEMA, HPMA, and GMAc were polymerized in the presence of the required amount of initiator, a fixed amount of water and various amounts of clay. Clay was first dispersed in the water for 24 hours, monomers were added, and the solution was stirred for one hour. Then, the samples were left to polymerise in an oven at 80 °C overnight. [9] The samples were then ground to a fine powder before XRD, TGA, FTIR measurement. [10] A selection of formulations of the (2 % clay)-polymer nanocomposites were studied depending on specific factors (observed after making the (1 % clay)-polymer nanocomposites) like processability, ease of handling on the rheometer, and ease to fine grind without contamination.

5.1 Clay-pHEMA Characterisation and Rheological Properties

2-hydroxyethyl methacrylate (HEMA) is a synthetic hydrophilic monomer which when polymerised has high mechanical strength used to prepare polymeric (i.e., pHEMA) hydrogels. Due to the biocompatible nature of pHEMA, and its similar properties to those of living tissues, it has been applied widely for drug delivery, implants, dental restorative materials [11] and as a major component in commercially important contact lenses. [12][13][14] The polymerisation of HEMA is based on the combination of methacrylate groups within its structure. It contains hydroxyl groups (-OH) that provide hydrophilicity and enables hydrogen bonding

with water molecules thus increasing the water uptake in the polymer matrix. [2][15]

5.1.1 Clay-pHEMA Nanocomposites









Table 5.1 shows images of the clay-pHEMA nanocomposites. The effect of different clays and clay-to-polymer ratios is visually observable. The pHEMA homopolymer is an elastic rubbery single block, water was observed to squeeze out of the sample when handling it out of the glass vial, but it did not readily re-sorb the water back afterwards. Adding L_{EL} to the composite ($1L_{EL}$ -pHEMA) changes some of the properties, the composite became softer, more elastic and some expelled water was present at the top of the sample vessel. This suggests that the existence of clay in the nanocomposite and the crosslinking that happens makes it harder for water to remain within the composite structure. The observations of $1L_{EL}$ -pHEMA are shared with $1L_{OG}$ -pHEMA and $1L_{RD}$ -pHEMA.

The $1L_{FN}$ -pHEMA sample was a more elastic white block than the pHEMA homopolymer but less elastic than the $1L_{EL}$ -pHEMA, water was present around the sample in the reaction vessel, but it was less than observed for $1L_{EL}$ -pHEMA, $1L_{OG}$ -pHEMA and $1L_{RD}$ -pHEMA, water was squeezed from the sample as it was pulled out from the glass vial after the reaction.

The final product from the $1L_{XL21}$ -pHEMA synthesis was a free-flowing suspension with no evidence of heterogeneity. The composite was easily handled with a syringe. A higher amount of crosslinker L_{XL21} ($2L_{XL21}$ -pHEMA) was assessed to determine if an elastic block could be achieved. However, the $2L_{XL21}$ -pHEMA had a similar flowing property but higher viscosity than $1L_{XL21}$ -pHEMA.

The $1C_{Na+}$ -pHEMA nanocomposite was a flaky material in turbid aqueous media, as the sample was pulled out of the glass vial it easily disintegrated as it was soft and weakly structured.

Table 5.1 General observation of clay-pHEMA nanocomposites, samples were investigated by pouring and poking with a small lab spatula.

pHEMA	1L_{EL}-pHEMA	1L_{FN}-pHEMA	1L_{OG}-pHEMA	1L_{RD}-pHEMA	1L_{XL21}-pHEMA	2L_{XL21}-pHEMA	1C_{Na+}-pHEMA
A white block of elastic solid gel	A white block of solid/elastic gel with ~ 20 % clear water on top	A white block solid gel with ~ 5 % clear water on top	A white block solid gel. ~ 20 % clear water on top	A white block of solid/elastic gel with ~ 20 % clear water on top	A white soft smooth flowing gel with little water around the sample	A white soft flowing gel. Less elastic than the 1L _{XL21} -pHEMA	A white flaky solid soft gel with ~ 20 % water
							

5.1.2 XRD Characterisation of Clay-pHEMA Nanocomposites

When a polymer is associated with dispersed nanoclay, the clay interlayer spacing changes depending on how well dispersed the clay is. The interlayer spacing also depends on how the polymer chains are associated with the clay platelets in the matrix and this depends on how dispersed the clay is and on the CEC of each particular clay. Taking this into consideration; clay dispersion plays an important role in the final properties of the clay-polymer nanocomposites which in our study depends mainly on the clay-to-polymer ratio. The clay-polymer nanocomposite systems have a well preserved repeated unit which allows for the use of (XRD) to determine the interlayer spacing after polymerisation. [3]

The XRD traces of pHEMA homopolymer, powder L_{EL} , and L_{EL} -pHEMA nanocomposites are presented in Figure 5.1. The X-ray diffraction trace of L_{EL} -pHEMA dominantly corresponds to the pHEMA. The lack of evidence of sharp and/or narrow reflections $2\theta = 5.8^\circ$ in the L_{EL} -pHEMA trace (due to d_{001} of L_{EL}) and the increasing baseline at $2\theta \leq 5^\circ$ suggest that the clay is well dispersed if not exfoliated. [16] The L_{EL} does have a weak d_{001} reflection, and so when dispersed in polymer it would be more difficult to observe especially at a low concentration so confirmation of exfoliated clay is also more difficult. [10] A well-dispersed clay suspension and also in the presence of monomer would support the likelihood of obtaining an exfoliated clay. [17]

The L_{EL} diffraction peak at around $2\theta = 19.4^\circ$ ($d = 4.75 \text{ \AA}$) was not observed in the $1L_{EL}$ -pHEMA XRD trace due to overlapping with the pHEMA reflection in that region. For all the pHEMA composites in this section, the presence of the pHEMA reflection at around $2\theta = 10^\circ$ to 23° makes it difficult to observe the reflection at $2\theta = 19.4^\circ$ and thus confirm the presence of clay in the XRD sampling area of the sample. However, the reflection at around $2\theta = 34.2^\circ$ ($d = 6.22 \text{ \AA}$) observed in the XRD trace of $1L_{EL}$ -pHEMA corresponds to the diffraction peak at $2\theta = 35.6^\circ$ ($d = 6.20 \text{ \AA}$) in L_{EL}

confirming the presence of clay. Overall, the XRD diffraction of the 1L_{EL}-pHEMA shows indications for clay exfoliation [18][19] in the dried nanocomposite. [3][8]

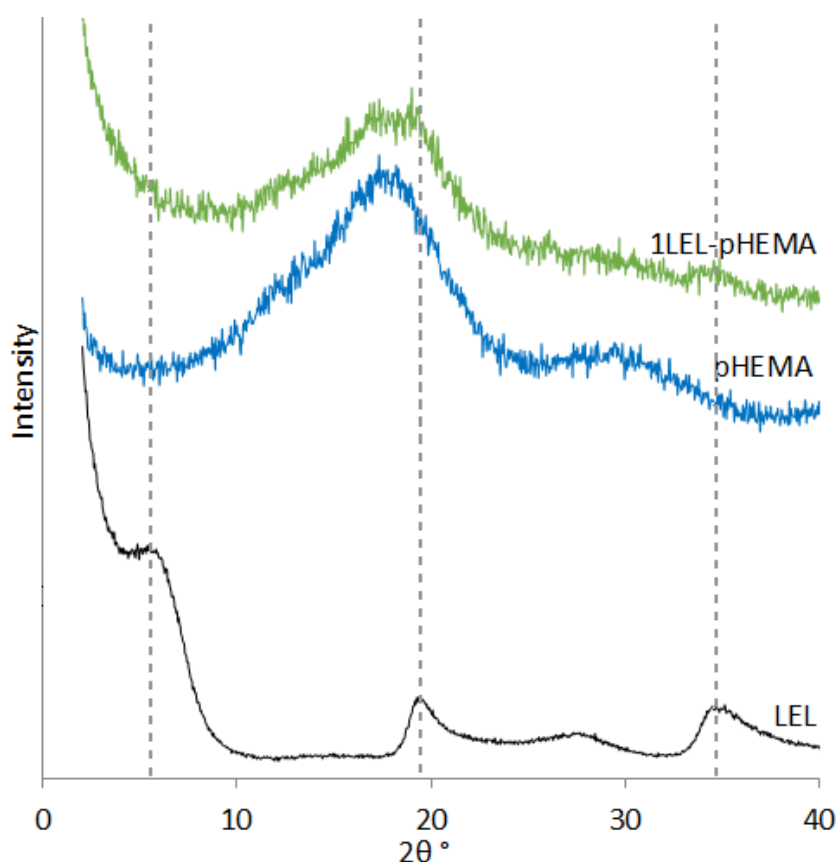


Figure 5.1 XRD profiles for powder L_{EL}, dried pHEMA homopolymer, and dried 1L_{EL}-pHEMA nanocomposites showing the differences as the polymer chains intercalate in between clay platelets as they disperse. All samples are ground powders.

The XRD traces for L_{FN}, pHEMA homopolymer, and 1L_{FN}-pHEMA nanocomposite are presented in Figure 5.2. Comparing the d-spacing values of L_{FN}, and the pHEMA with the d-spacing values from the XRD trace of the 1L_{FN}-pHEMA nanocomposite shows the interaction between the polymeric chains and the clay platelets. [3] The XRD trace of the 1L_{FN}-pHEMA is dominated by the pHEMA profile. The diffraction reflection d_{001} for L_{FN} which corresponds to a d-spacing of around $2\theta = 6.6^\circ$ ($d = 13.34 \text{ \AA}$) was observed in the 1L_{FN}-pHPMA nanocomposite with a slight shift to lower angle around $2\theta = 6.1^\circ$ ($d = 14.49 \text{ \AA}$). This indicates a microstructure composite. [16] The diffraction reflections in the XRD trace of 1L_{FN}-pHEMA at $2\theta = 18.6^\circ$ ($d = 4.77 \text{ \AA}$) and $2\theta = 27.9^\circ$ ($d = 3.19 \text{ \AA}$) are attributed to the polymer within the composite as a result of the pHEMA dominating and overlapping the L_{FN} reflections ($2\theta = 17.8^\circ$ ($d = 4.95 \text{ \AA}$) and $2\theta = 29.7^\circ$ ($d = 3.01 \text{ \AA}$) in the pHEMA

homopolymer). The clay presence in the composite may be the reason for the $2\theta = 18.6^\circ$ shift (and slight broadening) in the trace of the $1L_{FN}$ -pHEMA (Table 5.2) compared to pHEMA, which implies that the clay is being detected within the XRD sampling area. [18][19]

The diffraction reflection at around $2\theta = 34.9^\circ$ ($d = 2.57 \text{ \AA}$) in the trace of $1L_{FN}$ -pHEMA composite does, however, it confirms the presence of clay within the composite. Table 5.2 shows the peaks and the d-spacing related to each 2θ for easier comparison. This comparison shows the microstructure of $1L_{FN}$ -pHEMA.

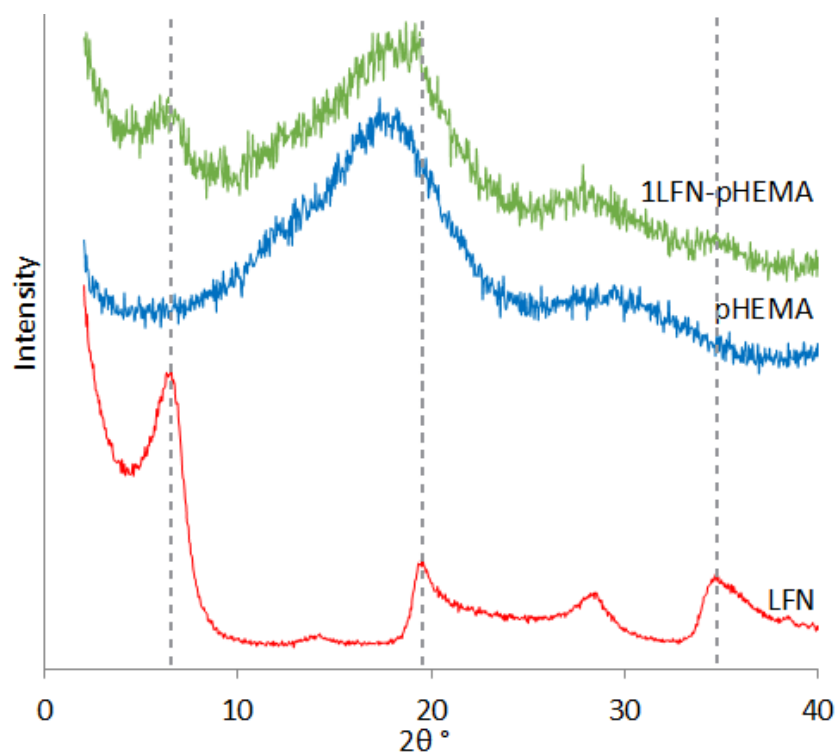


Figure 5.2 XRD profiles for powder L_{FN} , dried pHEMA homopolymer, and dried $1L_{FN}$ -pHEMA nanocomposites showing the differences as the polymer chains intercalate in between clay platelets as they disperse. All samples are ground powders.

Figure 5.3 shows the XRD traces of the L_{OG} pure clay, pHEMA homopolymer, and $1L_{OG}$ -pHEMA nanocomposites. A decreasing baseline at $2\theta \leq 5^\circ$ in the $1L_{OG}$ -pHEMA XRD trace suggests that the clay is well dispersed if not exfoliated. [16] Although there is a clear reflection at the d_{001} in the trace of the L_{OG} ; there is a lack of diffraction reflection around $2\theta = 7.1^\circ$ ($d = 12.45 \text{ \AA}$) in the XRD trace of the $1L_{OG}$ -pHEMA supporting well dispersed, if not exfoliated clay. [20] The reflection around $2\theta = 18.9^\circ$ ($d = 4.73 \text{ \AA}$) is mainly attributed to the polymer within the composite

with a shift to a higher angle ($2\theta = 17.8^\circ$ ($d = 4.95 \text{ \AA}$)) as the reflection of the clay and the reflection on the polymer have overlapped in the same region. The broad diffraction peak at around ($2\theta = 28.9^\circ$ ($d = 4.95 \text{ \AA}$)) is also attributed to the pHEMA polymer within the composite. The weak peak at around $2\theta = 34.2^\circ$ ($d = 2.62 \text{ \AA}$) in the 1LOG-pHEMA trace is attributed to a structural spacing d_{110} in the clay. [16][18][19]

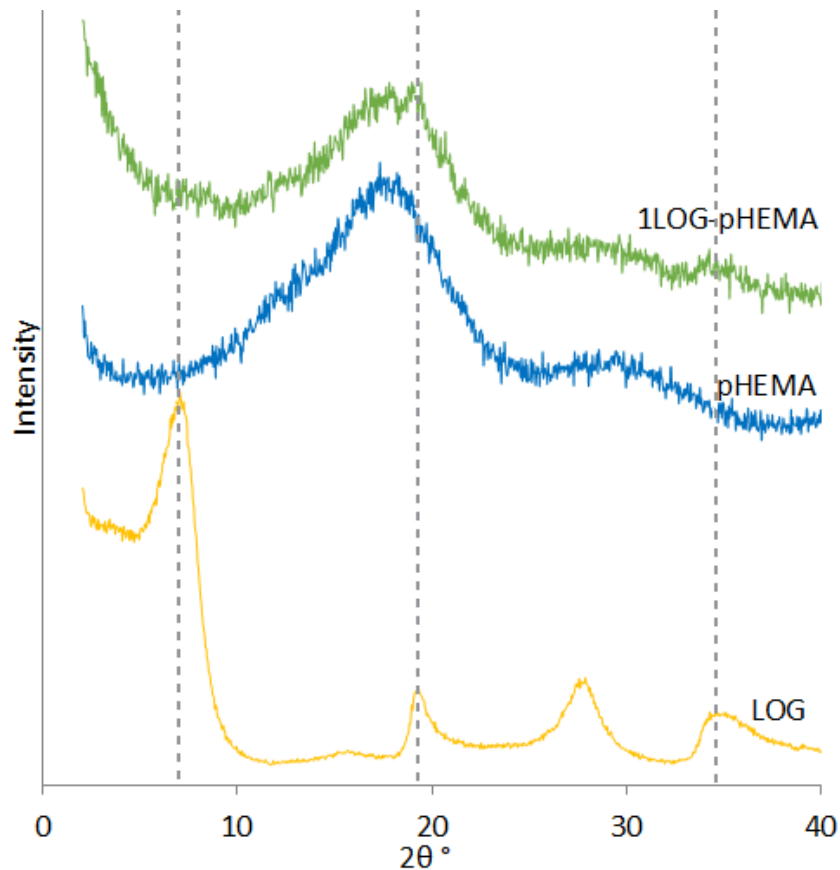


Figure 5.3 XRD profiles for powder LOG, dried pHEMA homopolymer, and dried 1LOG-pHEMA nanocomposites showing the differences as the polymer chains intercalate in between clay platelets as they disperse. All samples are ground powders.

Figure 5.4 shows the XRD profiles for pure L_{RD}, dried pHEMA homopolymer and L_{RD}-pHEMA nanocomposite. A decreasing baseline at $2\theta \leq 5^\circ$ was observed [16] and the XRD reflection related to the d_{001} in the trace of L_{RD} $2\theta = 6.5^\circ$ ($d = 13.60 \text{ \AA}$) was not observed in the XRD trace of L_{RD}-pHEMA, these observations can be indications of clay being well dispersed, probably mostly exfoliated in the nanocomposite.

The reflections at around $2\theta = 18.4^\circ$ ($d = 4.82 \text{ \AA}$) and $2\theta = 28.9^\circ$ ($d = 3.09 \text{ \AA}$) are attributed to the pHEMA within the nanocomposite. However, the reflection at

around $2\theta = 34.8^\circ$ ($d = 2.58 \text{ \AA}$) is an indication of the clay presence as it corresponds to the L_{RD} structural d_{110} (Table 5.2). [8] As was the case with $1L_{OG}$ -pHEMA, the decreasing baseline and the absence of the d_{001} diffraction reflection of L_{RD} at around $2\theta = 6.5^\circ$ in the XRD trace of $1L_{RD}$ -pHEMA suggest a very well dispersed if not exfoliated composite structure. [18][19]

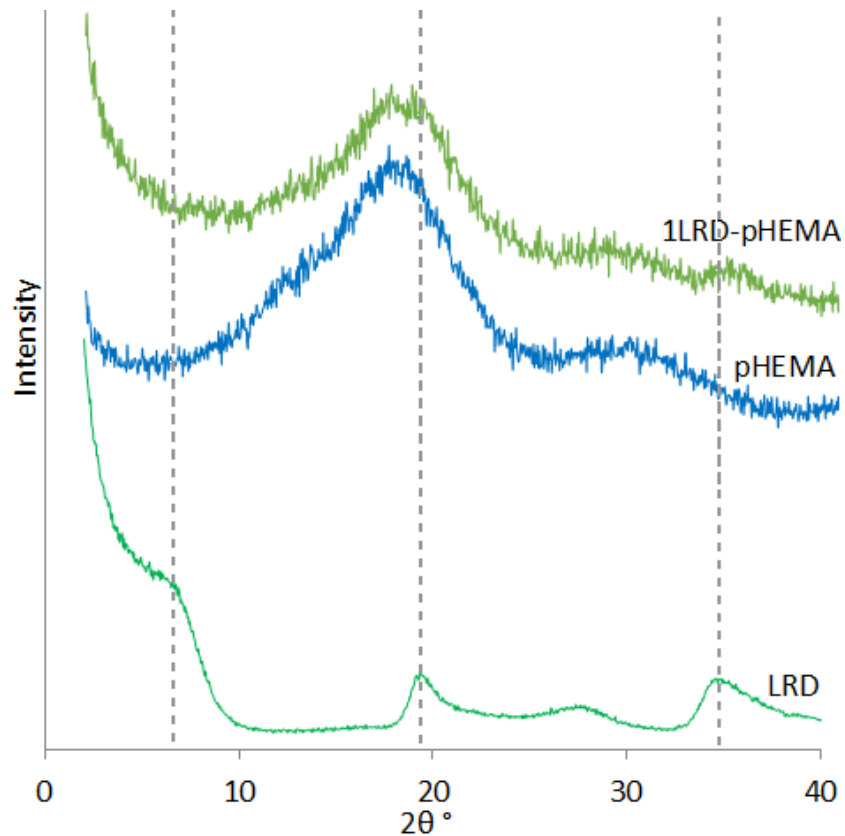


Figure 5.4 XRD profiles for powder L_{RD} , dried pHEMA homopolymer, and dried $1L_{RD}$ -pHEMA nanocomposites showing the differences as the polymer chains intercalate in between clay platelets as they disperse. All samples are ground powders.

Figure 5.5 shows the XRD traces of powder L_{XL21} , dried pHEMA homopolymer, and dried $1L_{XL21}$ -pHEMA and $2L_{XL21}$ -pHEMA nanocomposites. Both nanocomposites showed a decreasing baseline at $2\theta \leq 5^\circ$ and neither of the L_{XL21} -pHEMA nanocomposites showed any reflections corresponding to the d_{001} in the trace of L_{XL21} at around $2\theta = 6.4^\circ$ ($d = 13.81 \text{ \AA}$), these observations provide evidence for disordered and well dispersed if not exfoliated L_{XL21} platelets in the composite. [16][18][19][21]

The $1L_{XL21}$ -pHEMA reflection at around $2\theta = 18.0^\circ$ and $2L_{XL21}$ -pHEMA at around $2\theta = 19.3^\circ$ are mostly due to the polymer within the composite. However, the $2L_{XL21}$ -pHEMA shows a larger shift towards higher 2θ than the $1L_{XL21}$ -pHEMA as the clay content in $2L_{XL21}$ -pHEMA is twice as much as in the $1L_{XL21}$ -pHEMA. This shows that the amount of clay in the nanocomposite affects the XRD profile and that the L_{XL21} peak at that region was overlapped by the pHEMA in the $1L_{XL21}$ -pHEMA.

At around $2\theta = 34.7^\circ$ ($d = 2.58 \text{ \AA}$) both L_{XL21} -pHEMA composites show a reflection corresponding to the clay (L_{XL21} d_{110} structural spacing) within the composite structure, but the $2L_{XL21}$ -pHEMA shows a higher intensity reflection than $1L_{XL21}$ -pHEMA which is attributed to more clay content in the $2L_{XL21}$ -pHEMA nanocomposite, this same reflection also provides evidence about the presence of clay platelets in the composite. [22]

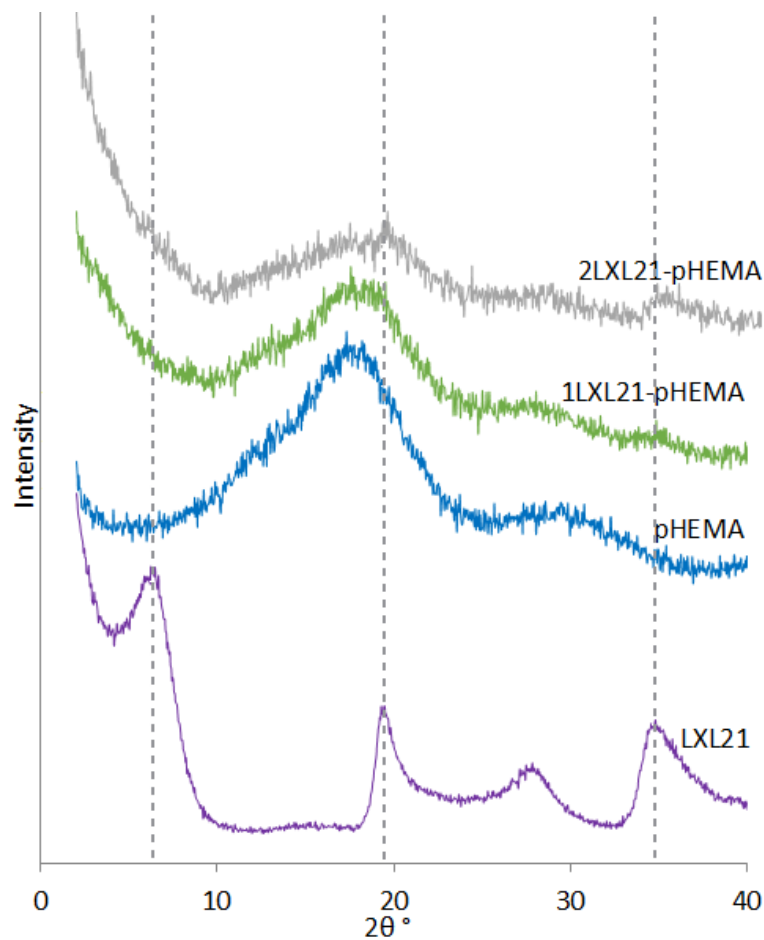


Figure 5.5 XRD profiles for powder L_{XL21} , dried pHEMA homopolymer, dried $1L_{XL21}$ -pHEMA, and dried $2L_{XL21}$ -pHEMA nanocomposites showing the differences as the polymer chains intercalate in between clay platelets as they disperse. All samples are ground powders.

Figure 5.6 shows the XRD traces of pure powder C_{Na^+} , dried pHEMA homopolymer, and dried $1C_{Na^+}$ -pHEMA nanocomposite. The XRD trace of $1C_{Na^+}$ -pHEMA showed no evidence of reflections at around $2\theta = 7.0^\circ$, however; there is a reflection at $2\theta = 3.7^\circ$ ($d = 23.9 \text{ \AA}$) which indicates a shift of the d_{001} for the C_{Na^+} indicating the clay has become intercalated. The reflection at $2\theta = 8.1^\circ$ relates to the d_{001} of the clay. The sharp reflection at around ($2\theta = 19.4^\circ$) in the $1C_{Na^+}$ -pHEMA is due to the clay and confirms its presence is an indication to that at around $2\theta = 34.6^\circ$. The broad reflections at $2\theta = 18^\circ$ and 29.6° are attributed to the polymer component of the clay-polymer nanocomposite.

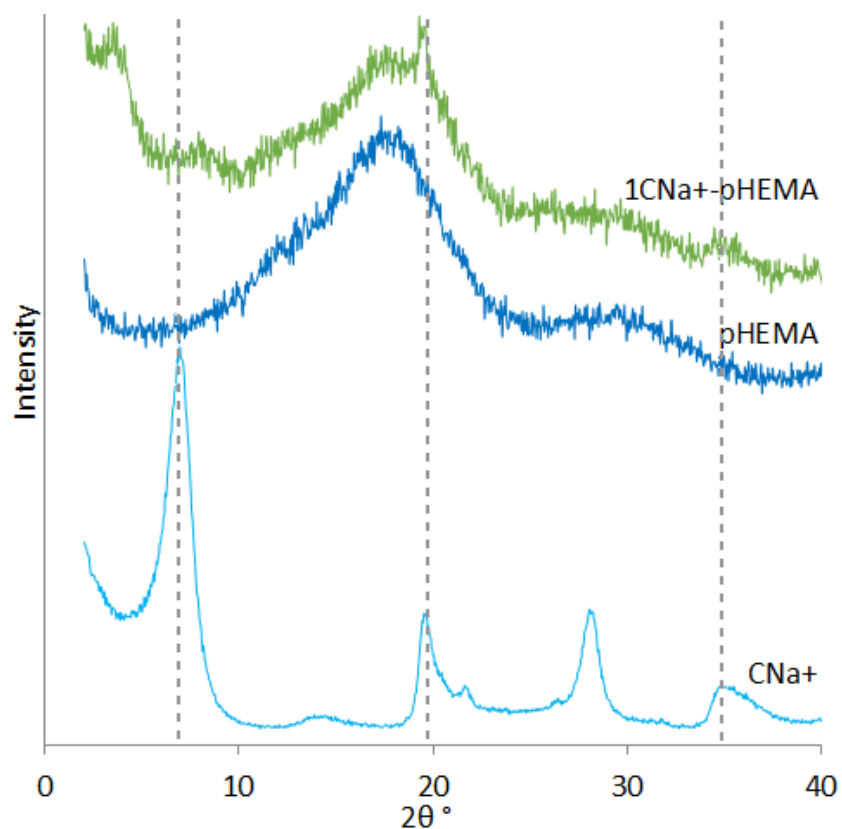


Figure 5.6 XRD profiles for powder C_{Na^+} , dried pHEMA homopolymer and dried $1C_{Na^+}$ -pHEMA nanocomposites showing the differences as the polymer chains intercalate in between clay platelets as they disperse. All samples are ground powders.

XRD characterisation of the clay-pHEMA nanocomposites showed that the composites are dominated by the pHEMA trace as amorphous structures with a lack for any strong reflections that might indicate otherwise. Some evidence of the clay presence within the composite structure was seen within the XRD traces of different clay-pHEMA nanocomposites. [20][23] This potentially suggests that the

clay platelets were exfoliated for most of the nanocomposite except for the L_{FN}-PHEMA as the composite was microstructured and the C_{Na+} platelets were intercalated. [1]

Table 5.2 Interplanar distances and 2θ of different clay (powder) and its corresponding clay-pHEMA nanocomposites samples obtained from XRD data

Sample	d ₀₀₁		d ₁₀₀		d ₁₁₀	
	2θ	d (Å)	2θ	d (Å)	2θ	d (Å)
LEL	5.8	15.24	19.4	4.57	34.5	2.60
1LEL-pHEMA	-	-	18.9	4.69	34.2	2.62
LFN	6.6	13.39	19.3	4.60	34.6	2.59
1LFN-pHEMA	6.1	14.49	18.6	4.77	34.9	2.57
LOG	7.1	12.45	19.1	4.65	34.6	2.59
1LOG-pHEMA	-	-	18.7	4.73	34.2	2.62
LRD	6.5	13.60	19.4	4.57	34.6	2.59
1LRD-pHEMA	7.1	12.45	18.4	4.82	34.8	2.58
LXL21	6.4	13.81	19.3	4.60	34.7	2.58
1LXL21-pHEMA	-	-	18.0	4.93	34.9	2.57
2LXL21-pHEMA	-	-	19.3	4.61	34.9	2.57
CNa+	7.0	12.63	19.5	4.55	34.7	2.58
1CNa+-pHEMA	8.1	10.6	19.4	4.57	34.6	2.59
	3.7	23.9	-	-	-	-

5.1.3 TGA Characterisation of Clay-pHEMA Nanocomposites

Thermal stability/behaviour of polymeric materials plays an important role in determining applications and processing conditions of polymeric nanocomposites. TGA is one technique used to characterise the thermal properties of polymeric materials where weight loss is monitored as a function of temperature. [12][24][25]

Figure 5.7 displays the thermal decomposition of the dried clay-pHEMA nanocomposite samples determined via TGA. Samples were heated from 25 °C to 900 °C at a constant rate of 20 °C/min. The weight loss associated with water evaporation starts as the temperature starts to increase. The weight loss associated with the thermal decomposition of the long pHEMA chains starts at 222 °C.[26] When the temperature exceeds 450 °C, pHEMA is considered to be completely thermally degraded with weight loss of 99.9 %.

TGA curves of (1 % clay)-pHEMA, Figure 5.7 shows the weight loss in three main stages. In “Stage 1” (temperature range 25 – 175 °C) weight loss can be attributed to the evaporation of free water. In “Stage 2”, the thermal decomposition onset of the clay-pHEMA nanocomposites shifts toward higher temperature range than that of pHEMA homopolymer (222 °C) by an average of 24 °C, and this the first sign of the enhancement of thermal stability of the clay-pHEMA nanocomposites. [20][22] Weight loss in “Stage 2” ends at around 400 - 475 °C and accounts for the biggest portion of the weight loss (up to 90 % for some nanocomposites). This is attributed to the decomposition and degradation of p(HEMA). [25][27] A different slope on the TGA curves represents “Stage 3” the final weight loss stage which is due to further degradation of polymer residues in the temperature range 475 - 600 °C and a total weight loss of 5 % on average. [12] After approximately 650 °C mainly the inorganic residues (i.e., Al₂O₃, MgO, and SiO₂) and carbonaceous char remain and there is no further weight loss. [20]

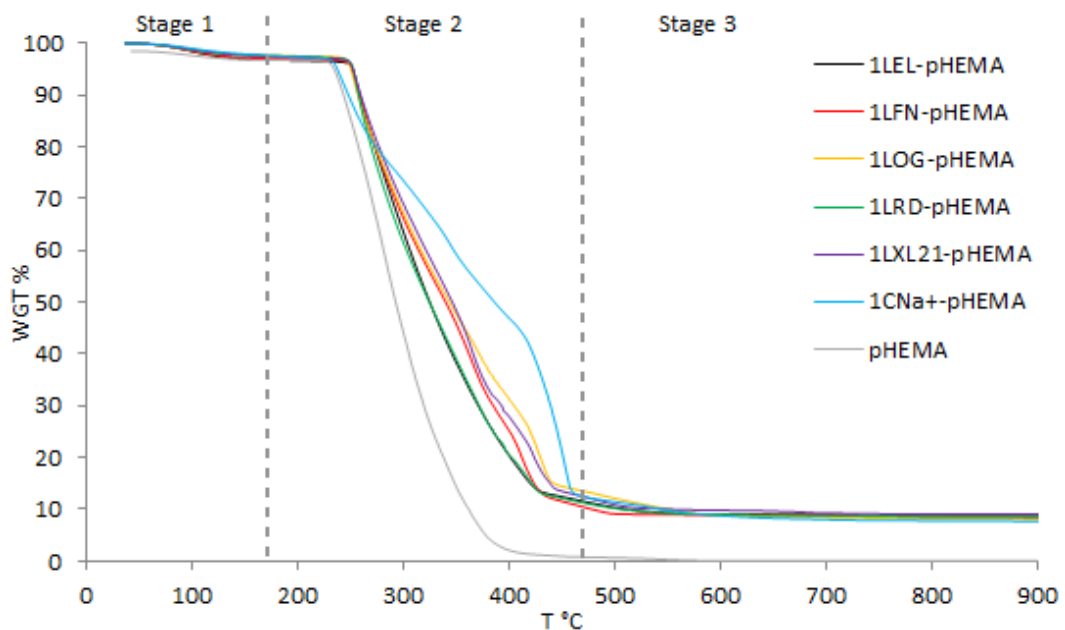


Figure 5.7 TGA thermograms of pHEMA homopolymer and 1clay-pHEMA nanocomposites. Indicating the three stages of weight loss. Stage 1 (25 – 175 °C), Stage 2 (175 – 475 °C), and stage 3 (475 – 700 °C).

pHEMA thermal stability is modified when crosslinked by clay platelets. The onset temperature increased from 222 °C to ~246 °C on average for all the Laponite[®]-pHEMA composites, where it did not change as much for the C_{Na+}-pHEMA

nanocomposites, however, its weight loss rate was different from all other composites “Stage 2” shows that the 1L_{EL}-pHEMA and 1L_{RD}-pHEMA degrade in almost an identical behaviour.

The weight loss behaviour can relate to the clay particle size, but that is not the only affecting factor, the clay CEC may also affect the thermal behaviour of the composites. Table 5.3 summarises the weight loss and degradation stages.

Table 5.3 TGA data of pHEMA homopolymer and its (1 % clay) and (2 % clay) nanocomposites, showing weight loss % at each stage and onset temperature.

Samples	Stage1: 25–175 °C	Stage2: 175–475 °C	Stage3: 475–600 °C	Total weight loss %	Onset Temp. °C
	Weight loss %				
1LEL-pHEMA	3.05	83.79	4.68	91.52	252
1LFN-pHEMA	2.79	84.26	4.34	91.39	251
1LOG-pHEMA	2.27	82.31	7.33	91.91	249
1LRD-pHEMA	2.04	83.22	6.15	91.41	242
1XL21-pHEMA	2.36	84.17	4.42	90.95	244
2XL21-pHEMA	1.31	73.77	6.74	81.82	241
1CNa+-pHEMA	1.87	83.92	4.55	90.34	226
pHEMA	3.06	94.98	1.86	99.9	222

Figure 5.8 shows the TGA curves for 1L_{XL21}-pHEMA, 2L_{XL21}-pHEMA, and pHEMA. The onset temperatures were not significantly different as the clay-to-polymer ratio changed. However, the onset temperature at which 1L_{XL21}-pHEMA and 2L_{XL21}-pHEMA nanocomposites degrade increased by 22 °C and 19 °C, respectively when compared to the pHEMA homopolymer.

The 2L_{XL21}-pHEMA degradation (“Stage 2”, Figure 5.8) ends at a lower temperature (403 °C) than the 1L_{XL21}-pHEMA (448 °C) perhaps due to the lower polymer content within it. The total weight loss for the 1L_{XL21}-pHEMA (90.95 %) was almost 10 % more than the total weight loss for the 2L_{XL21}-pHEMA (81.82 %). These percentages can be related to the amount of clay and polymer associated in each composite. After “Stage 2” carbonaceous char still present. On dry bases; the 1L_{XL21}-pHEMA has a 1:9 clay-to-polymer ratio and the weight loss curve of the pHEMA shows a weight loss of 99.9 %, this keeps only about 10% of the initial weight after decomposition which is on dry bases in 10 % of the 1L_{XL21}-pHEMA composite, and the same applies for the 2L_{XL21}-pHEMA which on dry bases has 2:8 clay-polymer ratio.

The clay-to-polymer ratio does not play a major role in enhancing the clay-pHEMA composite thermal stability as the onset temperature values are not significantly different and the weight loss rates through “Stage 2” are almost identical for both composites. [28]

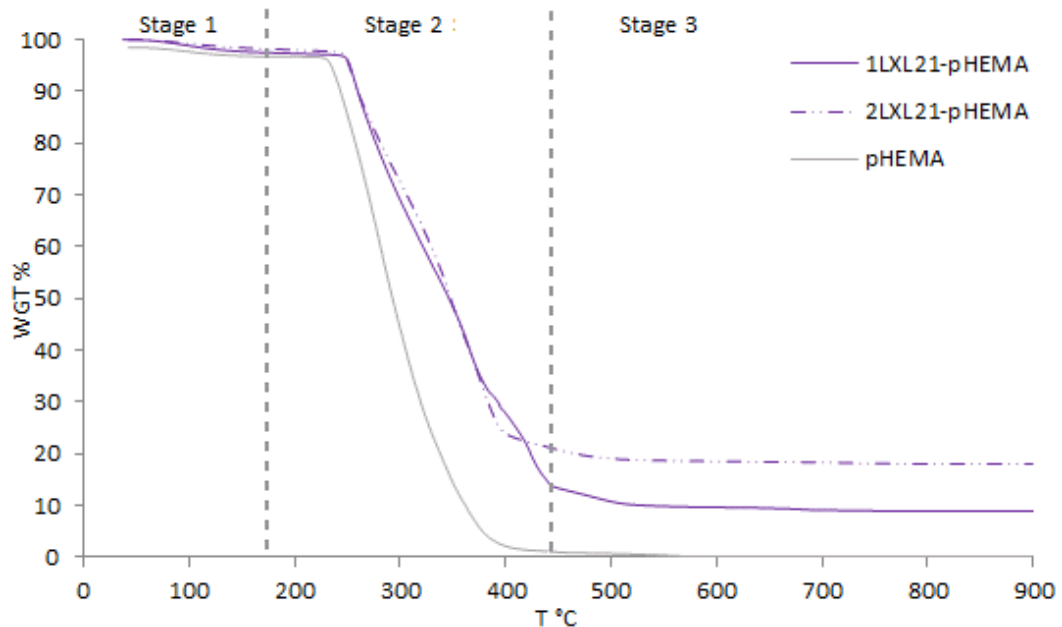


Figure 5.8 TGA thermograms of pHEMA homopolymer, 1LXL21-pHEMA, and 2LXL21-pHEMA nanocomposites. Indicating the three stages of weight loss. Stage 1 (25 – 175 °C), Stage 2 (175 – 475 °C), and stage 3 (475 – 700 °C).

The presence of clay platelets and carbonaceous char may also make it harder for the degraded polymers (as volatile gases) to exit from the nanocomposite structure. Figure 5.9 shows the pathways, which volatile decomposition products must pass through from A to B in homopolymer and the clay-polymer nanocomposite. The total distance significantly increases with the presence of the clay platelets. This makes it harder for volatile decomposition products to travel across the clay-polymer nanocomposite structure, which results in more polymeric chains kept in the clay-polymer matrix at lower temperature and enhances the thermal stability of the clay-pHEMA composites when compared to the neat pHEMA. [29][24]

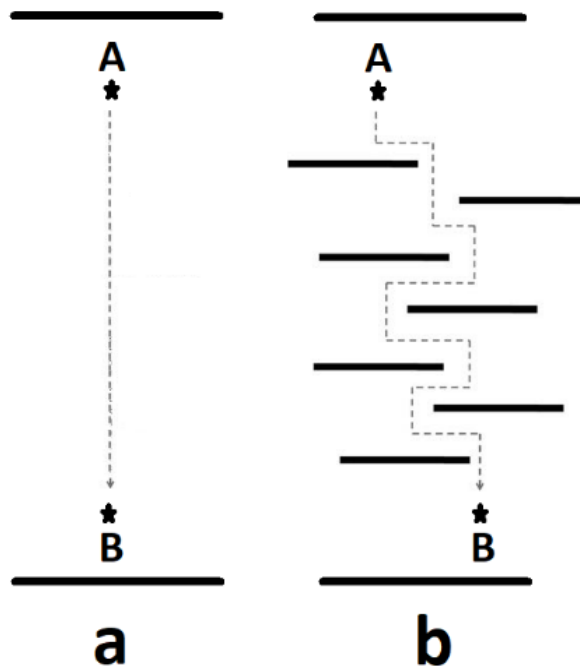


Figure 5.9 Models for the pathways of volatile decomposition products in a) Homopolymer and b) Clay-polymer nanocomposites. Modified from [30].

5.1.4 SEM Morphology Observation of Clay-pHEMA Nanocomposite

The clay-polymer nanocomposites were flash-frozen after the crosslinking process. The free water transforms into ice. This quenching process in liquid nitrogen and water solidification leads to a tubular polymer structure with channel pores. [31] As water solidification in the clay-polymer structure takes place the ice acts as a porogen. This process is called ice-templating, the polymer chains are rejected by the growing ice as the polymer solubility is lower in ice than in liquid water. As water leaves the system during freeze-drying a continuous polymer network is formed that takes the shape of the frozen water forming ice voids. [32] In this study, these voids are referred to as pores. [33] The size of these pores is related to the wettability of the clay-polymer nanocomposite; the more hydrophobicity the larger the pores. [34]

The influence of different clays on the structure of the nanocomposite is discussed in this section. Figure 5.10 shows SEM images of the fractured surface morphology

of the (1 % clay)-pHEMA nanocomposites. The poor quality images from some samples were unavoidable due to charging effects.

The images show similarities and differences between the different composites. The materials possess irregular rough surfaces [26] with a uniform and porous structure which may be a result of the homogeneity of the clay dispersion and clay-monomer mixtures before polymerisation. [25] It can be seen from the images that the nanocomposites have interconnected porous microstructures. This could dramatically facilitate the migration in and out of the nanocomposites or containing water or other materials. [17] [35]

L_{EL} , L_{OG} , and L_{RD} with pHEMA (Figure 5.10 a, c, and d) create similar morphologies, with thin and solid walls. Porosity is similar to a uniform pore distribution, pore size averaged around 5.7 μm for $1L_{EL}$ -pHEMA, 5.6 μm for $1L_{OG}$ -pHEMA, and 4.8 μm for $1L_{RD}$ -pHEMA. Table 5.4 shows the pore size average over 25 pores measured and the standard deviation values for all clay-pHEMA nanocomposites.

The $1L_{XL21}$ -pHEMA (Figure 5.10 e) has a smaller pore size (average 4.1 μm) when compared to $1L_{EL}$ -pHEMA, $1L_{OG}$ -pHEMA, and $1L_{RD}$ -pHEMA. The L_{XL21} has a higher CEC value than L_{EL} , L_{OG} , and L_{RD} which allows more crosslinking points.

The SEM image of $1L_{FN}$ -pHEMA (Figure 5.10 b) shows a regular “mountain valley” layered structure with a smoother surface morphology than other clay grades; the pore size averaged 4 μm . $1C_{Na+}$ -pHEMA (Figure 5.10 f) does show a porous layered structure with pore size average of 6.7 μm , C_{Na+} has a big particle size which makes it harder to form agglomerations as polymer chains have more area to interact with the clay platelets.

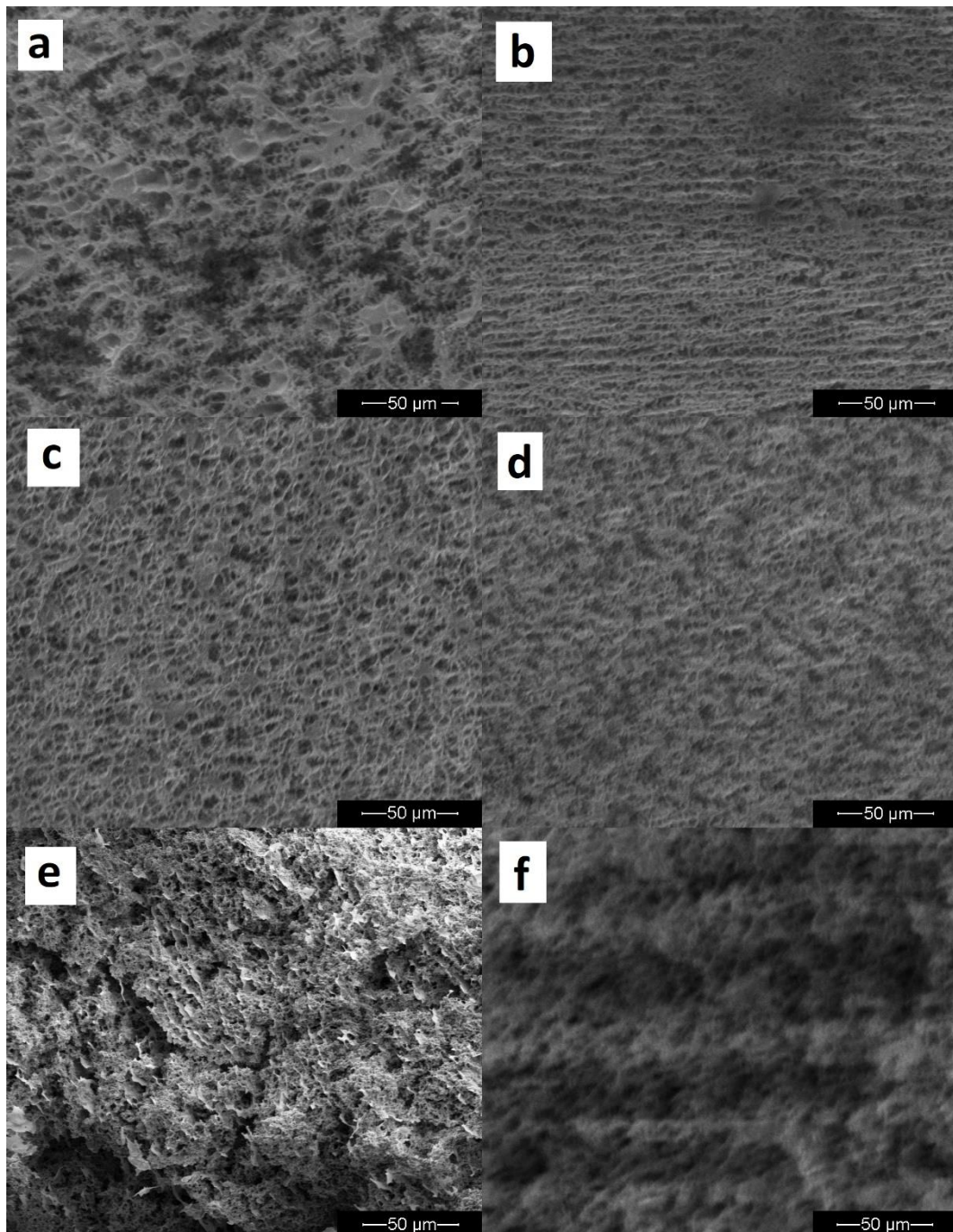


Figure 5.10 SEM images of (1% clay)-pHEMA nanocomposites showing microstructure and pore size differences as a result of the effect of clay grade used. a) 1LEL-pHEMA b) 1LFN-pHEMA c) 1LOG-pHEMA d) 1LRD-pHEMA e) 1LXL21-pHEMA f) 1CNa+-pHEMA.

Figure 5.11 shows the SEM images of L_{XL21} -pHEMA with different clay-to-polymer ratios. The $1L_{XL21}$ -pHEMA composite has a denser micro-network structure with smaller pore size than the $2L_{XL21}$ -pHEMA (4.3 and 6.7 μm , respectively). The $2L_{XL21}$ -pHEMA composite with a higher clay-to-polymer ratio creates more crosslink junctions with shorter polymeric chains, the result is a less dense microporous

structure with larger pore size. The 2L_{XL21}-pHEMA composite has a rougher surface morphology. The higher the clay content the more space clay platelets occupy and the faster the crosslinking, which results in shorter the polymeric chains. With more clay platelets more connections to polymer chains are created, which should show relatively higher mechanical strength and robustness. [36] Given these observations, the pore size and density can be controlled by controlling crosslinker dosage relative to polymer concentration, and by controlling the clay type used as a crosslinker. [17]

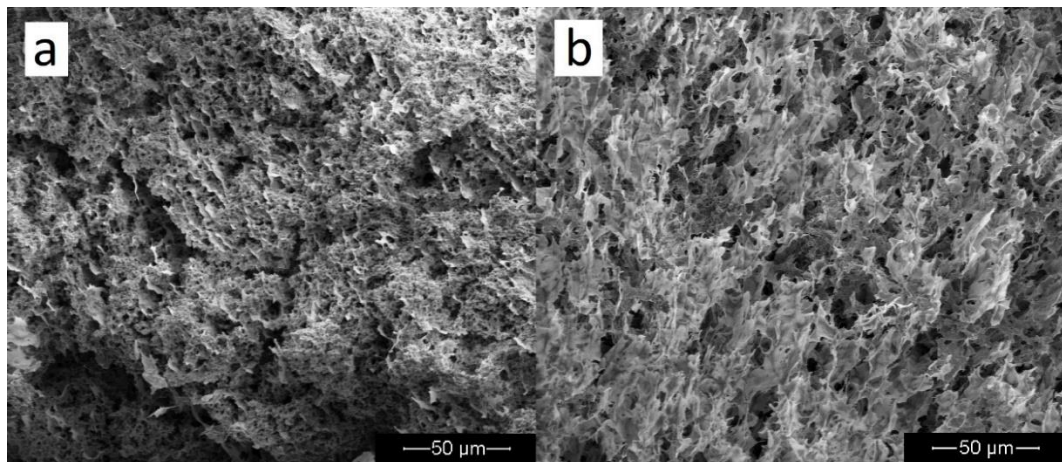


Figure 5.11 SEM images of LXL21-pHEMA nanocomposites. a) 1LXL21-pHEMA b) 2LXL21-pHEMA showing the effect of increasing clay content on the pore size and the microstructure.

Table 5.4 Average pore size and standard deviation of (n=25) for clay-pHEMA nanocomposites.

	Pore size (μm)	SD
1L_{EL}-pHEMA	5.7	2.1
1L_{FN}-pHEMA	4.0	0.9
1L_{OG}-pHEMA	5.6	0.9
1L_{RD}-pHEMA	4.8	1.0
1L_{XL21}-pHEMA	4.3	0.9
2L_{XL21}-pHEMA	6.7	1.8
1C_{Na+}-pHEMA	6.7	1.2

Figure 5.12 shows the relationship between the clay properties (particle size and CEC) and the average pore size determined by SEM. The CEC effect on the pore size is clearer to observe the higher the value the smaller the pore size.

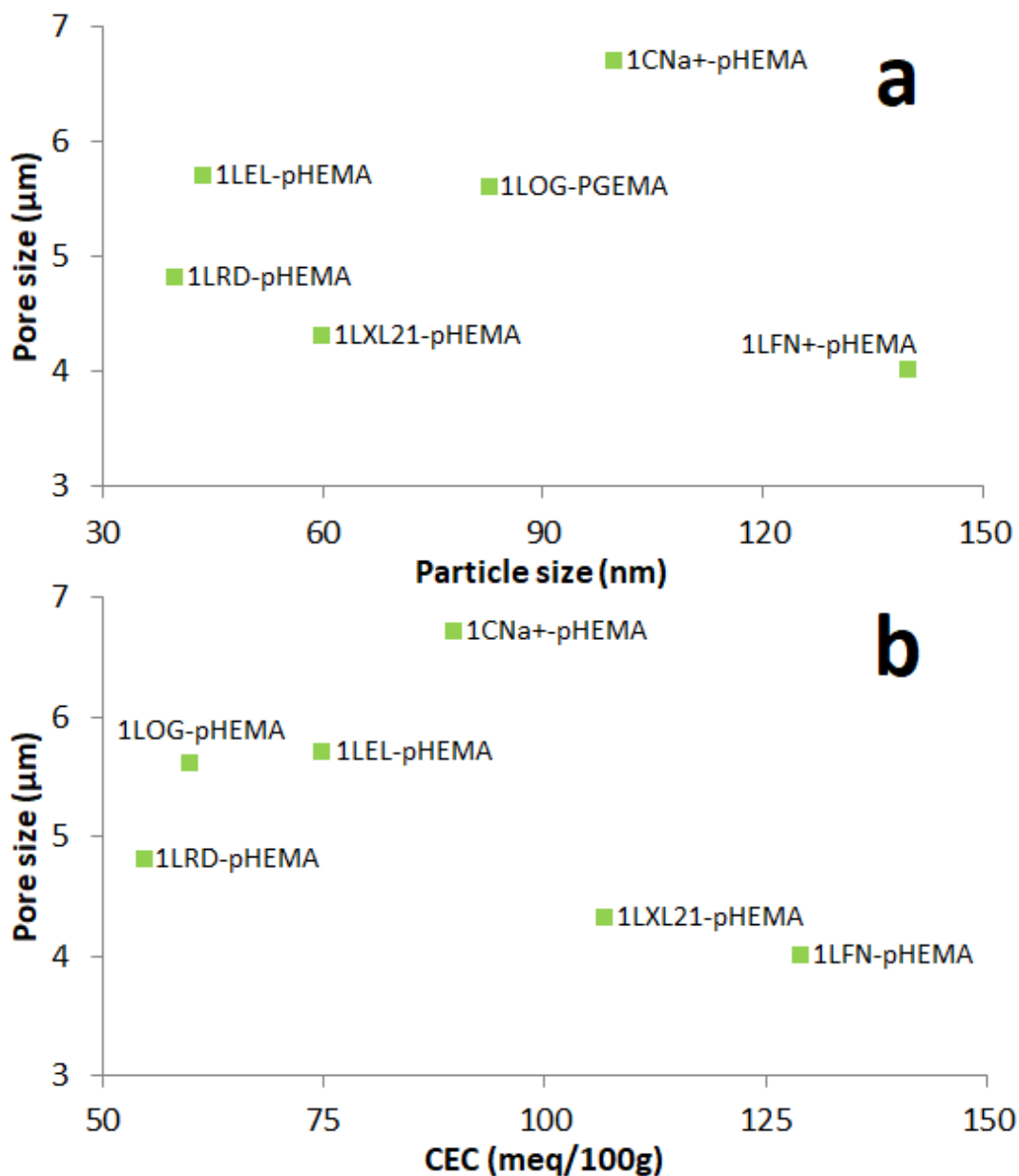


Figure 5.12 (1 % clay)-pHEMA composites pores size as a function of a) Clay particle size b) Clay CEC.

5.1.5 FTIR Spectroscopic Analysis of Clay-pHEMA Nanocomposites

To examine the nature of the interactions between the different clay types and the pHEMA in clay-pHEMA nanocomposites, FTIR spectra for the clay, pHEMA homopolymer, (1 % clay)-pHEMA, and (2 % clay)-pHEMA for selected clays were obtained to show any changes to the homopolymer FTIR fingerprint and whether there is any interaction between the polymer chain in the clay-polymer matrix. [37]

Figure 5.13 shows FTIR spectra in the spectral range (4000 - 400 cm^{-1}) for the monomer HEMA and the dried pHEMA homopolymer at room temperature. [10] Upon polymerisation, the stretching band due to C=C at $\sim 1636 \text{ cm}^{-1}$ in the HEMA monomer spectrum is no longer present. [37] The -OH stretching band of HEMA at 3425 cm^{-1} also shifts to a lower wavenumber in pHEMA (3391 cm^{-1}). The C=O band at 1715 cm^{-1} of HEMA shifts to a higher wavenumber (1718 cm^{-1}) upon polymerisation

The C-H stretching region has three bands at around (2985 , 2947 , and 2884) cm^{-1} . The C-H deformation region has bands at approximately 1460 cm^{-1} and 1450 cm^{-1} and 1388 cm^{-1} . Table 5.5 summarises the main band's positions for both HEMA monomer and pHEMA homopolymer.

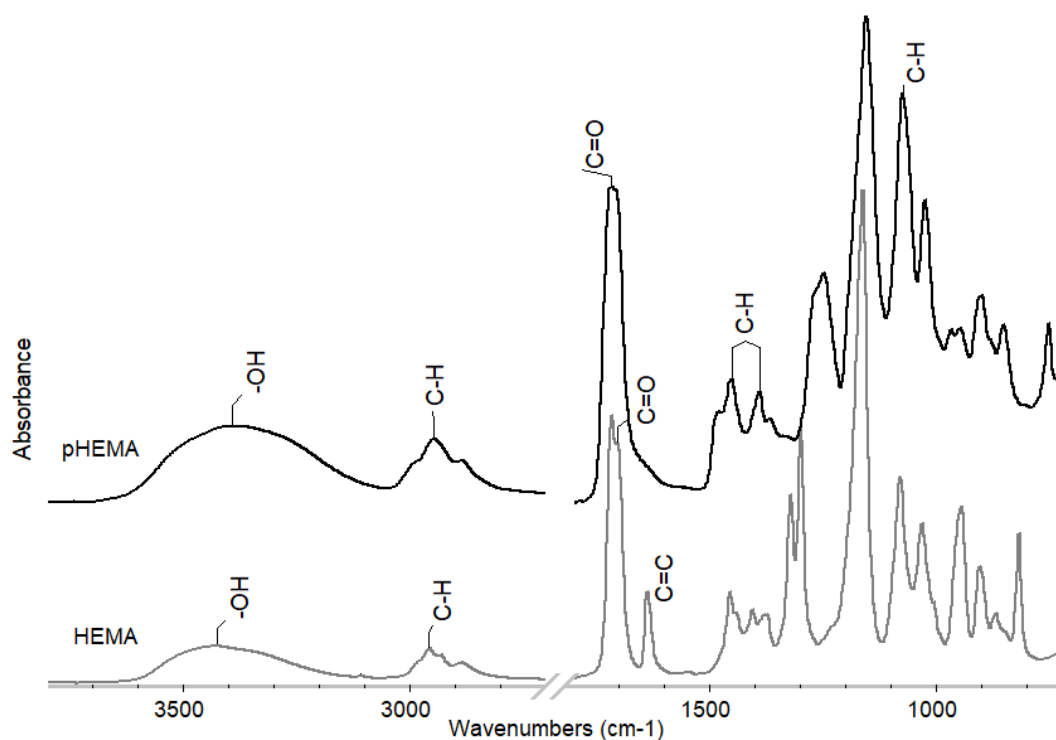


Figure 5.13 FTIR spectra of HEMA and pHEMA homopolymer showing the main characteristic bands in the range $3800 - 900 \text{ cm}^{-1}$.

Table 5.5 FTIR bands positions for HEMA monomer and pHEMA homopolymer.

	-OH	C-H			C=O	C=C	C-H		
HEMA	3425	2957	2930	2886	1715	1636	1453	1378	1076
pHEMA	3391	2985	2947	2884	1718	-	1450	1388	1071

Figure 5.14 (a) shows some of the major details of the FTIR spectra for 1L_{EL}-pHEMA nanocomposite compared to L_{EL} and pHEMA homopolymer. The 1L_{EL}-pHEMA spectrum also contains information on both of its components. The 3100 - 3700 cm⁻¹ in the -OH stretching region for the band of the 1L_{EL}-pHEMA shifts to a lower wavenumber when compared to the -OH band for the pHEMA (3384 and 3391 cm⁻¹, respectively) providing evidence of the association of hydrogen bonds with the addition of the nanoclay. [38] The C=O stretching band did not show any significant shifts from 1718 cm⁻¹ in pHEMA and 1717 cm⁻¹ in 1L_{EL}-pHEMA.

As the clay platelets are dispersed and the polymer chains find their way into the clay galleries, Si-O bands shift and show overlapping features at ~1120 cm⁻¹, ~1000 cm⁻¹ (in-plane Si-O) and ~1080 cm⁻¹ (out-of-plane Si-O). A significant variation in the Si-O stretching region of the 1L_{EL}-pHEMA in comparison with the spectra of L_{EL} can be observed. In the 1L_{EL}-pHEMA nanocomposites, well-separated Si-O peaks can be observed, which correspond to the in-plane (995 cm⁻¹) and out-of-plane Si-O (1070 cm⁻¹) modes. The out-of-plane Si-O mode at 1070 cm⁻¹ is not clearly observed since it overlaps a band of the polymer at the same position. However, its presence is judged (as was the case with the acrylamides) because of an increase at this position relative to the polymer band at 1150 cm⁻¹. The Si-O peaks in the 1L_{EL}-pHEMA composite are quite strong and a general shift toward higher wavenumber of the Si-O modes when compared with the L_{EL} indicates evidence for clay exfoliation. [39]

The clay-to-polymer ratio in the dried 1L_{EL}-pHEMA nanocomposite is 1:9. The band related to Si-O in the 1L_{EL}-pHEMA is positioned at 995 cm⁻¹, which has shifted to a higher wavenumber from 946 cm⁻¹ in the L_{EL}. This change suggests that the Si-O bond has been involved in the interaction between the polymer chains and the clay platelets. Table 5.6 show band positions for L_{EL}, pHEMA and 1L_{EL}-pHEMA composite.

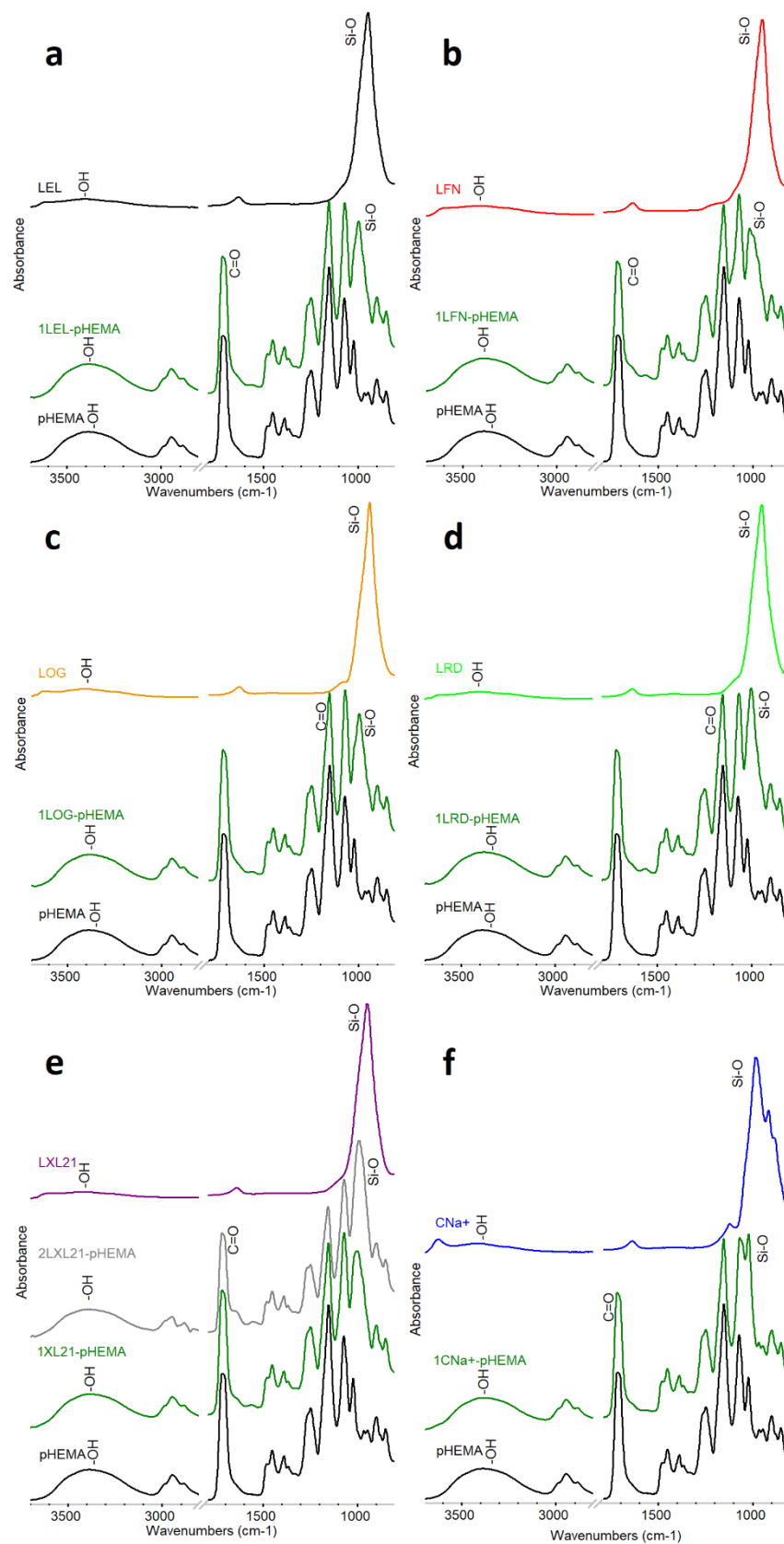


Figure 5.14 FTIR spectra for a) 1LEL-pHEMA, b) 1LFN-pHEMA, c) 1LOG-pHEMA, d) 1LRD-pHEMA, e) 1XL21-pHEMA, f) 1CNa+-pHEMA nanocomposites compared to the clay and homopolymer pGMAc. Samples are dried powder. Offset for clearance.

Figure 5.14 (b to f) shows a comparison between pHEMA, different clay types and the corresponding (1 % clay)-pHEMA and (2 % clay)-pHEMA. In general, most of the (1 % clay-pHEMA) composites FTIR spectra show a similar trend to the 1L_{EL}-pHEMA with the -OH band shifting to a lower wavenumber and the Si-O band shifting to a higher wavenumber and showing more details. Table 5.6 provides more details about bands positions for all clay-pHEMA nanocomposites with clay Si-O positions and the pHEMA homopolymer to support Figure 5.14 and for ease of comparison.

Figure 5.14 (e) shows spectra for L_{XL21}-pHEMA and different clay-to-polymer ratios in comparison with L_{XL21} and pHEMA. The 2L_{XL21}-pHEMA shows a similar trend, however; the Si-O shows a smaller shift to 990 cm⁻¹ when compared to the 1L_{XL21}-pHEMA (1000 cm⁻¹). The 2L_{XL21}-pHEMA also shows a higher intensity band at 1070 cm⁻¹ which may be evidence that the band at that wavenumber is the Si-O out-of-plane.

The 1C_{Na+}-pHEMA spectrum (Figure 5.14 (f)) shows a different behaviour as both the Si-O bands have similar intensities, the C_{Na+} is the only clay that had two different Si-O related bands and as the clay platelets are involved in the 1C_{Na+}-pHEMA both shift to a higher wavenumber.

Table 5.6 FTIR bands positions for clays, pHEMA, (1 % clay)-pHEMA, and 2L_{XL21}-pHEMA.

	-OH	Si-O	
pHEMA	3391	1071	-
L_E	3408	-	946
1L_{EL}-pHEMA	3384	1070	995
L_{FN}	3408	-	949
1L_{FN}-pHEMA	3383	1071	998
L_{OG}	3407	-	940
1L_{OG}-pHEMA	3384	1070	995
L_{RD}	3405	-	945
1L_{RD}-pHEMA	3384	1066	1000
L_{XL21}	3417	-	942
1L_{XL21}-pHEMA	3387	1070	1000
2L_{XL21}-pHEMA	3389	1070	990
C_{Na+}	3418	981	912
1C_{Na+}-pHEMA	3382	1067	1020

5.1.6 Rheological Analysis and Properties of Clay-pHEMA Nanocomposites

To make sure the test parameters were appropriate; an LVE check was required for a fully formed nanocomposite. A 1L_{EL}-pHEMA sample was placed on the rheometer. Time to reach equilibrium was determined by a time sweep as a first step. A strain sweep from 0.1 % to 100 % strain was then conducted at room temperature under arbitrarily chosen frequency for the fully polymerized nanocomposite sample. A strain of 1 % was selected for subsequent sweeps. [40] The results of the strain sweeps for 1L_{EL}-pHEMA are shown in Figure 5.15.

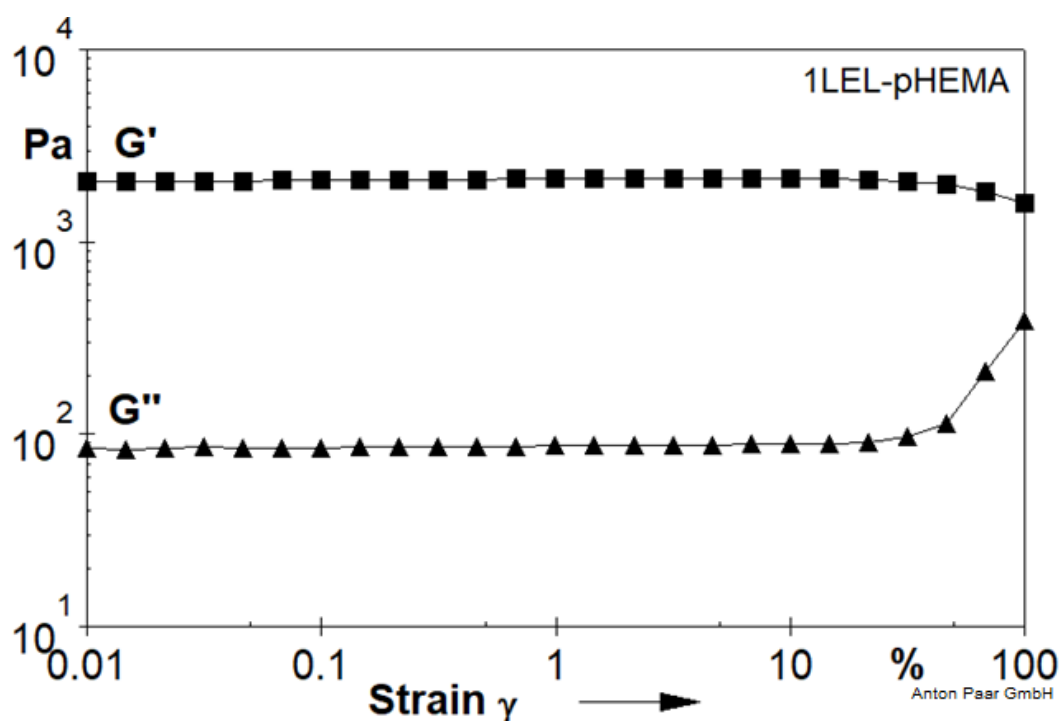


Figure 5.15 Strain sweep. The LVE limit was determined with respect to strain. G' was determined from 0.1 to 100 % strain for 1LEL-pHEMA.

5.1.6.1 Yield Stress for Clay-pHEMA Nanocomposites

The flow curves in Figure 5.16 show the yield stress values of the 1L_{XL21}-pHEMA and 2L_{XL21}-pHEMA nanocomposite. The increased elasticity caused by higher clay-to-polymer ratio leads to higher yield stress, the 2L_{XL21}-pHEMA has a higher resistance to flow (Table 5.7) due to more crosslinks between the clay platelets and the polymeric chains. The physical nature of the crosslinking between the clay and the

polymer chain give the composite more elasticity as there is no chemical bond present. This support the results from the SEM images which show that the 1L_{XL21}-pHEMA has a denser structure than the 2L_{XL21}-pHEMA due to more polymer and less crosslink point in the composite.

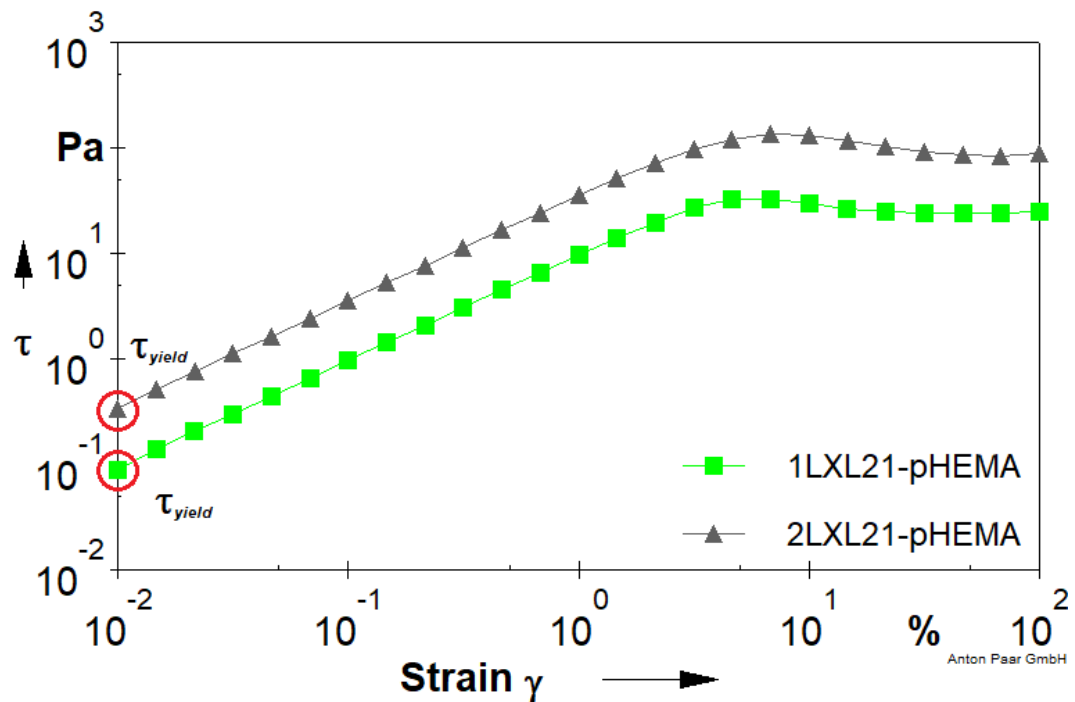


Figure 5.16 Flow curve showing yield stress for 1LXL21-pHEMA and 2LXL21-pHEMA nanocomposite.

Table 5.7 τ_{yield} (Pa.) as an average for n=3 and SD for the 1L_{XL21}-pHEMA and 2L_{XL21}-pHEMA.

Sample	τ_{yield}	SD
1L _{XL21} -pHEMA	0.0880	0.0024
2L _{XL21} -pHEMA	0.3313	0.0184

5.1.6.2 Storage (G') and Loss (G'') Moduli Behaviour for Clay-pHEMA Nanocomposite

5.1.6.2.1 Amplitude Sweep (Function of Strain)

Figure 5.17 shows the behaviour G' and G'' moduli as a function of strain for 1L_{XL21}-pHEMA and 2L_{XL21}-pHEMA, both composite show an elastic behaviour (linear) to a certain strain limit where G' decrease indicating the LVE. Table 5.8 show the LVE limits for both composites, the 2L_{XL21}-pHEMA has a larger LVE region compared to the 1L_{XL21}-pHEMA as a result of its higher elastic properties which support the findings from the yield stress test earlier.

As the composites reach the limits of the LVE range the G' and G'' moduli values change at a faster rate to the limit they crossover. The yield value at the crossover point is called the critical strain (γ_c) and the nanocomposite starts to change from gel-like material to a liquid-like material as G'' become higher in value than G' . This may happen as the crosslink point break and the polymer within the composite can move more freely. A thixotropy test may be ideal to provide more evidence to this assumption but due to time limitation, it was not done as a part of this experiment.

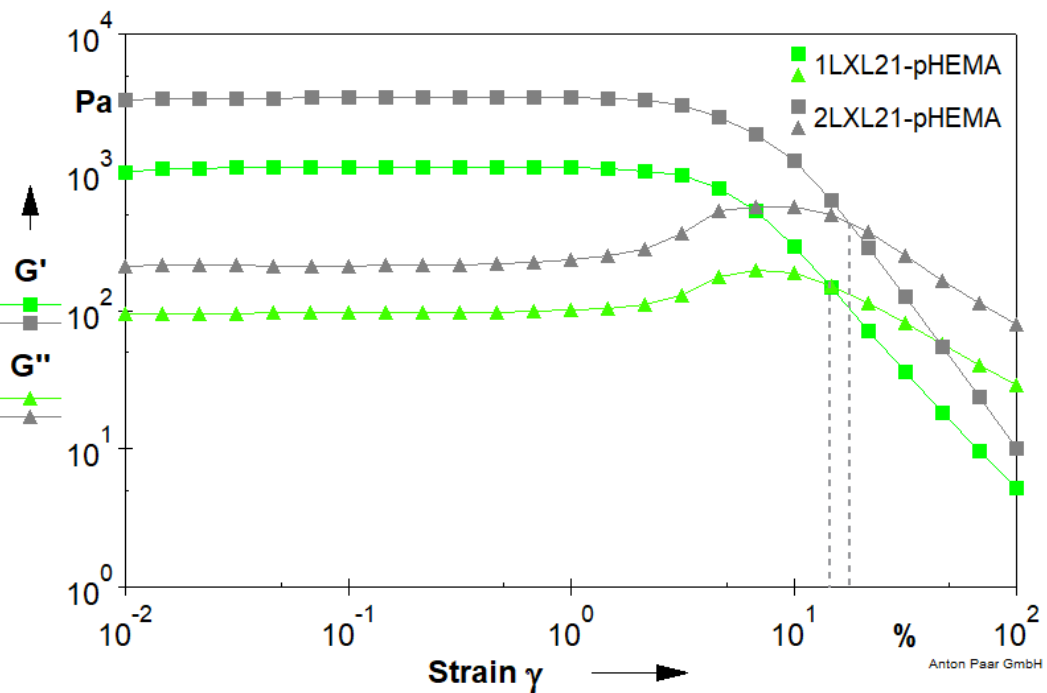


Figure 5.17 Evolution of storage modulus G' and loss modulus G'' as a function of strain from 0.01 % - 100 % for 1LXL21-pHEMA and 2LXL21-pHEMA nanocomposite. Transition point (solid-like to fluid-like) points.

Table 5.8 strain values and G' as an average of ($n=3$) for LVE region limits (strain % and G' Pa.) and Crossover transition point (solid-like to fluid-like) strain values.

	LVE		Crossover Point	
	Strain %	G' Pa.	Strain %	SD
1L _{XL21} -pHEMA	1.0003	1081	14.34	1.21
2L _{XL21} -pHEMA	1.4699	3406	17.66	0.67

5.1.6.2.2 Frequency Sweep (Function of Frequency)

The Frequency sweeps from 0.01 to 100 Hz were conducted at a strain of 1 % at room temperature for L_{XL21}-pHEMA at two different clay-to-polymer ratios. Both composites show no significant variation of the moduli values over the frequency

range (Figure 5.18). The composites show a frequency-independent behaviour at a strain of 1 %. The 2L_{XL21}-pHEMA composite shows higher modulus value when compared to the 1L_{XL21}-pHEMA as expected.

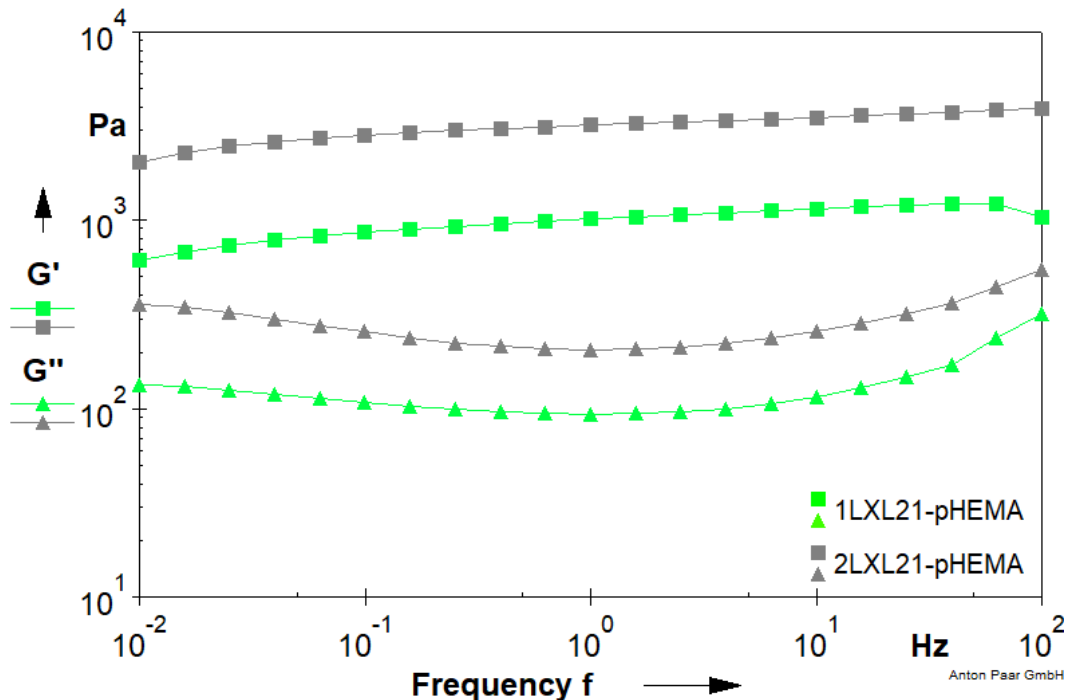


Figure 5.18 Evolution of storage modulus G' and loss modulus G'' as a function of frequency from 0.01 - 100 Hz for 1LXL21-pHEMA and 2LXL21-pHEMA nanocomposite.

5.2 Clay-pHPMA Characterisation and Rheological Properties

Hydroxypropyl methacrylate (HPMA) is a monomer with excellent chemical and biological stability. When polymerised; pHPMA becomes a water-immiscible polymer with great shrinkage and water resistance properties. [27][41][42]









5.2.1 Clay-pHPMA Nanocomposites

Table 5.9 shows photographs of the clay-pHPMA nanocomposites. The effect of different clays and clay-to-polymer ratios is observable upon testing the composites with a spatula for general observation and differences between the samples. The pHPMA homopolymer was an elastic rubbery block. The 1L_{EL}-pHPMA is a softer and more elastic composite when compared with the pHPMA homopolymer. There is also aqueous media on top of the sample which may be caused by the existence of

clay in the composite acting as a crosslinker bringing the polymer chains closer to one another affecting the size of the clay-polymer nanocomposite, which leads to a decrease in the amount of water the composite can hold. The 1L_{EL}-pHPMA shares these observations with the 1L_{OG}-pHPMA and the 1L_{RD}-pHPMA.

The 1L_{FN}-pHPMA is a more elastic white block composite than the pHPMA homopolymer but less elastic than the 1L_{EL}-pHPMA, 1L_{OG}-pHPMA and 1L_{RD}-pHPMA. There is evidence of aqueous media surrounding the sample forming a layer in the reaction vessel. The 1L_{XL21}-pHPMA is a liquid suspension and the product was easily handled with a syringe. As with pHPMA, 2L_{XL21}-pHPMA was prepared to establish which has higher viscoelastic properties. The 1C_{Na+}-pHPMA nanocomposite was a soft flaky material in water, as the sample was pulled out of the glass vial it disintegrated as it was soft and weakly structured.

Table 5.9 General observation of clay-pHPMA nanocomposites, samples were investigated by pouring/pulling and poking with a small lab spatula at room temperature.

pHPMA	1L_{EL}-pHPMA	1L_{FN}-pHPMA	1L_{OG}-pHPMA	1L_{RD}-pHPMA	1L_{XL21}-pHPMA	2L_{XL21}-pHPMA	1C_{Na+}-pHPMA
A white block of elastic solid gel	A white block of elastic solid gel with cloudy ~ 25 % cloudy water on top	A white block of elastic solid gel with cracks. ~ 15 % cloudy water on top	A white block of elastic solid gel with cracks. ~ 15 % cloudy water on top	A white block of elastic solid gel with ~ 25 % cloudy water on top	A white block of soft elastic free-flowing gel with ~ 5 % clear water on top	A white soft flowing gel. Less elastic than the 1L _{XL21} -pHEMA	A white block of soft elastic gel with cracks
							

5.2.2 XRD Characterisation of Clay-pHPMA Nanocomposites

The XRD traces of powder L_{EL} , pHPMA, homopolymer, and L_{EL} -pHEMA nanocomposites are presented in Figure 5.19 (a). The X-ray reflections predominantly corresponded to the pHPMA homopolymer. [10]

At low angle ($2\theta \leq 5^\circ$) the $1L_{EL}$ -pHPMA XRD reflection shows an increasing baseline toward low angle and no reflection was observed around that angle that can be related to the $2\theta = 5.8^\circ$ ($d = 15.24 \text{ \AA}$) in the XRD reflection of the L_{EL} , which suggests clay well dispersion if not exfoliation in the composite. The diffraction reflections at around $2\theta = 7.7^\circ$ ($d = 11.48 \text{ \AA}$) correspond to the polymer within the composite (pHPMA at $2\theta = 7.6^\circ$ ($d = 11.63 \text{ \AA}$)). [16][18][19]

At $2\theta = 17.8^\circ$ ($d = 4.99 \text{ \AA}$) the XRD trace of the $1L_{EL}$ -pHPMA shows a reflection which corresponds to the $2\theta = 17.7^\circ$ ($d = 5.01 \text{ \AA}$) pHPMA, this is the clearest reflection in the composite XRD. The L_{EL} diffraction reflection at $2\theta = 19.4^\circ$ ($d = 4.57 \text{ \AA}$) was not observed due to being overlapped by the wide pHPMA reflection (2θ in the range of $10^\circ - 25^\circ$), the case was the same for L_{EL} diffraction reflection $2\theta = 27.5^\circ$ ($d = 3.24 \text{ \AA}$) and the pHPMA diffraction reflection $2\theta = 29.8^\circ$ ($d = 3.00 \text{ \AA}$). The diffraction reflection at around $2\theta = 34.9^\circ$ ($d = 2.57 \text{ \AA}$) in the XRD trace of the $1L_{EL}$ -pHPMA correspond to the d_{110} in the XRD trace of the neat L_{EL} at $2\theta = 34.5^\circ$ ($d = 2.60 \text{ \AA}$), this diffraction shows the presence of L_{EL} in the nanocomposite matrix.

Most of the other clay-pHPMA XRD traces show similar behaviours to $1L_{EL}$ -pHPMA. However, some differences can easily be observed. Figure 5.19 (b) shows the XRD traces of $1L_{FN}$ -pHPMA and its components individually. The diffraction reflection at $2\theta = 6.6^\circ$ ($d = 13.35 \text{ \AA}$) in the trace of the $1L_{FN}$ -pHPMA correspond to the very clear sharp reflection of d_{001} in the XRD trace of L_{FN} $2\theta = 6.6^\circ$ ($d = 13.39 \text{ \AA}$). This observation provides evidence that the $1L_{FN}$ -pHPMA is a microstructure nanocomposite. [18]

The 1L_{OG}-pHPMA and 1L_{RD}-pHPMA nanocomposite XRD reflections Figure 5.19 (c and d) show similar behaviour to that of 1L_{EL}-pHPMA showing the same evidence of clay well dispersed if not exfoliated. [16][18][19] Table 5.10 provides the positions for the clay-pHPMA reflections as well as for the clay types and pHPMA homopolymer.

The 1L_{XL21}-pHPMA and 2L_{XL21}-pHPMA nanocomposite Figure 5.19 (e) show the effect of different clay-to-polymer ratios as different intensities and shifts of the diffraction reflection. The diffraction reflection at $2\theta = 6.6^\circ$ ($d = 13.35 \text{ \AA}$) in the trace of the 1L_{XL21}-pHPMA and 2L_{XL21}-pHPMA correspond to the reflection of d_{001} in the XRD trace of L_{FN} $2\theta = 6.4^\circ$ ($d = 13.81 \text{ \AA}$), these results suggest that both L_{XL21}-pHPMA are microstructure nanocomposite. The reflection at $2\theta = 17.4^\circ$ ($d = 5.10 \text{ \AA}$) in the XRD trace of the 1L_{XL21}-pHPMA has a higher intensity and is also closer to the angle of the reflection on the pHPMA XRD trace ($2\theta = 17.7^\circ$ ($d = 5.01 \text{ \AA}$)), whereas for the 2L_{XL21}-pHPMA corresponding reflection was at ($2\theta = 18.3^\circ$ ($d = 4.84 \text{ \AA}$)) with a shift to a higher angle towards the d_{100} of the clay (Table 5.10) as a result of more clay in it. The diffraction reflection related to the clay d_{110} intensity has also higher intensity in the 2L_{XL21}-pHPMA.

Figure 5.19 (f) shows the XRD trace of 1C_{Na+}-pHPMA nanocomposite, the decreasing baseline at angle $\geq 5^\circ$ shows evidence about the clay exfoliation in the nanocomposite. [16][18][19] No evidence of the pHPMA was observed in the nanocomposite trace. The reflection $2\theta = 8.3^\circ$ ($d = 10.70 \text{ \AA}$) is possibly due to the clay and represents a portion of collapsed clay, i.e. clay with no water or polymer present within the interlayer. The diffraction reflections at $2\theta = 19.5^\circ$ ($d = 4.56 \text{ \AA}$) and $2\theta = 34.7^\circ$ ($d = 2.58 \text{ \AA}$) are indications of the clay presence in the composite as they match the C_{Na+} d_{100} and d_{110} positions (Table 5.10). These results need further experimentation to be understood from a structural point.

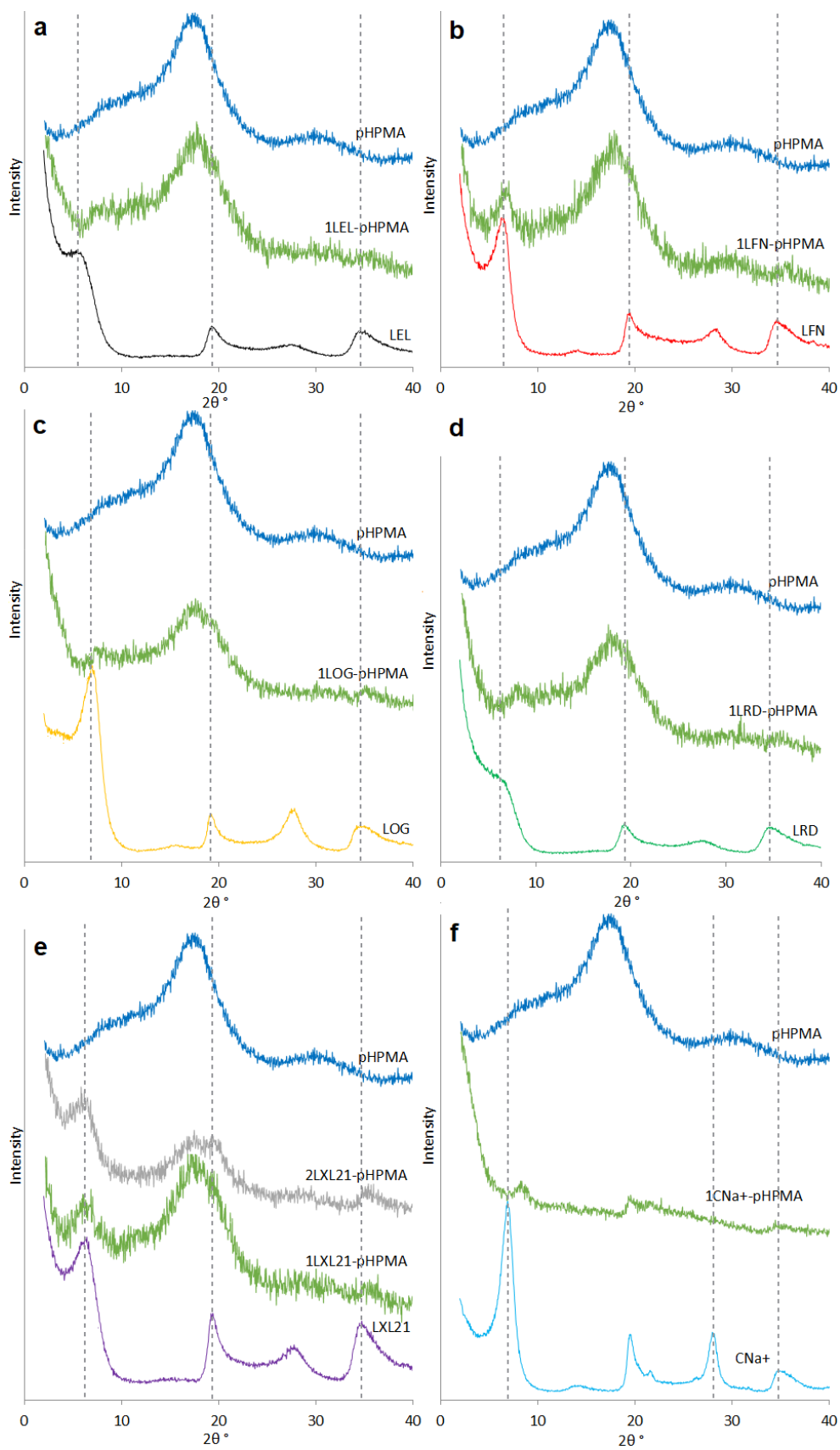


Figure 5.19 XRD traces for clays, pHPMA and its nanocomposite showing differences in the XRD traces. Intensities are irrelevant in value to the clay's traces. By clay the plots are a) LEL, b) LFN, c) LOG, d) LRD, e) LXL21, f) CNa+. All samples are ground powders and offset for clearance.

The diffraction reflections in the XRD trace of the clay-pHPMA indicates that clay in the dried nanocomposite was well dispersed as it mainly corresponds to the pHPMA. However, the composite still provides evidence about the clay incorporation in the composite structure. [3][8]

Table 5.10 Interplanar distances and 2θ of different clay (powder) and its corresponding clay-pHPMA nanocomposites samples obtained from XRD data.

Sample	d_{001}		d_{100}		d_{110}	
	2θ	d (Å)	2θ	d (Å)	2θ	d (Å)
pHPMA	7.6	11.63	17.7	5.01	-	-
LEL	5.8	15.24	19.4	4.57	34.5	2.60
1LEL-pHPMA	7.7	11.48	17.8	4.99	34.9	2.57
LFN	6.6	13.39	19.3	4.60	34.6	2.59
1LFN-pHPMA	6.6	13.35	17.7	5.02	35.1	2.56
LOG	7.1	12.45	19.1	4.65	34.6	2.59
1LOG-pHPMA	7.2	12.31	17.5	5.06	34.5	2.60
LRD	6.5	13.60	19.4	4.57	34.6	2.59
1LRD-pHPMA	7.5	11.85	17.1	5.18	34.7	2.58
LXL21	6.4	13.81	19.3	4.60	34.7	2.58
1LXL21-pHPMA	6.6	13.43	17.4	5.10	34.9	2.57
2LXL21-pHPMA	6.6	13.35	18.3	4.84	34.7	2.59
CNa+	7.0	12.63	19.5	4.55	34.7	2.58
1CNa+-pHPMA	8.3	10.60	19.5	4.56	34.7	2.58

5.2.3 TGA characterisation of Clay-pHPMA Nanocomposites

Figure 5.20 shows the TGA weight loss curves of pHPMA homopolymer and (1 % clay)-pHPMA nanocomposites. All (1 % clay)-pHPMA composites exhibited similar thermal behaviour with three stages of weight loss. The weight loss occurring in “Stage 1” (below 175 °C) was ascribed to the loss of free water in the samples. [27][43] The largest amount of weight loss occurs in the “Stage 2” between 220 - 460 °C [44][45] which is attributed to the decomposition of p(HPMA) organic skeleton and dehydroxylation. [46] As the temperatures go higher than 450 °C, the decomposition is due to further degradation of polymer residues with weight loss of 5 % on average. [12]

The thermal stability of pHPMA was modified when crosslinked with clay platelets. The pHPMA homopolymer onset temperature increased from 229 °C to ~243 °C on

average for the (1 % clay)-pHPMA composites. Table 5.11 shows the onset temperature for the clay-pHPMA. The 1L_{FN}-pHPMA has the lowest onset temperature of 230 °C which is still higher than the onset temperature of the pHPMA homopolymer.

The L_{OG}-pHPMA and 1L_{EL}-pHPMA composite had close onset temperatures of 240 °C and 241 °C respectively, however, the weight loss rates for both composites through “Stage 2” were different. 1L_{RD}-pHPMA, 1L_{XL21}-pHPMA had close onset temperatures (250 °C and 253 °C respectively) and had a similar weight loss behaviour to 1L_{EL}-pHPMA.

The L_{OG} and C_{Na+} corresponding pHPMA nanocomposites showed different weight loss behaviour through “Stage 2” when compared to other clay-pHPMA nanocomposites; this may be related to the clay grade as L_{OG} and C_{Na+} had different behaviours compared to the other clays when tested with TGA.

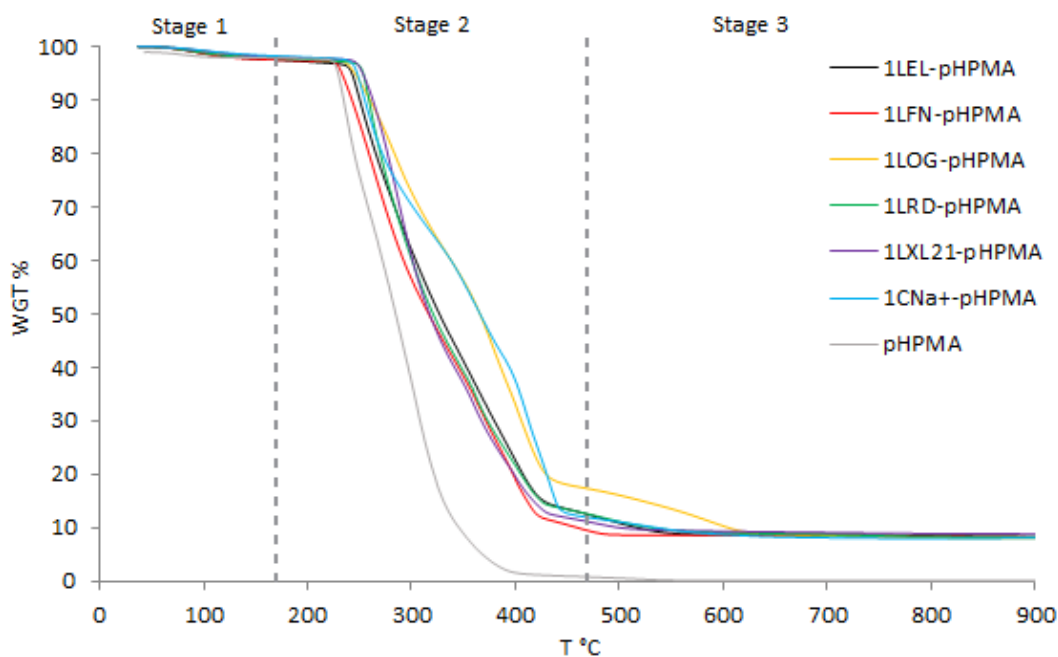


Figure 5.20 TGA thermograms of pHPMA homopolymer and 1clay-pHPMA nanocomposites indicating the three stages of weight loss. Stage 1 (25 – 175 °C), Stage 2 (175 – 460 °C), and stage 3 (460 – 600 °C).

Figure 5.21 shows a comparison between 1L_{XL21}-pHPMA and 2L_{XL21}-pHPMA. The onset temperature did not significantly change as the clay-to-polymer ratio

increased from 1L_{XL21}-pHPMA to 2L_{XL21}-pHPMA nanocomposites (253 °C and 254 °C respectively).

As the 2L_{XL21}-pHPMA contains a smaller proportion of polymer; “Stage 2” ends at a lower temperature than 1L_{XL21}-pHPMA. Knowing that the pHPMA total weight loss came up to 99.86 %, at the end of the weight loss process the total weight loss for 1L_{XL21}-pHPMA (91.68 %) and 2L_{XL21}-pHPMA (82.03 %) are as anticipated and are relative to the clay amounts in the dry base of both composites.

The clay-to-polymer ratio did not play a major role in enhancing the clay-pHPMA composite thermal stability as the onset temperature values were not significantly different and the weight loss rates through “Stage 2” were almost identical for both composites. [28]

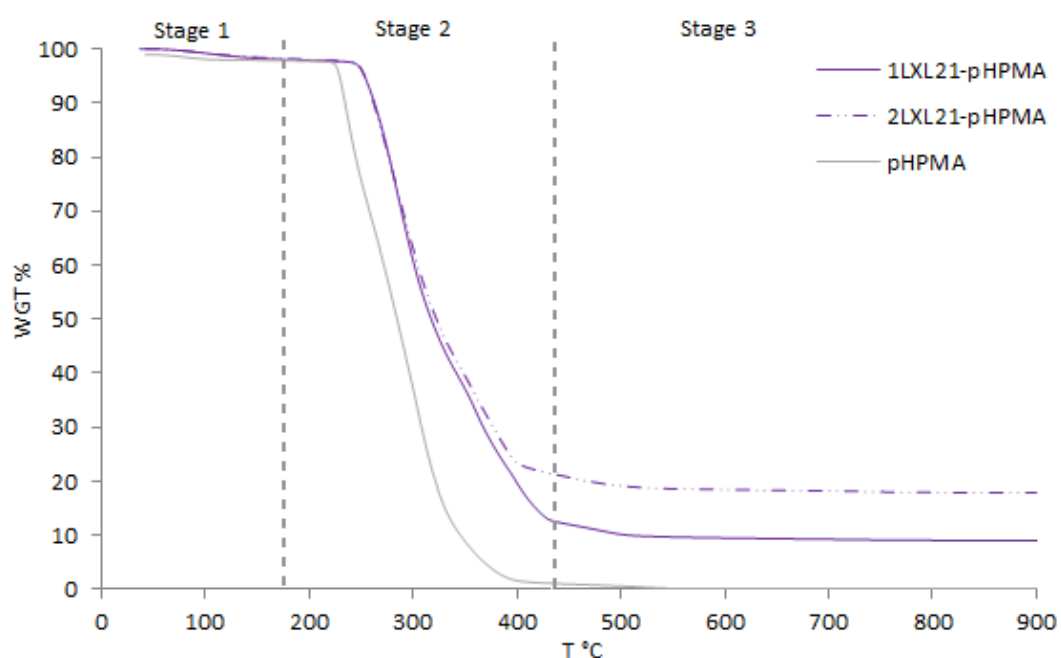


Figure 5.21 TGA thermograms of pHPMA homopolymer, 1LXL21-pHPMA, and 2LXL21-pHPMA nanocomposites indicating the three stages of weight loss. Stage 1 (25 – 175 °C), Stage 2 (175 – 460 °C), and stage 3 (475 – 600 °C).

Clay-pHPMA nanocomposites have good thermal stability up to 230 °C. Polymer degradation started at about 230 - 250 °C. The weight loss attributed to the degradation of polymeric chains had different behaviour according to different clays in the composite structure with the L_{OG}-pHPMA and C_{Na+}-pHPMA having

different behaviours mostly related to the clays in them. Table 5.11 summarises the weight loss and degradation stages.

Table 5.11 Summary of TGA data of pHPMA homopolymer and its (1 % clay) and (2 % clay) nanocomposites, showing weight loss at each stage, total weight loss and onset temperature.

	Stage1: 25–175°C	Stage2: 175–460 °C	Stage3: 460–600 °C	Total weight loss %	Onset Temp. °C
	Weight loss %				
pHPMA	1.99	96.62	1.25	99.86	229
1LEL-pHPMA	2.21	83.60	5.93	91.74	241
1LFN-pHPMA	1.98	86.51	3.32	91.81	230
1LOG-pHPMA	1.66	83.51	6.76	91.93	240
1LRD-pHPMA	1.68	83.58	6.51	91.77	250
1LXL21-pHPMA	1.59	86.03	4.06	91.68	253
2LXL21-pHPMA	1.51	75.96	4.56	82.03	254
1CNa+-pHPMA	1.24	86.32	4.34	91.90	245

5.2.4 SEM Morphology Observation of Clay-pHPMA Nanocomposites

Figure 5.22 shows an SEM examination of clay crosslinked pHPMA composites with porous networks and interconnected pores. Some clay-pHPMA nanocomposites images were not clear due to charging in the SEM chamber. [47] Table 5.12 shows the values for average pore size and the standard deviation for each clay-pHPMA composite over twenty five measured pores.

1LEL-pHPMA composite (Figure 5.22 a) created a high-density structure without a uniform pore distribution, pore size varied greatly and averaged around 5.9 μm . Table 5.12 shows standard deviation values next to average pore size. The structure has defined walls separating the pores. 1LRD-pHPMA show similar morphology to the 1LEL-pHPMA with higher pore density and smaller pore size with much less variation in size (3.7 μm , 0.7 SD).

The SEM image of 1LFN-pHPMA composite (Figure 5.22 b) created a low pore density structure with sharp “mountain-valley” morphology that appears to have a rougher surface than 1LEL-pHPMA and 1LRD-pHPMA, pore size averaged around 5.2 μm . The 1LFN-pHPMA image showed a layered effect “diagonally through the

image” which may be as a result of the L_{FN} larger particle size between all other Laponite[®] clays.

1L_{OG}-pHPMA composite (Figure 5.22 c) structure was a high-density structure with a low-density pore distribution and pore average of 3.4 μm . The 1L_{XL21}-pHPMA (Figure 5.22 e) exhibit a rough-textured morphology with a non-uniform, small high-density pore distribution (average 3.6 μm). 1C_{Na+}-pHEMA composite image (Figure 5.22 f) was not clear. The surface was rough-textured, non-uniform with a broad pore distribution (averaged around 4.5 μm) over a from 2.1 - 9.6 μm .

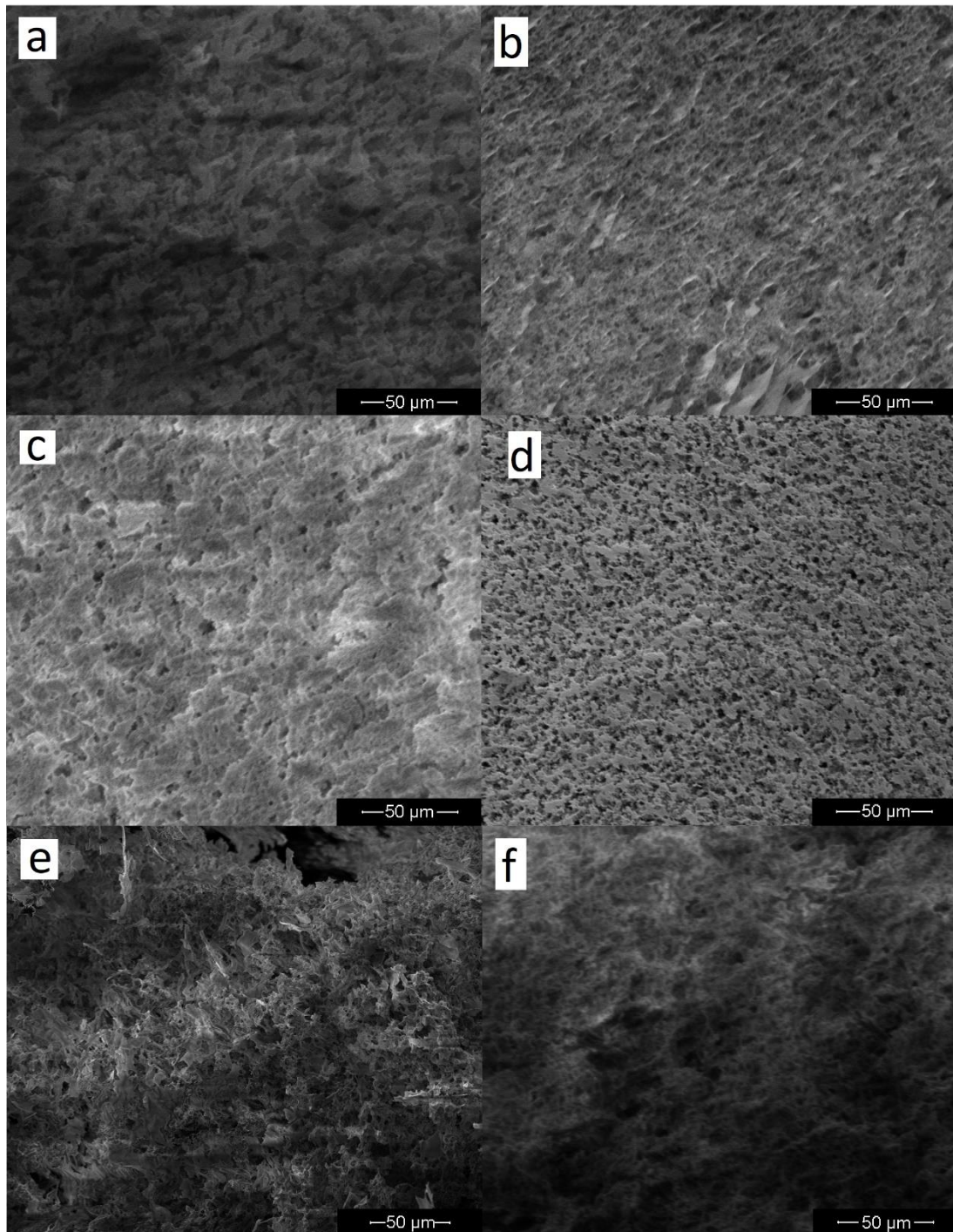


Figure 5.22 SEM images of (1% clay)-pHPMA nanocomposite showing microstructure and pore size differences as a result of clay types used. a) 1LEL-pHPMA b) 1LFN-pHPMA c) 1LOG-pHPMA d) 1LRD-pHPMA e) 1LXL21-pHPMA f) 1CNa+-pHPMA.

To observe the effect of different clay-to-polymer ratios on the morphology of clay-pHPMA, SEM images for 1L_{XL21}-pHPMA and 2L_{XL21}-pHPMA nanocomposites were obtained as shown in Figure 5.23.

The 1L_{XL21}-pHPMA nanocomposite (Figure 5.23 a) showed a non-uniform rough texture with a variety of pore size averaged around 3.6 μm (Table 5.12). On the other hand, the 2L_{XL21}-pHPMA nanocomposites (Figure 5.23 b), showed more uniform and wider pore distribution.

Increasing the clay content in the nanocomposites created more crosslink points and maybe a reason for tighter polymer chains resulting in a more uniform distribution of polymer between clay platelets. Which may explain the 2L_{XL21}-pHPMA composite more uniform structure and porosity which was more evenly distributed and with a pore size around 5.6 μm . This varied less than the pore size of the 1L_{XL21}-pHPAM composite. [36]

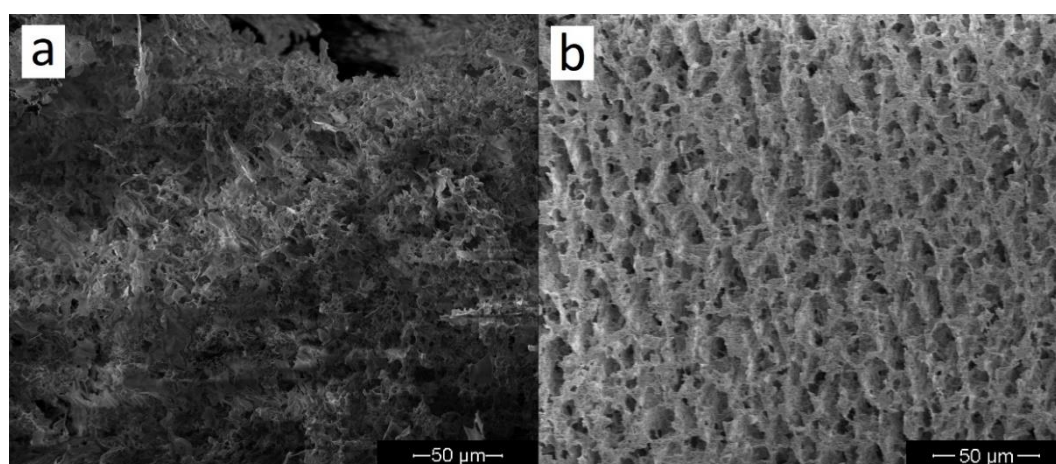


Figure 5.23 SEM images of LXL21-pHPMA nanocomposite on scale bar 50 μm . a) 1LXL21-pHPMA b) 2LXL21-pHPMA showing the effect of increasing clay content on the pore size and the microstructure.

Table 5.12 Average pore size and standard deviation of (n=25) for clay-pHPMA.

Sample	Pore size (μm)	SD
1LEL-pHPMA	5.9	2.1
1LFN-pHPMA	5.2	2.7
1LOG-pHPMA	3.4	1.5
1LRD-pHPMA	3.7	0.7
1LXL21-pHPMA	3.6	1.7
2LXL21-pHPMA	5.6	1.1
1CNa+ -pHPMA	4.5	2.1

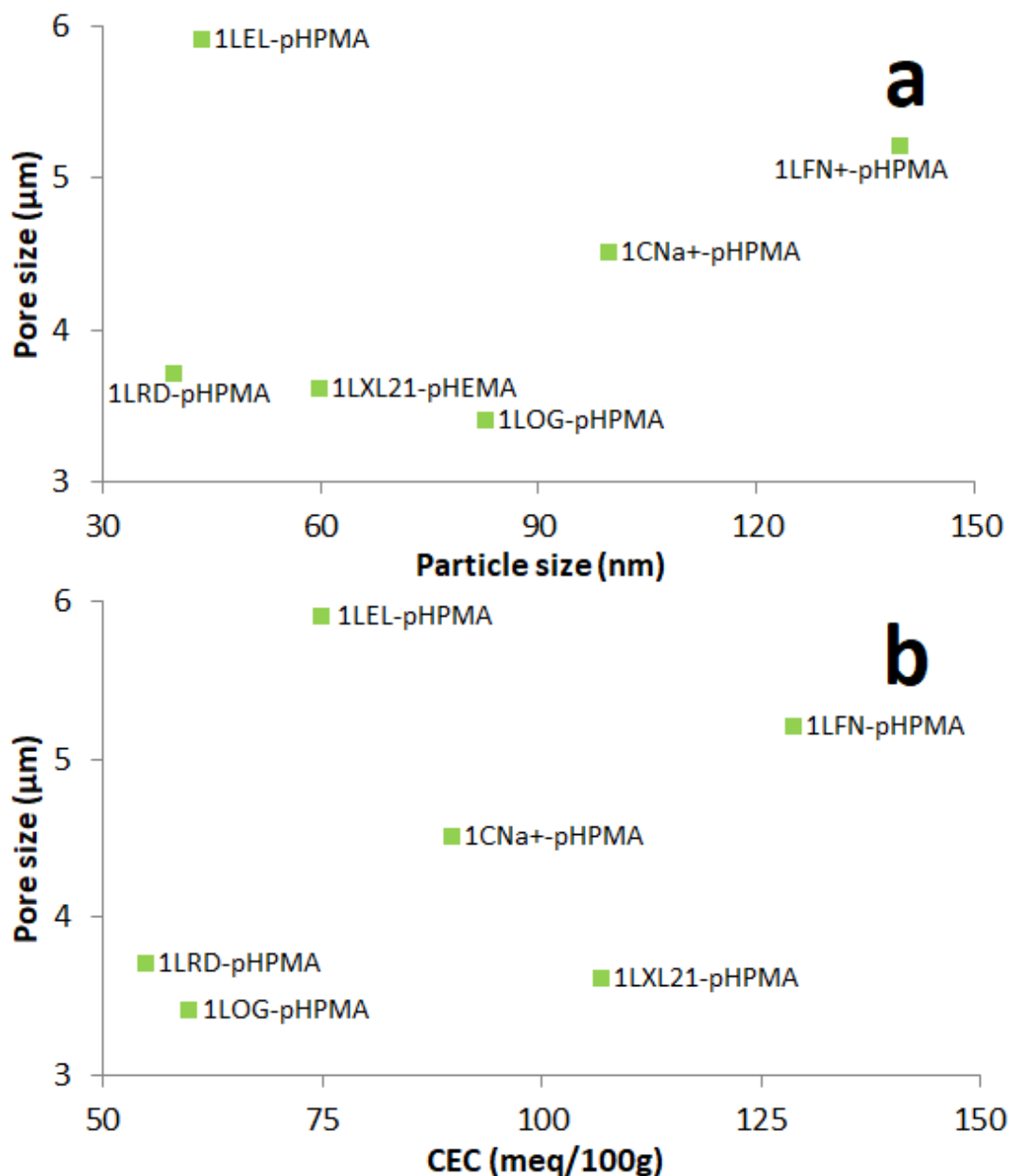


Figure 5.24 (1 % clay)-pHPMA composites pores size as a function of a) Clay particle size b) Clay CEC

5.2.5 FTIR Spectra Analysis of Clay-pHPMA Nanocomposites

FTIR spectra of HPMA monomer and dried pHPMA homopolymer at room temperature in Figure 5.25 support the successful polymerisation of pHPMA as the C=C band at 1636 cm^{-1} in the HPMA spectrum is no longer presented in the pHPMA spectrum. The characteristic OH stretching band at 3452 cm^{-1} in the HEMA spectrum has shifted to a lower wavenumber upon polymerisation (pHPMA, 3396 cm^{-1}). The band C=O stretching at 1716 cm^{-1} did not show a significant shift when

HPMA was polymerised (Table 5.13), neither did the C-H stretching bands between 3000 – 2880 cm^{-1} and 1460 – 1400 cm^{-1} . [41] Table 5.13 summarises the main band's positions for both HPMA monomer and pHPMA homopolymer.

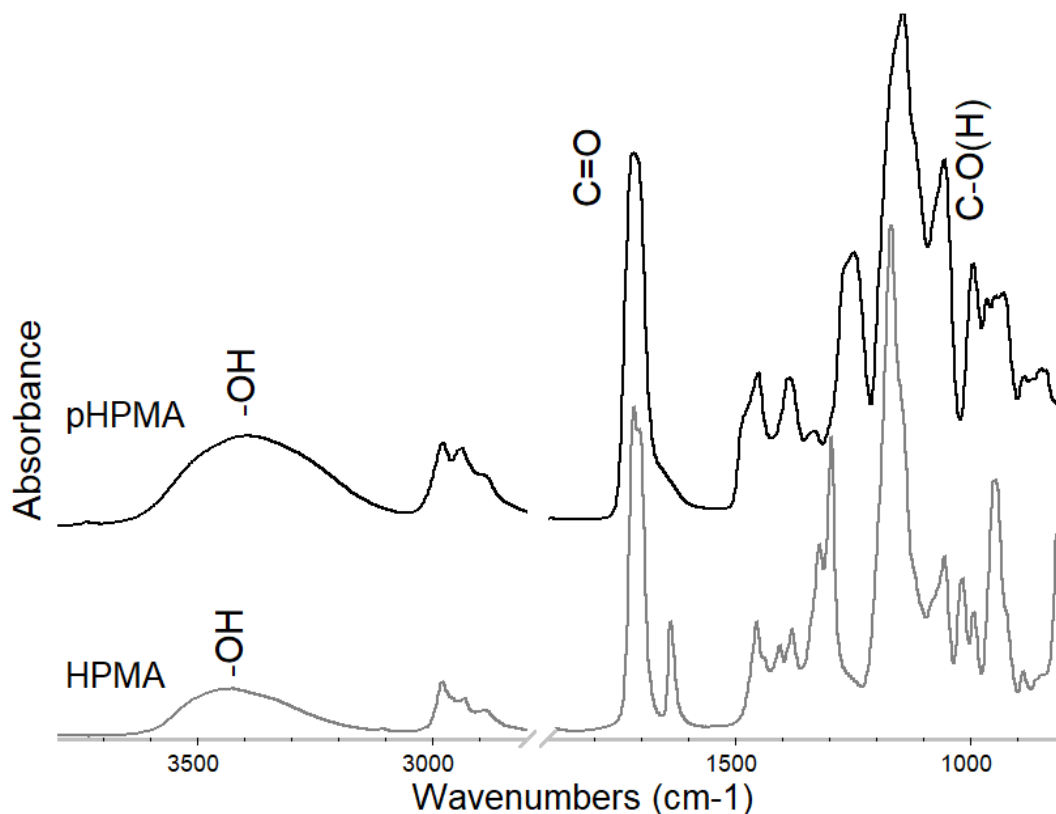


Figure 5.25 FTIR spectra of HPMA and pHPMA homopolymer showing the main characteristic peaks of pHPMA in the range 900 - 4000 cm^{-1} .

Table 5.13 FTIR peaks value for HPMA the monomer and pHPMA homopolymer.

	-OH	CH ₃		C=O	C-H		C-C	C-O(H)	
HPMA	3425	2978	2931	2889	1715	1453	1404	1166	1053
pHPMA	3396	2977	2938	2888	1717	1451	1386	1141	1053

FTIR spectra of the clay, homopolymer pHPMA, and their corresponding dried (1 % clay)-pHPMA and (2 % clay)-pHPMA nanocomposites are presented in Figure 5.26. FTIR spectra of the (1 % clay)-pHPMA nanocomposites exhibit characteristics of both clay and pHPMA which confirm the presence of both the clay and the pHPMA in the composite structure. [26]

Figure 5.26 (a) shows the details of interest for dried 1L_{EL}-pHPMA nanocomposite compared to L_{EL} and dried pHPMA homopolymer. From 3100 - 3700 cm^{-1} in the -OH stretching region the -OH band shifts to a higher wavenumber (3403 cm^{-1}) in the

1L_{EL}-pHPMA composite spectrum when compared to the pHPMA homopolymer (3403 cm⁻¹), this provides evidence of the association of hydrogen bonds as the polymer chain is crosslinked by the nanoclay platelets. [38] The C=O stretching band does not show any significant shift when comparing the 1L_{EL}-pHPMA crosslinked to the homopolymer pHPAM (1718 cm⁻¹ for 1L_{EL}-pHPMA to 1717 cm⁻¹ for pHPMA), implying that the C=O is not involved in the interactions.

The Si-O band in the 1L_{EL}-pHPMA composite spectrum is the one positioned at 990 cm⁻¹; this band has shifted from a lower wavenumber (946 cm⁻¹) in the L_{EL}. This shift may be due to the involvement of the Si-O in the crosslinking process between the clay platelets and the pHPMA chains. However as the clay platelets are separated, another Si-O band becomes more dominant in the composite spectrum at 1054 cm⁻¹, this may be the Si-O out-of-plane band, and it overlaps with the C-O from the polymer within the composite. Table 5.14 show bands positions for L_{EL}, pHPMA and 1L_{EL}-pHPMA composite.

Most of the (1 % clay)-pHPMA nanocomposites follow the same trend and behave in a very similar manner when different clay types crosslink the pHPMA chains, however, some difference still exists as the clay types have different properties.

Figure 5.26 (e) shows the 1L_{XL21}-pHPMA and 2L_{XL21}-pHPMA nanocomposites compared to L_{XL21} and pHPMA homopolymer. Both composites show bands at 1054 cm⁻¹ (Si-O out-of-plane) and it has a higher intensity in the 2L_{XL21}-pHPMA which provide more evidence that this band is related to the clay within the composite.

Figure 5.26 (f) shows the dried 1C_{Na+}-pHPMA nanocomposite compared to C_{Na+} and pHPMA homopolymer. The C_{Na+} show two Si-O bands (Table 5.14), as the C_{Na+} crosslinks the pHPMA chains the Si-O band shifts to a higher wavenumber to 994 cm⁻¹ and sharp bands to be observed at around 1055 cm⁻¹ which provides more evidence that the band at around 1055 cm⁻¹ is both polymer and clay.

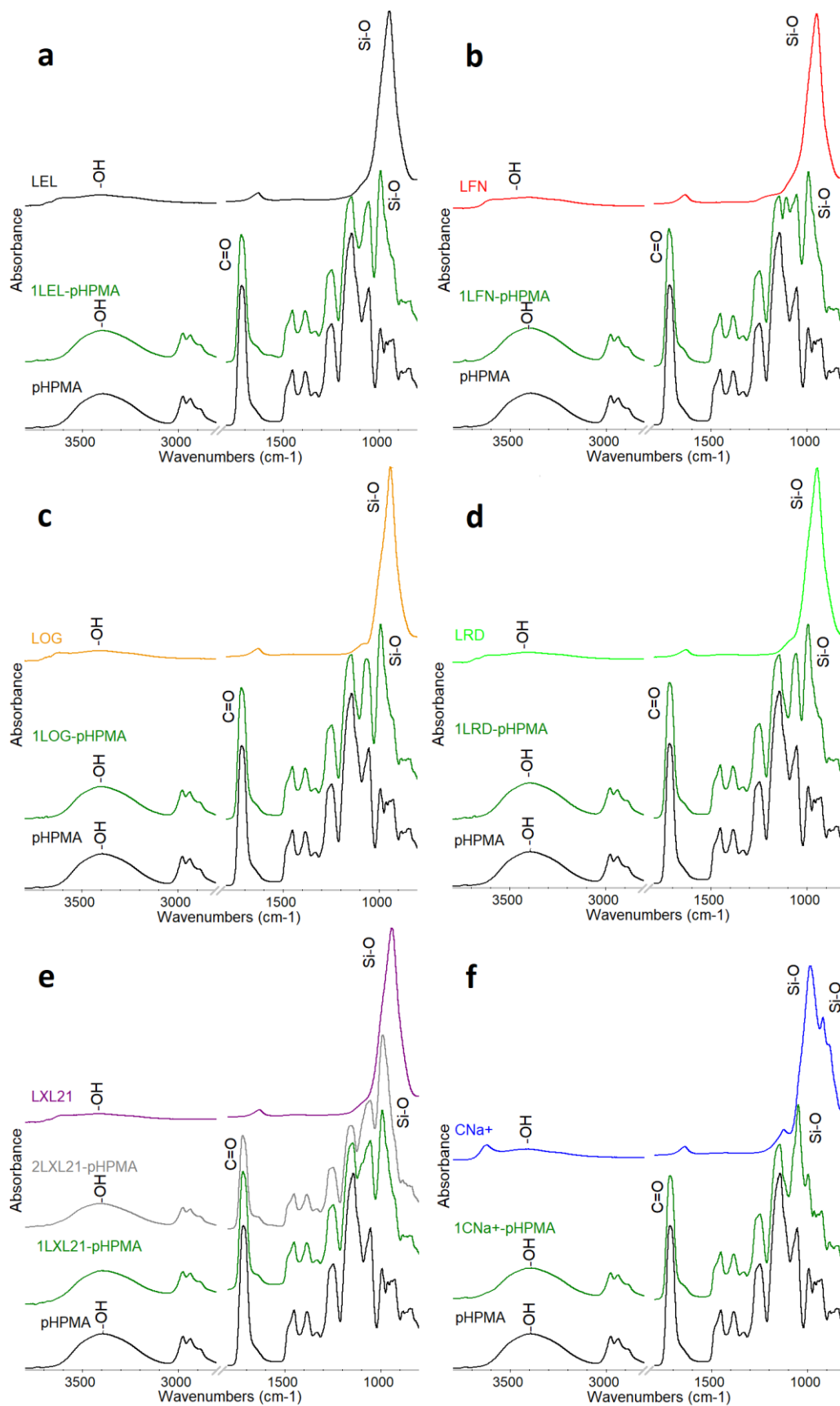


Figure 5.26 FTIR spectra of clay, pHPMA homopolymer, and their corresponding nanocomposite (a) 1LEL, b) 1LFN, c) 1LOG, d) 1LRD, e) 1LXL21, f) 1CNa+), indicating major bands positions and offset for clearance. All samples are dried powder.

Table 5.14 FTIR peaks for pHPMA, (1 % clay)-pHPMA, and 2LXL21-pHPMA.

Sample	-OH	Si-O	
pHPMA	3396	-	-
L _{EL}	3408	-	946
1L _{EL} -pHPMA	3403	1054	990
L _{FN}	3408	-	949
1L _{FN} -pHPMA	3403	1054	990
L _{OG}	3407	-	940
1L _{OG} -pHPMA	3403	-	990
L _{RD}	3405	-	945
1L _{RD} -pHPMA	3393	1056	992
L _{XL21}	3417	-	942
1L _{XL21} -pHPMA	3392	1054	990
2L _{XL21} -pHPMA	3410	1054	988
C _{Na+}	3418	981	912
1C _{Na+} -pHPMA	3392	1046	994

5.2.6 Rheological Analysis and Properties of Clay-pHPMA Nanocomposites

5.2.6.1 Yield Stress for Clay-pHPMA Nanocomposites

The flow curves in Figure 5.27 shows the yield stress of the 1L_{XL21}-pHPMA and 2L_{XL21}-pHPMA nanocomposites. As expected, the higher the clay-to-polymer ratio in the nanocomposite the larger the yield stress values (Table 5.15).

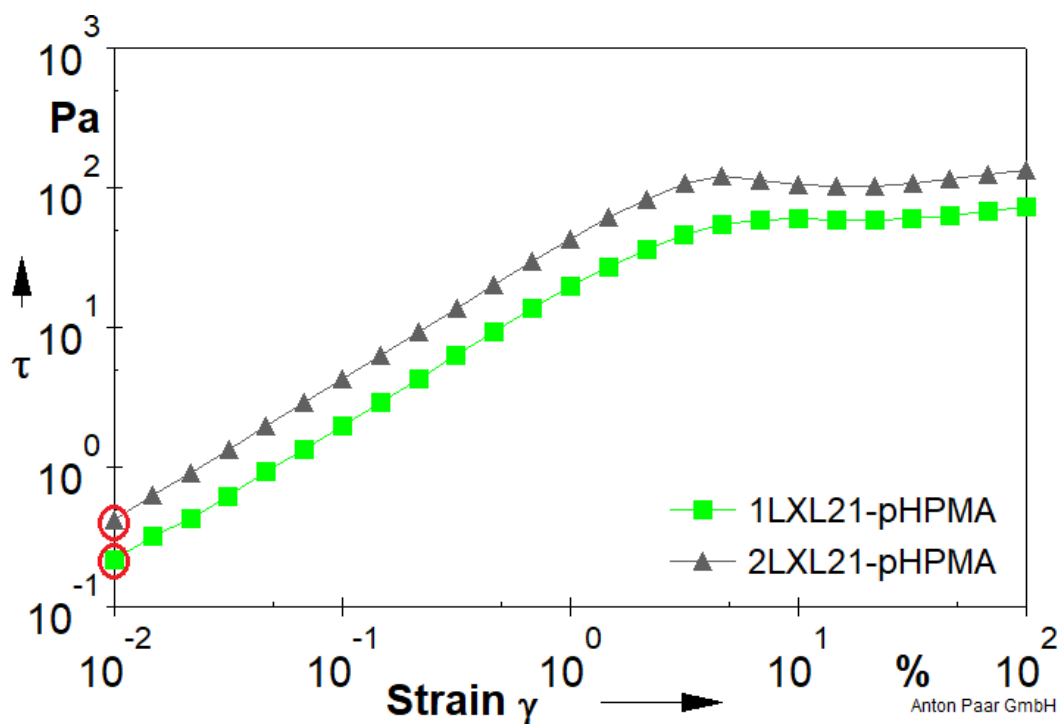


Figure 5.27 Flow curves show yield stress for 1LXL21-pHPMA and 2LXL21-pHPMA nanocomposites.

Table 5.15 τ_{yield} (Pa.) as an average from n=3 and SD for the 1LXL21-pHPMA and 2LXL21-pHPMA.

Sample	τ_{yield}	SD
1L _{XL21} -pHEMA	0.222	0.022
2L _{XL21} -pHEMA	0.442	0.071

The increased elasticity caused by the presence of more crosslinks between the clay platelets and the polymeric chains leads to higher yield stress and higher resistance to flow. This was observed in the SEM images, for the 2L_{XL21}-pHPMA nanocomposite which had a more uniform structure with more pore distribution and less density structure when compared to the 1L_{XL21}-pHPMA.

5.2.6.2 Storage (G') and Loss (G'') Moduli Behaviour for Clay-pHPMA Nanocomposites

5.2.6.2.1 Amplitude sweep (Function of Strain)

Figure 5.28 shows the behaviour G' and G'' on a strain sweep for 1L_{XL21}-pHPMA and 2L_{XL21}-pHPMA. Both composites show an elastic behaviour to a certain limit whereupon the G' values (2885 Pa, 4144 Pa for 1L_{XL21}-pHPAM and 2L_{XL21}-pHPMA, respectively) start to change. The change in G' towards lower values indicated the limit of the LVE region where the change for such is irreversible.

Table 5.16 shows the crossover value for the two different clay-to-polymer ratios, the change of value to where the G' and G'' crossover show the effect of the clay on the composite on the critical strain (γ_c). The γ_c is where the nanocomposite starts to change from a gel-like material to a liquid-like material as G'' become larger in value than G' .

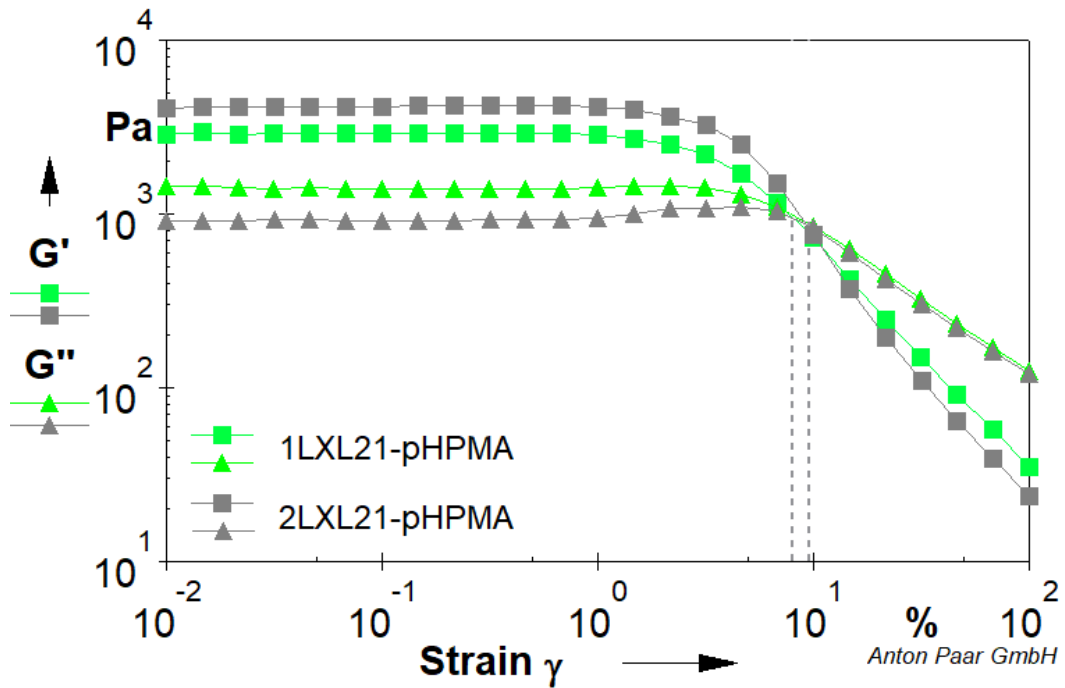


Figure 5.28 Evolution of storage modulus G' and loss modulus G'' as a function of strain from 0.01 % - 100 % for 1LXL21-pHPMA and 2LXL21-pHPMA nanocomposite. Transition point (gel-like to fluid-like) points.

Table 5.16 LVE region limits (strain % and G' Pa.). Crossover transition point strain values for 1LXL21-pHPMA and 2LXL21-pHPMA nanocomposite as an average of (n=3).

Sample	LVE		Crossover Point	
	Strain %	G' Pa.	Strain %	SD
1L _{XL21} -pHPMA	0.68	2885.11	7.556	1.301
2L _{XL21} -pHPMA	1.00	4144.58	9.393	2.496

5.2.6.2.2 Frequency Sweep (Function of Frequency)

Figure 5.29 shows the behaviour of G' and G'' as a function of frequency for 1L_{XL21}-pHPMA and 2L_{XL21}-pHPMA. The 2L_{XL21}-pHPMA nanocomposites have higher elastic properties until a certain limit ($f = 10$ Hz, $G' = 5825$ Pa.) when compared to 1L_{XL21}-pHPMA nanocomposite as expected before. The figure also shows that both composites are frequency dependant from as low as 0.01 Hz.

The 1L_{XL21}-pHPMA composites; the change in G'' increases at a much higher rate with increasing frequency while G' show a constant change rate until it reaches the critical value and the material transforms to a liquid-like composite (Table 5.17). This may be due to a smaller number of crosslink points getting broken when compared to the 2L_{XL21}-pHPMA.

Table 5.17 (n=3) G' Pa and frequency Hz at the crossover transition point for 1LXL21-pHPMA nanocomposite.

Sample	Crossover Point		
	G' Pa	Frequency Hz	SD
1LXL21-pHPMA	7093.47	26.36	4.90

Following the 2LXL21-pHPMA composite moduli curves shows a slower change rate for the G'' when compared the 1LXL21-pHPMA G'' . However, the behaviour of the viscoelastic moduli of the 2LXL21-pHPAM still shows that the values of the moduli are getting closer to one another and a crossover point is to be expected at frequency larger than 100 Hz.

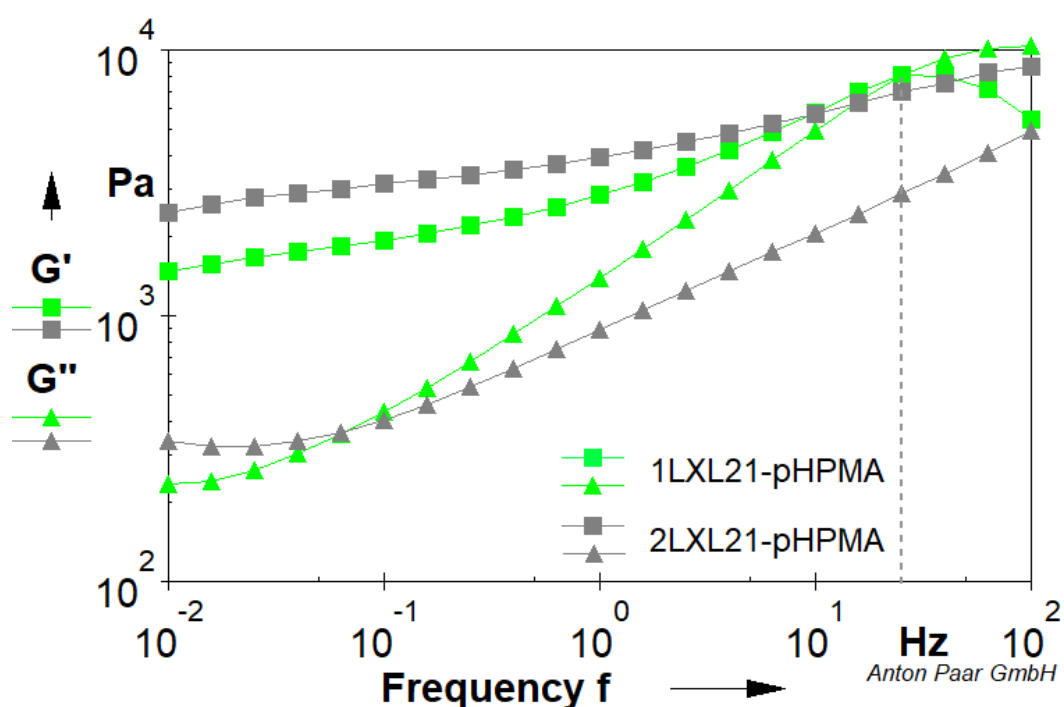


Figure 5.29 Evolution of storage modulus G' and loss modulus G'' as a function of frequency from 0.01 Hz – 100 Hz for 1LXL21-pHPMA and 2LXL21-pHPMA nanocomposite. Transition point (solid-like to fluid-like) points.

5.3 Clay-pGMAc Characterisation and Rheological Properties








Glycidyl methacrylate (GMAc) is a reactive monomer with an epoxide ring which offers it an opportunity to enter a wide range of chemical reactions. (GMAc) can be polymerised and copolymerised by free radical polymerisation where initiators attack the methacrylic double bonds. [48] It is a low-cost monomer as it is used to

produce epoxy-functional methacrylic resins which are industrially employed as coatings and adhesives. [49]

5.3.1 Clay-pGMAc Nanocomposite

Table 5.18 shows general observation on the pGMAc and (1 % clay)-pGMAc nanocomposite after polymerisation. The pGMAc homopolymer separated from the water after two days of polymerisation and the material sediments on the bottom of the vial. The composites were in general heterogeneous with two different components in the glass vial after polymerisation: a soft, white, and heterogeneous gel part filling most of the volume, and a white hard bead-like part at the bottom of the vial. The bead-like part was only analysed by FTIR to find out what it contains. The gel part was analysed further with TGA and XRD.

Table 5.18 General observation on pGMAc and 1clay-pGMAc nanocomposites, samples were investigated by pouring and poking with a small lab spatula.

pGMAc	1L _{EL} -pGMAc	1L _{FN} -pGMAc	1L _{OG} -pGMAc	1L _{RD} -pGMAc	1L _{XL21} -pGMAc	1C _{Na+} -pGMAc
<p>(Top) ~ 90% of the total volume, white soft heterogeneous polymer. 2 days after polymerisation ~ 10% of the total volume at the bottom and clear water on top.</p>	<p>(Top) ~ 80% of the total volume, very soft gel, observed heterogeneous composite as poured of the glass vial. (Bottom) ~ 20% of the total volume, white hard bead-like composite.</p>	<p>(Top) ~ 85% of the total volume, soft gel, observed heterogeneous composite as poured of the glass vial. (Bottom) ~ 25% of the total volume, white hard bead-like composite.</p>	<p>(Top) ~ 80% of the total volume, very soft gel, observed heterogeneous composite as poured of the glass vial. (Bottom) ~ 20% of the total volume, white hard bead-like composite smaller in size than the 1L_{EL}-pGMAc and 1L_{FN}-pGMAc.</p>	<p>(Top) ~ 80% of the total volume, very soft gel, observed heterogeneous composite as poured of the glass vial. (Bottom) ~ 20% of the total volume, white hard bead-like composite.</p>	<p>(Top) ~ 70% of the total volume, soft gel, observed heterogeneous composite as poured of the glass vial. (Bottom) ~ 30% of the total volume, white hard bead-like composite. with some having dimensions of 5x4 mm</p>	<p>(Top) ~ 70% of the total volume, yellow soft gel, observed heterogeneous composite as poured of the glass vial. (Bottom) ~ 30% of the total volume, white hard bead-like composite.</p>
						

5.3.2 XRD Characterisation of Clay-pGMAc Nanocomposites

GMAc is a functional monomer used to prepare homogeneous and heterogeneous polymer networks. [50] It is a monomer that is not easy to control the polymerisation process for, as it is a relevant epoxy-functional monomer. Figure 5.30 shows the XRD traces for the two different products after the polymerisation process of GMAc. The reflections for both products are almost the same showing amorphous polymer traces. Since both products XRD reflection has almost the same behaviour, the pGMAc will be used as a reference to compare the clay-pGMAc composites. The pGMAc also will be investigated further using TGA, SEM, FTIR and rheological tests.

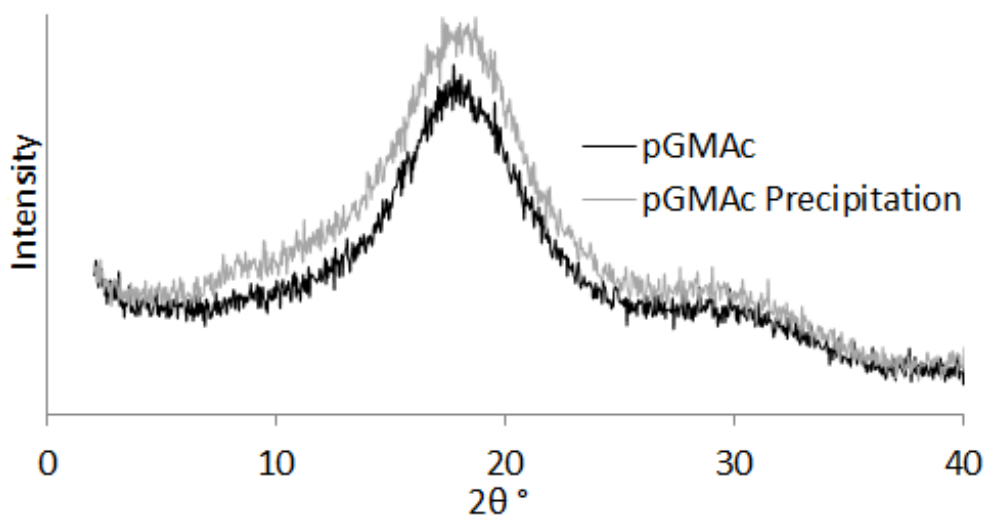


Figure 5.30 XRD profiles for powder pGMAc homopolymer and pGMAc precipitations showing the differences in the XRD traces. pGMAc homopolymer samples are ground powders, pGMAc precipitations samples were too hard to ground.

The XRD traces of L_{EL} , pGMAc, and $1L_{EL}$ -pGMAc nanocomposites are presented in Figure 5.31 (a). The XRD trace of $1L_{EL}$ -pGMAc is dominated by the pGMAc within the composite. Evidence of L_{EL} within the composite can also be observed. A decreasing baseline is observed at a low angle ($2\theta \leq 5^\circ$) and the lack of any diffractions in the region 2θ between $5.5^\circ - 6^\circ$ corresponding to the d_{001} spacing in the powder L_{EL} in the XRD trace for the $1L_{EL}$ -pGMAc composite suggests clay is well dispersed if not exfoliated in the composite structure. [16][18][19]. The reflection at $2\theta = 18.3^\circ$ ($d = 4.86 \text{ \AA}$) in the XRD trace of $1L_{EL}$ -pGMAc is a result of the presence of pGMAc within

the composite, however, another small sharp reflection can be observed at $2\theta = 19.4^\circ$ ($d = 4.58 \text{ \AA}$) which may be due to the d_{100} spacing in the L_{EL} .

No reflections were observed in the XRD trace $1L_{EL}$ -pGMAc composite at around $2\theta = 27^\circ$, this position is related to the pGMAc reflection at $2\theta = 29.8^\circ$ ($d = 3.00 \text{ \AA}$). It is also related to the d_{005} spacing in the L_{EL} at $2\theta = 27.5^\circ$ ($d = 3.24 \text{ \AA}$). Towards the right-side end of the XRD trace of the $1L_{EL}$ -pGMAc composite, a reflection at $2\theta = 35.0^\circ$ ($d = 2.57 \text{ \AA}$) can be observed corresponding to the d_{110} spacing in the L_{EL} , this reflection provides evidence about the clay presence in the $1L_{EL}$ -pGMAc structure.

Figure 5.31 shows the XRD traces of seven different clay-pGMAc nanocomposites in comparison with their components (clay type and pGMAc). Most of the composites follow the same trend as the pGMAc is crosslinked with different clay types, however, some differences are still to be mentioned. Figure 5.31 (b) shows the XRD traces of $1L_{FN}$ -pGMAc composite. A diffraction reflection is observed at $2\theta = 6.6^\circ$ ($d = 13.35 \text{ \AA}$) corresponding to the d_{001} in the L_{FN} . The presence of this reflection suggests that the $1L_{FN}$ -pGMAc is a microstructure nanocomposite. [19]

The $1L_{OG}$ -pGMAc and $1L_{RD}$ -pGMAc nanocomposites (Figure 5.31 (c and d)) have similar behaviours to that of $1L_{EL}$ -pGMAc. Table 5.18 shows the position of the reflection for different clay-pGMAc nanocomposites.

In Figure 5.31 (e) both composites with different L_{XL21} -to-polymer ratio show similar behaviours. The XRD trace of $2L_{XL21}$ -pGMAc has a reflection at $2\theta = 6.3^\circ$ ($d = 13.81 \text{ \AA}$) with position closer to the d_{001} of the L_{XL21} than the $1L_{XL21}$ -pGMAc as a result of more clay contained in the $2L_{XL21}$ -pGMAc composite. The XRD observations of the L_{XL21} -pGMAc suggests that both nanocomposites are microstructure composites.

Figure 5.31 (f) shows the XRD trace of $1C_{Na+}$ -pGMAc nanocomposite. A decreasing baseline is observed at a low angle ($\leq 5^\circ$) in the XRD trace for the $1C_{Na+}$ -pGMAc composite which suggests clay exfoliation in the composite structure. [16][18][19] The diffraction reflections at $2\theta = 19.5^\circ$ ($d = 4.56 \text{ \AA}$) is an indication of the clay presence in the composite as they match the C_{Na+} d_{100} and (Table 5.19).

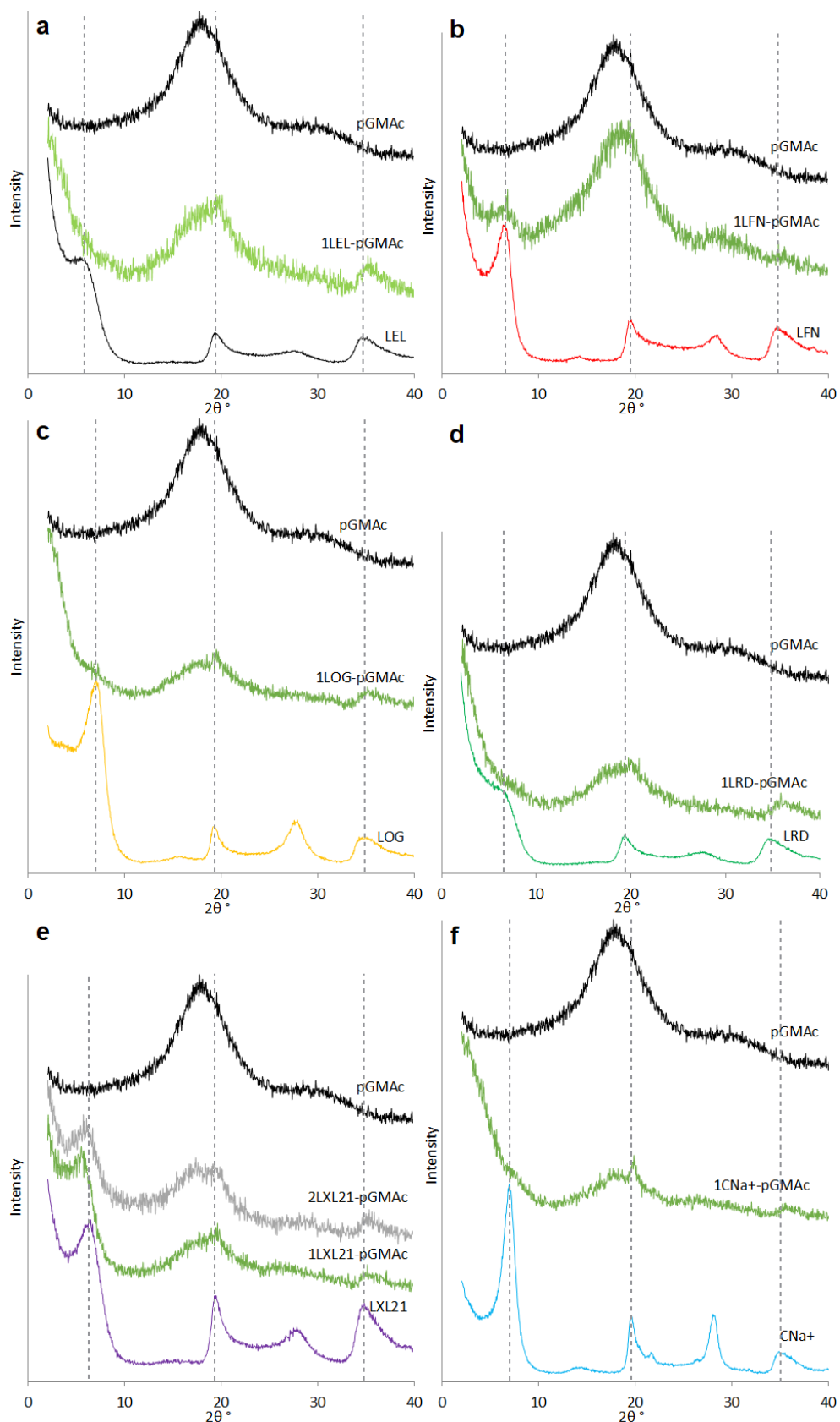


Figure 5.31 XRD profiles for powder clay, pGMAc homopolymer and its related nanocomposite showing the differences in the XRD traces as the polymer chains intercalate in between clay platelets as they disperse; by clay a) LEL, b) LFN, c) LOG, d) LRD, e) LXL21, f) CNa+. All samples are ground powders. Offset for clearance.

The fact that the d_{001} spacing is not observed or observed but as a weak reflection indicates that pGMAc chains penetrate through the interlayer spacing of the nano-clay. Which means that clay platelets in pGMAc nanocomposite can be well dispersed or can form a microstructure nanocomposites as was the case for the L_{FN} -pGMAc and the L_{XL21} -pGMAc. [1][2][51]

Table 5.19 Interplanar distances and 2θ of different clay (powder) and its corresponding clay-pGMAc nanocomposites samples obtained from XRD data.

Sample	d_{001}		d_{100}		d_{110}	
	2θ	d (Å)	2θ	d (Å)	2θ	d (Å)
pGMAc	-	-	18.1	4.89	-	-
L_{EL}	5.8	15.24	19.4	4.57	35.6	2.52
1L_{EL}-pGMAc	-	-	18.3	4.86	35.0	2.57
	-	-	19.4	4.58	-	-
L_{FN}	6.6	13.39	19.3	4.60	34.6	2.59
1L_{FN}-pGMAc	6.6	13.35	18.3	4.86	34.9	2.57
L_{OG}	7.1	12.45	19.1	4.65	34.6	2.59
1L_{OG}-pGMAc	-	-	18.0	4.94	34.8	2.58
	-	-	19.3	4.60	-	-
L_{RD}	6.5	13.60	19.4	4.57	34.6	2.59
1L_{RD}-pGMAc	-	-	18.2	4.87	34.7	2.58
	-	-	19.5	4.56	-	-
L_{XL21}	6.4	13.81	19.3	4.60	34.7	2.58
1L_{XL21}-pGMAc	5.8	15.29	18.3	4.85	34.5	2.60
	-	-	19.5	4.56	-	-
2L_{XL21}-pGMAc	6.3	14.03	17.3	5.11	34.4	2.61
	-	-	19.1	4.64	-	-
C_{Na+}	7.0	12.63	19.5	4.55	34.7	2.58
1C_{Na+}-pGMAc	-	-	19.5	4.54	34.9	2.57
	-	-	18.4	4.82	-	-

5.3.3 TGA Characterisation of Clay-pGMAc Nanocomposite

Figure 5.32 presents the thermal decomposition TGA curves for pGMAc homopolymer and (1 % clay)-pGMAc nanocomposites. Three different weight loss stages are observed throughout all the clay-pGMAc nanocomposites over the temperature range 25 - 900 °C (Table 5.20). [22] “Stage 1” corresponds to weight loss due to free water evaporation. At “Stage 2” the samples lost 50 - 85 % of the total weight loss in the temperature range of 250-500 °C, due to the degradation of pGMAc, the big variation in the wt% is mainly due to pGMAc-based nanocomposite

being not homogenous. [26] “Stage 2” also includes the weight loss attributed to the degradation of the epoxied group between 170 - 220 °C in pGMAc. [27] At temperatures higher 500 °C “Stage 3” the clay-pGMAc nanocomposites still showed the weight loss of about 5 -17 % which is mainly due to further degradation of polymer residues and dehydroxylation. The difference of the total weight loss at the end of “Stage 2” between pGMAc-based nanocomposite and all previously mentioned nanocomposites can be related to the polymer being precipitated out and thus more clay in the sample.

The thermal stability for pGMAc and clay-pGMAc nanocomposites is in a higher range (275 °C - 286 °C) than that of pHEMA and pHPMA nanocomposites. Clay-pGMAc nanocomposites have less total weight loss as clay-pGMAc composites which is a result of its heterogeneous nature as its polymerisation cannot be easily controlled due to the presence of the epoxide functional group.

pGMAc thermal stability is modified as it is crosslinked by the clay platelets. The onset temperature increased from ~238 °C for the homopolymer to ~280 °C for the clay-pGMAc nanocomposites. The 1L_{FN}-pGMAc composite is the fastest to start degrading with an onset temperature of 272 °C, it also lost less weight than other composites through “Stage 1” which suggest that it holds less water than all other clay-pGMAc nanocomposites.

1L_{EL}-pGMAc and 1L_{RD}-pGMAc composites had close onset temperature (278 °C and 275 °C, respectively), similar weight loss curves, and very close weight loss values. Whereas, L_{OG}-pGMAc and 1C_{Na+}-pGMAc have the same onset temperature at 286 °C. The L_{OG} and C_{Na+} corresponding nanocomposites showed the slowest weight loss rates in “Stage 2”; this observation was also the same for their pHPAM corresponding nanocomposite which suggests it is related to the clay types as L_{OG} and C_{Na+} were the most thermally stable clays.

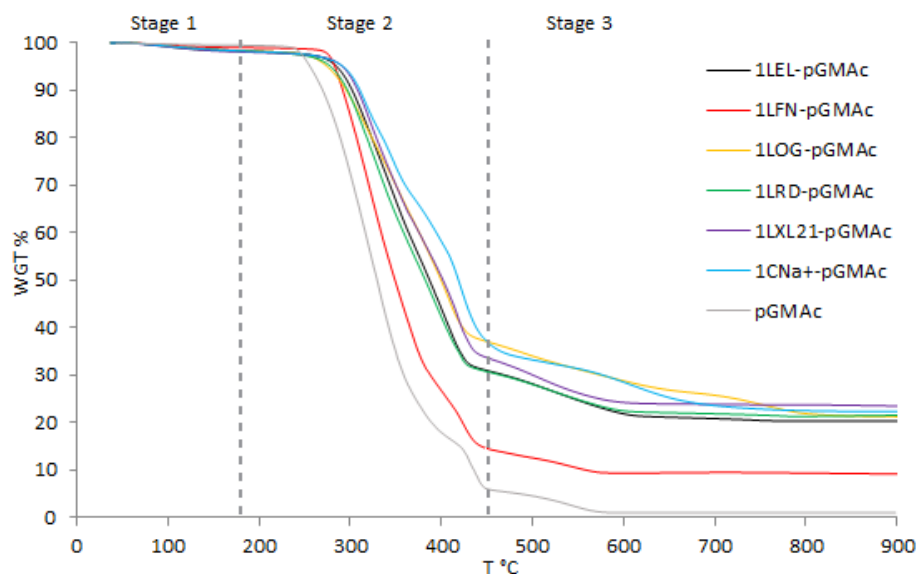


Figure 5.32 TGA thermograms of pGMAc homopolymer and 1clay-pGMAc nanocomposites. Indicating the three stages of weight loss. Stage 1 (25 - 175 °C), Stage 2 (175 - 450 °C), and stage 3 (460 - 800 °C).

Figure 5.33 shows the TGA weight loss curves for L_{XL21}-pGMAc with two different clay-to-polymer ratios. The onset temperature was not significantly different (285 °C for 1L_{XL21}-pGMAc, 284 °C for 2L_{XL21}-pGMAc) (Table 5.20) which does not show a strong thermal difference between both nanocomposites at these clay contents. Both composite also had a similar weight loss rate through “Stage 2”. As clay-pGMAc composites were heterogeneous, it was not possible to relate the total weight loss in 1L_{XL21}-pGMAc and 2L_{XL21}-pGMAc to the clay-to-polymer ratios.

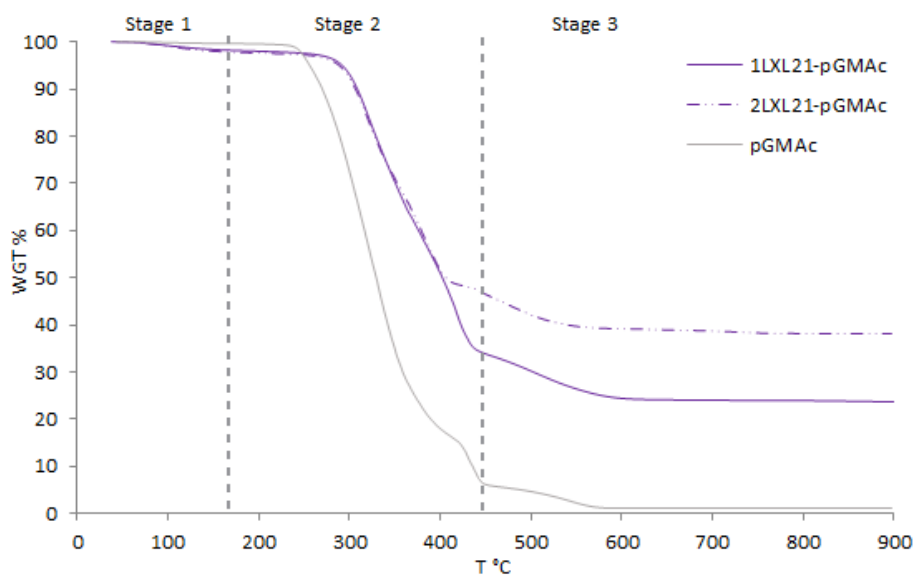


Figure 5.33 TGA thermograms of pGMAc homopolymer, 1LXL21-pGMAc, and 2LXL21-pGMAc nanocomposites. Indicating the three stages of weight loss. Stage 1 (25 - 175 °C), Stage 2 (175 - 450 °C), and stage 3 (450 - 800 °C).

Table 5.20 TGA data of pGMAc homopolymer and its (1 % clay) and (2 % clay) nanocomposites, showing weight loss at each stage and onset temperature.

Sample	Stage1: 25–175 °C	Stage2: 175–450 °C	Stage3: 450–800 °C	Total weight loss %	Onset Temp. °C
	Weight loss %				
1LEL-pGMAc	1.30	66.03	12.35	79.68	278
1LFN-pGMAc	0.84	84.61	5.39	90.84	272
1LOG-pGMAc	1.28	59.9	17.58	78.76	286
1LRD-pGMAc	1.41	66.39	10.65	78.45	275
1LXL21-pGMAc	1.51	63.55	11.46	76.52	285
2LXL21-pGMAc	1.96	49.05	11.06	62.07	284
1CNa+-pGMAc	1.27	61.07	15.33	77.67	286
pGMAc	0.29	93.92	4.76	98.97	238

5.3.4 SEM Morphology Observation of Clay-pGMAc Nanocomposites

Figure 5.34 shows SEM images of clay crosslinked pGMAc composites at 50 μm . The images show porous interconnected micro-scaled structure networks, with different morphologies and different pore distribution. [47][52]

1LEL-pGMAc nanocomposite (Figure 5.34 a) shows a uniform pore distribution structure, pore size averaged around 17.7 μm with a large variety in size (standard deviation = 7.5) (Table 5.21). The composite has thin well-defined walls separating the pores. The 1LRD-pGMAc composite (Figure 5.34 d) has a similar morphology with a smaller pore size of 7.2 μm

The SEM image of 1LFN-pGMAc composite (Figure 5.34 b) show a layered structure with a high pore density through individual layers. The surface is smoother when compared to the 1LEL-pGMAc composite surface. Pores found in layers averaged around 10.8 μm (Table 5.22). The 1LXL21-pGMAc composite (Figure 5.34 e) shows a layered surface similar to the 1LFN-pGMAc with a pore size and lower pore density through layers.

1LOG-pGMAc composite (Figure 5.34 c) showed a high-density and thick-walled structure with a low pore distribution and smaller size pores when compared to than 1LEL-pGMAc. Pore size averaged around 4.1 μm with a standard deviation of 2.3 (Table 5.21). 1CNa+-pGMAc composite (Figure 5.34 f) shows similar morphology

to that of the 1L_{OG}-pGMAc composite with pore size averaged at 4.7 μm (Table 5.21)

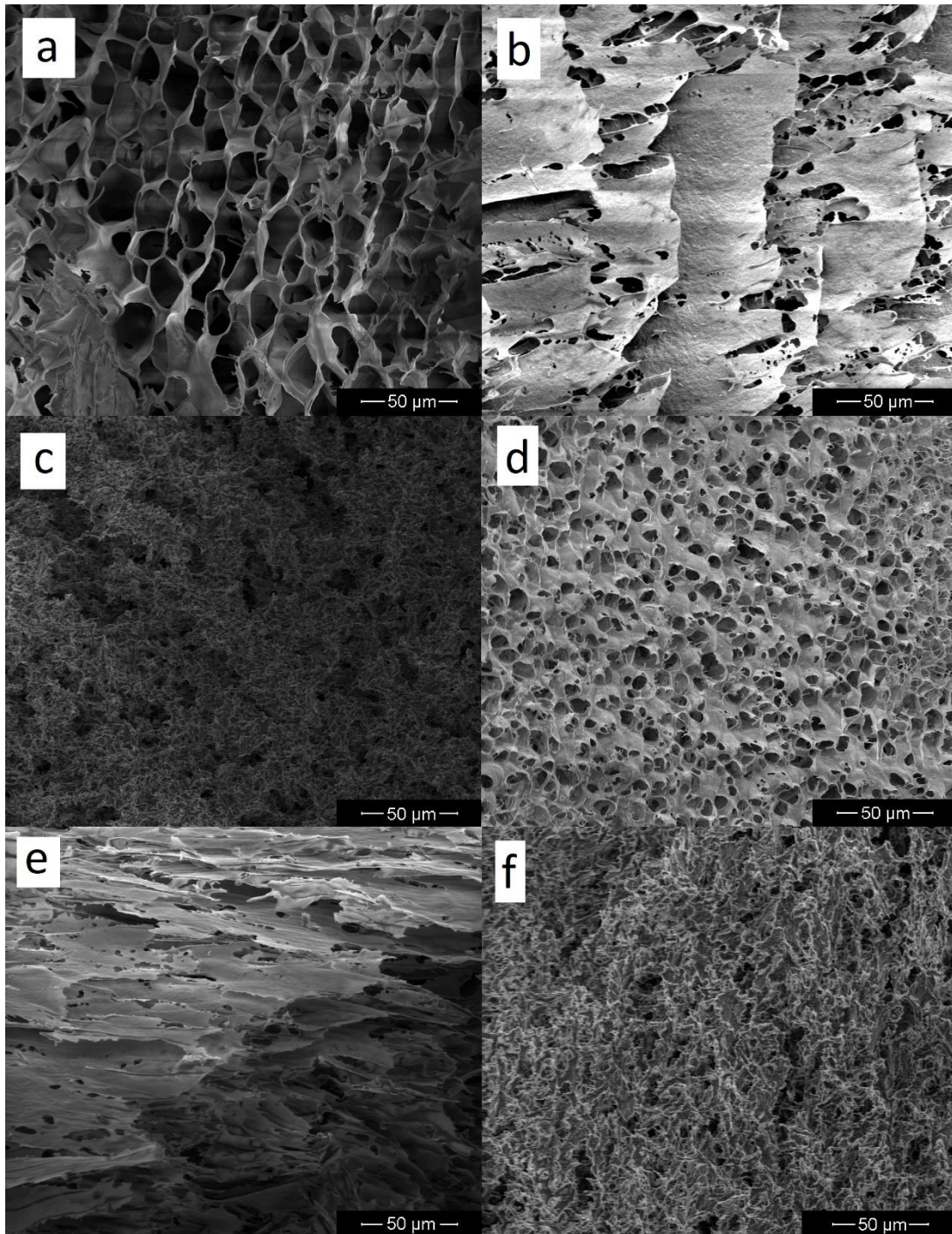


Figure 5.34 SEM images of (1 % clay)-pGMAc nanocomposite showing microstructure and pore size differences as a result of the effect of clay grade used. a) 1LEL-pGMAc b) 1LFN-pGMAc c) 1LOG-pGMAc d) 1LRD-pGMAc e) 1XL21-pGMAc f) 1CNa+-pGMAc.

Table 5.21 Average pore size and SD of (n=25) for (1 % clay)-pGMAc nanocomposite (LEL, LOG, LRD, CNa+).

Sample	Pore size (μm)	SD
1L _{EL} -pGMAc	17.7	7.5
1L _{OG} -pGMAc	4.1	2.3
1L _{RD} -pGMAc	7.2	2.6
1C _{Na+} -pGMAc	4.7	2.3

Figure 5.35 shows SEM images of the 1L_{FN}-pGMAc composite form at different profiles. The layers are stacked on top of each other in a uniform distribution, the layers of the space are interconnected through a collection of pores in each layer. The average distance separating the layers is around 4.2 with a variation from 2 – 13 μm . Table 5.22 shows the average pore size and the average distance between layers for L_{FN}-pGMAc and L_{XL21}-pGMAc nanocomposites.

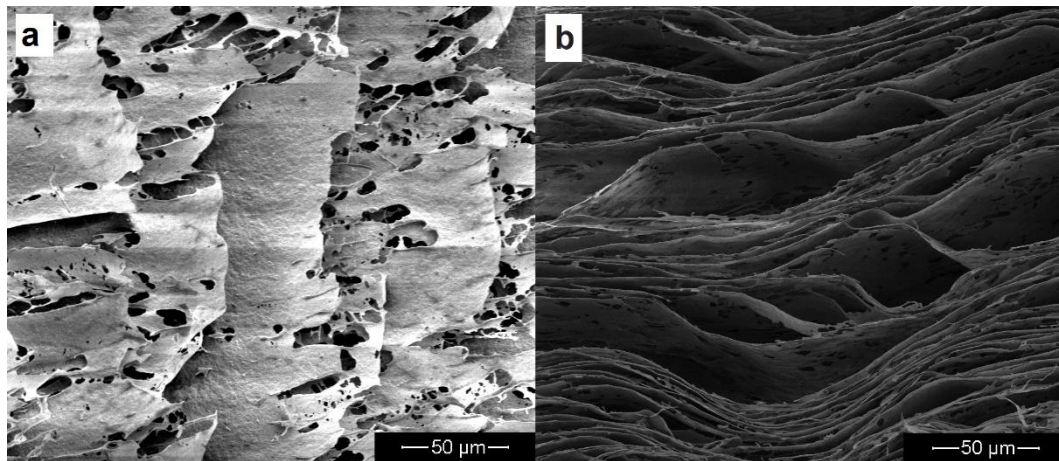


Figure 5.35 SEM images of LFN-pGMAc nanocomposite on scale bar 50 μm . a) A top view showing the voids in the 1L_{FN}-pGMAc thin layers. b) A cross-section showing the layers of LFN-pGMAc layers.

The 1L_{XL21}-pGMAc composite (Figure 5.36) also shows a layered effect with less distinct layers than the 1L_{FN}-pGMAc composite, layered surfaces are also rougher than the 1L_{FN}-pGMAc. Distance between the layers is on average of 6.7 μm (Table 5.22).

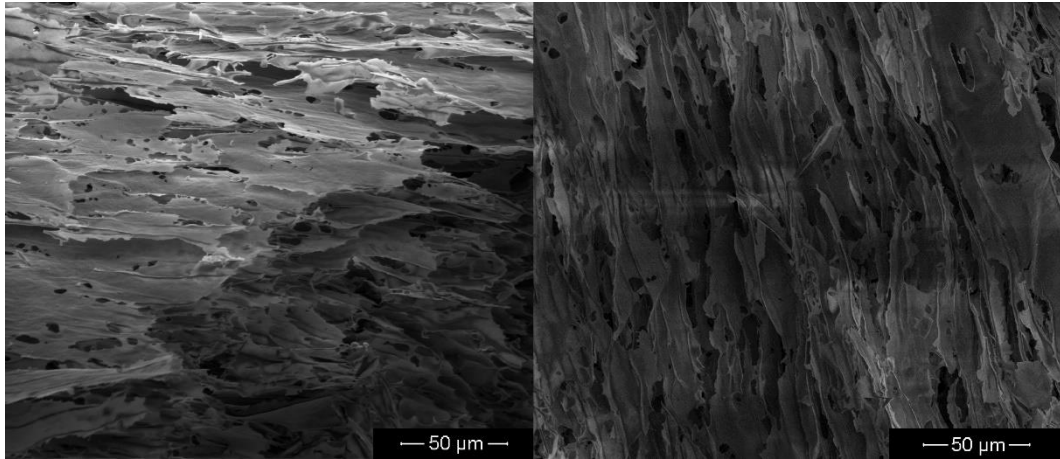


Figure 5.36 SEM images of 1LXL21-pGMAc from different angles showing its morphology from top and cross-section views.

The effect of different clay-to-polymer ratios on the morphology of clay-pGMAc was examined by comparing the SEM images of 1L_{XL21}-pGMAc and 2L_{XL21}-pGMAc nanocomposites. Figure 5.37 shows the SEM image of L_{XL21}-pGMAc composites at different magnifications for better recognition of the morphological differences.

The 1L_{XL21}-pGMAc (Figure 5.37 a and c) has an interconnected micro-scaled, smooth layered morphology with irregular voids in the layers, the size of the voids averaged around 4.1 μm. The distance between the layers was on average 6.7 μm.

By changing the clay-to-polymer ratio, the 2L_{XL21}-pGMAc nanocomposites (Figure 5.37 b and d) showed a layered, smoother textured surface with lower pore density, when compared to the 1L_{XL21}-pGMAc composite, [53] with an average of around 6.0 μm. The distance between the layers was on average 8.3 μm showing that the distance between layers (Table 5.22) is bigger. [36]

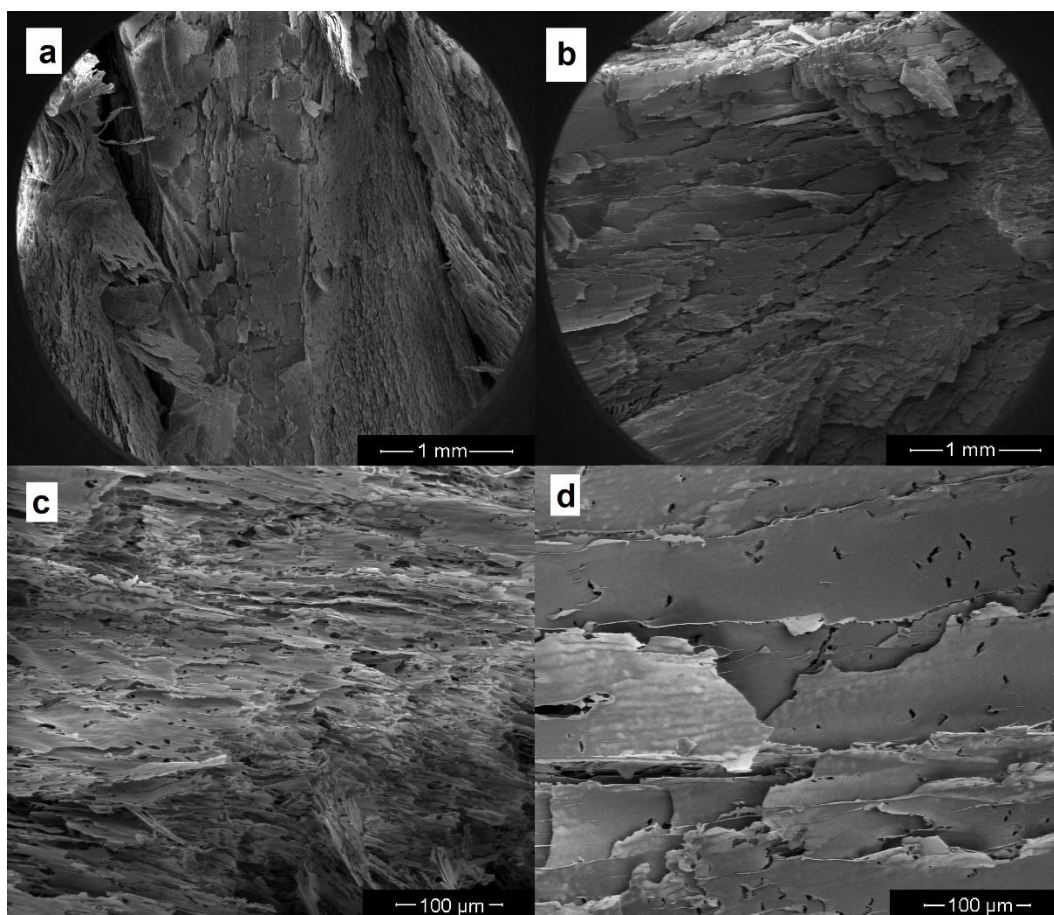


Figure 5.37 SEM images of LXL21-pGMAc nanocomposite on scale bar 1 mm and 100 μm . (a, c) 1LXL21-pGMAc (b, d) 2LXL21-pGMAc showing the effect of increasing clay content on the morphology of the microstructure.

Table 5.22 (n=25) distance between layers in the clay-pGMAc nanocomposite with a layered-like morphology and the size of the void in the layers.

Samples	Interlayer distance		layers voids	
	distance (μm)	SD	size (μm)	SD
1LFN-pGMAc	4.2	3.3	10.8	7.4
1LXL21-pGMAc	6.7	3.2	4.1	2.5
2LXL21-pGMAc	8.3	4.3	6.0	5.9

5.3.5 FTIR Spectra Analysis of Alay-pGMAc Nanocomposites

Figure 5.38 shows the FTIR spectra for GMAc monomer, pGMAc homopolymer, and the pGMAc hard precipitated material. The intensity of the C=C band at (1636 cm^{-1}) is less in both polymerisation products spectra than it is in the intensity in the GMAc monomer, this suggests that most of the monomer was polymerised. The pGMAc precipitation is also a fully polymerised material as observed by the same C=C band. [54]

In the pGMAc spectrum, the characteristic band at 3418 cm^{-1} correspond to the -OH, the C-H stretching vibration bands are observed at 2998, 2944, and 2888 cm^{-1} while the bands at 1451 and 1386 cm^{-1} corresponds to the C-H bend vibration. The peak at 1721 cm^{-1} corresponds to the C=O stretching which did not show a significant shift (1715 cm^{-1} in the GMAc spectrum). The bands at 1255, 907, 843, and 760 cm^{-1} correspond to the epoxide group. [55] Table 5.23 shows the positions of bands for GMAc, pGMAc homopolymer, and pGMAc precipitation.

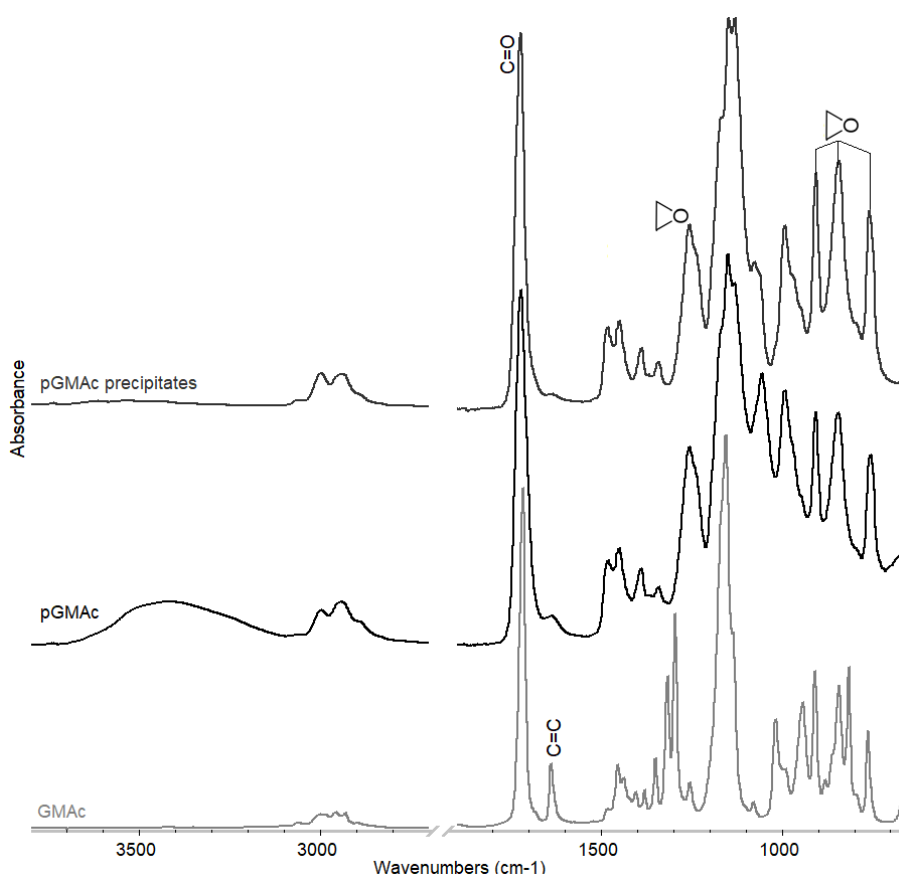


Figure 5.38 FTIR spectra of monomer GMAc and pGMAc homopolymer showing the main characteristic bands of pGMAc.

Table 5.23 FTIR peaks value for GMAc monomer, pGMAc homopolymer, and pGMAc precipitation.

Sample	-OH	C-H			C=O	C=C	C-H		Epoxide			
GMAc	-	2985	2958	2930	1715	1637	1453	1436	1294	907	842	761
pGMAc	3418	2977	2944	-	1721	1635	1451	1386	1255	905	843	784
pGMAc precipitation		2998	2987	2940	1722	1636	1448	1388	1255	905	842	757

FTIR spectra of the clay, homopolymer pGMAc, and the corresponding (1 % clay)-pGMAc and (2 % clay)-pGMAc nanocomposites are presented in Figure 5.39. FTIR spectra of the (1 % clay)-pGMAc nanocomposites exhibit evidence of containing both the clay and pGMAc in its structure.

Figure 5.39 (a) shows the details of interest in the FTIR spectrum for 1L_{EL}-pGMAc nanocomposite compared to L_{EL} and pGMAc homopolymer. The -OH stretching band shifted to lower wavenumber (3408 cm⁻¹) for the 1L_{EL}-pGMAc composite when compared to the pGMAc homopolymer (2418 cm⁻¹) which is not a significant shift to provide evidence of the association of hydrogen bonds with the addition of the nanoclay. [38] The C=O stretch band also did not shift significantly (1721 cm⁻¹ in pGMAc) (1722 cm⁻¹ in the 1L_{EL}-pGMAc). [27] The Si-O band in the L_{EL} at (946 cm⁻¹) shifted to a higher position upon crosslinking the pGMAc with the L_{EL}, the 1L_{EL}-pGMAc composite Si-O band was observed at 984 cm⁻¹. The 1L_{EL}-pGMAc band at 1060 cm⁻¹ is likely to be contributed to by the Si-O (out-of-plane) related band as it has a higher intensity after crosslinking than the 1055 cm⁻¹ in the pGMAc spectrum (relative to the pGMAc band at 1255 cm⁻¹). Most of the (1 % clay)-pGMAc nanocomposites have the same trend when examined with FTIR. However, there are some differences observed.

The 1L_{FN}-pGMAc nanocomposite in Figure 5.39 (b) shows a clear C=O band at 1722 cm⁻¹, this can be explained by the homogeneity of the composites as it had the least amount of precipitation after polymerisation and was the most homogeneous when compared to the other (1 % clay)-pGMAc composites. 1L_{OG}, pGMAc and 1L_{RD}-pGMAc composites Figure 5.39 (c and d) show similar results and shifts as the 1L_{EL}-pGMAc. Figure 5.39 (e) shows the 1L_{XL21}-pGMAc and 2L_{XL21}-pGMAc nanocomposites compared to L_{XL21} and pGMAc homopolymer. The 1L_{XL21}-pGMAc C=O stretch band shifted to around 1720 cm⁻¹ and has a lower intensity than the 2L_{XL21}-pGMAc as a result of more clay and less pGMAc in the composite, however, it did not show any significant difference in position when compared to the 1L_{XL21}-pGMAc (Table 5.24). The Si-O related bands have a lower wavenumber in the 2L_{XL21}-pGMAc composite (977 and 1057 cm⁻¹) than the Si-O bands for the 1L_{XL21}-pGMAc (982 and 1072 cm⁻¹).

Figure 5.39 (f) shows the 1C_{Na+}-pGMAc nanocomposite. The Si-O band in the 1C_{Na+}-pGMAc is 995 cm⁻¹ which has shifted to a higher wavenumber from 981 cm⁻¹ in the C_{Na+}.

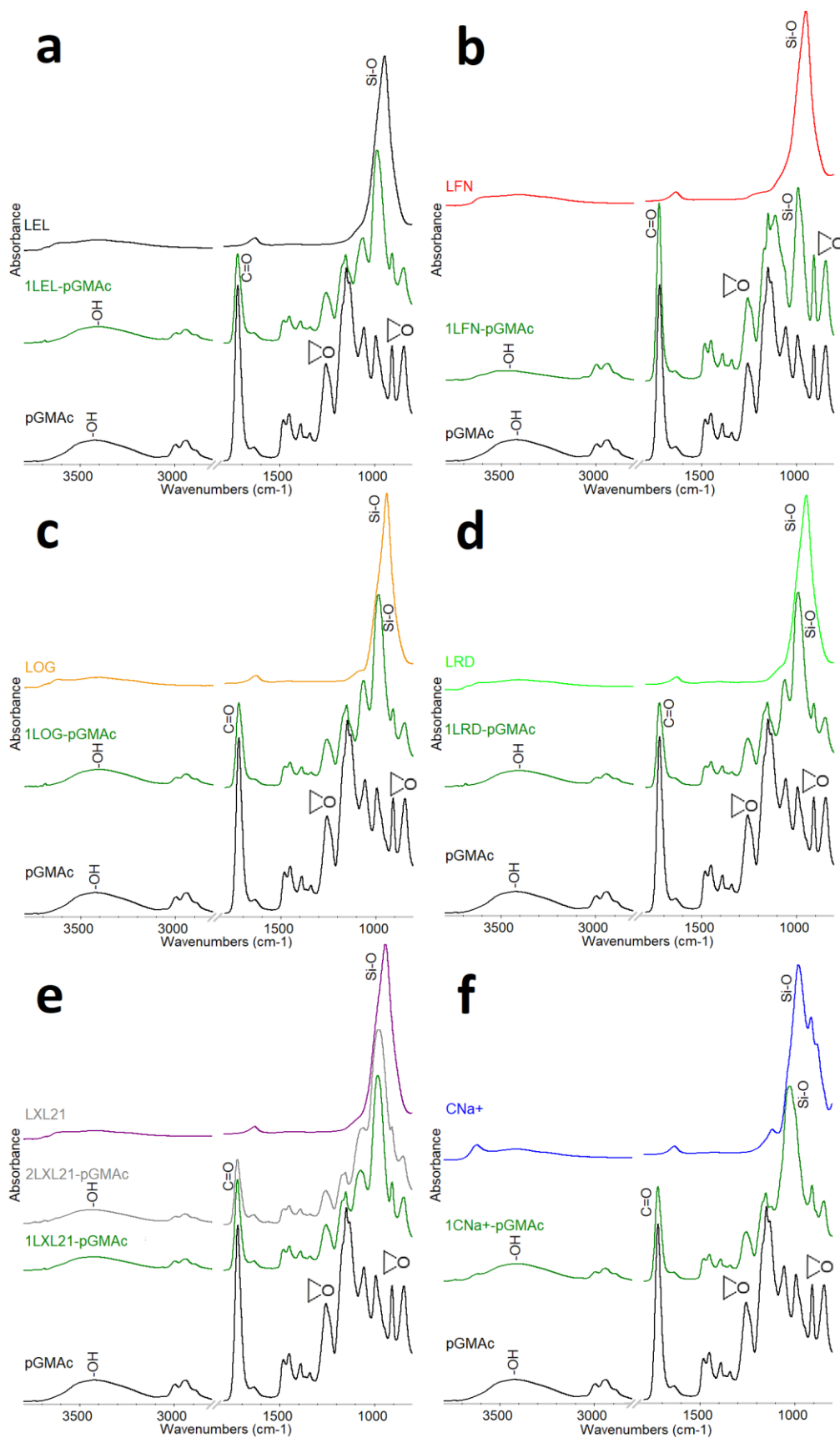


Figure 5.39 FTIR spectra of a) 1LEL-pGMAC, b) 1LFN-pGMAC, c) 1LOG-pGMAC, d) 1LRD-pGMAC, e) 1LXL21-pGMAC, f) 1CNa⁺-pGMAC nanocomposites compared to the clay and pGMAC. Offsite for clearance. All samples are dried powder.

Table 5.24 FTIR bands positions for clays, pGMAc, 1clay-pGMAc, and 2LXL21-pGMAc.

	-OH	C=C	Si-O	
pGMAc	3418	1636	-	-
L_{EL}	-	-	-	946
1L_{EL}-pGMAc	3408	1637	1060	984
L_{FN}	-	-	-	949
1L_{FN}-pGMAc	3501	1636	1072	981
L_{OG}	-	-	-	940
1L_{OG}-pGMAc	3399	1636	1062	983
L_{RD}	-	-	-	945
1L_{RD}-pGMAc	3396	1636	1060	989
L_{XL21}	-	-	-	942
1L_{XL21}-pGMAc	3418	1637	1072	982
2L_{XL21}-pGMAc	3440	1636	1057	976
C_{Na+}	-	-	-	912
1C_{Na+}-pGMAc	3411	1637	1024	995

5.3.6 Rheological Analysis and Properties of Clay-pGMAc Nanocomposites

5.3.6.1 Yield stress for clay-pGMAc nanocomposites

The flow curves in Figure 5.40 show the yield stress (τ_{stress}) points for the (1 % clay)-pGMAc nanocomposite. Values for τ_{stress} for the clay-pGMAc nanocomposites are presented in Table 5.25. 1L_{EL}-pGMAc and L_{RD}-pGMAc nanocomposites have higher yield stress values than other composites in the pGMAc related composites, this may be a result of the small particle size of the L_{EL} and L_{RD} when compared to other clays.

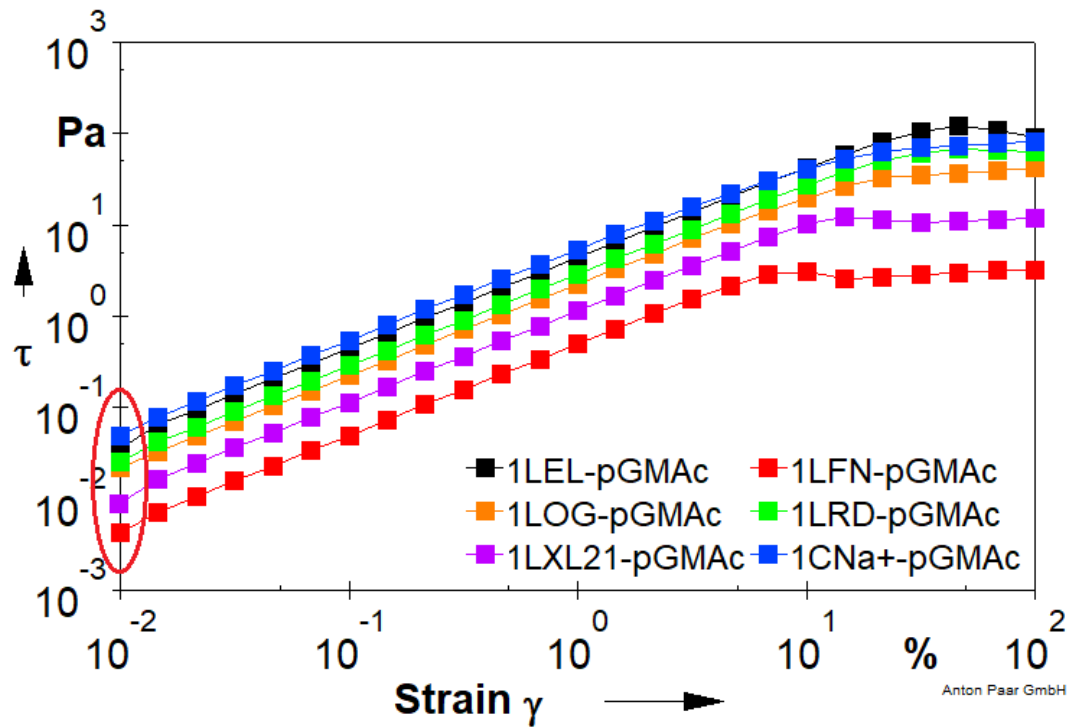


Figure 5.40 (n=3) Flow curve showing yield stress for 1clay-pGMAc. The first point on Y-axis is where the stress is high enough for the material to start flowing.

The smaller the clay platelets used to crosslink the pGMAc for a nanocomposite the larger the yield stress values when plotting the τ_{yield} as a function to the clay particle size (Table 5.25 and Figure 5.41). The clay effect on the yield stress value may not be observed directly from these values as the clay-pGMAc composites were heterogeneous in general. The 1CNa⁺-pGMAc with the largest particle size had the highest τ_{yield} value despite its particle size (550 nm), this may be related to the fact that 1CNa⁺-pGMAc squeezed more water when setup for testing on the rheometer than other hydrogels from this group.

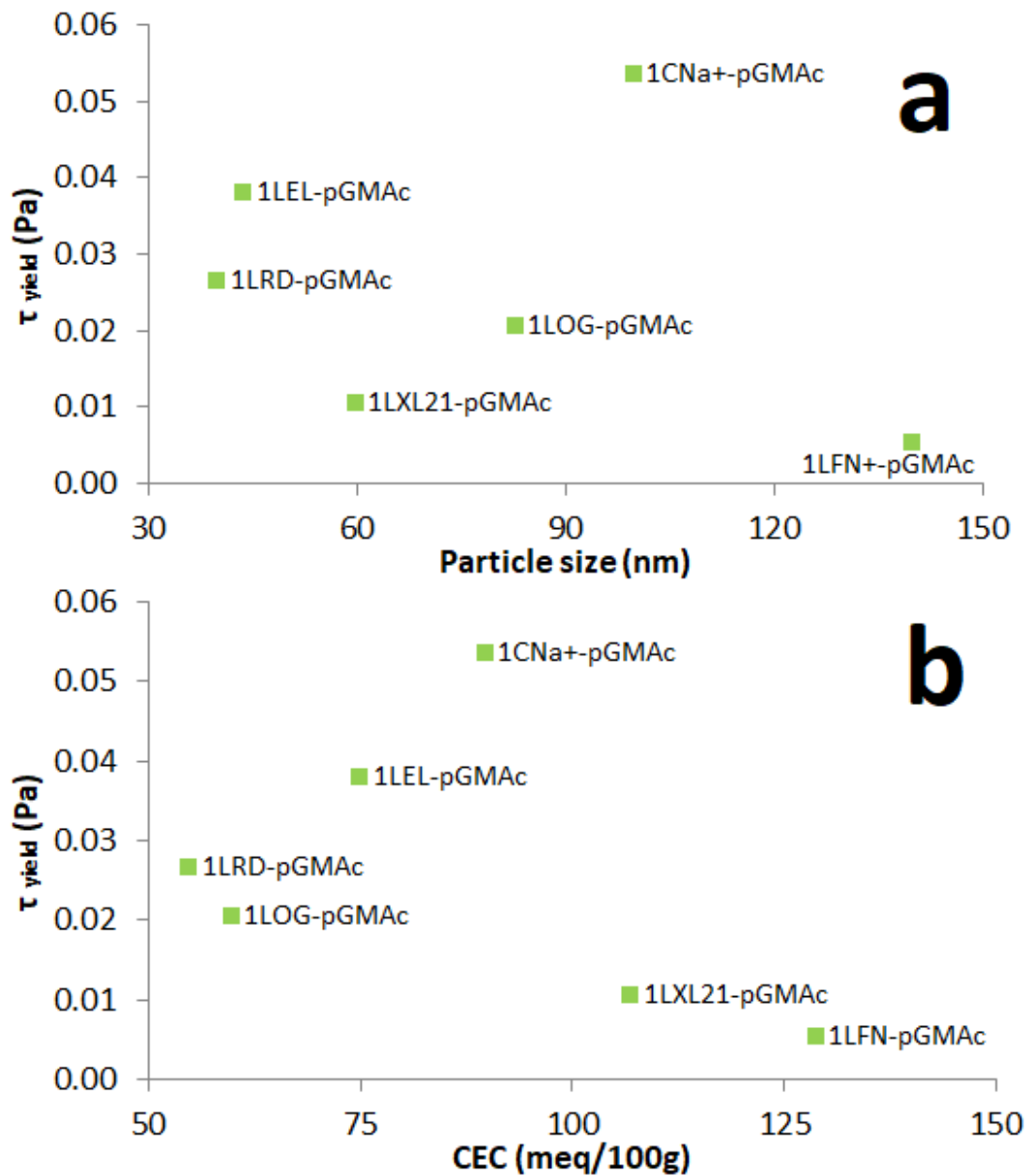


Figure 5.41 Yield stress for (1 % clay)-pGMAc nanocomposites as a function of a) Clay particle size, b) Clay CEC.

The flow curves in Figure 5.42 show the yield stress value points for 1L_{XL21}-pGMAc and 2L_{XL21}-pGMAc. As expected, the higher the clay-to-polymer ratio in the nanocomposite the larger the τ_{yield} values. The effect of the number of the crosslinking point is clear as per the values in Table 5.25.

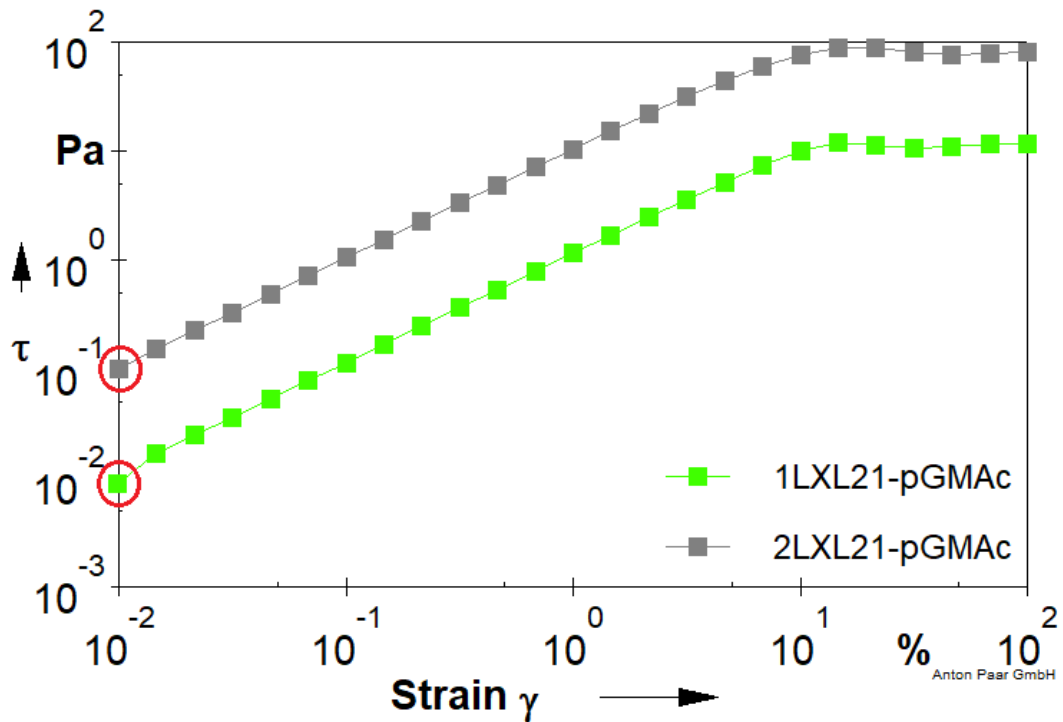


Figure 5.42 ($n=3$) Flow curve showing yield stress for 1LXL21-pGMAc and 2LXL21-pGMAc nanocomposite.

Table 5.25 ($n=3$) τ_{yield} (Pa.), SD and the corresponding clay particle size and CEC values for the (1 % clay)-pGMAc and 2LXL21-pGMAc.

Sample	Yield point	
	τ_{yield}	SD
1L _{EL} -pGMAc	0.0379	0.0044
1L _{FN} -pGMAc	0.0052	0.0012
1L _{OG} -pGMAc	0.0204	0.0025
1L _{RD} -pGMAc	0.0264	0.0018
1L _{XL21} -pGMAc	0.0103	0.0006
2L _{XL21} -pGMAc	0.0966	0.0038
1C _{Na+} -pGMAc	0.0534	0.0069

5.3.6.2 Storage (G') and Loss (G'') Moduli Behaviour for Clay-pGMAc Nanocomposites

5.3.6.2.1 Amplitude Sweep (Function of Strain)

Figure 5.43 shows the storage (G') and loss (G'') moduli behaviour over a strain sweep for (1 % clay)-pGMAc. The critical strain (γ_c) value changes according to the clay used as a crosslinking agent. As with the yield stress values; composites which were crosslinked with small particle size clays (L_{EL} , L_{RD}) have higher γ_c value where larger particle size clays had lower γ_c value (Table 5.26). This behaviour did not

apply with 1L_{XL21}-pGMAc, this might be because this particular clay has a high CEC value compared to its particle size.

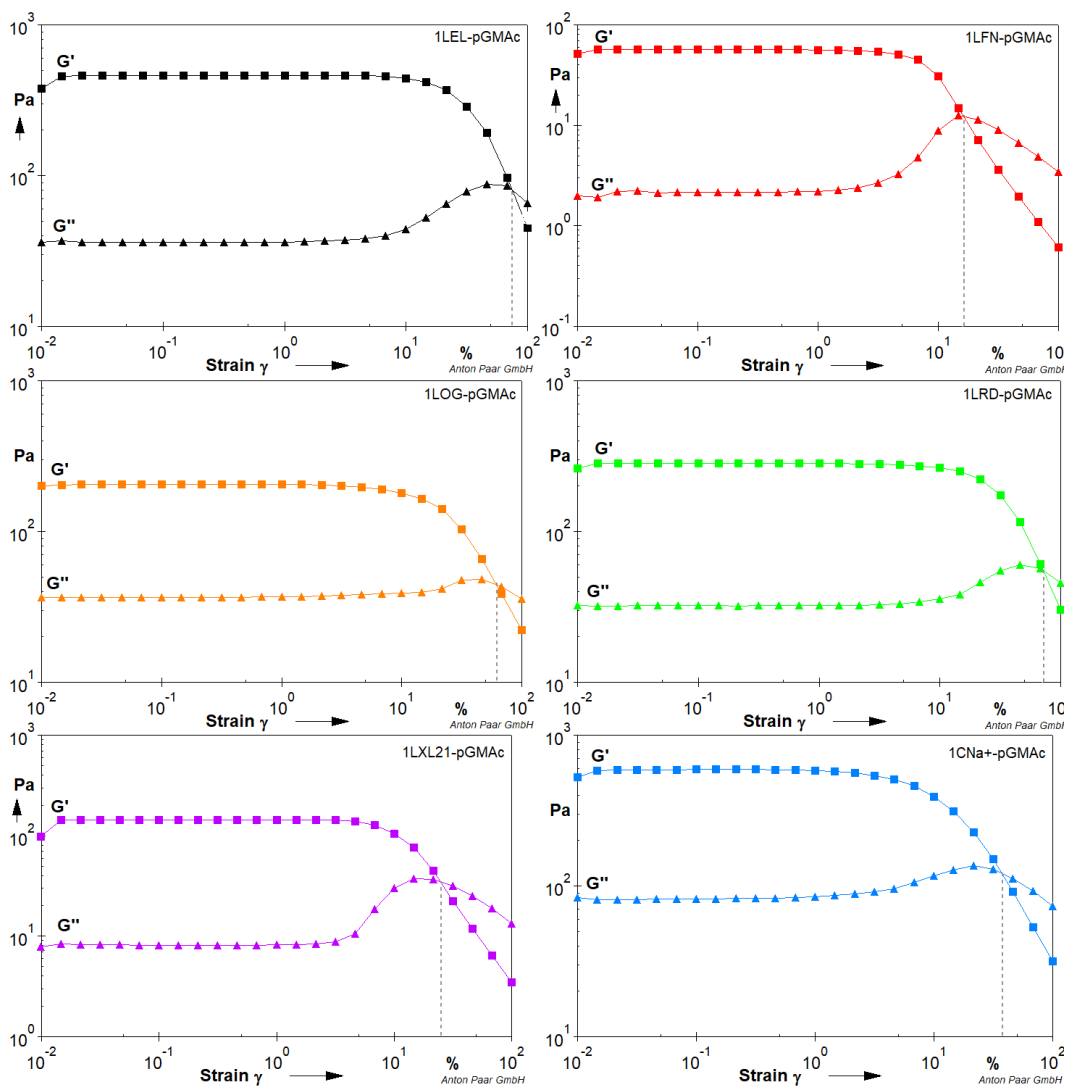


Figure 5.43 (n=3) Evolution of storage modulus G' and loss modulus G'' as a function of strain at a constant frequency from 0.01 % - 100 % strain; showing the LVE range and transition crossover point (gel-like to fluid-like) for (1 % clay)-pGMAc.

Clay-pGMAc composites with small particle size clays also showed a larger LVE range than other composites, these composites have higher elastic properties. This may be due to better distribution of clay platelets in the structure and more crosslink points as a result.

Table 5.26 average LVE region limits (strain % and G' Pa.) of (n=3). Crossover transition point (gel-like to liquid-like) strain values and moduli value for 1clay-pGMAc and 2LXL21-pGMAc nanocomposite.

Samples	LVE		Crossover point		
	Strain %	G' Pa	Critical Strain		G' Pa
			Strain %	SD	
1L _{EL} -pGMAc	16.90	399.00	74.75	28.65	80.31
1L _{FN} -pGMAc	04.19	51.80	16.29	00.94	12.21
1L _{OG} -pGMAc	07.10	190.00	61.86	21.20	44.28
1L _{RD} -pGMAc	11.50	259.00	71.92	18.25	55.37
1L _{XL21} -pGMAc	07.67	120.00	24.68	10.75	34.98
2L _{XL21} -pGMAc	03.72	931.00	35.72	5.49	146.73
1C _{Na+} -pGMAc	04.14	516.00	37.29	23.18	121.52

Figure 5.44 shows a strain sweep for 1L_{XL21}-pGMAc and 2L_{XL21}-pGMAc. Changing clay-to-polymer ratio increased the γ_c from 24.68 % to 35.72 %. More clay in the composite also increased the LVE range. The clay-to-polymer ratio had a large effect on the rheological properties via more crosslink points between the pGMAc chains and the clay platelets, giving the composite more elasticity and the ability to withstand higher strains. Related values are shown in Table 5.26 which shows the parameters for the crossover points and the for the LVE range.

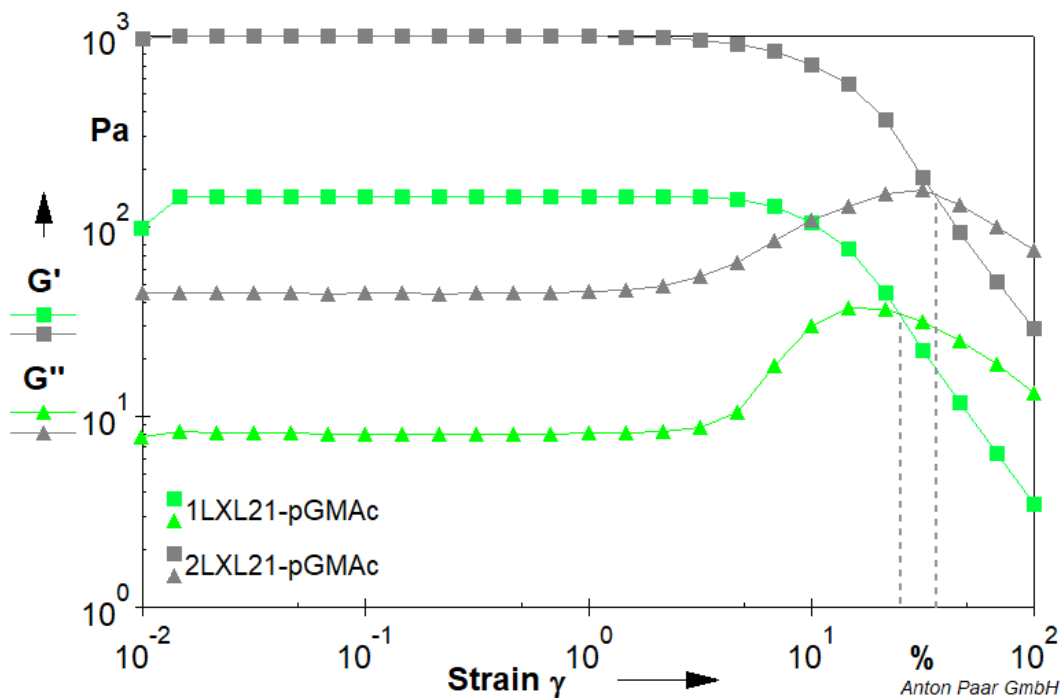


Figure 5.44 (n=3) Evolution of storage modulus (G') and loss modulus (G'') as a function of strain sweep from 0.01 % - 100 % strain showing the LVE range and transition point (gel-like to liquid-like) for 1LXL21-pGMAc and 2LXL21-pGMAc nanocomposite.

5.3.6.2.2 Frequency Sweep (Function of Frequency)

Figure 5.45 shows the G' and G'' behaviour as a function of frequency from 0.01 - 100 Hz for (1 % clay)-pGMAc nanocomposites. Gel-Like material behaviour is observed for all composites up to high frequency (Table 5.27). The crossover transition points show when the samples transform to a liquid-like material and they are all at high-frequency values. 1C_{Na+}-pGMAc (92.71 Hz, 529.00 Pa) had the highest crossover point followed by 1L_{OG}-pGMAc (91.55 Hz, 370.59 Pa), then 1L_{EL}-pGMAc and 1L_{XL21}-pGMAc had close values, whereas the 1L_{FN}-pGMAc had the lowest crossover point at (39.00 Hz, 26.39 Pa).

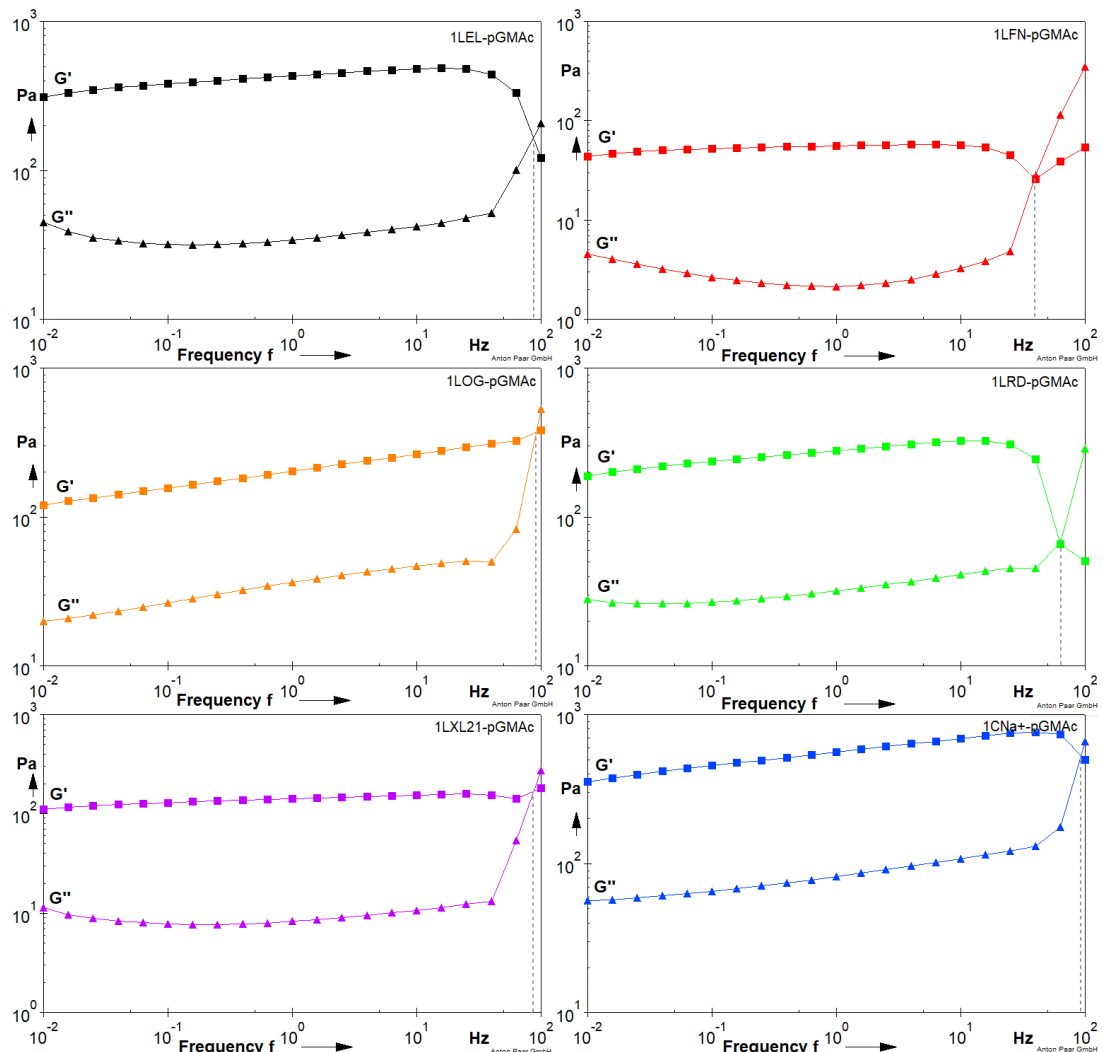


Figure 5.45 (n=3) Evolution of storage modulus G' and loss modulus G'' as a function of frequency from 0.01 - 100 Hz showing the transition point (solid-like to fluid-like) for (1 % clay)-pGMAc.

Table 5.27 (n=3) G' Pa and frequency Hz at the crossover transition point (gel-like to liquid-like) for (1 % clay)-pGMAc nanocomposite.

Sample	Crossover point		G' Pa
	Critical frequency		
	Frequency Hz	SD	
1L _{EL} -pGMAc	86.62	02.01	165.29
1L _{FN} -pGMAc	39.00	09.58	026.39
1L _{OG} -pGMAc	91.55	19.78	370.59
1L _{RD} -pGMAc	62.71	01.98	066.96
1L _{XL21} -pGMAc	87.15	16.73	169.18
1C _{Na+} -pGMAc	92.71	20.60	529.00

Figure 5.46 shows the G' and G'' moduli behaviour over a frequency sweeps for 1L_{XL21}-pGMAc and 2L_{XL21}-pGMAc composites. The higher clay-to-polymer ratio nanocomposites have higher elastic properties. No change of behaviour was observed for the 2L_{XL21}-pGMAc up to 100 Hz, while as mentioned earlier the 1L_{XL21}-pGMAc had a crossover point to a liquid-like material at around (987.15 Hz, 169.18 Pa) which can be related to the more homogeneous and more crosslinked 2L_{XL21}-pGMAc as a result of more clay and less polymer in the composite.

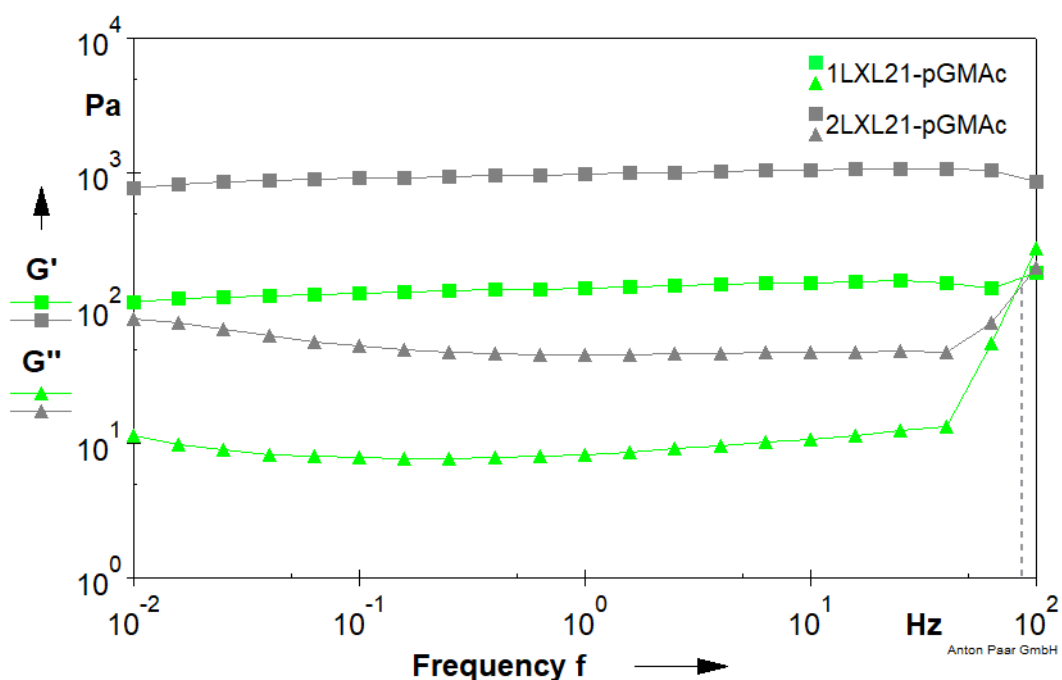


Figure 5.46 (n=3) Evolution of storage modulus (G') and loss modulus (G'') as a function of frequency from 0.01 Hz – 100 Hz showing the crossover transition point (gel-like to liquid-like) for 1LXL21-pGMAc and 2LXL21-pGMAc nanocomposite.

5.4 Summary

Chapter 5 studied the influence of clay type on the morphological and mechanical properties of clay crosslinked pHEMA, pHPMA and pGMAc nanocomposites.

The characterisation techniques used (XRD and FTIR) show evidence of clay platelets dispersion in the composite structure and the interaction between the clay platelets and the polymeric chains. The XRD shows an increasing baseline for $2\theta < 5^\circ$ which supports very well dispersed clay in the nanocomposite's matrix, however, the L_{FN} and L_{XL21} and C_{Na+} based nanocomposite showed evidence of forming intercalated or microstructure nanocomposites in some cases as mentioned earlier, which may be due to their higher CEC, but this still need further analysis.

The main spectroscopic changes observed for FTIR spectra shown for the nanocomposites are changes in intensity and band position associated with the water and Si-O of the clay when comparing the neat clay and the homopolymers to the clay-polymer composites (Table 5.6, Table 5.14, and Table 5.24). The Si-O stretching band shifts show that the clay platelets have separated because of inserting the polymeric chains between the layers. This observation supports the XRD observations indicating that the clay particles are either well dispersed or intercalated or microstructured. All these observations can be associated directly to the crosslinking action of the clay platelets.

As polymers were crosslinked with clay, they exhibited less total weight loss compared to the homopolymers as can be seen throughout "stage 2" of all nanocomposites mentioned earlier in this chapter. The TGA analysis showed that the onset temperature made a significant improvement for the clay-pHEMA and clay-pHPMA nanocomposites when compared to the homopolymers (Figure 5.7 and Figure 5.20), the pHEMA-based nanocomposites showed an average increase of the onset temperature of 24 °C (Table 5.2) and the pHPMA showed an increase of 14 °C (Table 5.11) on average. The clay-to-polymer ratios did not show a significant effect on the onset temperature or the total weight loss as discussed earlier, as when

calculated on dry-basis the remaining mass is mainly the clay, however, the weight loss behaviour between 300 – 400 °C was slower with the presence of clay and the decomposition occurs at significantly higher temperatures than for the pHEMA and pHPMA homopolymers. No trends relating to the clay platelet size or CEC were observed. The C_{Na^+} -based pHEMA and pHPMA nanocomposites require higher temperature for decomposition, this behaviour can relate to its different structure but still require more investigation.

pHEMA and pHPMA based composites exhibit interesting rheological properties with high yield stress region related to its hydrophobicity as a result of less water held in the hydrogel matrix. Most of the water involved in the synthesis process is squeezed out of the hydrogels as soon as they are placed between the rheometer parallel plates, and hard solid rubbery like materials are remaining to test, these hydrogels were mainly not capable of being tested and only the L_{XL21} -pHEMA and $1L_{XL21}$ -pHPMA hydrogels were used for rheological analysis. Figure 5.16 and Figure 5.17 show the effect of the L_{XL21} -to-PHEMA ratio effect on the τ_{yield} and LVE limits, the higher the L_{XL21} content higher the τ_{yield} and LVE limits, the case is the same for the L_{XL21} -pHPMA hydrogels as shown in Figure 5.27 and Figure 5.28. These results show an opposite trend to the effect of a clay-to-pDMAc ratio where the more clay the lower the LVE limits, which is a result of the polymers different nature. With pHEMA and pHPMA based hydrogels, the crosslinking point adds flexibility and increases the elasticity of the material were with pDMAc-based hydrogels the crosslinking points restrict the movement and flexibility of the polymeric chains.

The incorporation of clay in pGMAc (Section 5.3) affects the properties of the pGMAc and the resulting composite has different behaviour, pGMAc homopolymer tends not to form a 3D network. The pGMAc-related composites were heterogeneous as shown by the different TGA weight loss curves (Figure 5.32) and the synthesis of them would need to be optimised and required more investigation to get to a homogeneous nanocomposite/hydrogel with no precipitation of pGMAc

or clay platelets, as the XRD analysis and FTIR spectroscopy (Figure 5.30 and Figure 5.38) showed that the precipitations were mainly a pGMAc homopolymer.

The clay-pGMAc nanocomposite SEM images show a porous interconnected structure, a comparison between the effect of different clay types and the clay-to-polymer ratio showed there was no trend to follow and the morphology of the 1L_{FN}-pGMAc, 1L_{XL21}-pGMAc, and 2L_{XL21}-pGMAc was different from the other composite with clear layered morphology (Figure 5.35 and Figure 5.36).

No clear trend was observed between the clay type and the τ_{yield} for the clay-pGMAc nanocomposites as shown by Figure 5.41, and the case was the same for the LVE limits, this may be a result of the heterogeneous nature of the clay-pGMAc nanocomposites which require further investigations. However, the effect of clay-to-polymer ratio was similar to the clay-pHEMA and clay-PPMA behaviour as indicated in Figure 5.42 and Figure 5.43.

5.5 References

- [1] H. Kang *et al.*, “Polymerization Kinetics of Poly(2-Hydroxyethyl Methacrylate) Hydrogels and Nanocomposite Materials,” *Macromolecules*, vol. 5, no. 1, pp. 449–456, Jan. 2013.
- [2] D. S. Achilias and P. I. Sifaka, “Polymerization kinetics of poly(2-hydroxyethyl methacrylate) hydrogels and nanocomposite materials,” *Processes*, vol. 5, no. 2, Jun. 2017.
- [3] E. A. Stefanescu, W. H. Daly, and I. I. Negulescu, “Hybrid polymer/clay nanocomposites: Effect of clay size on the structure of multilayered films,” *Macromol. Mater. Eng.*, vol. 293, no. 8, pp. 651–656, Aug. 2008.
- [4] K. Haraguchi, H. J. Li, L. Song, and K. Murata, “Tunable optical and swelling/deswelling properties associated with control of the coil-to-globule transition of poly(N-isopropylacrylamide) in polymer - Clay nanocomposite gels,” *Macromolecules*, vol. 40, no. 19, pp. 6973–6980, Sep. 2007.
- [5] L. Mengatto, M. G. Ferreyra, A. Rubiolo, I. Rintoul, and J. Luna, “Hydrophilic and hydrophobic interactions in cross-linked chitosan membranes,” *Mater. Chem. Phys.*, vol. 139, no. 1, pp. 181–186, Apr. 2013.
- [6] L. J. Macdougall, M. M. Pérez-Madrigal, M. C. Arno, and A. P. Dove, “Nonswelling Thiol-Yne Cross-Linked Hydrogel Materials as Cytocompatible Soft Tissue Scaffolds,” *Biomacromolecules*, vol. 19, no. 5, pp. 1378–1388, May 2018.
- [7] L. Liang *et al.*, “Surfaces with reversible hydrophilic/hydrophobic characteristics on cross-linked poly(N-isopropylacrylamide) hydrogels,” *Langmuir*, vol. 16, no. 21, pp. 8016–8023, Oct. 2000.
- [8] K. Haraguchi, R. Farnworth, A. Ohbayashi, and T. Takehisa, “Compositional effects on mechanical properties of nanocomposite hydrogels composed of poly(N,N-dimethylacrylamide) and clay,” *Macromolecules*, vol. 36, no. 15, pp.

5732–5741, Jul. 2003.

- [9] E. Karpushkin, M. Dušková-Smrčková, M. Šlouf, and K. Dušek, "Rheology and porosity control of poly(2-hydroxyethyl methacrylate) hydrogels," *Polymer (Guildf)*, vol. 54, no. 2, pp. 661–672, Jan. 2013.
- [10] Zainuddin, D. J. T. Hill, A. K. Whittaker, and T. V. Chirila, "In-vitro study of the spontaneous calcification of PHEMA-based hydrogels in simulated body fluid," *J. Mater. Sci. Mater. Med.*, vol. 17, no. 12, pp. 1245–1254, Dec. 2006.
- [11] I. Ahmad *et al.*, "Photoinitiated Polymerization of 2-Hydroxyethyl Methacrylate by Riboflavin/Triethanolamine in Aqueous Solution: A Kinetic Study," *ISRN Pharm.*, vol. 2013, pp. 1–7, 2013.
- [12] H. Rashid, M. Ahmad, M. U. Minhas, M. Sohail, and M. F. Aamir, "Synthesis and characterization of poly(hydroxyethyl methacrylate-co-methacrylic acid) cross li muhammad farooq View project A Bioequivalence Study of Two Commercial Brands of Cephadrine View project SEE PROFILE," *Artic. Journal-Chemical Soc. Pakistan*, vol. 37, no. 05, pp. 999–1007, 2015.
- [13] J. V. M. Weaver *et al.*, "Stimulus-Responsive Water-Soluble Polymers Based on 2-Hydroxyethyl Methacrylate," *Macromolecules*, vol. 37, no. 7, pp. 2395–2403, Apr. 2004.
- [14] K. L. Beers, S. Boo, S. G. Gaynor, and K. Matyjaszewski, "Atom transfer radical polymerization of 2-hydroxyethyl methacrylate," *Macromolecules*, vol. 32, no. 18, pp. 5772–5776, 1999.
- [15] C. Maldonado-Codina and N. Efron, "Hydrogel Lenses Materials and Manufacture_ A Review," *Optom. Pract.*, vol. 4, pp. 101–115, 2003.
- [16] A. M. Asiri, "Nanocomposites and Importance of Nanofiller in Nanocomposites," *Dev. Prospect. Appl. Nanosci. Nanotechnol.*, no. January, pp. 157–179, 2016.

- [17] Q. Li, X. Chen, Q. Tang, H. Xu, B. He, and Y. Qin, "Imbibition of polypyrrole into three-dimensional poly(hydroxyethyl methacrylate/glycerol) gel electrolyte for robust quasi-solid-state dye-sensitized solar cells," *J. Mater. Chem. A*, vol. 1, no. 27, pp. 8055–8060, 2013.
- [18] C. Statement, "Multi-Scale Effects on Deformation Mechanisms of Polymer Nanocomposites : Experimental Characterisation and Numerical Study," *Scan. Electron Microsc.*, vol. 1994, no. April, 1994.
- [19] N. Ghaemi, S. S. Madaeni, A. Alizadeh, H. Rajabi, and P. Daraei, "Preparation, characterization and performance of polyethersulfone/organically modified montmorillonite nanocomposite membranes in removal of pesticides," *J. Memb. Sci.*, vol. 382, no. 1–2, pp. 135–147, 2011.
- [20] J. M. Yeh, S. J. Liou, and Y. W. Chang, "Polyacrylamide-clay nanocomposite materials prepared by photopolymerization with acrylamide as an intercalating agent," *J. Appl. Polym. Sci.*, vol. 91, no. 6, pp. 3489–3496, Mar. 2004.
- [21] M. Alexandre and P. Dubois, "Polymer-layered silicate nanocomposites: Preparation, properties and uses of a new class of materials," *Mater. Sci. Eng. R Reports*, vol. 28, no. 1, pp. 1–63, Jun. 2000.
- [22] J. M. Yeh *et al.*, "Enhancement of corrosion protection effect of poly(o-ethoxyaniline) via the formation of poly(o-ethoxyaniline)-clay nanocomposite materials," *Polymer (Guildf.)*, vol. 43, no. 9, pp. 2729–2736, Mar. 2002.
- [23] T. N. Blanton, D. Majumdar, and S. M. Melpolder, "MICROSTRUCTURE OF CLAY-POLYMER COMPOSITES," vol. 42. JCPDS-International Centre for Diffraction Data, New York, pp. 562–568, 2000.
- [24] P. K. Paul, S. A. Hussain, D. Bhattacharjee, and M. Pal, "Preparation of polystyrene-clay nanocomposite by solution intercalation technique," *Bull. Mater. Sci.*, vol. 36, no. 3, pp. 361–366, Jun. 2013.

- [25] S. Mallakpour and M. Dinari, "Biomodification of cloisite Na + with L-methionine amino acid and preparation of poly(vinyl alcohol)/organoclay nanocomposite films," *J. Appl. Polym. Sci.*, vol. 124, no. 5, pp. 4322–4330, Jun. 2012.
- [26] F. F. Fang, J. H. Kim, H. J. Choi, and C. A. Kim, "Synthesis and electrorheological response of nano-sized laponite stabilized poly(methyl methacrylate) spheres," *Colloid Polym. Sci.*, vol. 287, no. 6, pp. 745–749, 2009.
- [27] M. Zhai, F. Ma, J. Li, B. Wan, and N. Yu, "Preparation and properties of cryogel based on poly(hydroxypropyl methacrylate)," *J. Biomater. Sci. Polym. Ed.*, vol. 29, no. 12, pp. 1401–1425, Aug. 2018.
- [28] S. Khanlari and M. Kokabi, "Thermal stability, aging properties, and flame resistance of NR-based nanocomposite," *J. Appl. Polym. Sci.*, vol. 119, no. 2, pp. 855–862, Jan. 2011.
- [29] G. Chen, S. Liu, S. Chen, and Z. Qi, "FTIR Spectra, Thermal Properties, and Dispersibility of a Polystyrene/Montmorillonite Nanocomposite," *Macromol. Chem. Phys.*, vol. 202, pp. 1189–1193, 2001.
- [30] S. Pricle, P. Posocco, G. Scocchi, and M. Fermeglia, "Handbook of Nanophysics: Functional Nanomaterials: Polymer–Clay Nanocomposites Sabrina," CRC Press, 2011.
- [31] H. W. Kang, Y. Tabata, and Y. Ikada, "Fabrication of porous gelatin scaffolds for tissue engineering," *Biomaterials*, vol. 20, no. 14, pp. 1339–1344, Jul. 1999.
- [32] T. M. Freyman, I. V. Yannas, and L. J. Gibson, "Cellular materials as porous scaffolds for tissue engineering," *Prog. Mater. Sci.*, vol. 46, no. 3–4, pp. 273–282, 2001.

- [33] J. Grenier, H. Duval, F. Barou, P. Lv, B. David, and D. Letourneur, "Mechanisms of pore formation in hydrogel scaffolds textured by freeze-drying," *Acta Biomater.*, vol. 94, pp. 195–203, Aug. 2019.
- [34] S. Sornkamnerd, M. K. Okajima, and T. Kaneko, "Tough and Porous Hydrogels Prepared by Simple Lyophilization of LC Gels," *ACS Omega*, vol. 2, no. 8, pp. 5304–5314, 2017.
- [35] A. Zhu, G. Li, and J. Jiang, "Novel poly(2-hydroxyethyl methacrylate-acrylamid)/clay nanocomposite gels with enhanced mechanical strength," *J. Macromol. Sci. Part B Phys.*, vol. 51, no. 5, pp. 1002–1010, May 2012.
- [36] W. Dong, C. Huang, Y. Wang, Y. Sun, P. Ma, and M. Chen, "Superior mechanical properties of double-network hydrogels reinforced by carbon nanotubes without organic modification," *Int. J. Mol. Sci.*, vol. 14, no. 11, pp. 22380–22394, Nov. 2013.
- [37] D. Çimen, F. Yılmaz, / Hacettepe, J. Biol, D. Çimen, and F. Yılmaz, "Bovine Serum Albumin Adsorption by Dye Derived Poly(hydroxyethyl methacrylate) [PHEMA] Membranes Boya Takılı Poli(hidroksietil metakrilat) [PHEMA] Membranlarla Sığır Serum Albümin Adsorpsiyonu," *Chem*, vol. 43, no. 3, pp. 213–223, 2015.
- [38] S. Morita, "Hydrogen-bonds structure in poly(2-hydroxyethyl methacrylate) studied by temperature-dependent infrared spectroscopy," *Front. Chem.*, vol. 2, no. MAR, 2014.
- [39] J. Díez, L. Barral, R. Bellas, J. López, C. Ramírez, and A. Rodríguez, "Exfoliated/intercalated silicate/hot styrene butadiene rubber nanocomposites: Structure-properties relationship," *J. Appl. Polym. Sci.*, vol. 125, no. SUPPL. 1, Jul. 2012.
- [40] J. M. Zuidema, C. J. Rivet, R. J. Gilbert, and F. A. Morrison, "A protocol for rheological characterization of hydrogels for tissue engineering strategies," *J.*

Biomed. Mater. Res. - Part B Appl. Biomater., vol. 102, no. 5, pp. 1063–1073, 2014.

- [41] T. Sentoukas and S. Pispas, "Poly(dimethylaminoethyl methacrylate)-b-poly(hydroxypropyl methacrylate) copolymers: Synthesis and pH/thermo-responsive behavior in aqueous solutions," *J. Polym. Sci. Part A Polym. Chem.*, vol. 56, no. 17, pp. 1962–1977, Sep. 2018.
- [42] N. Rocha, J. F. J. Coelho, J. R. Gois, M. H. Gil, P. M. O. F. Gonçalves, and J. T. Guthrie, "Poly(vinyl chloride)-b-poly(hydroxypropyl acrylate)-b-Poly(vinyl chloride): Understanding the synthesis of an amphiphilic PVC block copolymer on a pilot scale," *J. Vinyl Addit. Technol.*, vol. 19, no. 2, pp. 94–104, Jun. 2013.
- [43] V. M. Gun'ko, I. N. Savina, and S. V. Mikhalovsky, "Cryogels: Morphological, structural and adsorption characterisation," *Adv. Colloid Interface Sci.*, vol. 187–188, pp. 1–46, 2013.
- [44] S. H. Nair, K. C. Pawar, J. P. Jog, and M. V. Badiger, "Swelling and mechanical behavior of modified poly(vinyl alcohol)/laponite nanocomposite membranes," *J. Appl. Polym. Sci.*, vol. 103, no. 5, pp. 2896–2903, Mar. 2007.
- [45] T. Çelik and M. F. Coşkun, "Dielectric and thermal properties of the methacrylate polymer bearing chalcone side group," *J. Mol. Struct.*, vol. 1157, pp. 239–246, Apr. 2018.
- [46] S. J. Gerber and E. Erasmus, "Electronic effects of metal hexacyanoferrates: An XPS and FTIR study," *Mater. Chem. Phys.*, vol. 203, pp. 73–81, Jan. 2018.
- [47] S. M. Choi, D. Singh, Y. W. Cho, T. H. Oh, and S. S. Han, "Three-dimensional porous HPMA-co-DMAEM hydrogels for biomedical application," *Colloid Polym. Sci.*, vol. 291, no. 5, pp. 1121–1133, May 2013.
- [48] M. H. Nasirtabrizi and S. Mohebalizadeh, "Glycidyl methacrylate polymers

containing indole groups: Synthesis and characterization," *Iran. Polym. J. (English Ed.)*, vol. 20, no. 7, pp. 579–586, 2011.

- [49] M. Benaglia, A. Alberti, L. Giorgini, F. Magnoni, and S. Tozzi, "Poly(glycidyl methacrylate): A highly versatile polymeric building block for post-polymerization modifications," *Polym. Chem.*, vol. 4, no. 1, pp. 124–132, Jan. 2013.
- [50] P. F. Cañamero, J. L. De La Fuente, E. L. Madruga, and M. Fernández-García, "Atom transfer radical polymerization of glycidyl methacrylate: A functional monomer," *Macromol. Chem. Phys.*, vol. 205, no. 16, pp. 2221–2228, Nov. 2004.
- [51] M. Çelik and M. Önal, "Synthesis and characterization of Poly(glycidyl methacrylate)/Na-montmorillonite nanocomposites," *J. Appl. Polym. Sci.*, vol. 94, Nov. 2004.
- [52] G. Jin, M. P. Prabhakaran, D. Kai, S. K. Annamalai, K. D. Arunachalam, and S. Ramakrishna, "Tissue engineered plant extracts as nanofibrous wound dressing," *Biomaterials*, vol. 34, no. 3, pp. 724–734, Jan. 2013.
- [53] D. Kai, M. P. Prabhakaran, B. Stahl, M. Eblenkamp, E. Wintermantel, and S. Ramakrishna, "Mechanical properties and in vitro behavior of nanofiberhydrogel composites for tissue engineering applications," *Nanotechnology*, vol. 23, no. 9, Mar. 2012.
- [54] N. D. Boscher, F. Hilt, D. Duday, G. Frache, T. Fouquet, and P. Choquet, "Atmospheric pressure plasma initiated chemical vapor deposition using ultra-short square pulse dielectric barrier discharge," *Plasma Process. Polym.*, vol. 12, no. 1, pp. 66–74, Jan. 2015.
- [55] W. N. E. van Dijk-Wotthuis, O. Franssen, H. Talsma, M. J. van Steenbergen, J. J. Kettenes-van den Bosch, and W. E. Hennink, "Synthesis, Characterization, and Polymerization of Glycidyl Methacrylate Derivatized Dextran,"

Macromolecules, vol. 28, no. 18, pp. 6317–6322, Aug. 1995.

6

Comparison Between Different Polymer-Based Nanocomposites/Hydrogels with L_{XL21} as a Crosslinking Agent

Chapter 6 Comparison Between Different Polymer-based nanocomposites/Hydrogels with L_{XL21} as a Crosslinking Agent

6.1 XRD Analysis of L_{XL21}-Polymer Nanocomposites

Most of the XRD traces described in Chapters 3 - 5 were predominated by the polymer within the composites. Some L_{XL21}-polymer nanocomposites show clay dispersion as a decreasing baseline at angles between 2 and 5 °2θ providing evidence for clay exfoliation, were other L_{XL21}-polymer provides evidence for intercalation and microstructures. However, all the XRD traces provide evidence of L_{XL21} within the composite.

Figure 6.1 (a) shows the XRD traces of L_{XL21} and L_{XL21}-Acrylamide based nanocomposites, the L_{XL21}-pNIPAM was an intercalated nanocomposite while the L_{XL21}-pDMAc results suggest an exfoliated nanocomposite (if not then very well dispersed). These differences are polymer related, as the conditions and synthesis steps were similar for both Acrylamides. Figure 6.1 (b) shows the XRD traces for L_{XL21}-Methacrylate based nanocomposites and it shows a similar observation as mentioned earlier for the L_{XL21}-Acrylamide, where L_{XL21}-pHEMA nanocomposites show an exfoliated structure, and the L_{XL21}-pHPMA and L_{XL21}-pGMAc show evidence for microstructure nanocomposites. Table 6.1 summaries the XRD results for all L_{XL21} nanocomposites.

The L_{XL21}-based nanocomposites XRD results show that the polymer type can affect how clay is dispersed in the nanocomposite and it is not just a clay property-related phenomena. However, these results require further chemical and structural analysis in the future.

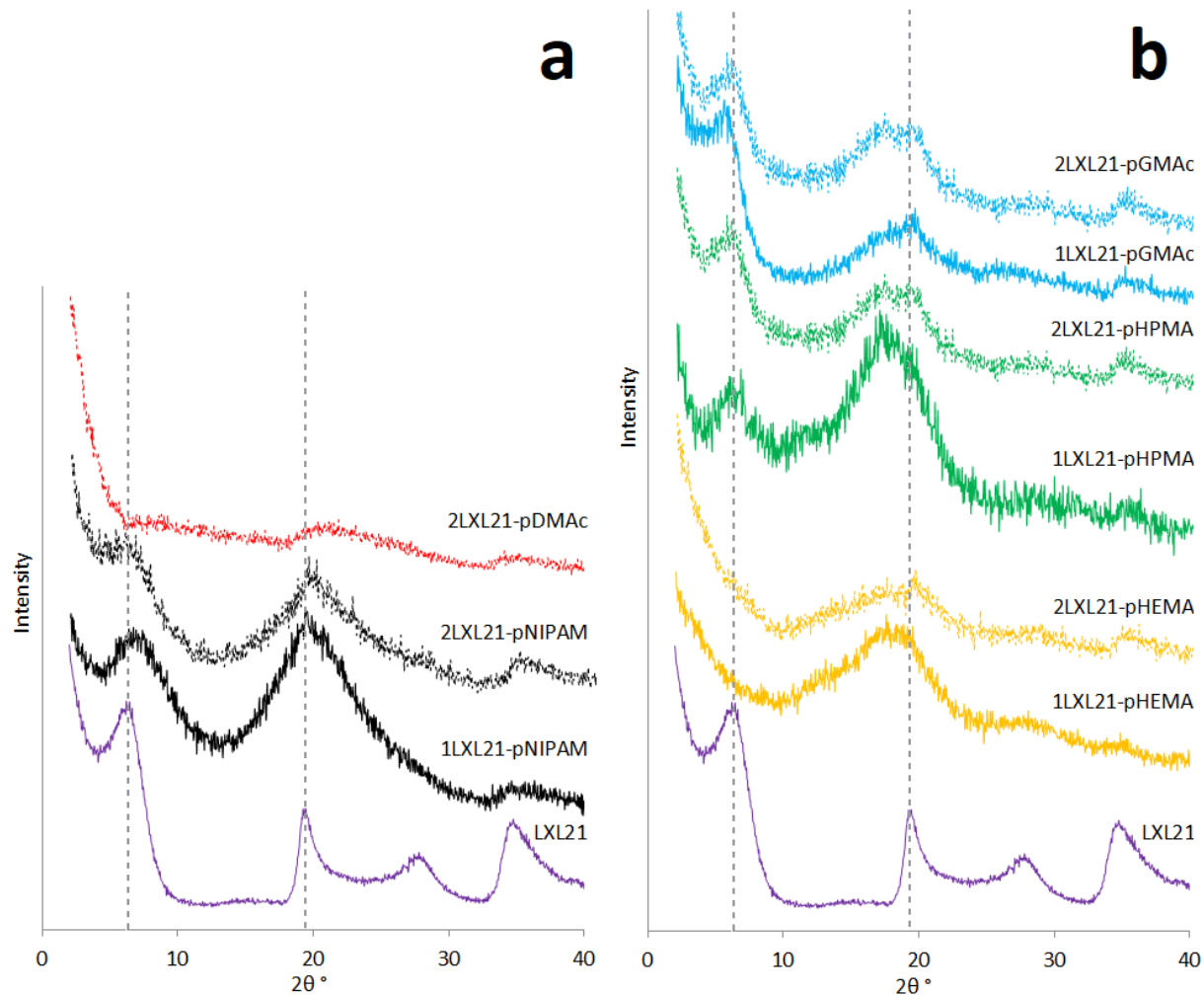


Figure 6.1 XRD traces of a)LXL21-acrylamides and b)LXL21-methacrylate nanocomposites at two clay-to-polymer ratios.

Table 6.1 2 θ and d-spacing for LXL21-polymer nanocomposites.

Sample	d_{001}		d_{100}		d_{110}	
	2 θ	d (Å)	2 θ	d (Å)	2 θ	d (Å)
L_{XL21}	6.2	14.2	19.4	4.6	34.7	2.6
pNIPAM	7.4	12.0	20.2	4.4	-	-
1L_{XL21}-pNIPAM	7.1	12.4	19.9	4.5	34.7	2.6
2L_{XL21}-pNIPAM	5.9	15.0	19.8	4.5	34.7	2.6
pDMAc	-	-	-	-	-	-
2L_{XL21}-pDMAc	8.6	10.3	20.8	4.3	34.5	2.6
pHEMA	-	-	17.9	5.0	-	-
1L_{XL21}-pHEMA	-	-	18.0	4.9	34.9	2.6
2L_{XL21}-pHEMA	-	-	19.3	4.6	34.9	2.6
pHPMA	7.6	11.6	17.7	5.0	-	-
1L_{XL21}-pHPMA	6.6	13.4	17.4	5.1	34.7	2.6
2L_{XL21}-pHPMA	6.6	13.4	19.5	4.6	34.7	2.6
pGMAc	-	-	18.1	4.89	-	-
1L_{XL21}-pGMAc	5.8	15.2	18.3	4.8	34.4	2.6
	-	-	19.1	4.6	-	-
2L_{XL21}-pGMAc	6.3	14.0	17.3	5.1	34.4	2.6
	-	-	19.1	4.6	-	-

6.2 SEM Imaging Analysis of L_{XL21}-Polymer Nanocomposites

Comparing the SEM images of clay-polymer composites that were crosslinked with the same clay (L_{XL21}) at same clay-to-polymer ratio showed its effect on the polymer composite morphology and pore size.

The pNIPAM-based composite pore sizes did not show any dependency on the clay-to-polymer ratio (Figure 6.2, Table 6.2). Pore size was on average 6.4 μm for the 1L_{XL21}-pNIPAM and 6.3 μm for the 2L_{XL21}-pNIPAM nanocomposites. However, the pDMAc-based composites showed a larger pore size average and a bigger variety. Both acrylamide-based polymer composites showed a clear layered effect at higher clay content which was related to the presence of clay in the structure (Figure 6.3, Figure 6.4 (top row)).

The methacrylate-based composites showed similar average pore sizes to each other relative to their clay loading, the clay-to-polymer ratio effect was also observed to increase the average pore size in methacrylate-based nanocomposites. The L_{XL21}-pGMAc nanocomposites showed a large variety of pore sizes as a result of its heterogeneous nature.

The 2_{LXL21}-(methacrylate-based) nanocomposites showed surfaces with similar pore size and distribution when compared to 1_{LXL21}-(methacrylate-based) ones. This suggests the higher clay content helped to form a clearer layered structure (2_{LXL21}-pGMAc) (Figure 6.3, Figure 6.4 (bottom row)).

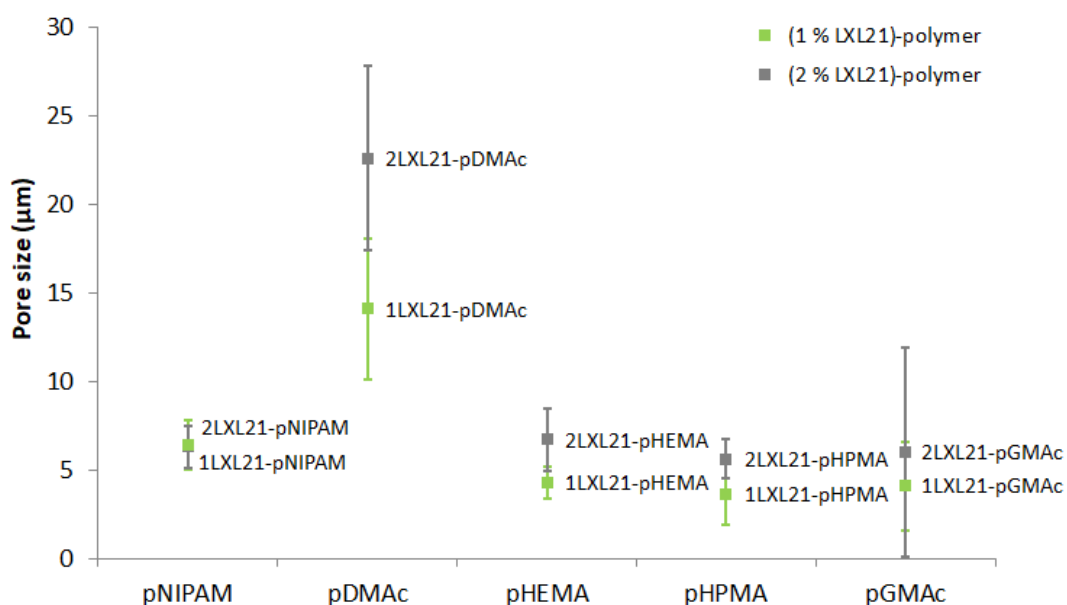


Figure 6.2 LXL21-polymer average pore size and standard deviation as measured from (n = 25) as measured from the SEM images.

Table 6.2 LXL21-polymer pore size as an average and standard deviation of (n=25) at two clay-to-polymer ratios from SEM images.

Sample	Pore size (μm)	SD
1 _{LXL21} -pNIPAM	6.4	1.4
2 _{LXL21} -pNIPAM	6.3	1.2
1 _{LXL21} -pDMAc	14.1	4.0
2 _{LXL21} -pDMAc	22.6	5.2
1 _{LXL21} -pHEMA	4.3	0.9
2 _{LXL21} -pHEMA	6.7	1.8
1 _{LXL21} -pHPMA	3.6	1.7
2 _{LXL21} -pHPMA	5.6	1.1
1 _{LXL21} -pGMAc	4.1	2.5
2 _{LXL21} -pGMAc	6.0	5.9

The SEM images and the pore size analysis showed that the average pore size and the morphology of the clay-polymer composites depended on the polymer used, however, the clay had an influence on the morphology as observed by the layered effect on the 2_{LXL21}-polymer composites.

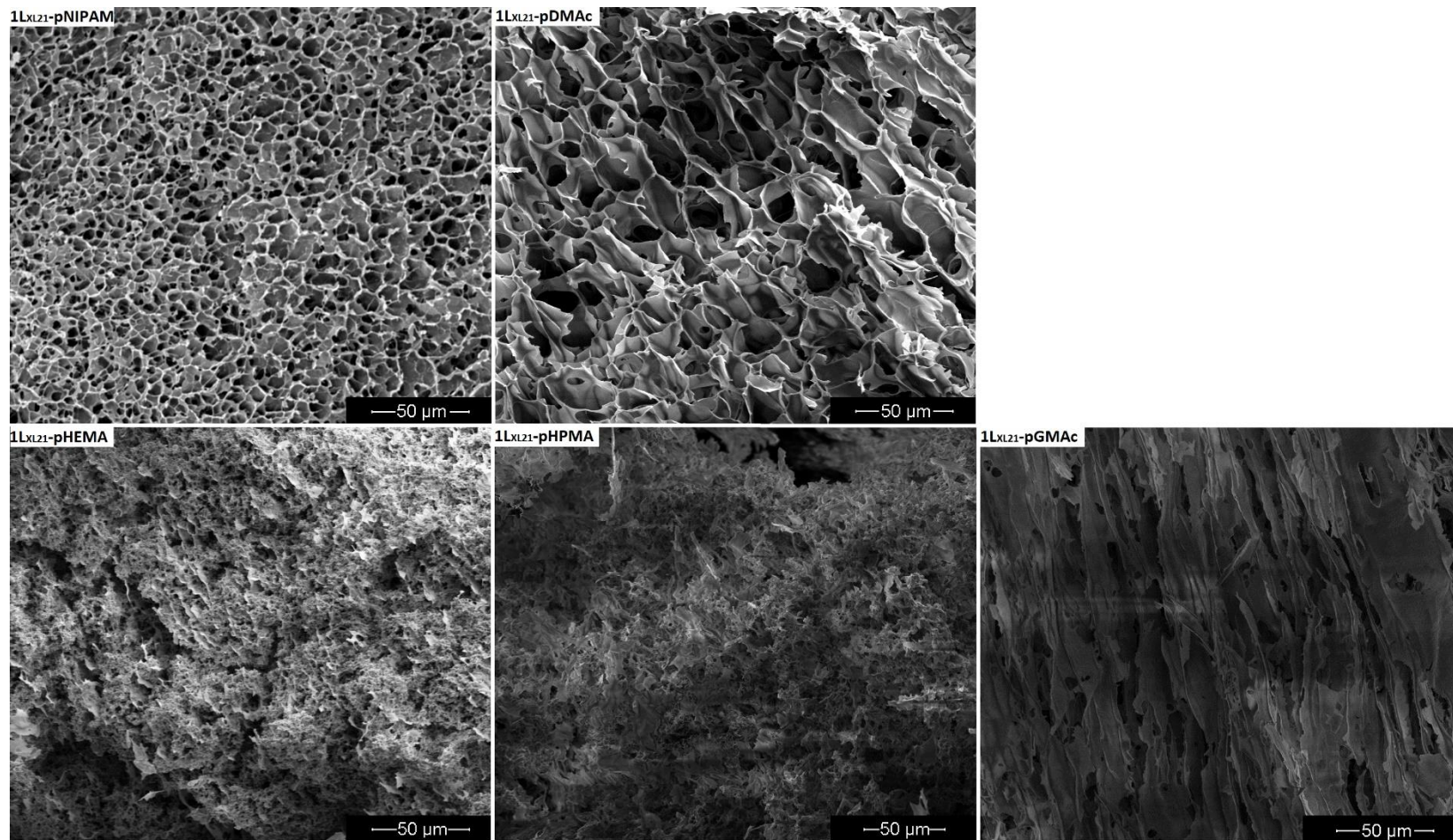


Figure 6.3 SEM images of 1LXL21-polymer nanocomposites on scale bar 50 μm showing microstructure and pore size differences as a result of the effect of the polymer type used. top) 1LXL21-(acrylamide-based), bottom) 1LXL21-(methacrylate-based).

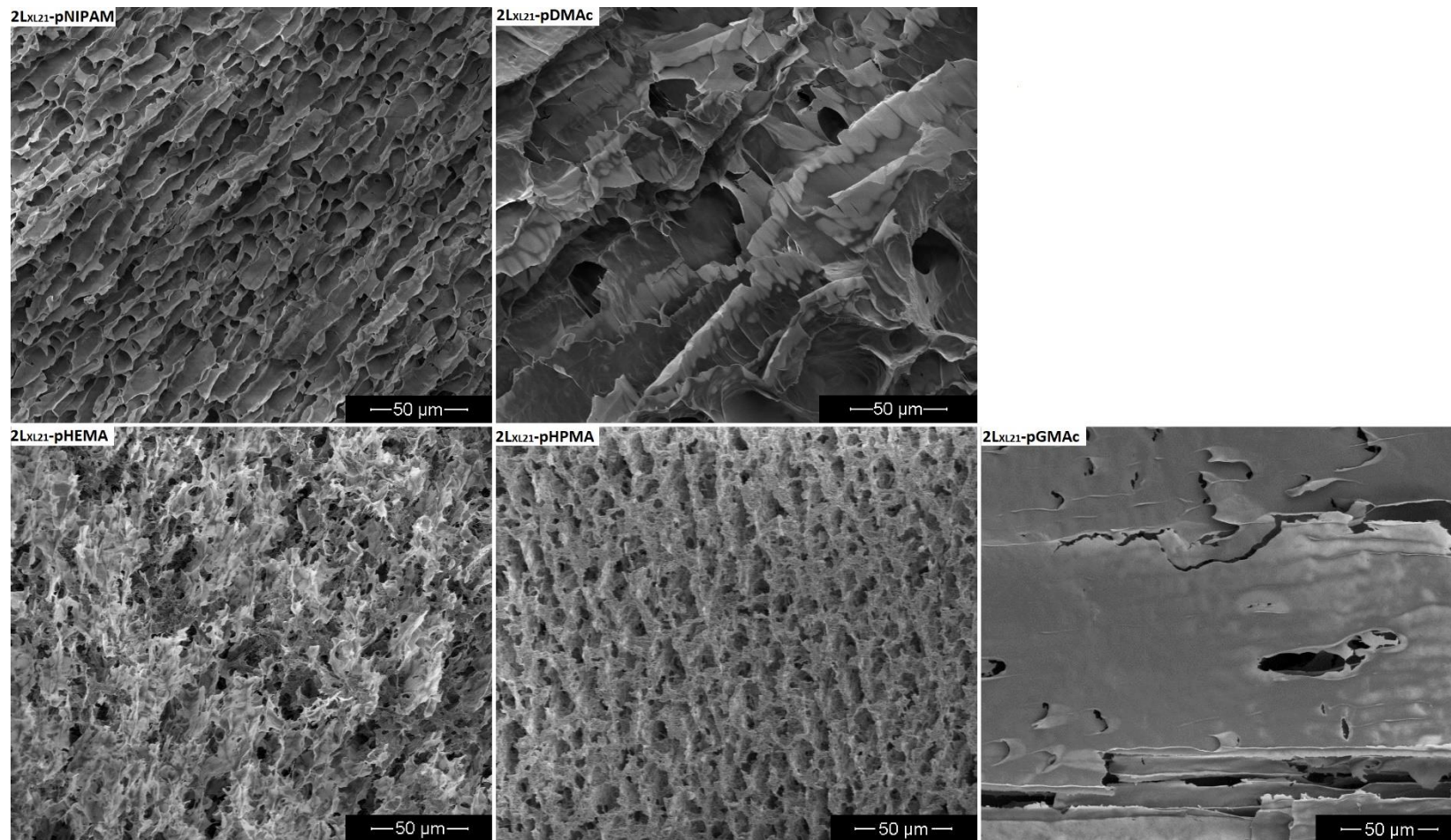


Figure 6.4 SEM images of 2LXL21-polymer nanocomposites on scale bar 50 μm showing microstructure and pore size differences as a result of the effect of the polymer type used. top) 2LXL21-(acrylamide-based), bottom) 2LXL21-(methacrylate-based)

6.3 Rheological Analysis and Properties of L_{XL21} -Polymer Hydrogels

6.3.1 Yield Stress of L_{XL21} -Polymer Hydrogels

Figure 6.5 shows the yield stress of the L_{XL21} -polymer hydrogels at two different clay-to-polymer ratios, this comparison showed the differences based on the type of polymer used in the hydrogel.

Acrylamide-based hydrogels showed dependency on the clay-to-polymer ratio; the $1L_{XL21}$ -(acrylamide-based) hydrogels yield stress values were significantly lower (0.0006 for the $1L_{XL21}$ -pNIPAM and 0.0041 for the $1L_{XL21}$ -pDMAc) when compared to the yield stress of the $2L_{XL21}$ -(acrylamide-based) hydrogels (0.0402 for the $2L_{XL21}$ -pNIPAM and 0.0232 for the $2L_{XL21}$ -pDMAc). These results showed that the pDMAc-based hydrogels were stiffer than the pNIPAM-based hydrogels (at 1% clay content), however, the clay content had a great effect on the rheological properties of the acrylamide-based hydrogels as with increasing the clay content there was a smaller difference in the yield stress values.

Methacrylate-based hydrogels showed similar behaviour of dependency on the polymer used and the clay-to-polymer ratio. The pHPMA-based hydrogels showed higher yield stress than the pHEMA-based hydrogels as illustrated in Figure 6.5 and Table 6.3. The pGMAc-based hydrogels showed similar behaviour with a different value range because of the heterogeneous nature of pGMAc-based hydrogels

The increased elasticity caused by the presence of more crosslinks between the clay platelets and the polymeric chains led to higher yield stress and higher resistance to flow.

The methacrylate-based hydrogels showed a higher yield stress range when compared to the acrylamide-based hydrogels, which was a result of the nature of the polymer used. This observation is related to the fact the pHEMA and pHPMA homopolymers are harder gels than the acrylamide-based homopolymers.

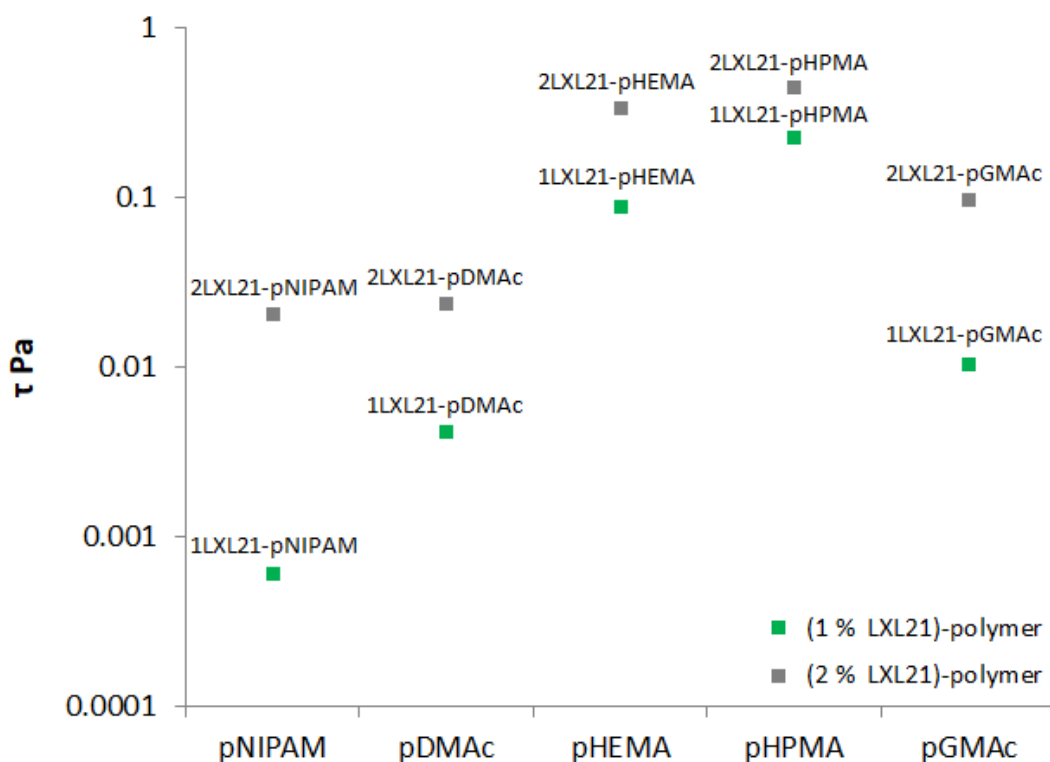


Figure 6.5 Yield stress of LXL21-polymer hydrogels at two clay-to-polymer ratios showing the effect of different polymers used to synthesis the hydrogels (from left) pNIPAM, pDMAc, PHEMA, pHPMA, and pGMAc.

Table 6.3 Average yield stress of (n = 3) for LXL21-polymer hydrogels at 40 °C at two different clay-to-polymer ratios.

Sample	τ_{yield}
1 % L_{XL21}	0.0044
1 L_{XL21} -pNIPAM	0.0006
2 L_{XL21} -pNIPAM	0.0204
1 L_{XL21} -pDMAc	0.0041
2 L_{XL21} -pDMAc	0.0232
1 L_{XL21} -pHEMA	0.0880
2 L_{XL21} -pHEMA	0.3313
1 L_{XL21} -pHPMA	0.2217
2 L_{XL21} -pHPMA	0.4417
1 L_{XL21} -pGMAc	0.0103
2 L_{XL21} -pGMAc	0.0966

6.3.2 LVE Region of LXL21-Polymer Hydrogels

As the methacrylate-based hydrogels were harder as gels and had a higher resistance to flow, their elasticities are expected to be on a lower range than the acrylamide-based hydrogels as was the case for the pHEMA and pHPMA based

hydrogels. Figure 6.6 shows the differences in the LVE limits for the different L_{XL21} -polymer hydrogels at two different clay-to-polymer ratios.

The effect of clay-to-polymer ratio was not the same when comparing the acrylamide-based hydrogels to each other, this may be a result of the highly elastic nature of the pDMAc; as the $1L_{XL21}$ -pDMAc contains more pDMAc than the $2L_{XL21}$ -pDMAc it showed a larger LVE limit (10 % strain), with more clay in the hydrogels as the case with the $2L_{XL21}$ -pDMAc more crosslinking points are created limiting the movement of the elastic pDMAc chains (pHEMA and pHPMA)-based hydrogels showed a similar trend; where the elasticity of the hydrogels increased with increasing clay content.

Table 6.4 shows the average LVE limits for all L_{XL21} -polymer hydrogels.

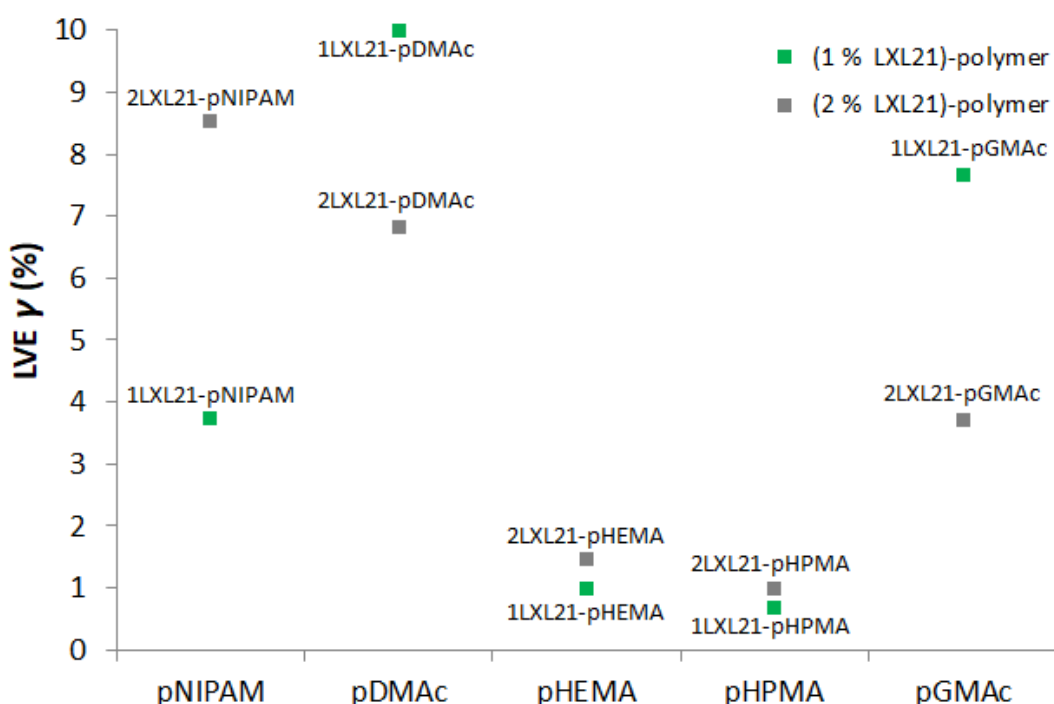


Figure 6.6 LVE limits of L_{XL21} -polymer hydrogels at two clay-to-polymer ratios showing the effect of different polymers used to synthesis the hydrogels (from left) pNIPAM, pDMAc, PHEMA, pHPMA, and pGMAc.

Table 6.4 Average LVE limits of ($n = 3$) for LXL21-polymer hydrogels at 40 °C at two different clay-to-polymer ratios.

Sample	LVE limit γ (%)
1L _{LXL21} -pNIPAM	3.75
2L _{LXL21} -pNIPAM	8.52
1L _{LXL21} -pDMAc	10.00
2L _{LXL21} -pDMAc	6.81
1L _{LXL21} -pHEMA	1.00
2L _{LXL21} -pHEMA	1.47
1L _{LXL21} -pHPMA	0.68
2L _{LXL21} -pHPMA	1.00
1L _{LXL21} -pGMAc	7.67
2L _{LXL21} -pGMAc	3.72

6.4 Summary

The properties of the composite are related to the polymer used to synthesize them and it has a greater influence on the final composite property than the nature of the clay used as a crosslinking agent. The acrylamide-based composites/hydrogels create soft, free-flowing or easily handled, hydrophilic, highly elastic gels as opposed to the methacrylate-based polymers which create hard, hydrophobic gels with low elasticity. However, the clay-to-polymer ratio effect still can be observed within the rheological analysis.

The XRD shows that the polymer can affect the way the clay disperses in the nanocomposite. Even in the same group of polymer, the L_{LXL21} behaved differently as it was intercalated with the pNIPAM-based nanocomposite and it was well-dispersed with the pDMAc-based nanocomposites. The case was the same as the methacrylate-based nanocomposite.

The rheological differences between the L_{LXL21}-based hydrogels are easily observed looking at the yield stress and the LVE region values, these differences also can be mainly related to the polymer within the hydrogel, however, the nature of clay dispersion have an effect that requires more analysis to be specified.

7

Conclusions and Further work

Chapter 7 Conclusions and Further Work

The principal aim of this thesis was to explore the effect of different clay types (Laponite® and Cloisite®) and concentrations as crosslinking agents on different polymers in clay-polymer nanocomposites. This work was performed to better understand how the properties of clays change the final characteristics and mechanical properties of the synthesised clay-polymer nanocomposite. Such clay-polymer composites are attractive materials in different industries such as the medical and biological fields as they show excellent potential as drug delivery systems and cell scaffolds. The difficulty of crosslinked composites lies in the processing of these materials, making them unsuited to certain clinical applications, the result of this work has shown how clay's different properties affect the mechanical stability of the nanocomposites when used as crosslinkers for different polymers.

Chapter 3 detailed the chemical properties of the different clays investigated using different elemental, and characterisation (e.g. spectroscopic) methods, which helped to better understand their differences. For example, fluorine-containing clays showed different thermal behaviour when compared to other clays when studied using the TGA as they showed two stages of weight loss instead of three stages as with the other clay grades. The XRD data showed information about the structure and dispersion of the clay within the polymer, however, the smaller platelets sized clays did make the description more difficult since they showed only weak reflections at small angles ($< 7^{\circ}2\theta$). Later, in Chapter 3, the viscosities and yield stresses from rheological tests of clays dispersed at five different wt.% and rheological tests were determined and related to the clay's platelet sizes and CEC values of each clay (see below). The comparison between different clay suspensions was the first step on how clay properties can affect the clay-polymer composite properties and how to compare them, it also helps to relate or eliminate any complications of clay suspensions like high clay contents which make testing or mixing hard. Understanding clay suspensions wt.% also helps to find an entrance to

what the effective concentration is which might help to design the properties of clay-polymer hydrogels, for example, keeping the hydrogel easy to inject.

The XRD analysis showed that clays were broadly similar in nature. All clays have d_{001} and d_{100} in the ranges 2θ (5 - 7 °) and (19.2 – 19.6 °), respectively. The smaller platelet size clays, L_{EL} and L_{RD} had a weak reflection at d_{001} and a smaller d_{001} spacing (4.86 Å and 5.86 Å, respectively) whereas clays with large platelet size like L_{FN} , L_{OG} and C_{Na+} had a sharp and clear reflection for the d_{001} and spacings of 6.54, 7.02, and 6.94 Å, respectively. The XRF analysis nature of not being able to detect some elements made it hard to confirm all the elemental differences. The XRF data showed some elemental differences between the clays when comparing the same concentrations as provided by the manufacturer. Clays with smaller platelet size like L_{EL} and L_{RD} showed total weight losses of 15.9 % for L_{EL} and 14.8 % for L_{RD} on the TGA plots, whereas clays with large platelet size like L_{FN} and C_{Na+} had less weight loss of 13.1 % and 12.1 %, respectively. L_{OG} and C_{Na+} had a higher dehydroxylation onset temperature than all other clays, and for understanding the reasons for this behaviour more investigation is needed.

The rheological tests for different clay dispersions showed the effects of different clays on their rheological and mechanical properties. Low clay concentration dispersions (< 5 wt.%) showed higher viscosities and yield stresses for the larger platelet clays, whereas with higher clay concentrations (> 5 wt.%), the larger platelet clays showed lower viscosity and yield stresses (Figure 3.11 and Figure 3.12). A shear thinning behaviour was observed as a result of clay platelets, as the force affecting the hydrogel increases the clay platelets gets in line with the flow direction, this leads to improvement as the platelets help to direct the flow making it easier to flow in the right direction and to avoid turbulence. The clay platelet size also plays a role in the rheological behaviour of the clay dispersions; larger clay-platelets size dispersions (L_{FN} , L_{OG} , and C_{Na+}) show a lower viscosity values when compared to other smaller clay-platelets size dispersions (L_{EL} , L_{RD} , and L_{XL21}) as shown in Figure 3.12.

The structural, thermal, morphological, and chemical properties of clay-(acrylamide-based) nanocomposites were studied using SEM imaging, TGA, XRD and FTIR spectroscopy in Chapter 4. The data represent the effect clays cause as crosslinkers in pNIPAM and pDMAc. This chapter also highlighted the rheological properties of pNIPAM-based hydrogels as they pass through their LCST, it also showed a comparison between the properties of these hydrogels at temperatures above and below LCST. Moreover, the effect of different clay properties and clay-to-polymer ratios on the properties of these nanocomposite hydrogels were studied.

The effect of clays on the composites were observed in the SEM images. Most composites showed a clear interconnected porous network as demonstrated in Figure 4.13. The L_{OG} -pNIPAM had a different morphology from all other composites that is related to the nature of pNIPAM with a clear porous interconnected structure as shown in Figure 4.12. Table 4.4 shows the average pore size and standard deviation for all clay-pNIPAM nanocomposites and Figure 4.16 helps to understand the effect of the clay type and its properties on the pore size on the nanocomposite. The clay CEC showed a clear effect on the pore size, with higher CEC values resulting in smaller pore sized nanocomposites, this is believed to be related to the ability of clay platelets to create more crosslinking points in the matrix (i.e. via the exchangeable cations). The main infrared spectroscopic differences observed for pNIPAM-based composites were those in intensity and band position associated with water and Si-O when compared to the neat clay and the pNIPAM homopolymer (Table 4.5). These can be associated directly to the redistribution of water molecules within the presence of clay, and to the separation of the clay layers by the polymer.

The rheological analysis showed that below the LCST of pNIPAM the G' values of the pNIPAM composites are closer to each other as a result of the bigger effect of the pNIPAM chains at such temperature, however the effect of the clay platelet size can still be observed as larger clay-platelet hydrogels showed higher G' values with L_{FN} -pNIPAM and C_{Na^+} -pNIPAM showing values up to 20 times higher than $1L_{EL}$ -pNIPAM

and L_{RD} -pNIPAM even at 20 °C. Figure 4.29 shows the effect of clay-to-polymer ratio on the elasticity of the clay-pNIPAM hydrogels, with more clay content (and less polymer) $2L_{EL}$ -pNIPAM, $2L_{RD}$ -pNIPAM, and $2L_{XL21}$ -PNIPAM showed higher G' values than their corresponding (1 % clay)-pNIPAM at 40 °C. The case was the same at 20 °C except for the L_{XL21} -pNIPAM hydrogels which may be a result of the L_{XL21} larger platelet size. Clay-pNIPAM nanocomposites with higher G' values based on clay type or clay-to-polymer ratio are expected to show higher yield stress values. Table 4.7 clearly shows this effect with the pNIPAM based hydrogels when comparing the τ_{yield} for the (2 % clay)-pNIPAM and (1 % clay)-pNIPAM hydrogels (0.0003 Pa for $1L_{EL}$ -pNIPAM to 0.0034 Pa for $2L_{EL}$ -pNIPAM, 0.0005 Pa for $1L_{RD}$ -pNIPAM to 0.0168 Pa for $2L_{RD}$ -pNIPAM, and 0.0006 Pa for $1L_{XL21}$ -pNIPAM to 0.0204 Pa for $2L_{XL21}$ -pNIPAM at 40 °C). The effect of clay-to-polymer ratios and clay properties on the LVE limits of the clay-pNIPAM hydrogels are shown in Figure 4.32 and Table 4.8, L_{XL21} -pNIPAM showed larger LVE as a result of the L_{XL21} larger platelet size and higher CEC when compared to the L_{EL} and L_{RD} . The amplitude sweeps also showed the different behaviour of these hydrogels based on temperature and the effect of changing the polymer chains conformation from coil-to-globule.

These results can be compared to those of Haraguchi *et al.* who developed clay-pNIPAM nanocomposites composed of a water-swelling inorganic clay [1] using a preparation technique similar to that used herein. [2][3][4] The novelty in this work is the incorporation of six different clay grades to compare the effect of clay properties on the final composite/hydrogel which was not found in literature as most of the researchers investigated only L_{RD} and L_{XLG} .

Chapter 4 also presents characterisation of the clay-pDMAc nanocomposites and highlights the effect of different clays and clay-to-polymer ratios on their properties as well as the differences between the pNIPAM-based and pDMAc-based nanocomposites. The pDMAc homopolymer and some clay-pDMAc nanocomposites were not easy to analyse as a result of their elastic nature even after drying. The pDMAc-based composites have similar XRD and FTIR results, their FTIR spectra showed shifts in their Si-O stretching bands to higher wavenumbers in a trend that

was similar to the pNIPAM-based nanocomposites. The L_{XL21}-pDMAc nanocomposite was the exception which showed three different Si-O bands (rather than two), this behaviour was only observed with this composite and highlights a different interaction mechanism related to L_{XL21} and pDMAc only. The SEM images (Figure 4.40 and Figure 4.41) and pore size analysis results (Table 4.14) showed morphological differences; an interconnected network structure was seen for all composites and a clear layered structure was observed for the (2 % clay)-pDMAc composite and especially for those containing L_{FN} and L_{XL21}. Figure 4.48 (b) shows the pore size is smaller with higher CEC, and that they can be divided into two distinct groups based on their CEC value.

Rheological analysis was performed for all clays at both clay-to-polymer ratios for pDMAc-based composites. The higher clay content in the hydrogel resulted in a higher τ_{yield} values (Figure 4.54 and Table 4.16), which is a result of more clay in the clay-polymer hydrogel dispersions creating more crosslinking points between the clay platelets and polymer chains, and thus restricting the movement of polymer chains. Generally, the (1 % clay)-pDMAc hydrogels showed a lower τ_{yield} with larger platelet size, and the (1 % clay)-pDMAc hydrogels also showed a trend of lower τ_{yield} for clay with higher CEC. The LVE limits are influenced by clay-to-polymer ratio and the clay platelet size, effects can be observed with higher LVE limit for the (1 % clay)-pDMAc hydrogels where pDMAc flexible chains are less restricted by a fewer number of crosslinkers than for the (2 % clay)-pDMAc hydrogels. A clear decrease in the LVE limit with larger platelet size for the clay-pDMAc nanocomposites at both clay-to-polymer ratios was also noted as shown in Figure 4.56 and Table 4.17.

In previous research by Barker [5] DMAc was used as a copolymer in pNIPAM/DMAc hydrogels as a means to raise the LCST (relative to that of pNIPAM). LCST was found to depend on the amount of the hydrophilic comonomer (DMAc) present in the system; it resulted in expanded and flexible globules above the LCST of each particular system. [5][6] This study used pDMAc as a single polymer and investigated the effect of different clays on the pDMAc-based composite/hydrogel.

Studying the rheological properties of such hydrogels was also introduced in this study as a new way of understanding the behaviour of such materials.

Characterisation of various methacrylate-based nanocomposite formulations is presented in Chapter 5. The same techniques mentioned earlier were used to assess the differences caused by the clay on the clay-polymer nanocomposites and hydrogels. Rheology tests revealed that the viscoelasticity of the hydrogels changes by varying the quantity of the crosslinking agent beside the effect of the crosslinking agent (clay) properties on it.

The incorporation of clay into pGMAc (Section 5.3) affects the properties of the pGMAc, since pGMAc homopolymer tends not to form a 3D network, with the incorporation of clay dispersed platelets a 3D structure of the composite is formed by crosslinking the pGMAc chains. Homogenous samples were not present as portions were observed to precipitate. The XRD analysis and FTIR spectroscopy (Figure 5.30 and Figure 38) showed that the precipitations that were formed mainly consisted of pGMAc homopolymer with no clay presence. The clay-pGMAc nanocomposites were porous interconnected structures as shown by the SEM images, a comparison between the effect of different clay types and the clay-to-polymer ratio showed no trend to follow and the morphology of the 1L_{FN}-pGMAc, 1L_{XL21}-pGMAc, and 2L_{XL21}-pGMAc was different from the other composite with clear layered morphology (Figure 5.35 and Figure 5.36). The τ_{yield} and the LVE limits for the clay-pGMAc nanocomposites showed no clear relation between the yield values and the clay properties (Figure 5.41), , this may be a result of the heterogeneous nature of the clay-pGMAc nanocomposites which require further investigations.

Attempts to assess the rheology of pHEMA-based and pHPMA-based hydrogels at different clay-to-polymer ratios were unsuccessful. The low elasticity and hydrophobic nature (water leaves the materials with the smallest load applied) made it difficult to use the rheology setup available and keep the tests comparable. The TGA analysis showed that the onset degradation temperature improved for the clay-pHEMA and clay-pHPMA nanocomposites when compared to the

homopolymers (Figure 5.7 and Figure 5.20), the pHEMA-based nanocomposites showed an increase of 24 °C (Table 5.2) on average and the pHPMA showed an increase of 14 °C (Table 5.11) on average. However, the clay-to-polymer ratios did not show an effect on the onset degradation temperature or on the total polymer weight loss. The weight loss rate between 300 – 400 °C was slower with the presence of clay. No trends were observed that can relate to the clay platelet size or CEC.

pHEMA and pHPMA based composites exhibit interesting yield stress values and low viscoelastic regions related to its hydrophobicity. Most of the water involved in the synthesis process is squeezed out of the hydrogels as soon as they are placed between the rheometer parallel plates, these hydrogels were mainly not capable of being tested except for the 1L_{XL21}-pHEMA and 1L_{XL21}-pHPMA hydrogels. Figure 5.16 and Figure 5.17 show the effect of the L_{XL21}-to-pHEMA ratio on the τ_{yield} and LVE limits; the higher the L_{XL21} content the higher the τ_{yield} and LVE limits, as is the case for the L_{XL21}-pHPMA hydrogels as shown in Figure 5.27 and Figure 5.28. These results show an opposite trend to the effect of a clay-to-pDMAc ratio where the more clay the lower the LVE limits. This is a result of the polymers different nature, with pHEMA and pHPMA based hydrogels, the crosslinking points add flexibility and increases the elasticity of the material were with pDMAc-based hydrogels the crosslinking points restrict the movement and flexibility of the polymeric chains.

Dimitris S. Achilias *et al.* examined the polymerisation of pHEMA with several relative amounts of nano-clay in order to investigate the effect of the crosslinker density on the polymerisation of HEMA. [7]. pHPMA was used generally as a copolymer to control different properties of pNIPAM/HPMA and pDMAc/HPMA such as temperature sensitivity and hydrogel optical transparency. [8][9] This study introduced HEMA and HPMA individually as single polymers to study the effect of different clays on the clay-pHEMA and clay-pHPMA composites/hydrogels.

The effect of the clay type and content was the main concern in this study, the polymers used were classified into two categories based on their chemical structure

(acrylamide and methacrylate). A comparison between all the different polymers used was shown in Chapter 6. All nanocomposites were crosslinked using L_{XL21}, all L_{XL21}-polymer nanocomposites were easier to handle than other clay-polymer nanocomposites especially compared with pHEMA and pHPMA.

The polymers used in this thesis are mostly biocompatible. The porous 3D nature of the clay-polymer hydrogels synthesised offers the potential for different medical applications and cell viability studies. These initial tests and comparisons provided more details about the ability to engineer the mechanical properties of the clay-polymer hydrogels, which offer a lot of potential for different medical applications like cartilage applications, injectable treatment of synthetic joints, bone fracture treatment (microcrack filling), skin and wound management, and drug delivery vehicles.

7.1 Further Work

- Clay suspensions have been observed to remain in a gel phase for periods of times exceeding months at room temperature. A clearer understanding of the properties of these suspensions for extended periods of times would be achieved by the examination of the physical properties after extended timeframes.
- More detailed studies about the effect of clay loading on the rheological properties of clay suspensions over a wider range of clay loading. More defined elemental analysis would also be beneficial to better understand the differences in clay behaviour and the relationship between the clay elemental content and its CEC.
- Clay suspension viscosity and yield stress are affected by the salt content of the clay. Conductivity measurement can provide a better view about the extent of salt present and factors that affect the clay suspension properties and as a result the clay-polymer hydrogel properties.

- The pGMAc-based nanocomposites/hydrogels show a heterogeneous nature. This behaviour requires more investigation and analysis to understand the cause and how to overcome such phenomena.
- Swelling-deswelling experiments to measure the effect of water content on the nanocomposites. This would help to understand whether the materials are losing free or bonded water.
- Rheological data to be generated for all clay-polymer ranges to cover more detailed experiments including:
 1. Time dependency creep recovery test and thixotropy loop test to know if all hydrogels are self-healing or not and whether the polymer chains or the crosslinks that get damaged on certain loading and how long it takes to rebuild its structure if needed
 2. Yield stress and viscosity measurement for hydrogels that contain different water ratios and clay-to polymer ratios.
 3. Detailed test about the behaviour of the storage and loss moduli and the factors that affect the transition point.
- Low angle XRD and Transmission electron microscopy (TEM) can be performed for a better image about the clay dispersion in the clay-polymer nanocomposites.
- A selection of comonomers can be incorporated into the clay-pNIPAM system, and an examined of these systems for swelling-deswelling capacities, rheological and mechanical properties. The addition of a comonomer to a pNIPAM-based system can control its LCST; adding a hydrophilic comonomer raises the pNIPAM LCST while adding a hydrophobic comonomer reduces the pNIPAM LCST.

7.2 References

- [1] K. Haraguchi and T. Takehisa, "Nanocomposite Hydrogels: A Unique Organic–Inorganic Network Structure with Extraordinary Mechanical, Optical, and Swelling/Deswelling Properties," *Adv. Mater. - ADVAN MATER*, vol. 14, Aug. 2002.
- [2] K. Haraguchi, R. Farnworth, A. Ohbayashi, and T. Takehisa, "Compositional effects on mechanical properties of nanocomposite hydrogels composed of poly(N,N-dimethylacrylamide) and clay," *Macromolecules*, vol. 36, no. 15, pp. 5732–5741, 2003.
- [3] K. Haraguchi and H. J. Li, "Mechanical properties and structure of polymer-clay nanocomposite gels with high clay content," *Macromolecules*, vol. 39, no. 5, pp. 1898–1905, Mar. 2006.
- [4] H. Kang *et al.*, "Polymerization Kinetics of Poly(2-Hydroxyethyl Methacrylate) Hydrogels and Nanocomposite Materials," *Macromolecules*, vol. 5, no. 1, pp. 449–456, Jan. 2013.
- [5] I. C. Barker, J. M. G. Cowie, T. N. Huckerby, D. A. Shaw, I. Soutar, and L. Swanson, "Studies of the 'Smart' thermoresponsive behavior of copolymers of N-isopropylacrylamide and N,N-dimethylacrylamide in dilute aqueous solution," *Macromolecules*, vol. 36, no. 20, pp. 7765–7770, Oct. 2003.
- [6] R. H. Dosh, A. Essa, N. Jordan-Mahy, C. Sammon, and C. L. Le Maitre, "Use of hydrogel scaffolds to develop an in vitro 3D culture model of human intestinal epithelium," *Acta Biomater.*, vol. 62, pp. 128–143, 2017.
- [7] D. S. Achilias and P. I. Sifaka, "Polymerization kinetics of poly(2-hydroxyethyl methacrylate) hydrogels and nanocomposite materials," *Processes*, vol. 5, no. 2, Jun. 2017.
- [8] K. Demirelli, M. F. Coşkun, E. Kaya, and M. Coşkun, "Investigation of the thermal decomposition of poly(2-hydroxypropyl methacrylate)," *Polym.*

Degrad. Stab., vol. 78, no. 2, pp. 333–339, 2002.

- [9] S. M. Choi, D. Singh, Y. W. Cho, T. H. Oh, and S. S. Han, “Three-dimensional porous HPMA-co-DMAEM hydrogels for biomedical application,” *Colloid Polym. Sci.*, vol. 291, no. 5, pp. 1121–1133, May 2013.